UNIVERSITÀ POLITECNICA DELLE MARCHE
Department of Civil, Environmental and Building Engineering and Architecture

Doctoral Course in Civil, Environmental and Building Engineering and Architecture

XXXIII Cycle

Curriculum in Civil, Environmental and Building Engineering and Architecture

An improved procedure for the seismic fragility analysis of existing bridges and implementation within a comprehensive probabilistic framework for the risk assessment

PhD Candidate:
Lucia Minnucci

Supervisor:
Prof. Fabrizio Gara

Contents

Abstract

The safety of infrastructural systems is of paramount importance since high socio-economic impacts on the society would be expected in case of disruptions or, even worse, people life could be seriously endangered in case of severe damages or collapses.

Unfortunately, several cases of bridge failures have been registered in the last decades all over the world, mainly induced by natural hazards and often exacerbated by human errors and lack of maintenance. The relevance of the issue at hand pushed the scientific community to develop always more accurate probabilistic tools for the risk assessment, with particular attention to the seismic problem. The major vulnerabilities of the system must be preliminary characterised to proceed with a proper risk analysis, aimed at forecasting post-scenario consequences and limit the impact on the society in case of earthquakes (or other natural hazardous events).

The analysis of the vulnerability of bridges is classically carried out through the adoption of fragility curves, which express the probability of exceedance of a certain performance level conditioned to a certain level of hazard intensity. However, it is common practice to use fragility curves as synthetic tools providing a global overview of the bridge vulnerability, with scarce attention to the damage extension or the evolution of different failure mechanisms that may potentially verify within the structure. Indeed, it is worth noting that bridges may show different damage mechanisms, occurring in one or multiple structural components, that differently contribute to the overall fragility of the system and potentially lead to different post-disaster scenarios.

In light of this drawback and considering also that, more in general, an optimal, comprehensive and robust probabilistic framework is not available yet, the present Thesis aims to provide some insights and original contributions for a state-of-the-art enrichment in the field of the safety of infrastructural systems. Advancements are indeed made on the following main subjects: fragility curves, with an innovative approach for a proper estimation of the bridge vulnerability, based on both a quantitative and qualitative assessment of failure mechanisms that may occur during a seismic event; analysis of Soil-Structure Interaction (SSI) effects through simple formulas estimating the behaviour of pile foundations (a common choice in case of bridge structures) and easy to be implemented for a reliable fragility and risk analysis; proposal of a holistic framework for the risk assessment and the quantification of consequences of a hazardous event in monetary terms, taking into account aspects such as SSI, degradation, maintenance and retrofit; analysis of the effects of uncertainties affecting the combined pile-soil system for the probabilistic characterization of impedance functions and kinematic response factors of deep foundations in homogeneous soils.

Concerning the first point, the fragility analysis proposed in this Thesis is based on an innovative methodology that aims to investigate the structural behaviour at a deeper and useful level of detail for the successive quantification of consequences related to the

bridges' performance. The methodology focuses on the analysis of the most probable failure mechanisms occurring in a bridge structure in presence of an earthquake with a special attention to the characterization of their concomitance and their extension in dependence of the seismic intensity.

In order to consider the effects of the compliance at the foundation level, which is recognized to be fundamental for an accurate description of the bridge response, the SSI analysis is carried out exploiting simple formulas estimating a Lumped Parameter Model (LPM) available in the literature for the modelling of the behaviour of deep foundations in homogeneous soils. The formulas are used to efficiently reproduce the adopted LPM in case of end-bearing pile foundations in different geometric and mechanical configurations and are suitable for an easy implementation in finite element software for analyses in the time domain.

A probabilistic conditional approach is used throughout the Thesis, with a stochastic ground motion model for the hazard characterization and earthquakes generation.

The Italian transport system is chosen as scenario for the applications of the present Thesis, since it is particularly emblematic due to the high vulnerability and the important critical issues presented by the existing road network. Many bridges constituting the network, indeed, date back to the beginning of the last century and their standards are often far away from those required by the current design codes. In addition, traffic limitations are increasingly required, as well as provisional safety measures against the growth of service loads, which is a relevant problem for the existing infrastructural network as recently reminded by a consistent number of bridge collapses. Moreover, a significant group of bridges and viaducts suffered from the seismic events recently occurred in 2016, which particularly hit the Central Italy.

Two different bridge typologies are considered, namely: Reinforced Concrete Link Slab bridges and Steel- Concrete Composite bridges. Being very widespread, such typologies result representative of most of the bridges and viaducts present over the Italian territory, and examples can also be found in the international panorama. Moreover, the choice of significative case studies follows multiple purposes. The first is to show the potentialities of the proposed fragility estimation methodology and the relevance of the SSI problem in the bridge vulnerability assessment. The second is to characterise the vulnerability of the Italian infrastructures with a higher level of detail, including degradation and SSI phenomena. The third is related to the choice of structural configurations suitable for the characterization of a regional scenario, such as the one of Marche region. Indeed, the regional scenario appears to be a strategic compromise for an accurate description of the bridges' behaviour without the need for too high computational efforts deriving from the modelling of each single structure.

In this Thesis a comprehensive framework is also proposed to include aspects like retrofit, maintenance, degradation, structural health monitoring, SSI and vertical load assessment, in addition to the evaluation of seismic risk, and to consider the associated uncertainties

that determine the probabilistic nature of the problem. A strategy for the proper analysis of consequences at network level associated to the results deriving from the fragility assessment is proposed, concerning direct and indirect costs, to integrate the already available methodologies in the literature with an approach characterized by a higher level of detail. The framework is applied to one of the main routes in the Marche region, after a detailed investigation work on the required regional data. The versatility of both the proposed fragility methodology and the framework is suitable for further applications involving bridge typologies and road network scenarios other than the one examined, as well as other natural hazards may be considered without modifying the proposed tools.

To conclude, possible improvements of the framework are illustrated and commented, especially with reference to the SSI problem. In particular, a focus on the behaviour of deep foundations in homogeneous soils is made, with the aim of characterizing the response of the combined soil-piles system, in several geometrical and mechanical configurations, under the effects of uncertainties deriving from both the soil and the pile most representative parameters. A probabilistic approach is used to evaluate the SSI phenomena in terms of impedance functions and kinematic response factors. Results reveal useful for the probabilistic characterization of the SSI effects at both kinematic and inertial analysis level. The approach should be included into the proposed holistic framework for a fully probabilistic assessment of the bridge vulnerability.

List of Figures

List of Tables

1. Introduction

Bridges and viaducts have a key role in transportation systems, since they represent an economic and social connection among cities and countries. The key role of bridges in the community life dates back to ancient civilizations, when bridges and viaducts represented not only a mean of transport for people and goods, but also a sign of conquest of the territory. From ancient to modern times, the development of big cities was always accompanied by the realization of bridges: it is enough to consider the extraordinary number of civil engineering works related to the building of bridges in the centuries of expansion of the Roman Empire.

From a structural point of view, the XIX century represented a flourishing period for the discovery and the application of new structural systems and architectures for bridges. From the traditional masonry and wood structures, new materials started to be employed, first and foremost reinforced concrete and steel. Thanks to the higher performances associated to the use of innovative building materials, also new structural solutions were adopted, such as long span bridges or suspension bridges. The introduction of alternative structural schemes gained interest also in the field of architecture, with an increasing attention in the harmonization of materials and geometries in urban and environmental contexts. Nevertheless, the adoption of various and increasingly elaborated structural solutions necessarily introduced new and different potential structural vulnerabilities, whose importance has been often recognized only after disastrous events caused by structural deficiencies against natural hazards. As earliest examples of inadequacy of bridge structures respect to natural actions, it is worth remembering the collapse of numerous bridges of new realization after the San Fernando earthquake in 1971 and the Loma Prieta, California earthquake in 1989 (Mahin, 1991; Mitchell et al., 1991).

Numerous examples of bridge failures can be mentioned in the last 50 years, as a result of which dedicated research studies have been carried out through more accurate numerical models to investigate the structural aspects that may be the primary responsible for direct consequences. In order to mitigate losses after the occurrence of a natural event, nowadays it is a well-established practice the adoption of performance-based approaches for both design and assessment, where different performance levels are defined as representative of damage or failure conditions on the bridge components and a certain level of intensity for the natural hazard is associated with them as target for the optimal structural performance. The most significative context of application of performance-based procedures falls in the design and assessment of structures with regard to seismic action, since earthquakes represent a source of hazard worldwide widespread. National and international codes received the progresses of the scientific community on the research topic in the last 20 years, so that a real design philosophy grown, the so called Performance Based Earthquake Engineering (PBEE) (Cornell & Krawinkler, 2000; Porter, 2003; Mohele & Deierlein, 2004). Given the intrinsic variable nature of seismic action, the PBEE procedures evolved towards a probabilistic format, in which

uncertainties associated to both the input and the structure characteristics are explicitly taken into account for a more reliable quantification of seismic risk and losses. Fragility, vulnerability and risk curves became a common tool in the scientific community for the investigation of structural performance, and bridges resulted one of the main characters of the still ongoing research (Karim & Yamazaki, 2003; Nielson & DesRoches, 2007; Mangalathu et al., 2016; Stefanidou & Kappos, 2019).

Efforts of the research community have been put into the characterization not only of the bridge expected performance in occurrence of a seismic event, but also in the quantification of consequences that disastrous events related to earthquakes may have on the functionality of road networks, especially when emergency actions are necessary. In fact, differently from other civil structures, failure of bridges as part of infrastructural systems can compromise the efficiency of rescue interventions as well as reduce the performance of the transport system for a long time, with high potential consequences in economic and health-related activities (EQE, 1994; EQE, 1995; Basoz & Kiremidjian, 1998; Kaiser et al., 2012). Thus, bridge vulnerability becomes a central point in the resilience of communities. The robustness of bridges and more in general of infrastructural systems can contribute to reduce overall economic losses and fatalities when natural events occur (Fekete, 2011; Deodatis et al., 2014). Moreover, the complexity of the potential post-earthquake scenarios has made the scientific community sensitive to social and economic aspects, so that the analysis and organization of the historical data connected to bridge damage and the engineering of recovery plans for infrastructural systems is a frontier of the research (Chang et al., 2012; Kongar et al., 2017).

1.1 Research Motivation

To date, the probabilistic tool widely accepted by the community to assess and characterize the vulnerability of structural systems is represented by fragility curves, which are commonly applied to both buildings and bridges with the main aim of providing a synthetic representation of the overall system tendency to develop damage in occurrence of natural hazardous events. However, in the case of bridges, information on the overall fragility may be not sufficient to finalize the risk analysis (e.g. to evaluate losses) because a wider spectrum of different failure modes with respect to buildings may develop (e.g., bridge failure may be attained due to maximum forces or stroke on bearings, forces on piers, abutments and decks) and the failure scenario may vary sensibly from case to case, in particular for existing bridges.

The need for a reliable fragility evaluation appears urgent in case of existing bridge structures. In the European context, the case of the Italian infrastructure system appears emblematic for the presence of numerous road networks showing important critical issues. After the collapse of numerous bridges and viaducts in the last 10 years, the evaluation of the performance of existing bridges and the forecasting of direct and indirect consequences of exposure to natural hazards has proved to be of primary importance for

the Italian context. In particular, among the mentioned cases, 10 bridges collapsed between 2015 and 2020, causing the loss of human lives. The causes of the collapses can be attributed to the scarce maintenance of ageing parts of the structures, the uncontrolled increase of traffic loads during service life, the inadequacy of structural details against vertical and seismic actions. The collapse of Polcevera viaduct in Genova in 2018 is a clear example of the inefficiency of the bridge management on the Italian territory, with huge consequences in terms of direct costs, economic repercussions on the regional businesses and environmental problems connected to the traffic emissions and the demolition/reconstruction operations. It is worth remembering also the collapse of several other Italian bridges that caused similar scenarios: the Carasco bridge in 2013, the Petrulla viaduct on the Ravanusa-Licata road link in 2014, the Annone viaduct in Lecco in 2016, the Torino-Savona bridge in 2019, the Caprigliola bridge in Massa Carrara in 2020. A further consideration on the importance of bridges in the Italian territory is that the Italian bridge stock counts a large number of ancient bridges that connect small villages and cities, whose role is fundamental for the survival of local communities. The social and historical value of the Italian bridge heritage must be preserved against natural hazards such as the last Centre Italy earthquake in 2016 (Durante et al., 2018).

Two main deficiencies can be found concerning the management of the Italian existing bridge stock. The first one concerns the lack of useful information about the structural behaviour of the Italian existing bridges, especially with regards to seismic actions, for the successive forecast of damage or failure scenarios. In particular, it is common practice to verify the structural performance of a single structure, according to the Italian national seismic code (Ministero delle Infrastrutture e dei Trasporti, 2018), in case of structural deficiencies or after a seismic event. In this case, results are specific and accurate, but cannot be extended for the characterization of the bridge typology. Alternatively, few works are available dealing with the analysis of Italian bridge classes (Borzi et al., 2015), but the information that come along with them may result too general for a reliable description of the expected behaviour at the road network (local or regional) level. On the contrary, a compromise between a too deep level of detail and a simplistic analysis of the bridge stock is needed. The second aspect is related to the absence of an organic protocol of inspection, assessment and maintenance. Latest attempts to provide a comprehensive procedure (Ministero delle Infrastrutture e dei Trasporti, 2020) mainly focus on the preliminary operations to the assessment of the risk towards different types of hazard, at various levels of accuracy depending on the bridge importance. Despite it is well known that the forecasting of possible scenarios after a disastrous event has a fundamental importance and must be strictly connected to the operations for the risk mitigation, a detailed analysis about the consequences of failure on the infrastructural network functionality is still missing.

1.2 Objectives and Outline of Thesis

This Thesis represents a first answer to the aforementioned issues concerning the analysis of the structural performance of existing bridges with a particular attention on the available tools for a reliable evaluation of the bridges' vulnerability and the associated consequences. The evaluation of the bridges' performance is made with reference to the seismic action, that may be considered the most widespread source of hazard all over the world and it is recognized as extremely important on the Italian national territory. The bridges' behaviour is characterized through the building of fragility curves, at both global and component level. An improved approach for the evaluation of fragility is proposed with the aim of putting in evidence the structural deficiencies at a suitable level of detail for the quantification of direct and indirect consequences. The approach allows to analyse the evolution of the failure mechanisms most likely to occur under two different perspectives: the first concerns the evaluation of the concomitance of different failure mechanisms within the structural system, the second aims to quantify the extension of damage or collapse phenomena associated to one or more structural components. The introduction of the proposed approach has a twofold purpose: to provide an insight on the structural behaviour of some common bridge typologies and to evaluate the implications of the inadequacy of the structural performance in terms of direct and indirect consequences. The methodology is indeed applied to two bridge typologies that result very widespread worldwide and on the Italian territory. The choice of the structural characteristics of the case studies belonging to the examined typologies is carried out taking into account the available information about existing bridges in the Marche region, in order to provide a description of the bridge behaviour at a suitable level of detail for the accurate estimate of consequences and characterize the regional stock as well. The analysis of bridge fragility takes into account also aspects related to the development of degradation phenomena and the presence of compliance at level foundation, being Soil Structure Interaction (SSI) phenomena strongly affecting the bridge response. The structural performance at component level is associated to different limit states, that represent not only different structural behaviours but also different levels of loss, computable as direct and indirect costs. Thus, the analysis of consequences, here treated in economic terms, follows the fragility step and represents a fundamental part in the proposed fully comprehensive framework for the accurate evaluation of bridge failure implications at road network level. The proposed framework deals with various aspects connected to a reliable analysis of the bridge performance in a probabilistic perspective, aims to integrate the already available tools and results flexible for the assessment of various bridge typologies. Moreover, as an innovative aspect in this context, the role of SSI in the quantification of indirect costs associated to the road network functionality is explicitly included. Basing on the available developed tools within the Thesis, an application of the framework is carried out on the examined regional context for the quantification of costs related to the functionality of bridges belonging to two main routes in the Marche region, based on the available information and the previous fragility results.

This Thesis is organized in 6 principal Chapters, as described in the following. Chapter 2 describes the adopted methodology for the analysis of bridge seismic fragility, focusing on both the global behaviour and the performance of the bridge components. A recall on the PEER's PBEE framework is provided and an overview on the available literature on existing bridges in Italy and worldwide is offered, highlighting the weaknesses in the Italian bridge context. Within the PEER's framework, an innovative approach is proposed for the building of the fragility curves to evaluate the concomitance of different failure modes and the extension of damage on the bridge components within each bridge structure. The characterization of such aspects reveals fundamental in the scheduling of maintenance works and for an optimal appropriation of economic resources. In order to provide a reliable description of the bridge fragility, non-negligible effects of Soil-Structure Interaction phenomena associated to deep foundations, typical for bridge structures, are investigated through the adoption of a new simplified formulation for a Lumped Parameter Model (LPM) (Morici et al., 2019) able to catch the behaviour of the soil-pile coupled system and easily manageable for the numerical modelling of the bridge structures.

In Chapter 3, an overview on the Italian and the regional bridge stocks is provided, with a focus on two main traffic routes in the Marche region. The characterization of the regional bridge inventory is carried out for the first time, listing the recollected data according to significative parameters for the bridges' description. A statistical analysis on the available information is made as a preliminary step to the selection of the case studies and the determination of the bridge classes most representative of the regional scenario. As a result, two main bridge typologies are individuated, the Reinforced Concrete with Link Slab decks (RCLS) and the Steel-Concrete Composite decks (SCC). Being the interest on existing structures, a recall on the Italian seismic codes in force at the time of design is offered. Finally, current codes and norms concerning bridges are commented.

Chapter 4 illustrates the adopted case studies and the numerical modelling in the open-source platform OpenSees (McKenna et al., 2015). The models are parametrically built to easily manage changes in the geometrical configurations and the mechanical parameters. Being the case studies representative of existing bridges, a simulated design project for piers and superstructures is developed and the modelling includes ageing effects related to the occurrence of corrosion. Moreover, a typical deep foundation for bridge piers is numerically implemented through the adoption of the Lumped Parameter Model developed by Morici et al. (2019) to quantify the SSI effects on vertical elements. Various Engineering Demand Parameters (EDPs) are adopted to monitor the structural performance at the varying of the seismic intensity, and associated performance thresholds are set to quantify the occurrence of different levels of damage on the bridge components. Peculiarities of each deck typology are explicitly considered in the definition of the EDPs.

In Chapter 5, results of the seismic analyses are illustrated and thoroughly commented, with a comparison between different case studies and different analysis assumptions. Fragility curves are built at level component in order to highlight the main sources of vulnerability for each bridge typology. The evolution of damage along the structure is monitored through the analysis of fragility at each bridge structural joint. As a result of the application of the proposed novel methodology for the fragility analysis, the number of involved elements in the considered failure mechanisms and the concomitance of different failure modes are analysed. It comes out that elements belonging to the superstructure, rarely considered in the quantification of fragility, are usually involved in the considered failure mechanisms and may noticeably contribute to the fragility of the overall structural system. Finally, the influence of ageing and compliant base on the fragility of the bridge components is shown and commented. As a result, the coupling of ageing and SSI effects may produce a high variation in the fragility of key components.

Chapter 6 introduces a global framework in which the adopted methodology for the fragility estimation represents a preliminary step for the evaluation of consequences. The framework leads to an innovative detailed and easy-to-compute quantification of indirect costs associated to the functionality of road networks. Various efficiency indicators are assumed to represent the impact of bridge damage on the viability and the environment after a seismic event. The framework treats also the evaluation of the capacity towards vertical loads, a not negligible aspect for existing bridges and the associated functionality. An application of the framework is carried out referring to one of the two considered road networks in the regional territory and basing on the results obtained in the previous Chapters. The framework is built in order to be suitable for applications concerning other bridge typologies and referring to alternative sources of hazard than the seismic one.

Finally, in Chapter 7 results about the ongoing research about a new probabilistic approach for the analysis of SSI effects on deep foundations are shown. The adoption of a non-deterministic methodology for the characterization of the behaviour of the pile-soil system represents a fundamental step to the improvement of current practices for a reliable evaluation of risk on existing bridges. A novel probabilistic analysis of significative deep foundation case studies is carried out, with the aim of characterizing the embedded system response in dependence of three main parameters affected by an intrinsic variability. The variability of the response is observed on the impedance functions and the kinematic response factors, then quantified through the evaluation of mean values, standard deviations and coefficients of variations for the definition of representative probabilistic distributions. A sensitivity analysis is carried out to individuate the most significant parameters affecting the variability of the pile-soil coupled response. The ongoing studies represent an insight on the SSI problem as part of the proposed general framework for the existing bridge assessment.

1.3 Chapter's references

Basoz, N., & Kiremidjian, A. S. (1998). *Evaluation of bridge damage data from the Loma Prieta and Northridge, California earthquakes* (No. MCEER-98-0004).

Borzi, B., Ceresa, P., Franchin, P., Noto, F., Calvi, G. M., & Pinto, P. E. (2015). Seismic vulnerability of the Italian roadway bridge stock. *Earthquake Spectra*, *31*(4), 2137-2161.

Chang, L., Elnashai, A. S., & Spencer Jr, B. F. (2012). Post-earthquake modelling of transportation networks. *Structure and infrastructure Engineering*, *8*(10), 893-911.

Cornell, C.A., Krawinkler, H. (2000). *Progress and challenges in seismic performance assessment*. PEER Center News, 3(2).

Deodatis, G., Ellingwood, B. R., & Frangopol, D. M. (Eds.). (2014). *Safety, reliability, risk and life-cycle performance of structures and infrastructures*. CRC Press.

Durante, M. G., Di Sarno, L., Zimmaro, P., & Stewart, J. P. (2018). Damage to roadway infrastructure from 2016 Central Italy earthquake sequence. *Earthquake spectra*, *34*(4), 1721-1737.

EQE, 1994. The January 17, 1994 Northridge, California earthquake: an EQE summary report.

EQE, 1995. The January 17, 1995 Kobe earthquake: an EQE summary report.

Fekete, A. (2011). Common criteria for the assessment of critical infrastructures. *International Journal of Disaster Risk Science*, *2*(1), 15-24.

Kaiser, A., Holden, C., Beavan, J., Beetham, D., Benites, R., Celentano, A., ... & Denys, P. (2012). The Mw 6.2 Christchurch earthquake of February 2011: preliminary report. *New Zealand journal of geology and geophysics*, *55*(1), 67-90.

Karim, K.R., & Yamazaki, F. (2003). A simplified method of constructing fragility curves for highway bridges. *Earthquake Engineering and Structural Dynamics*, 32, 1603– 1626.

Kongar, I., Esposito, S., & Giovinazzi, S. (2017). Post-earthquake assessment and management for infrastructure systems: learning from the Canterbury (New Zealand) and L'Aquila (Italy) earthquakes. *Bulletin of earthquake engineering*, *15*(2), 589-620.

Mahin, S. A. (1991). The Loma Prieta Earthquake: Implications of Structural Damage.

Mangalathu, S., Jeon, J. S., Padgett, J. E., & DesRoches, R. (2016). ANCOVA-based grouping of bridge classes for seismic fragility assessment. *Engineering Structures*, *123*, 379-394.

McKeena, F., Fenves, G., & Scott, M. (2015). Open System for Earthquake Engineering Simulation (OpenSees). *Pacific Earthquake Engineering Research Center* (PEER), University of California: Berkeley, CA.

Ministero delle Infrastrutture e dei Trasporti, D.M.17.01.2018, *Aggiornamento delle "Norme Tecniche per le Costruzioni"*, G.U. n.42, 20.02.2018 (in Italian).

Ministero delle Infrastrutture e dei Trasporti, *Linee Guida per la Classificazione e Gestione del Rischio, la Valutazione della Sicurezza ed il Monitoraggio dei Ponti Esistenti*, 17.04.2020 (in Italian).

Mitchell, D., Tinawi, R., & Sexsmith, R. G. (1991). Performance of bridges in the 1989 Loma Prieta earthquake–lessons for Canadian designers. *Canadian Journal of Civil Engineering*, *18*(4), 711-734.

Moehle, J., & Deierlein, G. G. (2004, August). A framework methodology for performance-based earthquake engineering. In *13th world conference on earthquake engineering* (Vol. 679).

Morici, M., Minnucci, L., Carbonari, S., Dezi, F., & Leoni, G. (2019). Simple formulas for estimating a lumped parameter model to reproduce impedances of end-bearing pile foundations. *Soil Dynamics and Earthquake Engineering*, *121*, 341-355.

Nielson, B.G., & DesRoches, R. (2007). Seismic fragility curves for typical highway bridge classes in the Central and South-eastern United States. *Earthquake Spectra*, *23*, 615–633.

Porter, K. A. (2003, July). An overview of PEER's performance-based earthquake engineering methodology. In *Proceedings of ninth international conference on applications of statistics and probability in civil engineering* (pp. 1-8).

Stefanidou, S. P., & Kappos, A. J. (2019). Bridge-specific fragility analysis: when is it really necessary?. *Bulletin of earthquake engineering*, *17*(4), 2245-2280.

2. Methodology for the vulnerability estimation of existing bridges

As an engineering concept, the vulnerability (or damageability) is measured in terms of the degree of an undesirable outcome, called loss, as repair costs, life-safety impacts, loss of functionality, or in terms of environmental degradation, quality of life, historical value, and other similar measures (Porter, 2018). The vulnerability is also related to one or more sources of hazard, so that loss measures are often expressed in terms of the probability distribution of loss conditioned on the natural excitation. The analyses of hazard and vulnerability are fundamental passages for the quantification of risk and losses, that in turn represent a first step for any activity aimed to the disaster prevention (Coburn & Spence, 2003).

In the next sections, an explanation of the loss analysis framework is provided, focusing on the concepts of hazard, fragility and risk in the seismic analysis context (§2.1). In Italy, the seismic problem is strongly perceived regarding existing structures, due to the catastrophic consequences that followed the seismic events that hit the national territory in the last century. The sensitization on the performance of existing bridges has become more relevant than ever in the last decade, since the importance of such infrastructures is widely acknowledged. To deepen the topic, a particular attention is payed on the evaluation of fragility curves, which are a common tool to evaluate the behaviour of structural and infrastructural systems with regard to different probabilities of hazard occurrence by now (§2.2). The risk analysis leads to the evaluation of potential economic, environmental and social consequences, against which it is necessary to draw up some risk-management decision (§2.3). Such decisions usually involve the choice between different alternative scenarios of action, and often require the analyst to assess the efficiency of the decision-making repeating the analyses under the different conditions of each alternative, in order to achieve the best balance for the intended risk mitigation purpose. In the closure of the Chapter (§2.4), the adopted methodology for the analysis of existing bridges vulnerability is illustrated and commented. In this Section, a novel methodology for the evaluation of bridge fragility is presented, concerning the analysis of the concomitance of failure modes and the extension of damage along the bridge after the occurrence of a seismic event. Moreover, given the importance of the topic in case of bridge structures, a focus on the methodology adopted for the analysis of SSI effects under pier foundations is provided in §2.5. In this Section, a simple and efficient approach for the building of a Lumped Parameter Model is described and validated through preliminary applications under bridge piers. The proposed methodologies allow for a detailed and accurate analysis of the bridge response under seismic excitation.

2.1 Seismic Hazard, Fragility and Risk analysis

During last decades the attention to the problem of seismic risk assessment grew significantly due to severe earthquakes occurred worldwide and dedicated frameworks and research projects were developed and proposed to improve the state of art in this field. Nowadays, seismic risk assessment is one of the main issues in civil and building engineering research.

The first seismic risk estimation studies were published between the end of the 1960s and the beginning of the 1970s (Cornell, 1968; Algermissen, 1972; Grandori & Benedetti, 1973; Whitman et al., 1975). At the beginning, studies conceived the risk as a measure of the seismic hazard, with a strong geological and geophysical matrix, and many studies dealt with the development and the improving of models describing local, regional and macro-regional seismic scenarios for the definition of hazard maps (Atkinson, 2004). However, from an engineering point of view, the hazard of the site is not enough to characterize the global seismic risk of a generic structure, which also depends on its intrinsic vulnerabilities and the exposure conditions. At this scope, many works turned the attention to concepts of fragility, vulnerability and economic losses (PELEM, 1989; Chen et al., 1992; Chen et al., 2002; Giovinazzi & Lagomarsino, 2004). In the PEER framework (Porter, 2003), the risk evaluation passes through the definition of several quantities in a specific outline (Figure 2.1). The first step consists in the acquisition of available data about assets exposed to loss (exposure data or inventory). Then, the potential loss must be translated in one or more engineering attributes; in this second phase, also called asset analysis, all the geometrical, mechanical, economical and typological entities of interest for a risk assessment are investigated and made usable in the successive steps. The Hazard analysis follows, representing the probability that a seismic event exceeds a selected measure for shake severity in a certain time period. The Probabilistic Seismic Hazard Analysis (PSHA) is the most widely adopted, since it combines information from different seismic sources to characterize large geographical regions and identify the most critical areas. Finally, the Loss analysis is performed through a Vulnerability model recollecting information from previous steps and evaluating the probability of exceeding a certain level of loss, conditioned on the excitation level, through the Total Probability theorem (Porter, 2018). If the Vulnerability model, which represents the expected value of loss as a function of excitation, is replaced by a damageability or, more commonly, Fragility model, that expresses the probability of exceeding specified limit states as a function of environmental excitation, the risk analysis can be called Probabilistic Seismic Demand Hazard Analysis (PSDHA). The evaluation of seismic risk leads to the definition of protection measures and emergency management plans (Coburn & Spence, 2003), in a final phase called decision-making.

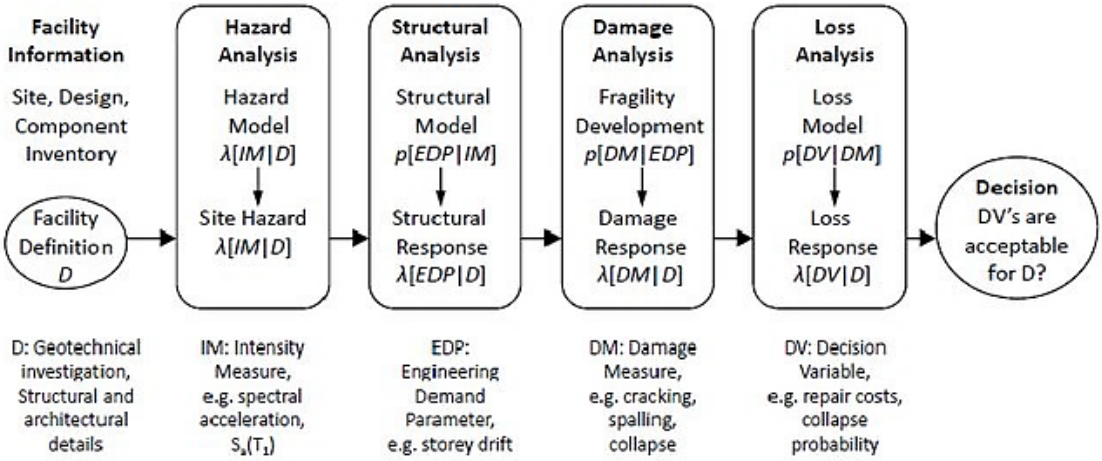

Figure 2.1. PEER framework for seismic risk assessment

In the PEER framework, PSHA and PSDHA represent the most relevant steps for engineering applications, and a brief insight on the subject is offered.

PSHA relies on the choice of a proper measure for the seismic intensity to characterize the seismic scenario in a certain site or area. This indicator, called *Intensity Measure* (*IM*), can be probabilistically described by means of seismic hazard curves, which represent the Mean Annual Frequency (MAF) of exceedance $\nu_{IM}(im)$ of an intensity level equal to im. The choice of a proper *IM* is conditioned to the fulfilment of two properties: efficiency, to provide a good estimate of seismic demand through a small number of ground motion records, and sufficiency, to represent the seismic scenario of the site consistently, without any further dependency on other seismological features (Luco & Cornell, 2007). It is fundamental to meet these requirements in order to ensure both a good estimation of the risk and the independence of PSHA and PSDHA in the PEER framework. Typically, in case of structural analysis, the Peak Ground Acceleration (PGA) and the Spectral acceleration at a certain vibrational period T (usually the first one) of the investigated structure, referring to a damped elastic pseudo-acceleration spectrum (Sa(T)) are chosen as *IM*s.

To estimate seismic hazard, the theorem of Total Probability is applied to combine the uncertain shaking at the site caused by a particular fault rupture and the occurrence frequency or probability of that rupture. This results in the following mathematical description of an *IM* based seismic hazard curve (Bazzurro & Cornell, 1999):

$$\begin{aligned} \nu_{IM}(im) &= \sum_{i=1}^{N} \left(\nu_{IM}(im)\right)_i \\ &= \sum_{i=1}^{N} \left(\nu_M(m_0)\right)_i \left\{ \iiint I[IM > im|m,r,\varepsilon] \cdot f_{M,R,\varepsilon}(m,r,\varepsilon) dm dr d\varepsilon \right\}_i \end{aligned} \quad (1)$$

where

- $\left(\nu_M(m_0)\right)_i$ is the mean annual rate of occurrence of earthquakes generated by source i with magnitude greater than m_0;
- $I[IM > im|m,r,\varepsilon]$ is an indicator function for the IM of a ground motion generated by source i of magnitude m, distance r and standard deviation ε from the median with respect to the level im. This indicator function is equal to 1 if $IM > im$ and 0 otherwise;
- $f_{M,R,\varepsilon}(m,r,\varepsilon)$ is the joint probability density function of the random variables magnitute M, distance R (of which m and r are samples) and ε for source i.

An example of Hazard curves for different Italian sites on different soil types is depicted in Figure 2.2. Figure 2.2a shows seismic hazard curves with the PGA selected as *IM*; the same is in Figure 2.2b, where the *IM* is the spectral acceleration at T* = 1 s.

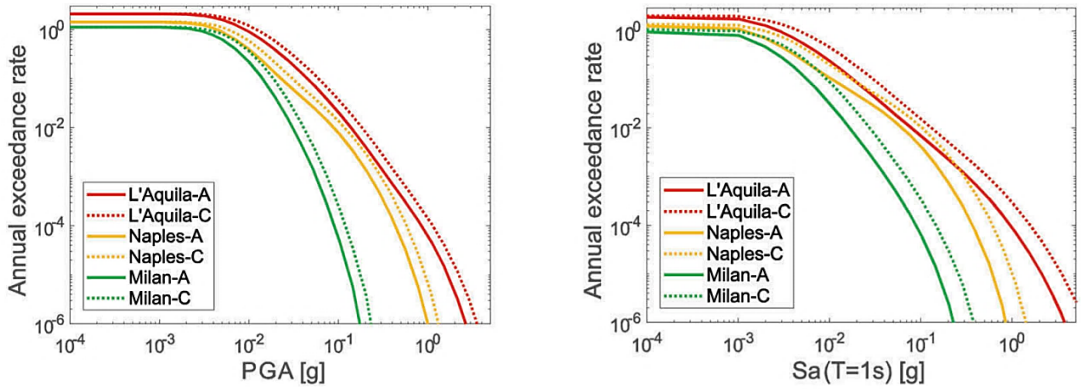

a) b)

Figure 2.2. Hazard curves for two spectral ordinates and soil types computed for the three Italian sites; (a) IM=PGA; (b) IM=Sa(T=1s) (from Iervolino et al 2018).

The correlation of *IM* to the predictive parameters m and r, and more in general also to additional variables such as fault type and local soil conditions at the site, can be obtained through empirical relationships, deriving from statistical regressions on earthquake parameter data, called Ground Motion Prediction Equations (GMPEs) (Boore & Atkinson, 2008) usually written in the following form:

$$lnIM = g(M,R,\theta) + \varepsilon\sigma_{lnIM} \quad (2)$$

where g represents the predictive functional form of the regression algorithm, σ_{lnIM} is the standard deviation of the natural logarithm of *IM* and θ the set of additional independent variables affecting the estimation of *IM*.

To proceed with the PSDHA, the probabilistic characterization of seismic hazard in PSHA comes with the selection of a set of ground motion samples to be used in the structural analyses. Despite the use of natural accelerograms is preferable due to the intrinsic variability of seismic signals, in case of limited databases or in case of lack of records, especially at highest *IM*s, ground motion simulation methods can be employed

to integrate or fully reproduce the features of the seismic records. The use of ground motion simulation methods allows to avoid the use of procedures such as strong scaling of accelerograms or spectral matching that may lead to less reliable results of PSDHA (Luco & Bazzurro, 2007). In this Thesis, artificial ground motion records are employed for the PSHA and PSDHA analyses, as explained in the following.

As previously recalled, PSDHA leads to the estimation of seismic risk as the convolution of the seismic Hazard with a Fragility model, through the Total Probability theorem. PSDHA can be mathematically formulated as follows:

$$\nu_D(d) = \int_{IM} G_{D|IM}(d|im)\,|d\nu_{IM}| \tag{3}$$

where $\nu_D(d)$ is the MAF of exceedance of the seismic demand value d in the considered *IM* domain, obtained convolving the seismic Hazard curve at each im, here represented as $|d\nu_{IM}|$ with the Fragility function $G_{D|IM}(d|im)$, the latter denoting the probability that the generic demand parameter D exceeds the associated demand threshold d conditional to the seismic intensity level im.

A Probabilistic Seismic Demand Model (PSDM) that mathematically links the condition $D \geq d$ of the generic EDP with the chosen *IM* is then represented by the fragility function $G_{D|IM}(d|im)$, which can be built by means of different approaches:

- Empiric approach: an empirical fragility function is created by fitting a function to approximate observational data, structured as ordered sets of seismic excitation (i.e. *IM* levels), a number of assets exposed to that level of excitation (i.e. values D for the considered EDP) and the number of those that failed when subjected to the environmental excitation (i.e. $D \geq d$);
- Judgment-based approach: a judgement-based fragility function is created by polling one or more people who have experience with the asset class in question, where the experts guess or judge failure probability as a function of environmental excitation.
- Analytical approach: the fragility function is derived respect to a selected EDP by creating and analysing a structural model of the asset class.

In this Thesis, fragility functions are obtained following an analytical approach.

In general, different analysis methods are available to build analytical fragility functions, among which three are the most commonly adopted for structural analysis (Jalayer & Cornell, 2009): Cloud analysis (Mackie & Stojadinovic, 2005a), Incremental Dynamic Analysis (IDA) (Vamvatsikos & Cornell, 2002) and Multiple-Stripe Analysis (MSA) (Mackie & Stojadinovic, 2005a; Bradley, 2013).

Cloud analysis consist in performing seismic analysis with a wide selection of unscaled ground motion time histories that form such a cloud of data points within the magnitude-distance (M, R) domain of possible earthquakes. As a result, the structural response,

monitored through a certain EDP, will appear as a cloud of points in the *IM*-EDP domain (Figure 2.3). In order to give a mathematical form to the cloud data points, regression techniques are applied to obtain a mean trend and the relative dispersion, which are then used to characterize a lognormal fragility function (Mackie & Stojadinovic, 2005a).

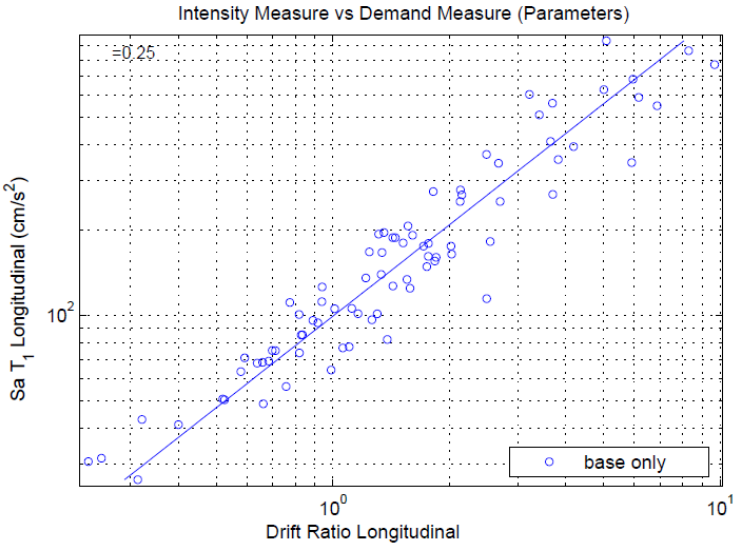

Figure 2.3. Example of PSDM adopting Cloud analysis (from Mackie & Stojadinovic, 2005a).

With regards to the other approach, IDA, it takes a smaller subset of ground motions with intensity incrementally increased in each analysis. This leads to the dynamic equivalent to the static pushover analysis, where the incremental parameter is the level of *IM*. The advantage of this approach is particularly evident in case of lack of seismic signals. As a result, EDP values are plotted against the corresponding value of the ground motion *IM* for each intensity level to produce a dynamic pushover curve for the structure and each scaled earthquake record (Vamvatsikos & Cornell, 2002) (Figure 2.4).

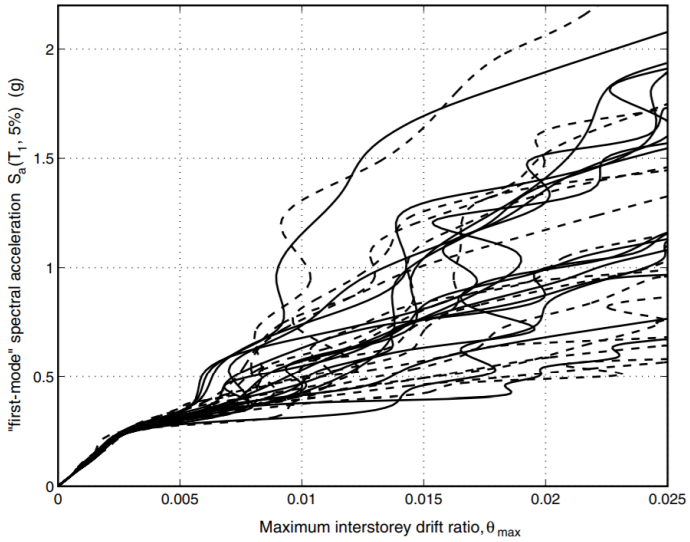

Figure 2.4. Example of IDA analysis (30 IDA curves) (from Vamvatsikos & Cornell, 2002).

By analogy with the IDA, the last analysis method, the MSA, consists of performing several nonlinear dynamic analyses at different intensity levels, in which the *IM*-hazard curve is discretised, throughout ground motions conditioned on the *IM*. This leads to the collection of stripes of EDP values, one for each *IM* level (Figure 2.5). It is noteworthy that, unlike IDA, different acceleration time series are used at different intensity levels, in order to catch the relevant changes of the ground motion target features of each *IM* level (Bradley et al., 2010) that may be lost with scaling procedures.

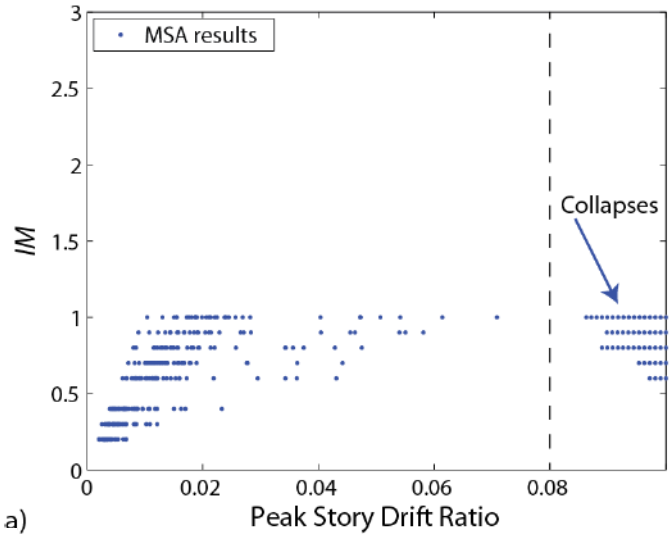

Figure 2.5. Example of MSA analysis (from Baker 2015).

All the above-mentioned analysis methods lead to the collection of data to be used for the estimation of the fragility function $G_{D|IM}(d|im)$. Many different statistical procedures exist to fit data and give a mathematical form to $G_{D|IM}(d|im)$ (Lallemant et al., 2015); among these, the lognormal cumulative distribution function (CDF) is the most common and classically adopted, being a reasonable assumption for a large set of cases (Ibarra & Krawinkler, 2005; Porter et al., 2007):

$$G_{D|IM}(d|im) = P[D \geq d \mid IM = im] \quad = \Phi\left(\frac{\ln\left(im/\theta\right)}{\beta}\right) \tag{4}$$

with $\Phi(\cdot)$ denoting the standard normal cumulative distribution function, θ the median fragility value (i.e., the *IM* level with 50% probability of exceedance), β the *IM* standard deviation. An example of fragility curve is furnished in Figure 2.6.

Basing on the above-mentioned results from the literature, in the next §2.4, the methodology adopted in this Thesis for the estimation of fragility is described. But first, an insight on fragility for existing bridges and an illustration of possible evolutions of the recalled PEER framework are introduced in §2.2 and §2.3.

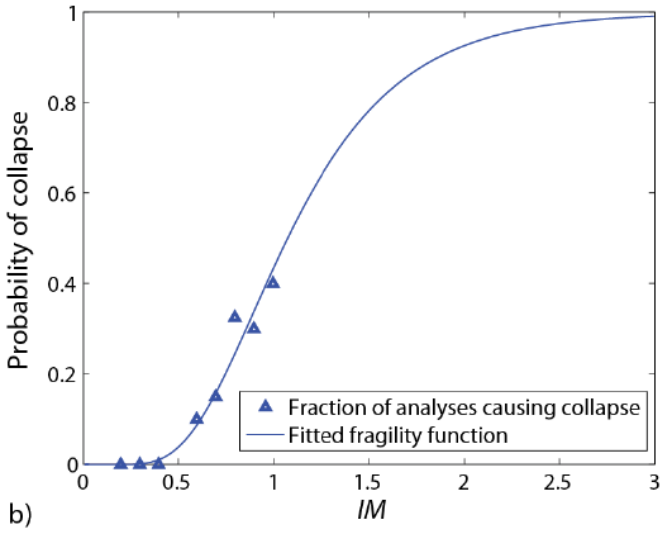

Figure 2.6. Example of fragility curve (from Baker 2015).

2.2 Common practice in fragility estimation of existing bridges

For what concerns the problem of bridges seismic vulnerability, fragility assessment is fundamental for a proper probabilistic characterization of the consequences of earthquakes on existing infrastructures. Major attention is paid to bridges of medium-high dimensions, due to their strategical role in the territorial network for viability, economic and social aspects.

Common practice is that of defining homogeneous fragility classes for cataloguing bridges based on their geometric and mechanical characteristics, deck cross section, static scheme and typology of vertical supporting elements (Nielson, 2005; Nielson & DesRoches, 2007a; Moschonas et al., 2009; Ramanthan, DesRoches & Padgett, 2010; Mangalathu, Jeon, Padgett & DesRoches, 2016). Moreover, since hazard sources, design rules, construction practices and bridge types vary from region to region, different research groups from different parts of the world developed fragility curves representative of bridge regional stocks.

A huge literature is available concerning seismic fragility assessment of highway bridges in different regions in the USA. Choi et al. (Choi et al., 2004), Nielson and DesRoches (Nielson & DesRoches, 2007a; Nielson & DesRoches, 2007b) and Padgett and DesRoches (Padgett & Des Roches, 2008; Padgett & DesRoches, 2009) developed fragility curves for as-built and retrofitted bridges in central and southern United States (CSUS). Pan et al. (Pan et al., 2010a; Pan et al., 2010b) conducted an extensive parametric study to evaluate the seismic response parameters for different bridge components of multi-span simply supported steel highway bridges in New York State. Ramanathan et al. (Ramanathan et al., 2010; Ramanathan et al., 2012) developed fragility curves for seismically and non-seismically designed bridges in CSUS. Mackie and Stojadinovic

(Mackie and Stojadinovic, 2005b) developed fragility curves for highway overpass bridges in western US and Ramanathan (Ramanathan, 2012) developed fragility curves for typical California bridge classes. In addition, several works have been recently developed towards a more efficient grouping of bridges into fragility classes for a more reliable risk assessment (Mangalathu et al., 2016; Mangalathu et al., 2017; Mangalathu et al., 2018).

Significant amount of research work has been carried out also in other several earthquake-prone countries such as Japan (Karim & Yamazaki, 2003; Akiyama, Frangopol, & Matsuzaki, 2011; Akiyama, Frangopol, & Mizuno, 2013), Canada (Tavares et al., 2012; Billah & Alam, 2013), Turkey (Avşar et al., 2011) or Greece (Moschonas et al., 2009). A complete review of the state of the art concerning bridge fragility assessment can be found in (Billah & Alam, 2015; Stefanidou & Kappos, 2019).

The most recent attempt to evaluate the fragility of the European bridge stock, involving the Italian existing infrastructures, was made withing the Syner-G project (Pitilakis, 2011). The proposed taxonomy is structured as an innovative modular classification that takes into account both the parameters considered of primary importance for the bridge classification (e.g., the construction material, the deck typology, the number of spans) and other optional parameters, to provide a further detail on the individuated macro bridge class (i.e., the selection of a reinforced or prestressed concrete for the deck), basing on the most recurrent bridge characteristics in the European context. The modular structure of the Syner-G classification allows expanding the proposed bridge classes or add further detail to the existing fragility curves taking into account additional parameters. The Syner-G bridge taxonomy is depicted in Figure 2.7.

In Italy, first efforts to characterize the seismic risk of existing bridges have been made by Codermatz et al. (Codermatz et al., 2003) and Franchetti et al. (Franchetti et al., 2008). In particular, Codermatz et al. followed the American HAZUS earthquake loss estimation methodology (HAZUS 99) to evaluate the risk level of bridges and tunnels of the Friuli-Venezia Giulia regional highway transportation network. Franchetti et al. constructed specific fragility curves comparing different damage analysis methods for 6 bridges in the Veneto region as a first investigation on the vulnerability of bridges in north-east Italy. Later, Miano et al. (Miano et al., 2015) updated available fragility curves with a Bayesian approach to improve risk estimation for highway bridges in the Campania region. At present, the most comprehensive research work on the fragility of existing Italian bridges has been carried out by Borzi et al. (Borzi et al., 2015). Since the approach by (Borzi et al., 2015) inspired the analysis of the examined bridge inventory, a more detailed description of the work by (Borzi et al., 2015) is provided in the next Chapter 3.

CATEGORY	SUB-CATEGORY	
Material (MM1) • Concrete (C) • Masonry (M) • Steel (S) • Iron (I) • Wood (W) • Mixed (MX)	**Material (MM2)** • Reinforced concrete (RC) • Post-tensioned or Pre-stressed reinforced concrete (PC) • Unreinforced masonry (URM) • Reinforced masonry (RM) • High strength concrete (HSC) • Average strength concrete (ASC) • Low strength concrete (LSC) • Adobe (A) • Fired brick (FB) • Hollow clay tile (HC) • Stone (S) • Lime mortar (LM) • Cement mortar (CM) • Mud mortar (MM) • Concrete masonry unit (CMU) • Autoclaved aerated concrete (AAC) • High % of voids (H%) • Low % of voids (L%) • Regular Cut (Rc) • Rubble (Ru)	
Type of Superstructure (TD1) • Girder bridge (Gb) • Arch bridge (Ab) • Suspension bridge (Spb) • Slab Bridge (Sb)	**Type of Deck (TD2)** • Solid slab (Ss) • Slab with voids (Sv) • Box girder (B) • Modern arch bridge (MA) • Ancient arch bridge (AA)	**Deck characteristics (DC)** [Here the width of the deck is explicitly given if known]
Deck Structural System (DSS) • Simply supported (SSu) • Continuous (Co)		
Pier to deck connection (PDC) • Not Isolated (monolithic) (NIs) • Isolated (through bearings) (Is)		
Type of pier to superstructure connection (TC1) • Single-column pier (ScP) • Multi-column piers (McP)	**Number of piers for column (NP)** [Here the number of piers for column is explicitly given if known]	
Type of section of the pier (TS1) • Cylindrical (Cy) • Rectangular (R) • Oblong (Ob) • Wall-type (W)	**Type of section of the pier (TS2)** • Solid (So) • Hollow (Ho)	**Height of the pier (HP)** [Here the height of piers is explicitly given if known]
Spans (Sp) • Single span (Ssp) • Multi spans (Ms)	**Spans characteristics (SC)** • Number of spans (Ns) - [Here the number of spans is explicitly given if known] • Span length (SL) - [Here the length of spans is explicitly given if known]	
Type of connection to the abutments (TCa) • Free (F) • Monolithic (M) • Isolated (through bearings, isolators) (Isl)		
Bridge Configuration (BC) • Regular (R) • Semi-regular (SR) • Irregular (IR)		
Level of seismicity (LS) • No seismic design (design for gravity loads only) (NSD) • Seismic design (SD)		

Figure 2.7. Syner-G bridge classification.

2.3 Beyond risk analysis: costs and consequences

An accurate analysis of fragility and, as a consequence, of risk reveals of major importance for bridge structures, since a failure or loss of functionality of these systems may have severe economic, social, and environmental impacts, especially within an infrastructural network (Frangopol & Soliman, 2016). From recent studies it appears that the consequences of failure are significantly more than just the cost of rebuilding or replacing the dysfunctional component, especially if the social and environmental impacts are included, in both the immediate and particularly long-term after a natural catastrophic event (Zhou, Banerjee, & Shinozuka, 2010; Bocchini, 2013; Dong et al., 2014).

Direct costs, which can be included within the PEER framework in the vulnerability estimation step as a measure of loss, are usually associated to the economic impact of restoration, retrofitting or demolition-reconstruction works for damaged structures. In order to mitigate this impact and optimally invest for the maintenance of a good structural performance, holistic life-cycle cost models for bridges have gained widespread interest in the last 20-30 years, in which different aspects of cost optimization are emphasized, such as maintenance costs, cost-benefit ratio for optimal reliability levels, repair costs for deterioration phenomena and many others (Chang & Shinozuka, 1996; Frangopol, 1999; Liu & Frangopol, 2005; Thoft-Christensen, 2009; Padgett et al., 2010; Frangopol et al., 2017; Zanini et al., 2017).

The sustainability of a bridge structure must be quantified also through the estimation of the social and environmental consequences, which result in additional *indirect costs*. Nowadays, the complexity of interconnection between cities and societies and the global issues concerning the environment on the planet ask for awareness on the efficiency of infrastructural systems from an overall point of view. In case of bridges as part of a road system, indirect costs are linked to the efficiency of the road network in terms of traffic. In fact, indirect losses refer to the increase of travel time due to the reduced functionality of the road network as well as the business interruption and the consequent alteration of socio-economic life; this also reflects on additional transportation costs and environmental implications (Kiremidjian et al. 2007; Dorra et al. 2013; Kilanitis & Sextos, 2019a). In occurrence of an earthquake, depending on the level of damage experienced by the strategic structures in the network, decision making on the degree of safety and usability of the single roads is necessary, so that local or widespread, partial or total closures are required (Alessandri et al., 2013). An intrinsic complication in the analysis of traffic flows after a seismic event is related to the spatial variability of the flow itself, that may involve different alternative ways to the principal one where the damage has occurred (Miller & Baker, 2016). The variability of traffic is also time-dependent, since repair or retrofit measures are gradually applied in order to restore the functionality of the network, so that the more efficient those measures, the quicker the full traffic capacity recovery (Alipour & Shafei, 2016). Many research studies grown in the last 20 years about the analysis of road networks subjected to natural hazards, with

the purpose of englobe hazard, fragility and loss concepts in comprehensive frameworks for the estimation of the risk and the post-event resilience. Examples of these studies can be found in (Werner et al., 2000; Padgett & DesRoches, 2007; Bocchini & Frangopol, 2011; Padgett & Tapia, 2013; Tapia & Padgett, 2016; Kilanitis & Sextos, 2019a; Kilanitis & Sextos, 2019b).

In the Italian context, despite the importance of the theme, very few works are available in the literature concerning the bridge risk management and the mitigation of direct and indirect losses on the relative road networks in Italy, all dating back to the last 10 years and involving northern-east areas in the most of cases (Zanini et al., 2013; Carturan et al., 2013; Carturan et al., 2014; Capacci et al., 2020). The need for a comprehensive framework to evaluate the bridge and the road network performance in such earthquake-prone areas as the Marche region in Central Italy is crucial. In this Thesis, a proposal for a holistic methodology for the evaluation of fragility, risk, direct and indirect costs is explained in Chapter 6. In the framework, the analysis of fragility of bridges belonging to different local or regional areas is central and exploits specific tools for the evaluation of some fundamental aspects affecting the bridge response not yet considered in existing holistic frameworks, such as the role of Soil Structure Interaction or the influence of the bridge damage at component level. The fragility analysis can be seen as a fundamental step of the framework and fully integrates with the evaluation of other aspects concerning the performance of bridges and infrastructural networks, such as the already mentioned analysis of risk and costs. The proposed methodology for the evaluation of fragility makes use of some innovative approaches that will be commented in the following §2.4.

2.4 Proposed probabilistic approach for the vulnerability estimation

In this section, the proposed and adopted tools for the evaluation of the fragility are presented. Firstly, a detailed description of the employed stochastic approach is provided in §2.4.1. This approach applies to the construction of fragility curves unless otherwise specified. Together with the classical representation of fragility described in §2.4.1, two novel procedures for the quantification of fragility are developed and presented in §2.4.2. The first (§2.4.2.1) is related to the analysis of the concomitance of different failure modes within the bridge structure at the occurrence of an earthquake event. The second (§2.4.2.2) focuses on the construction of fragility considering the number of elements involved into a certain failure mechanism. Both the approaches reveal useful for a detailed analysis of the bridge performance and the decision-making process that follows the post-earthquake damage scenario.

2.4.1 Probabilistic tool and stochastic ground motion model

A conditional probabilistic approach is employed in this study to assess the seismic vulnerability of the Marche bridges. In this work, the efficient and widely used MSA is adopted. Synthetic accelerograms are used, generated according to a stochastic ground motion model. Following the procedure used by Jalayer and Beck (2008), Scozzese et al.

(2019) and Scozzese et al. (2020), a simulation-based approach, called Subset Simulation (Au & Beck, 2003), is adopted for generating the *IM* hazard curve $\nu_{IM}(im)$ from a stochastic seismic scenario, along with different sets of pairs (horizontal components) of ground motion time series conditional to various *IM* levels. The stochastic ground motion model is based on two main random seismological parameters: the moment magnitude *M*, and the epicentral distance *R*. A Gutenberg-Richter recurrence law (Kramer, 2003) is used to describe the magnitude-frequency relationship of the seismic source:

$$\nu_M(m) = 10^{(a-bm)} \tag{5}$$

where *a* and *b* are parameters characterizing the mean number of earthquakes expected from the source and the regional seismicity, respectively. The assumed recurrence law, truncated within the range of magnitudes of interest [m_0, m_{max}], leads to the moment magnitude probability density function (PDF) (Kramer, 2003; Au & Beck, 2003; Scozzese et al., 2019):

$$f_M(m) = \beta \frac{e^{-\beta(m-m_0)}}{1 - e^{-\beta(m_{max}-m_0)}} \tag{6}$$

where $\beta = b^* \log_e(10)$, m_0 and m_{max} the minimum and maximum values of magnitude expected from the source.

According to the features of the potential seismic sources in the region, the probability density function of the epicentral distance is modelled as follow:

$$f_R(r) = \begin{cases} \dfrac{2r}{r_{max}} & if\ r < r_{max} \\ 0 & otherwise \end{cases} \tag{7}$$

which is obtained under the hypothesis that the source produces random earthquakes with equal likelihood anywhere within a distance from the site r_{max}. The soil condition is described by a deterministic value of the shear-wave velocity parameter V_{S30} (Boore & Joyner, 1997).

The source-based ground motion model proposed in (Atkinson & Silva, 2000) is used in this study, as well as in (Au & Beck, 2003; Jalayer & Beck, 2008; Dall'Asta et al., 2017; Scozzese et al., 2019). This model, combined with the stochastic point source simulation method (Boore, 2003), is employed to generate ground motion time series according to the samples of *M*, *R*. The ground motions record-to-record variability is accounted by means of a Gaussian white noise process.

Based on the outcomes of the extensive parametric study performed by Scozzese et al. (2020), and in order to achieve a level of accuracy comparable to that of robust direct simulation methods (i.e., Monte Carlo-like methods), the following setup of analysis is adopted:

1) the IM hazard curve is discretised in 20 IM levels equally spaced in the log-log plane, thus MSA analysis is performed at 20 stripes;

2) a set of 20 ground motion pairs of samples (along the two orthogonal directions X and Y) is used at each IM level, for a total amount of analysis equal to 400 for every case study;

3) IM hazard curve truncation at sufficiently low MAF levels (i.e., $n_{IM} = 10^{-5}$ year^{-1}), with the aim of accounting for rare seismic events contribution.

For what concerns the choice of the *IM*, the most practical and used ones for bridges are the peak ground acceleration (PGA) (Padgett & Des Roches, 2008; Stefanidou & Kappos, 2017) and the spectral acceleration at the period T*=1.0 s, Sa(1.0) (Ramanathan, 2012). More precisely, given the bidirectional nature of the seismic input, the spectral acceleration (at period T*) of the maximum horizontal component (Iervolino et al., 2018), i.e., $IM = \max(S_{a,X}(T^*), S_{a,Y}(T^*))$, is herein adopted as IM.

As recalled above, the fragility function $G_{D|IM}(d|im)$ denotes the probability of exceeding a given threshold value d of a demand parameter D, given a value im of the seismic intensity IM. As a result of the structural analysis performed according to MSA, at each IM level the fraction of ground motions satisfying the exceedance condition $D \geq d$ can be computed. As suggested by (Baker 2015), and as widely accepted within the scientific community (Baker & Cornell 2005; Straub & Der Kiureghian 2008), an appropriate fragility fitting strategy for this type of data is maximum likelihood, according to which the fragility function parameters $(\hat{\theta}, \hat{\beta})$ are obtained by maximizing the logarithm of the likelihood function (Baker 2015):

$$\{\hat{\theta}, \hat{\beta}\} = \underset{\theta,\beta}{\operatorname{argmax}} \sum_{i=1}^{N_{IM}} \left\{ ln \binom{N_{GM}}{N_{di}} + N_{di} ln\, \Phi\left(\frac{\ln\,(im_i/\theta)}{\beta}\right) + (N_{GM} - N_{di}) ln \left[1 - \Phi\left(\frac{\ln\,(im_i/\theta)}{\beta}\right)\right]\right\} \tag{8}$$

where N_{IM} is the number of IM levels, N_{GM} is the total number of ground motion samples adopted at each IM level (assumed as constant all over the IMs) and N_{di} is the fraction of ground motion samples leading to $D \geq d$.

2.4.2 Proposed methodology

The maximum likelihood fitting strategy previously explained can be adopted not only for the evaluation of the fragility at the element level, where the element is a single pier or a single bearing, but also for the bridge component (i.e. the collection of the piers, the collection of the bearings, …) fragility estimation. Classically, fragility curves for bridge components (i.e. piers, abutments, bearings and so on) are derived as the envelope of fragility curves for each element belonging to the considered component, counting how

many ground motion samples led to the exceeding of the performance threshold by *at least one* element, the one with the worst performance at each *IM* level.

In the sequel, a novel procedure for the fragility analysis of bridges is proposed, aimed at overcoming drawbacks of the classical approach that classically derives fragility curves as the envelope of fragility curves relevant to each element belonging to the considered component. The proposed strategy aims to obtain: *i*) a qualitative estimate of the bridge's vulnerabilities (analysis of the failure modes) and *ii*) a quantitative assessment of the damage extent over the bridge (analysis of the damage extensions). These objectives are obtained by providing *multiple damage fragility curves*, obtained by considering the possible combinations of failure scenarios, and *quantitative fragility curves*, obtained by investigating each failure mechanisms and focusing on the number of elements or components involved in the damage mechanism.

For the purpose of the approach presentation, failure is herein defined as the exceeding of a threshold value for a selected bridge response parameter that controls the behaviour and the evolution of damage in the key structural components of the bridge. Different response parameters can be considered to control all the possible failure mechanisms in the bridge, which can affect piers, abutments, bearings, and so on. Failures may thus occur in different components and are expressed by the threshold overcome of the relevant response parameter controlling the evolution of damage of the component. A Limit state is described by a set of thresholds relevant to different potential failures. Different set of thresholds (limit states) can be of interest, according to different performance of the structure, e.g. serviceability or ultimate limit states. Limit states are considered one by one in the following. So, failures may concern thresholds relevant to different response parameters and may occur in different components.

For the purpose of this study, failure events are grouped in families related to parameters of interest, and each family is denoted by a capital letter (e.g. A, B, C, …). For instance, one might have the following failure modes: A, pier flexural failure; B, pier shear brittle failure; C, bearings failure due to maximum stroke attainment.

Failure of given type, e.g. A, may occur in one or more components of the family and the failure on each component is denoted by A_k, with $k = 1, \dots N_{Ak}$, where N_{Ak} is the number of components that may suffer the type of failure A. Consequently, the failure event A occurs if one or more events A_k occur in one or more components, i.e.

$$A = \bigcup_k A_k \tag{9}$$

The fragility curve relevant to the occurrence of event A, hereafter called Mode A-fragility curve, describes the probability of occurrence of A, conditional to seismic intensity im, and is defined as

$$G_A(im) = P[A|im] \tag{10}$$

while

$$G_{A_k}(im) = P[A_k|im] \tag{11}$$

denotes the fragility curve of a single element of the family A and will be called Mode A component-fragility curve.

Different failure modes $(A, B, C, \dots)$ are considered and the event

$$F = \bigcup (A, B, C, \dots) \tag{12}$$

is denoted as the global failure, to which the Global fragility curve

$$G_F(im) = P[F|im] \tag{13}$$

is associated.

Based on this information, two types of analysis and organization of the outcomes of seismic response are proposed: the failure mode analysis and the damage extension analysis, each providing a different information about the system vulnerability and a different support to the risk assessment and the decision-making process.

2.4.2.1 Analysis of the failure modes

The analysis is oriented to provide qualitative information about the bridge vulnerability, giving evidence to typical or recurrent failure modes. The outcome of the analysis not only provides a classification of the most recurrent failure modes of the bridge but also makes it possible to investigate their possible interactions, providing probabilities of joint events depending on the seismic intensity im. Results may be useful to choose the most effective type of retrofit action for the bridge oriented to the seismic risk mitigation.

For this purpose, the event F is partitioned into subsets of disjoint events M_l, with $l = 1, \dots N_M$, considering all the N_M possible combinations of failure types, such as the occurrence of only one failure mode and the coupling of two or more failure modes. As an example, if three failure modes A, B and C are possible, F is partitioned into seven sets (Figure 2.8): $F \setminus \cup(B, C)$, $F \setminus \cup(A, C)$, $F \setminus \cup(A, B)$, $\cap(A, C) \setminus B$, $\cap(B, C) \setminus A$, $\cap(A, B) \setminus C$, $\cap(A, B, C)$.

The probability of occurrence of F is the sum of the probability of M_l, i.e.

$$P[F] = \sum_l P\,[M_l] \tag{14}$$

and the fragility curve

$$G_{M_l}(im) = P[M_l|im] \tag{15}$$

describes the *l*-th failure scenario (combination of given damage modes).

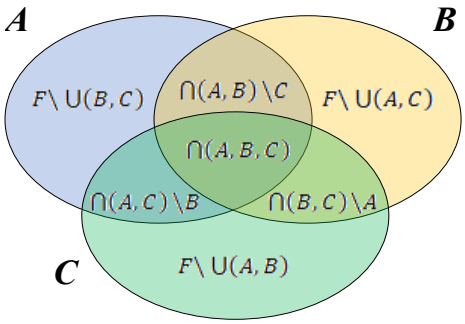

Figure 2.8. Analysis of failure modes concurring to the global failure F: example with three failure modes A, B and C.

As a result, the construction of the *multiple damage fragility curves* $G_{M_l}(im) = P[M_l|im]$ can be directly compared to the global fragility curve of the bridge $G_F(im) = P[F|im]$, that can be expressed as the envelope of the failure modes fragilities (see previous Eq.(14)). An example of realization of *multiple damage fragility curves* is shown in Figure 2.9, where different combination of failure modes are evaluated. In the case of Figure 2.9, the overcoming of damage performance level is associated to the components through a capital letter, following this criterion: B = damage on bearings; C = damage on cross beams; P = damage on piers. The global fragility results as a sum of the contribution of single or multiple failure modes occurring simultaneously at varying of *IM*. Since different numbers of mechanisms may be involved in damage at the varying of *IM*, *multiple damage fragility curves* do not necessarily have an increasing trend, so that the classical lognormal cumulative distribution function may be inadequate to fit the results. The resulting polygonal chain is considered sufficient to comment fragility results, and the research of an optimal fitting strategy is beyond the purposes of this work.

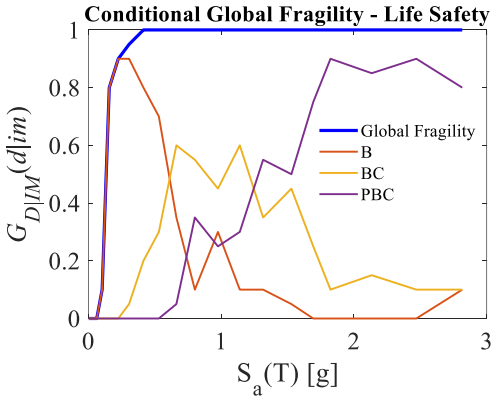

Figure 2.9. Probabilities of occurrence of damage mechanisms at Life Safety Limit State for combined mechanisms; in blue, the global fragility curve as the envelope of the single fragility curves.

2.4.2.2 *Analysis of the damage extension*

With reference to a specific failure mode, the analysis aims to provide a quantitative evaluation of the failure extension; the outcomes can be of interest for the assessment of losses due to earthquakes, since reconstruction or repair costs depend on the effective number of components affected by damage. In this case, the single failure type, e.g. A, is studied and the event is partitioned, based on its N_{Ak} components, in order to obtain information about the damage extension. This partition is based on the number of damaged elements, e.g. subsets S_{m}, m=1…N_{S}, may concern failures occurring in 1 element, 2 elements, … all the $N_{\mathrm{Ak}} = N_{\mathrm{S}}$ elements.

It is evident that each subset may collect failures of the same family occurring at different locations along the bridge because only the failure number is counted. In this sense, the approach may be not able to provide information about the distribution of damage but only about the damage extension.

The number of components is often high and it is generally useful to provide a rougher partition, $N_{\mathrm{S}} < N_{\mathrm{Ak}}$, joining some subsets, for example by considering situations for which failures involve increasing percentages of the overall elements of the family (e.g. up to 25%, from 25% to 50%, from 50% to 75% and from 75% to 100%), as schematically depicted in Figure 2.10 where the failure mode A is studied and S_1, S_2 and S_3 are used for events involving damage in the 25%, 50% and 75% of the elements of the family.

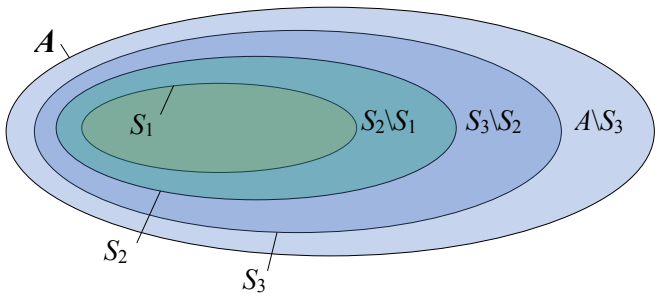

Figure 2.10. Analysis of the damage extension for the failure mode A: different subsets of damaged components.

As a consequence, subsets of disjoint events D_m can be considered, such that

$$\begin{cases} D_m = S_m & m = 1 \\ D_m = S_m / S_{m-1} & m = 2, \dots, N_D \end{cases} \tag{16}$$

being N_D the total number of possible combinations. It follows that the probability of A can also be defined as follows.

$$P[A] = \sum_{m=1}^{N_D} P[D_m] = P[S_1] + \sum_{m=2}^{N_D} P[S_m \backslash S_{m-1}] \tag{17}$$

There are different postprocessing analyses which can be consequently performed, each aimed to highlight a specific perspective of the damage situation. One might be interested in the fragility curves of disjointed failure subsets

$$G_{D_m}(im) = P[D_m|im] \tag{18}$$

relevant to specific intervals of damage extension (e.g., between 25% and 50% of damaged elements).

One might be also interested in assessing how the probability of a specific damage condition (e.g., 25% damaged elements) varies over the seismic intensity levels, thus a fragility curve expressed by

$$G_{S_m}(im) = P[S_m|im] \tag{19}$$

can be used. Finally, the exceedance probability of a given damage condition can be expressed through the following fragility function

$$G_{\bar{S}_m}(im) = P[\bar{S}_m|im] \tag{20}$$

in which $\bar{S}_m$ denotes the complementary event of S_m.

Herein, we will call this new fragility functions as the *quantitative fragility functions*. Since the quantitative fragility functions represent the probability that *at least* $X = N_S$ elements ($X \geq N_S$) experienced damage, each curve will have an increasing trend with the IM, as shown in the following Figure 2.11a.

Another possible construction of *quantitative fragility curves* that takes into account the number of elements that overcome a performance level requires to evaluate the *exact* percentage of elements that, at each IM level, undergo damage (i.e. $X = N_S$). In this case, different percentages result as complementary, and the sum of the probabilities of exceedance associated to different percentages is equal to the probability of exceedance of the entire element family, since the latter means that *at least one* element is subjected to damage, as previously explained. Also in this case, it is clear that fragility curves do not necessarily have an increasing trend; on the contrary, as *IM* level increases, an increase on the exceedance probabilities associated to higher percentages of involved elements is expected (Figure 2.11b). In this case, the adoption of the classical parametric lognormal cumulative distribution function is inadequate to fit the results. Herein, we will call this second type of fragility curves *discrete quantitative fragility curves*. The adoption of an optimal fitting strategy for these curves is beyond the purposes of this work.

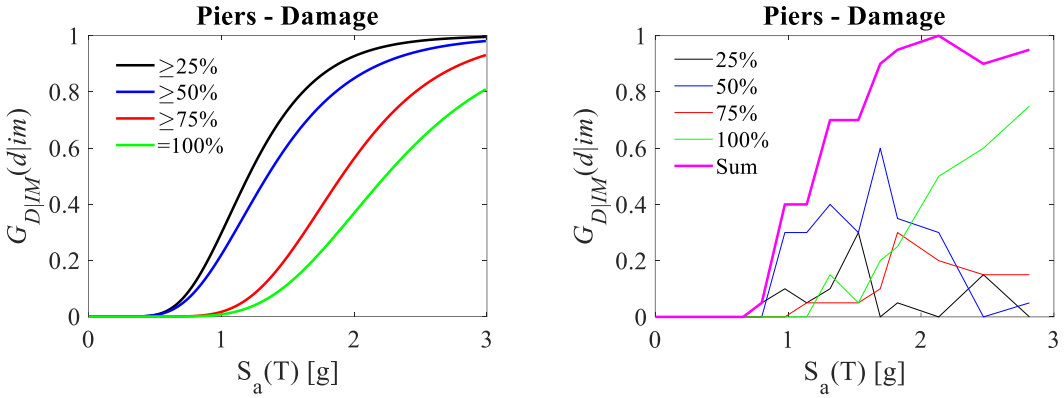

Figure 2.11. Example of (a) a quantitative fragility function and (b) a discrete quantitative fragility function: different percentages on the total number of bridge piers experiencing $D \geq d$ at Damage Limit State. In magenta, the non-fitted version of the fragility curve for piers.

2.5 Adopted methodology for the evaluation of Soil-Structure Interaction effects on the bridge fragility

A further effort to accurately define the bridge response under seismic excitation consists in the proper consideration of SSI effects on the bridge foundations. At this scope, several approaches can be adopted, from the most onerous from the computational point of view, in which both the structure, the foundation and the soil are explicitly modelled (Karapetrou et al., 2015), to the substructure method, that splits the analysis of the superstructure from the analysis of the subsoil domain, under the hypothesis of a linear or linear equivalent behaviour for the soil (Wolf, 1985; Carbonari et al., 2012). In the latter case, two could be the outcomes of the SSI analysis: the direct use of the derived Impedance and Foundation Input Motion (FIM) functions, which describe the behaviour of the combined system foundation-soil, for the superstructure analysis in the frequency domain of interest (Bolisetti et al., 2015), or the further simplification of these functions through the approximation with a Lumped Parameter Model (LPM), obtained by assembling springs, masses and dashpots, which could be more easily employed for structural analysis and applied in the time domain, where the nonlinear response of the superstructure can be observed (Carbonari et al., 2018).

In line with the need of simplification of SSI analysis procedures, in the wake of the work started by Carbonari et al. (Carbonari et al., 2018), Morici et al. (Morici et al., 2019) presented a LPM for the approximation of the dynamic impedances of pile groups and provided closed-form formulas for estimating parameters of the model for foundations in homogeneous soil deposits in case of end-bearing piles. The analysed foundations are characterized by a different number of piles (single pile or pile groups) crossing a deformable shallow soil layer of different stiffness and embedded for three diameters into

an underlying bedrock. The lumped model can capture the roto-translational, vertical and torsional behaviour that characterises the response of pile groups. The dataset is obtained by performing dynamic analyses of soil-foundation systems in homogenous soil deposits by means of the numerical model developed by Dezi et al. (Dezi et al., 2016), which provides impedances of pile groups, and by optimising parameters of the lumped models through a linear regression approach. Formulas, that may be implemented in simple spreadsheets, allow defining restraint systems that can be physically reproduced in common software for structural analysis, avoiding the (*i*) evaluation of the dynamic impedance functions and the (*ii*) LPMs selection and calibration process.

In this Thesis, the formulas estimating the LPM by (Carbonari et al., 2018) and proposed in (Morici et al., 2019) is adopted. In the following, a recall on the adopted tools for the building of the LPM and the main results obtained in the work by Morici et al. (Morici et al., 2019) with reference to bridge pier foundations are presented. In particular, the efficiency of the proposed formulas in assuring a reliable evaluation of the seismic response of bridge piers, with respect to that obtained from a more rigorous approach for the analysis of the SSI problem, are presented and discussed with reference to some case studies. Indeed, the seismic SSI analysis of four bridge piers founded on different soils is performed and the proposed LPM, with parameters estimated by the proposed closed formulas, is adopted to simulate the soil-foundation dynamic behaviour. Inertial interaction analyses are thus performed without the need of a frequency domain analysis of the soil-foundation system, assuming the foundation input motion to be equal to the free-field one. Results of the analyses are compared with those achieved through a rigorous approach considering the actual frequency-dependent soil-foundation impedances and foundation input motion. Results of fixed base applications are included to highlight the significance of the SSI problem for the selected analysis cases.

2.5.1 Recall of adopted tools

2.5.1.1 Numerical model for the dynamic analysis of the soil-foundation system

Impedances are obtained performing dynamic analyses of case studies through the numerical model developed by Dezi et al. (Dezi et al., 2016); piles are modelled with 2-node beam elements with third order and linear polynomials for the interpolation of transverse and longitudinal displacements, respectively, while the soil is assumed to be constituted by independent horizontal infinite visco-elastic layers. Displacement components of the soil are not physically included in the problem formulation since the soil-pile interaction and the radiation damping are taken into account in the frequency domain by means of elastodynamic Green's functions available in the literature, inherited from the plane strain problem (Dobry et al., 1982; Gazetas & Dobry, 1984; Makris & Gazetas, 1993). The presence of a rigid cap is accounted for by constraining displacements of the pile heads. The model allows performing kinematic soil-foundation interaction analysis of pile groups with generic number of piles, layout and piles

inclination and permits the derivation of the soil-foundation impedance matrix through the problem condensation on the rigid cap degrees of freedom.

Taking into account the investigated soil-foundation layout (Figure 2.12a) and the variability of geometric and mechanical parameters that will be considered in the sequel for the formulas calibration, some applications are herein presented to show the suitability of the model in estimating impedances of the selected end-bearing foundations. Potential critical scenarios constituted by low pile slenderness ratios and high impendence contrasts between the deformable layer and the bedrock are included. Components of impedance matrixes obtained with the numerical model developed Dezi et al. (Dezi et al., 2016) are compared with those obtained from a refined 3D finite element model, developed in ANSYS. In details, geometric and mechanical properties of soils and foundations are reported in Figure 2.12b in a non-dimensional form, derived from the formal application of the Buckingham's theorem (Buckingham, 1914).

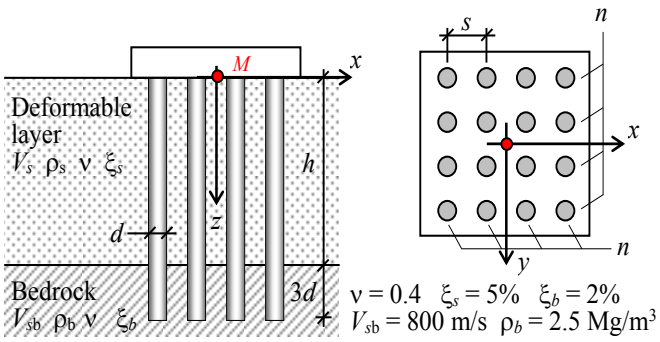

(a)

n	$\frac{s}{d}$	$\frac{h}{d}$	$\frac{E_p}{\rho_s V_s^2}$	& $\frac{\rho_p}{\rho_s}$
2	2.0	14	1500	1.6058
4	4.0	28	150	1.2854

(b)

Figure 2.12. (a) Soil-foundation layouts and (b) selection of geometric and mechanical parameters.

Taking into account the double symmetry of case studies, and considering the reference system frame of Figure 2.12a, the non-dimensional soil-foundation impedance matrix assumes the form

$$\boldsymbol{\Pi}(a_0) = \begin{bmatrix} \Pi_x(a_0) & 0 & 0 & 0 & \Pi_{x-ry}(a_0) & 0 \\ & \Pi_x(a_0) & 0 & -\Pi_{x-ry}(a_0) & 0 & 0 \\ & & \Pi_z(a_0) & 0 & 0 & 0 \\ & & & \Pi_{ry}(a_0) & 0 & 0 \\ & sym & & & \Pi_{ry}(a_0) & 0 \\ & & & & & \Pi_{rz}(a_0) \end{bmatrix} \quad (21)$$

where

$$\Pi_i(a_0) = \frac{\Im_i}{\rho_s V_s^2 d} \qquad \text{with } i = x, z \quad (22a)$$

$$\Pi_{ri}(a_0) = \frac{\Im_{ri}}{\rho_s V_s^2 d^3} \qquad \text{with } i = x, z \tag{22b}$$

$$\Pi_{x-ry}(a_0) = \frac{\Im_{x-ry}}{\rho_s V_s^2 d^2} \tag{22c}$$

are the non-dimensional transverse, rotational and coupled roto-translational impedances of the soil-foundation systems, obtained starting from the relevant dimensional components $\Im_i$, $\Im_{ri}$ and $\Im_{x-ry}$ (with $i = x, z$). In Equations (21) and (22), $a_0 = \omega d/V_s$ is non-dimensional circular frequency.

The refined 3D model is developed adopting 8-node linear brick elements to model a quarter of a cylindrical soil portion with radius R and height H satisfying conditions $R/d = 70$ and $H/d = 70$ (Figure 2.13a). A viscoelastic material model is adopted for the soil and infinite elements are provided at the boundaries to absorb the outgoing waves, satisfying the radiation condition. Piles are modelled with 2-node cubic beam elements and their physical dimensions are considered removing the relevant soil cylinders (Figure 2.13b). The beam-solid coupling is assured exploiting potentials of the adopted software. Piles are connected at the head by a rigid constraint (Figure 2.13b) and meshing criteria aimed at obtaining an as much as possible structured mesh and assuring a sufficient number of nodes per wavelength are adopted. Some accuracy analyses are preliminarily performed to define the mesh dimension in order to balance results reliability with computational efforts; the selected mesh dimension assures that the propagation of waves with frequency up to 15 Hz is well captured. Analogously to (Dezi et al., 2016), a highly refined vertical mesh is used for the pile (0.5 m), since the computational effort is overall very low.

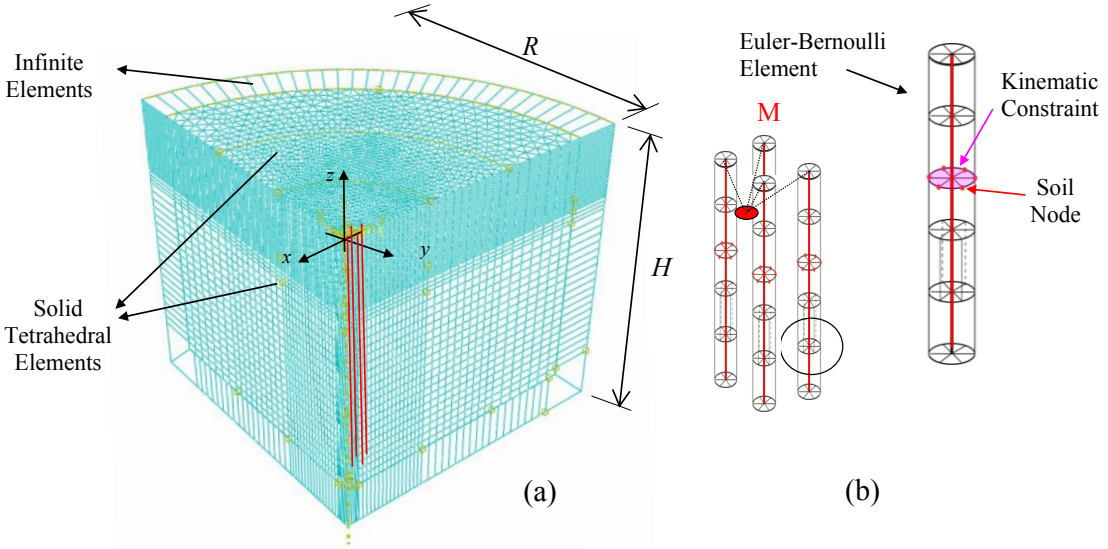

Figure 2.13. 3D refined finite element model.

Soil-foundation impedances from the refined 3D model are obtained by imposing unit steady harmonic displacements at the fully restrained master node and evaluating the

relevant reaction forces; symmetry or emisymmetry conditions are imposed at boundaries, depending on the investigated component of the impedance matrix.

For the sake of brevity only some results obtained from the applications are shown in the sequel. Figure 2.14 refers to the non-dimensional real and imaginary parts of the translational, vertical, rotational and coupled roto-translational impedances of the 2x2 pile group with $s/d = 4$, $h/d = 14$ and different $E_p/(\rho_s V_s^2)$ ratios. Results of the 3D refined finite element model are reported with symbols while continuous lines are used for results of the adopted model. Cut-off effects are evident in the horizontal, vertical and coupled roto-translational impedances, especially in the case of soft soils, while for stiff soils effects appear of less significance. Also, for the rotational impedance, cut-off effects do not modify sensibly the overall trends of both real and imaginary parts. From an engineering point of view, despite it is not able to capture local trends of impedances due to cut-off effects, the numerical model developed by Dezi et al. (Dezi et al., 2016) is overall capable of reproducing the behaviour of soil-foundation systems evaluated through the 3D refined model in the frequency range 0÷10 Hz, which may be considered of practical interest in earthquake engineering because it both includes the highest energy content of earthquakes and the fundamental frequencies of civil structures.

Similarly, Figure 2.15 refers to the non-dimensional real and imaginary parts of the translational, vertical, rotational and coupled roto-translational impedances of the 4x4 pile group with $s/d = 2$, $h/d = 28$ and different $E_p/(\rho_s V_s^2)$ ratios. As expected, in view of the higher soil layer thickness overlying the bedrock, cut-off effects are less important and only clearly evident for the coupled roto-translational behaviour of the selected case studies.With reference to the horizontal impedance, the adopted model (Dezi et al., 2016) slightly underpredicts the response of the 3D model in the case of stiff soils and overpredicts that relevant to soft soils, in the low frequency range. Greatest inaccuracies affect the vertical stiffness in the case of soft soils and the coupled roto-translational one, for both stiff and soft soils; in these cases, the response differs of about 20% from that of the 3D refined solid model.

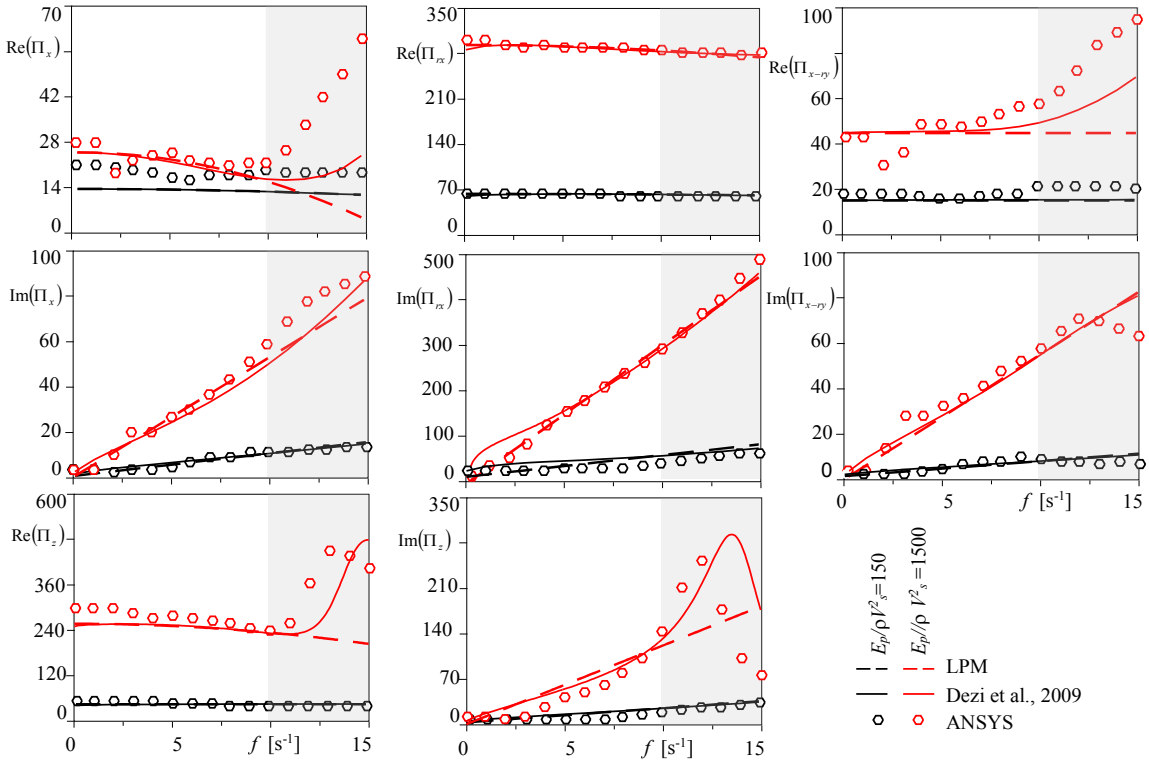

Figure 2.14. Impedances of 2x2 pile groups with s/d = 4, h/d = 14 and different E_p/E_s ratios.

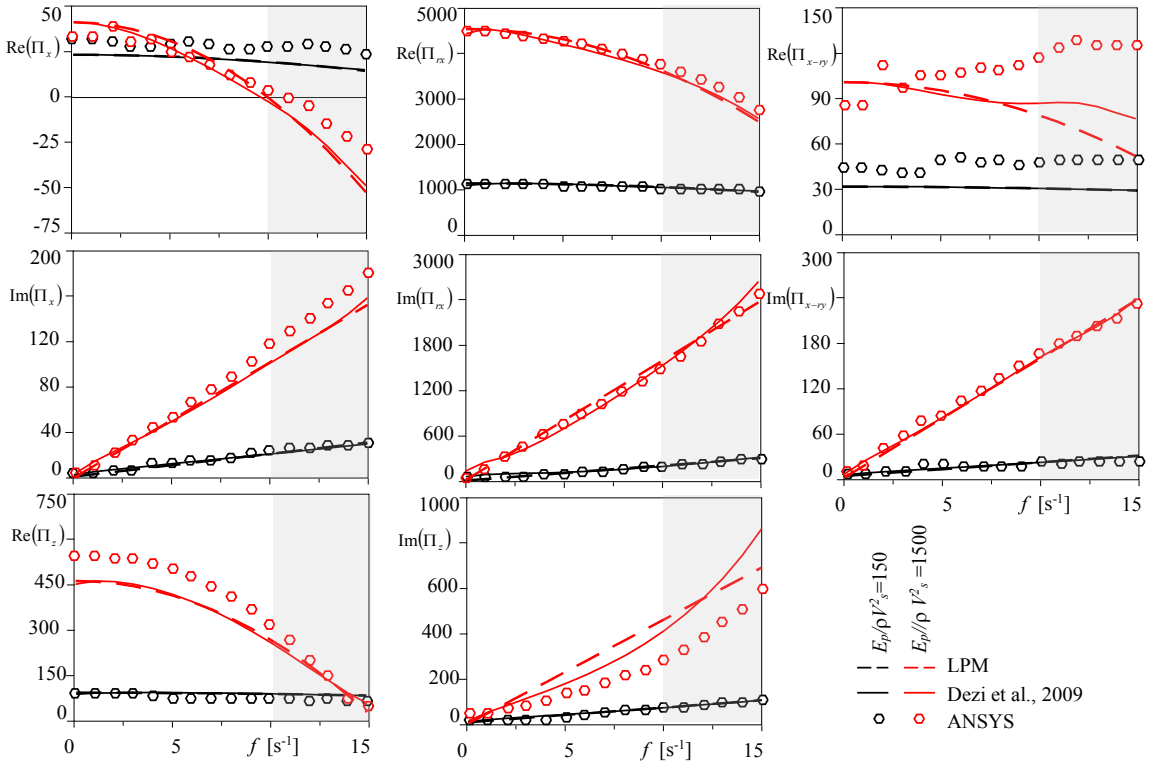

Figure 2.15. Impedances of 4x4 pile groups with s/d = 2, h/d = 28 and different E_p/E_s ratios.

2.5.1.2 Lumped Parameter Model

The lumped model presented by Carbonari et al. (Carbonari et al., 2018) and depicted in Figure 2.16 is considered in this work. As already stated, because of the symmetry of the system, the foundation is characterised by uncoupled vertical and torsional responses, whereas horizontal displacements and relevant rotations are coupled as usual for deep foundations. Furthermore, the double symmetry of the system makes the roto-translational responses uncoupled between planes *xz* and *yz*, too. The adopted LPM reflects above aspects and is obtained assembling independent sub-LPMs, as presented in Figure 2.16, which refer the uncoupled behaviours of the soil-foundation systems. The square layout of the pile group implies that the whole system is characterized by 18 parameters, namely: translational and rotational masses, lumped at the master node of the rigid cap (4 parameters), elastic and viscous constants that define the relevant spring-dashpot elements also applied at the master node (8 parameters) and additional eccentric springs, dashpots and masses (3 parameters), connected to the master node by rigid links of different lengths (3 parameters). Eccentric components are introduced to catch the coupling between the rotation and the translation in *x* and *y* directions.

Following a formal non-dimensional approach (Buckingham, 1914) for the formulation of the system impedance matrix, the following expressions hold for parameters of the lumped model

$$k_i = \rho_s V_s^2 d\left(\Omega_1 - \Omega_4 \frac{d}{h_{ki}}\right), m_i = \rho_s d^3\left(\Omega_2 - \Omega_5 \frac{d}{h_{mi}}\right), \quad c_i = \rho_s V_s d^2\left(\Omega_3 - \Omega_6 \frac{d}{h_{ci}}\right) \tag{23a, b, c}$$

$$k_{ih} = \Omega_4 \frac{\rho_s V_s^2 d^2}{h_{ki}}, m_{ih} = \Omega_5 \frac{\rho_s d^4}{h_{mi}}, c_{ih} = \Omega_6 \frac{\rho_s V_s d^3}{h_{ci}} \tag{24d, e, f}$$

$$k_{ri} = \rho_s V_s^2 d^3\left(\Omega_7 - \Omega_4 \frac{h_{ki}}{d}\right), I_i = \rho_s d^5\left(\Omega_8 - \Omega_5 \frac{h_{mi}}{d}\right), \quad c_{ri} = \rho_s V_s d^4\left(\Omega_9 - \Omega_6 \frac{h_{ci}}{d}\right) \tag{25g, h, i}$$

$$k_z = \Omega_{10}\rho_s V_s^2 d\ , m_z = \Omega_{11}\rho_s d^3\ , c_z = \Omega_{12}\rho_s V_s d^2 \tag{26j, k, l}$$

$$k_{rz} = \Omega_{13}\rho_s V_s^2 d^3\ , I_z = \Omega_{14}\rho_s d^5\ , c_{rz} = \Omega_{15}\rho_s V_s d^4 \tag{27m, n, o}$$

where Ωi ($i = 1 \ldots 15$) are the non-zero non-dimensional components of the lumped system impedance matrix

$$\tilde{\boldsymbol{\Pi}}(\boldsymbol{\Omega}, a_0) = \bar{\boldsymbol{K}}(\boldsymbol{\Omega}) - a_0^2 \bar{\boldsymbol{M}}(\boldsymbol{\Omega}) + i a_0 \bar{\boldsymbol{C}}(\boldsymbol{\Omega}) \tag{24}$$

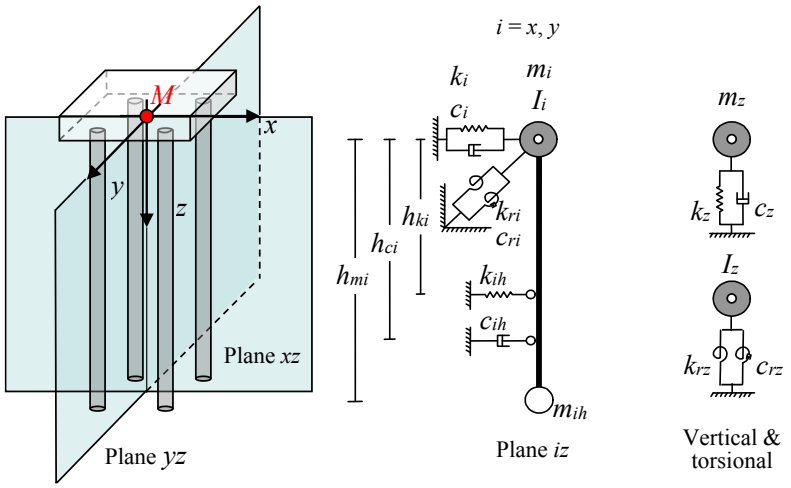

Figure 2.16. Assemblage of uncoupled LPMs.

In Equation (24),

$$\overline{\mathbf{K}} = \begin{bmatrix} \Omega_1 & 0 & 0 & 0 & \Omega_4 & 0 \\ & \Omega_1 & 0 & -\Omega_4 & 0 & 0 \\ & & \Omega_{10} & 0 & 0 & 0 \\ & & & \Omega_7 & 0 & 0 \\ & sym & & & \Omega_7 & 0 \\ & & & & & \Omega_{13} \end{bmatrix} \quad \overline{\mathbf{M}} = \begin{bmatrix} \Omega_2 & 0 & 0 & 0 & \Omega_5 & 0 \\ & \Omega_2 & 0 & -\Omega_5 & 0 & 0 \\ & & \Omega_{11} & 0 & 0 & 0 \\ & & & \Omega_8 & 0 & 0 \\ & sym & & & \Omega_8 & 0 \\ & & & & & \Omega_{14} \end{bmatrix} \tag{25a, b}$$

$$\overline{\mathbf{C}} = \begin{bmatrix} \Omega_3 & 0 & 0 & 0 & \Omega_6 & 0 \\ & \Omega_3 & 0 & -\Omega_6 & 0 & 0 \\ & & \Omega_{12} & 0 & 0 & 0 \\ & & & \Omega_9 & 0 & 0 \\ & sym & & & \Omega_9 & 0 \\ & & & & & \Omega_{15} \end{bmatrix} \tag{25c}$$

Parameters h_{ki}, h_{ci}, h_{mi} appearing at the right-hand side of Equations (23) are arbitrarily chosen according to the following conditions

$$\begin{cases} \operatorname{sgn} h_{ki} = \operatorname{sgn} \Omega_4 \\ \left|\frac{\Omega_4}{\Omega_1}\right| d \le |h_{ki}| \le \left|\frac{\Omega_7}{\Omega_4}\right| d \end{cases} \quad \begin{cases} \operatorname{sgn} h_{mi} = \operatorname{sgn} \Omega_5 \\ \left|\frac{\Omega_5}{\Omega_2}\right| d \le |h_{mi}| \le \left|\frac{\Omega_8}{\Omega_5}\right| d \end{cases} \quad \begin{cases} \operatorname{sgn} h_{ci} = \operatorname{sgn} \Omega_6 \\ \left|\frac{\Omega_6}{\Omega_3}\right| d \le |h_{mi}| \le \left|\frac{\Omega_9}{\Omega_6}\right| d \end{cases} \tag{26a, b, c}$$

in order to assure positive signs to springs and dashpots coefficients, as well as masses. It is worth noting that real parts of the LPM impedance matrix are second order parabolas in the non-dimensional frequency a_0, while imaginary parts vary linearly. The non-dimensional parameters Ω_i ($i = 1 \ldots 15$) of the LPM impedance matrix appearing in Equation (23) have to be calibrated to reproduce components of the soil-foundation impedance matrix (21) evaluated with a dedicated software (e.g. Dezi et al., 2016, Padrón

et al., 2008). Details of a linear least square calibration strategy that allows computing the best set of parameters of the lumped system can be found in (Carbonari et al., 2018). In Figure 2.14 and Figure 2.15 impedances of LPMs suitably calibrated with the mentioned procedure are shown with dashed lines. The adopted lumped system is able to well capture trends of impedances (both real and imaginary parts) in the frequency range 0÷10 Hz.

2.5.2 Formulas for estimating LPM parameters of end-bearing pile groups

Closed-form empirical formulas to estimate parameters parameters Ω_i of the LPMs representative of square r.c. end-bearing pile groups are presented in this section. A wide number of cases, representative of foundations with square layouts constituted by reinforced concrete piles embedded in deformable homogeneous shallow soils from low to high stiffness and socked for 3 diameters in the underlying seismic bedrock (Figure 2.17a), are considered; the LPM parameters are calibrated to best fit the soil-foundation impedances in the frequency range 0÷10 Hz. In details, analysis cases are obtained by varying the number of piles *n*, the pile spacing-diameter ratio *s/d*, the pile length-diameter ratio *h/d* and the stiffness ratio $E_p/(\rho_s V_s^2)$, where E_p is the Young modulus of the pile material and ρ_s and V_s are the density and the shear wave velocity of the soil, respectively. Values attributed to the above non-dimensional parameters are listed in Figure 2.17b. For all cases, a constant Poisson's ratio $\nu = 0.4$ and soil hysteretic damping ratios $\xi_s = 0.05$ are assumed. Fixed values for the pile-soil density ratio ρ_p/ρ_s are assumed for each $E_p/(\rho_s V_s^2)$ratio since preliminary applications revealed that the influence of ρ_p/ρ_s on impedances is limited. Combination of parameters generates a total of 1470 analysis cases, which constitute the dataset from which formulas are calibrated. It is worth noting that the optimization procedure is constrained to give positive definite matrices and positive masses, to guarantee the system implementation in commercial software for structural analysis (which generally do not allow introducing negative masses). Positivity of masses in some cases enforces solutions with null mass values; this circumstance is typical of impedance functions characterized by almost flat real parts or slightly increasing with frequency in the selected frequency range of calibration. (e.g. some translational or rotational terms of Figure 2.14 and Figure 2.15).

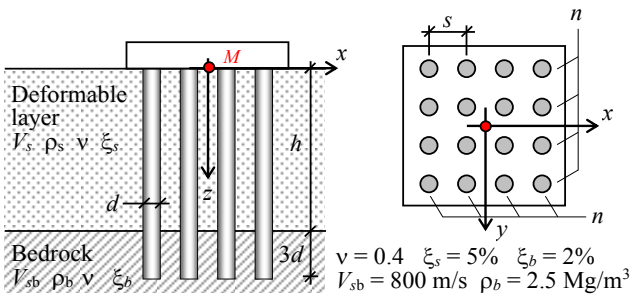

(a)

n	$\frac{s}{d}$	$\frac{h}{d}$	$\frac{E_p}{\rho_s V_s^2}$ & $\frac{\rho_p}{\rho_s}$	
1	2.0	12	2000	1.67
2	2.5	14	1500	1.6058
3	3.0	16	1000	1.5416
4	3.5	18	442	1.4700
5	4.0	20	300	1.3802
		22	150	1.2854
		24	94	1.2500
		26		
		28		
		30		

(b)

Figure 2.17. (a) Scheme of investigated soil-foundation systems and (b) non-dimensional parameters.

Expressions defined for the generic non-dimensional parameter Ω_i ($i = 1 \ldots 15$) are reported below.

$$\Omega_{1,4,5,6} = \alpha_i \left(\frac{s}{d}\right)^{\beta_i} \left(\frac{\rho_p}{\rho_s}\right)^{\chi_i} \left(\frac{E_p}{\rho_s V_s^2}\right)^{\delta_i} \tag{27a}$$

$$\Omega_{2,3,13,14,15} = \left(\frac{s}{d}\right)^{\alpha_i} \left(\frac{\rho_p}{\rho_s}\right)^{\beta_i} \left[\chi_i \left(\frac{E_p}{\rho_s V_s^2}\right)^2 + \delta_i \frac{E_p}{\rho_s V_s^2} + \varepsilon_i\right] \tag{27b}$$

$$\Omega_7 = \left(\alpha_i \left(\frac{s}{d}\right)^{\lambda} + \beta_i\right) \left[\chi_i \left(\frac{E_p}{\rho_s V_s^2}\right)^2 + \delta_i \frac{E_p}{\rho_s V_s^2} + \varepsilon_i\right] \left(\frac{\rho_p}{\rho_s}\right)^{\varphi_i} \left(\frac{L}{d}\right)^{\phi_i} \tag{27c}$$

$$\Omega_{8,9} = \left[\alpha_i \left(\frac{s}{d}\right)^{2\lambda} + \beta_i \left(\frac{s}{d}\right)^{\lambda} + \chi_i\right] \left[\delta_i \left(\frac{E_p}{\rho_s V_s^2}\right)^2 + \varepsilon_i \frac{E_p}{\rho_s V_s^2} + \varphi_i\right] \left(\frac{\rho_p}{\rho_s}\right)^{\phi_i} \left(ln \frac{L}{d}\right)^{\gamma_i} \tag{27d}$$

$$\Omega_{10} = \left(\frac{s}{d}\right)^{\alpha_i} \left[\beta_i \left(\frac{E_p}{\rho_s V_s^2}\right)^2 + \chi_i \frac{E_p}{\rho_s V_s^2} + \delta_i\right] \left(\frac{\rho_p}{\rho_s}\right)^{\varepsilon_i} \left(\frac{L}{d}\right)^{\varphi_i} \tag{27e}$$

$$\Omega_{11,12} = \psi_i \left(\frac{s}{d}\right)^{\alpha_i} \left(\frac{\rho_p}{\rho_s}\right)^{\beta_i} \left(\frac{E_p}{\rho_s V_s^2}\right)^{\chi_i} \left[\delta_i \left(\frac{L}{d}\right)^2 + \varepsilon_i \frac{L}{d} + \varphi_i\right] \tag{27f}$$

In Equation (27c and 27d)

$$\lambda = 0 \text{ for } n = 1 \tag{28a}$$

$$\lambda = 1 \text{ for } n > 1 \tag{28b}$$

while in Equation (27f)

$$\psi = 0 \text{ for } \frac{E_p}{\rho_s V_s^2} < \kappa_i \tag{28a}$$

$$\psi = 1 \text{ for } \frac{E_p}{\rho_s V_s^2} \geq \kappa_i \tag{28b}$$

Constants appearing in Equations (27) and (28) are reported in Table A in the Appendix at the end of this Thesis for foundations with different number of piles.

Figure 2.18 compares the non-dimensional parameters Ω_i optimised according to (Carbonari et al., 2018) with values obtained from the proposed formulas. Parameters Ω_1, Ω_3, Ω_4 are reproduced closely, with errors lower than 30% (dotted lines in Figure 2.18). On the contrary, parameters Ω_5, Ω_8 and Ω_{11}, representative of mass terms, present errors sensibly higher; all the remaining parameters are characterised by errors of about 30% (with few exceptions). Errors relevant to masses are due to perturbations induced by the positivity condition in the LPM calibration procedure. The overall suitability of the proposed formulas in capturing the optimised parameters of the LPMs is quantified through the coefficients of determination (R-squared coefficients) presented in Table 2.1. It should be noted that most of the computed R-squared parameters, including mean values obtained by averaging those of pile groups with different number of piles, are greater than 0.9, excepting those relevant to Ω_5. Furthermore, in a very high number of

cases, the R-squared coefficients are higher than 0.95. Finally, to provide a pictorial view of the formulas capabilities in predicting parameters of the optimised LPM, Figure 2.19 shows components Π_i of the non-dimensional impedance matrix for the 4x4 pile groups with s/d = 2.5, h/d = 18 and different ratios, obtained from the dynamic analysis (Dezi et al., 2016), from the LPM calibration (LPM_C) and from the proposed formulas (LPM_F). The proposed LPM, suitably calibrated, can approximate the soil-foundation dynamic stiffness very well in the optimization frequency range 0÷10 Hz with minor discrepancies affecting the imaginary parts at low frequencies, especially for the rotational (Π_{ry}) component. Differences between the dynamic behaviour of LPM_C and LPM_F are overall very limited and mainly affect the torsional impedance (Π_{rz}).

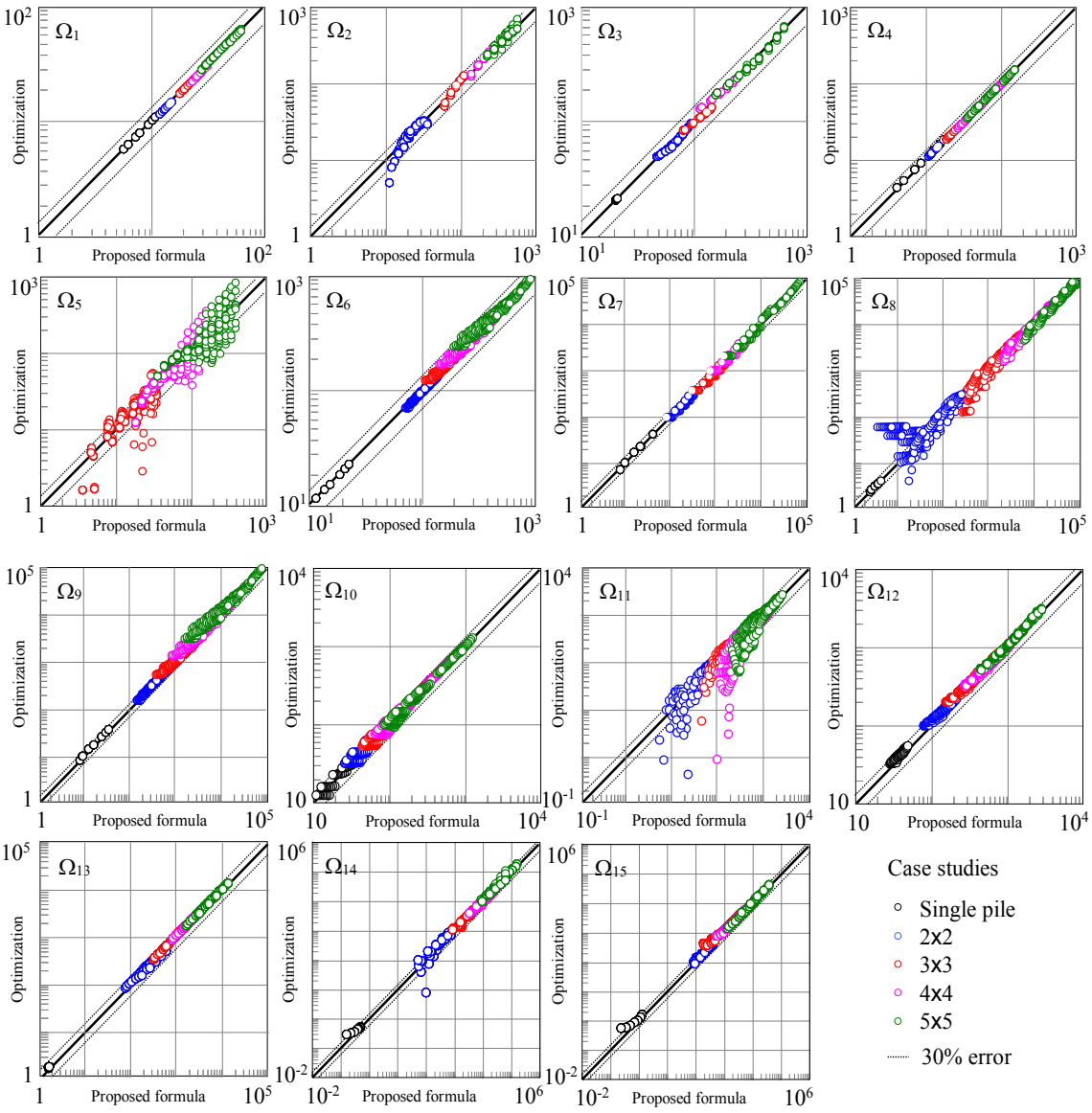

Figure 2.18. Comparisons between the optimized non-dimensional parameters of the LPMs and the proposed formulas.

Table 2.1. R-squared coefficients.

	Ω_1	Ω_2	Ω_3	Ω_4	Ω_5	Ω_6	Ω_7	Ω_8	Ω_9	Ω_{10}	Ω_{11}	Ω_{12}	Ω_{13}	Ω_{14}	Ω_{15}
1	1.00	---	0.81	1.00	---	1.00	1.00	1.00	1.00	0.99	---	0.91	0.94	1.00	0.99
2x2	1.00	0.89	0.98	1.00	---	1.00	0.99	0.94	0.99	1.00	0.98	0.97	1.00	0.94	0.97
3x3	1.00	0.93	0.99	1.00	0.79	1.00	0.99	0.94	0.99	1.00	0.97	0.98	1.00	0.99	0.99
4x4	1.00	0.97	0.99	1.00	0.72	1.00	0.99	0.98	0.99	1.00	0.93	0.99	1.00	0.99	1.00
5x5	1.00	0.97	0.99	1.00	0.72	1.00	0.99	0.98	0.99	1.00	0.93	0.99	1.00	0.99	1.00
Mean	**1.00**	**0.94**	**0.95**	**1.00**	**0.72**	**1.00**	**0.99**	**0.97**	**0.99**	**1.00**	**0.95**	**0.97**	**0.99**	**0.98**	**0.99**

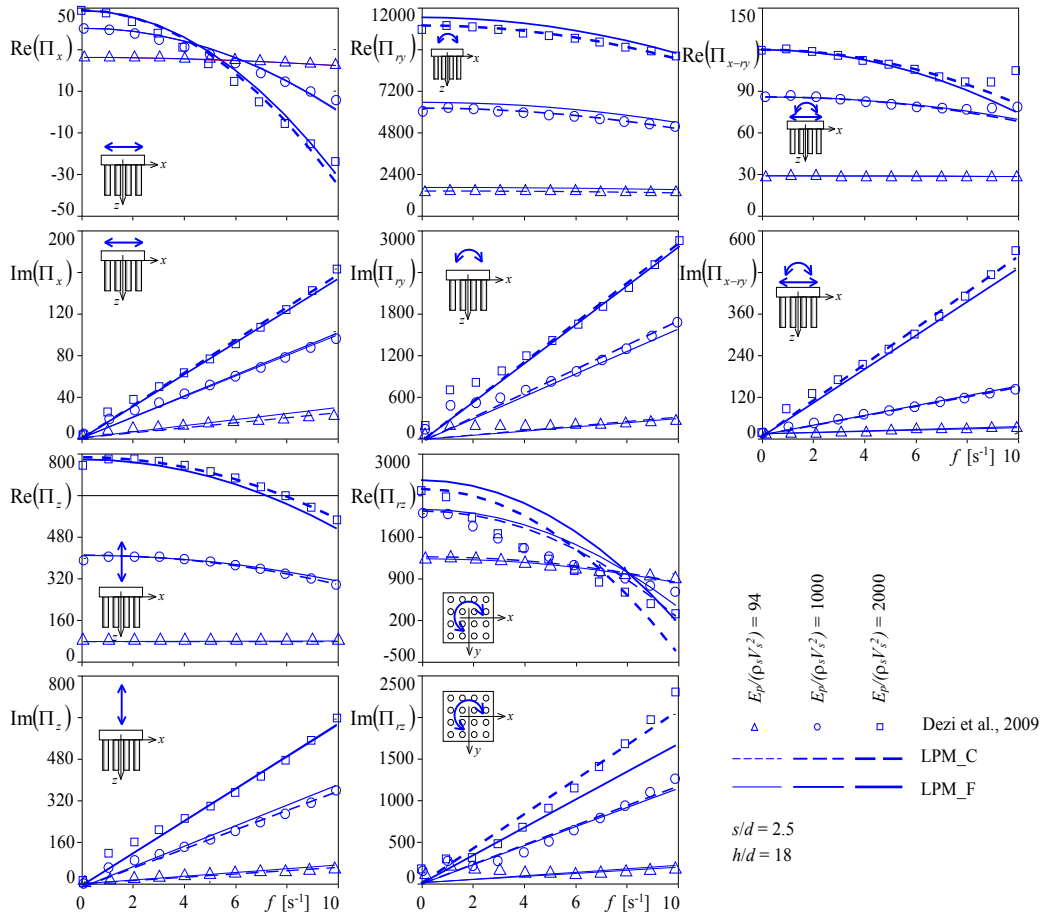

Figure 2.19. Impedances of 4x4 pile groups: comparisons of benchmarks with impedances of LPM_C and LPM_F.

2.5.3 Application of the proposed formulas

Proposed formulas can be exploited to simplify the computational effort of seismic SSI analysis of structures, in the framework of the substructure approach, which classically requires the definition of the frequency-dependent compliant structural restraints and the evaluation of the foundation input motion. Above quantities, usually obtained through frequency domain analysis of the soil-foundation system, have to be further elaborated in order to be used in time domain inertial SSI analysis of the superstructures: soil-

foundation impedances must be reproduced by means of calibrated lumped systems and time histories of the foundation input motion must be computed by the inverse Fourier transform. In this framework, proposed closed-form expressions directly provide parameters of the lumped system approximating the frequency-dependent impedance functions of the soil-foundation system, largely simplifying the overall procedure, especially if the free-field motion is assumed to be equal to the foundation input one.

2.5.3.1 Case studies

By assuming the foundation input motion to coincide with the free-field motion (Mamoon & Banerjee, 1990; Fan et al., 1991), formulas proposed in §2.5.2 are herein used to evaluate LPMs to perform SSI analyses of some bridge piers (Figure 2.20a) characterised by different fundamental periods. The scheme may be representative of the transverse response of multi-span bridges with decks not connected at the abutments in the transverse direction, or with dual load path mechanisms, for what concern the transverse seismic behaviour of inner piers (Capatti et al., 2017). Focusing on the deck and foundation displacements due to seismic actions acting in the x direction (i.e. transverse bridge direction), piers are modelled with rigid elements and the elastic deformability is lumped at end rotational viscoelastic springs with stiffness K_ϕ and damping C_ϕ (Figure 2.20b). Pile and bent caps are assumed to be rigid, with masses m_c and m_f, and moment of inertia I_c and I_f, respectively. Furthermore, m_d and m_p are the masses of the bridge deck belonging to the pier and the mass of the pier, respectively, while I_d is the deck moment of inertia. Finally, h_d, h_c, h_p and h_f are geometric parameters depicted in Figure 2.20b. Four piers (P1, P2, P3, P4), characterised by properties reported in Table 2.2, are considered and assumed to be founded on 2x2 and 4x4 reinforced concrete pile groups with h/d = 20 and s/d = 3, according to schemes of Figure 2.17a. Soft soil conditions (i.e $E_p/(\rho_s V_s^2)$ = 1000) are considered in order to promote significance of SSI effects. With reference to the soil-foundation systems, mechanic and geometric dimensional parameters are obtained assuming E_p = 30000 MPa and ρ_p = 2.5 t/m^3. Finally, 5% structural damping is introduced in terms of stiffness proportional damping.

The response of the bridge piers on Compliant Base (CB) (Figure 2.20b) are computed considering both the LPM, with parameter obtained through the proposed formulas (CB-LPM), and the soil-foundation impedances (CB-IMP) resulting from the numerical procedure of Dezi et al. (Dezi et al., 2016). Furthermore, the response of piers on Fixed Base (FB) (Figure 2.20c) is also computed in order to evaluate significance of SSI effects on the bridge response and suitably weight discrepancies between the rigorous and simplified evaluation of the soil-foundation impedances.

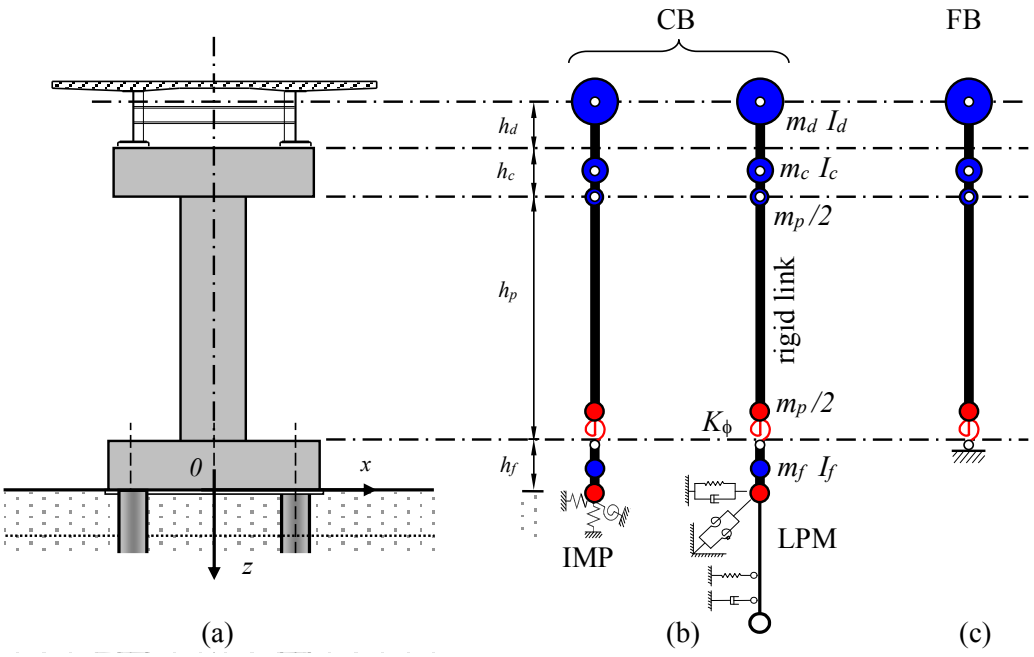

Figure 2.20. (a) Lateral view of one bridge pier; (b) CB models and (c) FB model.

Table 2.2. Superstructure and foundation parameters of bridge piers.

Superstructure	**P1**	**P2**	**P3**	**P4**
Foundation	**2x2**	**2x2**	**4x4**	**4x4**
m_d [t]	305.8	305.8	305.8	305.8
I_d [t m^2]	2466.6	2466.6	2466.6	2466.6
h_d [m]	0.59	0.59	0.59	0.59
m_c [t]	88.3	88.3	88.3	88.3
I_c [t m^2]	426.6	426.6	426.6	426.6
h_c [m]	1.80	1.80	1.80	1.80
m_p [t]	57.6	121.1	196.0	253.6
h_p [m]	5.0	10.5	17.0	22.0
h_f [m]	1.50	1.50	2.00	2.00
m_f [t]	95.6	95.6	326.2	326.2
I_f [t m^2]	217.0	217.0	1848.4	1848.4
K_ϕ [MN/rad]	23067.6	10984.6	6784.6	5242.6
FB period [s]	0.2001	0.50082	1.0076	1.4841

Since accuracy of LPMs in reproducing impedances of the soil-foundation system may vary with frequency, each pier, characterised by a specific fundamental period, is analysed considering seismic actions with different frequency contents, selected from both the Europeans Strong motion Database (ESD) (Ambraseys et al., 2004) and the Italian database Itaca (IT) (Luzi et al., 2017). The adopted earthquakes with high magnitude M_w registered by stations on different soil types are reported in Table 2.3, while Figure 2.21 shows the relevant acceleration time histories and Fourier amplitude spectra from which the earthquakes frequency content can be evaluated.

Table 2.3. Selected earthquakes.

ID	Earthquake	Station	Soil Type	Date	M_w	Δ[km]	PGA [g] (*x*)
ESD287	Campano Lucano	ST93	A	23/11/80	6.9	23	0.18
ESD290	Campano Lucano	ST96	A	23/11/80	6.9	32	0.32
ESD292	Campano Lucano	ST98	A	23/11/80	6.9	25	0.06
ESD428	Etolia	ST169	A	18/05/88	5.3	23	0.18
ESD593	Umbria-Marche	ST60	B	26/09/97	5.7	13	0.27
ESD595	Umbria-Marche	ST83	B	26/09/97	5.7	25	0.04
ESD601	Umbria-Marche	ST224	C	26/09/97	5.7	27	0.05
ESD759	Umbria-Marche	ST265	B	26/09/97	5.7	32	0.04
ESD4675	South Iceland	ST2487	A	17/06/00	6.5	13	0.13
ESD6965	Izmit (aftershock)	ST3270	D	13/09/99	5.8	27	0.07
ESD7089	Pasinler	ST557	A	10/07/01	5.4	32	0.02
IT74	Friuli	SRC0	A	11/09/76	5.1	16	0.07

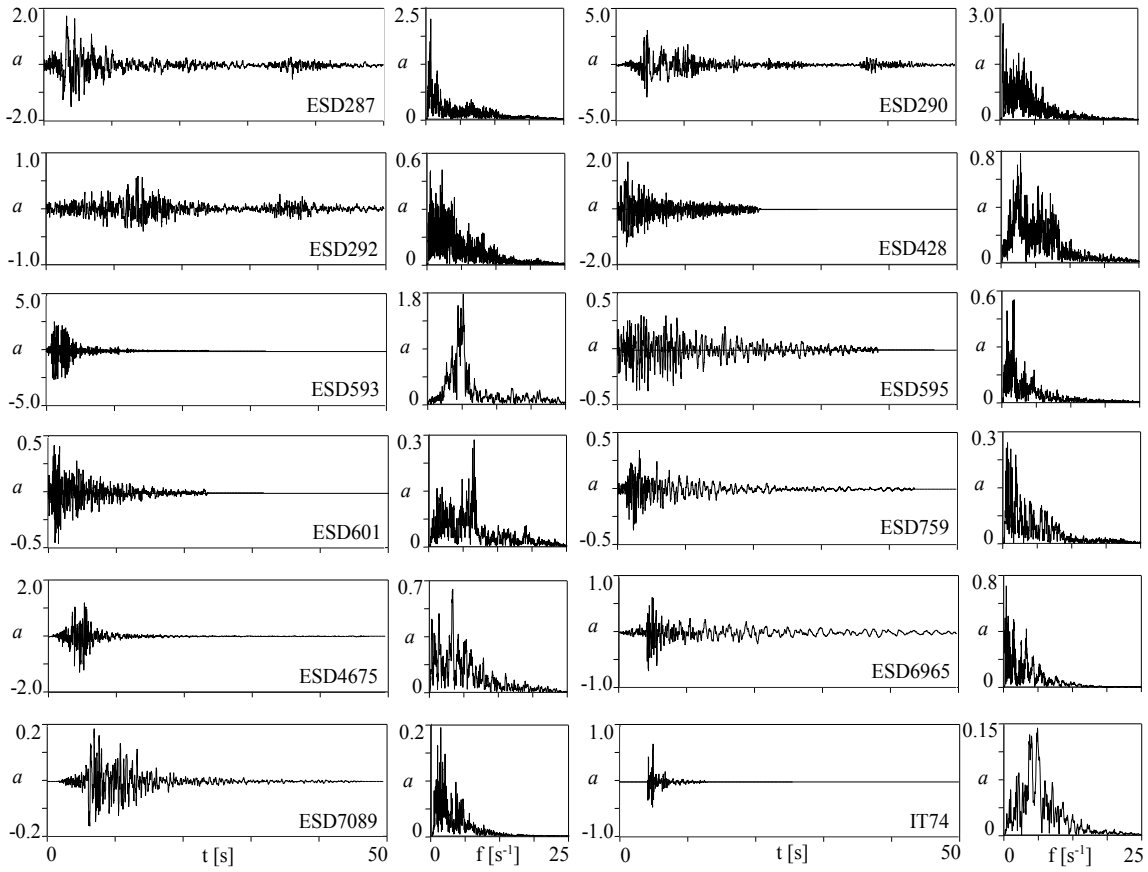

Figure 2.21. Acceleration time histories [m/s^2] and Fourier amplitude spectra [m/s^2] of the selected earthquakes.

The seismic inputs of CB models implementing the actual frequency-dependent soil foundation impedances are evaluated rigorously considering the Dezi et al. model (Dezi et al., 2016), which provides the foundation input motion from a kinematic interaction analysis of the soil foundation system. On the contrary, the seismic inputs of the FB models and of CB models implementing LPMs obtained through formulas of §2.5.2 are directly constituted by the selected free-field ground motions. It is worth mentioning that a rigorous evaluation of the foundation input motion for the CB models implies the computation of the soil-foundation system kinematic factors, through which the translational and rotational components of the seismic action are evaluated.

2.5.3.2 Main results

Results of applications are presented in terms of bridge deck relative displacements (with respect to the foundation) and foundation displacements, comparing results obtained from the two CB models (CB-IMP, implementing the actual frequency-dependent soil foundation impedances, and CB-LPM, assembled according to the proposed formulas). Results of FB applications are considered to quantify significance of SSI effects, i.e. to weight importance of discrepancies between the rigorous (CB-IMP) and simplified (CB-LPM) approach.

Figure 2.22 shows the deck relative displacement of P2 obtained for two of the selected accelerograms (ESD287 and ESD428); results from FB and CB-IMP models are compared in the first row of graphs while comparisons of results from the CB models (i.e. CB-IMP and CB-LPM) are addressed in the second row of graphs. The simple observation of time histories suggests that SSI significantly affects the superstructure response, as expected in view of the superstructure stiffness (case study P2 is representative of a stiff superstructure), and that these effects can be reasonably captured by adopting a simplified analysis approach which foresees the application of the free-field motion, instead of the foundation input one, to a CB structure assembled exploiting the proposed formulas. The latter consideration is justified by the almost superimposed responses of the CB-IMP and CB-LPM models.

Figure 2.23 shows similar results for P4, which is representative of a slender superstructure. In this case, SSI is less pronounced and responses of CB-IMP and CB-LPM models perfectly match.

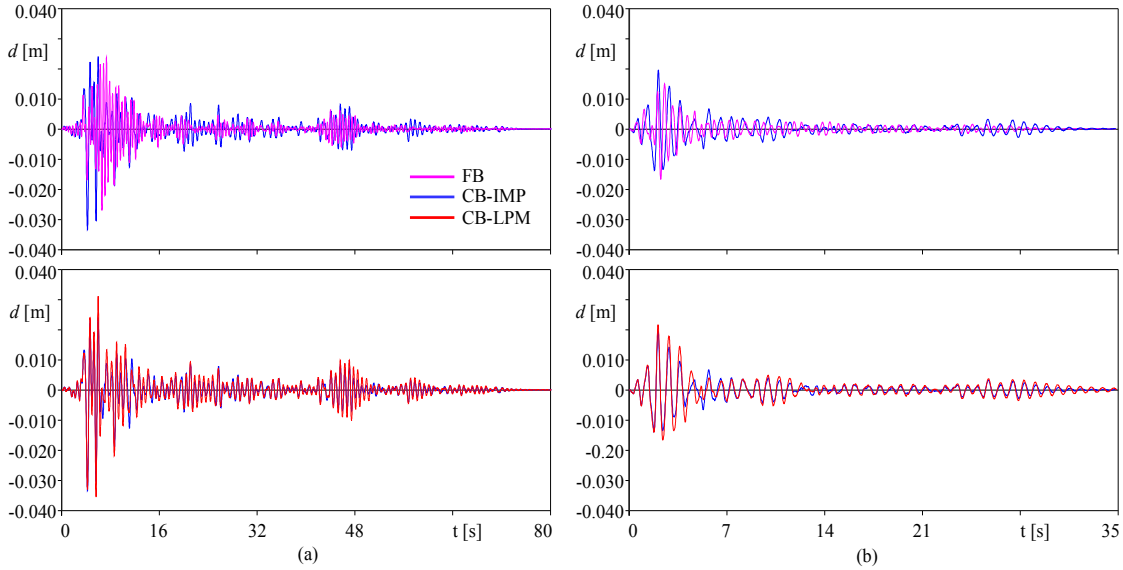

Figure 2.22. Deck displacements obtained from FB and CB models for (a) earthquake ESD287 and (b) earthquake ESD428 and for P2.

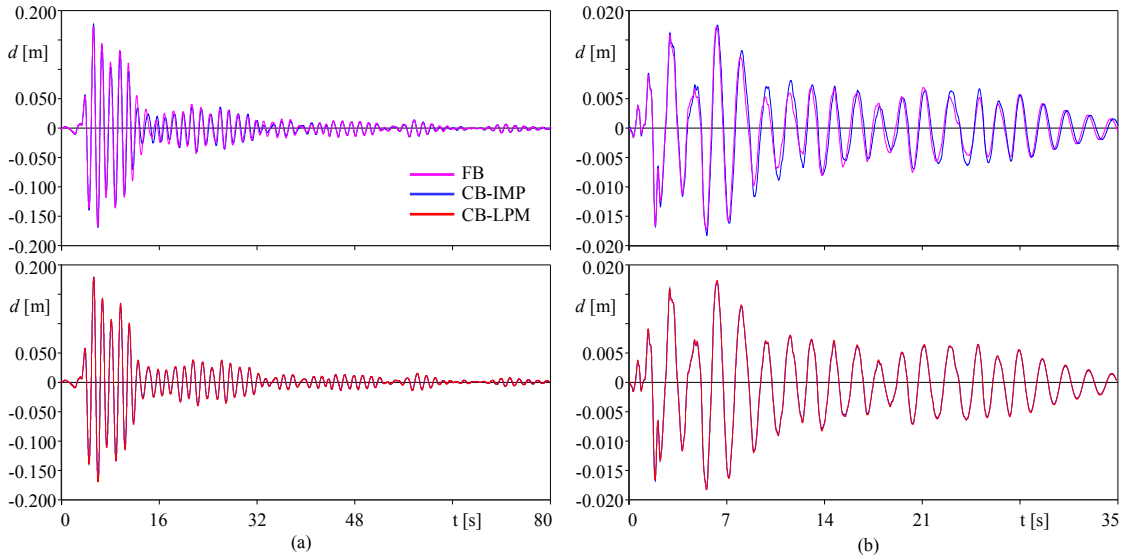

Figure 2.23. Deck displacements obtained from FB and CB models for (a) earthquake ESD287 and (b) earthquake ESD428 and for P4.

In order to facilitate the presentation of results from all applications, and to quantitatively express the formulas efficiency, metrics proposed by Kavrakov et al. (Kavrakov et al., 2018) are used in the sequel to compare time histories of displacements obtained from the different structural models. Metrics, quantifying discrepancies between two signals $x(t)$ and $y(t)$ in the time domain with respect to different properties, are expressed in the form:

$$M_i(x,y) = e^{-|A_i(x,y)|} \tag{29}$$

and assume values between 0 (completely discrepant signals) and 1 (no discrepancies between signals). In Equation (29), subscript i refers to the i-th particular property of the signals, for which the metric is constructed. Among those introduced in (Kavrakov et al., 2018), the phase metric M_φ, the peak metric M_p, the root mean square metric M_{rms}, the magnitude metric M_m, the wavelet metric M_w and the frequency normalised wavelet metric M_{wf} are herein considered. The phase metric accounts for the mean phase discrepancy between signals, with respect to a reference time delay T_C; the peak metric accounts for the difference in the maximum peak response while the root mean square metric quantify discrepancies of signals with respect to their average quantities. The magnitude metric accounts for discrepancies in the time-localized magnitude of the signals and is computed on the basis of the dynamic time warping algorithm (Sarin et al., 2010). Finally, the wavelet metric allows studying the overall signals discrepancies in the time-frequency plane while the frequency normalised wavelet metric allows to understand if the latter are due to the signal amplitudes or frequency content. Expressions of coefficients A_i of above metrics are reported below for the sake of completeness; further details can be found in (Kavrakov et al., 2018).

$$A_\phi = \frac{argmax_t\, x\,(t) * y(t)}{T_C} \tag{30a}$$

where T_C is assumed to be the fundamental frequency of the pier;

$$A_p = \frac{max_t|x(t)| - max_t|y(t)|}{max_t|x(t)|} \tag{30b}$$

$$A_{rms} = \frac{\sqrt{\int_t x^2(t)dt} - \sqrt{\int_t y^2(t)dt}}{\sqrt{\int_t x^2(t)dt}} \tag{30c}$$

$$A_m = \sqrt{\frac{\sum_{i=1}^{N_w}(x_w[i] - y_w[i])^2}{\sum_{i=1}^{N_w}(x_w[i])^2}} \tag{30d}$$

where x_w and y_w are the warped signals and N_w is the number of warped steps;

$$A_w = \frac{\int_a \int_t \left||W_x(a,t)| - |W_y(a,t)|\right| dt\, da}{\int_a \int_t |W_x(a,t)| dt\, da} \tag{30e}$$

where W_x and W_y are the wavelet coefficients of signals x and y, respectively, in the time-frequency plane, obtained by considering the Morlet wavelet, for which the scale a is inversely proportional to the frequency;

$$A_w = \frac{\int_a \int_t \left| \frac{|W_x(a,t)|}{max_a|W_x(a,t)|} - \frac{|W_y(a,t)|}{max_a|W_y(a,t)|} \right| dt\, da}{\int_a \int_t \frac{|W_x(a,t)|}{max_a|W_x(a,t)|} dt\, da} \tag{30f}$$

Figure 2.24 refers to the deck relative displacements and shows comparisons in terms of above metrics for all applications (i.e. for all piers and earthquakes) adopting "radar graphs". In details, each radar refers to a specific pier and each line within the radar refers to one of the selected earthquakes. Association of each line to the relevant earthquake goes beyond the aim of the figure, which intends to provide a pictorial view of the overall discrepancies between the superstructure responses obtained from FB and CB models for input motions characterised by different frequency contents, magnitudes, and acceleration amplitudes. In this sense, blue lines quantify discrepancies between responses of CB-IMP and CB-LPM models, while red lines quantify discrepancies between responses from FB and CB-LPM models. With reference to red lines, it can be observed that SSI effects diminish sensibly by increasing the superstructure slenderness; greater effects can be observed for P1 for which metrics are all in in the range 0.35÷0.60, with few exceptions relevant to M_p and M_{rms}. This implies that the response of the CB model is significantly different from that of the FB model, both in terms of amplitude and frequency content. For pier P2, discrepancies in terms of average quantities of signals (M_{rms}), maximum peak response (M_p) and time lag (M_φ) diminish (metrics are mainly in the range 0.40÷0.90) while differences in terms of time-localized magnitude (M_w) and frequency content (M_{wf}) remain important (metrics are in the range 0.35÷0.45). Piers P3 and P4 are less affected by SSI phenomena; both metrics quantifying discrepancies in terms of signal amplitude and frequency content are close to one (0.80÷1.00).

The effectiveness of the proposed formulas is providing reliable lumped systems to simulate the actual soil-foundation impedances is quantified through metrics depicted with blue lines in Figure 2.24. For P1 and P2 the response of the CB-LPM model agree quite well with that obtained from the CB-IMP model, implementing the actual soil-foundation impedances, both in terms of signals amplitude and frequency content; the relevant metrics, indeed, vary between 0.75 and 1.00, depending on the earthquake. Furthermore, discrepancies between the two CB models reduce significantly, passing from P1 to P4; in particular, for P3 and P4 the match is almost perfect.

With a similar approach, Figure 2.25 shows trends of the comparison metrics relevant to time histories of the foundation rotations, obtained from the CB-LPM and CB-IMP models. Previous considerations concerning deck displacements hold; overall the CB-LPM models are able to capture the response predicted with the more rigorous CB-IMP models with differences among them diminishing by increasing the superstructure slenderness.

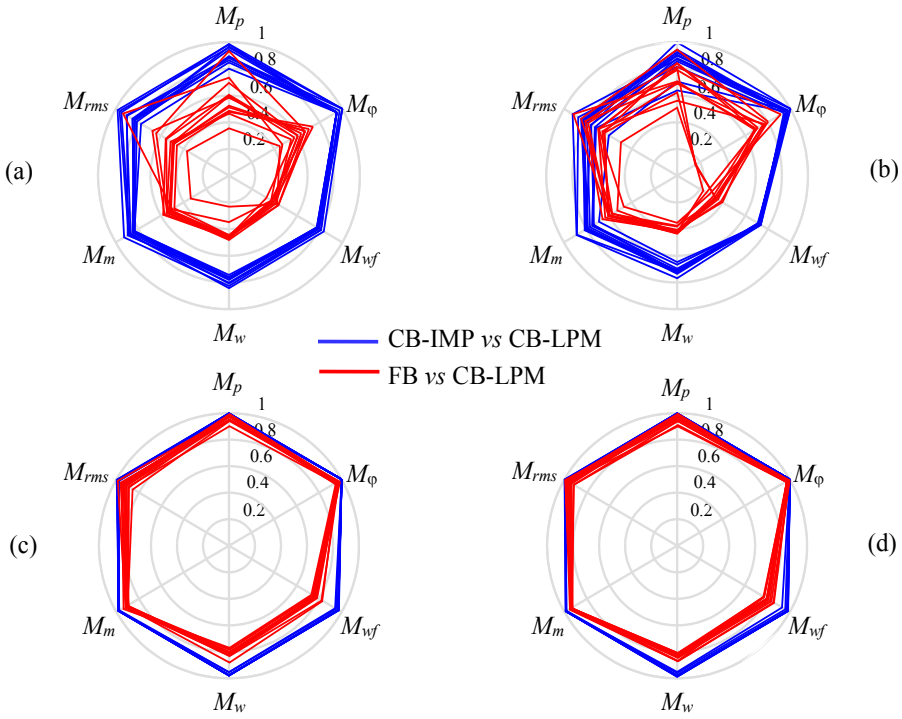

Figure 2.24. Comparison metrics for the deck displacements: (a) P1, (b) P2, (c) P3 and (d) P4.

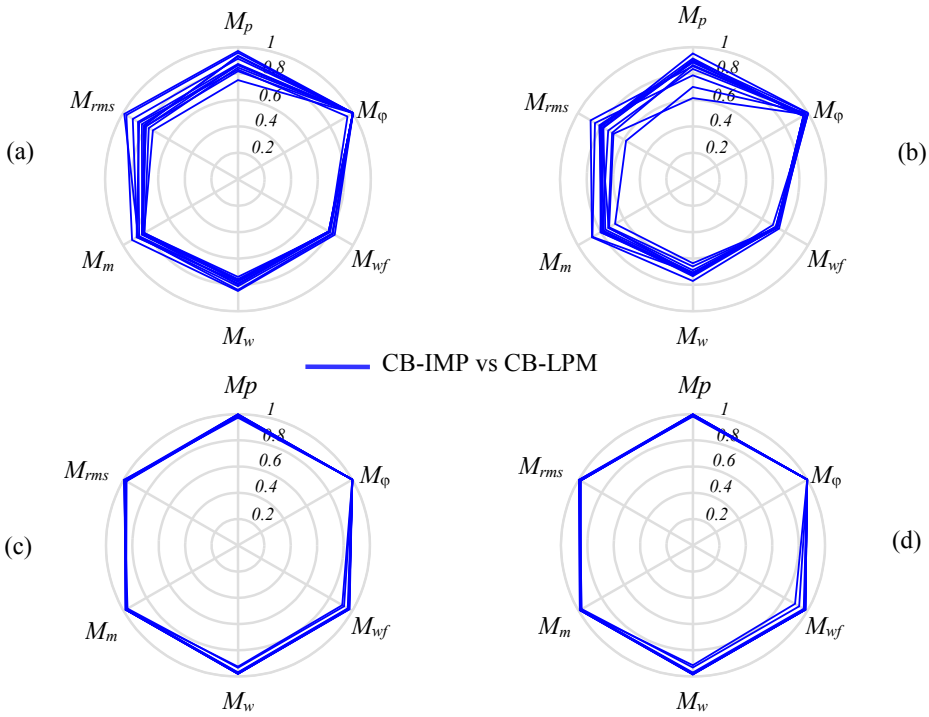

Figure 2.25. Comparison metrics for the foundation rotation: (a) P1, (b) P2, (c) P3 and (d) P4.

2.5.4 Conclusive remarks

With reference to end-bearing square pile groups, closed form expressions for evaluating parameters of the lumped system proposed by Carbonari et al. (2018) have been identified and calibrated. The lumped model can be adopted in the framework of the sub-structure approach to perform time domain inertial analyses of superstructures considering the coupled roto-translational, vertical and torsional behaviour of the soil-foundation system. Formulas, calibrated with a nonlinear least square procedure and whose independent variables are the main geometrical and mechanical properties of the soil-foundation systems, are overall able to well capture all the parameters of the lumped system and can be readily adopted by engineers through simple spreadsheets to define compliant restraints to perform inertial soil-structure interaction analyses. The applications provided in §2.5.3 demonstrate the potentials of the developed expressions in simplifying the analysis procedures while assuring a reliable prediction of the structural response, independently on the seismic input magnitude and frequency content.

In this Thesis, the proposed formulas will be used for the calculation of the constitutive LPM parameters for the implementation of the compliant base under the bridge piers. The modelling of springs, masses and dashpots representative of a typical pier foundation in a homogeneous soil will be described in the next §4.4. Effects of SSI modelled according to the presented formulation on the response of the piers and, more widely, of the bridge and the road network of belonging will be discussed in the following Chapters 5 and 6. In particular, the fragility analysis of the bridge typologies of interest will be carried out under the hypothesis of fixed and compliant base, and the most relevant differences will be put in evidence (Chapter 5). Moreover, the impact of these assumptions on the functionality of a road network will be investigated with an application on a principal traffic route in the Marche region (Chapter 6).

2.6 Chapter's references

Akiyama, M., Frangopol, D.M., & Matsuzaki, H. (2011). Lifecycle reliability of RC bridge piers under seismic and airborne chloride hazards. *Earthquake Engineering and Structural Dynamics*, *40*, 1671– 1687.

Akiyama, M., Frangopol, D.M., & Mizuno, K. (2013). Performance analysis of Tohoku-Shinkansen viaducts affected by the 2011 Great East Japan earthquake. *Structure and Infrastructure Engineering*. doi:10.1080/15732479. 2013.806559.

Alessandri, S., Giannini, R., & Paolacci, F. (2013). Aftershock risk assessment and the decision to open traffic on bridges. *Earthquake engineering & structural dynamics*, *42*(15), 2255-2275.

Algermissen, S. T. (1972). *A study of earthquake losses in the San Francisco Bay Area: Data and analysis*. US Department of Commerce, National Oceanic & Atmospheric Administration. Environmental Research Laboratories.

Alipour, A., & Shafei, B. (2016). Seismic resilience of transportation networks with deteriorating components. *Journal of Structural Engineering*, *142*(8), C4015015.

Ambraseys, N., Smit, P., Douglas, J., Margaris, B., Sigbjörnsson, R., Olafsson, S., ... & Costa, G. (2004). Internet site for European strong-motion data. *Bollettino di geofisica teorica ed applicata*, *45*(3), 113-129.

ANSYS Academic Research Mechanical, Release 18.1.

Atkinson, G. M. (2004, August). An overview of developments in seismic hazard analysis. In *13th World Conference on Earthquake Engineering* (pp. 1-6).

Atkinson, G. M., & Silva, W. (2000). Stochastic modeling of California ground motions. *Bulletin of the Seismological Society of America*, *90*(2), 255-274.

Au, S. K., & Beck, J. L. (2003). Subset simulation and its application to seismic risk based on dynamic analysis. *Journal of engineering mechanics*, *129*(8), 901-917.

Avşar, Ö., Yakut, A., & Caner, A. (2011). Analytical fragility curves for ordinary highway bridges in Turkey. *Earthquake Spectra*, *27*(4), 971-996.

Baker, J. W. (2015). Efficient analytical fragility function fitting using dynamic structural analysis. *Earthquake Spectra*, *31*(1), 579-599.

Baker, J. W., and Cornell, C. A. (2005). Vector-Valued Ground Motion Intensity Measures for Probabilistic Seismic Demand Analysis, Report No. 150, John A. Blume Earthquake Engineering Center, Stanford, CA, 321 pp.

Bazzurro, P., & Allin Cornell, C. (1999). Disaggregation of seismic hazard. *Bulletin of the Seismological Society of America*, *89*(2), 501-520.

Billah, A. H. M. M., & Alam, M. S. (2013). Seismic vulnerability assessment of a typical multi-span continuous concrete highway bridge in British Columbia. *Canadian Journal of Civil Engineering, Manuscript ID: CJCE-2013-0049R2*.

Billah, A. H. M. M., & Alam, M. S. (2015). Seismic fragility assessment of highway bridges: a state-of-the-art review. *Structure and Infrastructure Engineering*, *11*(6), 804-832.

Bocchini, P. (2013). Computational procedure for the assisted multi-phase resilience-oriented disaster management of transportation systems. *Safety, Reliability, Risk, and Life-Cycle Performance of Structures and Infrastructures*, 581-588.

Bocchini, P., & Frangopol, D. M. (2011). Generalized bridge network performance analysis with correlation and time-variant reliability. *Structural Safety*, *33*(2), 155-164.

Bolisetti, C., Whittaker, A. S., & Coleman, J. L. (2015). Frequency-and time-domain methods in soil-structure interaction analysis (No. INL/CON-15-35455). Idaho National Lab. (INL), Idaho Falls, ID (United States).

Boore, D. M. (2003). Simulation of ground motion using the stochastic method. *Pure and applied geophysics*, *160*(3-4), 635-676.

Boore, D. M., & Atkinson, G. M. (2008). Ground-motion prediction equations for the average horizontal component of PGA, PGV, and 5%-damped PSA at spectral periods between 0.01 s and 10.0 s. *Earthquake Spectra*, *24*(1), 99-138.

Boore, D. M., & Joyner, W. B. (1997). Site amplifications for generic rock sites. *Bulletin of the seismological society of America*, *87*(2), 327-341.

Borzi, B., Ceresa, P., Franchin, P., Noto, F., Calvi, G. M., & Pinto, P. E. (2015). Seismic vulnerability of the Italian roadway bridge stock. *Earthquake Spectra*, *31*(4), 2137-2161.

Bradley, B. A. (2013). Practice-oriented estimation of the seismic demand hazard using ground motions at few intensity levels. *Earthquake Engineering & Structural Dynamics*, *42*(14), 2167-2185.

Bradley, B. A., Cubrinovski, M., Dhakal, R. P., & MacRae, G. A. (2010). Probabilistic seismic performance and loss assessment of a bridge–foundation–soil system. *Soil Dynamics and Earthquake Engineering*, *30*(5), 395-411.

Buckingham, E. (1914). On physically similar systems; illustrations of the use of dimensional equations. *Physical review*, *4*(4), 345.

Cademartori, M., Sullivan, T. J., & Osmani, S. (2020). Displacement-based assessment of typical Italian RC bridges. *Bulletin of Eathquake Engineering*.

Capacci, L., Biondini, F., & Titi, A. (2020). Lifetime seismic resilience of aging bridges and road networks. *Structure and Infrastructure Engineering*, *16*(2), 266-286.

Capatti, M. C., Tropeano, G., Morici, M., Carbonari, S., Dezi, F., Leoni, G., & Silvestri, F. (2017). Implications of non-synchronous excitation induced by nonlinear site amplification and of soil-structure interaction on the seismic response of multi-span bridges founded on piles. *Bulletin of Earthquake Engineering*, *15*(11), 4963-4995.

Carbonari, S., Dezi, F., & Leoni, G. (2012). Nonlinear seismic behaviour of wall-frame dual systems accounting for soil–structure interaction. *Earthquake engineering & structural dynamics*, *41*(12), 1651-1672.

Carbonari, S., Morici, M., Dezi, F., & Leoni, G. (2018). A lumped parameter model for time-domain inertial soil-structure interaction analysis of structures on pile foundations. *Earthquake Engineering & Structural Dynamics*, *47*(11), 2147-2171.

Carturan, F., Pellegrino, C., Rossi, R., Gastaldi, M., & Modena, C. (2013). An integrated procedure for management of bridge networks in seismic areas. *Bulletin of Earthquake Engineering*, *11*(2), 543-559.

Carturan, F., Zanini, M. A., Pellegrino, C., & Modena, C. (2014). A unified framework for earthquake risk assessment of transportation networks and gross regional product. *Bulletin of earthquake engineering*, *12*(2), 795-806.

Chang, S. E., & Shinozuka, M. (1996). Life-cycle cost analysis with natural hazard risk. *Journal of infrastructure systems*, *2*(3), 118-126.

Chen, Y., Chen, Q.F., Liu, J., Chen, L., & Li, J. (2002). Seismic Hazard and Risk Analysis: A Simplified Approach. Science Press, Beijing, 228 pp.

Chen, Y., Chen, X.L., Fu, Z.X., Ying, Z.Q., & Yang, M.D. (1992). Estimating Losses from Earthquakes in China in the Forthcoming 50 Years. Seismological Press, Beijing, 60 pp.

Choi, E., DesRoches, R., & Nielson, B.G. (2004). Seismic fragility of typical bridges in moderate seismic zones. *Engineering Structures*, *26*, 187-199.

Coburn, A., & Spence, R. (2003). *Earthquake protection*. John Wiley & Sons.

Codermatz, R., Nicolich, R., & Slejko, D. (2003). Seismic risk assessments and GIS technology: applications to infrastructures in the Friuli–Venezia Giulia region (NE Italy). *Earthquake engineering & structural dynamics*, *32*(11), 1677-1690.

Cornell, C. A. (1968). Engineering seismic risk analysis. *Bulletin of the seismological society of America*, *58*(5), 1583-1606.

Dall'Asta, A., Scozzese, F., Ragni, L., & Tubaldi, E. (2017). Effect of the damper property variability on the seismic reliability of linear systems equipped with viscous dampers. *Bulletin of Earthquake Engineering*, *15*(11), 5025-5053.

Dezi, F., Carbonari, S., & Morici, M. (2016). A numerical model for the dynamic analysis of inclined pile groups. *Earthquake Engineering & Structural Dynamics*, *45*(1), 45-68.

Dobry, R., Vicente, E., O'Rourke, M., & Roesset, M. (1982). Horizontal stiffness and damping of single piles. *Journal of Geotechnical and Geoenvironmental Engineering*, *108*(GT3).

Dong, Y., Frangopol, D.M., & Saydam, D. (2014). Sustainability of highway bridge networks under seismic hazard. *Journal of Earthquake Engineering*, *18*, 41–66.

Dorra, E. M., Stafford, P. J., & Elghazouli, A. Y. (2013). Earthquake loss estimation for Greater Cairo and the national economic implications. *Bulletin of Earthquake Engineering*, *11*(4), 1217-1257.

Fan, K., Gazetas, G., Kaynia, A., Kausel, E., & Ahmad, S. (1991). Kinematic seismic response of single piles and pile groups. *Journal of Geotechnical Engineering*, *117*(12), 1860-1879.

FEMA. HAZUS 99. Estimated annualized earthquake losses for the U.S.A. Federal Emergency Management Agency, Washington D.C., 1999.

Franchetti, P., Grendene, M., Sleiko, D., & Modena, C. (2008). Seismic damage assessment for six RC bridges in the Veneto region (NE Italy). *Bollettino di geofisica applicata*, *49*(3-4), 513-532.

Frangopol, D. M. (1999). Life-cycle cost analysis for bridges. In *Bridge safety and reliability* (pp. 210-236). ASCE.

Frangopol, D. M., & Soliman, M. (2016). Life-cycle of structural systems: recent achievements and future directions. *Structure and infrastructure engineering*, *12*(1), 1-20.

Frangopol, D. M., Dong, Y., & Sabatino, S. (2017). Bridge life-cycle performance and cost: analysis, prediction, optimisation and decision-making. *Structure and Infrastructure Engineering*, *13*(10), 1239-1257.

Gazetas, G., & Dobry, R. (1984). Simple radiation damping model for piles and footings. *Journal of Engineering Mechanics*, *110*(6), 937-956.

Giovinazzi, S., & Lagomarsino, S. (2004, August). A macroseismic method for the vulnerability assessment of buildings. In *13th World Conference on Earthquake Engineering* (Vol. 896, pp. 1-6).

Grandori, G., & Benedetti, D. (1973). On the choice of the acceptable seismic risk. *Earthquake Engineering & Structural Dynamics*, *2*(1), 1-9.

Ibarra, L. F., & Krawinkler, H. (2005). *Global collapse of frame structures under seismic excitations* (pp. 29-51). Berkeley, CA: Pacific Earthquake Engineering Research Center.

Iervolino, I., Spillatura, A., & Bazzurro, P. (2018). Seismic reliability of code-conforming Italian buildings. *Journal of Earthquake Engineering*, *22*(sup2), 5-27.

Jalayer, F., & Beck, J. L. (2008). Effects of two alternative representations of ground-motion uncertainty on probabilistic seismic demand assessment of structures. *Earthquake Engineering & Structural Dynamics*, *37*(1), 61-79.

Jalayer, F., & Cornell, C. A. (2009). Alternative non-linear demand estimation methods for probability-based seismic assessments. *Earthquake Engineering & Structural Dynamics*, *38*(8), 951-972.

Karapetrou, S. T., Fotopoulou, S. D., & Pitilakis, K. D. (2015). Seismic vulnerability assessment of high-rise non-ductile RC buildings considering soil–structure interaction effects. *Soil Dynamics and Earthquake Engineering*, *73*, 42-57.

Karim, K.R., & Yamazaki, F. (2003). A simplified method of constructing fragility curves for highway bridges. *Earthquake Engineering and Structural Dynamics*, 32, 1603– 1626.

Kavrakov, I., Kareem, A., & Morgenthal, G. (2018). Quantification of the influence of aerodynamic model assumptions for dynamic analyses of bridges. In *40th IABSE Symposium, Tomorrow's Megastructures, Nantes, France*.

Kilanitis, I., & Sextos, A. (2019a). Integrated seismic risk and resilience assessment of roadway networks in earthquake prone areas. *Bulletin of earthquake engineering*, *17*(1), 181-210.

Kilanitis, I., & Sextos, A. (2019b). Impact of earthquake-induced bridge damage and time evolving traffic demand on the road network resilience. *Journal of traffic and transportation engineering (English edition)*, *6*(1), 35-48.

Kiremidjian, A. S., Stergiou, E., & Lee, R. (2007). Issues in seismic risk assessment of transportation networks. In *Earthquake geotechnical engineering* (pp. 461-480). Springer, Dordrecht.

Kramer, S.L., 2003. *Geotechnical Earthquake Engineering*, Prentice-Hall: Englewood Cliffs, NJ.

Lallemant, D., Kiremidjian, A., & Burton, H. (2015). Statistical procedures for developing earthquake damage fragility curves. *Earthquake Engineering & Structural Dynamics*, *44*(9), 1373-1389.

Liu, M., & Frangopol, D. M. (2005). Multiobjective maintenance planning optimization for deteriorating bridges considering condition, safety, and life-cycle cost. *Journal of Structural Engineering*, *131*(5), 833-842.

Luco, N., & Bazzurro, P. (2007). Does amplitude scaling of ground motion records result in biased nonlinear structural drift responses?. *Earthquake Engineering & Structural Dynamics*, *36*(13), 1813-1835.

Luco, N., & Cornell, C. A. (2007). Structure-specific scalar intensity measures for near-source and ordinary earthquake ground motions. *Earthquake Spectra*, *23*(2), 357-392.

Luzi, L., Pacor, F., & Puglia, R. (2017). Italian Accelerometric Archive v 2.3. Istituto Nazionale di Geofisica e Vulcanologia. *Dip. Prot. Civ. Naz*.

Mackie, K. R., & Stojadinović, B. (2005a). Comparison of incremental dynamic, cloud, and stripe methods for computing probabilistic seismic demand models. In *Structures Congress 2005: Metropolis and Beyond* (pp. 1-11).

Mackie, K., & Stojadinovic, B. (2005b). Fragility basis for California highway overpass bridge seismic decision making, (PEER Report 2005/02). Pacific Earthquake Engineering Research Center. Berkeley, CA: University of California.

Makris, N., & Gazetas, G. (1993). Displacement phase differences in a harmonically oscillating pile. *Geotechnique*, *43*(1), 135-150.

Mamoon, S. M., & Banerjee, P. K. (1990). Response of piles and pile groups to travelling SH-waves. *Earthquake engineering & structural dynamics*, *19*(4), 597-610.

Mangalathu, S., Heo, G., & Jeon, J. S. (2018). Artificial neural network based multi-dimensional fragility development of skewed concrete bridge classes. *Engineering Structures*, *162*, 166-176.

Mangalathu, S., Jeon, J. S., Padgett, J. E., & DesRoches, R. (2016). ANCOVA-based grouping of bridge classes for seismic fragility assessment. *Engineering Structures*, *123*, 379-394.

Mangalathu, S., Soleimani, F., & Jeon, J. S. (2017). Bridge classes for regional seismic risk assessment: Improving HAZUS models. *Engineering Structures*, *148*, 755-766.

Miano, A., Jalayer, F., De Risi, R., Prota, A., & Manfredi, G. (2015, July). A case-study on scenario-based probabilistic seismic loss assessment for a portfolio of bridges. In *Proceedings of the 12th International Conference on Applications of Statistics and Probability in Civil Engineering, ICASP12* (pp. 12-15).

Miller, M., & Baker, J. W. (2016). Coupling mode-destination accessibility with seismic risk assessment to identify at-risk communities. *Reliability Engineering & System Safety*, *147*, 60-71.

Moschonas, I. F., Kappos, A. J., Panetsos, P., Papadopoulos, V., Makarios, T., & Thanopoulos, P. (2009). Seismic fragility curves for Greek bridges: methodology and case studies. *Bulletin of Earthquake Engineering*, *7*(2), 439.

Nielson, B.G. (2005). Analytical fragility curves for highway bridges in moderate seismic zones (Doctoral dissertation, Georgia Institute of Technology).

Nielson, B.G., & DesRoches, R. (2007a). Seismic fragility curves for typical highway bridge classes in the Central and South-eastern United States. *Earthquake Spectra*, *23*, 615–633.

Nielson, B.G., & DesRoches, R. (2007b). Seismic fragility methodology for highway bridges using a component level approach. *Earthquake Engineering and Structural Dynamics*, *36*, 823– 839.

Padgett, J. E., & DesRoches, R. (2007). Bridge functionality relationships for improved seismic risk assessment of transportation networks. *Earthquake Spectra*, *23*(1), 115-130.

Padgett, J. E., & Tapia, C. (2013). Sustainability of natural hazard risk mitigation: Life cycle analysis of environmental indicators for bridge infrastructure. *Journal of Infrastructure Systems*, *19*(4), 395-408.

Padgett, J. E., Dennemann, K., & Ghosh, J. (2010). Risk-based seismic life-cycle cost–benefit (LCC-B) analysis for bridge retrofit assessment. *Structural Safety*, *32*(3), 165-173.

Padgett, J.E., & DesRoches, R. (2008). Methodology for the development of analytical fragility curves for retrofitted bridges. *Earthquake Engineering and Structural Dynamics*, *37*, 157– 174.

Padgett, J.E., & DesRoches, R. (2009). Retrofitted bridge fragility analysis for typical classes of multispan bridges. *Earthquake Spectra*, *25*, 117– 141.

Padrón, L. A., Aznárez, J. J., & Maeso, O. (2008). Dynamic analysis of piled foundations in stratified soils by a BEM–FEM model. *Soil Dynamics and Earthquake Engineering*, *28*(5), 333-346.

Pan, Y., Agrawal, A.K., Ghosn, M., & Alampalli, S. (2010a). Seismic fragility of multi-span simply supported steel highway bridges in New York State. I: Bridge modeling, parametric analysis, and retrofit design. *ASCE Journal of Bridge Engineering*, *15*, 448–461.

Pan, Y., Agrawal, A.K., Ghosn, M., & Alampalli, S. (2010b). Seismic fragility of multi-span simply supported steel highway bridges in New York State. II: Fragility analysis, fragility curves, and fragility surfaces. *ASCE Journal of Bridge Engineering*, *15*, 462–472.

PELEM (Panel of Earthquake Loss Estimation Methodology) (1989). Estimating Losses from Future Earthquakes, National Academy Press, 248 pp.

Pitilakis, K. (2011). Systemic seismic vulnerability and risk analysis for buildings, lifeline networks and infrastructures safety gain. *European Collaborative research Project*, *Deliverable D3.6*. (FP7-ENV-2009- 1-244061) http://www.syner-g.eu

Porter, K. A. (2003, July). An overview of PEER's performance-based earthquake engineering methodology. In *Proceedings of ninth international conference on applications of statistics and probability in civil engineering*.

Porter, K. (2018). A Beginner's Guide to Fragility, Vulnerability and Risk. University of Colorado Boulder, 110 pp.

Porter, K., Kennedy, R., & Bachman, R. (2007). Creating fragility functions for performance-based earthquake engineering. *Earthquake Spectra*, *23*(2), 471-489.

Ramanathan, K. N. (2012). *Next generation seismic fragility curves for California bridges incorporating the evolution in seismic design philosophy* (Doctoral dissertation, Georgia Institute of Technology).

Ramanathan, K., DesRoches, R., & Padgett, J. E. (2010). Analytical fragility curves for multispan continuous steel girder bridges in moderate seismic zones. *Transportation Research Record*, *2202*(1), 173-182.

Ramanathan, K., DesRoches, R., & Padgett, J.E. (2012). A comparison of pre- and post-seismic design considerations in moderate seismic zones through the fragility assessment of multi-span bridge classes. *Engineering Structures*, *45*, 559– 573.

Sarin, H., Kokkolaras, M., Hulbert, G., Papalambros, P., Barbat, S., & Yang, R. J. (2010). Comparing time histories for validation of simulation models: error measures and metrics. *Journal of dynamic systems, measurement, and control*, *132*(6).

Scozzese, F., Dall'Asta, A., & Tubaldi, E. (2019). Seismic risk sensitivity of structures equipped with anti-seismic devices with uncertain properties. *Structural Safety*, *77*, 30-47.

Scozzese, F., Tubaldi, E., & Dall'Asta, A. (2020). Assessment of the effectiveness of multiple-stripe analysis by using a stochastic earthquake input model. *Bulletin of Earthquake Engineering*, *18*(7), 3167-3203.

Stefanidou, S. P., & Kappos, A. J. (2017). Methodology for the development of bridge-specific fragility curves. *Earthquake Engineering & Structural Dynamics*, *46*(1), 73-93.

Stefanidou, S. P., & Kappos, A. J. (2019). Bridge-specific fragility analysis: when is it really necessary?. *Bulletin of earthquake engineering*, *17*(4), 2245-2280.

Straub, D., and Der Kiureghian, A., 2008. Improved seismic fragility modeling from empirical data, *Structural Safety 30*, 320–336.

Tapia, C., & Padgett, J. E. (2016). Multi-objective optimisation of bridge retrofit and post-event repair selection to enhance sustainability. *Structure and Infrastructure Engineering*, *12*(1), 93-107.

Tavares, D.H., Padgett, J.E., & Paultre, P. (2012). Fragility curves of typical as-built highway bridges in eastern Canada. *Engineering Structures*, *40*, 107– 118.

Thoft-Christensen, P. (2009). Life-cycle cost-benefit (LCCB) analysis of bridges from a user and social point of view. *Structures & Infrastructure Engineering*, *5*(1), 49-57.

Vamvatsikos, D., & Cornell, C. A. (2002). Incremental dynamic analysis. *Earthquake Engineering & Structural Dynamics*, *31*(3), 491-514.

Werner, S. D., Taylor, C. E., Moore, J. E., Walton, J. S., & Cho, S. (2000). *A risk-based methodology for assessing the seismic performance of highway systems*. Buffalo, NY: Multidisciplinary Center for Earthquake Engineering Research.

Whitman, R. V., Vanmarcke, E. H., de Neufville, R. L., Brennan, J. E. I., Cornell, C. A., & Biggs, J. M. (1975). Seismic design decision analysis. *Journal of the Structural Division*, *101*(5), 1067-1084.

Wolf, J.P. (1985). Dynamic Soil-Structure Interaction. Englewood, N.J: Prentice-Hall, Inc.

Zanini, M. A., Faleschini, F., Zampieri, P., Pellegrino, C., Gecchele, G., Gastaldi, M., & Rossi, R. (2017). Post-quake urban road network functionality assessment for seismic emergency management in historical centres. *Structure and Infrastructure Engineering*, *13*(9), 1117-1129.

Zanini, M. A., Pellegrino, C., Morbin, R., & Modena, C. (2013). Seismic vulnerability of bridges in transport networks subjected to environmental deterioration. *Bulletin of Earthquake Engineering*, *11*(2), 561-579.

Zhou, Y., Banerjee, S., & Shinozuka, M. (2010). Socio-economic effect of seismic retrofit of bridges for highway transportation networks: A pilot study. *Structure and Infrastructure Engineering*, *6*, 145–157.

3. Analysis of the Italian and regional existing bridges stock

3.1 The Italian bridge inventory

The Italian bridge inventory belongs to one of the most complex national road systems in the world. Over time the morphological and orographic features of the Italian territory led to the building of 1,068 structures, covering a length of 1,013 km out of a total of over 6,000 km of main network (highways). If we consider the entire Italian road network with a total length of 184,000 km, including local, municipal, provincial and regional roads, then the number of bridge structures rise to 61,000.

Differently from other countries in Europe or in the US, in Italy the management of the bridge inventory is not entrusted to a national Bridge Management System (BMS), that is an efficient instrument to monitor and assess the structural health of existing structures and infrastructural systems. The management of bridges is delegated to local authorities, such as Provinces and Regions. This leads to a fragmentation of information of all works of art. Moreover, such entities very often do not have a database of structures under their jurisdiction, since several works are of property of private operators.

Some attempts have been made to organize the information about the Italian bridges, both on local and national scale (Gattulli & Chiaramonte, 2005; Zonta et al., 2007; Pellegrino et al., 2011; Modena et al., 2014). As previously stated in §2.2, a recent study by Borzi et al. (Borzi et al., 2015) has been involved in providing indication, at national level, about the vulnerability of bridges and viaducts. The study focuses on the typology of reinforced concrete bridges, since this typology represents more than the 90% of the total (Pinto & Franchin, 2010). The information database contains about 17,000 bridges, of which only 485 are described exhaustively from a structural point of view. The Italian bridges involved in the database are represented in Figure 3.1.

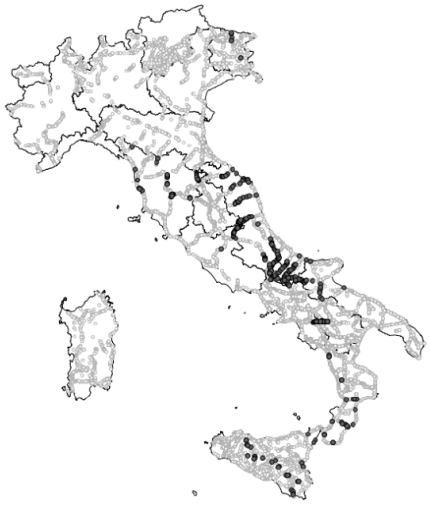

Figure 3.1. Stock of bridges identified by Borzi et al. (2015): the black circles represent the 485 bridges for which exhaustive information was obtained.

The bridge information has been classified according to several different parameters concerning the bridge geometry, the static scheme and the foundation type, basing on which the fragility analysis of the bridge structures is possible. The classification parameters and the distribution of the bridge data are depicted in Figure 3.2.

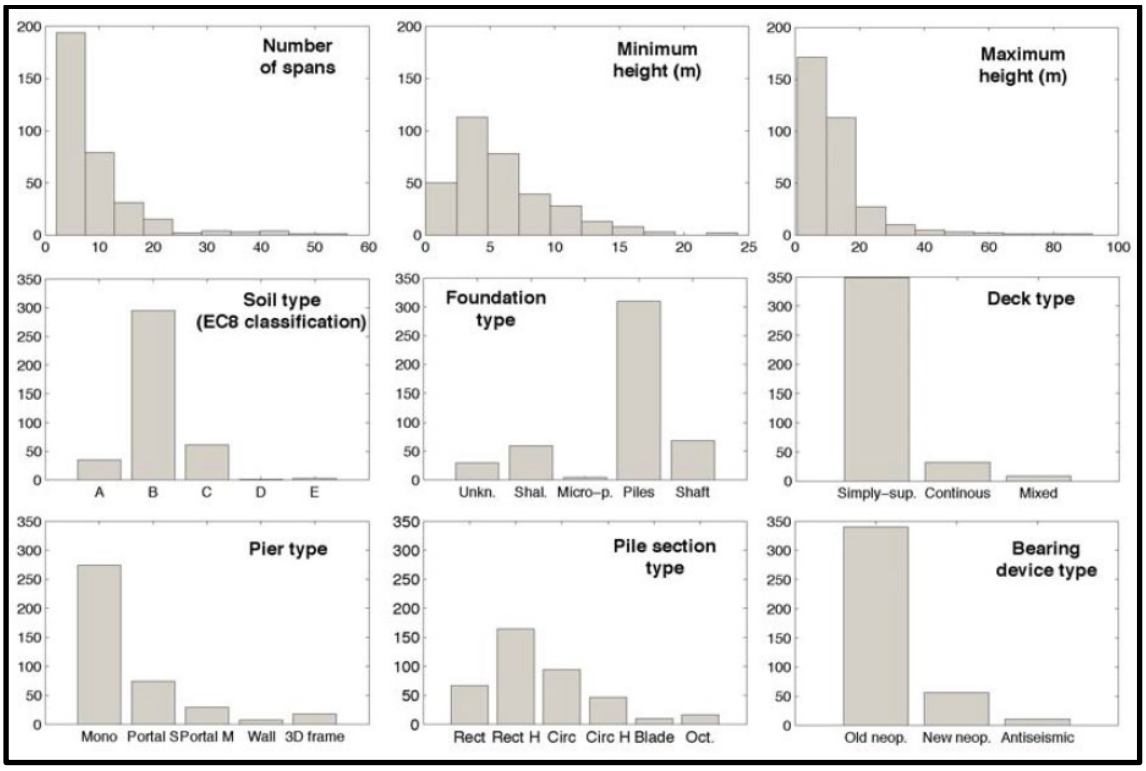

Figure 3.2. Distribution of the bridge parameters (Borzi et al., 2015).

In order to furtherly investigate the existing bridges' inventory and consider other typologies than the reinforced concrete bridges, in this Thesis the classification approach proposed by Borzi et al. (Borzi et al., 2015) is taken as a starting point for the analysis of the bridge structures within the Marche Region. In particular, two main road networks are considered, the SS76 and SS77 roads, along which about one hundred of bridges are located and classified according to different relevant parameters concerning structural schemes, materials and geometries. As later commented, the found bridge typologies result common not only on the regional territory, but also on national scale. In the next Chapter a description of the Marche regional bridge inventory and the relative classification are provided.

3.2 The Marche Region bridge inventory

The Marche Region is crossed by a high number of viaducts and bridges being the territorial orography very complex. There are 286 viaducts and overpasses connecting the hinterland to the coast and along the coastal development of the motorway A14. In particular, there are three main roadways connecting the West side to the East one where

the available structural and geotechnical information about bridges is sufficient to provide a representative classification of the medium and large size bridge structures in the regional context (Figure 3.1). In this Thesis, the longest two out of these three main roads are considered to evaluate the seismic performance and the regional viability.

The first considered main road is the highway SS76 of Val d'Esino, which crosses from West to East the Umbria and Marche territories being one of their most important road axes for both economic and touristic reasons. It is a double carriageway road with mainly two lanes per direction, with a total length of 75 km connecting Fossato di Vico, in Umbria Region, to Falconara Marittima, in the Marche Region. Along SS76 a total of 30 bridge structures can be found. A picture of the SS76 geographical location and extension is provided in Figure 3.3.

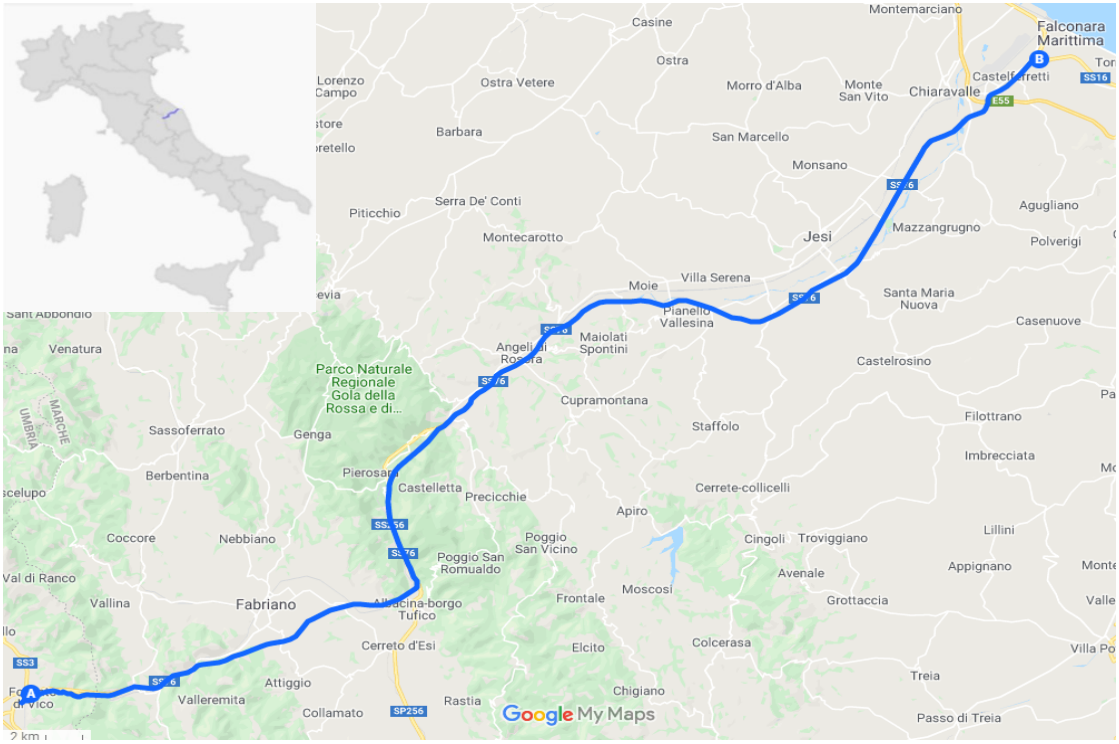

Figure 3.3. Highway SS76 (Google Maps).

The second considered main road is the highway SS77 of Val di Chienti, which connects the city of Foligno, in Umbria Region, to the city of Civitanova Marche, with a total length of 95 km crossing the Apennines. Along SS77 a total of 60 bridges can be found. A picture of the SS77 geographical location and extension is provided in Figure 3.4.

The collection of data about the existing bridges of SS76 and SS77 have allowed a first macro classification into two structural categories: Reinforced Concrete (RC) decks and Steel-Concrete Composite (SCC) decks. All the bridges present RC substructures (piers and abutments), and no masonry bridges have been identified along the considered highways. The geographical distribution of RC and SSC viaducts is collected in Figure 3.5 and Figure 3.6.

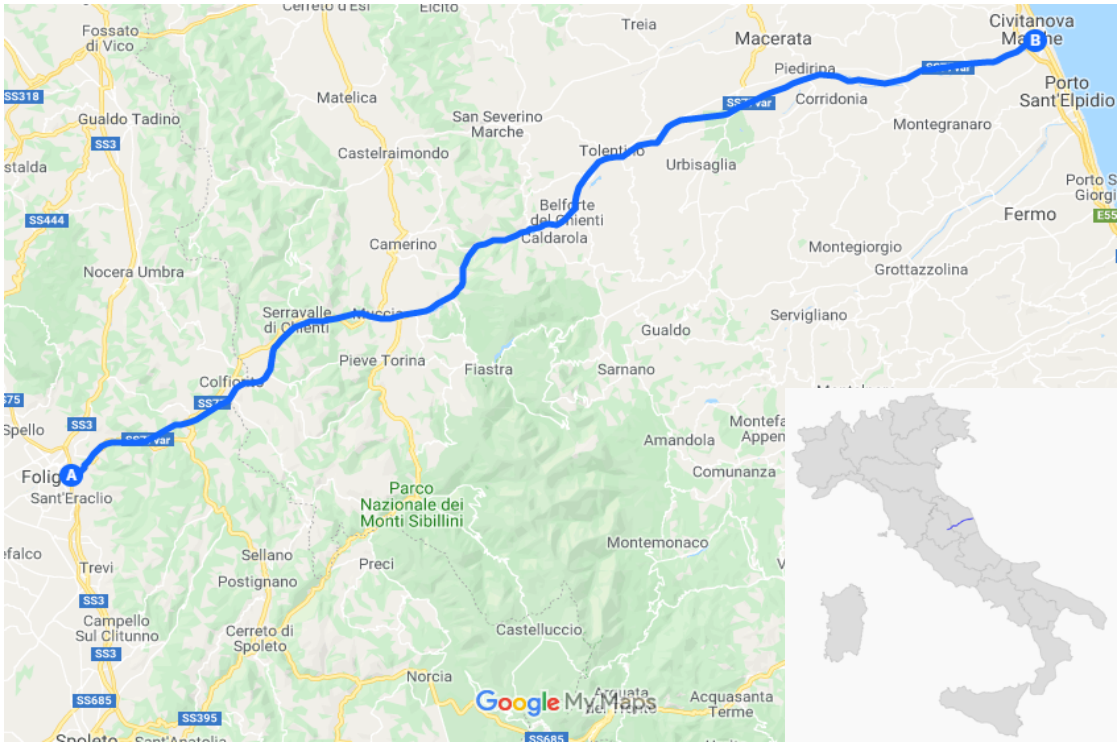

Figure 3.4. Highway SS77 (Google Maps).

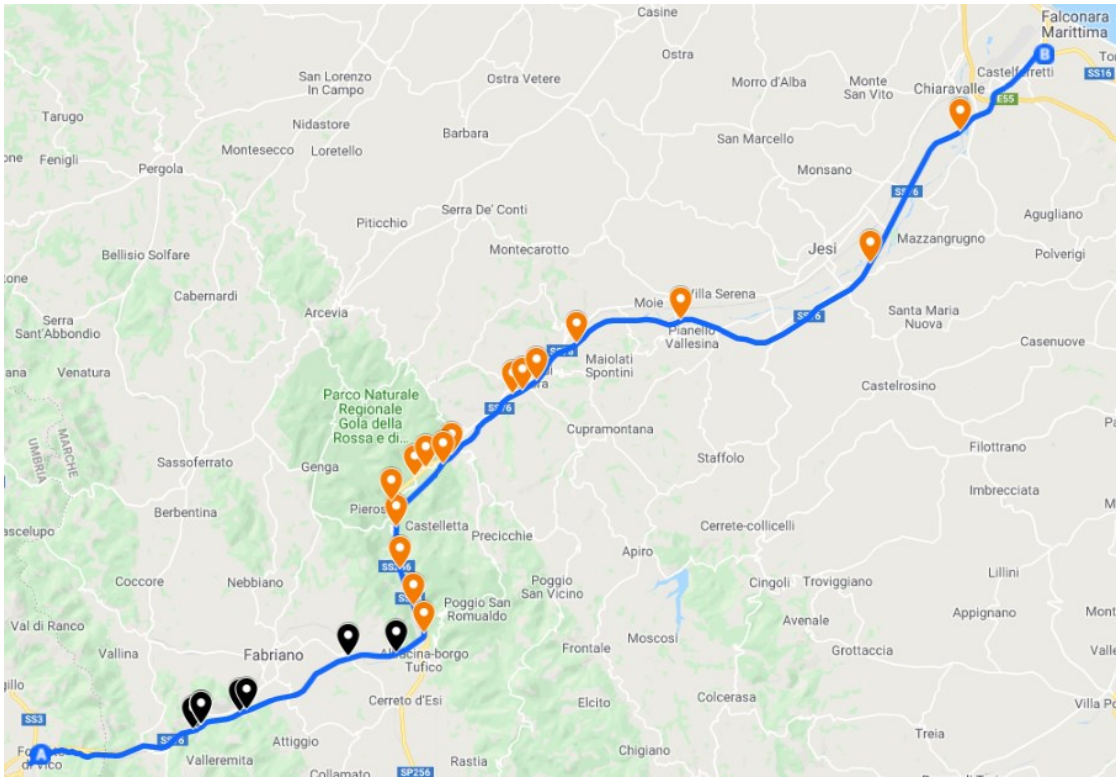

Figure 3.5. Surveyed bridges along SS76. Orange marker: viaducts with RC deck; black marker: viaducts with SCC deck.

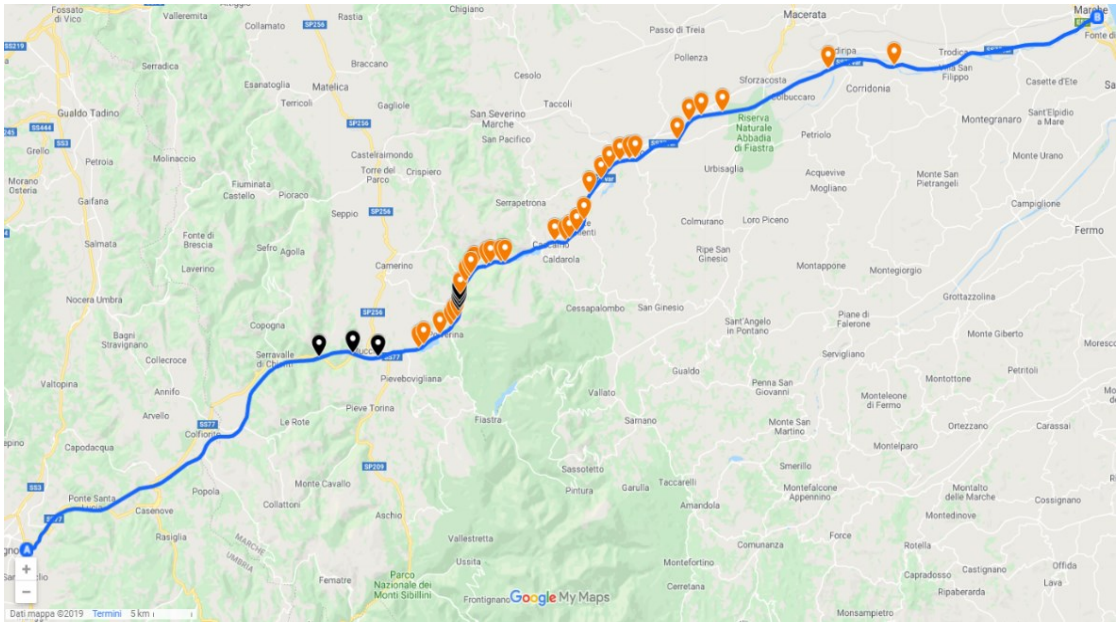

Figure 3.6. Surveyed bridges along SS77. Orange marker: viaducts with RC deck; black marker: viaducts with SCC deck.

The collected information has a different level of detail, basing on the available documentation and the results of web and site surveys. Only 28 bridges out of a total of 90 present an extensive description about structural and geometrical features. The information has been organized into a structured dataset, with the following classification categories:

- **Geographical position of the bridge**
  - Progressive kilometres (from West to East)
  - Nearest residential area
- **General information**
  - Name of the work
  - Age of construction
  - Age of design
  - Total length [m]
- **Deck**
  - Materials
  - Static scheme
  - Typology
  - Number of spans
  - Mean span length [m]
  - Maximum/Minimum span length ratio
- **Piers**
  - Materials
  - Static scheme
  - Cross section

    - Cross section dimensions
    - Mean height [m]
    - Maximum/Minimum pier height ratio
- **Bearings**
    - Typology
- **Foundations**
    - Typology
- **Soil and Location information**
    - Reference PGA
    - Topographic Category T
    - Topographic amplification coefficient S_t

The following Tables show the built-up database. The bridges with a higher level of detail are highlighted in green.

Table 3.1. Surveyed bridges along SS76: geographical position and general information.

SS76					
Geographical Position		General Information			
KM	Nearest residential area	Name	Age of construction	Age of design	Total length [m]
8944	Campodiegoli	Giano Ovest (Dx)	1981 - 2000	1981 -1997	125
8967	Campodiegoli	Giano Ovest (Sx)	1981 - 2000	1981 -1997	124
9129	Campodiegoli	Camporegio (Dx)	1981 - 2000	1986	120.46
9140	Campodiegoli	Camporegio (Sx)	1981 - 2000	1986	119
9430	Campodiegoli	Valleremita (Solo Sx)	1981 - 2000	1986	259
9484	Campodiegoli	Valleremita I (Solo Dx)	1981- 2000	1986	34
9575	Campodiegoli	Valleremita II	1981 - 2000	1986	127
11553	Fabriano	Malvaioli (Sx)	1981- 2000		35
11569	Fabriano	Malvaioli (Dx)	1961 - 1980	1961 -1965	35
11939	Fabriano	Vetralla (Dx)	1961 - 1980		83
11943	Fabriano	Vetralla (Sx)	1981 - 2000		83
17922	Albacina	Giano Est (Dx)	1961 - 1980	1961 -1965	534
17914	Albacina	Giano Est (Sx)	1981 - 2000		536
20235	Albacina	Albacina (Dx)	1961 - 1980		437
20298	Albacina	Albacina (Sx)	1981 - 2000		312
23334	Albacina	Esino	1965		167
27064	Valtreara	Mariani	1967		127
29164	Valtreara	Gattuccio			118
30515	Genga	Esino II	1967		73
32183	Genga	Esino III	1970		113
32894	Genga	Esino IV	1970		113
34465	Serra San Quirico	Gola Della Rossa	1975		707
37886	Serra San Quirico	Serra San Quirico	1975 - 1981		256.1
38814	Angeli di Rosora	Angeli	1970 - 1980		151
39363	Angeli di Mergo	Esinante	1975 - 1981		224.4
40246	Angeli	Collefreddo	1961 - 1980		97
43040	Macine Borgo Loreto	Spontini	1980		232
48782	Castelbellino	Castelbellino	1970 - 1980	1970 - 1980	85.1
59915	Jesi	Esino I		1970 - 1971	256
68169	Piane	Esino II		1970 - 1971	256

Table 3.2. Surveyed bridges along SS76: deck structural information (PRC = Prestressed Reinforced Concrete).

SS76							
General Information	Deck						
Name	Material	Static scheme	Typology		N° spans	L_{mean} [m]	L_{max} /L_{min}
Giano Ovest (Dx)	SCC	Reticular Continuous Box Girder	Continuous Slab	2 Girders with internal braces	4		
Giano Ovest (Sx)	SCC	Reticular Continuous Box Girder	Continuous Slab	2 Girders with internal braces	4		
Camporegio (Dx)	SCC	Reticular Continuous Box Girder	Continuous Slab	2 Girders with internal braces	3	35.35	1.48
Camporegio (Sx)	SCC	Reticular Continuous Box Girder	Continuous Slab	2 Girders with internal braces	3	37	1.55
Valleremita (Sx)	SCC	Reticular Box Girder	Slab with Joints	2 Girders with internal braces	6	40.5	1.38
Valleremita I (Dx)	SCC	Reticular Continuous Box Girder	Continuous Slab	2 Girders	1	34	
Valleremita II	SCC	Reticular Continuous Box Girder	Continuous Slab	2 Girders with internal braces	3	44	1.26
Malvaioli (Sx)	SCC		Continuous Slab		1		
Malvaioli (Dx)	SCC	Reticular Continuous Box Girder	Continuous Slab	2 Girders	1		
Vetralla (Dx)	SCC	Reticular Continuous Box Girder	Continuous Slab	2 Girders	2		
Vetralla (Sx)	SCC	Reticular Continuous Box Girder	Continuous Slab	2 Girders	2		
Giano Est (Dx)	SCC	Reticular Continuous Box Girder	Continuous Slab	2 Girders with internal braces	9		
Giano Est (Sx)	SCC	Reticular Continuous Box Girder	Continuous Slab	2 Girders with internal braces	9		
Albacina (Dx)	SCC	Reticular Continuous Box Girder	Continuous Slab	2 Girders with internal braces	7		
Albacina (Sx)	SCC	Reticular Continuous Box Girder	Continuous Slab	2 Girders with internal braces	5		
Esino	RC	Simply Supported Cross Section	Continuous Slab	5 Girders			
Mariani	RC	Simply Supported Cross Section		11 Girders			
Gattuccio	RC	Simply Supported Cross Section		11 Girders			

Esino II	RC	Simply Supported Cross Section	Slab with Joints	11 Girders			
Esino III	RC	Continuous Box Girder	Slab with Joints		3		
Esino IV	RC	Continuous Box Girder	Slab with Joints				
Gola Della Rossa	RC + PRC	Simply Supported Cross Section	Slab with Joints	9 Girders	24	30.83	1.32
Serra San Quirico	RC + PRC	Simply Supported Cross Section	Slab with Joints	9 Girders	8	31.9	1.32
Angeli	RC + PRC	Simply Supported Cross Section	Slab with Joints	9 Girders	5	30	1.32
Esinante	RC + PRC	Simply Supported Cross Section	Slab with Joints	9 Girders	8	28.37	1.3
Collefreddo	RC + PRC	Simply Supported Cross Section	Slab with Joints	9 Girders	3		
Spontini	RC + PRC	Simply Supported Cross Section	Slab with Joints	9 Girders	8	30.75	1.32
Castelbellino	RC + PRC	Simply Supported Cross Section	Slab with Joints	19 Girders	3	28.45	1.11
Esino I	RC + PRC	Simply Supported Cross Section	Slab with Joints	4 +3 (new) Girders	8	32.1	1
Esino II	RC + PRC	Simply Supported Cross Section	Slab with Joints	4 +3 (new) Girders	8	32.1	1

Table 3.3. Surveyed bridges along SS76: pier structural information.

SS76						
General Information	Piers					
Name	Material	Static scheme	Cross section	Dimensions [m]	H_{mean} (m)	H_{max} / H_{min}
Giano Ovest (Dx)	RC	Wall	Pseudo rectangular			
Giano Ovest (Sx)	RC	Wall	Pseudo rectangular	3,0x7,5		
Camporegio (Dx)	RC	Wall	Hollow pseudo rectangular	3,0x7,5	6.1	1.08
Camporegio (Sx)	RC	Wall	Hollow pseudo rectangular	3,0x7,5	7.12	1.52
Valleremita (Sx)	RC	Wall	Hollow pseudo rectangular	3,0x7,5	12.49	3.2
Valleremita I (Dx)	RC	Wall	Hollow pseudo rectangular	3,0x7,5		
Valleremita II	RC	Wall	Hollow pseudo rectangular		11.5	1.87
Malvaioli (Sx)						
Malvaioli (Dx)						
Vetralla (Dx)	RC	Wall	Hollow pseudo rectangular			
Vetralla (Sx)	RC	Wall	Hollow pseudo rectangular			
Giano Est (Dx)	RC	Single pier	Pseudo rectangular			
Giano Est (Sx)	RC	Single pier	Pseudo rectangular			

Albacina (Dx)	RC	Single pier	Pseudo rectangular			
Albacina (Sx)	RC	Single pier	Pseudo rectangular			
Esino		Single pier	Circular			
Mariani	RC	2 piers frame	Circular			
Gattuccio	RC	2 piers frame	Circular			
Esino II	RC	Wall	Rectangular			
Esino III		Wall	Rectangular			
Esino IV	RC	Wall	Rectangular	1.8		
Gola Della Rossa	RC	Single pier/2 piers frame	Octagonal	1.5	9.94	4.23
Serra San Quirico	RC	Single pier/2 piers frame	Octagonal	1.8	7.2	2.27
Angeli	RC	Single pier/2 piers frame	Octagonal	1.8	5.62	1.5
Esinante	RC	Single pier/2 piers frame	Octagonal		5.76	1.37
Collefreddo	RC	Single pier	Octagonal	1.8		
Spontini	RC	Single pier/2 piers frame	Octagonal	1,80x2,60	8.18	2.27
Castelbellino	RC	2 piers frame	Rectangular	1.5	5	2.33
Esino I	RC	3 piers frame	Circular	1.5	7	1
Esino II	RC	3 piers frame	Circular		7.6	1

Table 3.4. Surveyed bridges along SS76: bearings, foundation and soil and location information.

SS76					
General Information	Bearings	Foundation	Soil and Location information		
Name	Typology	Typology	PGA_{ref}	T	St
Giano Ovest (Dx)					
Giano Ovest (Sx)					
Camporegio (Dx)	Confined elastomeric	Parallelepiped foundation plinth	0.107	T1	St = 1
Camporegio (Sx)	Confined elastomeric	Parallelepiped foundation plinth	0.107	T1	St = 1
Valleremita (Sx)	Confined elastomeric	Parallelepiped foundation plinth	0.107	T1	St = 1
Valleremita I (Dx)	Confined elastomeric	Parallelepiped foundation plinth	0.107	T1	St = 1
Valleremita II	Confined elastomeric	Parallelepiped foundation plinth	0.107	T1	St = 1
Malvaioli (Sx)					
Malvaioli (Dx)					

Vetralla (Dx)					
Vetralla (Sx)					
Giano Est (Dx)					
Giano Est (Sx)					
Albacina (Dx)					
Albacina (Sx)					
Esino					
Mariani					
Gattuccio					
Esino II					
Esino III					
Esino IV					
Gola Della Rossa	Reinforced neoprene	Parallelepiped foundation plinth	0.107	T1	St = 1
Serra San Quirico	Reinforced neoprene	Drilled foundation piles	0.107	T1	St = 1
Angeli	Reinforced neoprene	Drilled foundation piles	0.107	T1	St = 1
Esinante	Reinforced neoprene	Drilled foundation piles	0.107	T1	St = 1
Collefreddo					
Spontini	Reinforced neoprene	Drilled foundation piles	0.107	T1	St = 1
Castelbellino	Reinforced neoprene	Drilled foundation piles	0.107	T1	St = 1
Esino I	Reinforced neoprene	Drilled foundation piles	0.107	T1	St = 1
Esino II	Reinforced neoprene	Drilled foundation piles	0.107	T1	St = 1

Table 3.5. Surveyed bridges along SS77: geographical position and general information.

SS77					
Geographical Position		General Information			
KM	Nearest residential area	Name	Age of construction	Age of design	Total length [m]
28431	Gelagna Bassa	Chienti I (Sx)	2001 - 2016		320
28516	Gelagna Bassa	Chienti I (Dx)	2001 - 2016		270
31152	Muccia	Chienti II (Dx)	2001 - 2016		430
31392	Muccia	Chienti II (Sx)	2001 - 2016		190
33137	Muccia	Muccia (Sx)	2001 - 2016		280
33187	Muccia	Muccia (Dx)	2001 - 2016		310
36341	Pievebovigliana	Le Fratte Ovest	2001 - 2009		130
36785	Pievebovigliana	Le Fratte Est	2001 - 2009		105
38198	Polverina	Polverina (Dx)	2001 - 2009		230
38223	Polverina	Polverina (Sx)	2001 - 2009		204

39254	Polverina	Altino (Dx)	2001 - 2009		135
39286	Polverina	Altino (Sx)	2001 - 2009		110
39654	Polverina	San Giusto (Dx)	2001 - 2009		123
39671	Polverina	San Giusto (Sx)	2001 - 2009		86
40068	Valdiea	Baroglia (Dx)	2001 - 2009		171
40074	Valdiea	Baroglia (Sx)			174
40375	Valdiea	Varano I (Sx)	2001 - 2009		110
40395	Valdiea	Varano I (Dx)	2001 - 2009		110
40758	Valdiea	Valdiea (Dx)	1963		70
40758	Valdiea	Valdiea (Sx)	1981 - 2012		70
52683	Valdiea	Madonna Del Rosario (Dx)	1991-1996	1991	72.4
52696	Valdiea	Madonna Del Rosario (Sx)	1991-1996	1991	107.80
52941	Valdiea	Sasso Rosso I (Dx)	1981-2000	1991	316.7
52955	Valdiea	Sasso Rosso I (Sx)	1981-2000	1991	316.7
53427	Valdiea	Sasso Rosso II (Sx)	1981-2000	1991	107.8
53433	Valdiea	Sasso Rosso II (Sx)	1981-2000	1991	107.8
54408	Bistocco	Fiungo I (Dx)			45
54416	Bistocco	Fiungo I (Sx)			45
54795	Bistocco	Fiungo II (Sx)	1981-2000		177.8
54838	Bistocco	Fiungo II (Dx)	1981-2000		142.1
55070	Bistocco	Fiungo III (Dx)	1981-2000		284.9
55083	Bistocco	Fiungo III (Sx)	1981-2000		272.05
55560	Bistocco	Campolarzo (Dx)	1981-2000	1981 -1990	317
55575	Bistocco	Campolarzo (Sx)	1981-2000	1981 -1990	317
56542	Bistocco	Madonna Di Bistocco (Sx)	1961-1980		71
56554	Bistocco	Madonna Di Bistocco (Dx)	1961-1980		70
56921	Bistocco	Eremo Di San Benedetto (Dx)	1961-1980		60
56952	Bistocco	Eremo San Benedetto (Sx)	1961-1980		66
57700	Colle e Valle Valcimarra	Valcimarra Ovest (Dx)	1981-2000		100
57723	Colle e Valle Valcimarra	Valcimarra Ovest (Sx)	1981-2000		132
58024	Colle e Valle Valcimarra	Valcimarra Est (Sx)	1981-2000	1984	135
58035	Colle e Valle Valcimarra	Valcimarra Est (Dx)	1981-2000	1984	135
62213	Caldarola	Caldarola	1961-1980	1969	355
63024	Belforte del Chienti	Fosso Conce	1961-1980	1969	215
63455	Belforte del Chienti	Savini	1961-1980	1969	434
64247	Belforte del Chienti	Belforte	1961-1980	1969	541.8
65168	Belforte del Chienti	Santa Maria (Dx)	1981-2000		104

65178	Belforte del Chienti	Santa Maria (Sx)	1981-2000		114
67126	Le Grazie	Le Grazie	1961-1980	1970	500
68539	Le Grazie	Cesolone	1981-2000		105
69487	Le Grazie	Chienti I	1961-1990	1961 - 1980	249.1
70544	Tolentino	Tolentino	1961-1980		535.8
71279	Tolentino	Paterno	1981-2000		125
71788	Tolentino	Ancajano	1981-2000		107
75326	Tolentino	Chienti II			105
76951	Piane della Rancia	La Rancia	1981-2000		107
77979	Piane della Rancia	Il Castello	1981-2000	1980	354
79655	Piane della Rancia	Chienti	1981-2000		70
88362	Piediripa	Fiastra	1981-2000	1975	142.8
93565	Piediripa	Chienti III	1981-2000	1975	249.1

Table 3.6. Surveyed bridges along SS77: deck structural information (PRC = Prestressed Reinforced Concrete).

SS77							
General Information	Deck						
Name	Material	Static scheme	Typology		N° spans	L_{mean} [m]	L_{max} /L_{min}
Chienti I (Sx)	SCC	Continuous Reticular Box Girder	Continuous Slab	2 Girders with internal braces	6		
Chienti I (Dx)	SCC	Continuous Reticular Box Girder	Continuous Slab	2 Girders with internal braces	5		
Chienti II (Dx)	SCC	Continuous Reticular Box Girder	Continuous Slab	2 Girders with internal braces			
Chienti II (Sx)	SCC	Continuous Reticular Box Girder	Continuous Slab	2 Girders with internal braces			
Muccia (Sx)	SCC	Countinous Girder	Continuous Slab		6		
Muccia (Dx)	SCC	Countinous Girder	Continuous Slab		6		
Le Fratte Ovest	RC	Simply Supported Cross Section	Continuous Slab	4 Girders	9		
Le Fratte Est	RC	Simply Supported Cross Section	Continuous Slab	4 Girders	5		
Polverina (Dx)	SCC	Continuous Cross Section	Continuous Slab	3 Girders with cross frames	7		
Polverina (Sx)	SCC	Continuous Cross Section	Continuous Slab	3 Girders with cross frames	6		
Altino (Dx)	SCC	Continuous Cross Section	Continuous Slab	3 Girders with cross frames	7		
Altino (Sx)	SCC	Continuous Cross Section	Continuous Slab	3 Girders with cross frames	6		

San Giusto (Dx)	SCC	Continuous Cross Section	Continuous Slab	3 Girders with cross frames	4		
San Giusto (Sx)	SCC	Continuous Cross Section	Continuous Slab	3 Girders with cross frames	3		
Baroglia (Dx)	SCC	Continuous Cross Section	Continuous Slab	3 Girders with cross frames	4		
Baroglia (Sx)	SCC	Continuous Cross Section	Continuous Slab	3 Girders with cross frames	3		
Varano I (Sx)	RC	Continuous Box Girder	Slab with Joints				
Varano I (Dx)	RC	Continuous Box Girder	Slab with Joints				
Valdiea (Dx)	RC	Simply Supported Cross Section	Continuous Slab				
Valdiea (Sx)	RC	Simply Supported Cross Section	Continuous Slab				
Madonna Del Rosario (Dx)	RC + PRC	Simply Supported Cross Section	Continuous Slab	4 Girders with 5 cross frames	3	34.5	1
Madonna Del Rosario (Sx)	RC + PRC	Simply Supported Cross Section	Continuous Slab	4 Girders with 5 cross frames	2	34.5	1
Sasso Rosso I (Dx)	RC + PRC	Simply Supported Cross Section	Continuous Slab	4 Girders with 5 cross frames	9	35.4	1
Sasso Rosso I (Sx)	RC + PRC	Simply Supported Cross Section	Continuous Slab	4 Girders with 5 cross frames	9	35.4	1
Sasso Rosso II (Sx)	RC + PRC	Simply Supported Cross Section	Continuous Slab	4 Girders with 5 cross frames	9	34.5	1
Sasso Rosso II (Sx)	RC + PRC	Simply Supported Cross Section	Continuous Slab	4 Girders with 5 cross frames	9	34.5	1
Fiungo I (Dx)	RC	Box Girder			3		
Fiungo I (Sx)	RC	Box Girder					
Fiungo II (Sx)	RC + PRC	Simply Supported Cross Section	Continuous Slab	4 Girders with 5 cross frames	5	35.7	1
Fiungo II (Dx)	RC + PRC	Simply Supported Cross Section	Continuous Slab	4 Girders with 5 cross frames	4	35.7	1
Fiungo III (Dx)	RC + PRC	Simply Supported Cross Section	Continuous Slab	4 Girders with 5 cross frames	8	35.7	1
Fiungo III (Sx)	RC + PRC	Simply Supported Cross Section	Continuous Slab	4 Girders with 5 cross frames	7+1	35.7	1
Campolarzo (Dx)	RC + PRC	Simply Supported Cross Section	Continuous Slab	4 Girders with 5 cross frames	9	35.4	1
Campolarzo (Sx)	RC + PRC	Simply Supported Cross Section	Continuous Slab	4 Girders with 5 cross frames	9		
Madonna Di Bistocco (Sx)	RC	Open Cross Section	Slab with Joints	4 Girders	3		
Madonna Di Bistocco (Dx)	RC	Open Cross Section	Slab with Joints	4 Girders			
Eremo Di San Benedetto (Dx)	RC	Open Cross Section	Continuous Slab	6 Girders	2		
Eremo San Benedetto (Sx)	RC	Open Cross Section	Continuous Slab	6 Girders	2		
Valcimarra Ovest (Dx)	RC	Open Cross Section	Slab with Joints	6 Girders	3		
Valcimarra Ovest (Sx)	RC	Open Cross Section	Slab with Joints	6 Girders	3		
Valcimarra Est (Sx)	RC + PRC	Simply Supported Cross Section	Continuous Slab	6 Girders with 2 cross frames	4	33.06	1

Valcimarra Est (Dx)	RC + PRC	Simply Supported Cross Section	Continuous Slab	6 Girders with 2 cross frames	4	33.06	1
Caldarola	RC + PRC	Simply Supported Cross Section	Slab with Joints	6 Girders with 5 cross frames	11	36.2	1
Fosso Conce	RC + PRC	Simply Supported Cross Section	Slab with Joints	6 Girders with 5 cross frames	6	36.2	1
Savini	RC + PRC	Simply Supported Cross Section	Slab with Joints	6 Girders with 5 cross frames	12	36.2	1
Belforte	RC + PRC	Simply Supported Cross Section	Slab with Joints	6 Girders with 5 cross frames	15	36.2	1
Santa Maria (Dx)	RC	Simply Supported Cross Section	Continuous Slab	5 Girders with cross frames			
Santa Maria (Sx)	RC	Simply Supported Cross Section	Continuous Slab	5 Girders with cross frames	3		
Le Grazie	RC + PRC	Simply Supported Cross Section	Slab with Joints	6 Girders with 4 cross frames	14	35.7	1
Cesolone	RC	Simply Supported Cross Section	Slab with Joints	10 Girders			
Chienti I	RC + PRC	Simply Supported Cross Section	Slab with Joints	6 Girders with 4 cross frames	7	35.7	1
Tolentino	RC + PRC	Simply Supported Cross Section	Slab with Joints	6 Girders with 5 cross frames	12	44.65	1.27
Paterno	RC	Simply Supported Cross Section	Slab with Joints	6 Girders with cross frames	3		
Ancajano			Slab with Joints		3		
Chienti II			Slab with Joints				
La Rancia	RC	Simply Supported Cross Section	Slab with Joints	6 Girders with cross frames	3		
Il Castello	RC + PRC	Simply Supported Cross Section	Slab with Joints	6 Girders with cross frames	10	35.4	1
Chienti	RC	Simply Supported Cross Section	Continuous Slab	8 Girders with cross frames	3		
Fiastra	RC + PRC	Simply Supported Cross Section	Slab with Joints	6 Girders with 5 cross frames	4	35.7	1
Chienti III	RC + PRC	Simply Supported Cross Section	Slab with Joints	6 Girders with 5 cross frames	7	35.7	1

Table 3.7. Surveyed bridges along SS77: pier structural information.

SS77						
General Information	Piers					
Name	Material	Static scheme	Cross section	Dimensions [m]	H_{mean} (m)	H_{max} / H_{min}
Chienti I (Sx)	RC	Single pier	Pseudo rectangular			
Chienti I (Dx)	RC	Single pier	Pseudo rectangular			
Chienti II (Dx)	RC	Single pier	Pseudo rectangular			
Chienti II (Sx)	RC	Single pier	Pseudo rectangular			
Muccia (Sx)	RC	Single pier	Circular			
Muccia (Dx)	RC	Single pier	Circular			
Le Fratte Ovest	RC	Wall	Pseudo rectangular			
Le Fratte Est	RC	Wall	Pseudo rectangular			
Polverina (Dx)	RC	Wall	Pseudo rectangular			

Polverina (Sx)	RC	Wall	Pseudo rectangular			
Altino (Dx)	RC	Wall	Pseudo rectangular			
Altino (Sx)	RC	Wall	Pseudo rectangular			
San Giusto (Dx)	RC	Wall	Pseudo rectangular			
San Giusto (Sx)	RC	Wall	Pseudo rectangular			
Baroglia (Dx)	RC	Wall	Pseudo rectangular			
Baroglia (Sx)	RC	Wall	Pseudo rectangular			
Varano I (Sx)		Single pier	Circular			
Varano I (Dx)		Single pier	Circular			
Valdiea (Dx)		Single pier	Pseudo rectangular			
Valdiea (Sx)		Single pier	Pseudo rectangular			
Madonna Del Rosario (Dx)	RC	Single pier	Circular	2.5	1.5	1
Madonna Del Rosario (Sx)	RC	Single pier	Circular	2.5	3.5	1
Sasso Rosso I (Dx)	RC	Single pier	Circular	2.5	1.26	2.43
Sasso Rosso I (Sx)	RC	Single pier	Circular	2.5	1.14	2.43
Sasso Rosso II (Sx)	RC	Single pier	Circular	2.5	1.75	1.33
Sasso Rosso II (Sx)	RC	Single pier	Circular	2.5	1.75	1.33
Fiungo I (Dx)	RC	Single pier	Circular			
Fiungo I (Sx)	RC	Single pier	Circular			
Fiungo II (Sx)	RC	Single pier	Hollow circular	2.8	5.25	1.16
Fiungo II (Dx)	RC	Single pier	Hollow circular	2.8	5.59	1.16
Fiungo III (Dx)	RC	Single pier	Hollow circular	2.8	5.44	1.47
Fiungo III (Sx)	RC	Single pier	Hollow circular	2.8	5.57	1.29
Campolarzo (Dx)	RC	Single pier	Circular/Rectangular	2.5	4.21	1.27
Campolarzo (Sx)	RC	Single pier	Circular/Rectangular	2.5	4.34	1.27
Madonna Di Bistocco (Sx)	RC	Single pier	Circular			
Madonna Di Bistocco (Dx)	RC	Single pier	Circular			
Eremo Di San Benedetto (Dx)	RC	Single pier	Circular			
Eremo San Benedetto (Sx)	RC	Single pier	Circular			
Valcimarra Ovest (Dx)	RC	Single pier	Circular			
Valcimarra Ovest (Sx)	RC	Single pier	Circular			
Valcimarra Est (Sx)	RC	Single pier	Circular	2.5	8.45	1.1
Valcimarra Est (Dx)	RC	Single pier	Circular	2.5	8.35	1.11
Caldarola	RC	Wall	Hollow rectangular wall	2,5x9,0	14.12	6.94
Fosso Conce	RC	Wall	Hollow rectangular wall	2,5x9,0	11.84	2.35
Savini	RC	Wall	Hollow rectangular wall	2,5x9,0	15.41	1.3
Belforte	RC	Wall	Hollow rectangular wall	2,5x9,0	9.32	2.68
Santa Maria (Dx)	RC	6 piers frame	Circular			

Santa Maria (Sx)	RC	6 piers frame	Circular			
Le Grazie	RC	Wall	Pseudo rectangular wall	2,60x9,50	11.2	1.4
Cesolone	RC	Wall	Pseudo rectangular wall			
Chienti I	RC	2 piers frame	Circular	2.2	6.54	1.47
Tolentino	RC	2 piers frame	Pseudo rectangular	2.2	5.3	3.27
Paterno	RC	2 piers frame	Circular			
Ancajano						
Chienti II						
La Rancia	RC	2 piers frame	Circular			
Il Castello	RC	2 piers frame	Circular	2.2	5.67	1.87
Chienti	RC	2 piers frame	Circular			
Fiastra	RC	2 piers frame	Circular	2.2	5	1
Chienti III	RC	2 piers frame	Circular	2.2	6	1

Table 3.8. Surveyed bridges along SS77: bearings, foundation and soil and location information.

SS77					
General Information	Bearings	Foundation	Soil		
Name	Typology	Typology	PGA_{rif}	T	St
Chienti I (Sx)					
Chienti I (Dx)					
Chienti II (Dx)					
Chienti II (Sx)					
Muccia (Sx)					
Muccia (Dx)					
Le Fratte Ovest					
Le Fratte Est					
Polverina (Dx)					
Polverina (Sx)					
Altino (Dx)					
Altino (Sx)					
San Giusto (Dx)					
San Giusto (Sx)					
Baroglia (Dx)					
Baroglia (Sx)					
Varano I (Sx)					
Varano I (Dx)					
Valdiea (Dx)					
Valdiea (Sx)					
Madonna Del Rosario (Dx)	Steel and PTFE	Micropiles and jet grouting	0.107	T1	St = 1
Madonna Del Rosario (Sx)	Steel and PTFE	Micropiles and jet grouting	0.107	T1	St = 1

Sasso Rosso I (Dx)	Steel and PTFE	Deep foundation	0.107	T1	St = 1
Sasso Rosso I (Sx)	Steel and PTFE	Deep foundation	0.107	T1	St = 1
Sasso Rosso II (Sx)	Steel and PTFE	Deep foundation	0.107	T1	St = 1
Sasso Rosso II (Sx)	Steel and PTFE	Deep foundation	0.107	T1	St = 1
Fiungo I (Dx)					
Fiungo I (Sx)					
Fiungo II (Sx)	Steel and PTFE	Deep foundation	0.107	T1	St = 1
Fiungo II (Dx)	Steel Hinges	Deep foundation	0.107	T1	St = 1
Fiungo III (Dx)	Steel and PTFE	Deep foundation	0.107	T1	St = 1
Fiungo III (Sx)	Steel and PTFE	Deep foundation	0.107	T1	St = 1
Campolarzo (Dx)	Steel and PTFE	Deep foundation	0.107	T1	St = 1
Campolarzo (Sx)	Steel and PTFE	Deep foundation	0.107	T1	St = 1
Madonna Di Bistocco (Sx)					
Madonna Di Bistocco (Dx)					
Eremo Di San Benedetto (Dx)					
Eremo San Benedetto (Sx)					
Valcimarra Ovest (Dx)					
Valcimarra Ovest (Sx)					
Valcimarra Est (Sx)	Confined elastomeric	Deep foundation	0.102	T1	St = 1
Valcimarra Est (Dx)	Confined elastomeric	Deep foundation	0.102	T1	St = 1
Caldarola	Reinforced neoprene	Deep foundation	0.098	T1	St = 1
Fosso Conce	Reinforced neoprene	Deep foundation	0.098	T1	St = 1
Savini	Reinforced neoprene	Drilled foundation piles	0.098	T1	St = 1
Belforte	Reinforced neoprene	Drilled foundation piles	0.098	T1	St = 1
Santa Maria (Dx)					
Santa Maria (Sx)					
Le Grazie	Reinforced neoprene	Drilled foundation piles	0.098	T1	St = 1
Cesolone					
Chienti I	Reinforced neoprene	Drilled foundation piles	0.096	T1	St = 1
Tolentino	Confined elastomeric	Deep foundation	0.095	T1	St = 1
Paterno					
Ancajano					
Chienti II					
La Rancia					
Il Castello		Drilled foundation piles	0.095	T1	St = 1
Chienti					
Fiastra	Steel and PTFE	Drilled foundation piles	0.095	T1	St = 1
Chienti III	Reinforced neoprene	Drilled foundation piles	0.091	T1	St = 1

3.2.1 Statistical analyses on the dataset

As a second phase of the analysis of the information about bridges in the Marche Region, the dataset has been reprocessed in order to identify the main characteristics of a representative bridge prototype to be used as a case study for the evaluation of the seismic and traffic performance in the regional context.

The first statistic elaboration concerns the age of building and construction (whereas available), useful to identify the corresponding design rules for a simulated project. Three time bands have been chosen, corresponding to the most important changes in the Italian codes about bridges design. It turns out that the number of "old" bridges in the Marche Region (i.e. with more than 50 years) is higher than the number of the newest ones. This means that a reliable analysis of the bridge inventory should be done taking into account old codes and old design rules. A histogram about the distribution of bridge ages is depicted in Figure 3.7. The second elaboration is about the total length of the viaducts (Figure 3.8). The most populated categories are relative to lengths comprised between 50 and 150 m and between 200 and 350 m.

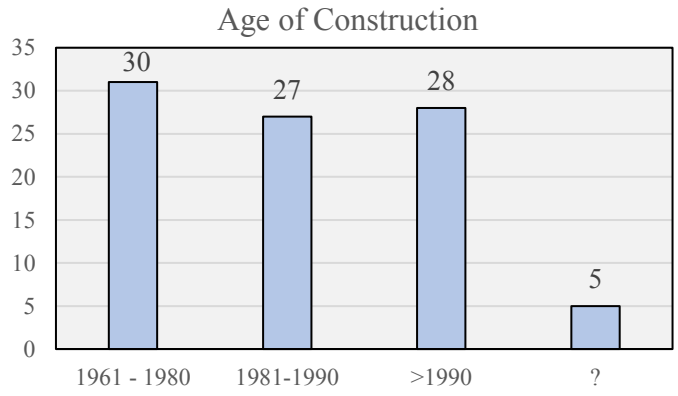

Figure 3.7. Statistics about the age of construction of bridges on SS76 and SS77.

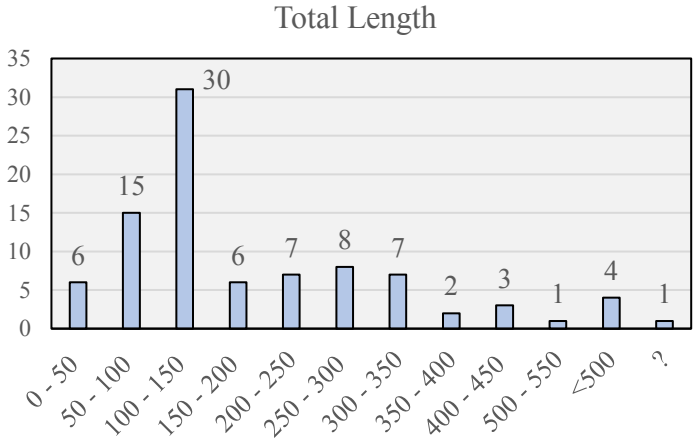

Figure 3.8. Statistics about the total length of construction of bridges on SS76 and SS77.

The analysis of the geographical distribution of the surveyed bridges shows that 2 out of 3 viaducts have a RC deck (Figure 3.9). More than half are simply supported decks (Figure 3.10). In order to summarize the information, almost the totality of the simply supported decks are RC decks, while bridges with continuous spans have SCC decks (Figure 3.11).

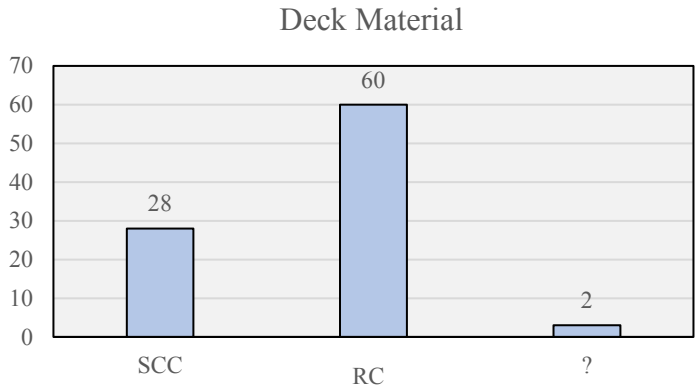

Figure 3.9. Deck construction material of bridges on SS76 and SS77.

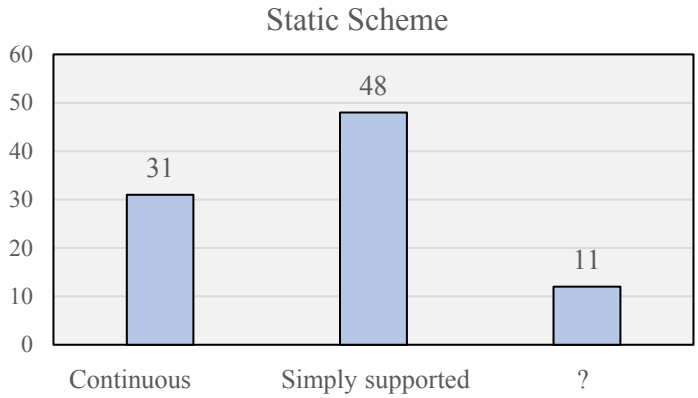

Figure 3.10. Statistics about the static scheme of bridges on SS76 and SS77.

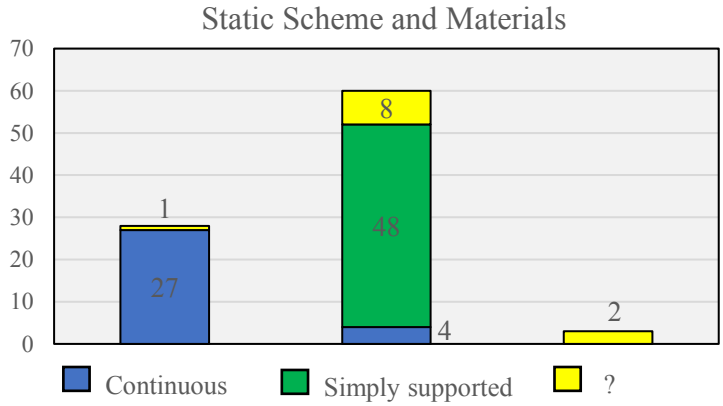

Figure 3.11. Distribution of static schemes basing and deck construction material on SS76 and SS77.

In Figure 3.12 the distribution of the deck cross sections is represented, with more than 60% of bridges realized with open girders, a typic typology for simply supported spans, and almost the total of the remaining decks presents a box girder cross section, with different configurations depending on the construction material (RC or SCC). Similarly to Figure 3.11, a summarising view of the existing decks can be provided through the following Figure 3.13.

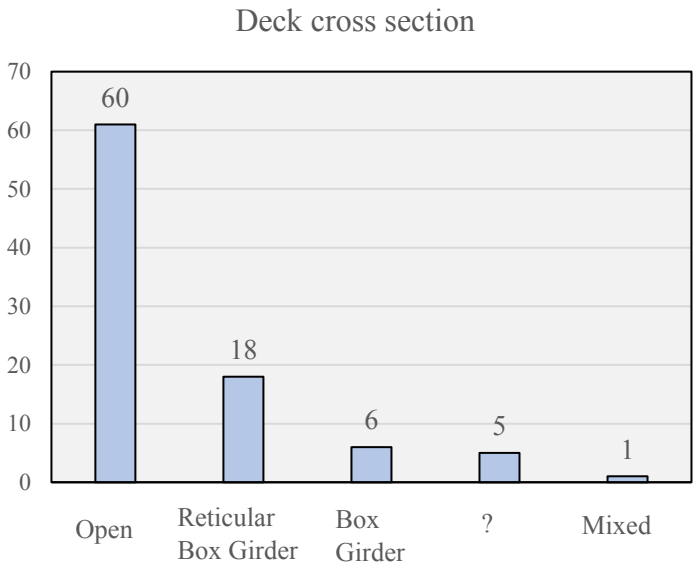

Figure 3.12. Distribution of deck cross sections of bridges on SS76 and SS77.

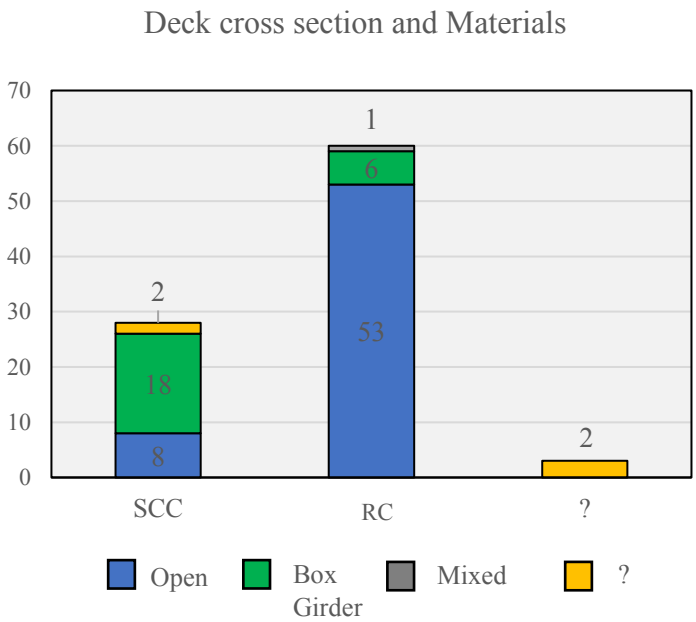

Figure 3.13. Distribution of deck typology basing on the deck construction material of bridges on SS76 and SS77.

Moving on to the analysis of the spans (Figure 3.14), it can be seen that 3-span bridges alone represent 20% of the bridges for which information are collected. Another very common value are bridges with 9 spans. Concerning the number of spans, it was not possible to have information on the number of spans of 20% of the population. For bridges with a complete set of information, it turns out that the spans are typically long from 20 to 40 metres (Figure 3.15a), the most usual configuration provides for equal length spans and a little percentage presents limited changes in the difference between the maximum and the minimum length (max 40%) (Figure 3.15b).

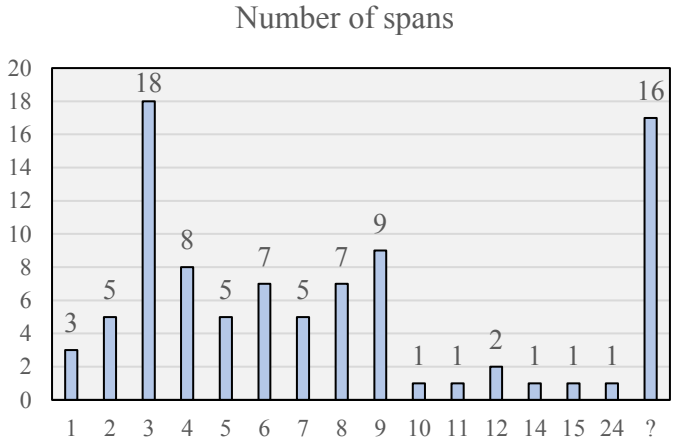

Figure 3.14. Statistics about the number of spans of bridges on SS76 and SS77.

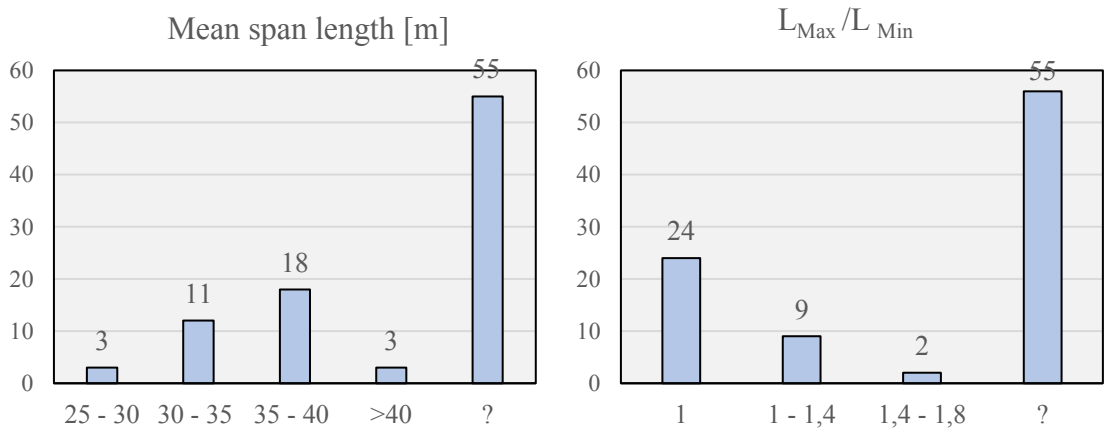

Figure 3.15. Statistics about (a) the mean span length of bridges and (b) the ratio between maximum and minimum length of bridges on SS76 and SS77.

Concerning the piers, in Figure 3.16 the distribution of the typologies is shown. The static scheme of single pier covers more than 40% of the surveyed bridges, followed by the wall scheme (30%) and the frame (20%). Within the latter, the majority of bridges presents two columns (Figure 3.17).

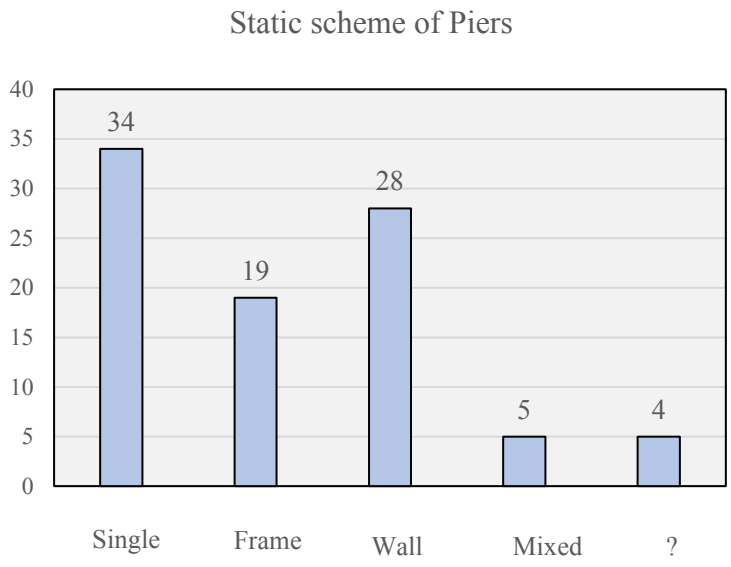

Figure 3.16. Distribution of pier static schemes of bridges on SS76 and SS77.

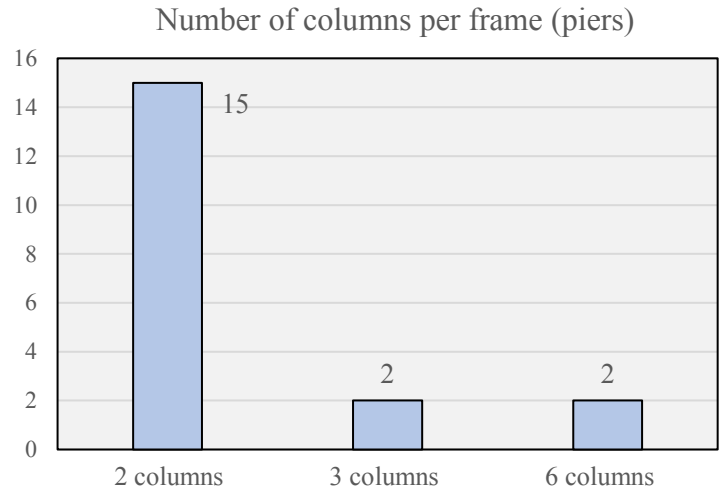

Figure 3.17. Distribution of the number of columns in frame piers.

Concerning the mean height of the piers, for bridges with a complete set of information, it turns out that the spans are typically high from 4,5 to 6 metres (Figure 3.18), and a significant percentage is covered by piers from 6 to 9 m. Similarly to the spans, the most usual configuration provides for equal height piers and a little percentage presents limited changes in the difference between the maximum and the minimum length (max 40%) (Figure 3.19). The most common cross section is the circular one, which represents the 40% of the total. 31 of the investigated bridges have a wall pier, while the remaining have rectangular or pseudo-rectangular cross sections (Figure 3.20).

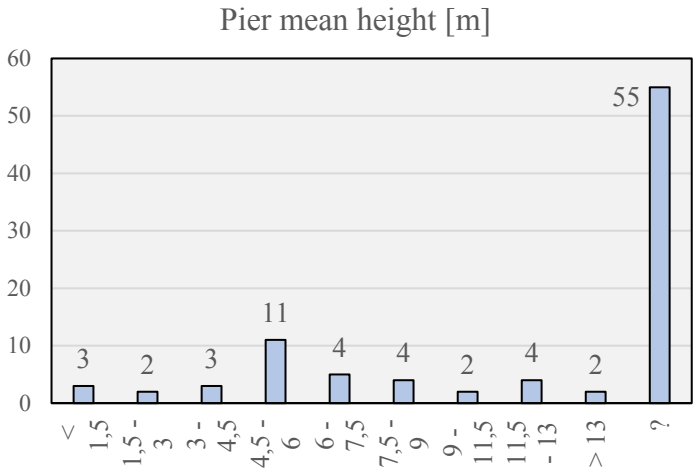

Figure 3.18. Statistics about the mean pier height of bridges on SS76 and SS77.

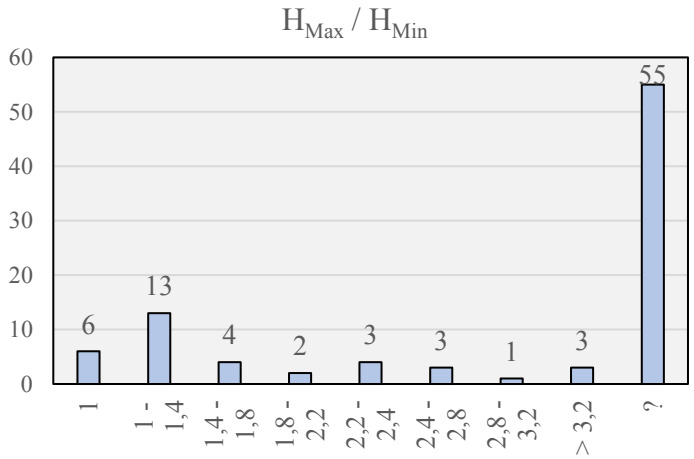

Figure 3.19. Statistics about the ratio between maximum and minimum height of bridges on SS76 and SS77.

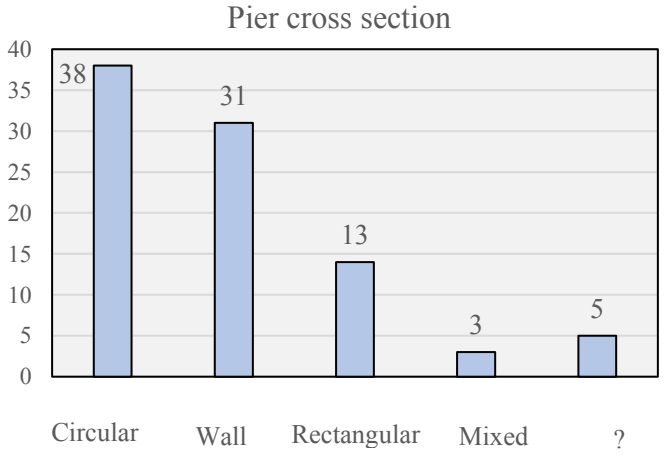

Figure 3.20. Distribution of pier cross sections of bridges on SS76 and SS77.

3.3 Previous and Current Design Codes for Italian Bridges

The numerous seismic events that involved the Italian territory in the XX century brought important changes in the seismic design philosophy both for buildings and for bridges. Since the beginning of 1900 the aim of the design codes started to be the mitigation of damages due to the occurrence of seismic events, through the progressive investigation of three fundamental aspects: the seismic classification of the Italian territory, the design of earthquake-proof buildings and the structural adjustment for existing structures. It is possible to classify the norms issued by the Italian governance about civil structures and infrastructures in 4 groups, each of which related to one or more particular seismic episodes:

- 1st generation Norms – from 1909 to '60s (in occurrence of the Messina earthquake in 1908);
- 2nd generation Norms – from '60s to 1980 (in occurrence of the Belice earthquake in 1968)
- 3rd generation Norms – from 1980 to 2000 (after the Friuli and the Irpinia earthquakes in 1976)
- 4th generation Norms – from 2000 to date (the Umbria-Marche earthquake in 1997, the L'Aquila earthquake in 2008, the Emilia earthquake in 2012, the earthquake in Central Italy of Amatrice-Norcia-Visso in 2016)

The analysis of the database showed that the majority of viaducts in the Marche region dates back to ages of construction when the actual design codes were not available. In particular, the existing Marche bridges and viaducts refer mainly to the 2nd and 3rd generation Norms. In the following Paragraphs, an illustration of the most important design rules and codes in seismic and civil engineering for the considered existing bridges and viaducts is offered. In particular, the first two sections concern the design codes before and after the emanation of Italian NTC2008, respectively. Then, the last section is dedicated to the new Italian Guidelines for existing bridges, approved in April 2020.

3.3.1 Pre-NTC2008 Codes

The formal introduction of the 2nd generation Norms coincides with the emanation of the Law n. 64/1974 and the consequent approval through the Ministerial Decree 03/03/1975. Two main aspects formed the innovation in the Italian design codes: the first is the introduction of a seismic classification for the Italian municipalities basing on the concept of degree of seismic intensity; the second concerns the concept of elastic response spectrum and the introduction of the dynamic analyses as a valid instrument to calculate the structural performance in occurrence of an earthquake. Both the concepts were introduced numerically in the design through the following formulations:

- for an equivalent static analysis, allowed in case of simple static schemes, the structure is subjected to a system of horizontal forces, parallel to the direction of the seismic action, whose resultant can be calculated as follows:

$$F_h = CRW$$

where $C = (S-2)/100$ is the coefficient of seismic intensity; S ($S \geq 2$) is the degree of seismicity; R is the response coefficient in the considered direction; W is the total weight of the structural masses.
Similarly, for the vertical direction:

$$F_v = mCW$$

where $m = 2$.

- for a dynamic analysis in linear elastic field, the elastic response spectrum in acceleration must be used in the modal analysis with the following relation:

$$\frac{a}{g} = CR$$

where a is the spectral acceleration, g is the gravity acceleration, R is (as above) a function of the fundamental vibration period, being:
$T_0 < 0{,}8$ s $\rightarrow R = 0{,}862/{T_0}^{2/3}$;
$T_0 \geq 0{,}8$ s $\rightarrow R = 1$;
T_0 unknown $\rightarrow R = 1$.

Concerning bridge structures, the Ministerial Circular n. 384 14/02/1962 established a classification based on the load typology in transit:

- bridges of I category: for the transit of military and civil loads;
- bridges of II category: for the transit of civil loads only (typically on local roads).

According to the specific category and the importance of the pertaining road, different load schemes were applied. No significant improvements about the seismic design of bridges were still approved. The assessment of the structure under vertical and horizontal loads was conducted according to the Admissible Stresses (AS) method.

After the Friuli and the Irpinia earthquakes, it became necessary to improve the classification of the Italian regions in a seismic perspective, basing not on the already happened events, but rather on a reliable forecasting of the future shakings depending on the previous cases. A 3rd generation of Norms started with the Ministerial Decrees of 03/06/1981 and 29/02/1984, in which the Italian territory is classified according to the first probabilistic study by the National Research Council (CNR) in three seismic zones, from the highest to the lowest associated seismic intensity (Figure 3.21):

- I category: $C = 0.10$;
- II category: $C = 0.07$;
- III category: $C = 0.04$.

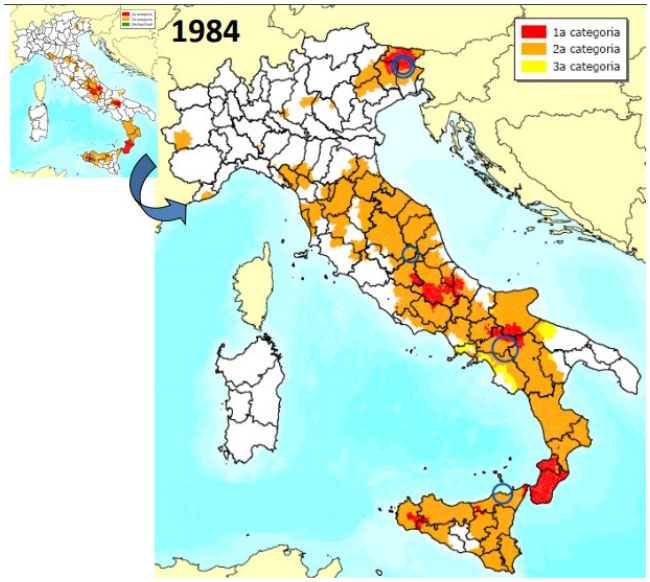

Figure 3.21. Evolution of the seismic classification on the Italian territory from 2nd to 3rd generation rules: red = I category (high seismicity); orange = II category (medium seismicity); yellow = III category (low seismicity).

With the Ministerial Decree of 19/06/1984 the diversification of the seismic performance of structures is introduced through the coefficient of seismic protection I, to be used in case of strategic and particular bridges and buildings. The previous formulations for equivalent static and dynamic analyses changed in the following:

- for horizonal actions:

$$F_h = CIRW$$

- for vertical actions:

$$F_h = mIRW$$

- for dynamic analysis:

$$\frac{a}{g} = CIR$$

where $I = 1.0$ for standard bridges and buildings, $I = 1.2$ for works with higher risk basing on the relative use category, $I = 1.4$ for works with a strategic and fundamental role in case of emergency.

Another important aspect introduced with the 3rd generation Norms was related to the current concept of performance-based design. Two different seismic events ruled the design and the assessment of the structures: the service earthquake, with a return period of 70 years, and the disruptive earthquake, with a 475-years return period. As a consequence, two different Limit States were introduced, which still represent two fundamental performance levels in the current design procedures: the Damage Limit State

(DLS), which represents a threshold within the structures shows limited structural and non-structural damages, calculated according to specific parameters (e.g. the interstory drift for buildings), and the Ultimate Limit State (ULS), related to the structural capacity towards vertical loads which must be ensured for the *life-safety*, even if both in structural and non-structural parts the building is severely damaged. A first attempt to take into account properly DLS and ULS was provided by the Ministerial Decree of 09/01/1996, which received the Eurocodes 2 and 3 about the calculation of load combinations with specific load amplification coefficients:

- for Ultimate Limit States:

$$F_d = \gamma_g G_k + \gamma_p P_k + \gamma_q \left[Q_{1k} + \sum_{i=2}^{n} \psi_{0i} Q_{ik} \right]$$

  where

  G_k the characteristic value of the permanent actions;

  P_k the characteristic value of the precompression strength;

  Q_{1k} the characteristic value of the variable action considered as principal;

  Q_{ik} the characteristic value of the other variable (independent) actions;

  γ_g = 1,4 (1,0 if in favour of security);

  γ_p = 1,2 (0,9 if in favour of security);

  γ_q = 1,5 (0 if in favour of security);

  ψ_{0i} the combination coefficient, whose value depends on the considered variable action in the combination.

- for Damage Limit States:

$$F_d = G_k + P_k + Q_{1k} + \sum_{i=2}^{n} \psi_{01} Q_{ik} \text{ (rare combination)}$$

$$F_d = G_k + P_k + \psi_{11} Q_{1k} + \sum_{i=2}^{n} \psi_{21} Q_{ik} \text{ (frequent combination)}$$

$$F_d = G_k + P_k + \sum_{i=2}^{n} \psi_{21} Q_{ik} \text{ (quasi-permanent combination)}$$

  where $\gamma_g = \gamma_p = \gamma_q = 1$ and ψ_0, ψ_1, ψ_2 with tabular values associated to different probabilities of occurrence of the considered variable action.

Concerning bridge structures, for the first time with the Ministerial Decree 02/08/1980 the seismic action is properly considered in the load combinations to assess the structural performance with both the Admissible Stresses method and the new semi-probabilistic Limit State method. In particular, the actions that was necessary to consider in the design of road bridges were the following:

g_1 = structural self-weight;

g_2 = permanent loads;

g_3 = other permanent loads;

ε_1 = distortions (pretensioning excluded);

ε_2= concrete shrinkage;

ε_3= thermal variations;

q_1 = vehicular loads;

q_2 = dynamic increment of vehicular loads;

q_3 = longitudinal braking action;

q_4 = centrifugal action;

q_5 = wind action;

q_6 = seismic action;

q_7 = friction resistance at bearings;

q_8 = actions on railings;

q_9 = other variable loads.

With the Ministerial Decree of 04/05/1990 the coefficient of structure β is introduced, related to the static scheme and the ductility characteristics of the bridge. The suggested values in case of lack of additive surveys were: $\beta = 1.0$ for frame structures (i.e. girders directly connected to the piers, frame piers for actions in the frame plane, etc.); $\beta = 1.2$ for limited ductility and isostatic structures (i.e. single pier bridges and frame piers for actions out of the frame plane); $\beta = 2.5$ for bearings and shear keys. An additional information was added in the Circular n. 34233 25/02/1991, where it was assumed that the coefficient of seismic protection I can be assumed equal to 1.0 for all the bridge structures, excepting for the ones with exceptional strategic importance.

3.3.2 Post-NTC2008 Codes

After the L'Aquila earthquake, happened on 06/04/2008 (which registered 330 deaths), the Ministerial Decree of 14/01/2008 finally entered into force revolutionizing the existing codes in the field of seismic design. The new "Norme Tecniche per le Costruzioni", or NTC2008, introduced different novelties, among which:

- a new criterion for the calculation of the seismic acceleration at site, going beyond the concept of seismic zone (which implied the evaluation of a unique acceleration value in the same seismic area) and providing a local evaluation of the local expected acceleration;

- the introduction of amplification site coefficient;
- the introduction of the coefficient of topography;
- the evaluation of the seismic actions basing on the so-called reference period (V_R), as a combination of the nominal structural life (V_N), depending on the structural typology, with the coefficient of use (C_U), depending on the importance of the structure in the territory. The reference period can be directly related to the exceedance probability P_R of a seismic event occurrence, basing on which the evaluation of the seismic hazard can be carried out.

In order to comply with the Eurocodes, after the Central Italy earthquakes in 2016, an upgraded version of NTC2008, the new NTC2018 has been approved with the Ministerial Decree of 17/01/2018, in which some adjustments in the field of seismic engineering are made. Among the modifications, the abolition of soil classes S1 and S2 and the removal of any mention to the AS method.

Concerning bridge structures, from NTC2008 the structure must be designed to show dissipative mechanisms only in correspondence of piers or dedicated dissipative devices, involving the maximum possible number of supporting elements in flexural inelastic behaviours and excluding fragile ones (shear ruptures). An elastic behaviour is expected (and also required) for deck, bearings (in case of not-dissipative devices), foundations and abutments, where plastic deformations are avoided through the adoption of the resistance hierarchy in the design project. Also, any mention to the AS method for the bridge assessment has been removed. Currently, from NTC2018, no fundamental information about the seismic design have been added. Only two bridge categories have been inherited from previous codes: bridges for the transit of all types of mobile loads, and pedestrian walkways.

3.3.3 Italian 2020 Guidelines for existing bridges

From the previous Paragraphs it is evident that a large effort has been put in the improvement of the design rules in the seismic context through the years, being the earthquake the most relevant type of hazard on the Italian territory. The insight of the seismic behaviour of new structures takes wide space and allows to realize an efficient design capable of mitigating risks associated to the occurrence of seismic events.

It is worth remembering that a peculiarity of the Italian territory is that the large majority of structures belongs to periods prior to the introduction of current seismic norms. In particular, more than 80% of Italian buildings date back to the 70's, when the first proposals of seismic design rules were just a draft of nowadays codes. Moreover, a 15% are prior 1918 and in the most of cases located in high seismicity zones as well. With more than 12 million buildings (including residential buildings, hospitals, commercial structures), only about 800'000 have less than 20 years.

Nevertheless, it is true that few norms regarding the maintenance problem are concomitant to the seismic design ones in Italy. The problem of maintenance is of primary importance, not only for bridges, but also for strategic structures, buildings belonging to

the national cultural heritage (ancient churches, cathedrals, temples, castles, theatres and so on), civil facilities with social and economic relevance. In case of bridges, the consequences of a bad or null maintenance can be disastrous for the entire society due to the primary importance of such structures in emergency, economic and social context.

As already introduced in §3.1, differently from some European countries, in Italy there is not a national database of existing bridge structures, nor a national norm where the operations of inspection, intervention and works for maintenance are encoded. The responsibility of those actions is delegated to local, regional or private handlers, with no fixed time scheduling nor standard protocols for the coordination among involved partners. In the last 100 years, only three attempts to introduce efficient rules about the maintenance have been made:

- Ministerial Circular n. 6736 19/07/1967: after the collapse of two arcades of the bridge in the city of Ariccia, the Department of Public Works recognized the need of a coordination in the visual inspection operations, in order to periodically monitor the status of health of the considered bridge;
- Ministerial Circular n. 34233 25/02/1991: presupposing that all the handlers must have a complete knowledge of their works, 4 fundamental phases for maintenance are outlined, that is vigilance by specialised personnel, cadenced inspections with a final report, ordinary or extraordinary maintenance, static restoration interventions;
- Ministerial Decree 14/01/2008 and Ministerial Circular n. 617 02/02/2009: tests are encoded to characterize the mechanical properties of structural materials.

In order to provide an efficient procedure for the management of existing bridges, on 17th April 2020 the Ministry of Infrastructure and Transport drew up new Guidelines that address three fundamental aspects: the survey and the risk classification, the safety assessment and the monitoring of existing works with a total length greater than 6.0 m. The novelty of these Guidelines lays in a multi-level approach, that from the direct survey of the bridge structures, the analysis of the available design documentation and/or the evaluation of the boundary conditions leads to a *class of attention*, basing on which the successive assessments, whereas necessary, are made. Depending on the most significant risks for the examined bridges, related to their structural peculiarities and the environmental context, 4 specific *classes of attention* (CoA) can be evaluated: the structural and foundational CoA, related to the structural capacity respect to the vertical loads; the seismic CoA, related to the structural capacity against earthquake action induced phenomena; the landslide CoA, related to the occurrence of landslide phenomena; the hydraulic CoA, related to the occurrence of flood events and fluvial erosions. These 4 specific CoA are then recombined to furnish a global *class of attention.*

The classification in one of five global *classes of attention* recollects the outcomes of the analyses in terms of hazard, fragility and exposure, and results not only in fundamental instructions for potential restoration works or maintenance interventions, but also in useful information to evaluate the resilience of the road network of pertinence. The

introduction of a multi-level approach is necessary given the large number of existing infrastructures on the national territory, so that the complexity of the numerous actions is calibrated depending on the need and the urgency, as applicable. One of the natural consequences of the application of this method is already outlined as a future target within 2025, that is the complete digitalization and the informatic management of the entire Italian bridge stock through BIM software and BMSs. Figure 3.22 illustrates in a schematic representation the content of the new Guidelines. In the coloured boxes the five *classes of attention* are illustrated, from the highest (in red) to the lowest (in green).

The adoption of accurate instruments such as the fragility curves and the risk curves may offer a more reliable view of the structural capacity in case of a high *class of attention*, which implies a deeper level of investigation and assessment (Level 4). The fragility analysis may reveal also fundamental in case of bridges and viaducts of strategic importance for a thorough evaluation of the resilience of the road network of pertinence (Level 5).

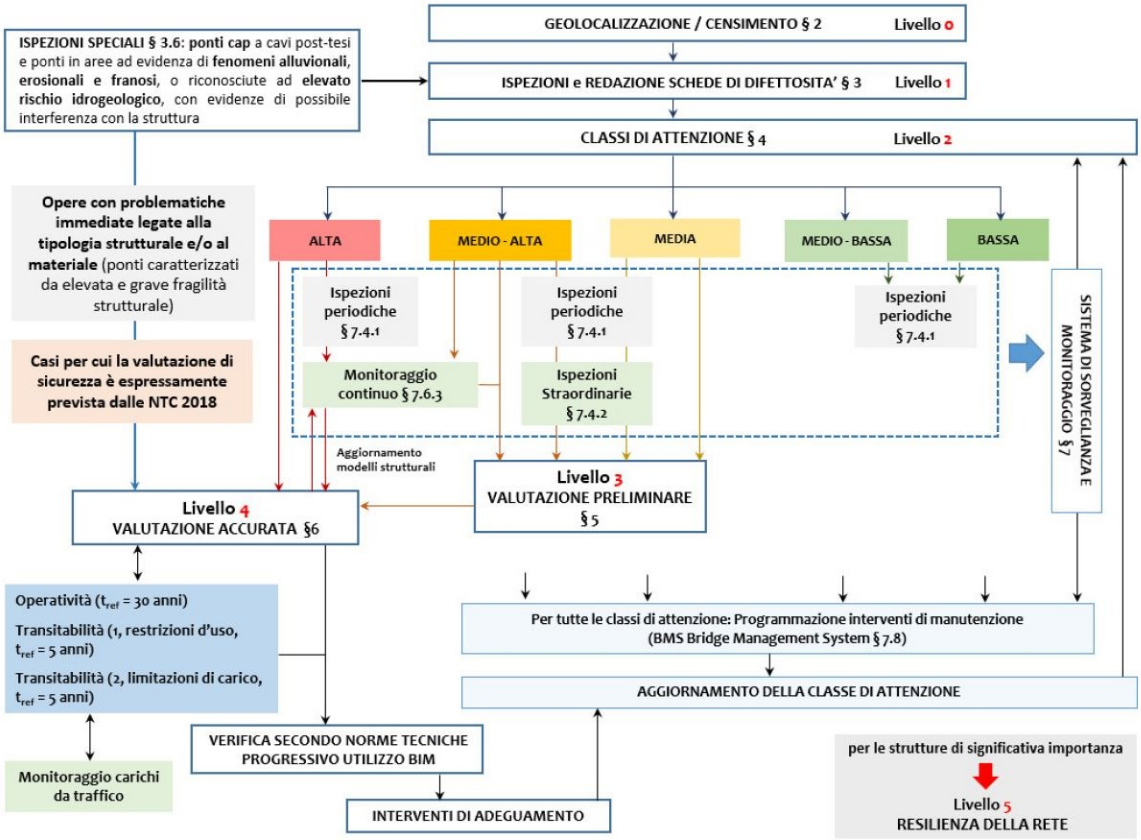

Figure 3.22. Multi-level approach and logical relations among different levels of analysis in the new Guidelines for existing bridges (in Italian).

In the following Chapters, the fragility analysis of two most common bridge typologies on the Italian territory, the Reinforced Concrete with Link Slab (RCLS) bridges and the Steel-Concrete Composite (SCC) bridges, is carried out on significant case studies for the characterization of the bridge inventory in the Marche region. Then, results of fragility

analysis are applied for the evaluation of direct and indirect consequences at road network level, according to a wider framework in which the Guidelines can be included. Indeed, the fragility analysis represents a necessary step for the assessment of the adequacy of the structure respect to the current codes and for the forecasting of potential risks.

3.4 Chapter's references

Borzi, B., Ceresa, P., Franchin, P., Noto, F., Calvi, G. M., & Pinto, P. E. (2015). Seismic vulnerability of the Italian roadway bridge stock. *Earthquake Spectra*, *31*(4), 2137-2161.

C.S.LL.PP., C.M. n. 617 02.02.2009, *Istruzioni per l'applicazione delle «Nuove norme tecniche per le costruzioni» di cui al decreto ministeriale 14 gennaio 2008* (in Italian).

EN 1992, 2004. *Eurocode 2: Design of Concrete Structures*. 1st ed. Brussels: BSi.

EN 1993, 2005. *Eurocode 3: Design of Steel Structures*. London: BSI, 2005. Print.

Gattulli, V., & Chiaramonte, L. (2005). Condition assessment by visual inspection for a bridge management system. *Computer-Aided Civil and Infrastructure Engineering*, *20*(2), 95-107.

Ministero dei Lavori Pubblici, C.M n. 34233 25.02.1991, *Istruzioni relative alla normativa tecnica dei ponti stradali* (in Italian).

Ministero dei Lavori Pubblici, C.M n. 6736 19.07.1967, *Controllo delle condizioni di stabilità delle opere d'arte stradali* (in Italian).

Ministero dei Lavori Pubblici, C.M. n.384 14.02.1962, *Norme relative ai carichi per il calcolo dei ponti stradali*, (in Italian).

Ministero dei Lavori Pubblici, D.M 02.08.1980, *Criteri generali e prescrizioni tecniche per la progettazione, esecuzione e collaudo di ponti stradali*, G.U. n.308, 10.11.1980 (in Italian).

Ministero dei Lavori Pubblici, D.M 04.05.1990, *Aggiornamento delle norme tecniche per la progettazione, la esecuzione e il collaudo dei ponti stradali*, G.U. n.24, 29.01.1991 (in Italian).

Ministero dei Lavori Pubblici, D.M. 03.03.1975, *Approvazione delle norme tecniche per le costruzioni in zone sismiche*, G.U. n.93, 08.04.1975 (in Italian).

Ministero dei Lavori Pubblici, D.M. 03.06.1981, *Classificazione "a bassa sismicità" S=6 del territorio dei comuni delle regioni Basilicata, Campania e Puglia, e classificazione sismica S=9 del territorio del comune di S. Maria la Carità*, G.U. n.162, 15.06.1981 (in Italian).

Ministero dei Lavori Pubblici, D.M. 09.01.1996, *Norme tecniche per il calcolo, l'esecuzione ed il collaudo delle strutture in cemento armato, normale e precompresso e per le strutture metalliche*, G.U. n.29, 05.02.1996 (in Italian).

Ministero dei Lavori Pubblici, D.M. 19.06.1984, *Norme Tecniche relative alle costruzioni sismiche*, G.U. n.208, 30.07.1984 (in Italian).

Ministero dei Lavori Pubblici, D.M. 29.02.1984, *Dichiarazione di zona sismica del comune di Tornolo*, G.U. n.89, 29.03.1989 (in Italian).

Ministero dei Lavori Pubblici, Law n.64 02.02.1974, *Provvedimenti per le costruzioni con particolari prescrizioni per le zone sismiche*, G.U. n.76, 21.03.1974 (in Italian).

Ministero delle Infrastrutture e dei Trasporti, D.M.14.01.2008, *Norme Tecniche per le Costruzioni*, G.U. n.51, 29.02.2008 (in Italian).

Ministero delle Infrastrutture e dei Trasporti, D.M.17.01.2018, *Aggiornamento delle "Norme Tecniche per le Costruzioni"*, G.U. n.42, 20.02.2018 (in Italian).

Ministero delle Infrastrutture e dei Trasporti, *Linee Guida per la Classificazione e Gestione del Rischio, la Valutazione della Sicurezza ed il Monitoraggio dei Ponti Esistenti*, 17.04.2020 (in Italian).

Modena, C., Tecchio, G., Pellegrino, C., da Porto, F., Zanini, M. A., & Donà, M. (2014). Retrofitting and refurbishment of existing road bridges. *Maintenance and safety of aging infrastructure*, 469-533.

Pellegrino, C., Pipinato, A., & Modena, C. (2011). A simplified management procedure for bridge network maintenance. *Structure and Infrastructure Engineering*, *7*(5), 341-351.

Pinto, P. E., & Franchin, P. (2010). Issues in the upgrade of Italian highway structures. *Journal of Earthquake Engineering*, 14, 1221-1252.

Zonta, D., Zandonini, R., & Bortot, F. (2007). A reliability-based bridge management concept. *Structures & Infrastructure Engineering*, *3*(3), 215-235.

4. Case studies and numerical models

Although the bridge classification on large scale represents a practical tool to obtain summary information on the fragility of the existing infrastructures, a reliable prediction of the behaviour of small or medium-size bridge sets requires a deeper level of detail, in which the most common and at the same time specific structural characteristics found within the selected networked system are explicitly modelled for the evaluation of the seismic response, as concluded by (Borzi et al., 2015; Stefanidou & Kappos, 2017; Stefanidou & Kappos, 2019). This "intermediate" level of analysis is a necessary compromise to avoid too much expensive computational efforts associated to a refined structural modelling and to offer an accurate evaluation of the seismic performance of the bridge set at once.

In this Thesis, the analysis of the regional bridge stock of the Marche region represents a starting point to investigate two most widespread bridge typologies both in the Marche Region and in the Italian context, the Reinforced Concrete with Link Slab (RCLS) and the Steel-Concrete Composite (SCC) bridges. The aim of this analysis is to furnish a deepening on the behaviour of these two bridge categories taking into account the most recurrent structural characteristics in the regional context and adding information to the existing fragility analyses on wider scale.

In this Chapter, the case studies for the investigation of the behaviour of RCLS and the SCC bridges are described. Simulated design projects are carried out according to the norms at the time of the bridge construction to reproduce the structural resistances to employ in the seismic analyses. A detailed description of the considered geometries and materials is provided, as well as of the adopted Finite Element models for the structural analysis. A dedicated paragraph about the structural peculiarities is added for each bridge typology and a dedicated modelling is derived. In particular, an innovative aspect is introduced in the bridge modelling for what concerns the superstructure, where possible failure mechanisms are recognized and considered for the analysis of the bridge response. In case of RCLS bridges, link slabs are explicitly modelled with an elastic-plastic behaviour. In case of SCC bridges, potential plasticization phenomena on the superstructure involve the cross beams, which are known to be directly involved in the transferring mechanisms of the shear forces from the superstructure to the bearings. For this reason, a dedicated detailed study on the behaviour of cross beams under seismic excitation is carried out and an equivalent modelling of the cross beams is introduced in the global bridge FE model. Finally, in the last section the choice of the most relevant EDPs to monitor the response of the bridges is illustrated, basing on which the fragility curves will be built.

4.1 Reinforced Concrete with Link Slab (RCLS) bridges

Among the several bridges classes, Reinforced Concrete with Link Slab (RCLS) bridges are highly representative of the Italian existing infrastructural network (Briseghella et al., 2004) and, at the same time, can be commonly found in the infrastructural stock of many other countries (Caner & Zia, 1998; Caner et al., 2002; Sevgili & Caner, 2009; Wang et al., 2019).

Link Slab (LS) decks consist in simply-supported beams, realized with reinforced or pre-stressed concrete girders completed with a RC slab cast in situ, and linked at the slab level over the piers in a later stage with respect to the main structure. The first proposal for the use of LSs for simply-supported beam bridges dates back to the late 1970s (Loveall, 1985), as one of the structural solutions for jointless bridges. LSs can be realized by means of either sheathed rebars or with standard longitudinal slab reinforcement, both positioned in correspondence of the gap between adjacent simply girders, covering the so called "debond length". A schematic representation of the two technical solutions can be found in Figure 4.1.

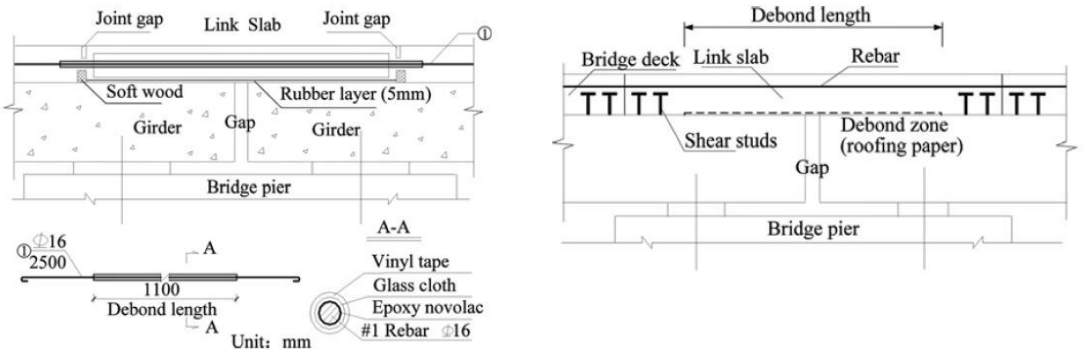

a) b)

Figure 4.1. Schematic representation of (a) debonded rebar link slab and (b) debonded link slab (from Wang et al., 2019).

The LS solution combines advantages of the statically determinate scheme for vertical loads (the linking portions of the slab are cast in the last stage of the bridge construction) with the advantages of continuous decks in terms of durability and good driving stability and comfort. Indeed, one of the main advantages of LSs on expansion joints consists in a lower wear vulnerability produced by debris and atmospheric agents: water leaking through the joints is the major cause of deterioration of bridge girder bearings and supporting structures, while debris accumulation in the joints restrains deck expansion and causes damage to the bridge. Moreover, the LS avoids the use of expensive expansion joints, which suffer of impact damage caused by heavy trucks passage. The use of LSs avoids those drawbacks and results in a lower maintenance effort and costs.

Since the construction technique is cheaper and quicker than standard of deck joints rebuilding, and offers better results in a long-term perspective, LSs are also widely used as retrofit interventions (Wing & Kowalski, 2005; Lam et al., 2008).

Particular care should be taken to preserve and maintain the optimal behaviour of LS bridges. Indeed, many studies have been conducted on the problem of slab cracking and the consequent reinforcement corrosion in correspondence of the links (Alampalli & Yannotti, 1998), resulting in innovative design approaches and solutions (Richardson, 1989; Caner & Zia, 1998; Okeil & El-Safty, 2005; Ulku et al., 2009) or in the use of innovative materials for LSs to improve the structural performance (Li et al., 2003; El-Safty, 2008; Lepech & Li, 2009).

Not least, LSs are required to give continuity to the deck, eliminating the span separation problem and the possible damage caused by unseating that can occur during an earthquake. In case of continuous decks, it is well known that structural problems can arise not only in vertical and supporting elements, but also on elements belonging to the superstructure, mainly as a consequence of the transverse bending of girder constrained by fixed abutments and deformable piers (Bruneau et al., 1996; Itani et al., 2004; Carbonari et al., 2016; Dezi et al., 2018; Tubaldi & Dall'Asta, 2012; Tubaldi et al., 2010; Tubaldi et al., 2011). Moreover, LS between adjacent spans might represent a weakness point and a potential source of failure for the entire bridge, to be considered in addition to classical seismic vulnerabilities generally involved in multi-span bridges (Padgett & DesRoches 2008; Kawashima, 2010).

According to the state of art on the topic, many authors have proposed new design solutions for materials (i.e. FRPs) and geometric details aimed at mitigating cracking phenomena and increasing LS bridges capacity (Kim, Fischer & Li, 2004; Lepech & Li, 2009; Zheng, Zhang & Xia, 2018). A large number of scientific works has focused on the effectiveness of LSs as retrofit technique in presence of live and thermal loads (Caner & Zia, 1998; Zhan, Shao & Liu, 2013).

Nevertheless, very few works available within the literature deal with seismic assessment of LS bridges. Caner et al. (Caner et al., 2002) assessed the effectiveness of LSs as seismic retrofitting strategy for a 4 simple-spans pre-stressed concrete highway overpass, by using multimode response spectrum and linear Time History (TH) analyses. Nielson (Nielson, 2005) analysed Multi Span Simply Supported Slab (MSSS) bridges as one of the most common bridge class in Central and Southeastern United States, assigning an elastic behaviour to the deck in presence of seismic action and considering only piers, bearings and abutments as the representative components of the bridge system. Sevgili & Caner (Sevgili & Caner, 2009) analysed the seismic response of skewed multi-span simply-supported decks retrofitted with LSs through 48 different finite element models to assess the efficiency of LSs with different skew angles, performing both response spectra and linear and nonlinear TH analyses using 5 records from the 1999 Marmara earthquakes.

The wide use of this engineering solution deserves a deeper investigation on the topic, considering that in most cases existing LS bridges were designed according to old standards, which lack attention and detailing with respect to seismic loads. In particular, existing bridges were realized without complying with the modern capacity design rules, so that ruptures may potentially involve different system components according to several possible failure mechanisms, without excluding brittle collapses. The problem highlighted above concerns countries all over the world, where a large number of short and medium span bridges have simply-supported girders linked at the slab level (Wang et al., 2019).

4.1.1 Geometries

Two multi-span simply supported pre-stressed concrete bridges are considered as case studies. Geometrical and mechanical characteristics are suitable to make the case studies general examples in order to highlight the vulnerabilities of existing bridges belonging to the selected bridge class. The geometries have been selected on the basis of the most recurrent geometries for the RCLS bridges on the SS76 and SS77 roads, statistically analysed in previous Chapter 3. Moreover, a detailed analysis of SS76 (which will be adopted as case study for the traffic simulations and costs evaluation in Chapter 6) allowed to distinguish the most recurrent number of spans between RCLS and SCC bridges so that it has been possible to reliably approximate the observed real geometries with the different numerical models.

Table 4.1 offers a comparison between real bridge data and the assumed geometries (the latter marked with an asterisk). The analysis of the dataset on the SS76 showed that for RCLS bridges the most frequent number of spans is 5 and 10, assuming a mean length of each simply supported span equal to 25 m. As a result, the LS bridge deck models are constituted by simply supported spans of L_{span} = 25 m, composed of a cast-on-site wide slab B = 12.50 m on three V-shape pre-stressed concrete girder beams. This geometry for the deck cross-section is a typical choice for pre-stressed concrete girders. A statistic view of the ratio L/B, where L is the total length of the bridge, is depicted in the chart in Figure 4.2. It is evident that the choice of the two L/B ratios is in good accordance with the distribution of the real deck geometries. Depending on the case study, the LS bridge deck has a total length L equal to 131 m (L/B = 10) or 263.5 m (L/B = 20), with N_{spans} = 5 or N_{spans} =10 respectively.

Table 4.1. Comparison between RCLS bridges on SS76 and geometries of the case studies.

Name	Latitude	Longitude	L/B	L/B*	N_{spans}	N_{spans}*
Esino	43.35283	12.99907	12	10	6	5
Mariani	43.38307	12.98459	14	10	7	5
Gattuccio	43.40177	12.98202	11	10	6	5
Esino II	43.41353	12.97982	7	10	3	5
Esino III	43.42413	12.9945	10	10	5	5
Esino IV	43.42808	13.00125	10	10	5	5
Gola della Rossa	43.43616	13.02023	54	20	27	10
Serra San Quirico	43.45587	13.04715	22	20	11	10
Angeli	43.46201	13.05673	14	10	7	5
Esinante	43.46414	13.06303	20	20	10	10
Collefreddo	43.46808	13.07012	9	10	5	5
Spontini	43.4847	13.09555	20	20	10	10
Castelbellino	43.49459	13.15893	7	10	4	5
Esino I	43.52131	13.27668	21	20	11	10
Esino II	43.5811	13.33345	21	20	11	10

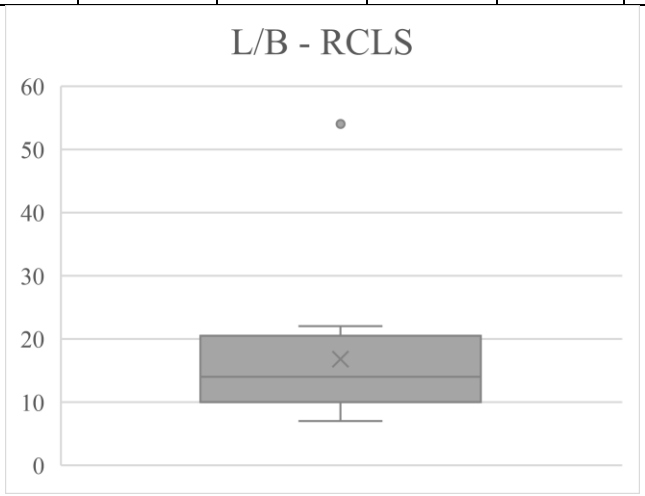

Figure 4.2. Statistical analysis of the ration L/B for RCLS bridges on the SS76 road.

Under each side of the spans (at both piers and abutments), a set of 3 neoprene semi-rigid bearings are installed (Figure 4.3). The bearings mechanical behaviour is the same along the two horizontal directions.

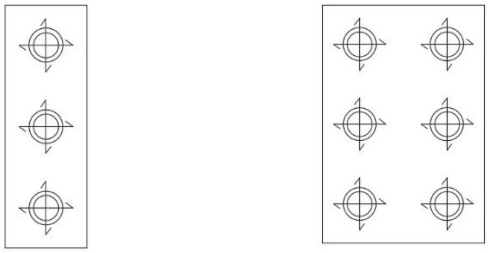

a) b)

Figure 4.3. Static scheme of bearings: (a) abutments, (b) piers.

Spans present connections at the slab level realized through the kinematic links, made by DYWIDAG bar groups and diameter Ø40 mm. An example of kinematic link was shown in Figure 4.1. The link zone between two adjacent spans is 20 cm long. The bar arrangement is made according to the static scheme in the longitudinal direction, where a fixed constraint is located at the abutment on the right side, and according to the relevant distribution of axial forces (due to seismic actions in the longitudinal direction of the bridge) as described in the following. For the sake of brevity, an illustration of the case L/B = 10 is furnished in Figure 4.4. The case study with L/B = 20 is analogously built. A set of 5 bars connects the right side of the bridge to the abutment; starting from there, the number of bars reduces by moving towards the other abutment, according to configuration depicted in Figure 4.4: 4 bars on pier n. 4, 3 bars on pier n. 3 and 2 bars on the la two piers (n. 1 and n. 2).

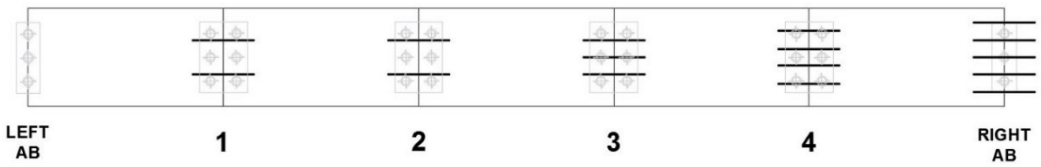

Figure 4.4. Scheme of link bar arrangement at the slab level – L/B = 10.

Vertical supporting elements are single piers with a full reinforced concrete circular cross section with a parallelepiped cap on top; a circular diameter D = 2 m and a constant ratio along the longitudinal development H/D = 5, where H is the pier height, are assumed. This choice perfectly matches the results of the statistical analysis on the pier geometries in Chapter 3. A schematic longitudinal perspective view of the bridge is provided in Figure 4.5.

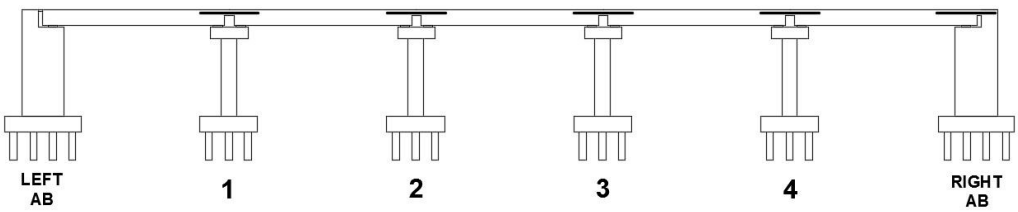

Figure 4.5. Scheme of the longitudinal perspective view of the bridge – L/B = 10.

It is assumed that the bridges were constructed in the 70's, before the emanation of seismic design codes at national and European level (Ministero delle Infrastrutture e dei Trasporti, 2018; EC8-2), and the design does not comply with capacity design rules.

4.1.2 Simulated design project basing on previous codes

A simulated design has been performed according to the Italian D.M. 03.03.1975 (Ministero dei Lavori Pubblici, 1975), considering both gravity and seismic loads. Gravity loads derive directly from the deck self-weight, while permanent loads, including the pavement, guard-rails and other building details of the superstructure, are assumed to be constant along the bridge and equal to 50 kN/m as distributed loads. Seismic loads are modelled as equivalent horizontal seismic forces applied separately along the transverse and longitudinal direction of the bridge in order to design piers and the link bars. More precisely, the equivalent seismic force F_h is calculated as a percentage of the deck self-weight:

$$F_h = C\ R\ W \tag{28}$$

where W is the self-weight of the relevant deck portion (a single span for each pier, one or more spans for the links), $C = \frac{S-2}{100}$ is the seismic intensity coefficient, S the level of seismicity and R is the response coefficient for the considered seismic direction. In this study, R = 1 and S = 9 are assumed, leading to a design seismic intensity C = 0.07.

Following the code requirements, the minimum longitudinal reinforcement ratio of 1% is assumed for the piers. From the simulated design, the optimal number of steel longitudinal rebars for all the bridge piers is found to be 59 with a constant diameter of 26 mm. Ø14 mm hoops are equally spaced at intervals of 25 cm along the pier shaft to address the shear force due to the design seismic load.

Material properties adopted for steel bars (both DYWIDAG and concrete reinforcement) and for concrete are summarised in Table 4.2. Steel and concrete mechanical properties of RCLS bridges.

More in detail, the pier circular cover has a characteristic compressive strength $f_{c,unconfined}$ = 25 MPa, while, due to the confinement provided by the hoops, the internal radius presents a compressive strength $f_{c,confined}$ = 26.75 MPa and an ultimate strain increased by about 50% from the original one. The DYWIDAG bars are pretensioned at 60% of steel yielding stress. For sake of completeness, the material constitutive laws are depicted in the charts of Figure 4.6. Finally, to sustain gravity and permanent loads, neoprene bearings with supporting area A = 157.5 cm^2, thickness t = 52 mm and shear modulus G = 1 MPa are adopted.

For the considered case studies, geometry and material properties are considered deterministic since the influence of seismic ground motion uncertainty is significantly larger than model parameter uncertainty on the structural response variability (Tubaldi et al., 2012).

Table 4.2. Steel and concrete mechanical properties of RCLS bridges.

	DYWIDAG steel bars	Steel reinforcement	Confined concrete	Unconfined concrete
Elastic modulus [MPa]	206000	206000	30000	30000
Yielding/Peak strength [MPa]	950 ($\sigma_{prestress}$ = 60% yielding)	435	26.75	25.00
Ultimate strength [MPa]	1050	540	0.200	0.200
Yielding/Peak strain [-]	0.0046	0.00207	0.002	0.0027
Ultimate strain [-]	0.04	0.12000	0.0060	0.0114

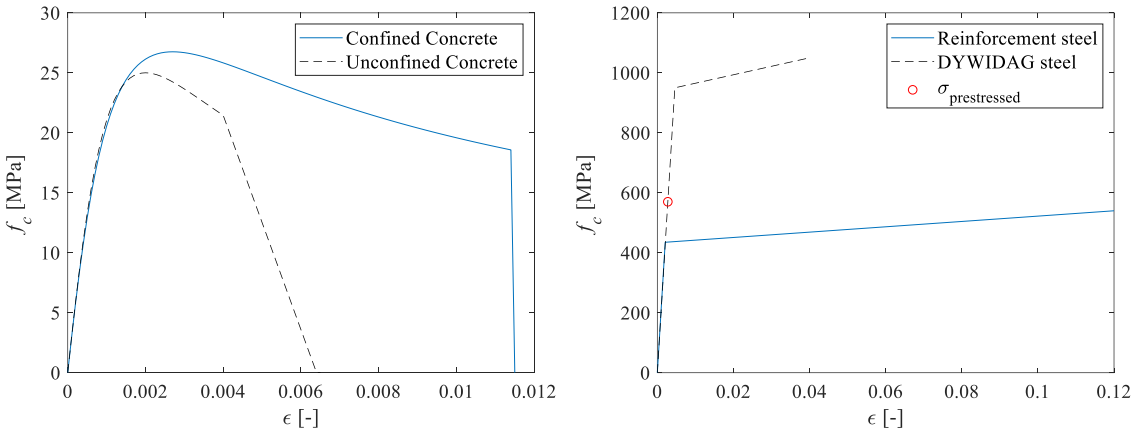

a) b)

Figure 4.6. a) Concrete constitutive law with and without confinement; b) Steel (DYWIDAG and concrete reinforcement) constitutive law.

4.1.3 Design details from Chiaravalle viaduct

An example of RCLS viaduct in the Marche territory is represented by the Chiaravalle Viaduct, located in Falconara Marittima (AN), in a strategic position as a part of the road junction connecting the road SS76 and the highway A14 to the Falconara airport, as illustrated in Figure 4.7. Given the large number of available structural and design details, the Chiaravalle viaduct has been taken as a reference point for the choice of some structural solutions for the decks of RCLS case studies.

a) b)

Figure 4.7. a) Inclusion of the bridge in the existing road network; b) Aerial view of the viaduct with indication of abutments.

The viaduct is 875 m long, composed of a 12.1 m wide bridge deck on 31 spans of 26.0 m length each. The bridge deck is formed by a cast on site slab on three simply supported V-shape girder beams in prestressed concrete (Figure 4.8). Links at the slab level are constituted by bar groups of Ø40 or 50 mm in a variable number from 3 to 7, as depicted in Figure 4.9a. The transverse distribution of bars in the deck cross section is governed by different bar positions (Figure 4.9b).

In particular, Figure 4.10 shows the structural detail of the connection between adjacent spans. The links are realized by means of the combination of a joint element positioned on the slab extrados and a system of steel threaded bars at about 100 mm from the slab extrados. The first ones act in compression, while the second ones are pre-tensioned bars. The bars are inserted in steel or synthetic material sheaths, which allow to absorb rotations between adjacent spans during the bar tensioning. After the tensioning, the containment sheaths are injected with an epoxy protection material. Above the joint elements a continuous road pavement is realized, which, although it is susceptible to cracking, prevents the water leaking and the resultant joint corrosion and degradation.

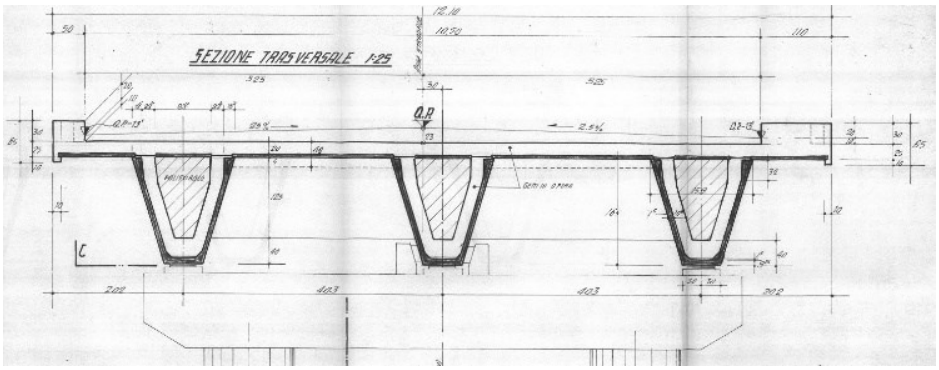

Figure 4.8. Cross section of the Chiaravalle viaduct.

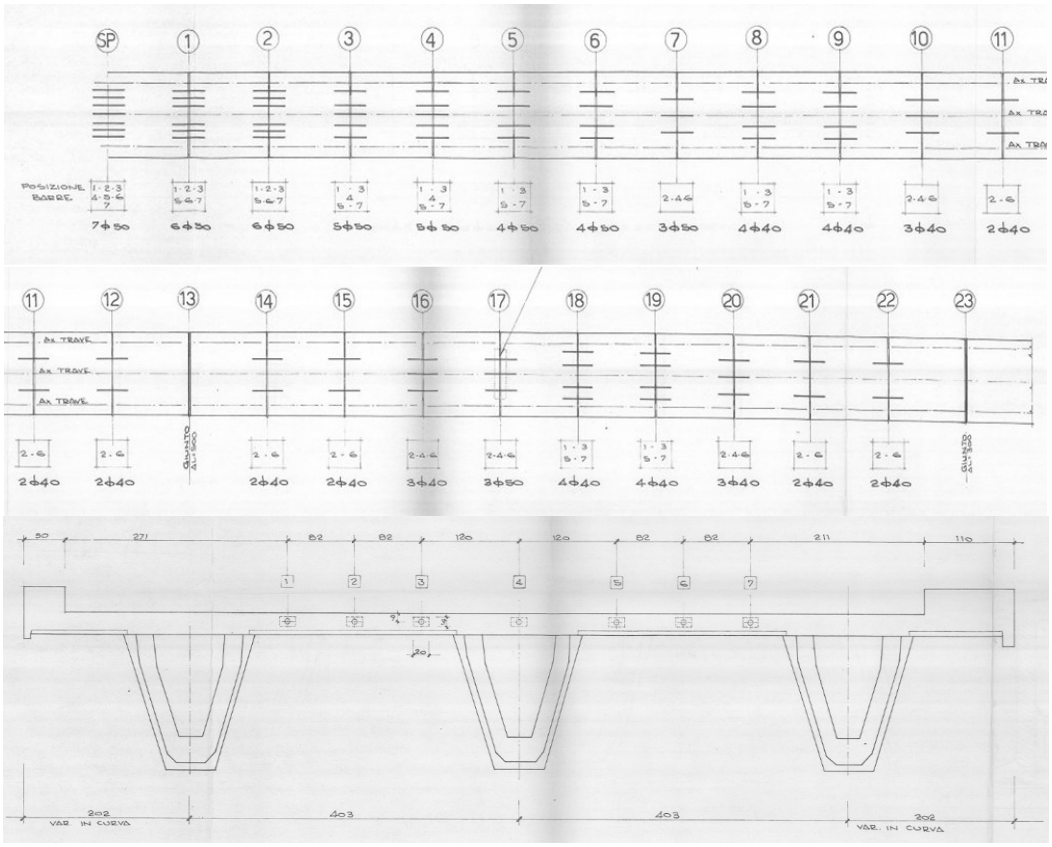

(a)

(b)

Figure 4.9. (a) Location of link bars from abutment A to pier 23; (b) pre-stressed concrete deck cross-section. Source: design project of the road links among SS76 road, A14 highway, Falconara airport and SS16 road, ANAS, 18.02.1986.

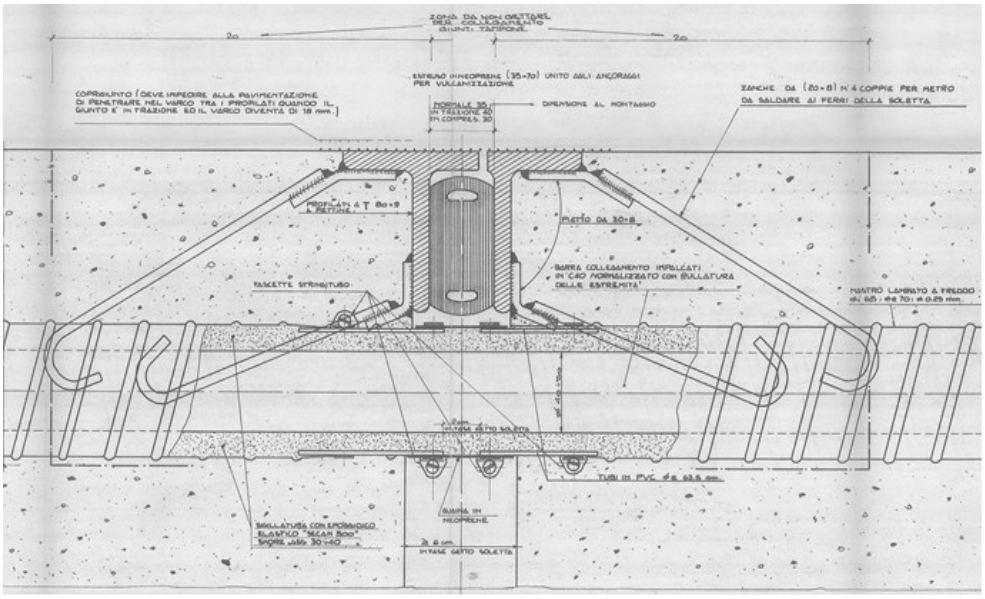

Figure 4.10. Detail of the joining elements between the decks (link slabs). Source: design project of the road links among SS76 road, A14 highway, Falconara airport and SS16 road, ANAS, 18.02. 1986.

4.1.4 RCLS bridges FE modelling

A three-dimensional nonlinear model of the RCLS bridges is developed in OpenSees (McKenna et al., 2015). Since no plastic deformation is expected on the deck girders, the latter are modelled as *elasticBeamColumn* elements. In order to reproduce the classical design configuration depicted in Figure 4.10, the LS elements are assumed to have a total length of 20 cm and they are discretised in sub-elements as follows: two symmetric external portions (5 cm long each) reproducing link bars covered by the concrete slab, and a central sub-element (10 cm long) simulating the bare bars of the link. According to the previous geometry, LS are modelled as displacement-based frame elements (*dispBeamColumn* element) with fiber section to catch the bar stress state. Within the cross section, bars are modelled through a straight layer of bars with *Steel02* elastic-plastic law and pretension stress equal to 60% of yielding stress; bars are positioned along the longitudinal direction in a variable number according to the scheme in Figure 4.4. In the external portions, the concrete slabs adopt a fiber rectangular cross section with *Concrete01* material.

Piers caps are assumed as rigid elements and are modelled by *rigidLink beam* elements connecting the deck beam ends to the bearings. Bearings are modelled through *zeroLength* elements with *Steel01* uniaxial material having an elastic-plastic law to simulate the deformability of the bearing. The constitutive law of neoprene bearings is derived from the User Manual of AVS procedure (DSTE/PRS & UNIBAS – Autostrade per l'Italia S.p.A., 2019). In particular, the bearings have an elastic behaviour (governed by the elastic stiffness k) until the maximum force (i.e. the force at which the sliding occurs) is reached. The elastic stiffness is proportional to the shear modulus of the neoprene G, the supporting area of the device A and the device thickness t:

$$k = \frac{GA}{t} \tag{29}$$

Two mechanisms can determine the maximum force carried by the bearings: the first is the sliding mechanism between concrete surface and neoprene; the second is a fragile one, which occurs when neoprene fails for shear stress. Two friction coefficients can be determined for each mechanism, and the minimum one is adopted to calculate the force at which sliding occurs, according to the following Eq. (6):

$$\mu = min\left(\frac{\gamma_{lim} GA}{w}; \mu_0\right) \tag{30}$$

where γ_{lim} is the maximum allowable shear strain for neoprene, assumed equal to 100% for existing bearings; w is the vertical load on the bearing; μ_0 is the sliding coefficient between concrete surface and neoprene, assumed equal to 0.25. In this case, $\frac{\gamma_{lim} GA}{w} < \mu_0$, so that the fragile rupture of the neoprene pads rules the bearing collapse.

Columns are modelled using displacement-based fiber elements (*dispBeamColumn* element), which are able to take into account the evolution of the plastic hinge at the base of the pier. Concrete is described by *Concrete01* (no tensile strength), with parameters assumed according to (Mander et al., 1988). More in detail, the circular cover thickness follows a *Concrete01* behaviour with concrete compressive strength derived from the constitutive law depicted by blue line in Figure 4.6(a), while the pier core implements a *Concrete01* confined concrete material, according to the constitutive law depicted by black dashed line in Figure 4.6(a). Fibre sections of both the confined and unconfined parts are generated by using a circular shaped patch. Steel longitudinal rebars are constructed as line fibres with *Steel02* uniaxial material, and the *layer circ* command is used to place the bars along circular arches.

Seat type abutments resting on piles are considered, since this typology can be considered as the most widespread on the Italian road networks. The response of the abutments is modelled evaluating the contribution of both earth pressure and structural stiffness in longitudinal and transverse direction. In particular, along the longitudinal direction, the passive resistance mobilized at the abutment backwall is simulated using the hyperbolic soil model proposed by (Shamsabadi et al., 2007), assuming a granular soil type. The active and the transverse resistances are entirely assigned to the piles whose response is schematized with a trilinear force deformation law. The parameters characterizing the constitutive pile law are determined following the design recommendations of (CALTRANS, 2015) and (Choi, 2002), assuming a 7 kN/mm/pile resistance and considering as yielding force the inertial force proportional to the mass of the entire bridge deck to be carried by the foundation piles.

The bilinear contact element developed by (Muthukumar & DesRoches, 2006) is used to model the pounding between the deck and the left abutment, as well as between adjacent spans after the rupture of the link bars at the ultimate strain. In fact, the link bar ultimate capacity is explicitly accounted by the adoption of a *MinMax* material, that activates after the ultimate strain of the *Steel02* on the bars. A *Parallel* material allows to combine the *MinMax* and the *Steel02* on the bar fiber elements, as well as the *Impact* material for the pounding.

Distributed masses on deck and pier elements have been defined considering 2.5 t/m3 as RC density. A lumped nodal mass M is applied at the top end of each pier to simulate the pier cap. Gravity and permanent loads are directly derived from distributed and nodal masses and applied just before TH analysis. A schematic view of the 3D FE Model is depicted in Figure 4.11 and Figure 4.12.

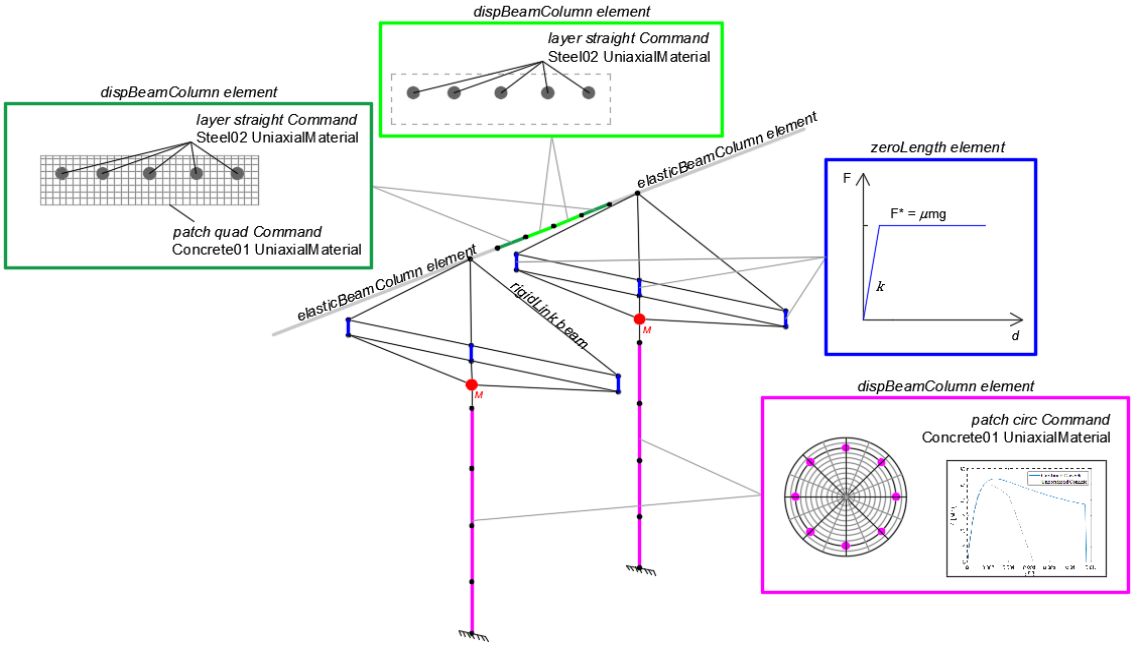

Figure 4.11. Finite Element Model of the RCLS bridges – deck, link slabs, bearings and piers.

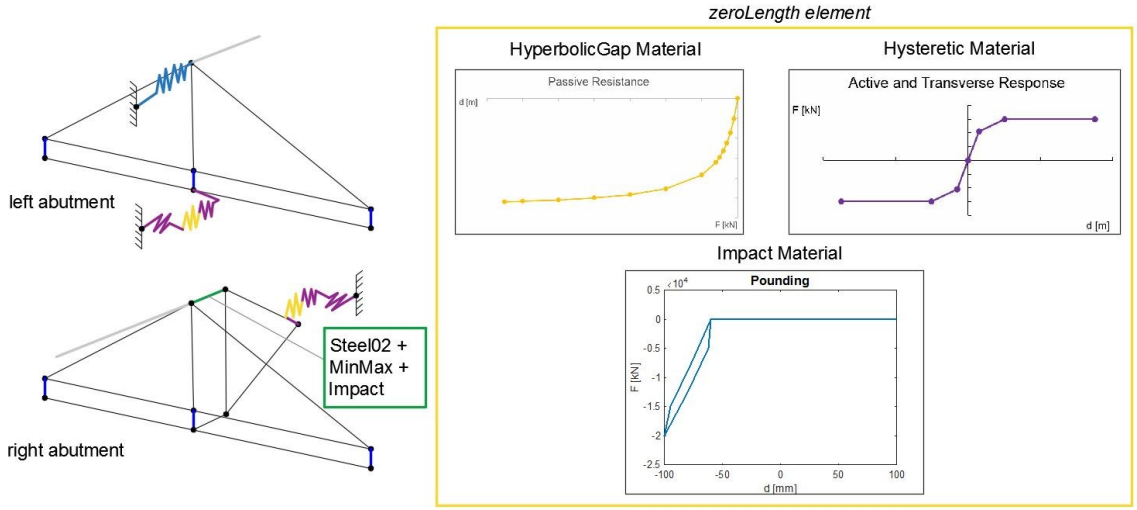

Figure 4.12. Finite Element Model of the RCLS bridges – abutments and pounding.

4.2 Steel-concrete composite (SCC) bridges

Steel-Concrete Composite (SCC) decks represent a very interesting typology, since they are a very common, economical, and efficient structural solution, especially for short and medium span lengths (Collings, 2005). Bridges with SCC decks are rapidly spreading both due to the availability of new materials (high-strength weldable steels, high-strength concretes), and to the progress achieved in construction and assembly technologies. The advantages offered by this structural typology are: lightness (high strength/weight ratio), slenderness, ease of construction of continuous decks with spans of different lengths and

with curvatures imposed by the road layout, low sensitivity to differential subsidence of foundations, the possibility of replacing structural elements, facilitating maintenance and possibly increasing their bearing capacity.

SCC bridges are generally characterized by a continuous SCC deck resting on reinforced concrete piers (Itani et al., 2004). The seismic performance of this bridge typology has been extensively discussed in many studies (Astaneh-Asl et al., 1994; Itani et al., 2004; Kawashima, 2010), and numerical investigation of their seismic response has also been carried out, as in (Nielson, 2005), (Padgett & DesRoches 2008) and Tubaldi et al. (Tubaldi & Dall'Asta, 2012; Tubaldi et al., 2010). These studies have highlighted the likelihood of damage to the various components (deck, bearings, piers) that lie in the seismic load paths.

In case of Italian existing bridges, it is quite common to find examples of bridges exhibiting a "dual load path" (Calvi, 2004; Tubaldi et al., 2010), since fixed bearings are adopted at abutments to avoid expensive expansion joints, realizing a rigid connection between the deck and the substructures. Usually, the design of bridge structures assures an almost linear behaviour for the SCC deck (EC8-2) subjected to permanent and seismic actions, while RC piers represent the main source of energy dissipation, whereas no other seismic protection strategy is adopted. Nevertheless, the transfer mechanisms arising from the dual load path necessarily involve the superstructure, and premature collapses due to fragile local failures may occur along the inertial forces path from the slab, where most of the mass is located, to the substructures (e.g. shear connection, truss cross-beams, supports), and may compromise the attended seismic performance (Bruneau et al., 1996; EERI, 1994).

Concerning local problems of composite decks subjected to seismic loads, only few works are available, mainly focusing on the behaviour of end cross beams (Zahrai & Bruneau, 1998; Zahrai & Bruneau, 1999a; Zahrai & Bruneau, 1999b; Bruneau et al., 1996; EERI1990; EERI, 1994) or on their effect on the shear connection behaviour (Carbonari et al., 2016; Carbonari et al., 2017; Dezi et al., 2018. In particular, results by Carbonari et al. (Carbonariet al., 2017) showed the key role of the metallic cross beams in the redistribution of the shear stresses deriving from the transverse seismic action. It was found that the shear forces have different trends in correspondence of the end cross beams (above the bearings), where the majority of the transverse seismic action is concentrated, as the relative stiffnesses change among the slab, the shear connection and the end cross beams themselves.

In the next Sections, significative case studies are evaluated to examine the behaviour of SCC bridges, considering geometries representative of the SCC bridges in the Marche regional context. A preliminary design project according to the AS method is realized for bridge piers. Considering the importance of the cross beams for both the local and the global performance of SCC decks, a dedicated study on the behaviour of these bridge components is carried out in §4.2.3. More in detail, the design and the assessment of the cross beams is carried out according to the existing codes at the construction time, then

an equivalent formulation and modelling for the cross beam system is analysed and applied to capture the occurring of local damage mechanisms. Finally, the FE modelling of the selected case studies is illustrated.

4.2.1 Geometries

It is assumed that the bridges were constructed in the 90s, before the emanation of seismic design codes at national and European level (Ministero delle Infrastrutture e dei Trasporti, 2018; EC8-2), and the design does not comply with capacity design rules.

Three multi-span continuous SCC deck bridges are considered as case studies. Geometrical and mechanical characteristics are suitable to make the case studies general examples in order to highlight the vulnerabilities of existing bridges belonging to the selected bridge class. The geometries have been selected on the basis of the most recurrent geometries for the SCC bridges on the SS76 and SS77 roads, statistically analysed in previous Chapter 3.

Table 4.3 offers a comparison between real bridge data and the assumed geometries (the latter marked with an asterisk).

Table 4.3. Comparison between SCC bridges on SS76 and geometries of the case studies.

Name	Latitude	Longitude	L/B	L/B*	N_{spans}	N_{spans}*
Giano Ovest (Sx)	43.31086	12.85769	4	4	1	1
Giano Ovest (Dx)	43.31086	12.85769	7	8	2	2
Camporegio	43.3115	12.85983	10	8	3	2
Valleremita (Sx)	43.31471	12.86608	21	20	5	5
Valleremita (Dx)	43.31471	12.86608	22	20	5	5
Malvaioli (Sx)	43.31868	12.88675	4	4	1	1
Malvaioli (Dx)	43.31868	12.88675	4	4	1	1
Vetralla (Sx)	43.32007	12.89125	8	8	2	2
Vetralla (Dx)	43.32007	12.89125	8	8	2	2
Giano Est	43.34425	12.95745	44	20	11	5
Albacina (Sx)	43.34534	12.98265	27	20	7	5
Albacina (Dx)	43.34534	12.98265	37	20	9	5

The analysis of the dataset on the SS76 showed that for SCC bridges the most frequent number of spans is 1, 2 and 5, assuming a mean length for the central spans span equal to 50 m. As a result, the SCC bridge deck models are constituted by continuous spans of L_{span} = 50 m, composed of a cast-on-site 12.50 m wide, 0.25 m thick slab on two I-shape

steel girder beams. This geometry for the deck cross-section is a typical choice for SCC decks. The external span length are equal to αL_{span} =40 m, with α=0.8 according to an optimization criterion to minimize the bending moments illustrated in the Figure 4.13. Depending on the case study, the LS bridge deck has a total length L of 50 m (L/B = 4), 100 m (L/B = 8) or 230 m (L/B = 20), with N_{spans} = 1, N_{spans} = 2 or N_{spans} =5 respectively. A statistic view of the ratio L/B is depicted in the chart in Figure 4.14. It is evident that the choice of the two L/B ratios is in good accordance with the distribution of the real deck geometries.

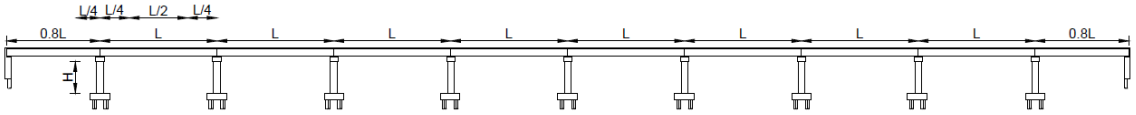

Figure 4.13. Longitudinal development of a typical SCC bridge.

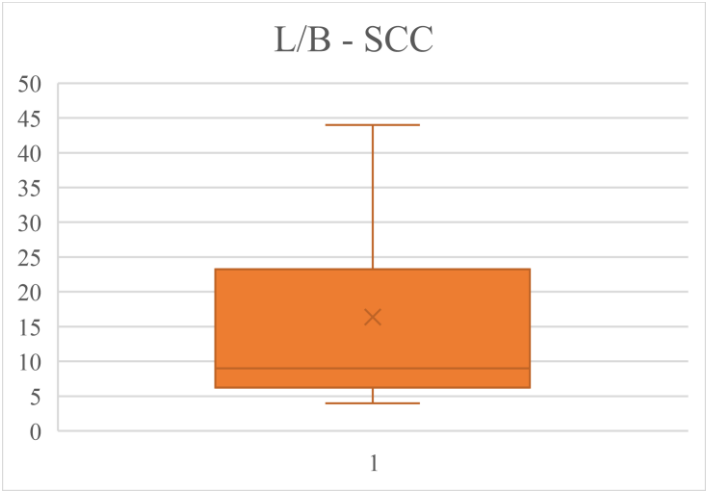

Figure 4.14. Statistical analysis of the ration L/B for RCLS bridges on the SS76 road.

Each span is characterized by two cross sections, one at the middle-span and the other above the supports, according to the following scheme (Figure 4.15)

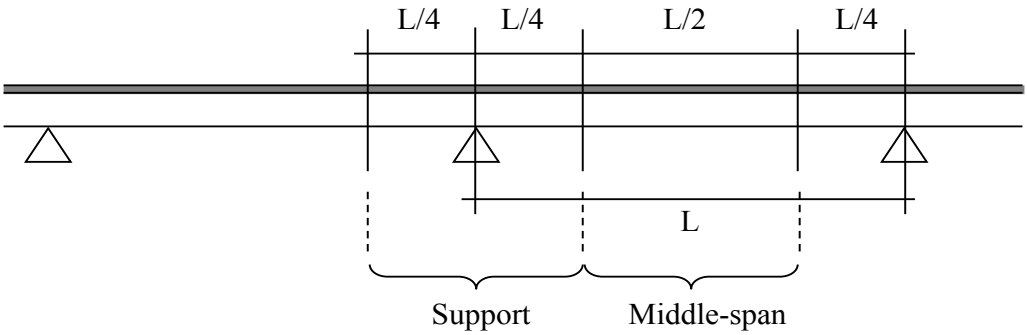

Figure 4.15. Longitudinal scheme of the subdivision of the deck into different cross sections.

Each cross section is composed by two I-shaped steel girders at a distance of 6 m, connected to the concrete slab by means of Nielson's studs to realize the shear connection. Figure 4.16 and Figure 4.17 show the deck cross section and the thicknesses of the steel girders at the supports and the middle-span, respectively.

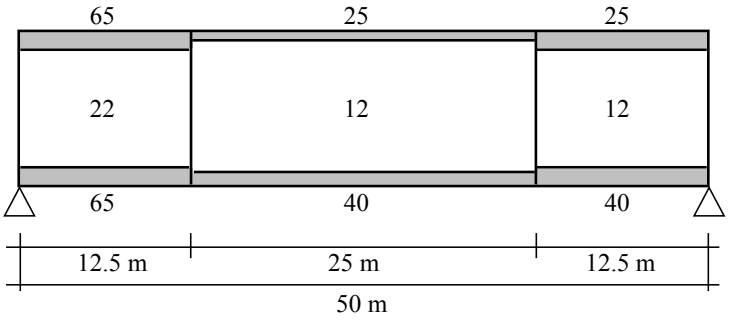

Figure 4.16. Thicknesses of plates in the deck cross sections.

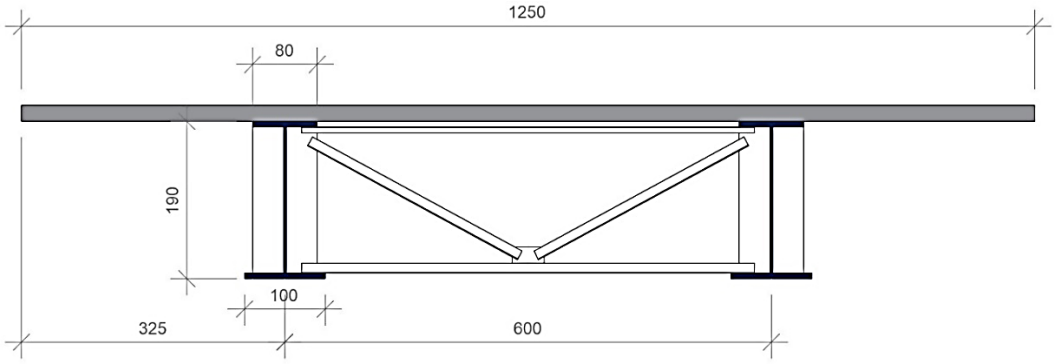

Figure 4.17. Cross section of the deck.

The girders are strengthened in the transverse direction by a reticular V-shaped structure in correspondence of each support cross section. Truss cross beams, composed by member cross-sections reported in Figure 4.18, are not directly connected to the slab and have been designed according to the D.M. 04/05/1990 (Ministero dei Lavori Pubblici, 1990) for wind and seismic loads, as it will be commented in the following §4.2.3.1.

The deck restraints are defined to allow free elongations at service conditions and are not modified for the dynamic situation, so that seismic actions in the transverse direction of the bridges are resisted by only one bearing at each support while a couple of bearings at only one support entrusts inertia forces in the longitudinal direction. The bridge static scheme is depicted in Figure 4.19.

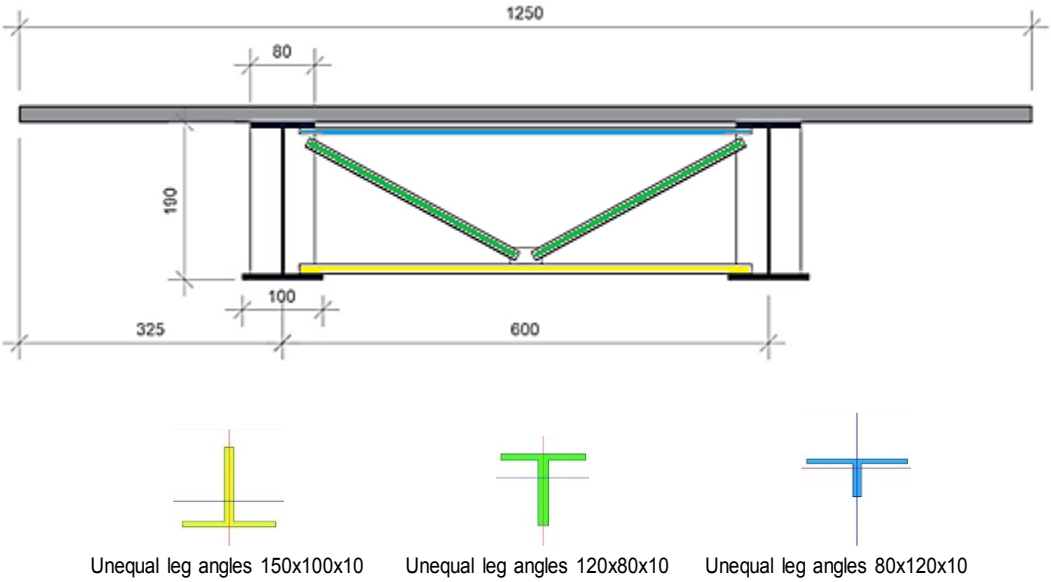

Figure 4.18. Cross sections of the beams constituting the truss end cross beams.

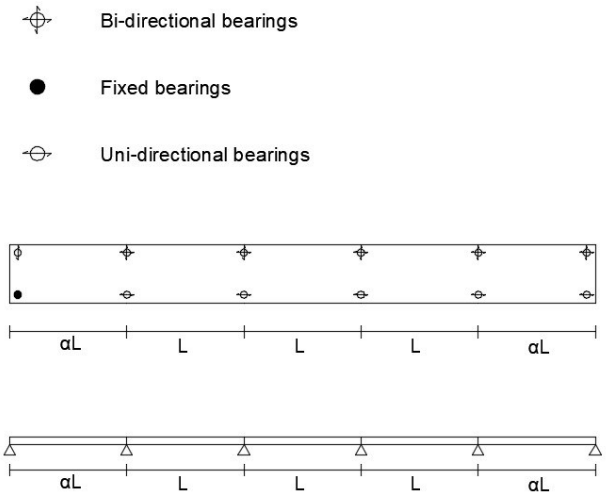

Figure 4.19. Deck static scheme.

Bearing devices are realized with the coupling of a poly-tetra-flour-ethylene (PTFE) surface and a steel surfaces, sliding whereas the movements are allowed. From Figure 4.19 it is possible to see that three typologies of bearings are adopted: fixed bearings, with no allowed movements in the horizontal plane; uni-directional bearings, sliding along one direction and fixed in the other one; bi-(or multi-)directional bearings, which can slide on both the horizontal directions. Two behaviours can be outlined. For the fixed direction, a rigid-perfectly plastic law can be formulated, where the maximum force carried by the bearings depends on the structural characteristic of the device, while the plastic behaviour is controlled by the friction coefficient between the surfaces in contact; typically, the shear rupture of the device is followed by the sliding between two steel surfaces. For the sliding direction, a rigid-perfectly plastic law can be adopted, where the maximum force

depends on the PTFE-steel friction coefficient until the partial loss of the support. After this stage, corresponding to the displacement d_1 in Figure 4.20b, a further sliding is allowed between steel surfaces. The complete loss of the support is indicated with d_2, when the maximum allowed displacement is overcome. Figure 4.20 shows the constitutive laws for the fixed and the sliding directions of PTFE-steel bearings.

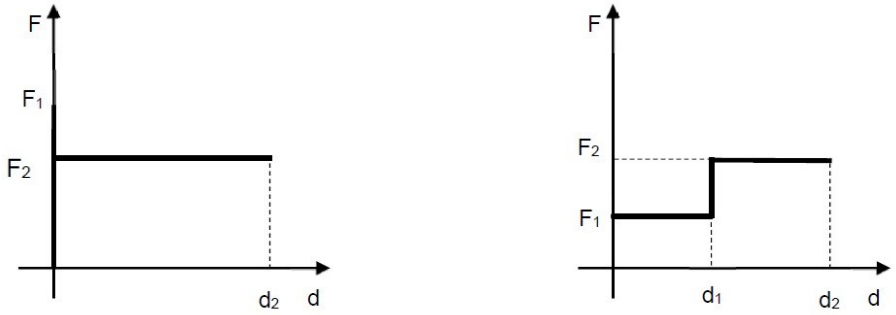

a) b)

Figure 4.20. Constitutive laws for bearings: (a) fixed direction; (b) sliding direction.

In case of uni- or multi-directional bearings, it is known from the literature that the friction between PTFE and steel depends on both the normal compression stress on the device, deriving from the applied vertical loads, and the sliding velocity v (Costantinou et al., 1990, Dolce et al., 2005):

$$\mu = \mu_{max} - (\mu_{max} - \mu_{min}) \cdot e^{-\alpha \cdot v} \tag{31}$$

in which μ_{max} is the coefficient of friction at high velocities, μ_{min} is the coefficient of friction at very low velocities and α is constant for a given pressure, temperature and condition of interfaces.

Each friction coefficient can be expressed as a function of the applied normal force N (Bowden & Tabor, 1964):

$$\mu_{max} = a_{max} \cdot N^{(n_{max}-1)} \tag{32}$$

$$\mu_{min} = a_{min} \cdot N^{(n_{min}-1)} \tag{33}$$

where $a_{max}, a_{min}, n_{max}, n_{min}$ are constants to build the friction model, to be calibrated basing on the experimental results. In this Thesis, results from the work by (Costantinou et al., 1990) are considered, as reported in Figure 4.21.

TABLE 1. Constants f_{max}, Df, a, and b

Type of Teflon (1)	Pressure (psi) (2)	Sliding direction (3)	f_{max} (%) (4)	Df (%) (5)	a (sec/in.) (6)	b (7)
UF	1,000	P	11.93	9.27	0.60	2.2
UF	2,000	P	8.70	6.95	0.60	2.3
UF	3,000	P	7.03	5.52	0.80	3.7
UF	6,500	P	5.72	4.85	0.50	4.3
15GF	1,000	P	14.61	10.60	0.60	2.1
15GF	2,000	P	10.08	5.80	0.55	1.4
15GF	3,000	P	8.49	4.17	0.60	1.3
15GF	6,500	P	5.27	3.12	0.70	2.2
25GF	1,000	P	13.20	7.66	0.65	1.4
25GF	2,000	P	11.20	6.33	0.65	1.4
25GF	3,000	P	9.60	5.20	0.32	1.5
25GF	6,500	P	5.89	2.70	0.90	1.8
UF	1,000	T	14.20	11.81	0.45	3
UF	2,000	T	10.50	8.78	0.70	4.4
UF	3,000	T	8.20	5.30	0.55	1.5
UF	6,500	T	5.50	4.39	0.45	3.2

Note: UF = unfilled Teflon; 15GF = glass-filled Teflon at 15%; 25GF = glass-filled Teflon at 25%; P = sliding parallel to lay; T = sliding perpendicular to lay; and 1,000 psi = 6.9 N/mm^2.

Figure 4.21. Parameters characterizing the friction model for PTFE-steel bearings (from Costantinou et al., 1990).

Nominal values for the friction coefficient between PTFE and steel as a function of the pressure only, at low temperatures, can be expressed in the following hyperbolic formulation (Figure 4.22):

$$0.08 \geq \mu_{nom} = \frac{1.2}{10 + p} \geq 0.03 \tag{34}$$

where p is expressed in MPa.

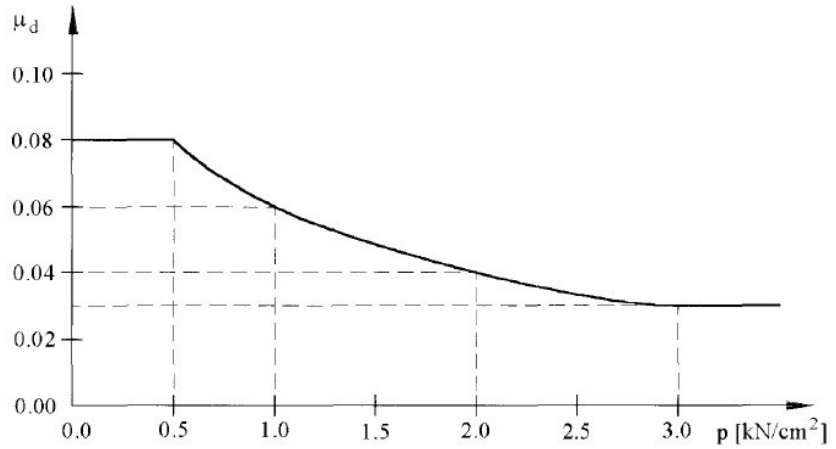

Figure 4.22. Relationship between friction coefficient and vertical pressure.

Vertical supporting elements are single piers with a full reinforced concrete circular cross section with a parallelepiped cap on top; a circular diameter D = 2.2 m and a constant ratio along the longitudinal development H/D = 5, where H is the pier height, are assumed. This choice perfectly matches the results of the statistical analysis on the pier geometries in Chapter 3.

4.2.2 Simulated design project basing on previous codes

A simulated design has been performed according to the Italian D.M. 03.03.1975 (Ministero dei Lavori Pubblici, 1975), considering both gravity and seismic loads. Gravity loads derive directly from the deck self-weight, while permanent loads, including the pavement, guard-rails and other building details of the superstructure, are assumed to be constant along the bridge. The sum of self-weights and permanents loads is assumed equal to 150 kN/m as distributed loads. Seismic loads are modelled as equivalent horizontal seismic forces in order to design the piers, analogously to §4.1.2.

Following the code requirements, the minimum longitudinal reinforcement ratio of 1% is assumed for the piers. From the simulated design, the optimal number of steel longitudinal rebars for all the bridge piers is found to be 55 with a constant diameter of 30 mm. Ø14 mm hoops are equally spaced at intervals of 25 cm along the pier shaft to address the shear force due to the design seismic load.

Material properties adopted for steel bars (concrete reinforcement), for girder steel and for concrete are summarised in Table 4.4. More in detail, the pier circular cover has a characteristic compressive strength $f_{c,unconfined}$ = 25 MPa, while, due to the confinement provided by the hoops, the internal radius presents a compressive strength $f_{c,confined}$ = 26.75 MPa and an ultimate strain increased by about 50% from the original one.

Table 4.4. Steel and concrete mechanical properties of SCC bridges.

	Carpentry steel	Steel reinforcement	Confined concrete	Unconfined concrete
Elastic modulus [MPa]	210000	206000	30000	30000
Yielding/Peak strength [MPa]	355	435	26.75	25.00
Ultimate strength [MPa]	470	540	0.200	0.200
Yielding/Peak strain [-]	0.0169	0.00207	0.002	0.0027
Ultimate strain [-]	0.1000	0.12000	0.0060	0.0114

Concerning the bearings, considering the vertical load on each bearing device, the maximum vertical load at the Ultimate Limit State can be calculated according to the load combinations from (Ministero dei Lavori Pubblici, 1980), as shown in the following Table 4.5. For the load nomenclature, see §3.3.1.

Table 4.5. Vertical load combinations at Ultimate Limit State (Ministero dei Lavori Pubblici, 1980)

G_{UI}	$1.35\ g + 1.5\ q_5 + q_6$
G_{UII}	$1.35\ g + 1.5\ (q_1+q_2) + 0.9\ q_5 + q_6$
G_{UIII}	$1.35\ g + 1.5\ (q_1+q_2+q_3) + 0.75\ q_5 + q_6$
G_{UIV}	$0.95\ g + 1.5\ (q_1+q_2+q_4) + 0.75\ q_5 + q_6$
G_{UV}	$0.9\ g + 1.5\ (q_1+q_2) + 0.6\ (q_3+q_4+q_5) + q_6$

For uni- or multi- directional bearings, the maximum thermal expansion to ensure in the transverse direction can be calculated basing on the maximum length of the deck and referring to a maximum thermal variation ΔT=40°C; for the thermal expansion coefficient of steel $\alpha = 1.2 \times 10^{-5}$, it is obtained:

$$\Delta l = \alpha \times \Delta T \times L = (1.2 \times 10^{-5}) \times 40 \times L \qquad (35)$$

A safety coefficient γ=1.5 is then applied for the Ultimate Limit State.

A simulated project can be carried out for each bridge configuration, choosing an appropriate device from available catalogues respecting the maximum allowable vertical load as well as the maximum transverse displacement Δl. In this Thesis, the characteristics of the bearing devices are taken from the *FIP Industriale* catalogues. Here below, Table 4.6 and Table 4.7 show the results from the evaluation of the vertical loads and the maximum transverse displacement, and the selected bearing devices, respectively, for the case study *L/B* = 20. To security advantage, results of the bearing design for *L/B* = 20 will be applied also to the other case studies. The selected devices allow maximum displacements of ±200 mm along mobile directions, maximum shear force at Ultimate Limit State V_{ULS} = 900 kN, maximum normal force at Service Limit State N_{SLS} = 6429 kN and maximum normal force at Ultimate Limit State N_{ULS} = 9000kN.

Table 4.6. Maximum vertical load and maximum transverse displacement of uni- and multi-directional bearings for the selected case study

Case study: *L/B* = 20	
N_{ULS} [kN]	8446.20
Δl [m]	$= (1.2 \times 10^{-5}) \times 40 \times 250 \times 1.5 = 0.18$

Table 4.7. Characteristics of the bearing devices: SF = fixed; SU = uni-directional; SM = bidirectional

Typology	N_{SLS} [kN]	N_{ULS} [kN]	V_{ULS} [kN]	Φ base [mm]	d_{max} [mm]	weight [kg]	Φ anchor bolts [mm]	n° anchor bolts [-]	Φ pintle [mm]
SF	6429	9000	900	560	-	274	55	4	140
SU	6429	9000	900	560	200	365	55	4	140
SM	6429	9000	-	550	200	250	-	-	55

Basing on results by (Costantinou et al., 1990), the design normal force on the devices can be used for the evaluation of the friction coefficients at high and low velocities, as depicted in Figure 4.23.

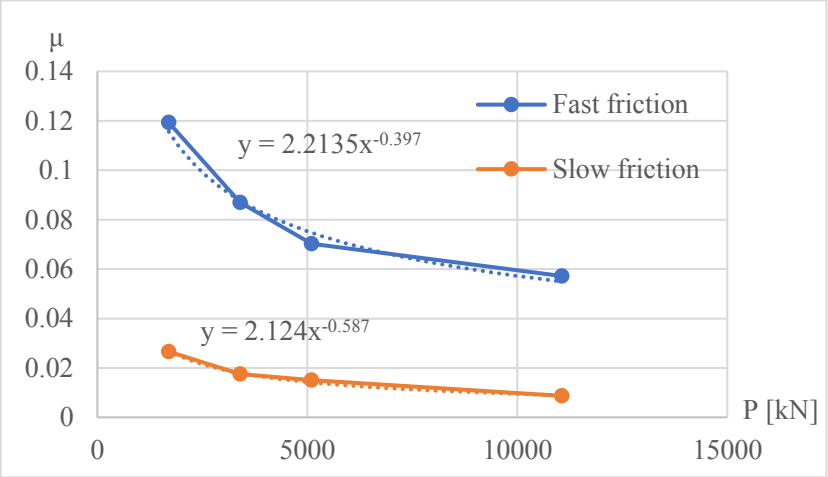

Figure 4.23. Friction coefficients at high and low velocities.

Depending on the geometry of the bearing device, the maximum resisting horizontal force in the fixed direction for fixed or uni-directional bearings can be calculated as the minimum between that provided by the pintles and that provided by the anchor bolts. Considering only the pure shear capacity of anchors or pintles, the resisting force V can be calculated according to Steelman et al. (2014) as follows:

$$V = \Phi n 0.6 f_u A_b$$

where Φ = strength reduction factor (taken as unity, to reflect nominal capacity); n = number of shear transfer elements; the 0.6 coefficient reflects the assumption that pure shear controls capacity; f_u = ultimate tensile strength of the material under consideration; and A_b = effective cross-sectional area of a single shear transfer element. The effective area was calculated as 80% of the nominal cross-sectional area for the threaded anchors into concrete.

From the design project, the minimum shear resistance derives from the anchor bolts and is equal to $V = 2326.41$ kN.

4.2.3 Behaviour of end cross beams

As previously introduced, in this section a further investigation is dedicated to the behaviour of the adopted reticular cross beams. According to (Carbonari et al., 2017; Dezi et al., 2018; Minnucci et al., 2019), the end cross beams have a key role in the redistribution of the transverse seismic action and basing on their stiffness a different trend of the shear forces can be observed in correspondence of the supports. The same studies proved also that the influence of the relative stiffnesses between the cross beams and the deck cross section can be caught only through appropriate refined modelling strategies, typically through 3D shell FE models. However, the computational effort deriving from a complete FE modelling of the structure is extremely high, so that it is necessary to adopt simplified methods to examine the behaviour of the deck under seismic actions, especially in the transverse direction, along which the major problems connected to the "dual load path" mechanisms arise. As first, the reticular cross beam system will be assessed according to the design criteria at the time of the bridge construction. Then, an equivalent simplified model by Carden et al. (Carden et al., 2007) will be adopted to investigate the behaviour of the reticular system.

4.2.3.1 Design and assessment with previous codes

Assuming that the considered case studies refer to an existing bridge antecedent the current Codes, the load combinations to be considered in the assessment of the deck cross section are defined in D.M. 04/05/1990 (Ministero dei Lavori Pubblici, 1990), D.M. 14/02/1992 (Ministero del Lavori Pubblici, 1992), D.M. 09/01/1996 (Ministero dei Lavori Pubblici, 1996). In particular, according to the AS method, the actions involved in the transverse direction are the wind load (*q5*) and the seismic force (*q6*), to be computed as follows: the wind load is regarded as equivalent to a static horizontal load in the orthogonal direction to the bridge axis equal to 250 kg/m^2 on the exposed surfaces; the seismic action can be evaluated according to the level of seismicity and the response coefficient as previously described in §3.3.1.

The load combinations to consider in case the AS method is adopted are reported in Table 4.8, where the loads other than wind and seismic action have already introduced in §3.3.1. In the following Table 4.9 the results of the most unfavourable load combinations for the transverse direction are shown.

Table 4.8. Most unfavourable load combinations in the AS method.

	g1	g2	g3	q1	q2	q3	q4	q5	q6	q7	q8	q9
AI	1	1	1	0	0	0	0	1	0	1	0	1
AII	1	1	1	1	1	0	0	0,6	0	1	1	1
AIII	1	1	1	1	1	1	0	0,2	0	1	1	1
AIV	1	1	1	1	1	0	1	0,2	0	1	1	1
AV	1	1	1	0	0	0	0	0	1	0	0	0

Table 4.9. Most unfavourable load combinations in the AS method.

AI	645.01 [kN]	g1+g2+q5+q7+q9
AII	387.00 [kN]	g1+g2+q1+q2+0.6*q5+q7+q8+q9
AV	635.81 [kN]	g1+g2+q6

The beam sections that compose the reticular system are assessed according to D.M. 02/08/1980 (Ministero dei Lavori Pubblici, 1980), as reported in the following Table 4.10. The assessment is satisfied if $\sigma_{adm}/\sigma > 1$.

In case of compressed elements, the assessment is satisfied if buckling phenomena are prevented. For this reason, the buckling of the compressed diagonal and the inferior beam is also verified following the AS method combinations, as shown in the following Table 4.11.

Table 4.10. Assessment of the reticular cross beam elements.

Compression/tension assessment				
UPPER HORIZONTAL BEAM (Double L 120x80x10)				
Combination	N [kN]	σ [MPa]	σ_{adm} [MPa]	$\sigma_{adm}/\sigma > 1$
AI	645.01	168.85	240	1.42
AII	387.00	101.31		2.37
AV	635.81	166.44		1.44
COMPRESSED DIAGONAL (Double L 80x120x10)				
Combination	N [kN]	σ [MPa]	σ_{adm} [MPa]	$\sigma_{adm}/\sigma > 1$
AI	351.88	92.12	240	2.61
AII	387.00	101.31		2.37
AV	173.43	45.40		5.29
TENSE DIAGONAL (Double L 80x120x10)				
Combination	N [kN]	σ [MPa]	σ_{adm} [MPa]	$\sigma_{adm}/\sigma > 1$
AI	351.88	92.12	240	2.61
AII	387.00	101.31		2.37
AV	173.43	45.40		5.29
LOWER HORIZONTAL BEAM (Double L 100x150x10)				
Combination	N [kN]	σ [MPa]	σ_{adm} [MPa]	$\sigma_{adm}/\sigma > 1$
AI	645.01	133.27	240	1.80
AII	387.00	79.96		3.00
AV	635.81	131.36		1.83

Table 4.11. Assessment of the compressed elements against buckling.

Compression/tension assessment						
COMPRESSED DIAGONAL (Double L 80x120x10)						
Combination	N [kN]	λ/λ_c [-]	ω [-]	σ [MPa]	σ_{adm} [MPa]	$\omega\sigma/\sigma_{adm} < 1$
AI	351.88	1.226	2.34	92.12	240	0.90
AII	387.00			101.31		0.99
AV	173.43			45.40		0.44
LOWER HORIZONTAL BEAM (Double L 100x150x10)						
Combination	N [kN]	λ/λ_c [-]	ω [-]	σ [MPa]	σ_{adm} [MPa]	$\omega\sigma/\sigma_{adm} < 1$
AI	645.01	0.767	1.48	133.27	240	0.82
AII	387.00			79.96		0.49
AV	635.81			131.36		0.81

4.2.3.2 Equivalent modelling of the cross-beam system

In order to simplify the structural modelling of the truss cross beams, an equivalent 2D model of the deck is built, representative of the deck portions above the bearings, which are known to be the main parts involved in the transfer mechanisms of the inertial forces. From previous studies (Carbonari et al., 2017; Dezi et al., 2018; Minnucci et al., 2019)), this portions can be assumed long about 2 m on each side of the bearings. Concerning SCC decks with a double I-shaped girder configuration, the results from the research by Carden et al. (Carden et al., 2007) are exploited. According to Carden et al. (Carden et al., 2007), the equivalent transverse stiffness of a deck girder on the supports can be modelled as a rotational and torsional spring system, where the different springs represent the flexural and torsional characteristics of the macro-system formed by steel girder, shear connection and web stiffeners, according to the following expression:

$$K_g = k_t + \frac{12EI_{ws}}{d_{gf}^3}(1-\rho) \tag{36}$$

where k_t is the equivalent torsional stiffness of the steel girder, EI_{ws} is the flexural stiffness of the web stiffeners, d_{gf} is the girder height between the plate centres, ρ is a coefficient that takes into account the rotational stiffness of the bearing devices and of the beam at the top, $k_{\theta b}$ and $k_{\theta s}$, respectively (Figure 4.24).

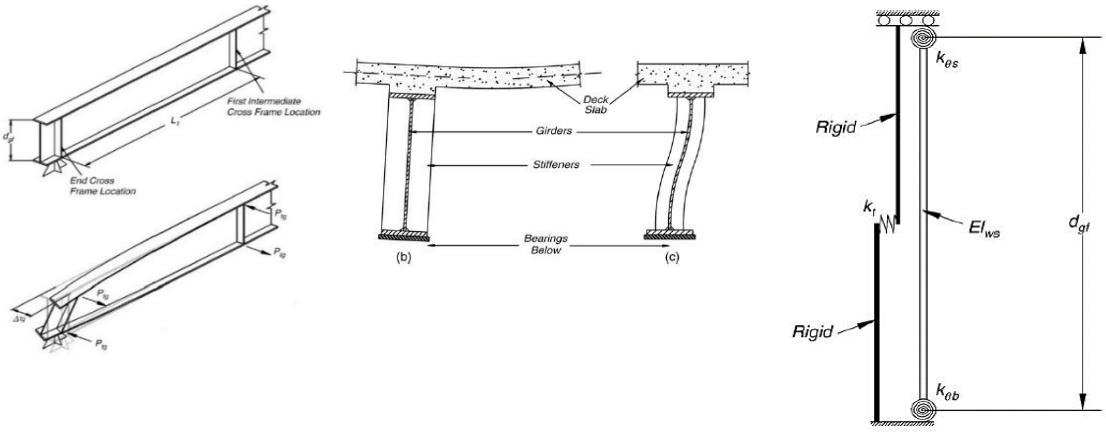

Figure 4.24. 2-D equivalent model.

The equivalent translational stiffness in the transverse direction of the combined system upper beam-slab can be also calibrated basing on the axial stiffnesses of the single parts, taking into account the slab longitudinal portion of interest:

$$K = K_{slab} + K_{truss} \tag{37}$$

The 2-D model is developed in SeismoStruct, v.2016 (Figure 4.25(a)). Each vertical element is characterized by the equivalent transverse stiffness K_{eg} and it is assumed to be elastic together with the upper horizontal elements, condensed in a single beam with stiffness equal to K. The diagonals and the lower horizontal element are built as force-based nonlinear fiber element, with the cross-sections illustrated in Figure 4.18. Both mechanical and geometric nonlinearities are introduced, considering a S355 steel material with the constitutive law reported in Figure 4.25(b) and local eccentricities equal to 1/200 of the diagonal length (simulating accidental imperfections).

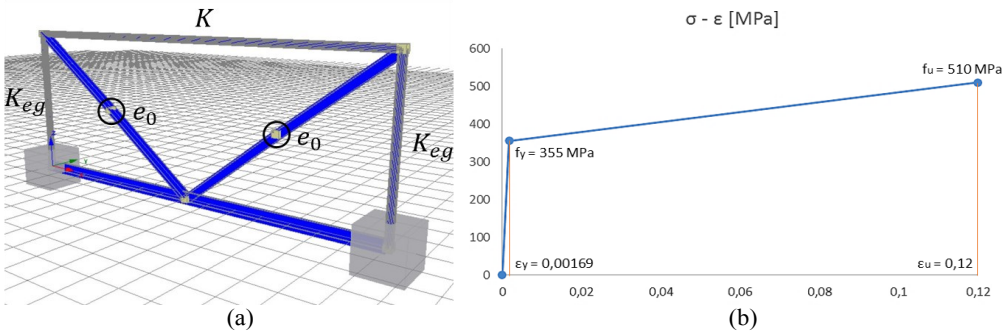

Figure 4.25. (a) 2-D FE equivalent model; (b) constitutive law – steel S355

The effects of seismic action in case of truss end cross beams are evaluated through pushover and cyclic nonlinear analyses, which can highlight the capacity of the system and the dissipative properties of the components. The maximum enforced displacement is equal to 0.1 m by 0.001 m steps. Known the maximum forces and displacements carried

by the components, cyclic time histories have been applied at different displacement levels, to quantify the dissipated energy and the equivalent stiffness and damping of the reticular system.

Figure 4.26 shows a view of the equivalent 2-D model under static increasing forces. From the analysis of the pushover curve from the applications (Figure 4.27), it can be clearly identified the buckling and the successive collapse of the compressed diagonal element in both the support and middle-span sections.

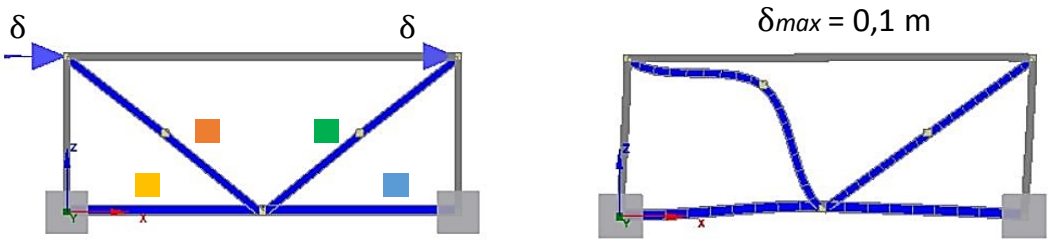

Figure 4.26. Nonlinear static analysis (pushover)

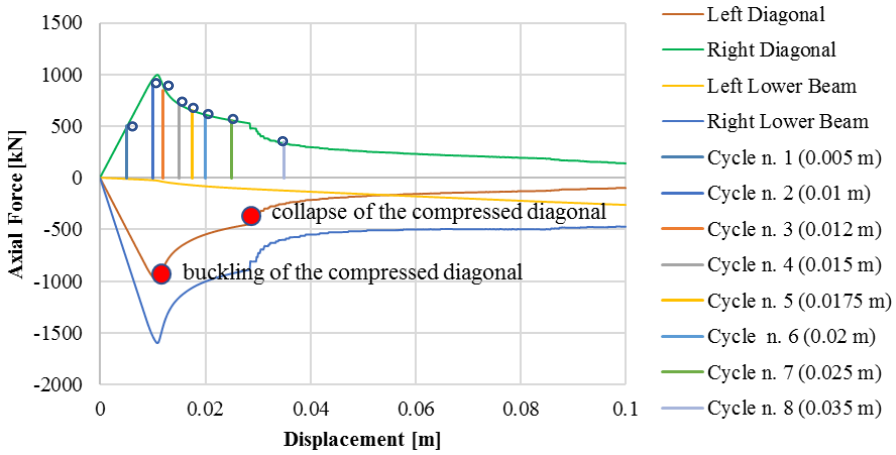

Figure 4.27. Results of nonlinear static analyses

Six different levels of displacement have been chosen on the pushover curve to carry out Static Time History analyses with a monotonic trend for the load factor to evaluate the dissipative capacities of the system (Figure 4.28). Results from the Static Time History analyses will be adopted in the next section to implement in the whole 3-D FE model of the SCC bridge the behaviour of the truss cross section.

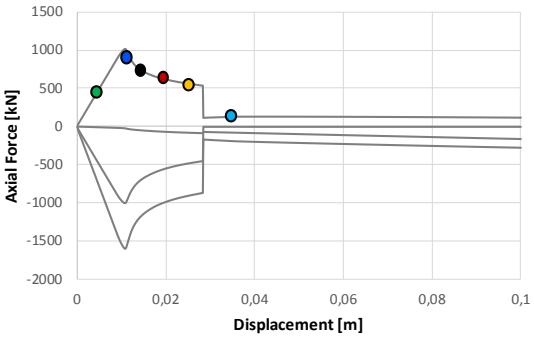

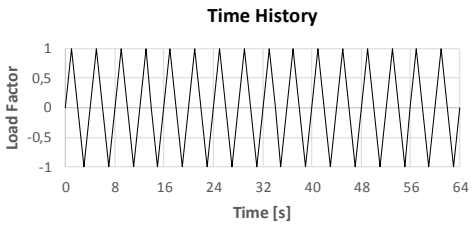

N° Cycle	δ*max* [m]
1	0,005
2	0,012
3	0,015
4	0,02
5	0,025
6	0,035

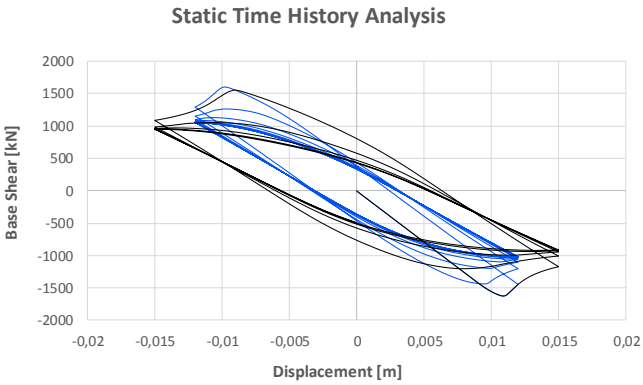

Figure 4.28. Monotonic static analyses and hysteretic cycles at different levels of displacement

4.2.4 SCC bridges FE modelling

A three-dimensional nonlinear model of the SCC bridges is developed in OpenSees (McKenna et al., 2015). Since no plastic deformation is expected on the deck girders, the latter are modelled as *elasticBeamColumn* elements.

Piers caps are assumed as rigid elements and are modelled by *rigidLink beam* elements connecting the deck beam ends to the bearings.

In order to apply the results on the behaviour of the reticular cross beam system obtained in the previous §4.2.3, the force-displacement response of the system, represented by the pushover curve in Figure 4.29a, can be approximated by the coupling of two materials from the OpenSees library Figure 4.29b):

- the first material is the elastic-perfectly plastic *Steel01* up to a maximum force equivalent to the post-collapse of the reticular system;
- the second material is the *Hysteretic*, which approximated the pre-collapse behaviour, with a maximum force equal to the difference between the buckling force and the maximum force of the elastic-plastic law.

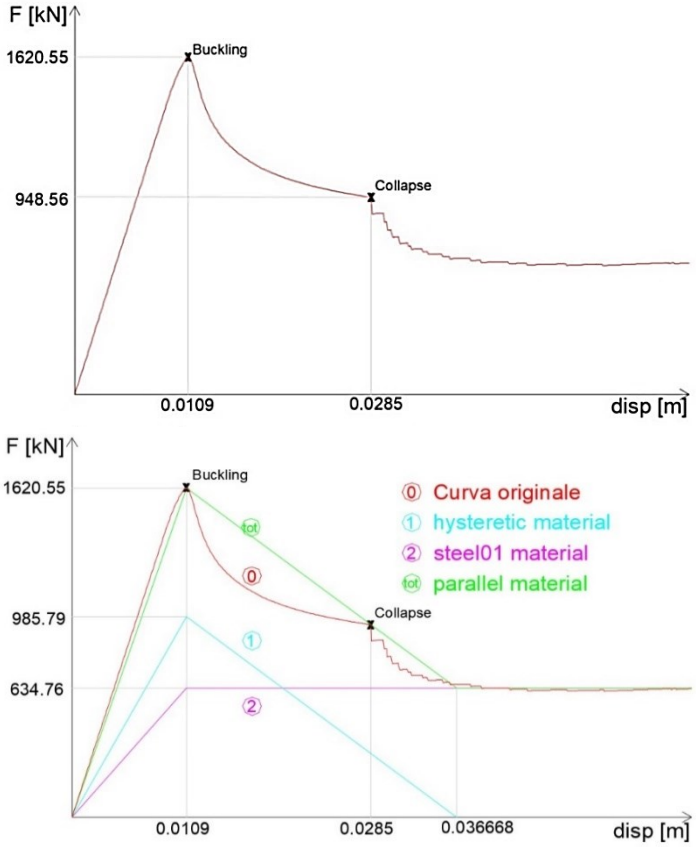

Figure 4.29. (a) Pushover curve of the reticular cross section and (b) Approximation of the force-displacement law with a material system in parallel

The combined behaviour of the *Steel01* and the *Hysteretic* materials is realized with an *Uniaxialmaterial Parallel* material assigned to the transverse direction of a *zeroLength* element in correspondence of each cross section above the supports, as depicted in Figure 4.30.

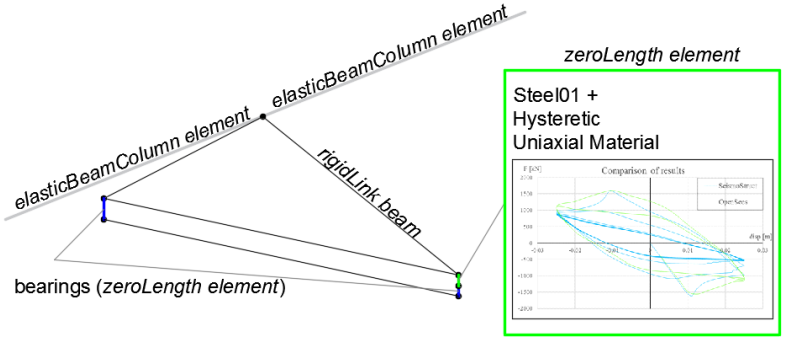

Figure 4.30. Modelling of the equivalent zeroLength element for the transverse reticular system.

The validation of the proposed element is carried out applying a monotonic cyclic load path (Figure 4.31) on both the 2D equivalent model in SeismoStruct and the equivalent parallel material in the transverse direction of the zeroLength element. The comparison

of results depicted in Figure 4.32 shows a good agreement between the two modelling strategies.

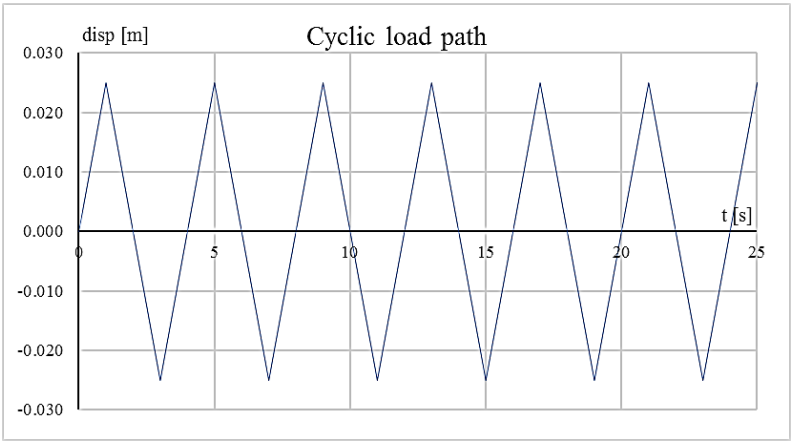

Figure 4.31. Cyclic load path

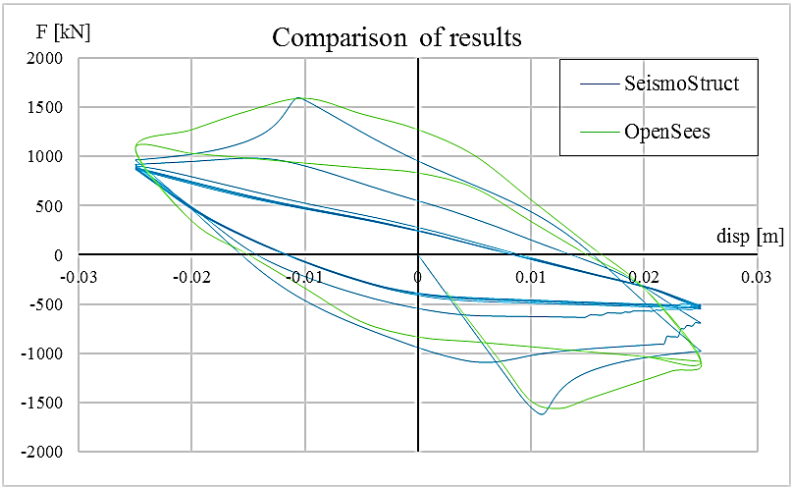

Figure 4.32. Comparison of results from SeismoStruct 2-D model and OpenSees equivalent zeroLength element

The modelling of the bearings is distinguished for the fixed and the sliding directions. In order to reproduce the expected behaviours of Figure 4.20, two different strategies are adopted. For fixed directions, the rigid-perfectly plastic law of Figure 4.20a can be approximated by the coupling of an *Elastic* uniaxial material and an Elastic Perfectly Plastic *ElasticPP* material. The first one acts till d^*= 0.001 m, then it fails due to a *MinMax* material. A *Parallel* material couples the initial stiffnesses of the *Elastic* and of the *ElasticPP* so that d^* corresponds to the maximum shear force F_1 carried by the selected device model. The plastic behaviour is governed by a friction coefficient between steel surfaces μ_f = 0.20. The modelling of the behaviour in the fixed directions is depicted in Figure 4.33.

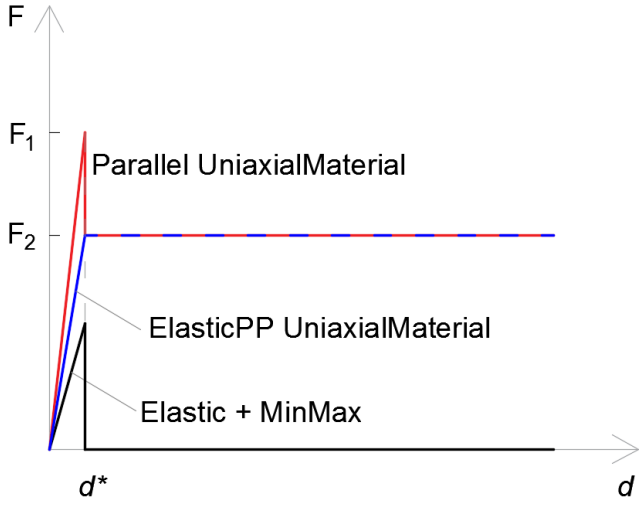

Figure 4.33. Modelling of the constitutive law for fixed directions (bearings).

In case of sliding directions, OpenSees offers the possibility of simulating the dependence of friction coefficient from both pressure and velocity through the *flatSliderBearing* element (Schellenberg, 2014) (Figure 4.34), for which the friction model is defined through the *Velocity and Normal Force Dependent Friction Material* (Dao, 2014) (Figure 4.35). The command line to model the *Velocity and Normal Force Dependent Friction Material* is described in Table 4.12.

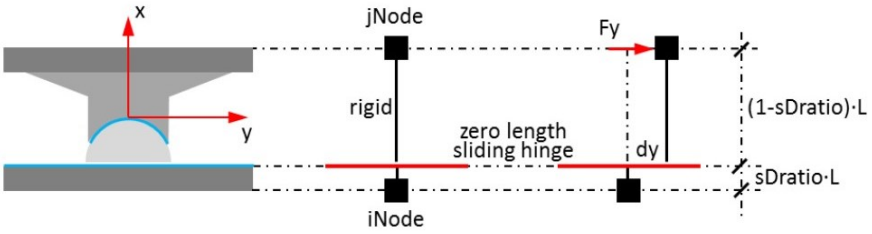

Figure 4.34. flatSliderBearing element in OpenSees.

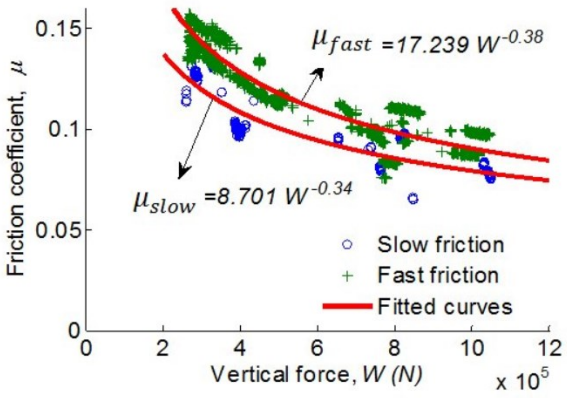

Figure 4.35. Example of friction coefficient vs. vertical force in the Velocity and Normal Force Dependent Friction Material in OpenSees.

Table 4.12. Command line for the Velocity and Normal Force Dependent Friction Material.

frictionModel VelNormalFrcDep $frnTag $aSlow $nSlow $aFast $nFast $alpha0 $alpha1 $alpha2 $maxMuFact

$frnTag	unique friction model object tag
$aSlow	constant for coefficient of friction at low velocity
$nSlow	exponent for coefficient of friction at low velocity
$aFast	constant for coefficient of friction at high velocity
$nFast	exponent for coefficient of friction at high velocity
$alpha0	constant rate parameter coefficient
$alpha1	linear rate parameter coefficient
$alpha2	quadratic rate parameter coefficient
$maxMuFact	factor for determining the maximum coefficient of friction. This value prevents the friction coefficient from exceeding an unrealistic maximum value when the normal force becomes very small. The maximum friction coefficient is determined from μFast, for example μ ≤ $maxMuFac*μFast.

It is possible to notice that all the required information to compile the command string are available from the simulated design project in §5.2.2. Even in this case, the initial stiffness is calibrated to impose the passage to the plastic behaviour at d^*= 0.001 m considering a friction coefficient $\mu = \mu_{nom}$ (34)). In this work, the intermediate loss of the bearing device is not modelled. The modelling of the behaviour in the sliding directions is depicted in Figure 4.36.

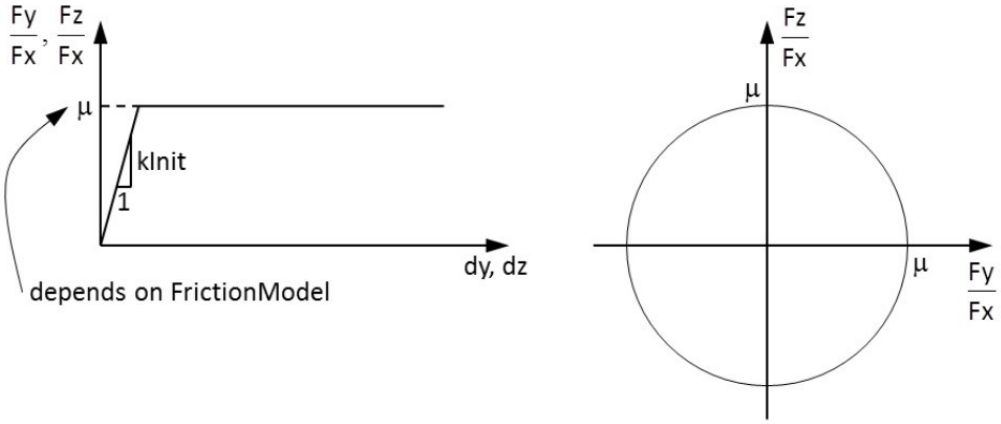

Figure 4.36. Modelling of the constitutive law for sliding directions (bearings).

Columns are modelled using displacement-based fiber elements (*dispBeamColumn* element), which are able to take into account the evolution of the plastic hinge at the base of the pier. Concrete is described by *Concrete01* (no tensile strength), with parameters assumed according to (Mander et al., 1988) and constitutive laws for both confined and unconfined concrete depicted in previous Figure 4.6(a). Fibre sections of both the confined and unconfined parts are generated by using a circular shaped patch. Steel

longitudinal rebars are constructed as line fibres with *Steel02* uniaxial material, and the *layer circ* command is used to place the bars along circular arches.

Seat type abutments resting on piles are considered, since this typology can be considered as the most widespread on the Italian road networks. The response of the abutments is modelled evaluating the contribution of both earth pressure and structural stiffness in longitudinal and transverse direction. In particular, along the longitudinal direction, the passive resistance of the abutment backwall is simulated using the hyperbolic soil model proposed by (Shamsabadi et al., 2007), assuming a granular soil type. The active and the transverse resistances are entirely assigned to the piles whose response is schematized with a trilinear force deformation law. The parameters characterizing the constitutive pile law are determined following the design recommendations of (CALTRANS, 2015) and (Choi, 2002), assuming a 7 kN/mm/pile resistance and considering as yielding force the inertial force proportional to the mass of the entire bridge deck to be carried by the foundation piles. The bilinear contact element developed by (Muthukumar & DesRoches, 2006) is used to model the pounding between the deck and the abutments.

Distributed masses on deck and pier elements have been defined considering 2.5 t/m3 as RC density. A lumped nodal mass M is applied at the top end of each pier to simulate the pier cap. Gravity and permanent loads are directly derived from distributed and nodal masses and applied just before TH analysis. A schematic view of the 3D FE Model is depicted in Figure 4.37 and Figure 4.38.

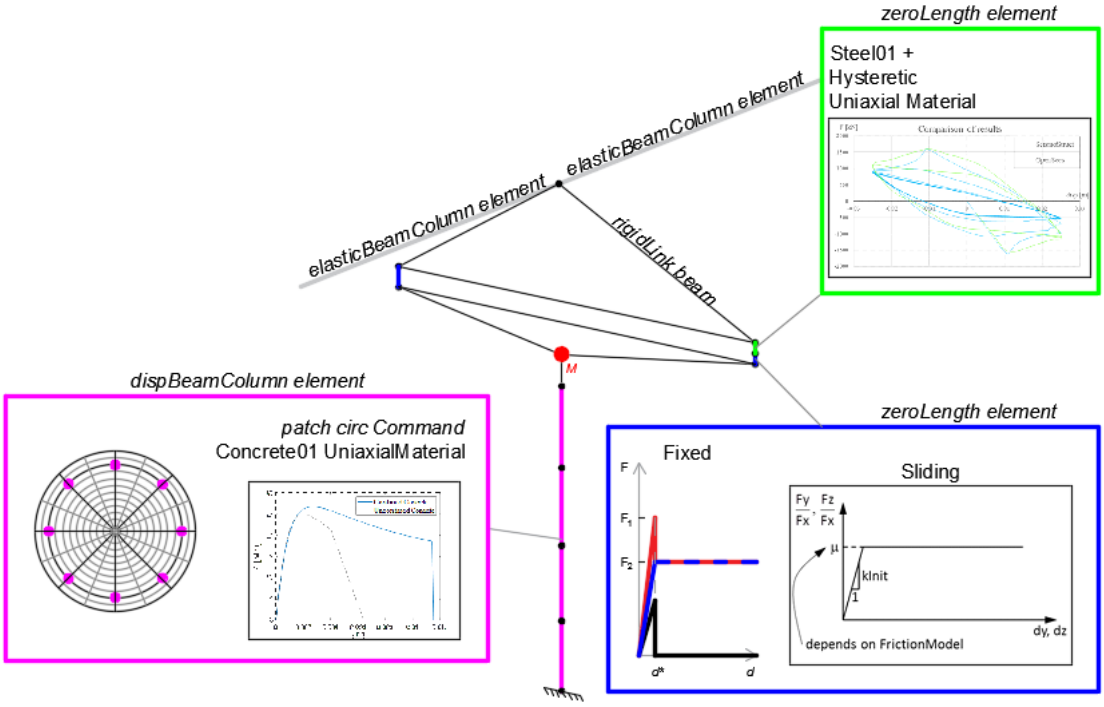

Figure 4.37. Finite Element Model of the SCC bridges – deck, link slabs, bearings and piers.

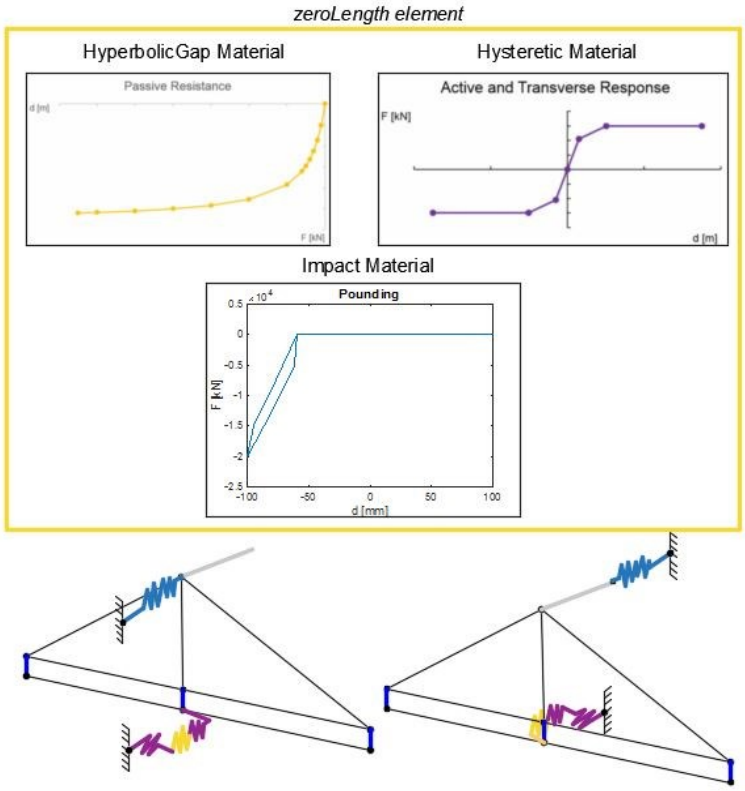

Figure 4.38. Finite Element Model of the SCC bridges – abutments.

4.3 Limit States and Damage Mechanisms

The Demand parameters *D* monitored to assess the structural response of the bridge are as follows:

1) pier maximum top-base relative displacement (related to the pier curvature χ), concerning the ductile mechanism of the pier;
2) bearings maximum displacement;
3) maximum strain on the link-slab steel bars, for RCLS bridges only;
4) maximum displacement in the transverse direction of the reticular cross beam system, for SCC bridges only;
5) abutment maximum longitudinal displacement for the passive response;
6) abutment maximum longitudinal displacement for the active response;
7) abutment maximum transverse displacement.

Three Performance Levels (PLs) are assessed: the first one is denoted as d_y and it is related to the onset of an irreversible damage condition (e.g., piers or bars yielding, compressed diagonal buckling for the reticular cross section); the second one is denoted as d_u and it is related to the attainment of the ultimate capacity of the bridge component (e.g., bars fracture, reticular system or pier collapse), potentially leading to the collapse of the whole system; the third one, d_{LS}, is an intermediary limit state, associated to an extensive damage

condition and related to the NTC2018 Life Safety limit state (Ministero delle Infrastrutture e dei Trasporti, 2018).

The limit values for each performance level and for all the observed bridge components are summarised in Table 4.13. The values assumed for the cross beams are consistent with the results obtained from static pushover analysis (see §4.2.3), while the limits assumed for the bearings and the piers are those recommended by the Italian code (Ministero delle Infrastrutture e dei Trasporti, 2018) and technical documents (DSTE/PRS & UNIBAS – Autostrade per l'Italia S.p.A., 2019) for bridge seismic vulnerability assessment. For PTFE-steel bearings, the damage limit state is not clearly associable to a physical phenomenon occurring on the devices, so that only the two heavier limit states are considered, the first associable to the shear rupture in case of fixed directions or to the maximum device displacement in exercise (from the technical schedules) in case of sliding directions, and the second to the complete loss of the support. The performance levels for piers in term of head displacements are obtained through a preliminary moment-curvature analysis starting from constitutive laws of materials. Concerning the demand thresholds for the abutments, the PLs are derived from the work by Ramanathan (Ramanathan, 2012).

It is worth to note that a shear-related response parameter for the piers is not considered. This is because it was preliminary assessed that brittle failure does not occur before the ductile one (shear overstrength), as can be observed in Figure 4.39.

Table 4.13. Performance levels and related demand threshold values for the bridge components.

Performance Level (PL)	Yielding/Damage (d_y)	Life Safety (d_{SL})	Collapse (d_u)
Link bars ε_{bar} [-]	0.0046	3/4 $\varepsilon_{bar,u}$	0.0400
Cross beam u_{cb} [m]	0.0109	3/4 u_{cb}	0.0285
RCLS Piers u_p [m]	0.077	3/4 $u_{p,u}$	0.234
SCC Piers u_p [m]	0.085	3/4 $u_{p,u}$	0.256
Neoprene Bearings u_b [m]	0.080	3/4 $u_{b,u}$	0.200
PTFE-Steel Fixed Bearings u_f [m]	-	0.001	0.400
PTFE-Steel Sliding Bearings u_s [m]	-	0.200	0.400
Abutment – Passive $u_{AB\text{-}P}$ [m]	0.037	1.000	1.000
Abutment – Active $u_{AB\text{-}A}$ [m]	0.00975	0.0072	1.000
Abutment – Transverse $u_{AB\text{-}T}$ [m]	0.00975	0.0072	1.000

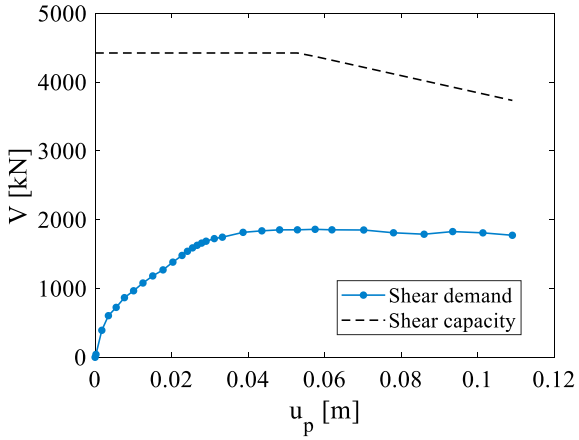

Figure 4.39. Comparison between pier shear capacity and shear demand (from static incremental analysis).

4.4 Modelling of Soil-Structure Interaction and degradation phenomena

As already mentioned, it is widely recognized that compliance of the foundation system of bridges may strongly affect the structural response (Anastasopoulos et al., 2015; Capatti et al., 2017; Carbonari et al., 2017; Stefanidou et al., 2017), with possible detrimental effects associated to deep foundations (Mylonakis & Gazetas, 2000; Carbonari et al., 2011), which are the most adopted solution in case of bridge piers and abutments. At the same time, considering that the examined case studied are representative of existing structures, effects of deterioration must be considered for a proper evaluation of the fragility. Regarding RCLS bridges, corrosion is recognized as the most influencing degradation phenomenon affecting the vulnerability of concrete structures, and can be reliably simulated through the reduction of the rebars' area, the worst consequence of corrosion for the bridge columns response (Rao et al., 2017a; Mangalathu et al., 2018). Regarding SCC bridges, the corrosion of metallic components adds to the corrosion on concrete elements. In particular, the corrosion on bearing devices may be of fundamental importance for the maintaining of their supporting function.

In order to capture the effects of the compliant base under the supporting elements, the Lumped Parameter Model (LPM) proposed by Morici et al. (Morici et al., 2019) and previously shown in §2.5 is adopted. The LPM approximates the dynamic impedances of pile groups and can be built through closed-form formulas for estimating parameters of the model for foundations in homogeneous soil deposits. The work by Morici et al. (Morici et al., 2019) represents the extension of the work by Carbonari et al. (Carbonari et al., 2018) for end-bearing single piles and pile groups. The approach results easy to calculate and implement in a FE model; moreover, the efficiency of the adopted model in reproducing impedances of pile foundations for inertial SSI analyses has been further demonstrated in the research by González et al. (González et al., 2019) to address the seismic response of bridge piers. The foundation can be described by the assemblage of

uncoupled springs, dashpots and masses in the 3-dimensional space, as depicted in Figure 4.40.

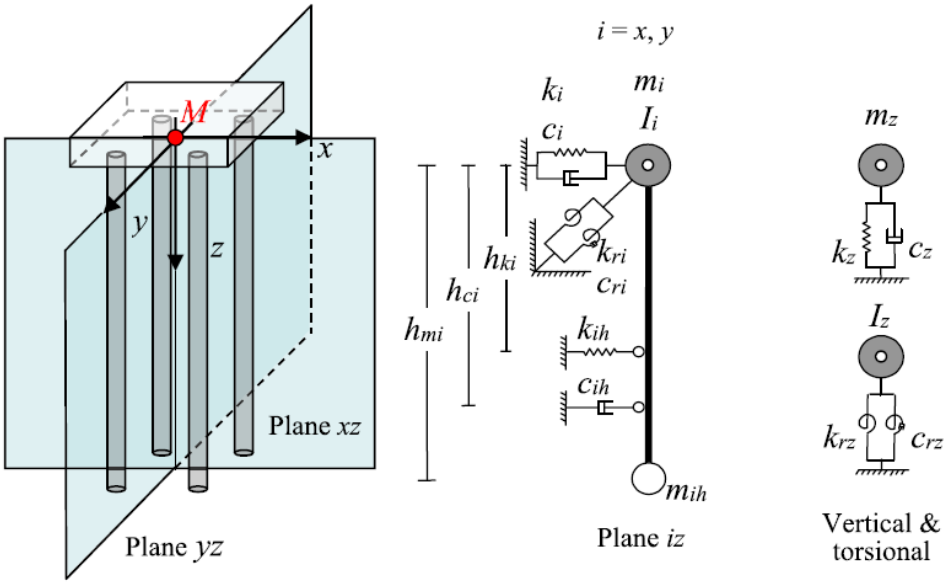

Figure 4.40. Assemblage of uncoupled LPMs.

In this Thesis, LPM parameters are chosen to reproduce the behaviour of an end-bearing pile foundation with geometric and mechanical characteristics deriving from the accomplishments of the requirements for the pier foundation under vertical loads. In particular, a 3x3 pile group foundation is considered with 12 m long and 3 m spaced piles, with circular cross section characterized by a diameter d = 1 m. The soil parameters are representative of a C soil class according to Eurocode 8 (CEN 2004), coherently with the most frequent soil characteristics at the investigated bridge sites in the Marche territory. Non-dimensional parameters and associated values for springs, masses and dashpots to be used for the LPM modelling are easily derived from the on-line available supplementary spreadsheet associated to the research paper by Morici et al. (Morici et al., 2019). Figure 4.41 and Figure 4.42 show the input data and the outcomes of the calculations in the graphical interface of the spreadsheet, respectively.

The LPM is simulated in the OpenSees platform as a combination of nodes, deformable and rigid elements connecting the translational and rotational masses of the foundation to the pier base. Springs and dashpots for the translational and rotational degrees of freedom are modelled through *zeroLength* elements. Whereas simultaneously present, the *Elastic* and the *Viscous* uniaxial materials, associated to springs and dashpots respectively, are combined using a *Parallel* material. Eccentric springs, dashpots and masses are connected to the base node of each bridge pier with a *rigidLink beam* element. Figure 4.43 schematically illustrates the realized FE model of the LPM.

Geometric pile group configuration

Type of pile foundations		End Bearing	
Number of piles	n	3	-
Piles Diameter	d	1.00	m
Piles Spacing	s	3.00	m
Piles Lenght	L	12.00	m

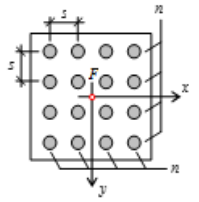

Input

Mecanichal Property Pile Group and Soil			
Mass Density of piles	ρ_p	2.5	Mg/m^3
Elastic Modulus of the piles	E_p	30000000	kN/m^2
Mass Density of Soil	ρ_s	1.75	Mg/m^3
Soil Shear Velocity	V_s	255	m/s
Soil Shear Modulus	G_s	113793.75	kN/m^2

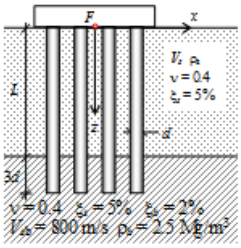

Non dimensional parameters

$\tilde{\Omega}_1$	24.27081 -	$\tilde{\Omega}_6$	106.64132 -	$\tilde{\Omega}_{11}$	0.00000 -
$\tilde{\Omega}_2$	97.58533 -	$\tilde{\Omega}_7$	1645.81417 -	$\tilde{\Omega}_{12}$	325.27024 -
$\tilde{\Omega}_3$	120.90252 -	$\tilde{\Omega}_8$	986.38293 -	$\tilde{\Omega}_{13}$	873.82309 -
$\tilde{\Omega}_4$	-32.47760 -	$\tilde{\Omega}_9$	1058.22486 -	$\tilde{\Omega}_{14}$	4674.79341 -
$\tilde{\Omega}_5$	-9.45390 -	$\tilde{\Omega}_{10}$	126.84833 -	$\tilde{\Omega}_{15}$	790.13146 -

Conditions and defition of h_{ki}, h_{mi}, h_{ci}

Conditions: Modulus of h_{ji}			$sgn(h_{ji})$	Select value:			Check
1.338	≤ $\lvert h_{ki} \rvert$ ≤	50.675	(-)	h_{ki} =	-1.60	m	OK
0.097	≤ $\lvert h_{mi} \rvert$ ≤	104.336	(-)	h_{mi} =	-0.50	m	OK
0.882	≤ $\lvert h_{ci} \rvert$ ≤	9.923	(+)	h_{ci} =	1.00	m	OK

Figure 4.41. LPM parameters - input.

LPM parameters

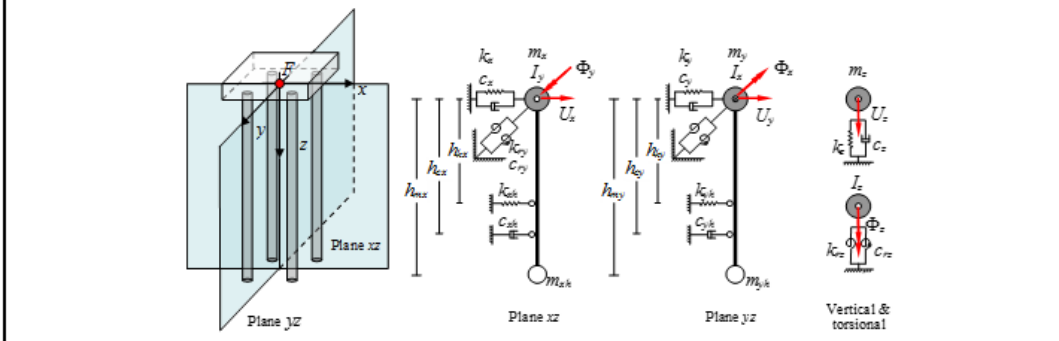

	Plane xz			Plane yz			Vertical & torsional	
k_x	452024.44	kN/m	k_y	452024.44	kN/m	k_z	14434547.09	kN/m
c_x	6364.06	kN s/m	c_y	6364.06	kN s/m	c_z	145151.85	kN s/m
m_x	137.69	Mg	m_y	137.69	Mg	m_z	0.00	Mg
k_{ry}	181370169.88	kN m	k_{rx}	181370169.88	kN m	k_{rz}	99435606.39	kN m
c_{ry}	424644.16	kN m s/rad	c_{rx}	424644.16	kN m s/rad	c_{rz}	352596.16	kN m s/rad
I_y	1717.90	Mg m^2	I_x	1717.90	Mg m^2	I_z	8180.89	Mg m^2
k_{xh}	-71121.09	kN/m	k_{yh}	-71121.09	kN/m	h_{ki}	-1.60	m
c_{xh}	47588.69	kN s/m	c_{yh}	47588.69	kN s/m	h_{mi}	-0.50	m
m_{xh}	33.09	Mg	m_{yh}	33.09	Mg	h_{ci}	1.00	m

Figure 4.42. LPM parameters - output.

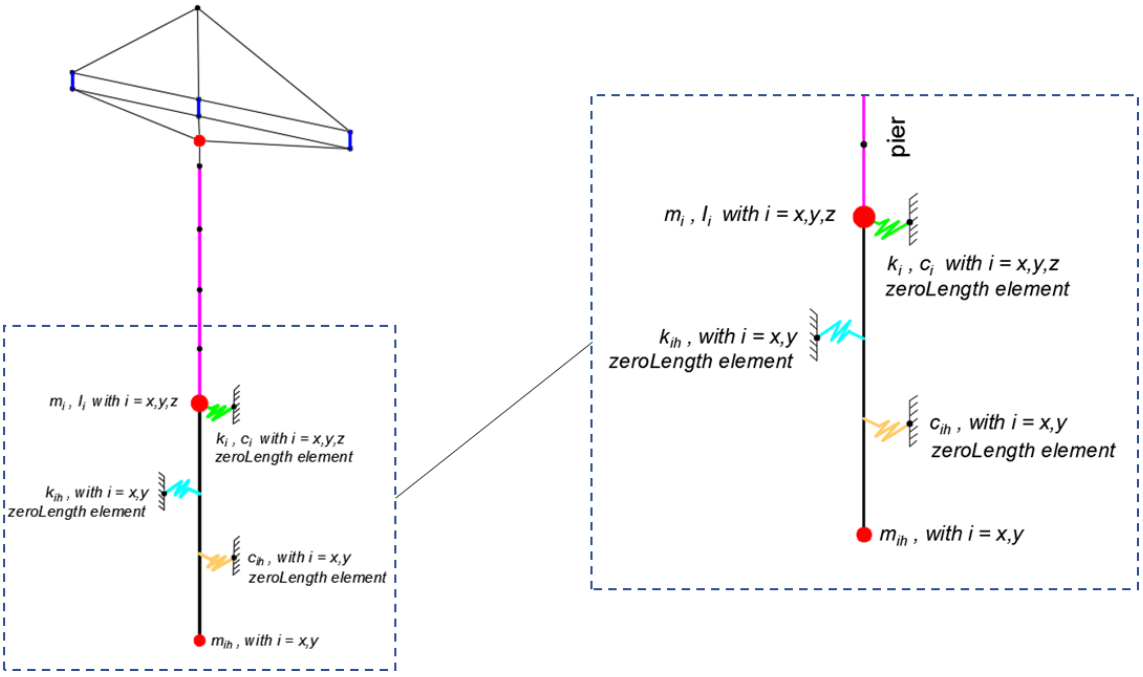

Figure 4.43. LPM modelling strategy in OpenSees.

For what concerns ageing, effects of degradation are simulated on the columns through the approach proposed by Ghosh & Padgett (2010), as a reduction of the nominal diameter of the longitudinal steel rebars depending on the elapsed time after the triggering of the corrosion phenomenon. Ageing on the PTFE-steel bearings is indirectly modelled as the loss of the maximum shear resistance in the fixed directions, since this depends from the reduction of dimensions of the shear-resisting parts of the bearing devices due to the corrosion action. Even in this case, the variation of geometric dimensions of the interested parts is calculated according to Ghosh & Padgett (2010).

Three ages are considered for the analysis of bridge fragility: the first represents the design conditions, when corrosion had not already started; in the second, the bridge is 25 y/o, at half its service life; in the third, the bridge is 50 y/o, that is in the actual conditions and at the end of the design service life.

Table 4.14 and Table 4.15 finally summarize the performed analysis cases for RCLS and SCC bridges considering both the effects of ageing and compliant base just described. In the tables, FB = fixed base analysis; CB = compliant base analysis (on piers) with the LPM.

Table 4.14. Analysis cases for RCLS bridges.

Age\ L/B ratio	L/B = 10	L/B = 20
Design conditions	FB, CB	FB, CB
25 y/o	FB, CB	FB, CB
50 y/o	FB, CB	FB, CB

Table 4.15. Analysis cases for SCC bridges.

Age\ L/B ratio	L/B = 4	L/B = 8	L/B = 20
Design conditions	FB	FB, CB	FB, CB
25 y/o	FB	FB, CB	FB, CB
50 y/o	FB	FB, CB	FB, CB

4.5 Chapter's references

Alampalli, S., & Yannotti, A. P. (1998). In-service performance of integral bridges and jointless decks. *Transportation research record*, *1624*(1), 1-7.

Anastasopoulos, I., Sakellariadis, L., & Agalianos, A. (2015). Seismic analysis of motorway bridges accounting for key structural components and nonlinear soil–structure interaction. *Soil Dynamics and Earthquake Engineering*, *78*, 127-141.

Astaneh-Asl, A., McMullin, K. M., & Cho, S. W. (1994). Seismic performance of steel bridges during the 1994 Northridge earthquake. In *Restructuring: America and Beyond* (pp. 1515-1527). ASCE.

Borzi, B., Ceresa, P., Franchin, P., Noto, F., Calvi, G. M., & Pinto, P. E. (2015). Seismic vulnerability of the Italian roadway bridge stock. *Earthquake Spectra*, *31*(4), 2137-2161.

Bowden, F.P., & Tabor, D. (1964). The friction and lubrication of solids – part II. Oxford University Press, London, Great Britain, 1964.

Briseghella, B., Siviero, E., & Zordan, T. (2004, January). A composite integral bridge in Trento, Italy: Design and Analysis. In *IABSE Symposium Report* (Vol. 88, No. 6, pp. 297-302). International Association for Bridge and Structural Engineering.

Bruneau, M., Wilson, J. C., & Tremblay, R. (1996). Performance of steel bridges during the 1995 Hyogo-ken Nanbu (Kobe, Japan) earthquake. *Canadian Journal of Civil Engineering*, *23*(3), 678-713.

CALTRANS (2015). Seismic design criteria, California Department of Transportation, Sacramento, California. (s.d.).

Calvi, G. M. (2004, August). Recent experience and innovative approaches in design and assessment of bridges. In *Proceedings of 13th World Conference on Earthquake Engineering* (pp. 1-6).

Caner, A., & Zia, P. (1998). Behavior and design of link slabs for jointless bridge decks. *PCI journal*, *43*, 68-81.

Caner, A., Dogan, E., & Zia, P. (2002). Seismic performance of multi simple-span bridges retrofitted with link slabs. *Journal of Bridge Engineering*, *7*(2), 85-93.

Capatti, M. C., Tropeano, G., Morici, M., Carbonari, S., Dezi, F., Leoni, G., & Silvestri, F. (2017). Implications of non-synchronous excitation induced by nonlinear site amplification and of soil-structure interaction on the seismic response of multi-span bridges founded on piles. *Bulletin of Earthquake Engineering*, *15*(11), 4963-4995.

Carbonari, S., Dezi, F., & Leoni, G. (2011). Seismic soil–structure interaction in multi-span bridges: application to a railway bridge. *Earthquake engineering & structural dynamics*, *40*(11), 1219-1239.

Carbonari, S., Gara, F., Dall'Asta, A., & Dezi, L. (2016, October). Shear Connection Local Problems in the Seismic Design of Steel-Concrete Composite Decks. In *Conference on Italian Concrete Days* (pp. 341-354). Springer, Cham.

Carbonari, S., Minnucci, L., Gara, F., Dezi, L., Dall'Asta, A. (2017). The Role of End Cross-beams on the Distribution of Seismic Induced Shear Actions on the Shear Connection in Steel-Concrete Composite Bridge Decks. *Atti delle XXVI Giornate Italiane della Costruzione in Acciaio*, Venezia 28-29/09/2017.

Carbonari, S., Morici, M., Dezi, F., & Leoni, G. (2018). A lumped parameter model for time-domain inertial soil-structure interaction analysis of structures on pile foundations. *Earthquake Engineering & Structural Dynamics*, *47*(11), 2147-2171.

Carbonari, S., Morici, M., Dezi, F., Gara, F., & Leoni, G. (2017). Soil-structure interaction effects in single bridge piers founded on inclined pile groups. *Soil Dynamics and Earthquake Engineering*, *92*, 52-67.

Carden, L. P., Buckle, I. G., & Itani, A. M. (2007). Transverse displacement capacity and stiffness of steel plate girder bridge superstructures for seismic loads. *Journal of Constructional Steel Research*, *63*(11), 1546-1559.

CEN, 2004. Eurocode 8 - Design of structures for earthquake resistance: EN 1998-1 - Part 1: General rules, seismic actions and rules for buildings.

Choi, E. (2002). Seismic Analysis and Retrofit of Mid-America Bridges [PhD Thesis]. Georgia Institute of Technology.

Collings, D. (2005). *Steel-concrete composite bridges*. Thomas Telford.

Constantinou, M., Mokha, A., & Reinhorn, A. (1990). Teflon bearings in base isolation II: Modeling. *Journal of Structural Engineering*, *116*(2), 455-474.

Dao, N. D. (2014). Velocity and Normal Force Dependent Friction, Univ. of Nevada, https://opensees.berkeley.edu/wiki/index.php/Velocity_and_Normal_Force_Dependent_Friction

Dezi, L., Carbonari, S., Dall'Asta, A., Gara, F., & Minnucci, L. (2018). Seismic behaviour of steel-concrete composite bridge decks. In *Steel and Steel-concrete composite structures in seismic areas: advances in research and design*. Research Project RP3, ReLUIS-DPC 2014-2018. Napoli: Doppia Voce. ISBN 978-88-89972-74-8, 451-478.

Dolce, M., Cardone, D., & Croatto, F. (2005). Frictional behavior of steel-PTFE interfaces for seismic isolation. *Bulletin of earthquake engineering*, *3*(1), 75-99.

DSTE/PRS & UNIBAS – Autostrade per l'Italia S.p.A. (2019). Manuale utente della procedura AVS per la valutazione della vulnerabilità e rischio sismico dei ponti e viadotti autostradali. In *Verifiche sismiche NTC 2018 – V01*, version 2.1.

Earthquake Engineering Research Institute. (1990). Lorna Prieta earthquake reconnaissance report. Spectra. supplement to vol. 6, Oakland, Calif.

Earthquake Engineering Research Institute. (1994). Northridge Earthquake Jan. 17, 1994, preliminary reconnaissance report. Oakland, Calif.

El-Safty, A. (2008). Extending the service life of bridges using CFRP laminates and continuous decks. In *Structures Congress 2008: Crossing Borders* (pp. 1-10).

EN1998-2 - Design of structures for earthquake resistance Part 2: Bridges, Brussels, Belgium.

Ghosh, J., & Padgett, J. E. (2010). Aging considerations in the development of time-dependent seismic fragility curves. *Journal of Structural Engineering*, *136*(12), 1497-1511.

González, F., Padrón, L. A., Carbonari, S., Morici, M., Aznárez, J. J., Dezi, F., & Leoni, G. (2019). Seismic response of bridge piers on pile groups for different soil damping models and lumped parameter representations of the foundation. *Earthquake Engineering & Structural Dynamics*, *48*(3), 306-327.

Itani, A. M., Bruneau, M., Carden, L., & Buckle, I. G. (2004). Seismic behavior of steel girder bridge superstructures. *Journal of Bridge Engineering*, *9*(3), 243-249.

Kawashima, K., 2010. Seismic damage in the past earthquakes, seismic design of urban infrastructure. Lecture note.

Kim, Y. Y., Fischer, G., & Li, V. C. (2004). Performance of bridge deck link slabs designed with ductile engineered cementitious composite. *Structural Journal*, *101*(6), 792-801.

Lam, C., Lai, D., Au, J., Lim, L., Young, W., & Tharmabala, B. (2008). Development of concrete link slabs to eliminate bridge expansion joints over piers. In *2008 Annual Conference of the Transportation Association of Canada*.

Lepech, M. D., & Li, V. C. (2009). Application of ECC for bridge deck link slabs. *Materials and Structures*, *42*(9), 1185.

Li, V. C., Fischer, G., Lepech, M., Qian, S., Weimann, M., and Wang, S. (2003). Durable link slabs for jointless bridge decks based on strain hardening cementitious composites. *Research Rep. No. RC 1438*, Michigan Dept. of Transportation, Lansing, Mich.

Loveall, C. L. (1985). Jointless bridge decks. *Civil Engineering*, *55*(11).

Mander, J. B., Priestley, M. J., & Park, R. (1988). Theoretical stress-strain model for confined concrete. *Journal of structural engineering*, *114*(8), 1804-1826.

Mangalathu, S., Jeon, J. S., & DesRoches, R. (2018). Critical uncertainty parameters influencing seismic performance of bridges using Lasso regression. *Earthquake Engineering & Structural Dynamics*, *47*(3), 784-801.

Mangalathu, S., Jeon, J. S., Padgett, J. E., & DesRoches, R. (2016). ANCOVA-based grouping of bridge classes for seismic fragility assessment. *Engineering Structures*, *123*, 379-394.

McKeena, F., Fenves, G., & Scott, M. (2015). Open System for Earthquake Engineering Simulation (OpenSees). *Pacific Earthquake Engineering Research Center* (PEER), University of California: Berkeley, CA.

Ministero dei Lavori Pubblici, D.M 02.08.1980, *Criteri generali e prescrizioni tecniche per la progettazione, esecuzione e collaudo di ponti stradali*, G.U. n.308, 10.11.1980 (in Italian).

Ministero dei Lavori Pubblici, D.M 04.05.1990, *Aggiornamento delle norme tecniche per la progettazione, la esecuzione e il collaudo dei ponti stradali*, G.U. n.24, 29.01.1991 (in Italian).

Ministero dei Lavori Pubblici, D.M 14.02.1992, *Norme tecniche per l'esecuzione delle opere in cemento armato normale e precompresso per le strutture metalliche*, G.U. n.65, 18.03.1992 (in Italian).

Ministero dei Lavori Pubblici, D.M. 03.03.1975, *Approvazione delle norme tecniche per le costruzioni in zone sismiche*, G.U. n.93, 08.04.1975 (in Italian).

Ministero dei Lavori Pubblici, D.M. 09.01.1996, *Norme tecniche per il calcolo, l'esecuzione ed il collaudo delle strutture in cemento armato, normale e precompresso e per le strutture metalliche*, G.U. n.29, 05.02.1996 (in Italian).

Ministero delle Infrastrutture e dei Trasporti (2018). D.M.17.01.2018, *Aggiornamento delle Norme Tecniche per le Costruzioni*, G.U. n.42, 20.02.2018.

Minnucci, L., Carbonari, S., Dall'Asta, A., Dezi, L., Gara, F. (2019). Local failure mechanisms of existing steel-concrete composite decks. *Atti delle XXVII Giornate Italiane della Costruzione in Acciaio*, Bologna 3-5/10/2019.

Morici, M., Minnucci, L., Carbonari, S., Dezi, F., & Leoni, G. (2019). Simple formulas for estimating a lumped parameter model to reproduce impedances of end-bearing pile foundations. *Soil Dynamics and Earthquake Engineering*, *121*, 341-355.

Muthukumar, S., & DesRoches, R. (2006). A Hertz contact model with non-linear damping for pounding simulation. *Earthquake engineering & structural dynamics*, *35*(7), 811-828.

Mylonakis, G., & Gazetas, G. (2000). Seismic soil-structure interaction: beneficial or detrimental?. *Journal of earthquake engineering*, *4*(3), 277-301.

Nielson, B.G. (2005). Analytical fragility curves for highway bridges in moderate seismic zones (Doctoral dissertation, Georgia Institute of Technology).

Nielson, B.G., & DesRoches, R. (2007). Seismic fragility curves for typical highway bridge classes in the Central and South-eastern United States. *Earthquake Spectra*, *23*, 615–633.

Okeil, A. M., & ElSafty, A. (2005). Partial continuity in bridge girders with jointless decks. *Practice Periodical on Structural Design and Construction*, *10*(4), 229-238.

Padgett, J.E., DesRoches, R., 2008. Methodology for the development of analytical fragility curves for retrofitted bridges. *Earthquake Engineering and Structural Dynamics*, **37**, 1157–1174.

Pitilakis, K. (2011). Systemic seismic vulnerability and risk analysis for buildings, lifeline networks and infrastructures safety gain. *European Collaborative research Project*, *Deliverable D3.6*. (FP7-ENV-2009- 1-244061) http://www.syner-g.eu

Ramanathan, K. N. (2012). *Next generation seismic fragility curves for California bridges incorporating the evolution in seismic design philosophy* (Doctoral dissertation, Georgia Institute of Technology).

Ramanathan, K., DesRoches, R., & Padgett, J. E. (2010). Analytical fragility curves for multispan continuous steel girder bridges in moderate seismic zones. *Transportation Research Record*, *2202*(1), 173-182.

Rao, A. S., Lepech, M. D., Kiremidjian, A. S., & Sun, X. Y. (2017a). Simplified structural deterioration model for reinforced concrete bridge piers under cyclic loading. *Structure and Infrastructure Engineering*, *13*(1), 55-66.

Richardson, D. R. (1989). *Simplified Design Procedures for the Removal of Expansion Joints from Bridges Using Partially Debonded, Continuous Decks* (Doctoral dissertation, North Carolina State University).

Schellenberg, A. (2014). Flast Slider Bearing Element. *OpenSees Command Manual, PEER*, https://opensees.berkeley.edu/wiki/index.php/Flat_Slider_Bearing_Element.

Sevgili, G., & Caner, A. (2009). Improved seismic response of multisimple-span skewed bridges retrofitted with link slabs. *Journal of Bridge Engineering*, *14*(6), 452-459.

Shamsabadi, A., Rollins, K. M., and Kapuskar, M., 2007. Nonlinear soil–abutment–bridge structure interaction for seismic performance-based design, *Journal of geotechnical and geoenvironmental engineering*, *133*(6), 707-720.

Steelman, J. S., Filipov, E. T., Fahnestock, L. A., Revell, J. R., LaFave, J. M., Hajjar, J. F., & Foutch, D. A. (2014). Experimental behavior of steel fixed bearings and implications for seismic bridge response. *Journal of Bridge Engineering*, *19*(8), A4014007.

Stefanidou, S. P., & Kappos, A. J. (2017). Methodology for the development of bridge-specific fragility curves. *Earthquake Engineering & Structural Dynamics*, *46*(1), 73-93.

Stefanidou, S. P., & Kappos, A. J. (2019). Bridge-specific fragility analysis: when is it really necessary?. *Bulletin of earthquake engineering*, *17*(4), 2245-2280.

Stefanidou, S. P., Sextos, A. G., Kotsoglou, A. N., Lesgidis, N., & Kappos, A. J. (2017). Soil-structure interaction effects in analysis of seismic fragility of bridges using an intensity-based ground motion selection procedure. *Engineering Structures*, *151*, 366-380.

Tubaldi, E., & Dall'Asta, A. (2012). Transverse free vibrations of continuous bridges with abutment restraint. *Earthquake engineering & structural dynamics*, *41*(9), 1319-1340.

Tubaldi, E., Barbato, M., & Dall'Asta, A. (2011). Influence of model parameter uncertainty on seismic transverse response and vulnerability of steel–concrete composite bridges with dual load path. *Journal of Structural Engineering*, *138*(3), 363-374.

Tubaldi, E., Barbato, M., & Dall'Asta, A. (2010). Transverse seismic response of continuous steel-concrete composite bridges exhibiting dual load path. *Earthquakes and Structures*, *1*(1), 21-41.

Ulku, E., Attanayake, U., & Aktan, H. (2009). Jointless bridge deck with link slabs: Design for durability. *Transportation Research Record*, *2131*(1), 68-78.

Wang, C., Shen, Y., Zou, Y., Zhuang, Y., & Li, T. (2019). Analysis of Mechanical Characteristics of Steel-Concrete Composite Flat Link Slab on Simply-Supported Beam Bridge. *KSCE Journal of Civil Engineering*, 1-10.

Wing, K. M., & Kowalsky, M. J. (2005). Behavior, analysis, and design of an instrumented link slab bridge. *Journal of Bridge Engineering*, *10*(3), 331-344.

Zahrai, S.M. & Bruneau, M. (1998). Impact of diaphragms on seismic response of straight slab-on-girder steel bridges. *Journal of Structural Engineering*, *124*(8): 938-947.

Zahrai, S.M. & Bruneau, M. (1999a). Ductile end-diaphragms for seismic retrofit of slab-on-girder steel bridges. *Journal of Structural Engineering*, *125*(1): 71-80.

Zahrai, S.M. & Bruneau, M. (1999b). Cyclic testing of ductile end diaphragms for slab-on-girder steel bridges. *Journal of Structural Engineering*, *125*(9): 987-996.

Zhan, X. F., Shao, X. D., & Liu, G. L. (2013). Thermal experiment of a reinforced approach pavement for semi-integral abutment jointless bridge. In *Advanced Materials Research* (Vol. 639, pp. 183-190). Trans Tech Publications.

Zheng, Y., Zhang, L. F., & Xia, L. P. (2018). Investigation of the behaviour of flexible and ductile ECC link slab reinforced with FRP. *Construction and Building Materials*, *166*, 694-711.

5. Fragility Analysis of existing bridges

This section presents and discusses the results from MSA in the form of fragility curves. The values of the parameters governing the seismic scenario (M, R, a, b, V_{S30}) are set in order to provide an *IM* hazard curve representative of medium-high seismicity in Italy, which is also the seismic characterization of great part of the Marche territory. More in detail, it has been assumed what follows: $m_0 = 5.5$, $m_{max} = 8$, $a = 4.35$; b=0.9, $r_{max} = 50$ km, and $V_{S30} = 255$ m/s, the latter representative of a deformable soil condition (Boore & Joyner, 1997). As anticipated before, the maximum component Sa(T*) is used in this study, where T* is equal to 1.0 s, a common choice for the analysis of bridge class fragility (Ramanathan, 2012; Mangalathu et al., 2018; Xie & DesRoches, 2019). The *IM* curve is shown in Figure 5.1, where the 20 *IM* levels selected to perform MSA analysis are highlighted by red circle markers. It is recalled that the *IM* curve discretization, as well as the number of samples per *IM* level (i.e., 20), have been set based on the results of a recently published paper (Scozzese et al., 2020).

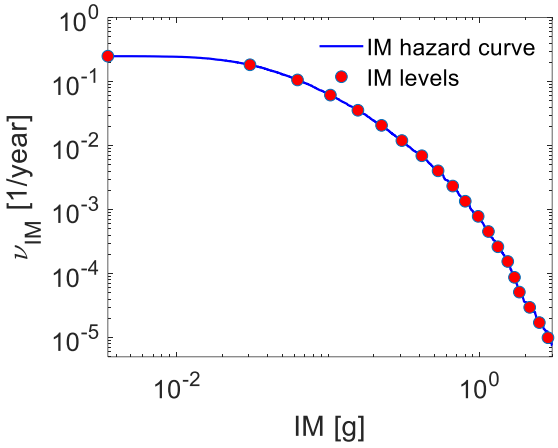

Figure 5.1. IM hazard curve for Sa(T) at T=1.0 s and discretization in 20 IM levels.

The analysis of the bridge response is carried out on different levels of investigation. As first, the behaviour of each component (i.e. piers, bearings, abutments, etc.) is discussed, considering the related EDPs at the different performance levels. The classical fragility representation is provided according to three types of charts: a comparison between different limit states for the same component is first depicted; then, the evolution of the elements' fragility along the bridge longitudinal development is illustrated; finally, a comparison between performances of different components at the same limit state is provided.

An insight on the fragility mechanisms follows, according to the methodology proposed in §2.4 for what concerns the analysis of failure modes and the damage extension. For the analysis of failure modes, as already mentioned, brittle failures on piers are not considered since the shear capacity largely overcomes the shear demand. In case of RCLS bridges,

ruptures of the bearings are imputable only to sliding mechanisms involving the neoprene pads, which are controllable by the analysis of the device displacements. A ductile failure mechanism is expected on links, which are monitored observing the elastic-plastic deformation of steel bars. Concerning abutments, the possible damage mechanisms are related to the longitudinal active and passive response as well as the transverse active one, so that three possible failure modes are individuated. This leads to the conclusion that for the considered case studies six different failure modes can be observed: the ductile failure of the piers, the displacement-related failure of the bearings, the strain-related failure of the links and the three displacement-related failure modes of the abutments. However, in order to synthesize the behaviour of the latter component, the analysis of failure modes will be carried out assuming a unique behaviour for the abutments, obtained from the envelope of the responses in longitudinal and transverse directions. In this way, the analysis of failure modes coincides with the analysis of the components, since a unique failure mode is associated to each element family, and four failure mode families will be investigated for RCLS bridges, consisting in the failure mechanisms on piers, link slab bars, bearings and abutments. In case of SCC bridges, the analysis of failure modes concerns the fragility of piers, cross beams, bearings and abutments. In the latter case, the approach adopted for RCLS bridges holds. For what concerns bearings, a double failure mode could be recognized, the first related to the behaviour in the fixed direction (a fragile one) and the second related to the sliding behaviour in the non-fixed directions (a ductile one). In order to synthetize the bearings' behaviour, a simplified approach is adopted to evaluate the fragility of the component, considering displacement-related (ductile) and force-related (brittle) damages together, corresponding to the different behaviours in sliding and fixed directions, respectively. This choice is made to offer an immediate insight on the different degrees of vulnerability of the structural components, that in case of bearings is represented by the highest probability of exceedance between ductile and fragile mechanisms. To further investigate the performance of bearings, the analysis of ductile and fragile mechanisms can be splitted and carried out through the same proposed methodology for the fragility.

The analysis of damage extension is carried out on both the bridge typologies evaluating the damage exceeding probability based on the number of elements involved for each family of elements, and, in case of multi-element families (i.e. links and bearings), on the number of sub-components. From the previous assumptions, it is evident that also in this case there is an overlapping between the extension of the failure modes and the extension of damage on the components, since they are univocally associated.

The analysis of the behaviour of each bridge typology and case study is firstly carried out basing on the hypothesis of fixed base for the vertical elements. Then, comparisons are made between the reference fixed base assumption and results from the introduction of ageing effects and the compliant base under the piers. The Soil-Structure Interaction is modelled through the Lumped Parameter Model proposed in the work by Morici et al. (Morici et al., 2019), while ageing effects derive from the stochastic modelling of corrosion on the piers' steel longitudinal bars and steel components of the bearings, as

described in previous Chapter 4. 400 time history analyses have been carried out for each of the 15 bridge case studies and the associated different analysis assumptions, for a total of 6000 seismic analyses. As a result, the peculiarities of the examined bridge typologies are individuated and major differences between the behaviours under the fixed base and the compliant base hypothesis are highlighted.

5.1 Fragility of RCLS bridges

The fragility curve for a certain bridge component is built as the envelope of the fragility curves of single elements that belong to the same element family, where the single elements are the piers, the abutments, each set of bearings above each pier and each set of link bars that covers the joints between adjacent spans (and the last span with the right abutment). For each component (piers, bearings, link-slab bars, abutments), results from the seismic analyses under the hypotheses of fixed base and the absence of degradation phenomena are presented in form of three types of charts: the comparison between different limit states for the same component; the evolution of the elements' fragility along the bridge longitudinal development through the fragility curves of the elements at each structural joint; finally, the comparison between performances of different components at the same limit state. The analysis of the failure modes and the damage extension follows, according to the proposed improved methodology for the evaluation of fragility. Then, a comparison between results of the examined different case studies is made to highlight typical vulnerabilities associated to the specific case study typology. Finally, results from the analysis with compliant base and the modelling of degradation are illustrated and commented.

5.1.1 Fixed base

5.1.1.1 L/B = 10

Results for case study L/B = 10 are firstly commented. As a classical representation of fragility, Figure 5.2 shows the fragility curves of element classes comparing different limit states.

Links are the most vulnerable elements at all the considered performance levels. The blue (Life Safety) and the red (Collapse) fragility curves are almost overlapping, which attests a rapid passage from the condition of extensive damage to the total failure of the component. On the contrary, the light damage condition (Damage limit state) is clearly distinguishable and associated to a certain event (i.e. $G_{D|IM}(d|im)$ = 100%) for very low *IM* (Sa(T)= 0.1g). A high vulnerability is also presented by the abutments, for the behaviour in active, transverse and passive response, in that order. In particular, light and extensive damage deriving from the active response are very likely to occur (i.e. $G_{D|IM}(d|im)$ > 50%) within Sa(T) = 1.0g, while Collapse has low probability of exceedance in the investigated IM range. Abutments are less vulnerable in the transverse direction, where the probability of exceedance light or extensive damage overcomes 50%

at higher *IM*s than in case of active response (0.6 g and 1.6 g, respectively), while collapse is visible only at very high spectral accelerations. In case of the passive response, extensive damage and collapse are not detected in the investigated frequency range. Light damage, extensive damage and collapse on bearings are reached with a 100% probability of occurrence for Sa(T)= 0.75g, 1.0g and 1.5g, respectively. Finally, piers present a low degree of vulnerability. Failures on piers at Life Safety and Collapse limit states are prevented by damage or ruptures on the superstructure and bearings.

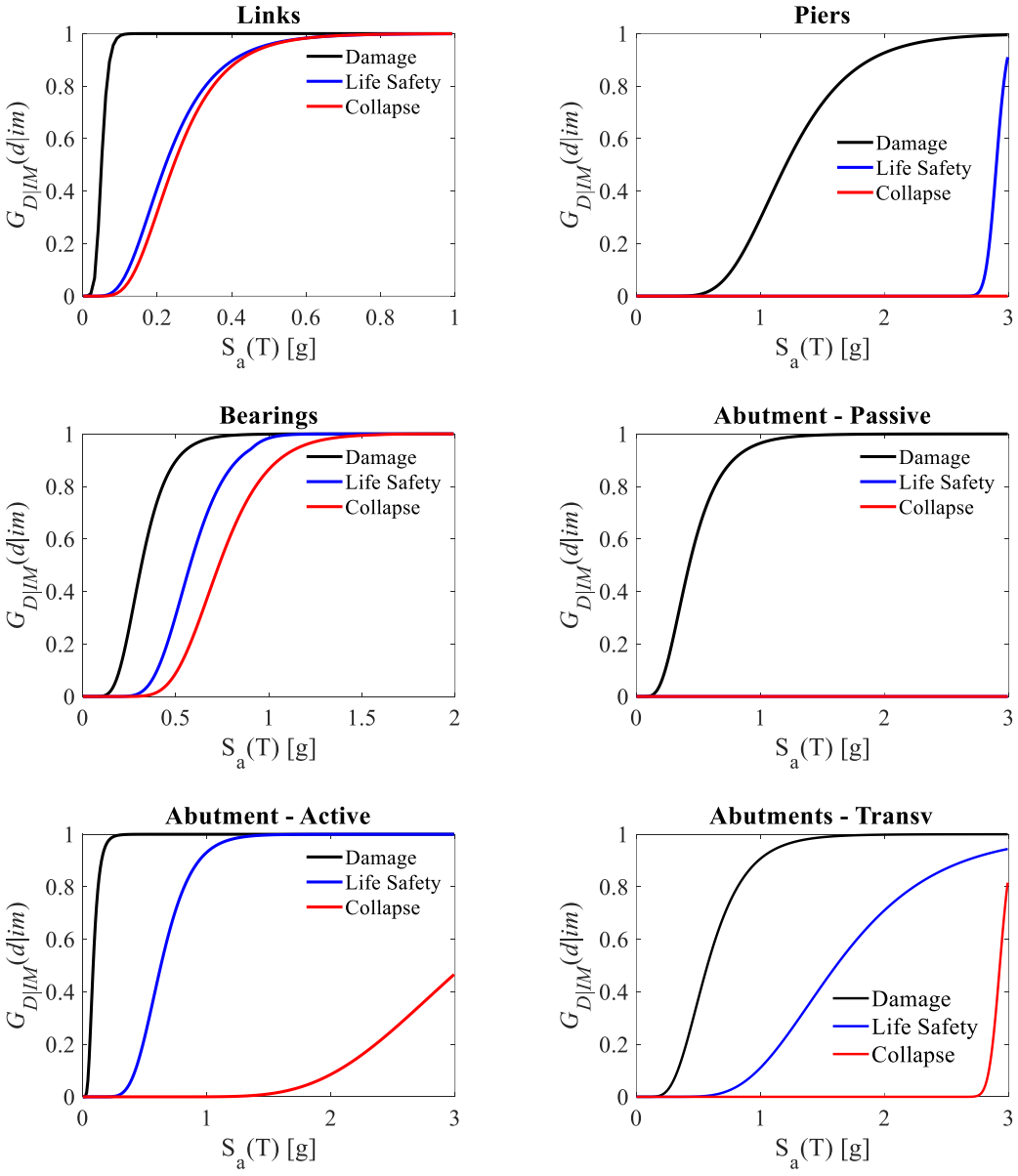

Figure 5.2. Fragility curves at different performance levels for bridge components – case study L/B = 10.

Results concerning the seismic demand on the link-slab bars are shown in Figure 5.3. In this case, the monitored demand parameter *D* is represented by the maximum strain attained on the bars. It is possible to underline the following aspects:

- at the Damage limit state, all the bar sets are strongly vulnerable, being the 50% of damage probability occurred at Sa(T) = 0.1-0.2g;
- the Collapse limit state distinguishes the structural behaviour among the bars, since bigger differences on the fragility curves can be noted;
- as the number of bar increases, the vulnerability of the bar set decreases;
- concerning joint n.5, link bars are strongly affected by the relative rotational flexibility between the abutment and the nearest pier.

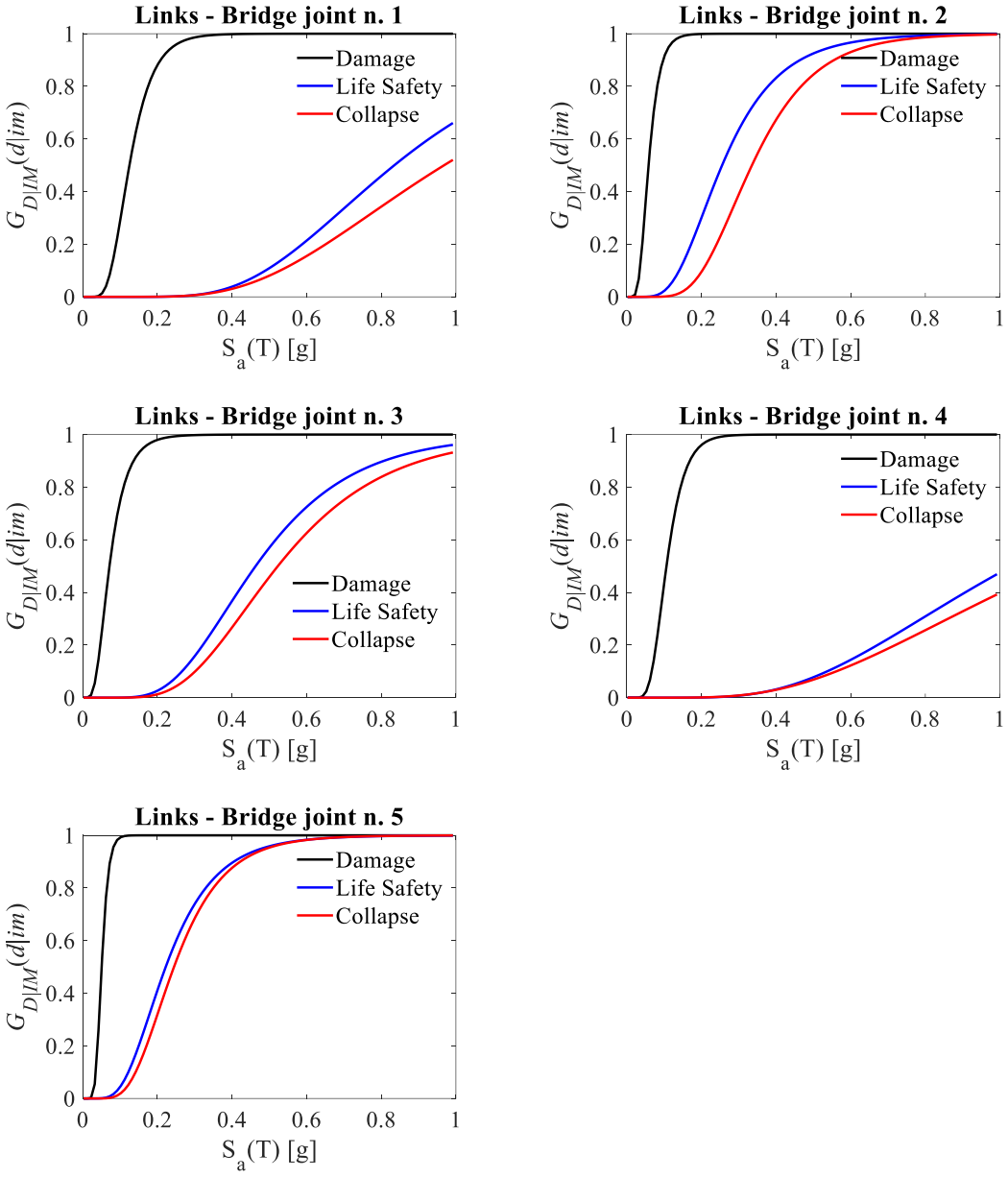

Figure 5.3. Fragility curves at different performance levels for link-slab bars – case study L/B = 10.

Results concerning the seismic demand on the bearings are shown in Figure 5.4. The monitored demand parameter *D* is the maximum horizontal displacement. In general, as

the number of link bars on the deck increases, the vulnerability of the bearings decreases, with greater resources in the plastic behaviour, since the difference between the fragility at Life Safety Limit state and Collapse limit state is appreciable. It is also worth mentioning that for all the bearings the 50% probability of exceeding damage and extensive damage is observed within Sa(T)=1.0g, and 50% probability of collapse verifies for Sa(T)>1.0g (Sa(T)=1.2g) only for bearings on the fourth pier. An exception is the set of bearings on the right abutment. In this case, the abutment flexibility scarcely affects the relative horizontal displacements of the devices, resulting in maximum displacements under the damage threshold.

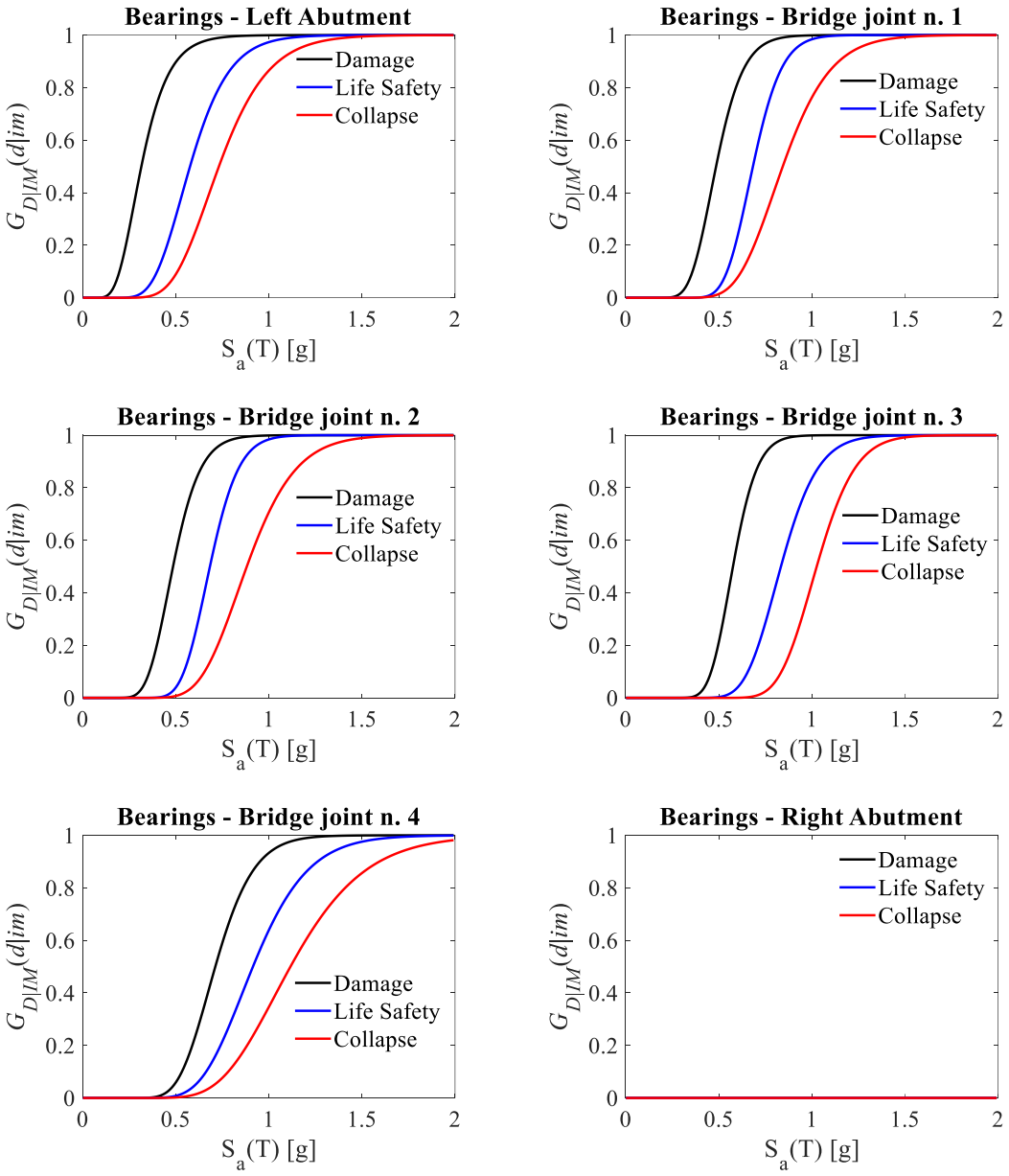

Figure 5.4. Fragility curves at different performance levels for bearings – case study L/B = 10.

Results concerning the seismic demand on the piers are shown in Figure 5.5. The monitored demand parameter is represented by the maximum top displacement. A symmetric behaviour can be observed looking at external and internal piers, where the latter experience damage at lower accelerations (the 50% probability of exceeding damage is at about Sa(T)=1.3g versus Sa(T)=2.0g for external piers). It is clear that unless bearing devices do not show a high probability of collapse at Sa(T)=1.0-1.2g, the piers are preserved against damage.

Figure 5.6 shows a comparison among fragility curves at the three considered limit states. As an overall comment, link-slab bars and bearings rule the vulnerability of the bridge at all the limit states. Furthermore, it is evident that piers are the less vulnerable elements of the structural system. The role of the abutments' fragility is noticeable only for Damage and Life Safety limit states. Effects of the component fragility on the global structural response are investigated in the following paragraphs.

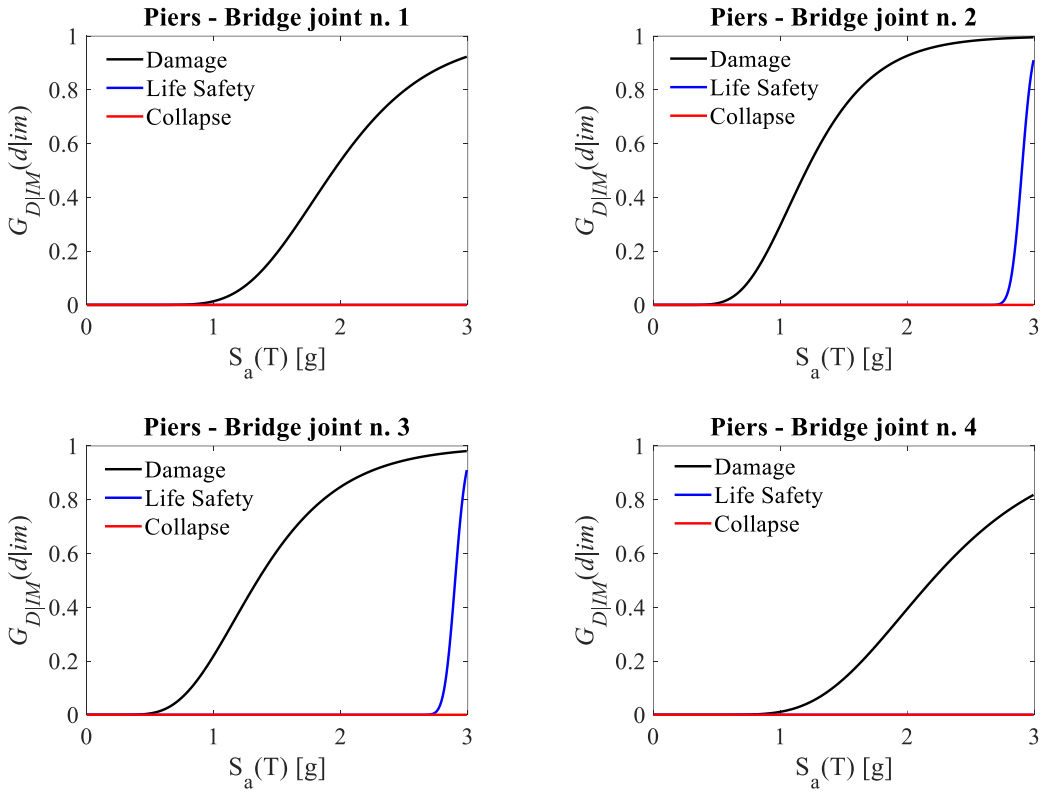

Figure 5.5. Fragility curves at different performance levels for piers – case study L/B = 10.

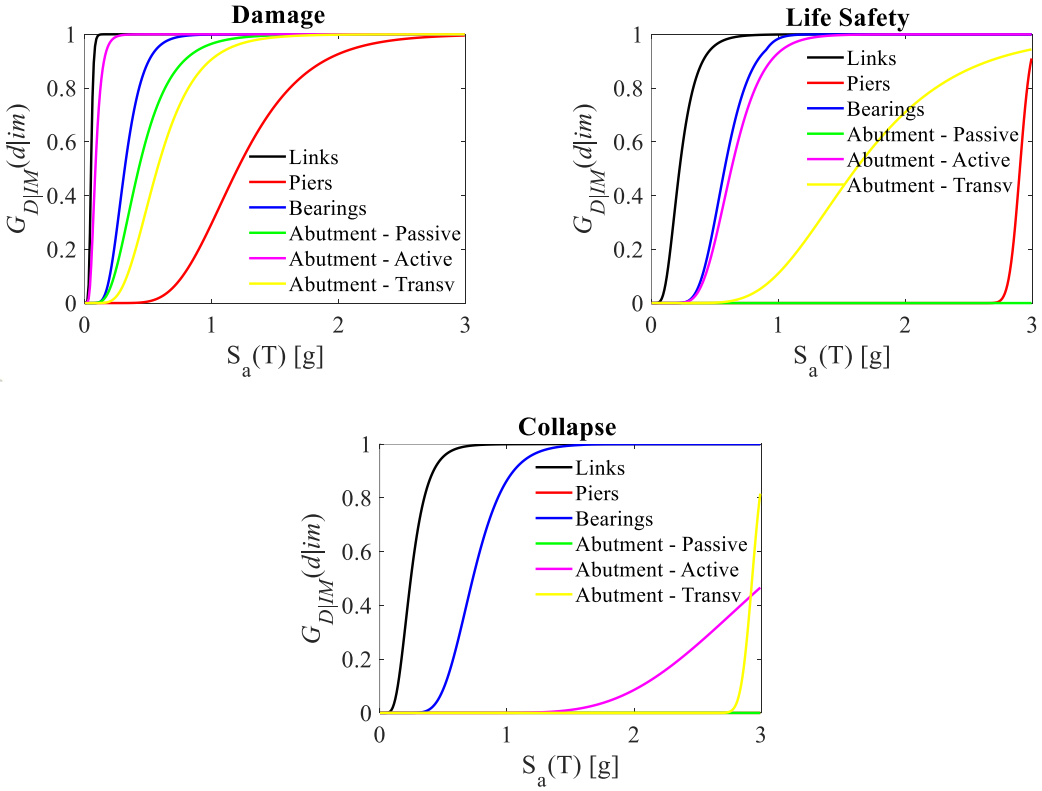

Figure 5.6. Fragility curves for different bridge components – case study L/B = 10.

Three sets of plots are reported in Figure 5.7 and Figure 5.8 to show the combination of damage mechanisms at the considered limit states, and for each of them a dedicated chart is represented to furnish a clearer view of the results. To indicate the different mechanisms, capital letters are employed in the following order: Mode-P = failure on piers; Mode-L = failure on link-slab bars; Mode-B = failure on bearings; Mode-A = failure on abutments (as the envelope of damage for passive, active and transverse movements). In the following, only the combinations of failure mechanisms that are responsible of non-null probabilities of failure occurrence are shown.

Figure 5.7 shows the behaviour of the bridge at Damage limit state considering the envelope (black solid line) of fragility curves of different components (see previous Figure 5.6) as representative of the whole structure. It is immediate to see that the global fragility curve is obtained from the concomitance of more than one damage mechanisms at the same time: excepting for low spectral accelerations, where the fragility of the system is governed by the damage of the abutments and the link-slab bars only, with peak probabilities of 80% and 15%, respectively, there is a strong correlation in the occurrence of damage for links and abutments (0.2g<Sa(T)<0.5g), links, bearings and abutments (0.5g<Sa(T)<1.0g) and all the component together, as shown with the orange line "PLBA" (Sa(T)>1.0g).

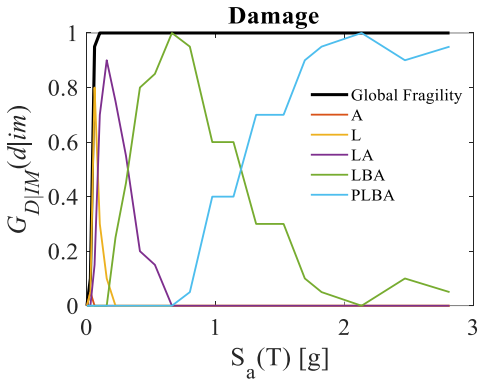

Figure 5.7. Probabilities of occurrence of Damage Limit State for combined mechanisms; in black, the global fragility curve as the envelope of the single fragility curves – case study L/B =10.

With an analogous perspective, the Life Safety limit state is examined (Figure 5.8a). In this case, the predominance of the damage on link-slab bars is evident to determine the global fragility, and it is immediate to notice that there is a rapid passage from the damage of link bars only (orange line) to the damage of link bars, bearings and abutments (green line) for Sa(T)>0.5g, attesting that, without considering the behaviour of the piers, the system loses progressively and rapidly resisting sources. The loss of the superstructure can be associated to the certain event for Sa(T)>1.0g. It is also worth noting that the failure modes related to abutments or bearings are never attained alone. Finally, at the Collapse limit state (Figure 5.8b), for Sa(T)<1.0g it is most probable that only link bars reach the collapse, while for Sa(T)>1.0g the collapse involves link bars and supporting devices always together. A slight influence of the abutments on the global collapse can be noted at high spectral accelerations (Sa(T)>2.0g).

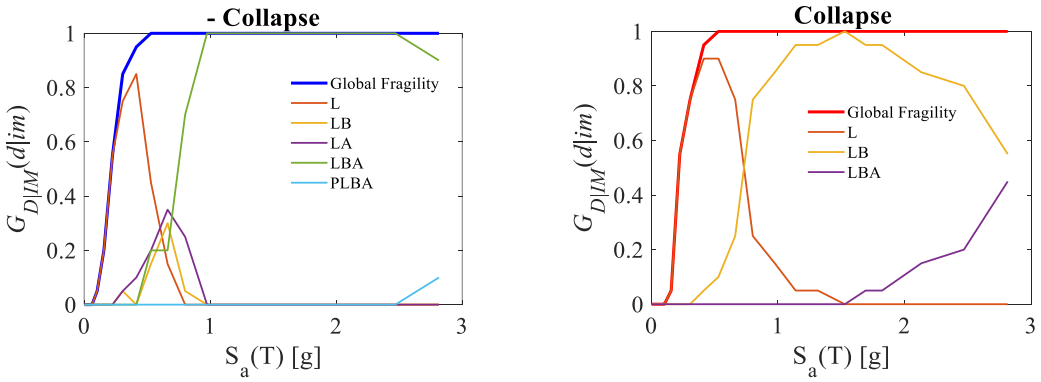

(a) (b)

Figure 5.8. Probabilities of occurrence of (a) Life Safety Limit State and (b) Collapse Limit State for combined mechanisms; in blue, the global fragility curve as the envelope of the single fragility curves – case study L/B =10.

Figure 5.9 shows fragility curves for link-slab bars at the considered limit states considering different percentages of link-slab bar sets (i.e. sets above each structural joint) that experience light damage, extensive damage or collapse. For instance, the 75% of

links is approximated to 3 sets over the total of 5. It is worth noting that at the Damage limit state, the probability of total damage (i.e. 100% of links) reaches its maximum for Sa(T)=0.3g, corresponding to a seismic event with 100 years return period, while the damage of more than half of the bar sets has the 50% probability of occurrence for a 18 years return period event. The behaviours at Life Safety and Collapse limit state are quite similar, according to the already observed behaviour on the fragility curves of the single bar sets (Figure 5.3). The 50% probability of extensive damage or collapse involving more than 50% of the bar sets corresponds to a return period less than the Life Safety event (250 vs 475 years).

A similar approach can be used to comment the bearings behaviour, which is illustrated in Figure 5.10. For Damage and Life Safety limit states the system offers a partially fragile behaviour, being almost equal the probabilities of damage occurrence for the 25% and the 50% of the supporting device sets. The total collapse of the bearings never happens, while the 50% probability that more than 4 sets over 6 (75%) reach the collapse corresponds to a return period of 650, 1000 and 1250 years for Damage, Life Safety and Collapse limit states, respectively.

Finally, looking at the piers behaviour in Figure 5.11, the 50% probability of damage is reached at Sa(T)=1.1g, 1.2g, 1.8g and 2.2g for 25%, 50%, 75% and 100% of the piers, respectively, corresponding to a minimum return period equal to 1600 years.

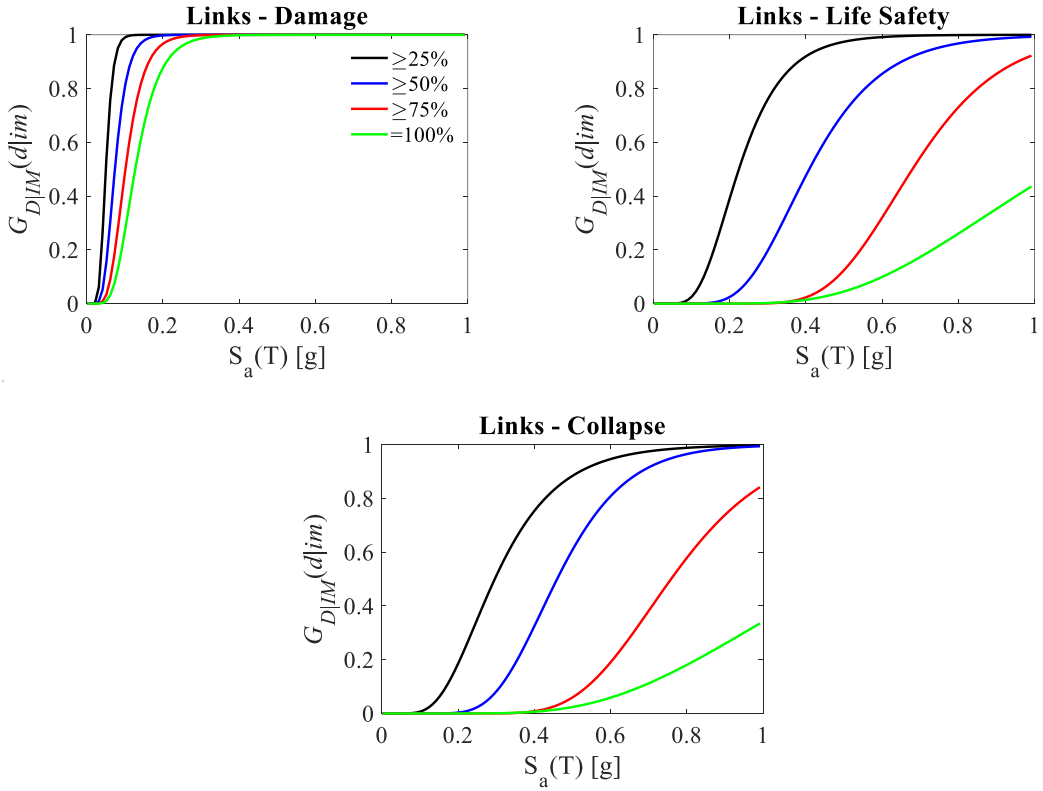

Figure 5.9. Fragility curves at Damage, Life Safety and Collapse limit states for link-slab bars: increasing percentages of involved elements (sets of link-slab bars) – case study L/B =10.

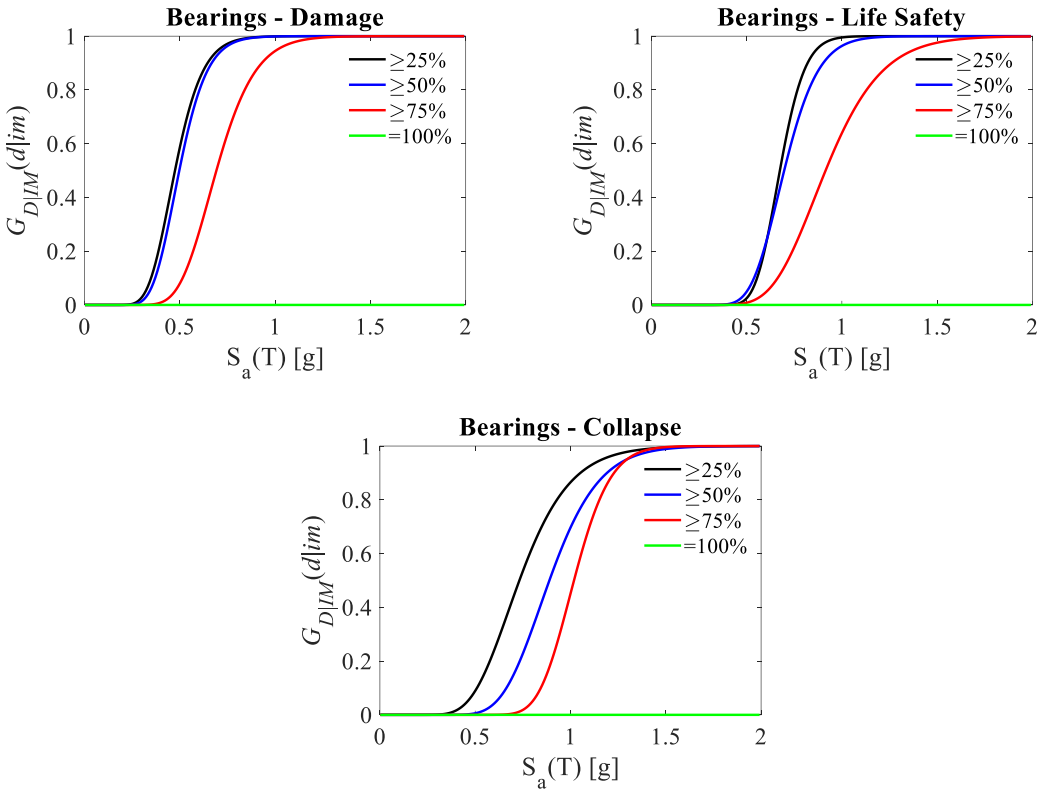

Figure 5.10. Bearings fragility curves: increasing involved sets of devices – case study L/B =10.

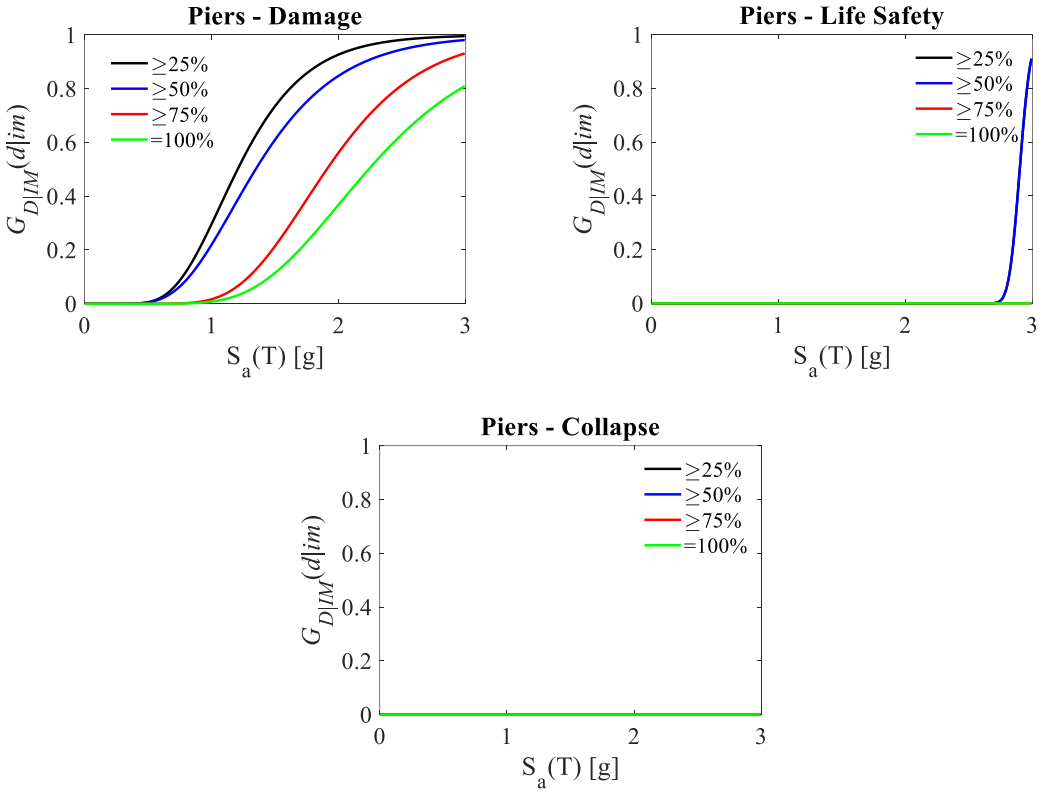

Figure 5.11. Pier fragility curves: increasing involved elements (single piers) – case study L/B =10.

Another possible representation of the previous results is shown in Figure 5.12, Figure 5.13 and Figure 5.14, where the discrete probability curves associated to the various percentages of involved elements for links, bearings and piers is compared to the probability of occurrence of damage on at least one element (magenta solid line). It is possible to highlight that the sum of the polygonal chains matches the magenta one and offers an immediate comprehension about how the damage or collapse mechanisms evolve with the increasing of the seismic intensity measure.

For example, for link-slab bars (Figure 5.12), at Sa(T)=0.75g, there is a probability of 95% that the 50% of the link bars overcomes the Life Safety limit state, while, for higher values of Sa(T), it is much more probable that at least 75% or 100% of bars undergoes severe damage.

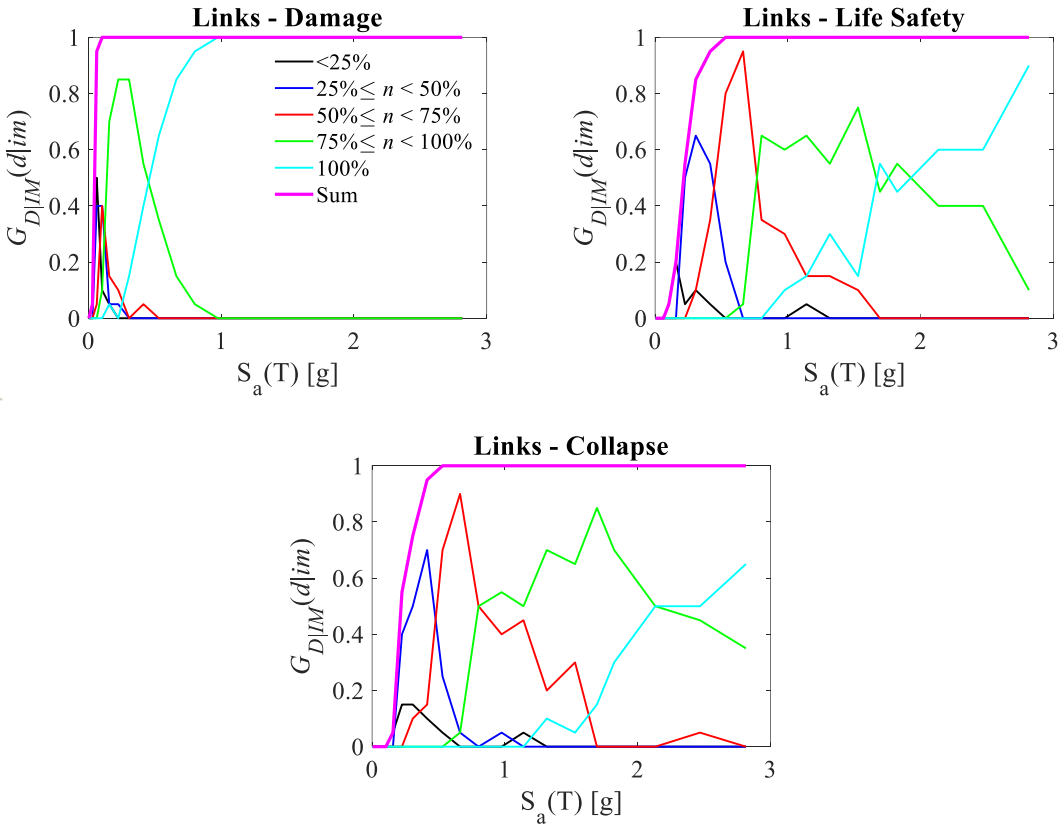

Figure 5.12. Probabilities of occurrence for different percentages of considered link-slab bars involved in damage mechanisms; in magenta, the sum of probabilities, being the magenta curve the envelope of the fragility curves (that means "at least one link-slab bar") – case study L/B =10.

The analysis of the curves for bearings in Figure 5.13 highlights a clear trend: for all the considered limit states, for spectral accelerations higher than Sa(T)=1.0g, there is an increasing probability that the 75% of devices experiences damage (or collapse for Collapse limit state).

Finally, it is worth commenting the behaviour of piers at Damage and Life Safety Limit States only, as depicted in Figure 5.14. In particular, concerning the Damage Limit State,

the highest percentages that contribute to the probability of having at least one pier damaged (the magenta solid line) are relative to the blue and green curves, corresponding to the 50% and the 100% of piers respectively. This means that the structural system is more prone to a rapid evolution of damage from half to the total of the vertical elements.

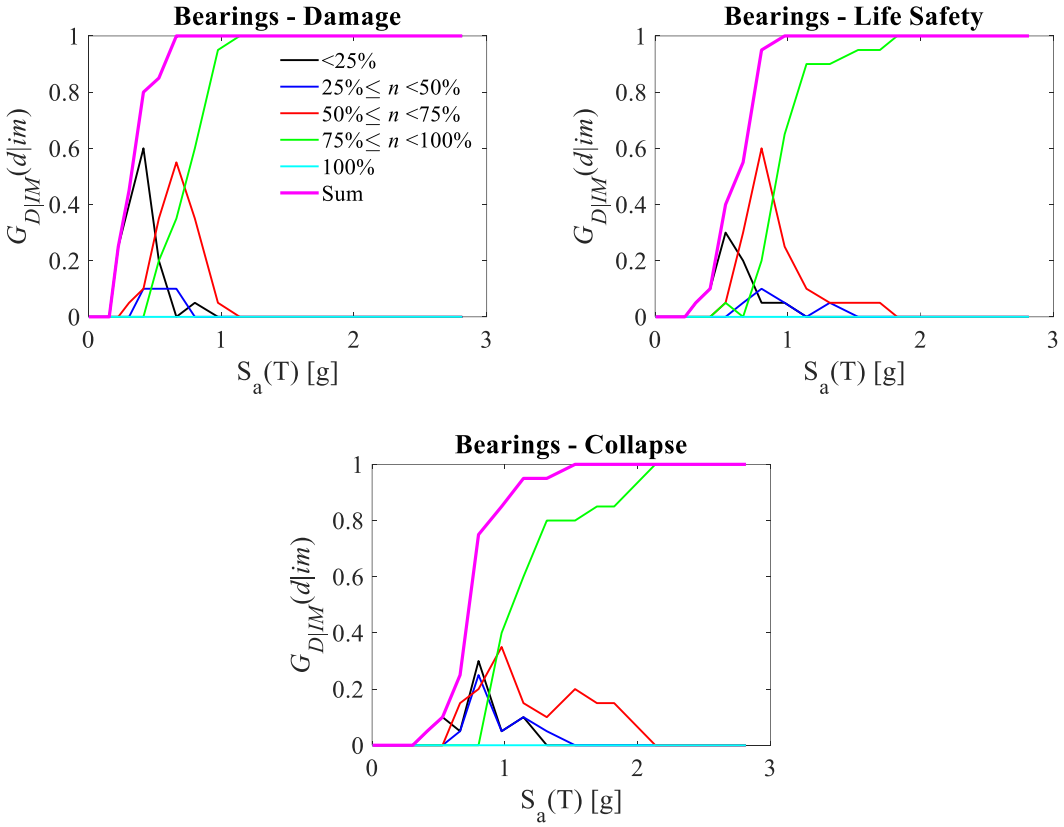

Figure 5.13. Probabilities of exceedance for different numbers of involved bearings – case study L/B =10.

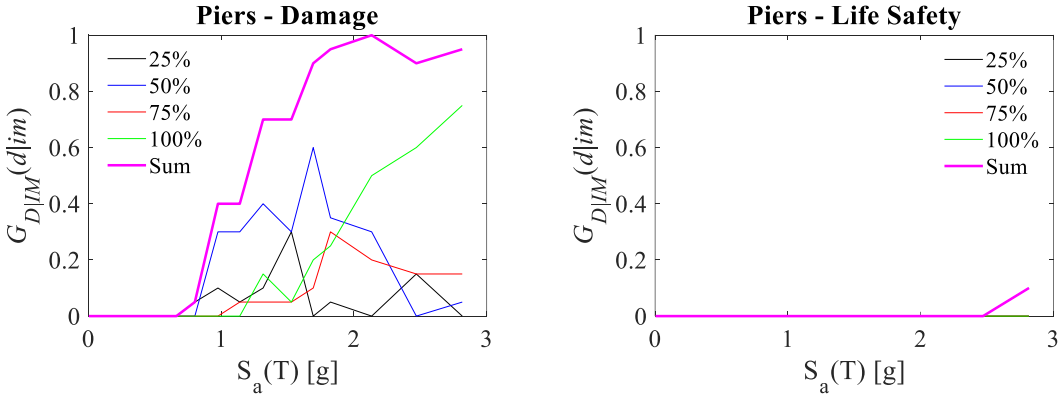

Figure 5.14. Probabilities of exceedance for different percentages of involved piers – case study L/B =10.

5.1.1.2 L/B = 20

Results for case study L/B = 20 are presented. Figure 5.15 shows the fragility curves of element classes comparing different limit states. Even in this case, links are the most vulnerable elements at all the considered performance levels. For Damage limit state, the behaviour of abutments in active, passive and transverse response follows. Piers present a low degree of vulnerability, especially at Life Safety and Collapse limit states. Failures on piers are prevented by damage or ruptures on the superstructure and the bearings. Collapse of the substructures may occur at very high spectral accelerations (50% probability of collapse is reached in abutment active response at Sa(T) = 2.8g).

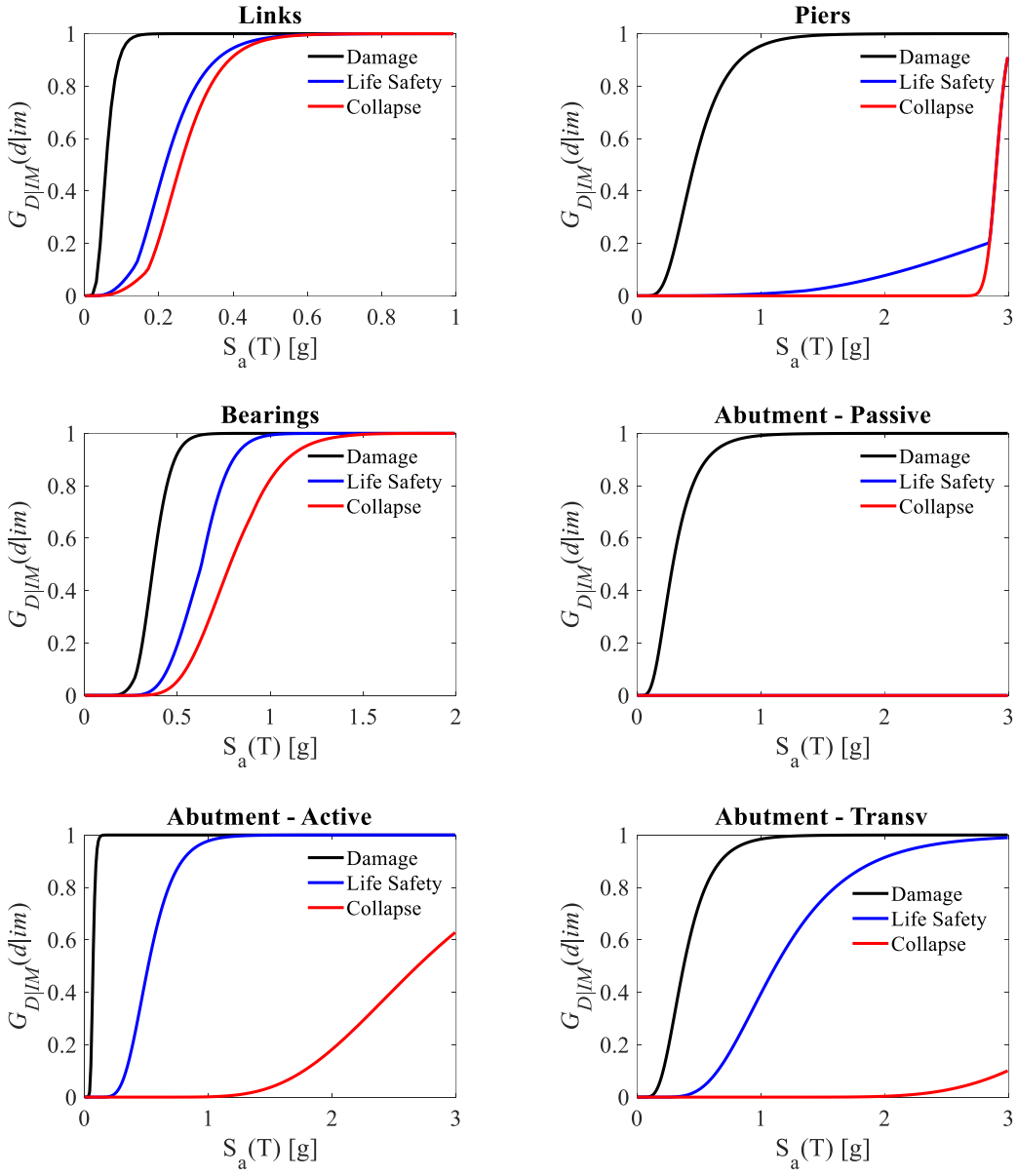

Figure 5.15. Fragility curves at different performance levels for bridge components – case study L/B = 20.

Results concerning the link-slab bars are shown in Figure 5.16 and Figure 5.17. At the Damage limit state, all the bar sets are strongly vulnerable, being the 50% of damage probability occurred at Sa(T) = 0.1-0.2g. The Life Safety and the Collapse limit states distinguish the structural behaviour among the bars, since bigger differences on the fragility curves can be noted; moreover, as the number of bar increases, the vulnerability of the bar set at Life Safety and Collapse limit states decreases. Concerning the last joint, link bars are strongly affected by the relative rotational flexibility between the abutment and the nearest pier.

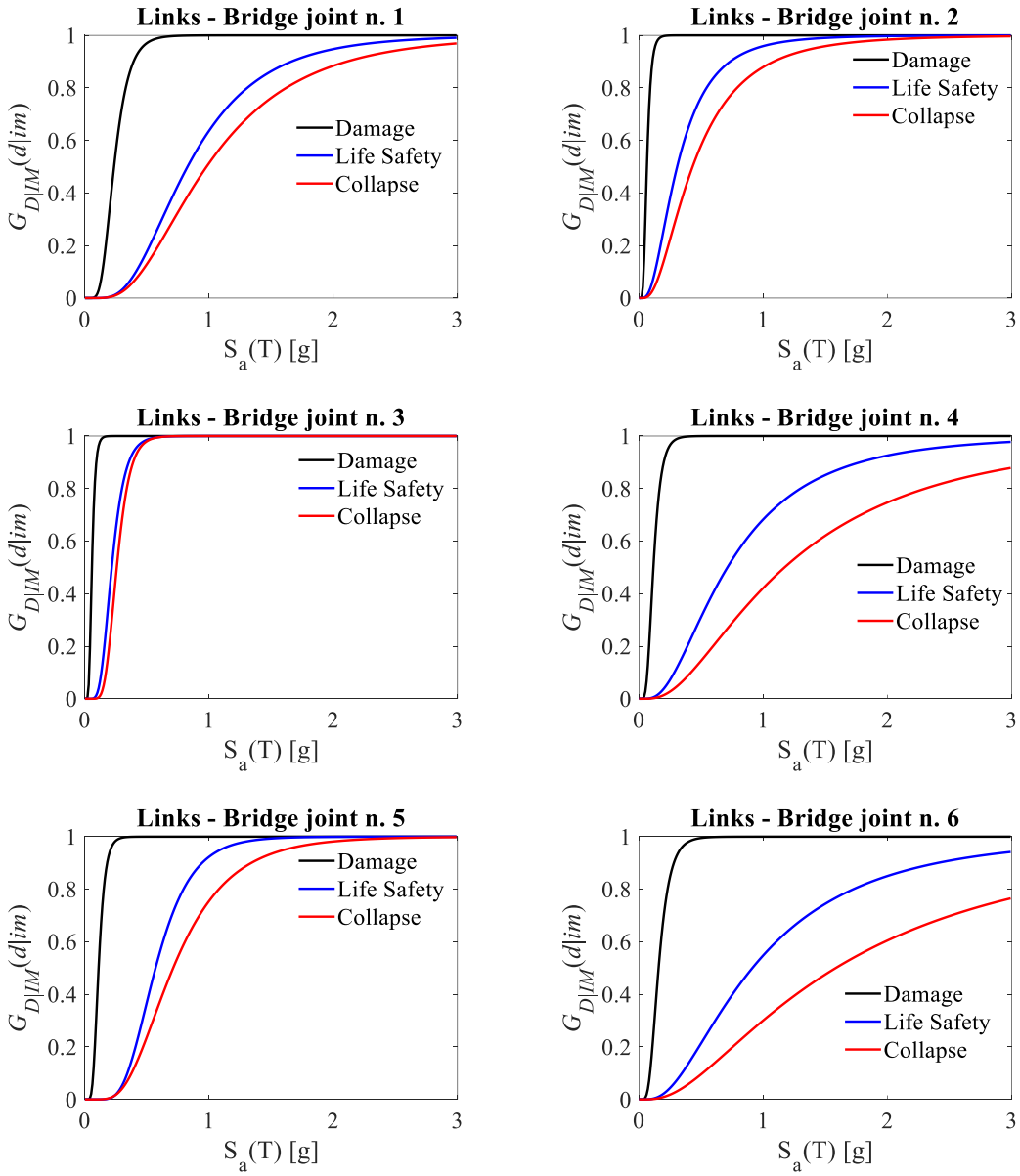

Figure 5.16. Fragility curves at different performance levels for link-slab bars (joints 1-6) – case study L/B = 20.

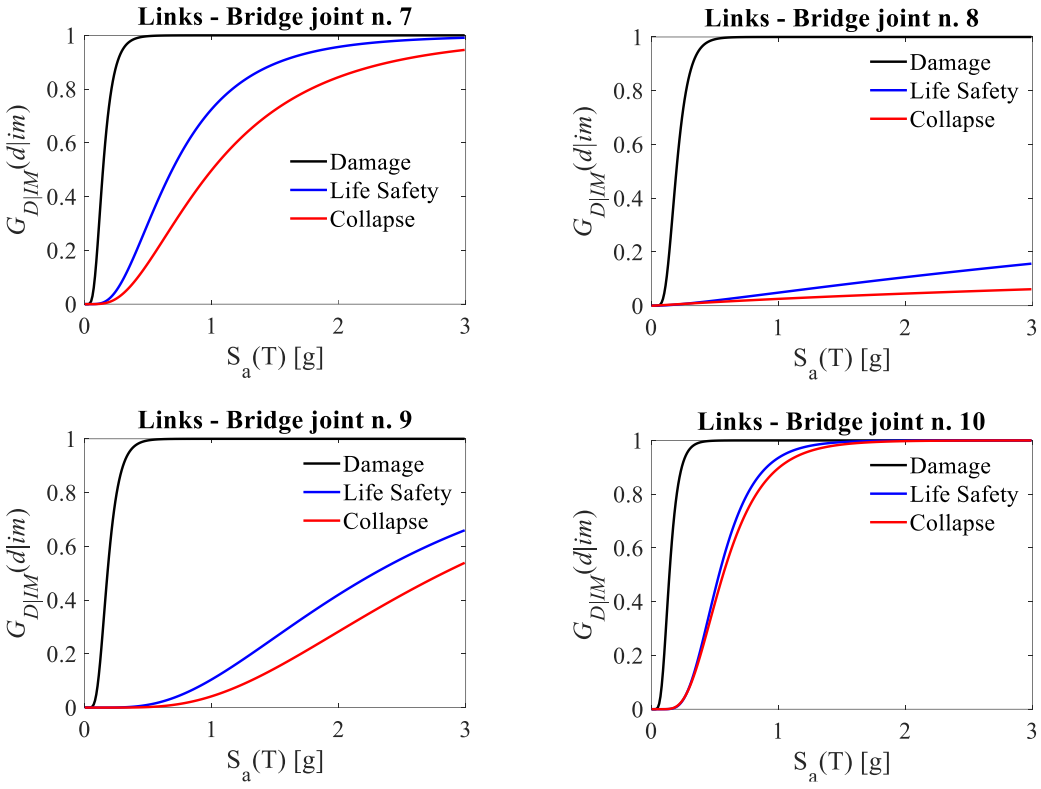

Figure 5.17. Fragility curves at different performance levels for link-slab bars (joints 7-10) – case study L/B = 20.

Results concerning the seismic demand on the bearings are shown in Figure 5.18 and Figure 5.19**Errore. L'origine riferimento non è stata trovata.**. Differently from the case study L/B = 10, there is not a univocal correspondence between the increment of the number of link bars and the decrease of the bearings' vulnerability. Nevertheless, at Damage limit state the vulnerability of devices is always and sensibly lower than the vulnerability of link bars. Moreover, for all the bearings the 50% probability of extensive damage at Life Safety limit state and Collapse is observed within Sa(T)=1.0g, and an almost uniform behaviour is offered along the structure. An exception is the set of bearings on the right abutment, where the relative horizontal displacements of the devices result under the damage threshold, resulting in a null probability of exceedance of the considered limit states in the whole *IM* range.

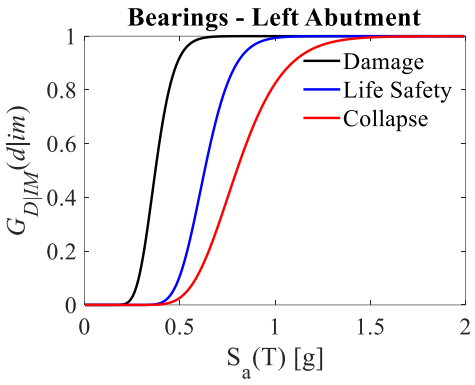

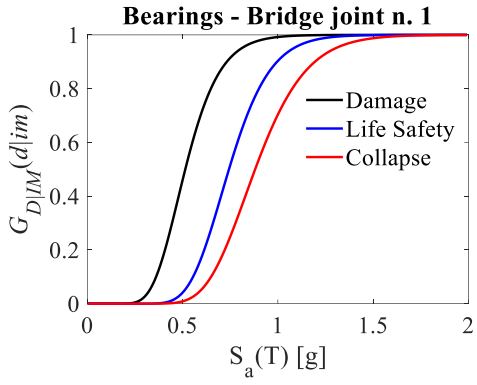

Figure 5.18. Fragility curves for bearings (left abutment and 1st joint)– case study L/B = 20.

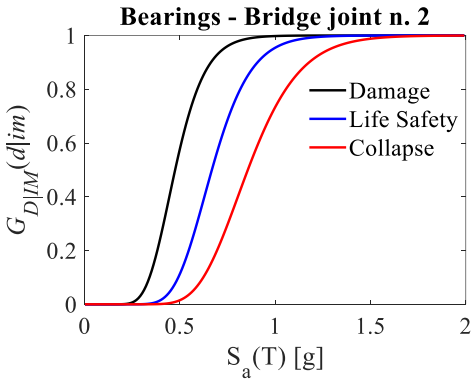

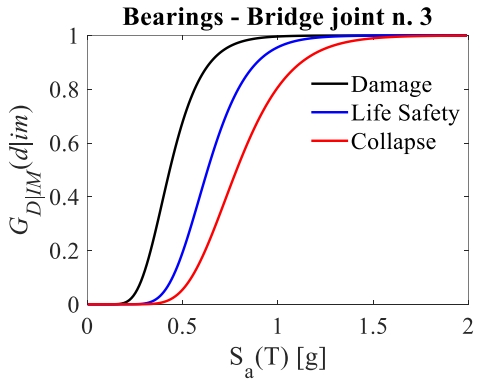

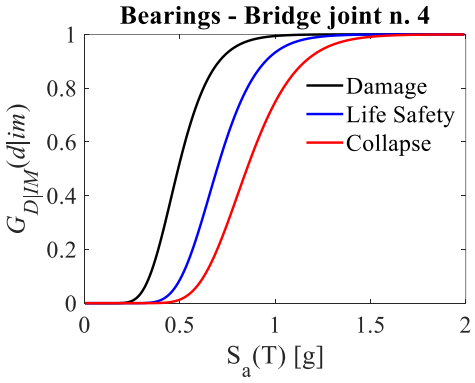

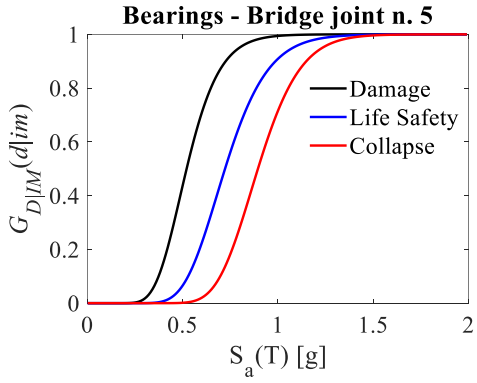

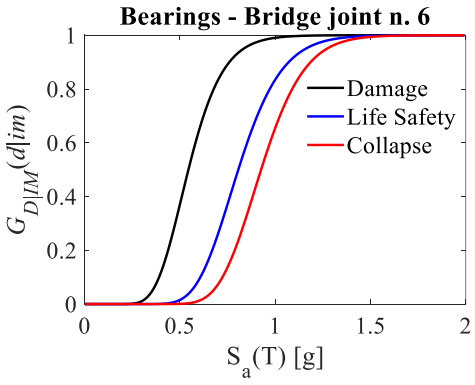

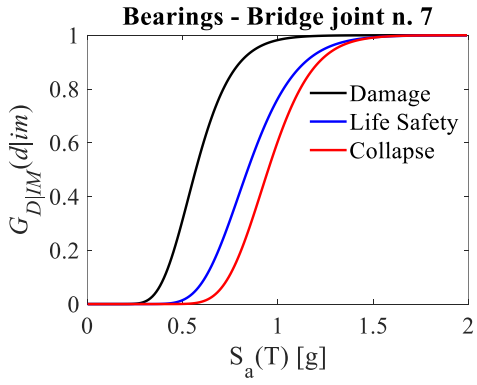

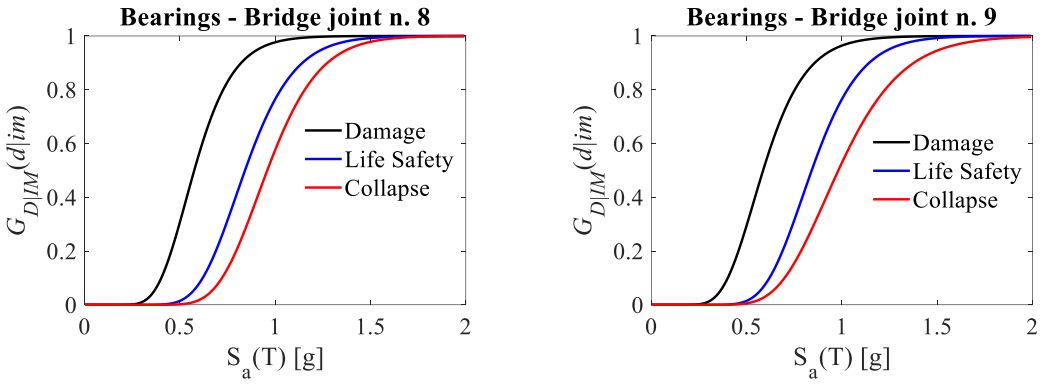

Figure 5.19. Fragility curves at different performance levels for bearings (joints 3-10) – case study L/B = 20.

Results concerning the piers' performance are shown in Figure 5.20 and Figure 5.20.
Fragility curves at different performance levels for piers (joints 1-6) – case study L/B = 20.

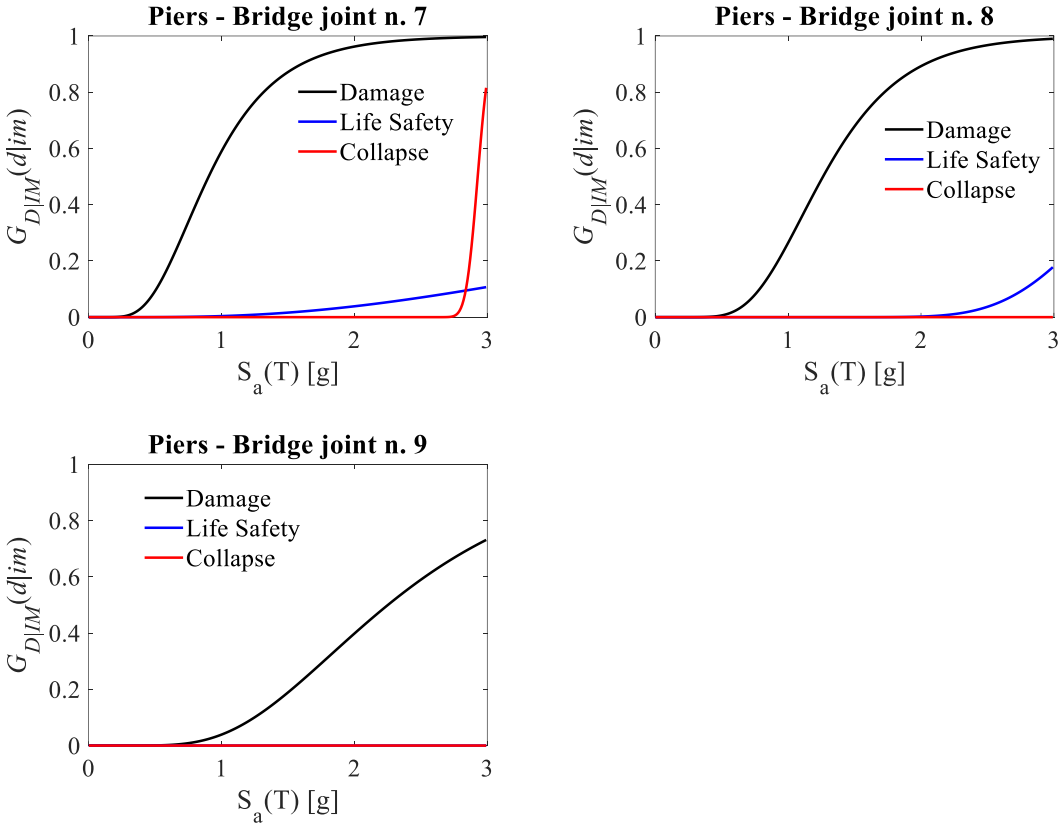

Figure 5.21. Analogously to L/B = 10, a symmetric behaviour can be observed. Internal piers experience damage at lower accelerations: the 50% probability of damage is at Sa(T)=0.55g for piers n. 2-6; it is at Sa(T)=0.95g for pier n. 7; it is at Sa(T)=1.25g for pier n. 8; finally, external piers have a 50% probability of overcoming Damage limit state at Sa(T)=2.0g. This trend could be justified by the increasing number of steel bars in the superstructure in correspondence of each pier; a different behaviour is reserved to the last

pier, where link bars present a high probability of experiencing damage. Extreme damage or collapses are prevented by the failure of bearing devices.

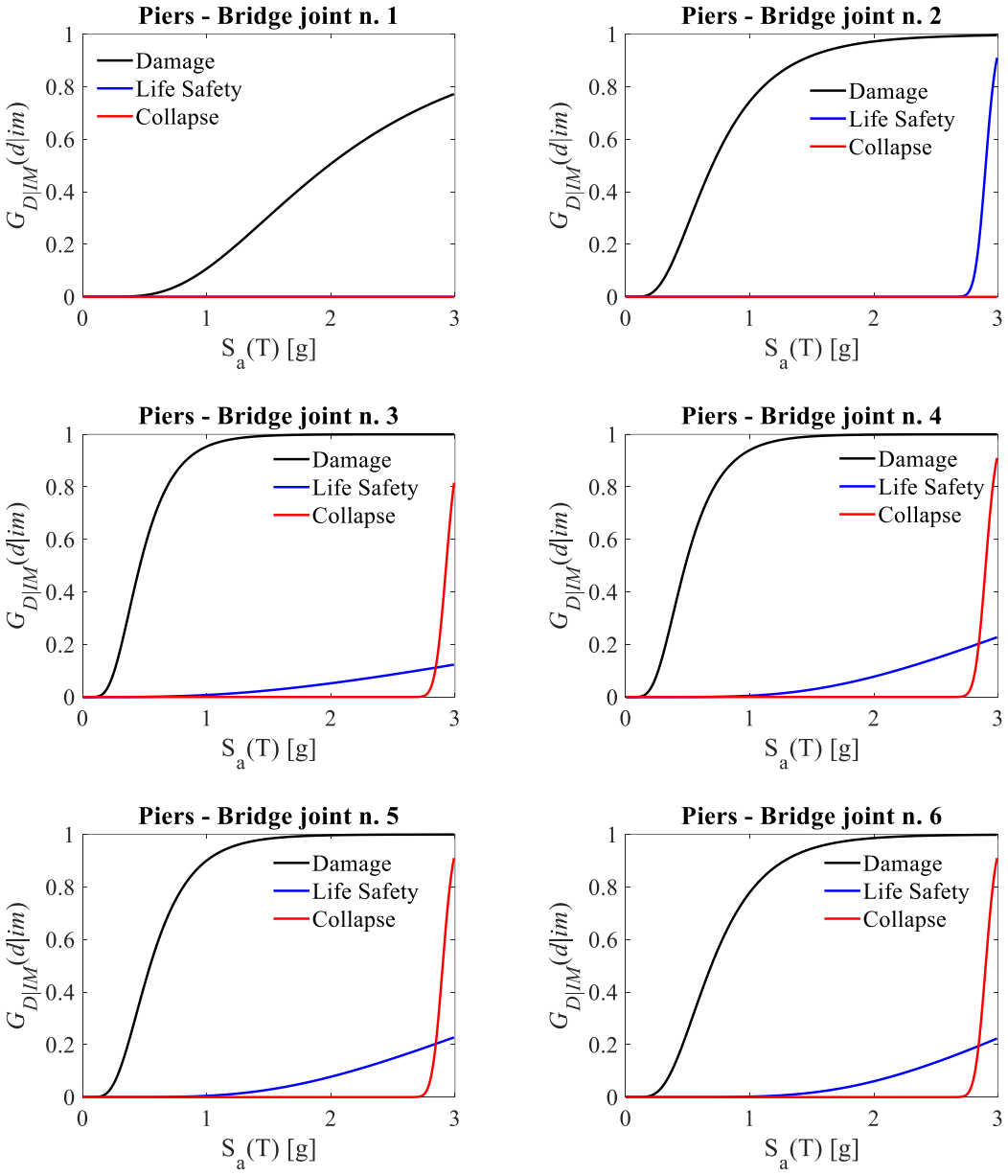

Figure 5.20. Fragility curves at different performance levels for piers (joints 1-6) – case study L/B = 20.

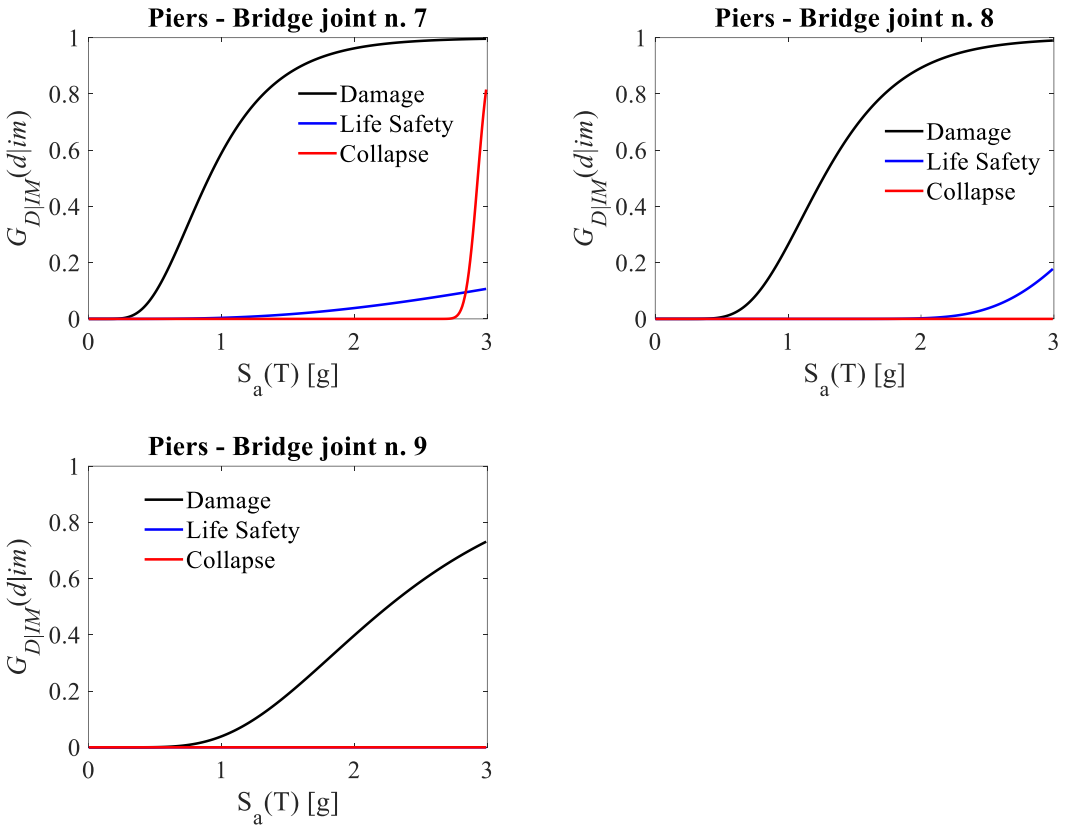

Figure 5.21. Fragility curves at different performance levels for piers (joints 7-9) – case study L/B = 20.

Figure 5.22 shows a comparison among fragility curves at the three considered limit states. As an overall comment, link-slab bars and bearings rule the vulnerability of the bridge at Collapse limit state, while a not negligible role is assumed by the active response of abutments not only at Damage limit state but also at Life Safety limit state. It can be seen that all the structural components experience damage (the probability of exceedance is close to 100%) within Sa(T)=1.0 g, while collapse of abutments and piers is prevented up to very high seismic intensities (Sa(T)=2.5g) with a return period equal to 100,000 years.

The combination of failure modes is shown in Figure 5.23, Figure 5.24, Figure 5.25, where the three performance levels are treated separately. For Damage limit state (Figure 5.23), the global fragility curve, obtained as the envelope of the single component fragilities, mainly depends from the fragility of link bars and abutments, which are the most vulnerable elements up to Sa(T)=0.5 g. Then, the curve is obtained from the concomitance of damage mechanisms on piers, links, bearings and abutments simultaneously. This analysis reveals that damage on piers are necessarily concomitant with damage on other structural elements.

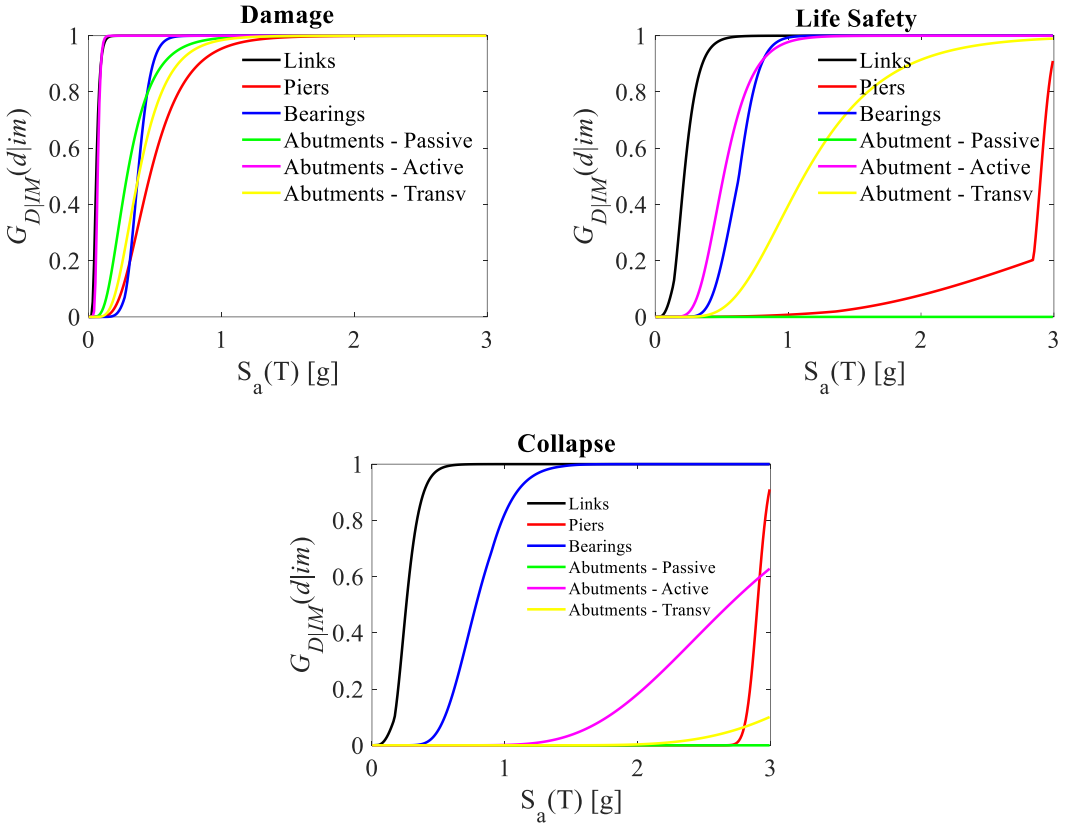

Figure 5.22. Fragility curves at slight damage, extensive damage and ultimate performance levels for different bridge components – case study L/B = 20, H/D = 5.

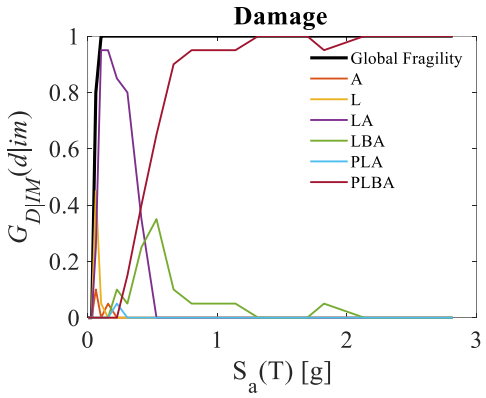

Figure 5.23. Probabilities of occurrence of Damage Limit State for combined mechanisms; in black, the global fragility curve as the envelope of the single fragility curves – case study L/B = 20.

With an analogous perspective, the Life Safety limit state is examined (Figure 5.24). In this case, the predominance of the damage on link-slab bars determines the global fragility up to Sa(T)=0.5g, and it is immediate to notice that there is a rapid passage from the damage of link bars only (orange line) to the damage of link bars, bearings and abutments (light blue line) for Sa(T)>0.5g, attesting that, without considering the behaviour of the

piers, the system loses progressively and rapidly resisting sources. The loss of the superstructure is complete for Sa(T)>1.0g.

Finally, at the Collapse limit state (Figure 5.25), for Sa(T)<0.5g it is most probable that only link bars reach the collapse, while for Sa(T)>0.5g the collapse involves link bars and supporting devices always together. An increasing influence of the abutments fragility on the overall fragility is noticeable for Sa(T)>1.3g, while a slight influence of the piers on the global collapse can be noted at very high spectral accelerations (Sa(T)>2.5g).

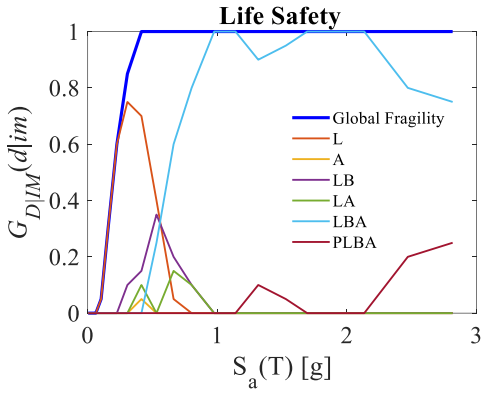

Figure 5.24. Probabilities of occurrence Life Safety Limit State for combined mechanisms; in blue, the global fragility curve as the envelope of the single fragility curves – case study L/B = 20, H/D = 5.

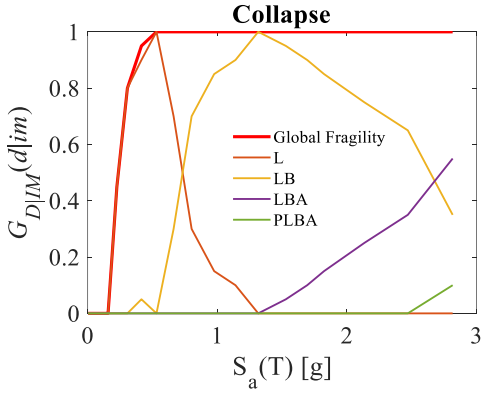

Figure 5.25. Probabilities of occurrence of Collapse Limit State for combined mechanisms; in blue, the global fragility curve as the envelope of the single fragility curves – case study L/B = 20, H/D = 5.

Figure 5.26 shows fragility curves for link-slab bars at the considered limit states considering different percentages of link-slab bar sets (i.e. sets above each structural joint) that experience light damage, extensive damage or collapse. For instance, in this case study the 50% of links is equivalent to 5 sets over the total of 10. It is worth noting that at the Damage limit state, the probability that total damage (i.e. 100% of links) verifies reaches its maximum for Sa(T)=0.6g, corresponding to a seismic event with 500 years return period, while the damage of more than half of the bar sets has the 50% probability of occurrence for a 100 years return period event. The behaviours at Life Safety and Collapse limit state are quite similar, considering that extreme damage or collapse of at

least 50% of the link sets is very likely to occur (≥50% probability) within Sa(T)=1.0g. In particular, 50% probability of extreme damage and collapse of at least 25% and 50% of link sets is expected for a seismic action Sa(T)=0.4g (with return period equal to 150 years) and Sa(T)=0.55g (with return period equal to 330 years), respectively.

A similar approach can be used to comment the bearings behaviour, which is illustrated in Figure 5.27. For Damage and Life Safety limit states the system offers a partially fragile behaviour, being almost equal the probabilities of damage occurrence for the 25% and the 50% of the supporting device sets. The total collapse of the bearings never happens, while the 50% probability that more than 7 sets over 11 (75%) reach the failure condition corresponds to a return period of 330, 660 and 1000 years for Damage, Life Safety and Collapse limit states, respectively.

Finally, looking at the piers behaviour in Figure 5.28, a 50% probability of damage is reached at Sa(T)=0.4g, 0.6g, 1.2g and 2.2g for 25%, 50%, 75% and 100% of the piers, respectively, corresponding to a minimum return period equal to 150 years. Similarly to the L/B=10 case study, failure on piers at Life Safety and Collapse limit states result as very unlikely to occur for seismic intensities lower than Sa(T)=2.5g.

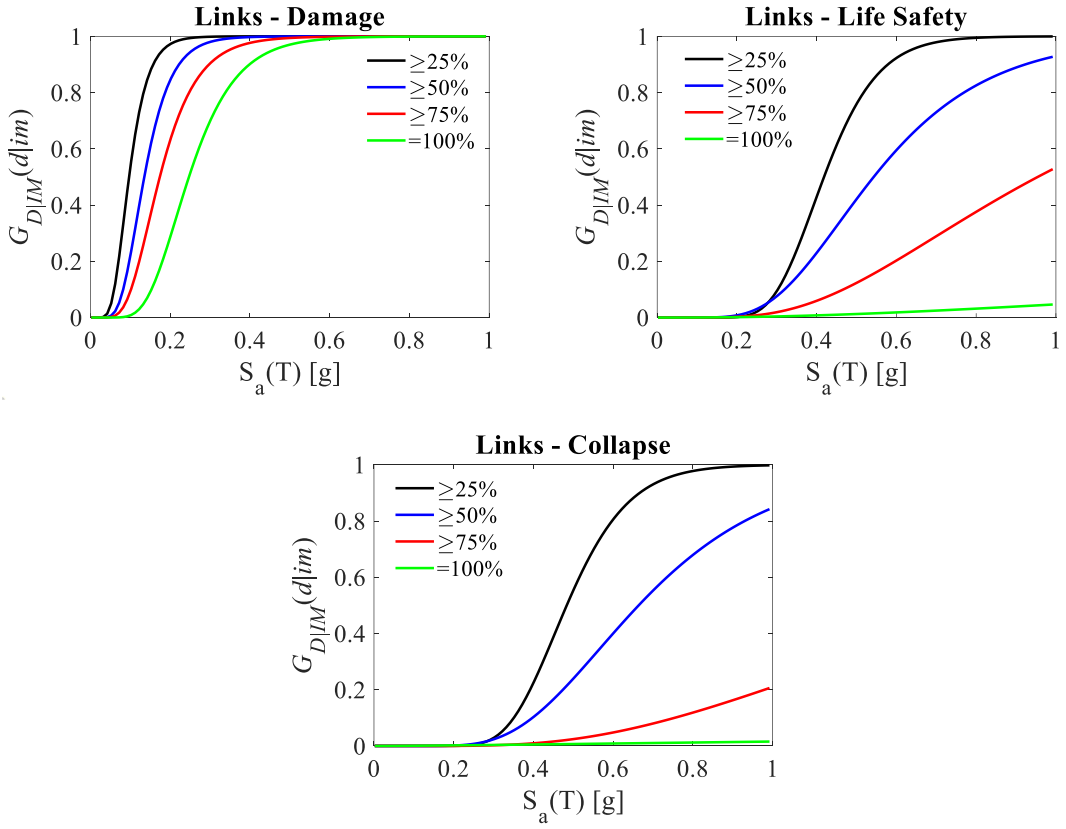

Figure 5.26. Fragility curves at Damage, Life Safety and Collapse limit states for link-slab bars: increasing percentages of involved elements (sets of link-slab bars) – case study L/B = 20.

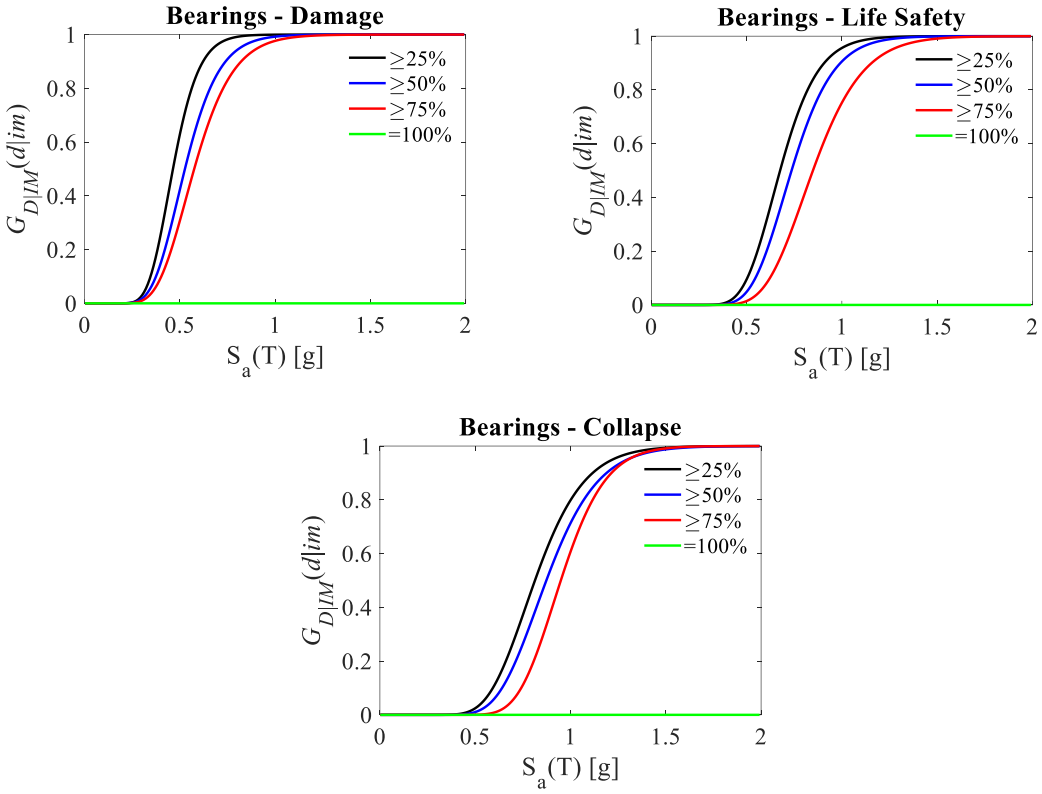

Figure 5.27. Bearings fragility curves: increasing involved sets of devices – case study L/B =20.

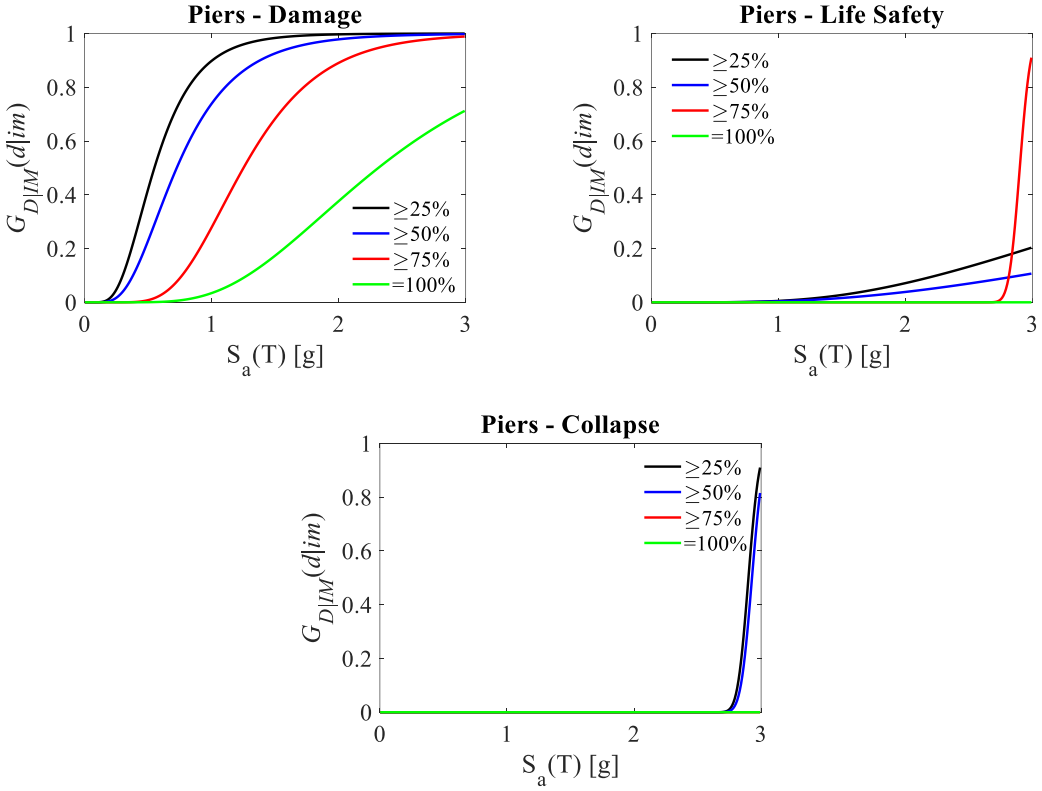

Figure 5.28. Pier fragility curves: increasing involved elements (single piers) – case study L/B =20.

Figure 5.29, Figure 5.30 and Figure 5.31 show the discrete probability curves associated to the various percentages of involved elements for links, bearings and piers compared to the probability of occurrence of damage on at least one element (magenta solid line).

For what concerns link-slab bars (Figure 5.29), damage never involves more than 75% of link bars, and in a short range of low *IM* values (up to 0.5g) a percentage of links comprised between 50% and 75% rapidly undergoes damage. At Life Safety limit state, it is very likely to occur that for low *IM* values (up to 0.5g) severe damage affects less than 25% of bars, while a percentage between 25 and 50% is strongly damaged up to 1.5g. More than 50% of link bars have a probability of exceeding severe damage higher than 50% only for very strong earthquakes (*IM* = 2.5g, with return period equal to 20'000 years). An analogous scenario is depicted for Collapse limit state.

The analysis of the curves for bearings in Figure 5.30 highlights that for all the considered limit states and Sa(T)>0.8g, there is an increasing probability that at least the 75% of devices experiences damage (or collapse in case of Collapse limit state). Finally, it is worth commenting the behaviour of piers at Damage limit state only, as depicted in Figure 5.31. A gradual development of damage can be detected with the increase of the seismic intensity since peaks of the red, green and cyan lines (corresponding to different increasing percentages of involved elements, at least the 50%) are clearly distinguishable and succeed each other at increasing *IM* values. Moreover, the damage of less than 50% of piers has a very low probability of exceedance (always inferior than 40%).

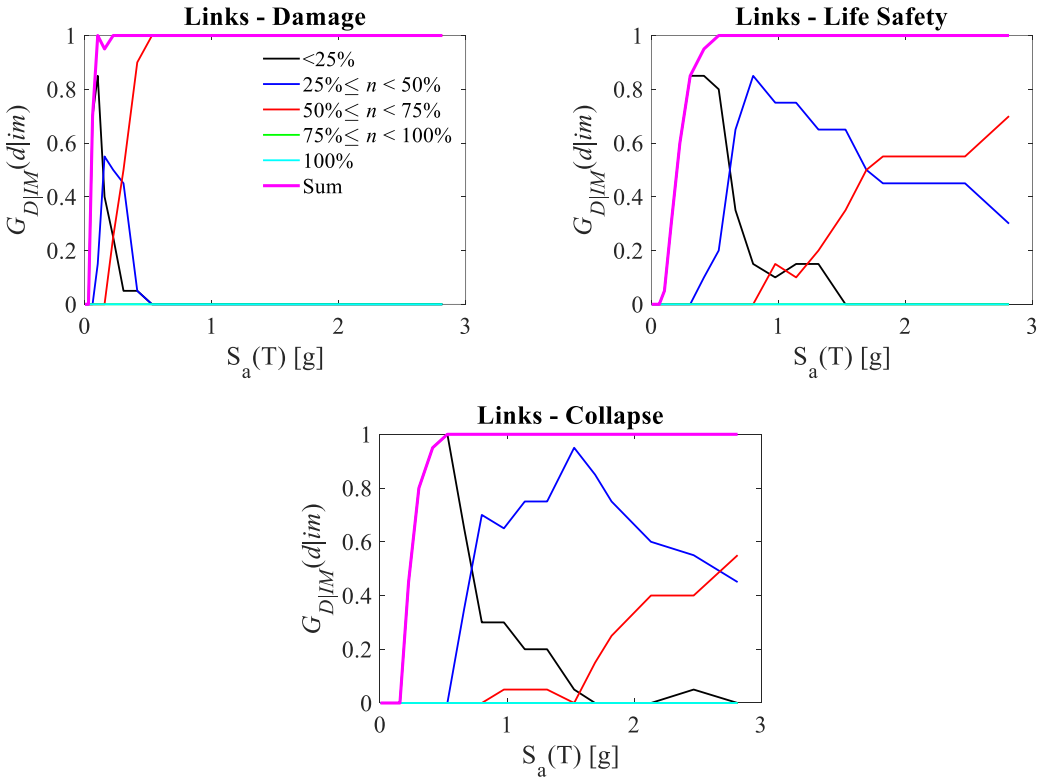

Figure 5.29. Probabilities of occurrence for different percentages of involved cross-beams – L/B = 20.

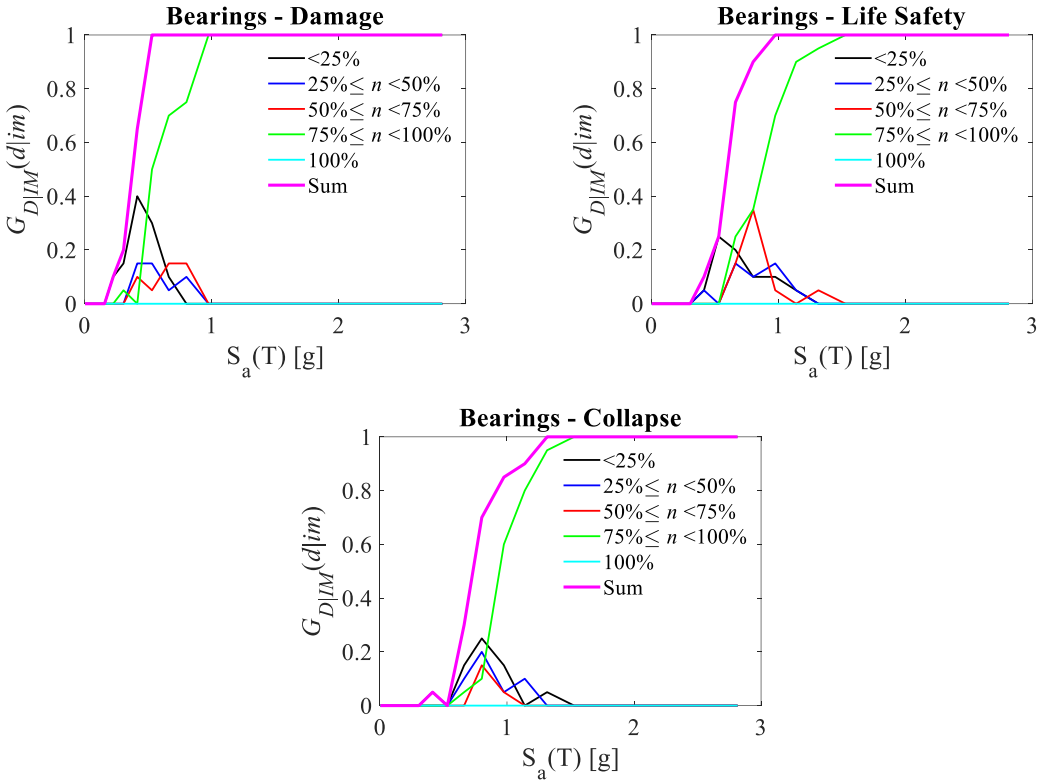

Figure 5.30. Probabilities of occurrence for different percentages of involved bearings – L/B =20.

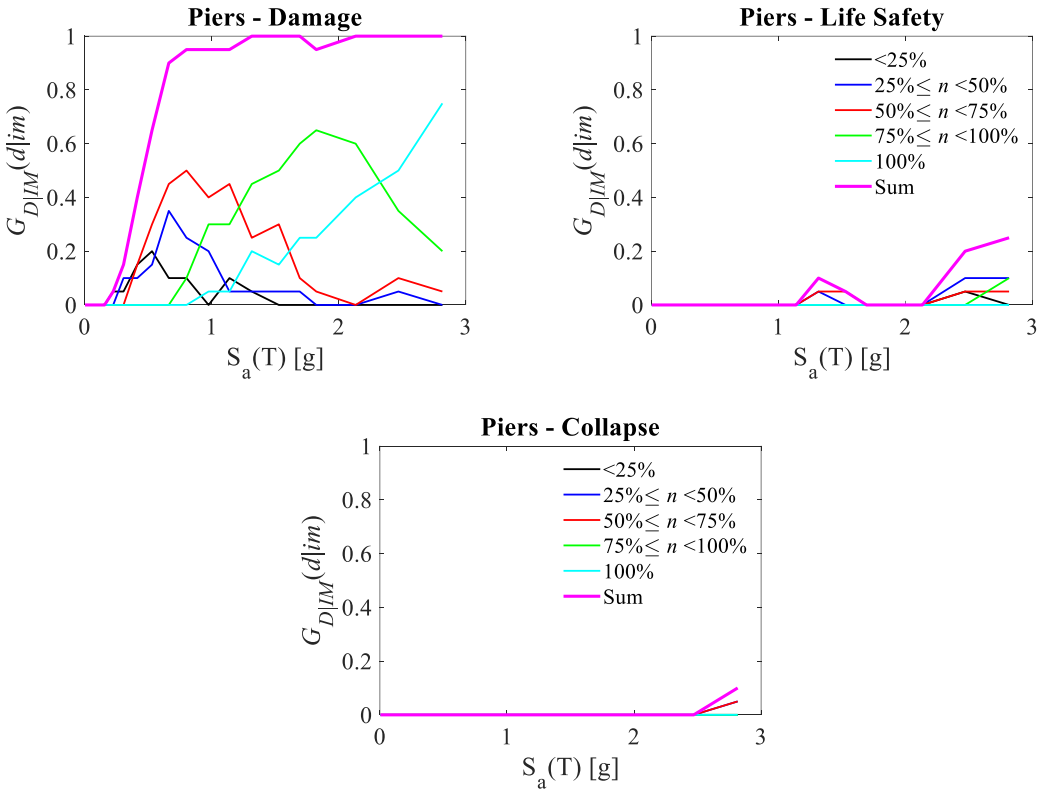

Figure 5.31. Probabilities of occurrence for different percentages of involved piers – case study L/B =20.

5.1.1.3 L/B = 10 vs L/B = 20

This section provides some comments on the comparison between the fragility results of RCLS bridges for the considered case studies. Fragility curves are illustrated with reference to the behaviour of the bridge components at the examined limit states in Figure 5.32.

For what concerns links, no appreciable differences are detectable between L/B = 10 and L/B = 20. Analysing the single link set fragility curves (Figure 5.3 and Figure 5.17), this result derives from the fragility of the link set in correspondence of the right abutment, which is the most vulnerable in both the structural configuration. In case of piers, the behaviour at Damage limit state is noticeably different. It appears that piers for the longer bridge are more vulnerable than piers of the shorter one. This can be associated to the higher influence of the abutment stiffness in the overall flexibility of the structure. Although a strong evidence can be observed at Life Safety limit state, it holds that very high seismic intensities are associated to a very low probability of exceedance of severe damage. In case of Collapse limit state, it can be concluded that no failure is expected for *IM*<2.5g (corresponding to a seismic event with return period equal to 20'000 years). Bearings of the case study L/B=10 are slightly more vulnerable than those of L/B=20, that can be correlated to the lower fragility of the piers for L/B=10 respect to L/B=20. Finally, due to the higher seismic action in the longitudinal direction, abutments of case study L/B=20 are more vulnerable than in case L/B=10.

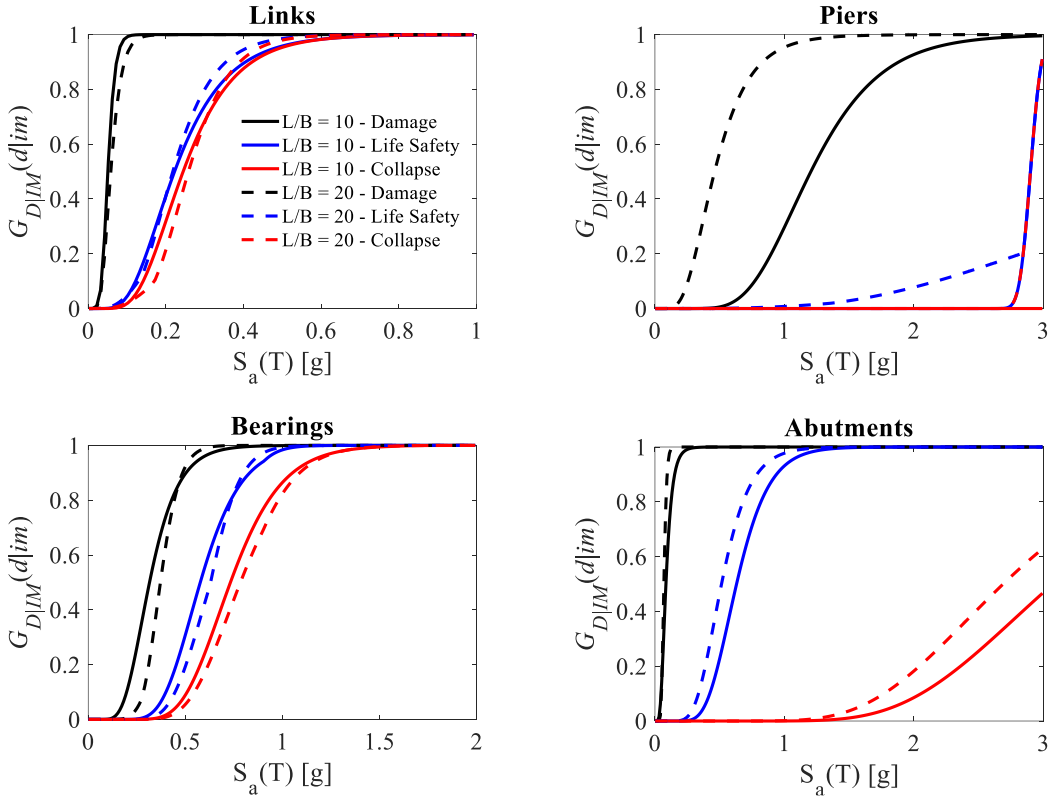

Figure 5.32. Comparison of fragility curves for the examind damage mechanisms on RCLS bridges.

5.1.2 Effects of compliant base and degradation

Analyses with different ageing conditions and the presence of compliance at foundation level under the piers are performed to highlight the degree of reliability of the models with design characteristics and fixed base in the face of an existing bridge structure. The following Figure 5.33 and Figure 5.34 provide a comparison between fragility curves for all the investigated case studies at different ageing and structural conditions referring to the structural configurations L/B = 10 and L/B = 20, respectively.

It is evident that effects of both ageing and SSI are mostly evident on piers, where they are explicitly modelled. Concerning this component, ageing (dot and dashed lines) changes the vulnerability of the structural component largely.

In case of L/B=10, the effect of ageing is appreciable at Damage and Life Safety limit states. In particular, starting from the fixed base condition (black line), the 50% of overcoming damage corresponds to lowering values of spectral acceleration up to almost half of the initial value (from Sa(T)=1.25g at design condition to Sa(T)=1.0g for 25-years ageing and Sa(T)=0.7g for 50 years ageing), that corresponds to a decrease of the frequency of occurrence of the corresponding earthquake event (from 2500 to 400 years return period). The presence of compliant base furtherly increases the vulnerability of piers, since higher displacements are expected in case of flexible foundation. In this case (grey curves) the design condition with compliant base almost overlaps the 25-years-ageing condition with fixed base. Ageing implies a reduction of the spectral accelerations where 50% probability of exceeding light damage occurs up to 1/3 (from 0.9g without ageing to 0.80g in the 25-years ageing condition and to 0.55g approximately for 50-years ageing condition). Ageing and compliant base have also a high impact on results at Life Safety limit state, although severe damage on piers is expected at very high values of *IM*, when all the other structural components have already experienced damage or collapse and the overall capacity of the bridge is compromised.

In case of L/B = 20, ageing and compliant base effects are mostly noticeable at Life Safety and Collapse limit states. In the former, starting from the fixed base condition (dark blue solid line), major differences can be observed in case of 25- and 50-years ageing for *IM*>2.0g and *IM*>1.0g, respectively, where $G_{D|IM}(d|im)$ is doubled. The presence of compliant base furtherly increases the vulnerability of piers and non-null differences between the design condition with fixed base and compliant base (light blue solid line) are shown for *IM*>1.5g. Adding effects of ageing to the presence of compliance on the foundations, worsening of the fragility condition is quantifiable with a growth of $G_{D|IM}(d|im)$ equal to 10-15%. In case of Collapse limit state, major differences are observed between the fixed base and the compliant base condition for *IM*>2.0g. The addition of ageing condition brings to a doubling of the probability of collapse exceedance, despite no substantial differences are shown between the 25-years and the 50-years conditions in the analysed *IM* range. It holds that $G_{D|IM}(d|im)$>50% verifies only at very high spectral accelerations (Sa(T)>2.8g).

It can be concluded that disregarding ageing and compliant base effects may lead to very high underestimates of the behaviour of piers. In case of short bridges (L/B=10), major errors may be observed at Damage limit state, while in case of long bridges (L/B=20) extensive damage and collapse condition may verify with a probability of exceedance up to four times higher than in case of fixed base and design conditions.

Few comments are offered for the other structural component. In general, in case of both short and long bridge configurations, no appreciable effects of ageing and compliant base on the piers are visible on bearings and abutments. Regarding the link behaviour, a slight reduction of the vulnerability at Collapse limit state is provided by the introduction of the compliance on the piers' foundation. It holds that the certain event associated to collapse verifies always within *IM*=1.0g.

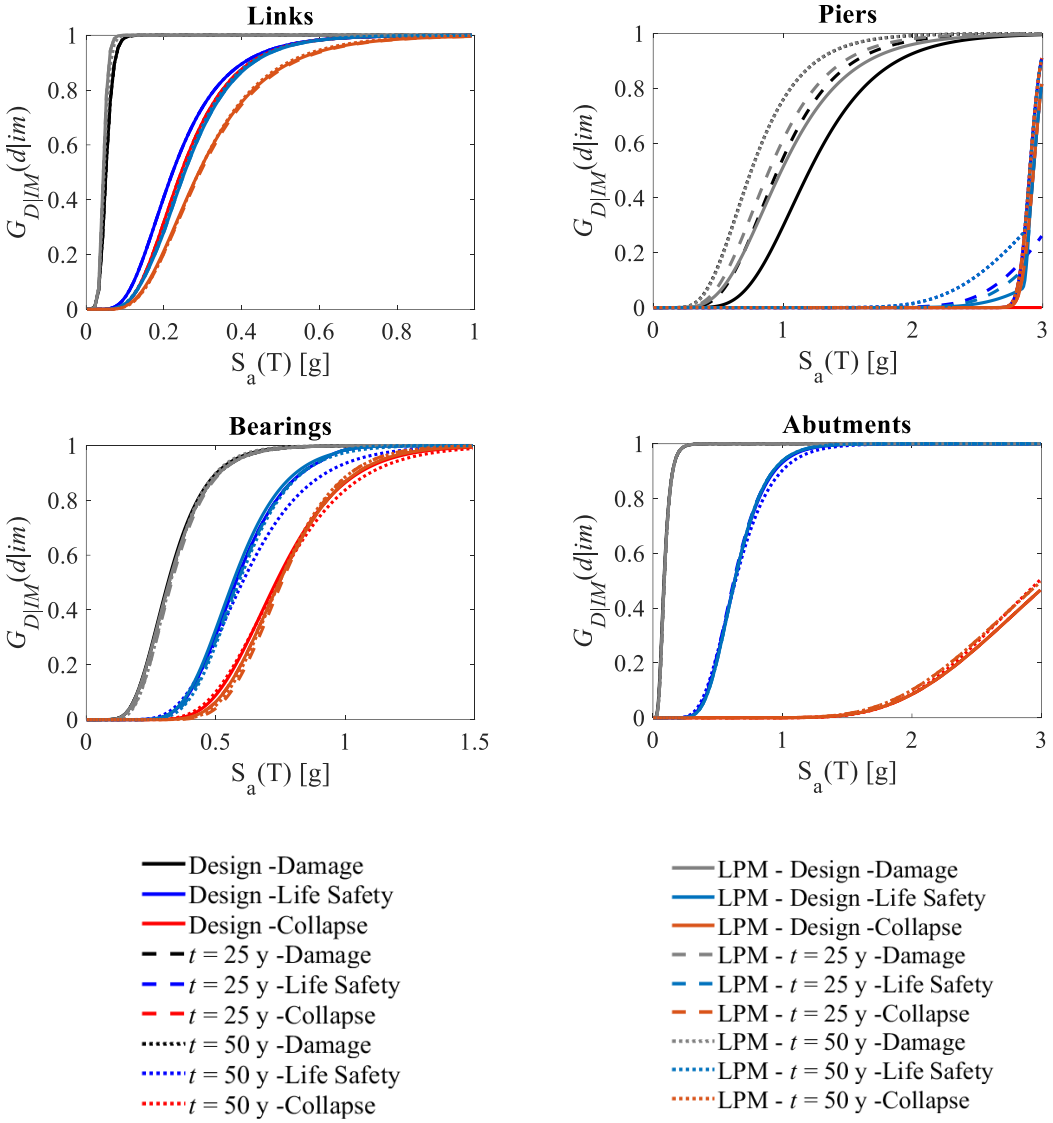

Figure 5.33. Comparison of fragility curves for different ageing conditions and compliance of the foundation system – case study L/B = 10.

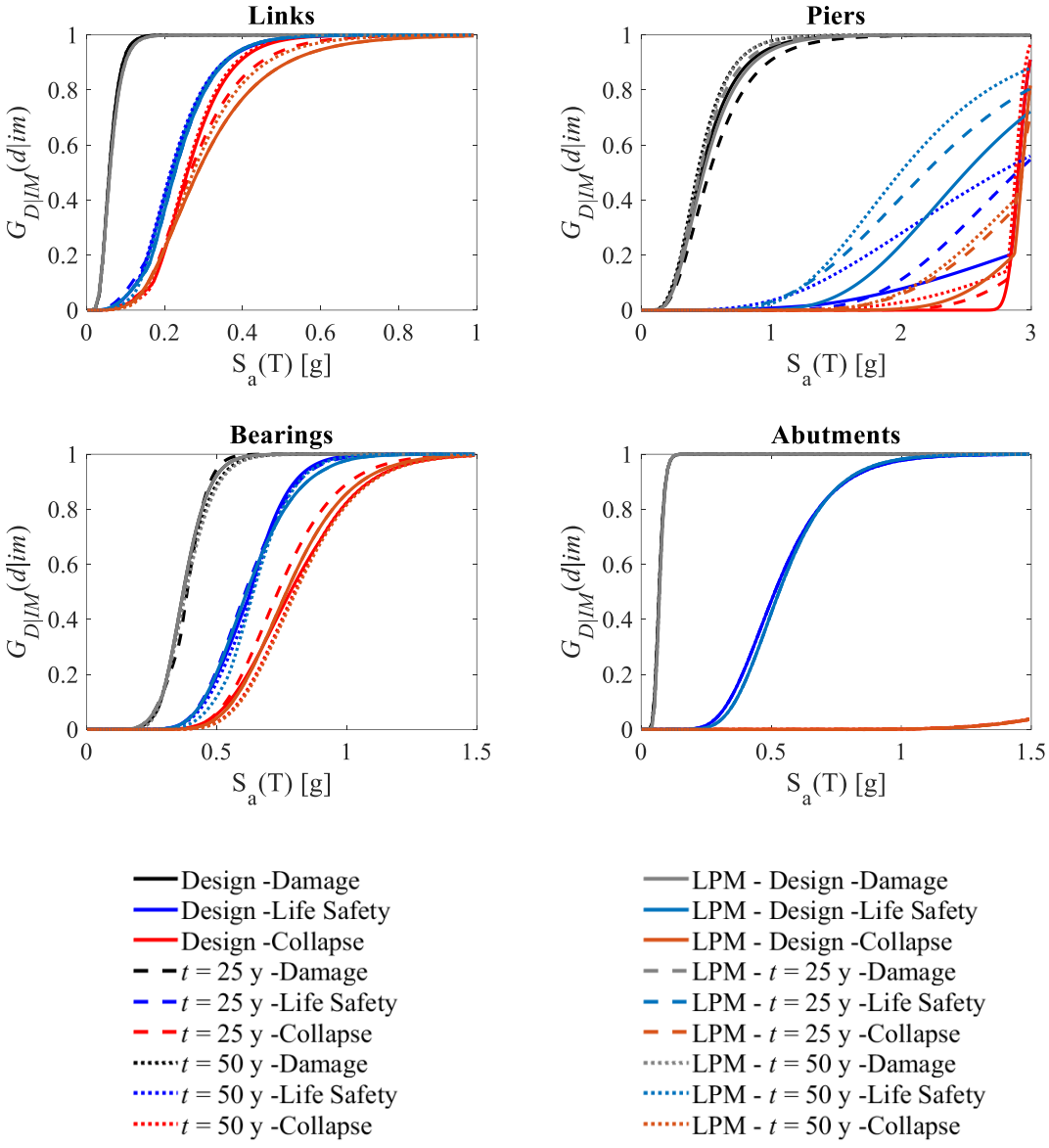

Figure 5.34. Comparison of fragility curves for different ageing conditions and compliance of the foundation system – case study L/B = 20.

5.2 Fragility of SCC bridges

Analogously to the RCLS bridges, the fragility curve for a certain SCC bridge component is built as the envelope of the fragility curves of single elements that belong to the same element family, where the single elements are the piers, the abutments, each set of bearings above each pier and the equivalent cross-beam system on each pier. For each component (piers, bearings, cross-beams, abutments), results from the seismic analyses under the hypotheses of fixed base and the absence of degradation phenomena are presented in form of three types of charts: the comparison between different limit states for the same component; the evolution of the elements' fragility along the bridge longitudinal development through the fragility curves of the elements at each structural joint; finally, the comparison between performances of different components at the same limit state. The analysis of the failure modes and the damage extension follows, according to the proposed improved methodology for the evaluation of fragility. Then, a comparison between results of the examined different case studies is made to highlight typical vulnerabilities associated to the case study typology. Finally, results from the analysis with compliant base and the modelling of degradation are illustrated and commented.

5.2.1 Fixed base

5.2.1.1 L/B = 4

Results for case study L/B = 4 are firstly commented. Figure 5.35 shows the fragility curves of element classes comparing different limit states. Different behaviours can be observed depending on the examined limit state. For Damage limit state, the active response of abutments presents the highest vulnerability among the failure modes occurring on the other structural components, while extensive damage as well as collapse condition are prevented. No significative failure mechanisms are appreciable on abutments in case of passive or transverse response. Cross beams present a high vulnerability at all the three considered limit states, since damage and collapse are very likely to occur (i.e. $G_{D|IM}(d|im)$ > 50%) within Sa(T)=0.5g, and the associated certain events (i.e. $G_{D|IM}(d|im)$ = 100%) are observed within Sa(T)=1.0g. As previously introduced, bearings are subject to extensive and complete damage only. In this case, the vulnerability of devices at Life Safety limit state is comparable to that of cross beams, while a larger capacity is offered at Collapse limit state, where higher probabilities of failure are expected at very high intensity measures (Sa(T) ≥ 2.0g).

Figure 5.36 shows the behaviour of the cross beams in correspondence of the bridge abutments. It is possible to appreciate a non-symmetric response since the reticular cross beam on the left abutment (the fixed one) presents a higher fragility at all the three considered limit states. Moreover, it is possible to observe that the principal difference in the behaviour of the two cross beams verifies at Life Safety limit state, where the extensive damage on the left abutment occurs at sensibly lower *IM*s (left offset of the curve). This can be correlated to the different stiffness provided by the bearing system

under the cross beams. However, in both cross beams a scarce range exists between the Life Safety and the Collapse limit state curves.

For what concerns bearings, the comparison between Figure 5.35 and Figure 5.37 reveals that the fragility at component level is determined by the higher fragility of the bearing system in correspondence of the left abutment, where both transverse and longitudinal shear forces are resisted.

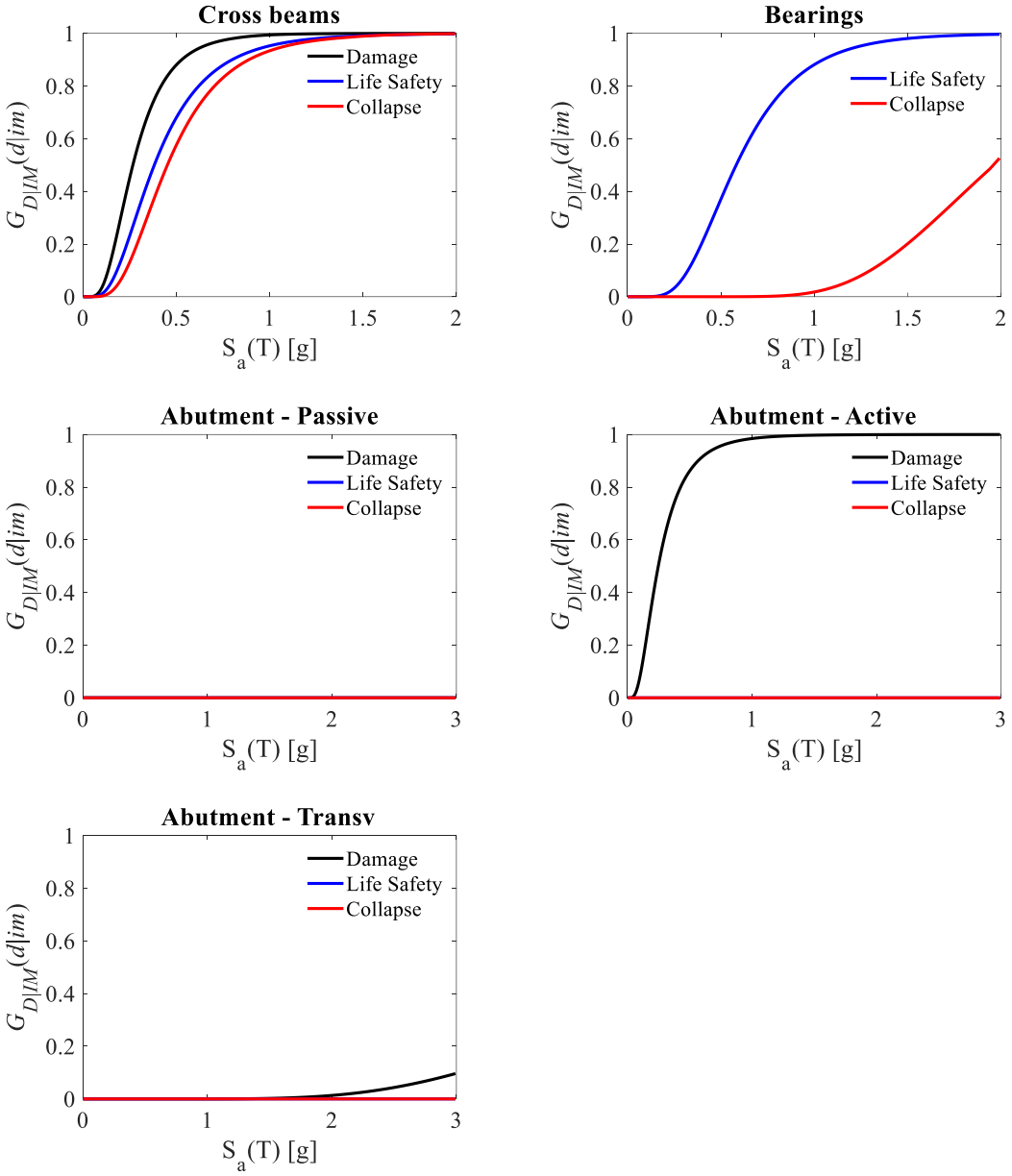

Figure 5.35. Fragility curves at different performance levels for bridge components – case study L/B = 4.

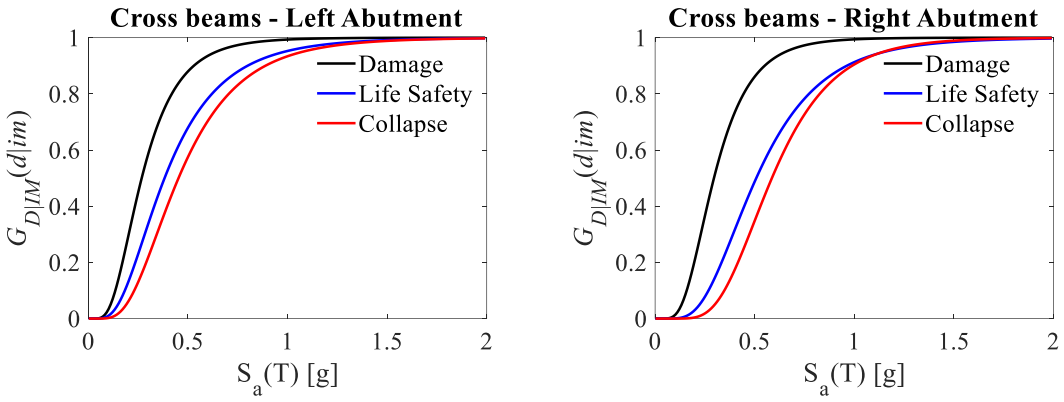

Figure 5.36. Fragility curves at different performance levels for cross-beams – case study L/B = 4.

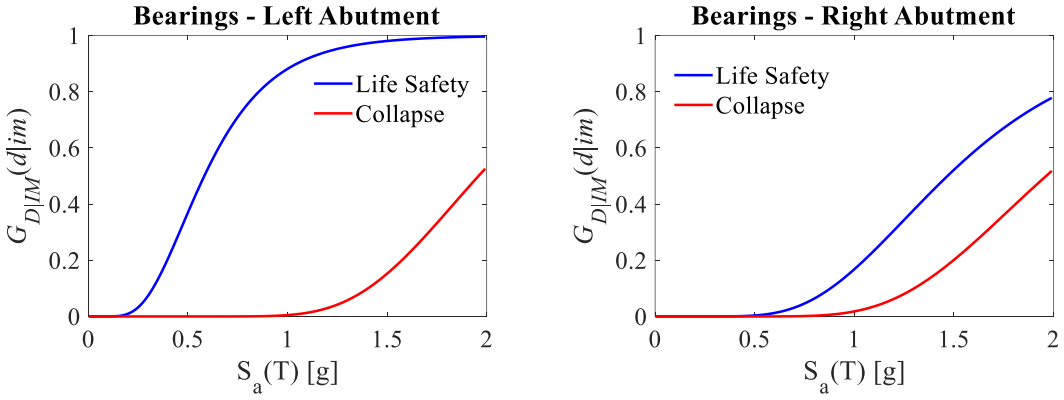

Figure 5.37. Fragility curves at different performance levels for bearings – case study L/B = 4.

Finally, Figure 5.38 represents fragility curves for different bridge components at the considered limit states. Damage limit state is governed by both abutments and cross beams; Life safety limit state mainly involves cross beams and bearings; collapse can be observed on cross beams only up to medium-high seismic intensities. As an overall conclusion, while damage may affect the entire bridge even at low *IM*s, collapse is unlikely to occur on the substructures.

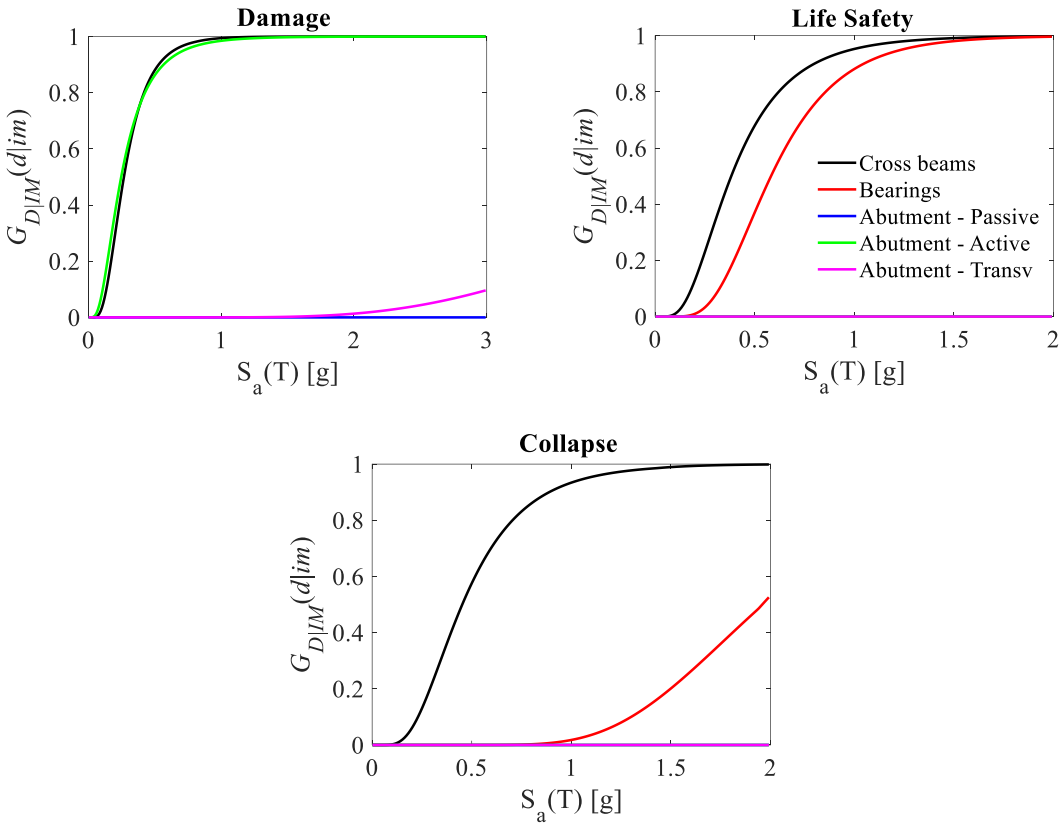

Figure 5.38. Fragility curves at different performance levels for bridge components – case study L/B = 4

Three sets of plots are reported in Figure 5.39 and Figure 5.40 to show the combination of damage mechanisms at the considered limit states, and for each of them a dedicated chart is represented to furnish a clearer view of the results. To indicate the different mechanisms, capital letters are employed in the following order: C = failure on cross beams; B = failure on bearings; A = failure on abutments (as the envelope of damage for passive, active and transverse movements).

Coherently with the results analysed in the classical fragility representation, cross beams have a fundamental role in the determination of the global fragility of the bridge. It appears that there is a strong correlation of damage on the superstructure and abutments, in case of Damage limit state, and on the superstructure and bearings, for Life Safety Limit State. At Collapse, the global fragility can be totally identified with the cross beams' fragility. The influence of bearings can be noted for high return period seismic actions (Sa(T)≥2.0g).

The extension damage analysis is not presented for the case study L/B = 4 given the low number of elements composing the families of element. A clear view on the behaviour of the single elements already emerges from the fragility analysis in the classical form.

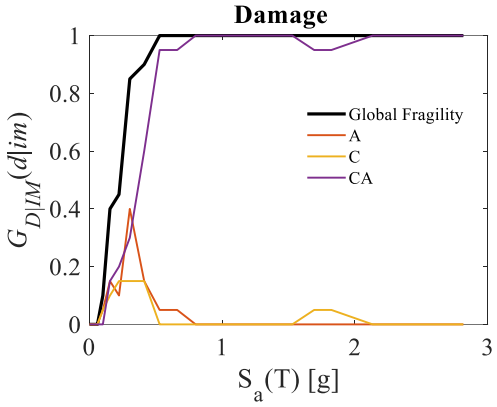

Figure 5.39. Probabilities of occurrence of Damage Limit State for combined mechanisms; in black, the global fragility curve as the envelope of the single fragility curves – case study L/B =4.

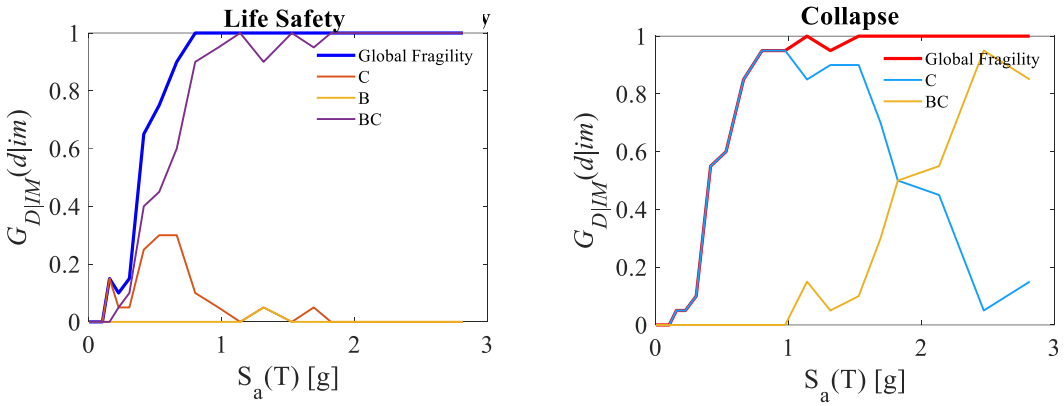

(a) (b)

Figure 5.40. Probabilities of exceedance of (a) Life Safety Limit State and (b) Collapse Limit State for combined mechanisms; in (a) blue and (b) red, the global fragility curve as the envelope of the single fragility curves – case study L/B =4.

5.2.1.2 L/B = 8

Results for case study L/B = 8 are presented. Figure 5.41 shows the fragility curves of element classes comparing different limit states. For what concerns abutments, the active response is responsible for a high vulnerability of the component at Damage limit state, while, at more severe limit states, no extensive damage nor ruptures are observed. A slight probability of exceeding the light damage condition is shown from the transverse response, but also in this case extensive damage and collapse are prevented in the considered *IM* range. No damage phenomena are observed relating to the passive response of the abutments. For what concerns cross beams, the behaviour of cross beams can be defined fragile, since the passage from the damage and the collapse condition is very "rapid" (it occurs at very close *IM* values and the fragility curves result almost overlapping). Bearings are investigated at Life Safety and Collapse limit states, resulting in a high vulnerability towards extensive damage. Finally, piers present a low degree of

vulnerability, especially at Life Safety and Collapse limit states. Failures on piers are prevented by damage or ruptures on the superstructure and the bearings. Collapse of the substructures may occur at medium-high spectral accelerations (50% probability of collapse is reached on bearings at Sa(T) = 1.5g).

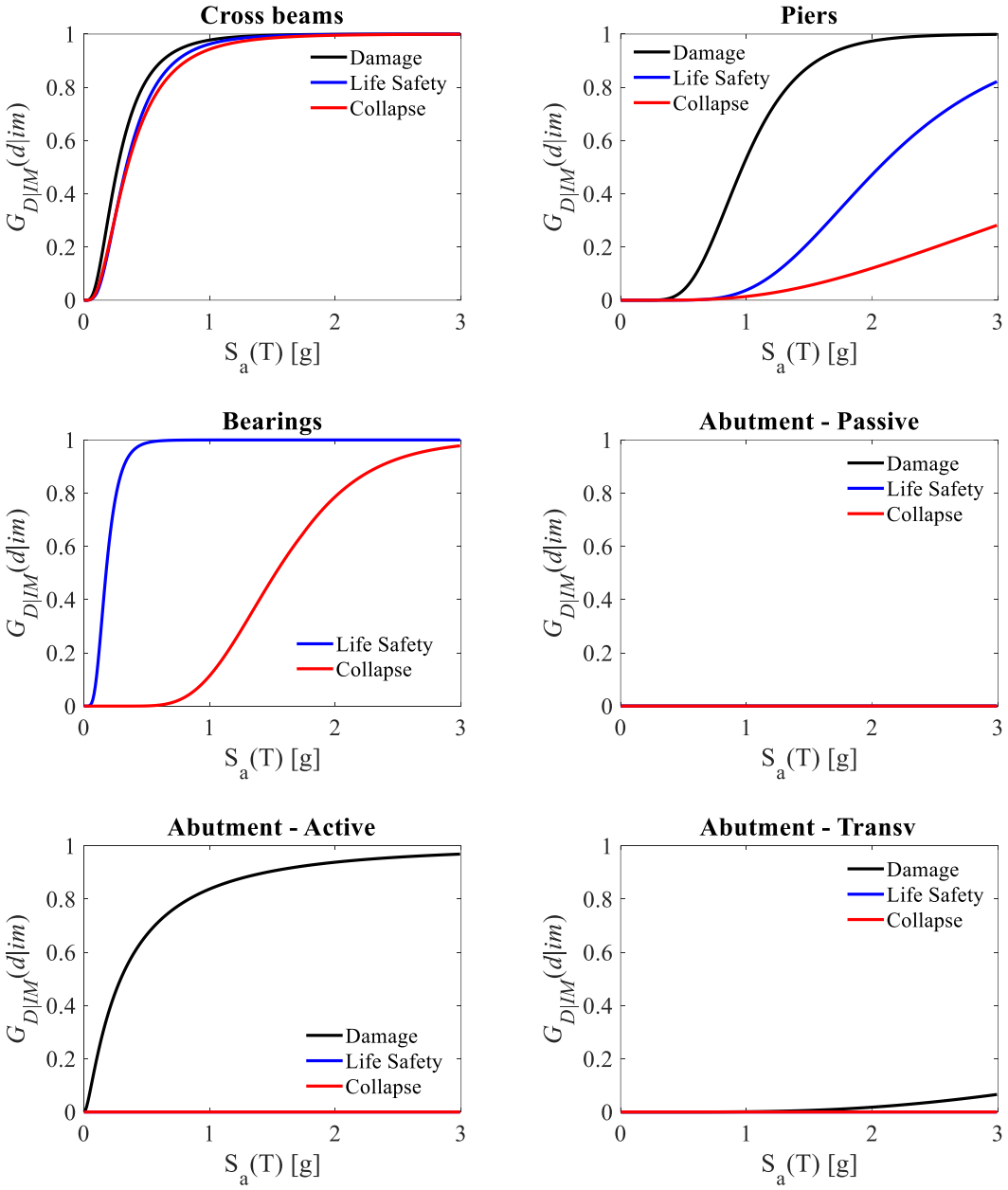

Figure 5.41. Fragility curves at different performance levels for bridge components – case study L/B = 8.

The behaviour of cross beams is analysed in Figure 5.42. It seems clear that the performance of end cross beams (i.e. in correspondence of abutments) reflects the expected trend for the shear forces. In particular, given the research on the behaviour of end cross beams illustrated in (Carbonari et al., 2017; Dezi et al., 2018; Minnucci et al., 2019), the most of inertial forces are absorbed by end cross sections and are transferred

from the concrete slab to the substructures through the cross beams. Since most of the shear action travels through the end cross beams, and the associated local deformation is higher than the corresponding one of the reticular system above the pier, external cross beams are much more likely to damage or collapse. However, it is also possible to recognize a fragile behaviour in all the cross beam systems, since the damage and collapse fragility curves almost overlap.

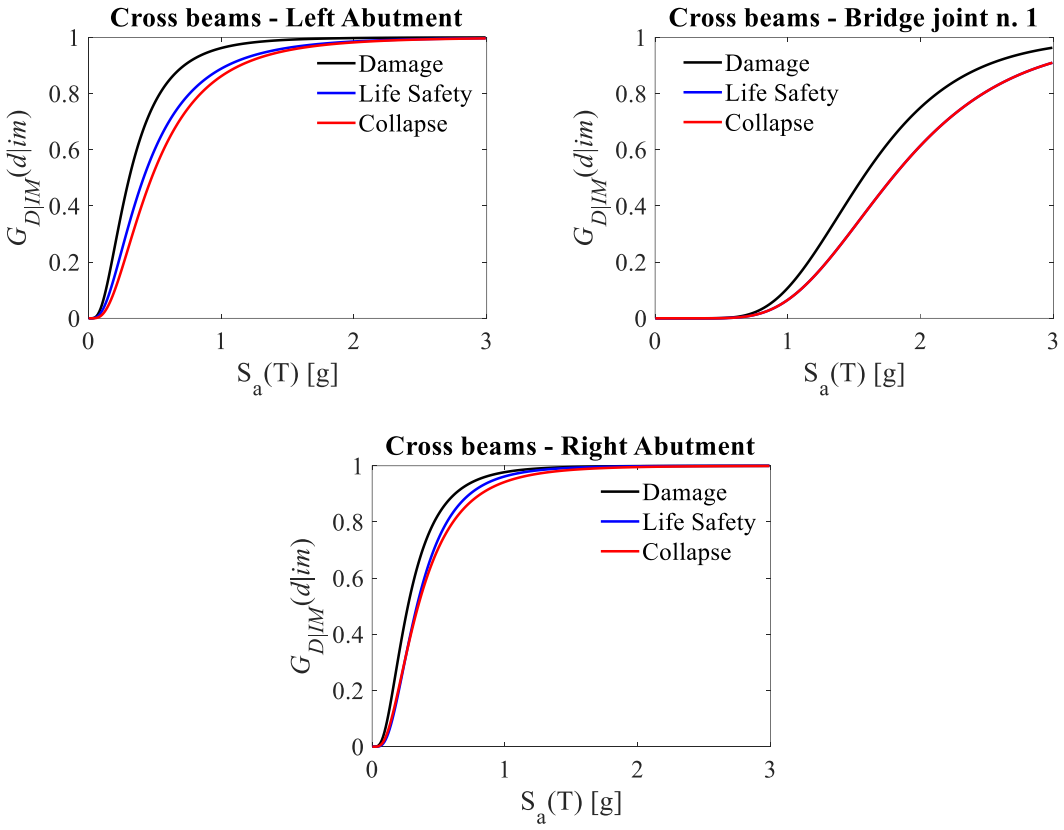

Figure 5.42. Fragility curves at different performance levels for cross beams – case study L/B = 8.

For what concerns bearings, the comparison between Figure 5.41 and Figure 5.43 reveals that the fragility at level component is determined by the fragility of the bearing system in correspondence of the left abutment, where both transverse and longitudinal shear forces are resisted. The performance of bearings is differentiated by the behaviour at Life Safety limit state, while fragility curves at Collapse limit state are comparable. This reveals that, once the bearing system corresponding to the left abutment (i.e. with the fixed device) is severely damaged, the behaviour of bearings becomes uniform.

Finally, a comparison between fragility curves of different bridge components at the examined limit states is offered in Figure 5.44. The damageability of cross beams and abutments (active response) is comparable at Damage limit state up to Sa(T)=0.3g. Then, a higher vulnerability of cross beams is noticeable, while piers are likely to damage (probability of overcoming Damage limit state higher than 50%) for Sa(T)>1.0g. Curves at Life Safety limit state show that extensive damage on bearings is expected at lower

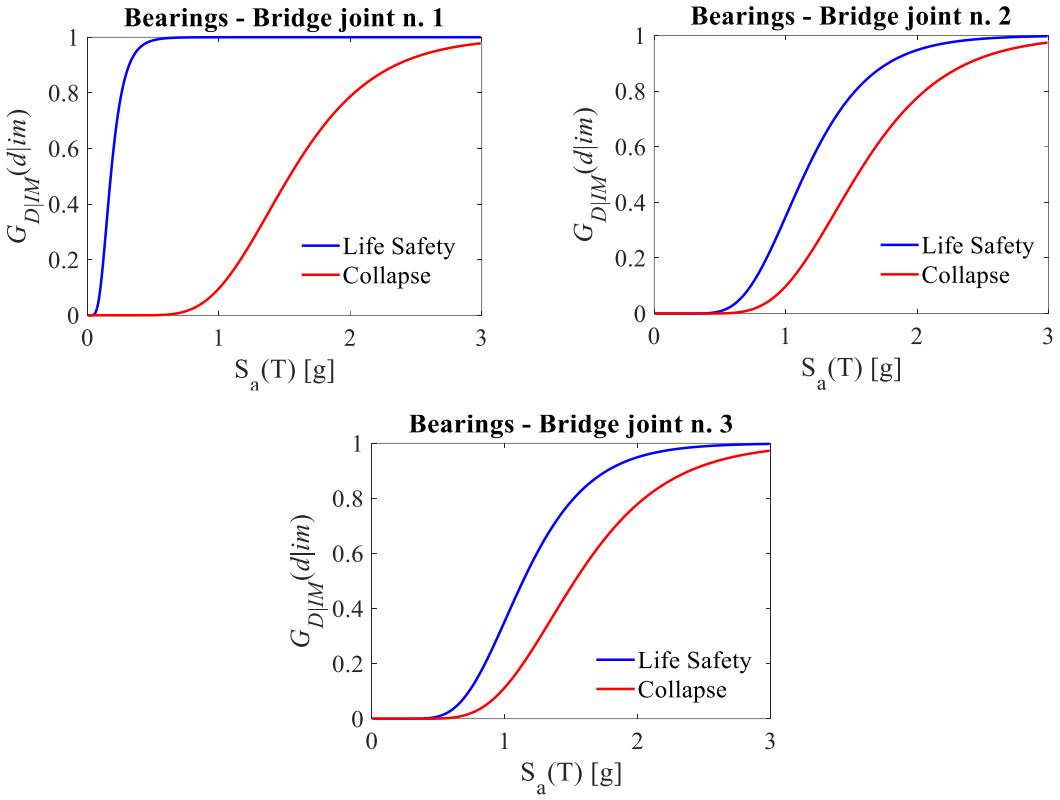

Figure 5.43. Fragility curves at different performance levels for bearings – case study L/B = 8.

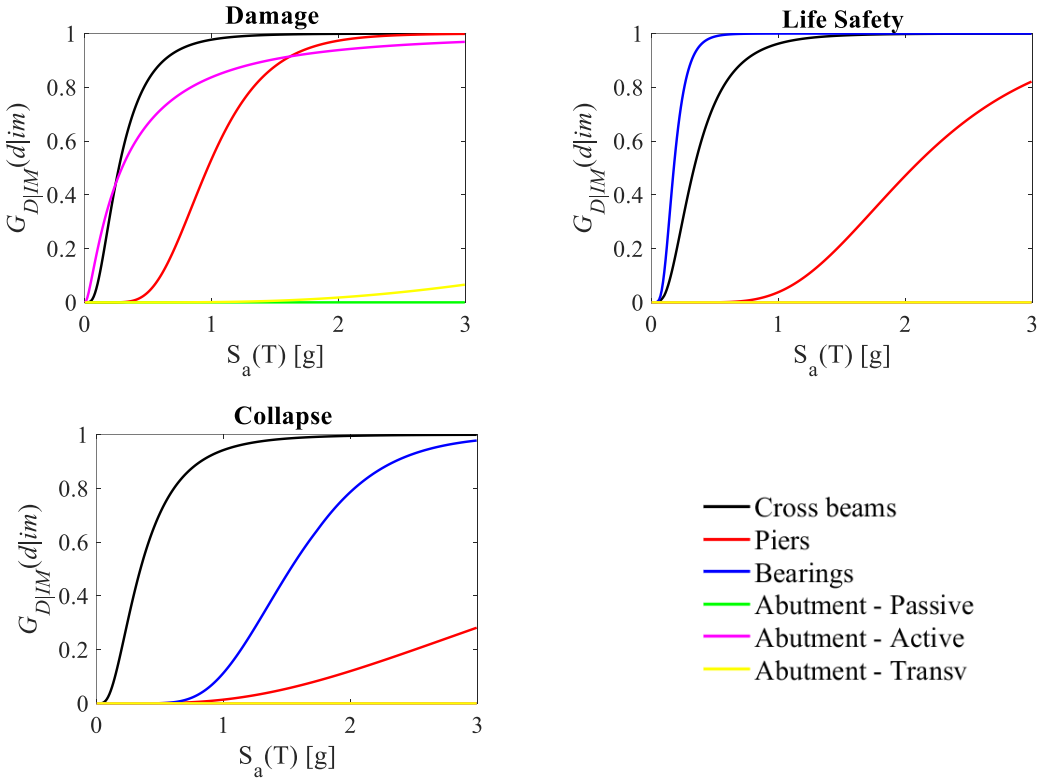

Figure 5.44. Fragility curves at different performance levels for bridge components – case study L/B = 8.

values of *IM* than in case of cross beams. This must be addressed to the occurrence of extensive damage on bearings in the longitudinal direction prior than in the transverse one, as shown in Figure 5.45. It is possible to see that damage on cross beams precedes damage on bearings in the transverse direction, as expected. Finally, Collapse limit state involves cross beams from very low spectral accelerations, while bearings are protected from total failure up to Sa(T) = 1.5g. For what concerns piers, both at Life Safety and Collapse limit state columns show a very low vulnerability level compared to other structural elements, so that the lack of functionality of the entire bridge structure can be attributed to cross beams or bearings only.

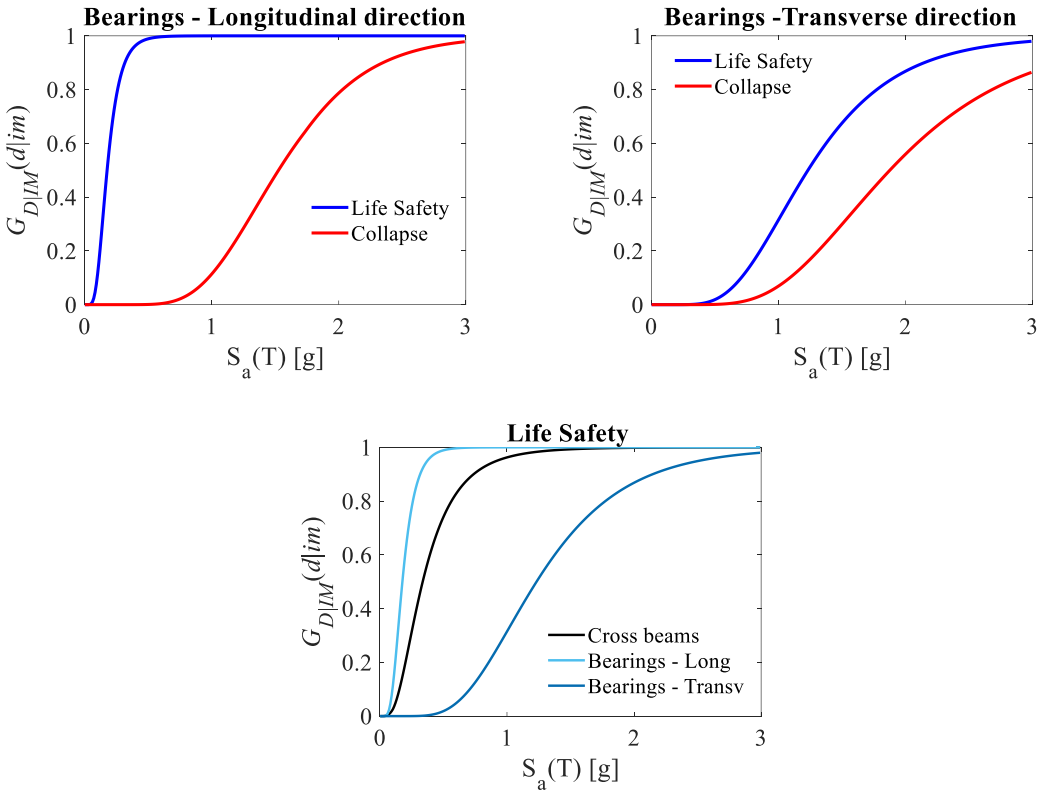

Figure 5.45. Fragility curves for bearings – behaviour in longitudinal and transverse direction and comparison with cross beams at Life Safety limit state – case study L/B = 8.

Figure 5.46 and Figure 5.47 show the combination of damage mechanisms at Damage, Life Safety and Collapse limit state, respectively. In addition to the already introduced nomenclature in the previous Section, the capital letter P is hereinafter used to characterize the fragility contribution of the piers to the global fragility of the bridge.

Figure 5.46 shows the behaviour of the bridge at Damage limit state considering the envelope (black solid line) of fragility curves of different components (see previous Figure 5.44) as representative of the whole structure. It is immediate to see that the global fragility curve is very often obtained from the concomitance of more than one damage mechanisms at the same time: excepting for low spectral accelerations, where the fragility of the system is governed by the damage of the abutments only, there is a strong

correlation in the occurrence of damage for cross beams and abutments (0.2g<Sa(T)<0.6g), and cross beams, piers and abutments, as shown with the light blue line "PCA" (Sa(T)>0.6g). It is also worth noting that no damage occurs on piers independently from other mechanisms.

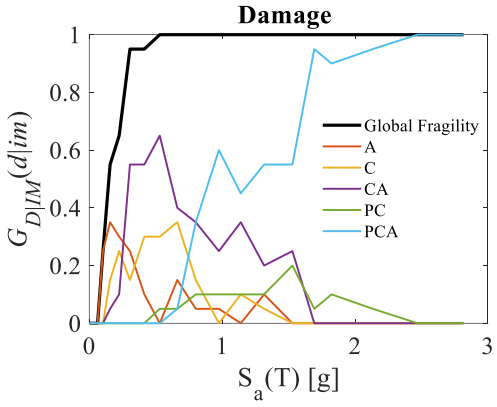

Figure 5.46. Probabilities of occurrence of damage mechanisms at Damage Limit State for combined mechanisms; in black, the global fragility curve as the envelope of the single fragility curves – case study L/B =8.

With an analogous perspective, the Life Safety limit state is examined (Figure 5.47a). In this case, the predominance of the damage on bearings largely influences the global fragility, and it is immediate to notice that there is a rapid passage from the damage of bearings only (orange line) to the concomitant damage of bearings and cross beams (yellow line) for Sa(T)>0.3g. It is possible to affirm that for a wide range of *IM* the Life Safety limit state is governed by damage on bearings and cross beams together. Even in this case, piers sensibly contribute to the global damage only at very high *IM*s (Sa(T)>2.0g).

Finally, Figure 5.47b shows the contribution of the component fragility at Collapse limit state. Up to Sa(T)=1.0g, collapse is observed mainly on cross beams and the overall failure is linked to the superstructure behaviour. From Sa(T)=1.0g to Sa(T)=2.0g, collapse involves also bearings. For Sa(T)>2.0g, the concomitance of failure on both cross beams and bearings is prevalent.

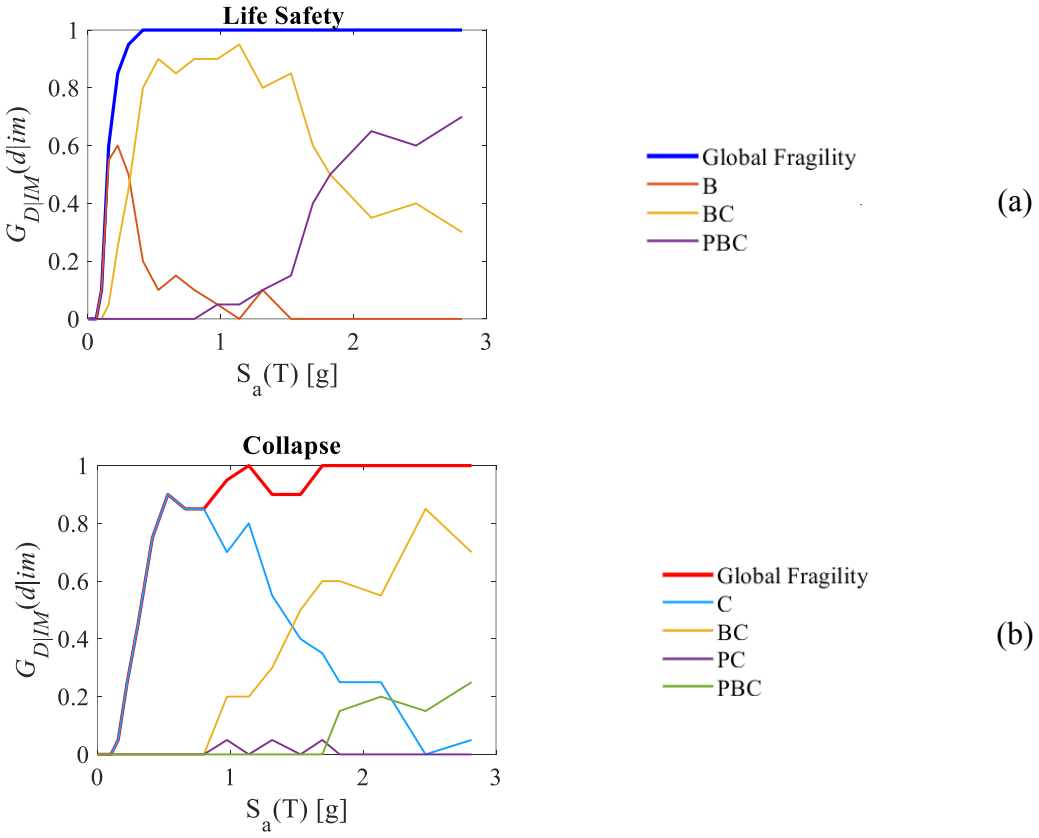

Figure 5.47. Probabilities of occurrence of damage mechanisms at (a) Life Safety limit state and (b) Collapse limit state for combined mechanisms; in (a) blue and (b) red, the global fragility curve as the envelope of the single fragility curves – case study L/B =8.

The analysis of damage extension on the different bridge components follows. Figure 5.48 shows fragility curves for cross beams at the considered limit states considering different percentages of involved elements that experience damage, extensive damage or collapse. In this case study the investigated range of involved elements is set equal to 33%, 66% and 100%, since the total number of cross beams is 3, so that the 33% represents at least 1 cross beams out of 3 and the 66% at least 2 cross beams out of 3. It is worth noting that for all the considered limit states failure on 2 out of 3 cross beams is much more probable than the failure of the total. This is clearly reflected in Figure 5.42, where the highest fragility is associated to the cross beam systems in correspondence of the abutments. The probability of total damage (i.e. 100% of cross beams) at the Damage limit state overcomes the 50% for Sa(T)=1.6g, which corresponds to a seismic event with 5000 years return period, while the damage of 2/3 cross beams has the 50% probability of exceedance for a 60 years return period event. The behaviours at Life Safety and Collapse limit state are quite similar, considering that extreme damage or collapse of at least 2 of the cross beams is very likely to occur ($G_{D|IM}(d|im)$>50%) within Sa(T)=0.5g. In particular, 50% probability of extreme damage and collapse of at least 33% and 66% of cross beams is expected for a seismic action Sa(T)=0.25g (with return period equal to 60 years) and Sa(T)=0.35g (with return period equal to 100 years), respectively.

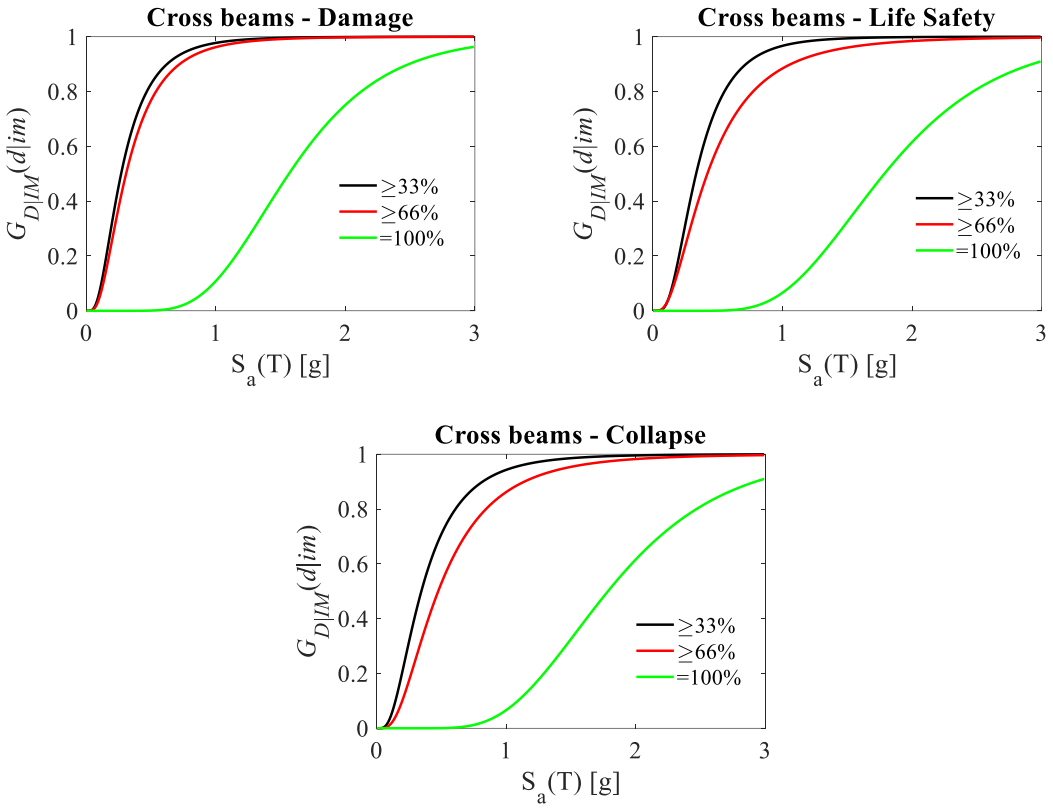

Figure 5.48. Fragility curves at different performance levels for cross beams: increasing percentages of involved elements – case study L/B =8.

For what concerns bearings (Figure 5.49), the higher fragility of the fixed device in correspondence of the left abutment determines a remarkable offset between curves representing failure on at least 1/3 sets of bearings (black solid line) and curves representing failure on more than 1 set of devices (red and green solid lines). Moreover, the red and the green fragility curves almost overlap, attesting that the other 2 bearing sets go to failure contemporary. It can be concluded that the behaviour of the bridge is strongly affected by the rupture of the fixed bearing device.

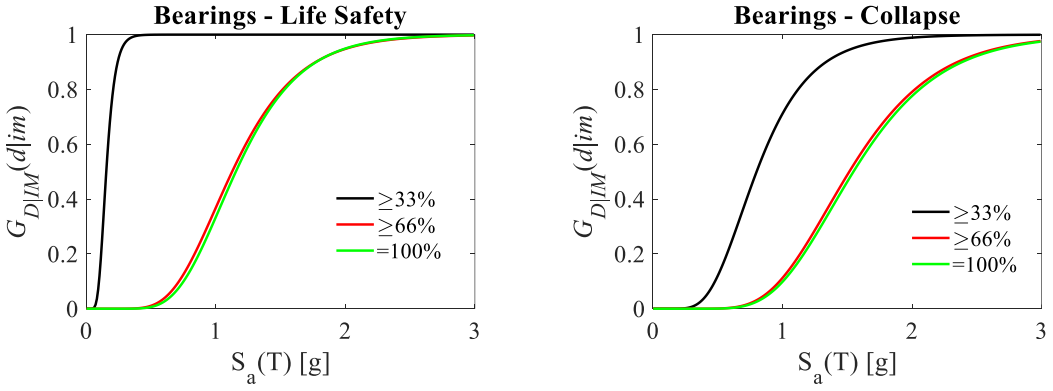

Figure 5.49. Fragility curves at slight damage, extensive damage and ultimate performance levels for bearings: increasing percentages of involved elements (sets of devices) – case study L/B =8.

5.2.1.3 L/B = 20

Fragility curves for bridge components of the case study L/B = 20 are here presented.

Figure 5.50 illustrates the fragility analysis on cross beams, piers, bearings (set of devices) and abutments at Damage, Life Safety and Collapse limit state. Analogously to the case L/B=10, For what concerns abutments, the active response is responsible for a high vulnerability of the component at Damage limit state, while, at more severe limit states, no extensive damage nor ruptures are observed. A slight probability of exceeding the light damage condition is shown from the transverse response, but also in this case extensive damage and collapse are prevented in the considered *IM* range. No damage phenomena are observed relating to the passive response of the abutments. A fragile behaviour can be attributed to cross beams, since curves for Damage, Life Safety and Collapse are very close and almost overlapping. On the contrary, in case of piers and bearings, the plastic resources of the substructures are much higher since Life Safety and Collapse are reached at very different accelerations (more than double for Collapse). It holds that failures on piers are prevented by damage or ruptures on the superstructure and the bearings. Collapse of the bearings may occur at medium-high spectral accelerations (50% probability of collapse is reached on bearings at Sa(T) = 1.5g), while $G_{D|IM}(d|im)$ never reaches 50% in the investigated *IM* range.

The fragility of cross beams along the bridge is analysed in Figure 5.51. A noticeable difference between the behaviour of the end cross beams and the central ones can be highlighted. The end cross beams result more vulnerable than the others, since damage, extreme damage or collapse may occur prior than damage in the central joints. This is coherent with the expected behaviour of the end cross sections for the adopted static scheme. For all the bridge sections, the occurrence of Collapse is immediate after reaching the Life Safety limit state, and no wide range is left between the elastic and the plastic behaviour. These aspects may compromise a good behaviour of the superstructure in case of even medium-low seismic intensities (Sa(T)<1.0g).

Figure 5.52 shows the fragility curves of bearings at different bridges sections. The fragility curves of bearings are comparable each other except for the case of bearings on the left abutment: here, the fixed behaviour in the longitudinal direction implies a concentration of forces that brings the rapid passage to the extensive damage condition within low *IM* levels (100% probability of severe damage is reached at 0.35g, i.e. for a 100 years return period earthquake).

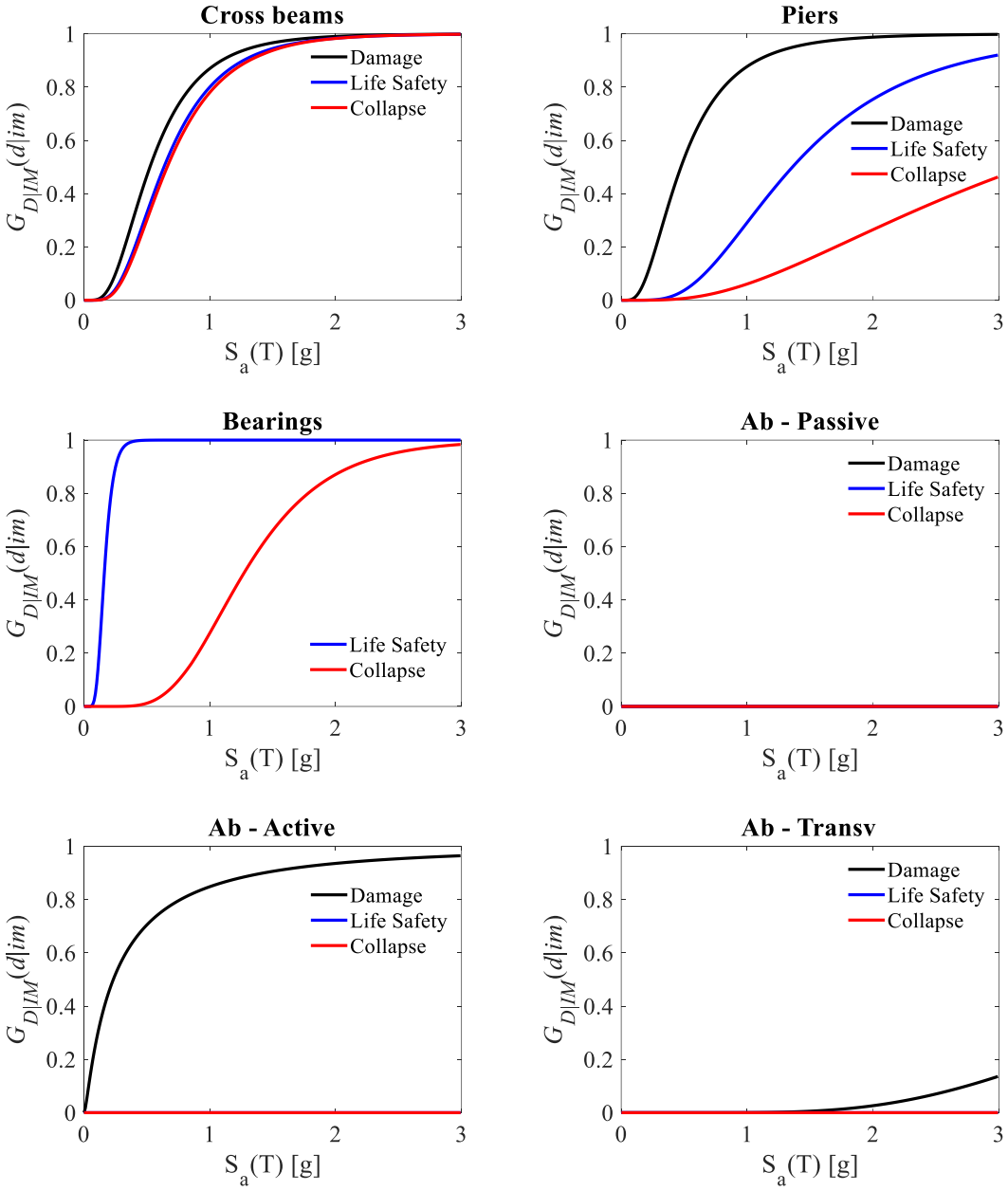

Figure 5.50. Fragility curves at different performance levels for bridge components – case study L/B = 20.

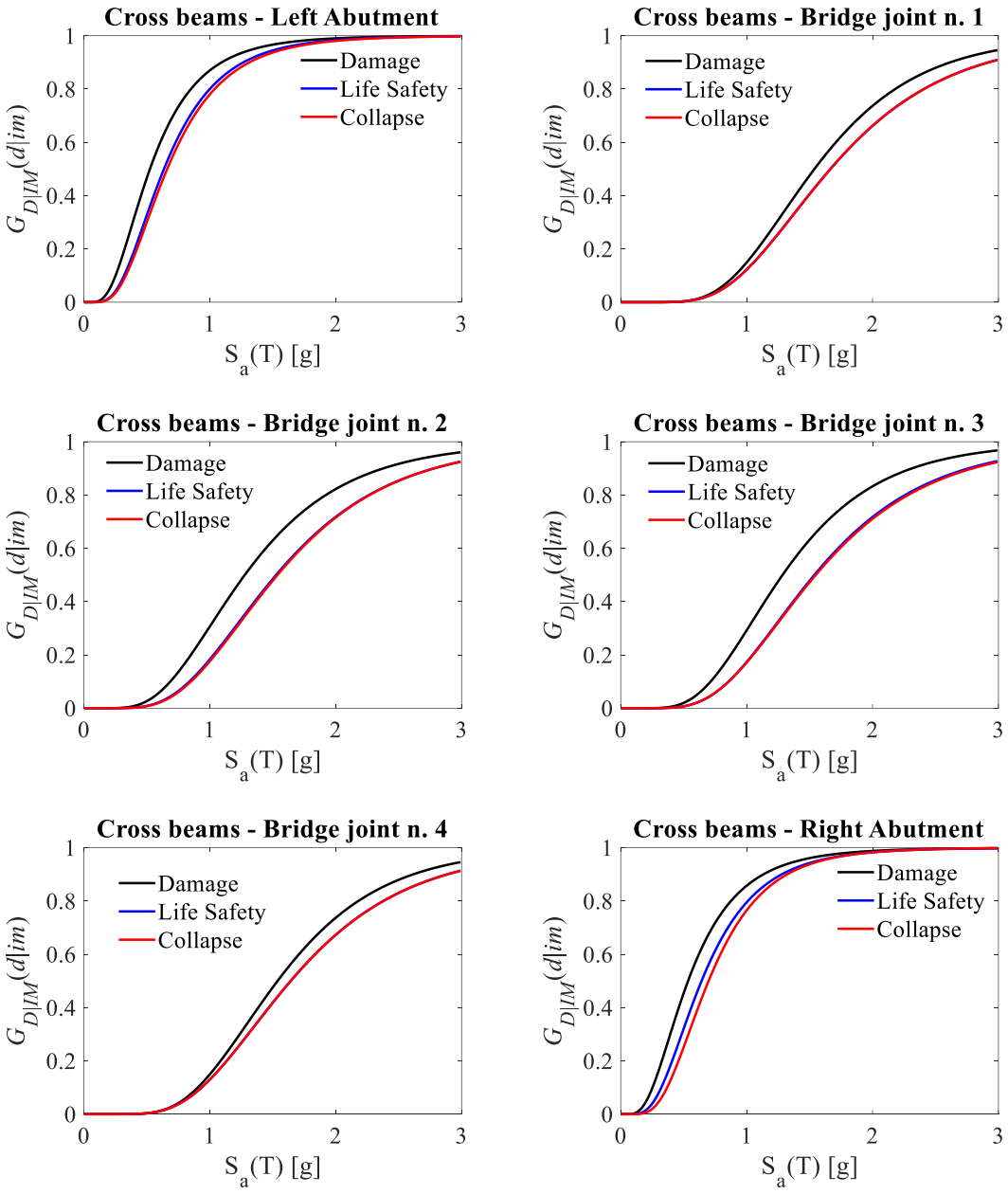

Figure 5.51. Fragility curves at different performance levels for cross-beams – case study L/B = 20.

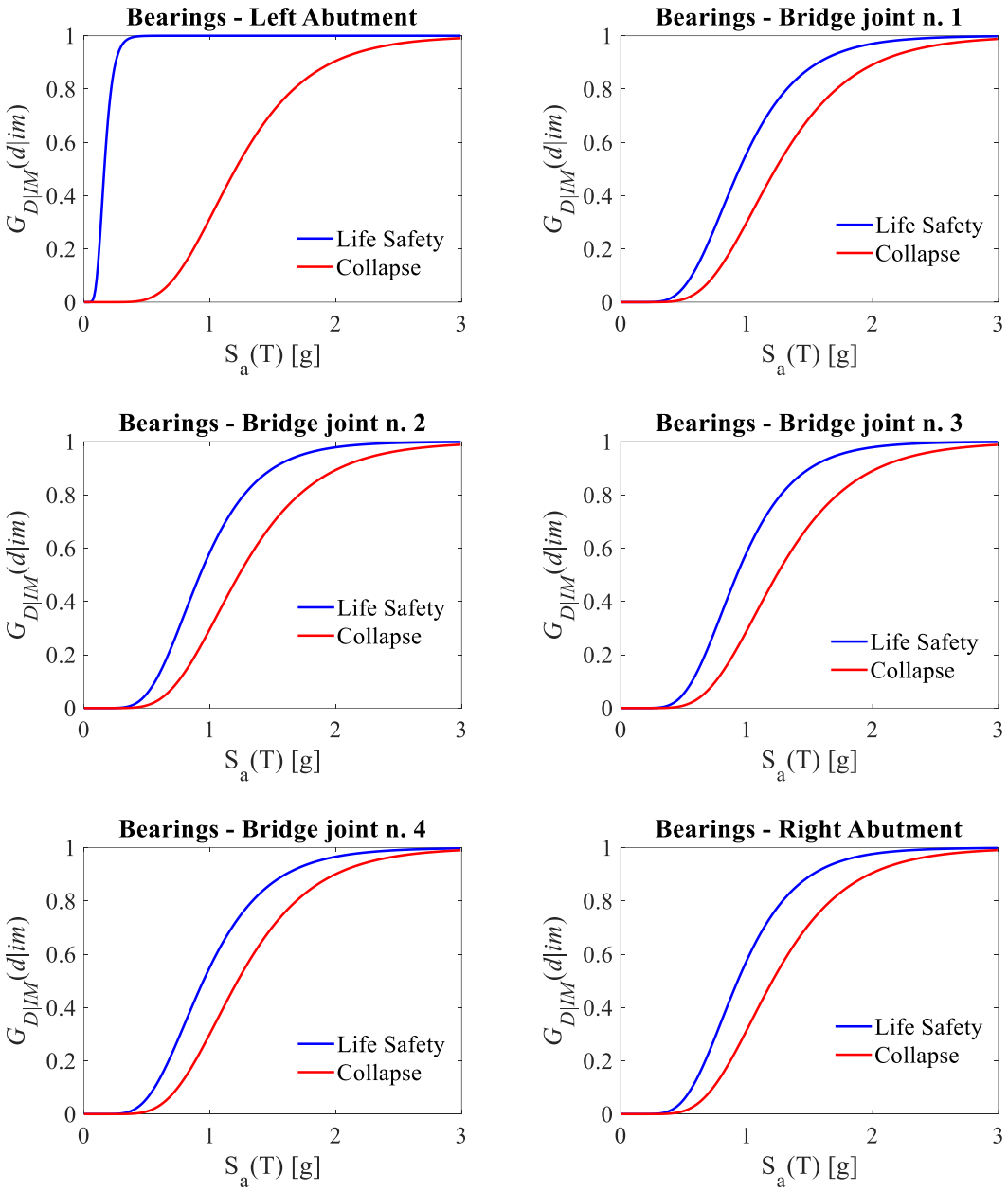

Figure 5.52. Fragility curves at different performance levels for bearings – case study L/B = 20.

Piers are examined in Figure 5.53. A higher fragility is observed on the central piers, where the same exceedance probability is associated to 1.5-2 times the spectral acceleration that causes failure on the external piers. Differently from the case study L/B=8, the vulnerability of piers at Damage limit state is comparable with that of cross beams, while a good performance remains at Life Safety and Collapse limit state, where piers are the less vulnerable components of the bridge. The higher vulnerability at Damage limit state may be explained considering that the involved structural masses in the seismic analysis are more than doubled (5 spans vs 2 spans for L/B=8), so that inertial forces are differently redistributed among structural elements in the elastic field.

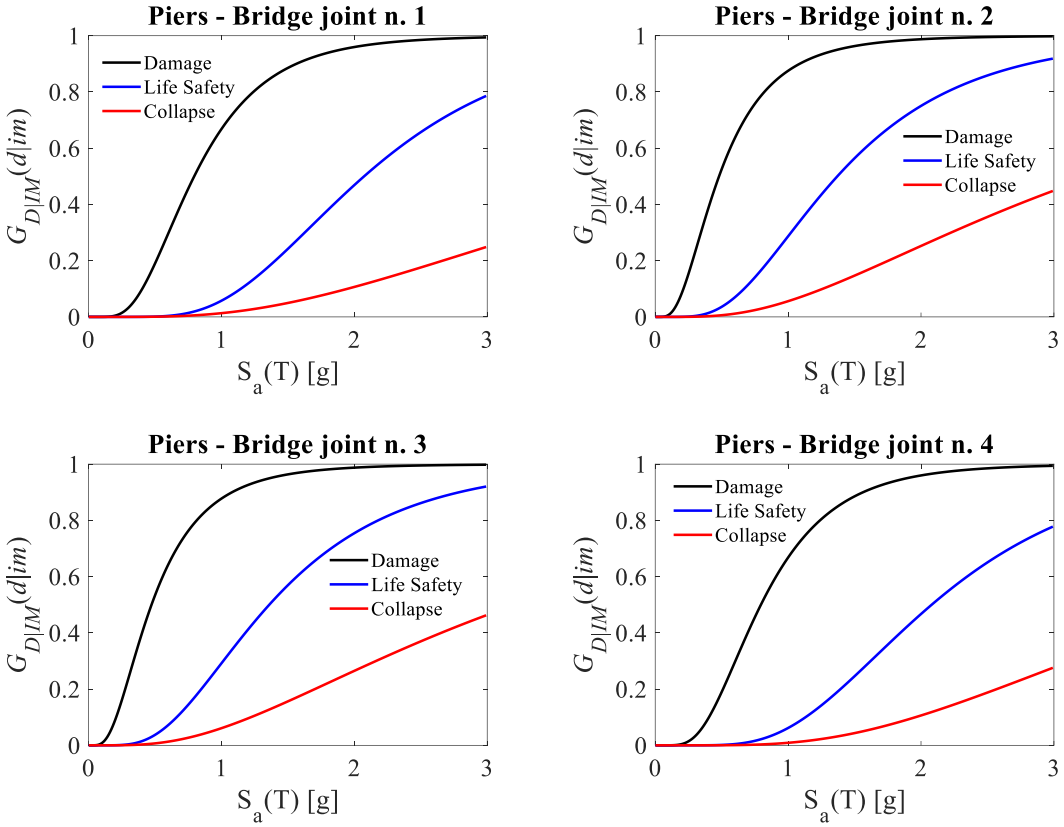

Figure 5.53. Fragility curves at different performance levels for piers – case study L/B = 20.

Figure 5.54 offers a comparison between fragility curves of different bridge components at the three examined performance levels. As already observed, the active response of abutments determines the higher fragility of the bridge system, followed by piers and cross beams to the same extent. Life Safety is primarily reached by bearings, where the longitudinal response determines a high vulnerability of the system. In fact, it is worth remembering that the bearings' fragility curve is obtained as the envelope of the fragilities in transverse and longitudinal direction, and a notable difference between them can be observed in Figure 5.55, where it is also possible to appreciate that failure on bearings for transverse seismic action occurs with a low probability of exceeding damage on the correspondent cross beam system, as expected. Cross beams and piers follow; more precisely, at Life Safety limit state, 50% damage on cross beams and piers is reached for Sa(T) = 0.6g and Sa(T) = 1.3g, respectively, while at Collapse limit state cross beams are sensibly more fragile than piers as well as other structural components, since the associated probabilities of exceedance are more than doubled. Finally, no appreciable failure is expected on abutments in the investigated *IM* range at Life Safety or Collapse limit state. Since piers have the lowest degree of fragility among the components, it can be concluded that the performance of the bridge is mainly governed by abutments in case of damage and by bearings at higher performance levels. Nevertheless, damage or collapse on the superstructure must not be neglected, since the consequences related to

the failure of cross beams may have a significative impact on the functionality of the bridge, as commented in the following Chapter 6.

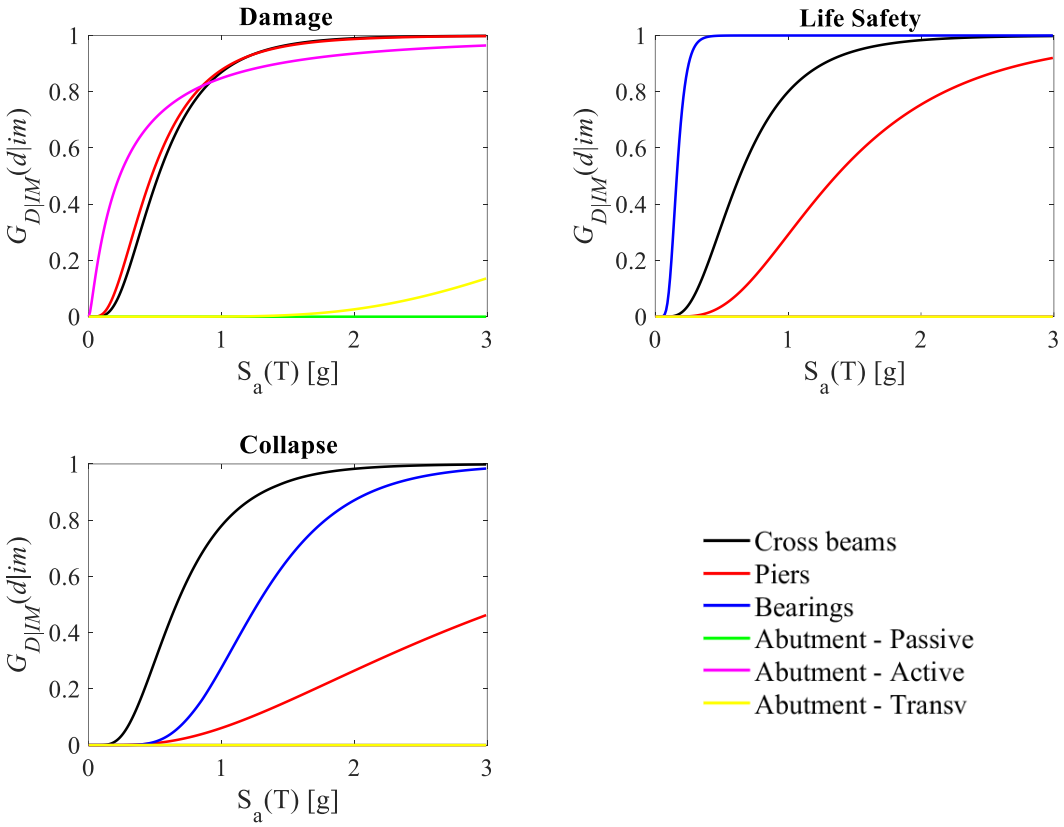

Figure 5.54. Fragility curves at different performance levels for bridge components – case study L/B = 20.

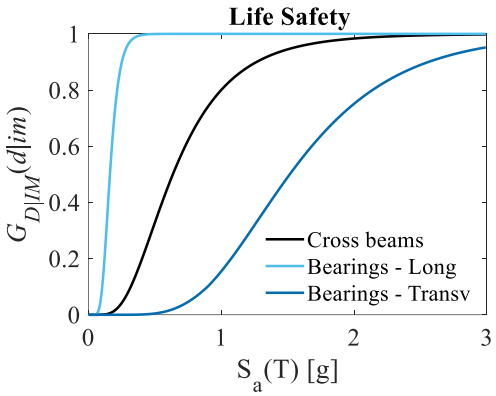

Figure 5.55. Fragility curves for bearings – behaviour in longitudinal and transverse direction and comparison with cross beams at Life Safety limit state – case study L/B = 20.

In order to analyse the impact of different failure modes on the fragility of the overall system, three plots are proposed in Figure 5.56a, Figure 5.56b and Figure 5.57, for Damage, Life Safety and Collapse limit states, respectively.

With regard to Damage limit state (Figure 5.56a), the overall fragility counts two main contributions: for low spectral accelerations (Sa(T)<0.5g), the damage of the entire structure can be identified with the damage of the abutments only (in active response, as already observed). From medium-high seismic intensities (Sa(T)>0.5g), damage on the abutments (A) is mainly correlated to the damage on the piers (P) and cross beams (C). It is interesting to notice that a contemporary damage on piers and cross beams is expected and characterizes the global fragility curve for most part of the investigated *IM* range.

The fragility at Life Safety limit state (Figure 5.56b) counts the contribution of three components: bearings, for low values of *IM* (Sa(T)<0.5g); bearings and cross beams (0.5g<Sa(T)<1.2g); bearings, cross beams and piers for high values of *IM* (Sa(T)>1.2g). Even in this case, damage on cross beams and piers only is always prevented. Finally, Figure 5.57 shows the contribution of the component fragility at Collapse limit state. Up to Sa(T)=1.0g, collapse is observed mainly on cross beams and the overall failure is linked to the superstructure behaviour. From Sa(T)=1.0g to Sa(T)=2.5g, collapse involves also bearings. The contribution of bearings and piers is scarce if the fragility is evaluated on these components alone. The influence of the fragility of piers can be appreciated for very high spectral accelerations (Sa(T)>2.5g).

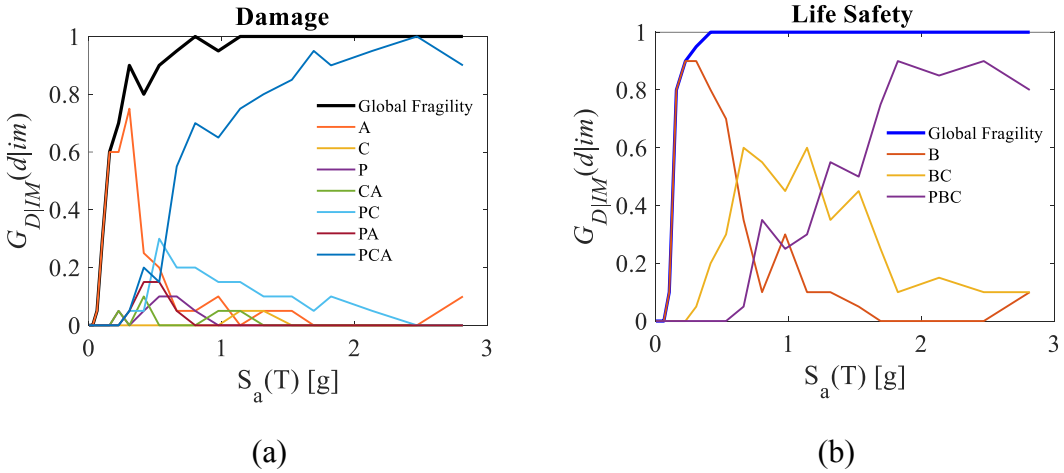

Figure 5.56. Probabilities of occurrence of (a) Damage limit state and (b) Life Safety limit state for combined mechanisms; in black and blue, the global fragility curve – case study L/B =20.

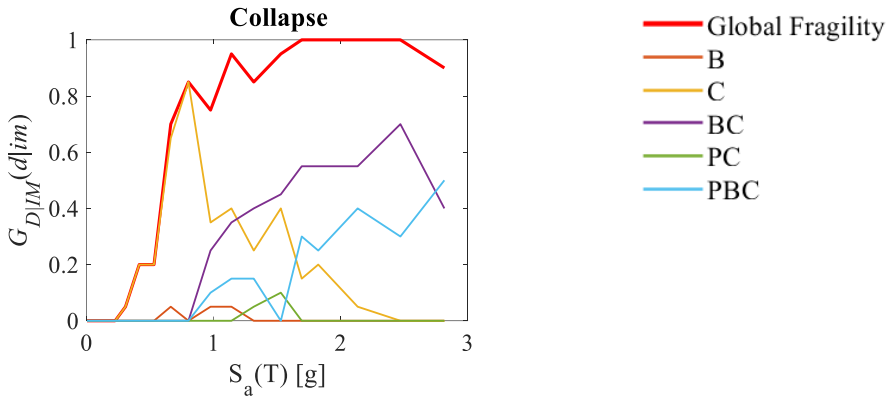

Figure 5.57. Probabilities of occurrence of damage mechanisms at Collapse Limit State; in blue, the global fragility curve– case study L/B =20.

The analysis of damage extension on the different bridge components follows. Figure 5.58 shows fragility curves for cross beams at the considered limit states considering different percentages of involved elements that experience damage, extensive damage or collapse. In this case study, the investigated range of involved elements is set equal to 25%, 50%, 75% and 100%. It is worth noting that for all the considered limit states failure on at least 25% of the cross beams (i.e. 1 out of 6) is much more probable than the failure of the 100%. This is clearly reflected in the classical representation of fragility shown in Figure 5.51, where the highest fragility is associated to the cross beam systems in correspondence of the abutments. It is also clear that once at least 75% of elements (i.e. 4 out of 6) are damaged or collapsed, the failure of all the cross beams is immediately reached (the red curve overlaps the green one). The probability of total damage at the Damage limit state overcomes the 50% for Sa(T)=1.6g, which corresponds to a seismic event with 5000 years return period, while the damage of 50% of cross beams has the 50% probability of occurrence for a 2850 years return period event. The behaviours at Life Safety and Collapse limit state are quite similar, considering that extreme damage or collapse of at least 25% of the cross beams is very likely to occur ($G_{D|IM}(d|im)$>50%) within Sa(T)=0.5g, while it becomes quite probable that at least 50% and 100% of the total fails for Sa(T)>1.0g and Sa(T)>1.5g, respectively.

For what concerns bearings (Figure 5.59), the higher fragility of the fixed device in correspondence of the left abutment determines a remarkable offset between curves representing failure on at least 1/6 sets of bearings (black solid line) and curves representing failure on more than 1 set of devices (red and green solid lines). Moreover, the red and the green fragility curves almost overlap, attesting that the remaining bearing sets go to failure contemporary. It can be concluded that the behaviour of the bridge is strongly affected by the rupture of the fixed device.

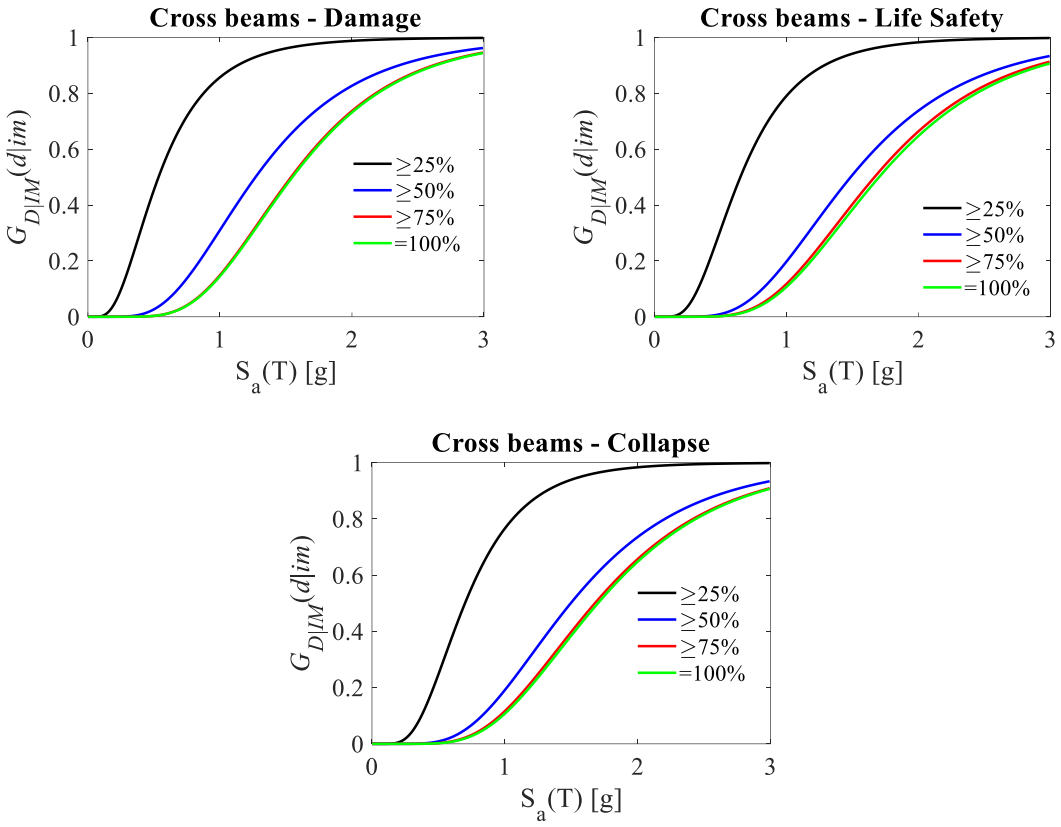

Figure 5.58. Fragility curves at different performance levels for cross beams: increasing percentages of involved elements – case study L/B =20.

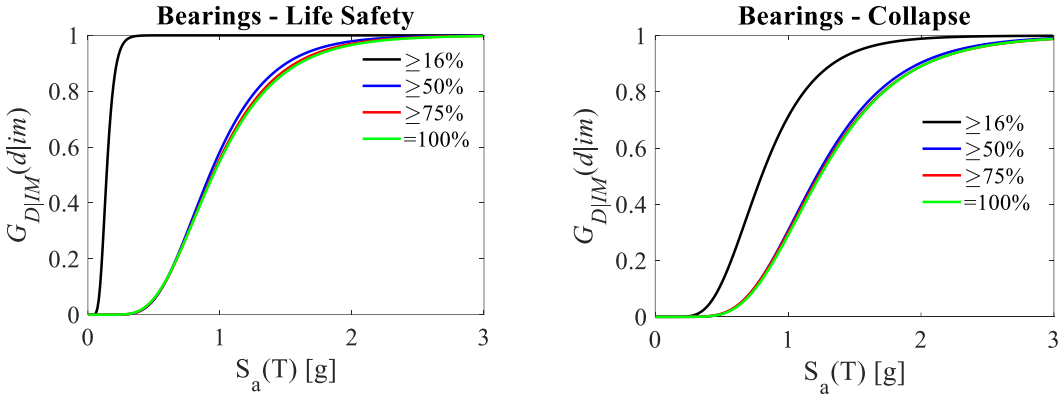

Figure 5.59. Fragility curves at slight damage, extensive damage and ultimate performance levels for bearings: increasing percentages of involved elements (sets of devices) – case study L/B =20.

Finally, looking at the fragility of piers in Figure 5.60, 2 out of 4 piers go failure contemporary at both Damage and Life Safety limit state. Then, the extension of damage up to 75% and 100% of the total determines an offset of the fragility curves on double values of the spectral acceleration. In case of Collapse, the probability that failure involves more than 1 element never overcomes 50% in the investigated *IM* domain.

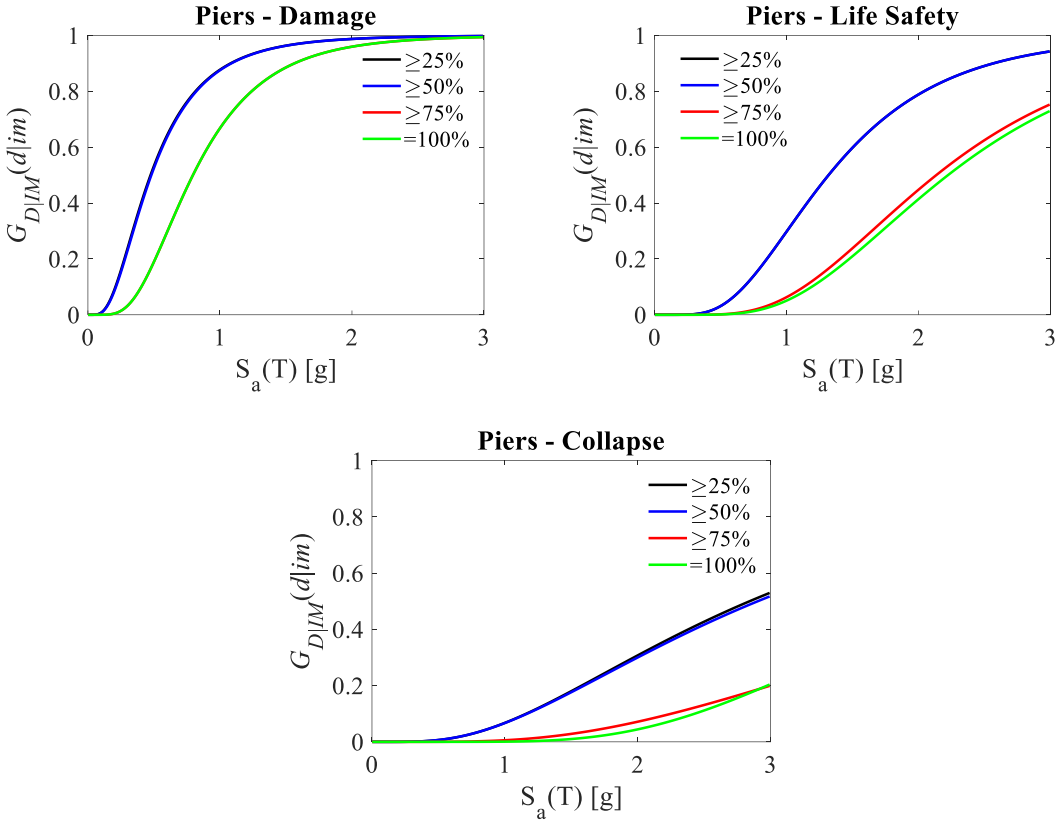

Figure 5.60. Fragility curves at different performance levels for piers: increasing percentages of involved elements – case study L/B =20.

For this case study, the analysis of damage extension can be specialized in case of cross beams, bearings and piers, since each of these components counts more than one element. The damage extension can be evaluated not only basing on a minimum number of elements going to failure, but also looking at different ranges on the total number of involved elements. This approach allows to identify the values of *IM* corresponding to a meaningful number of damaged or collapsed elements, an information that reveals useful for the analysis of potential direct and indirect consequences. Analogously to the already examined RCLS bridges, probability curves related to various percentage of involved elements are built and compared to the probability of occurrence of damage or collapse on one single element of the family, drawn with the magenta solid line.

Extension damage on cross beams is analysed through Figure 5.61. In case of Damage limit state, it is clear that there is a distinct passage to the plastic deformation from 2 (blue line) to all the cross beams (cyan line) at Sa(T)=1.5g. Only few cases present a progressive plasticization involving more than 50% of elements (red line). An analogous comment can be made on Life Safety and Collapse limit states, where the rapid transition from the failure of only 2 elements to the total is observed at Sa(T)=1.75g.

In case of bearings (Figure 5.62), the rupture of the fixed device on the left abutment governs the fragility of the family at Life Safety limit state up to Sa(T)=1.0g, where it

becomes very likely that the rupture of all the remaining devices occurs. At Collapse limit state, it is possible to conclude that the devices go to collapse simultaneously.

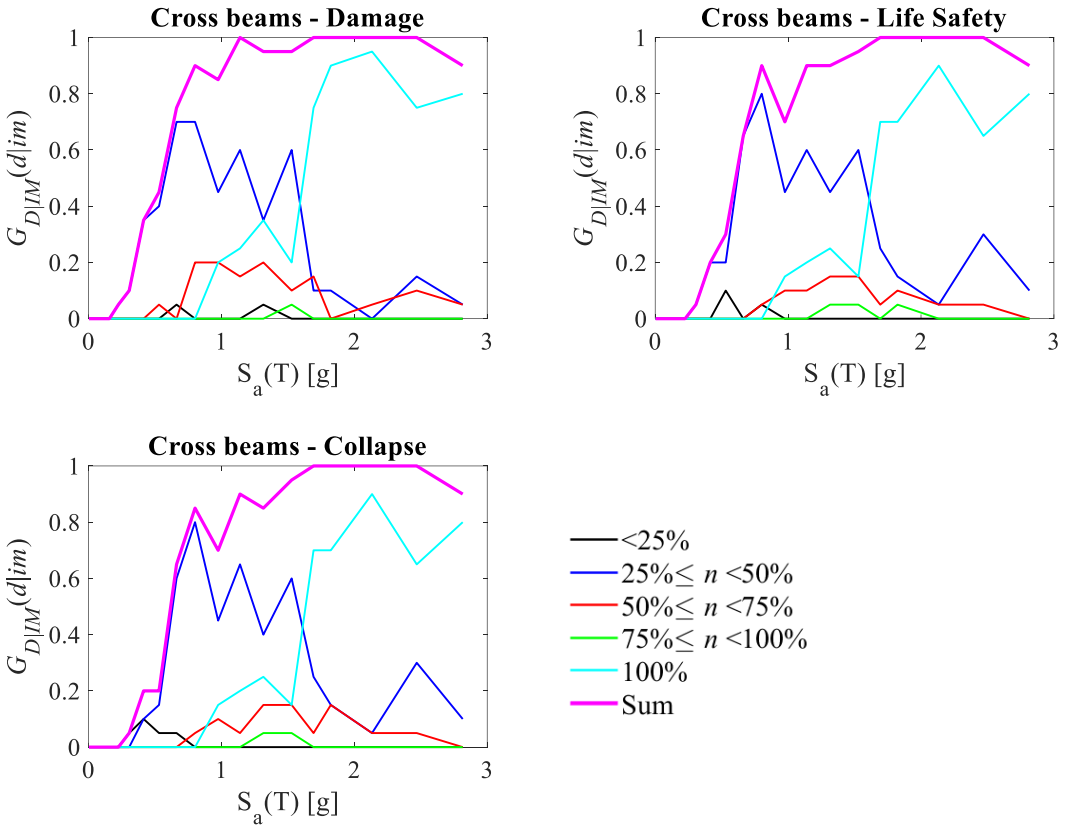

Figure 5.61. Probabilities of occurrence of damage mechanisms for different percentages of considered cross-beams involved; in magenta, the sum of probabilities, being the magenta curve the envelope of the fragility curves (that means "at least one cross-beam") – case study L/B =20.

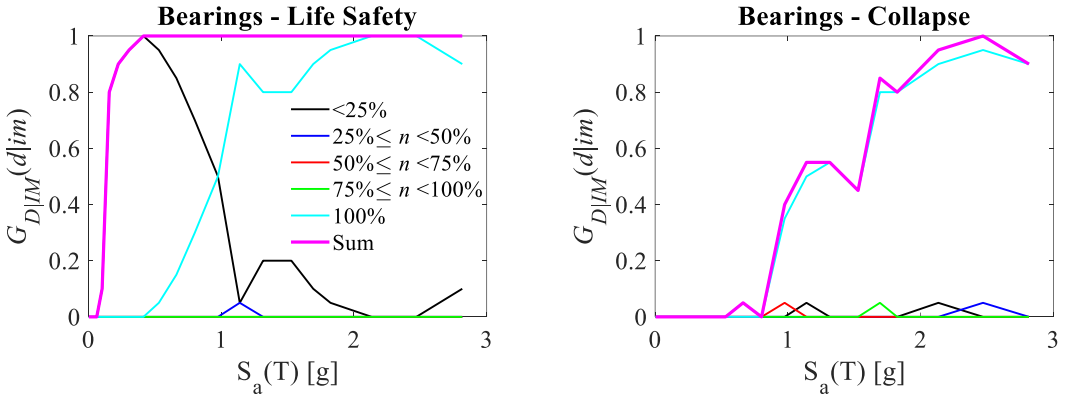

Figure 5.62. Probabilities of occurrence for different percentages of involved bearing devices – case study L/B =20.

In case of piers (Figure 5.63), the evolution of damage in both Damage and Life Safety limit state emerges as the direct passage from the damage on half of the piers to all the piers. No intermediate condition is appreciable. The evolution can be recognized with a

significative percentage (>50%) at Sa(T)=0.7g and Sa(T)=2.2g for Damage and Life Safety limit state, respectively. This means that all the piers are damaged for seismic actions with return period higher than 500 and 30,000 years. At Collapse limit state, the condition most likely to occur is associated to the failure of half of the piers, although the probability of collapse stood at low values (less than 50%) in all the considered *IM* domain.

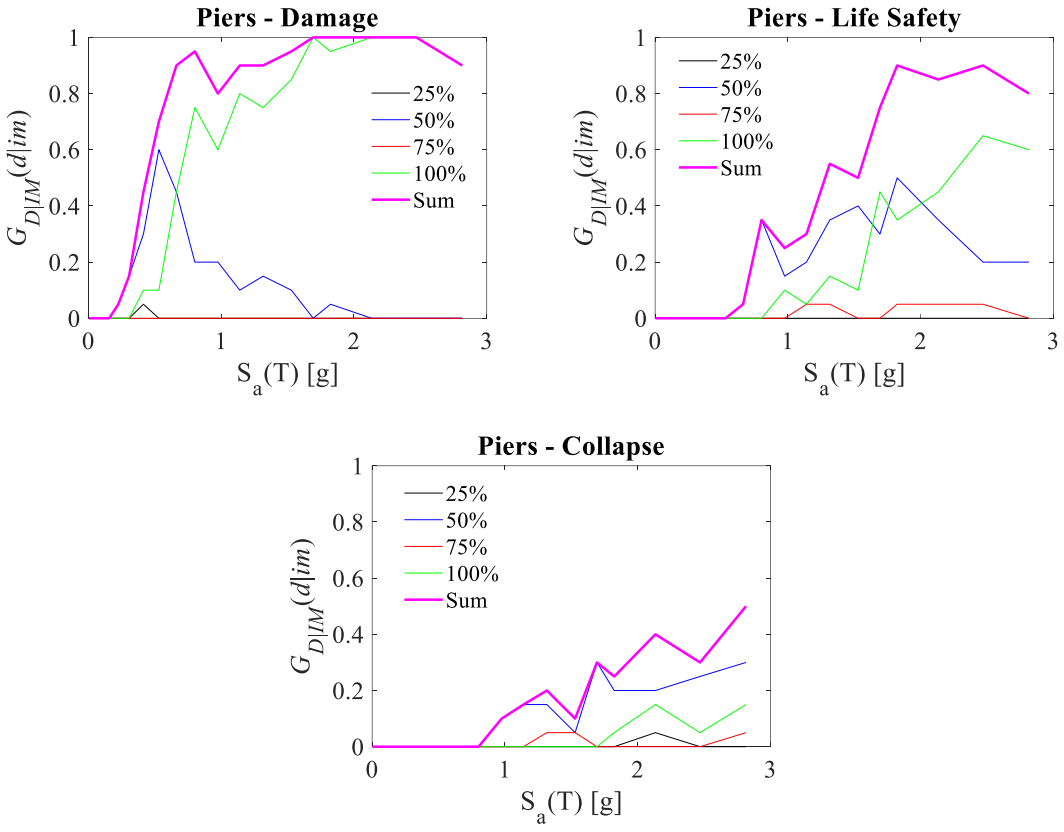

Figure 5.63. Probabilities of occurrence for different percentages of involved piers – case study L/B =20.

5.2.1.4 L/B = 4 vs L/B = 8 vs L/B = 20

This section provides some comments on the comparison between the fragility results of SCC bridges for the considered case studies. Fragility curves are illustrated with reference to the behaviour of the bridge components at the examined limit states in the following Figure 5.64, Figure 5.65, Figure 5.66 and Figure 5.67.

Figure 5.64 shows the comparison between fragility curves for cross beams at different limit states. A focus on the *IM* range 0<Sa(T)≤1.5g is made in order to investigate the behaviour of cross beams where the evolution of damage is expected. It is possible to recognize a similarity between the case studies L/B=4 and L/B=8, in which the vulnerability of the component is higher than that observed in case of L/B=20. Differences tend to decrease as the severity of damage increases, even if a clear offset of

the L/B=20 fragility curve is still appreciable. This information contributes to outline the different behaviour between short and long bridges.

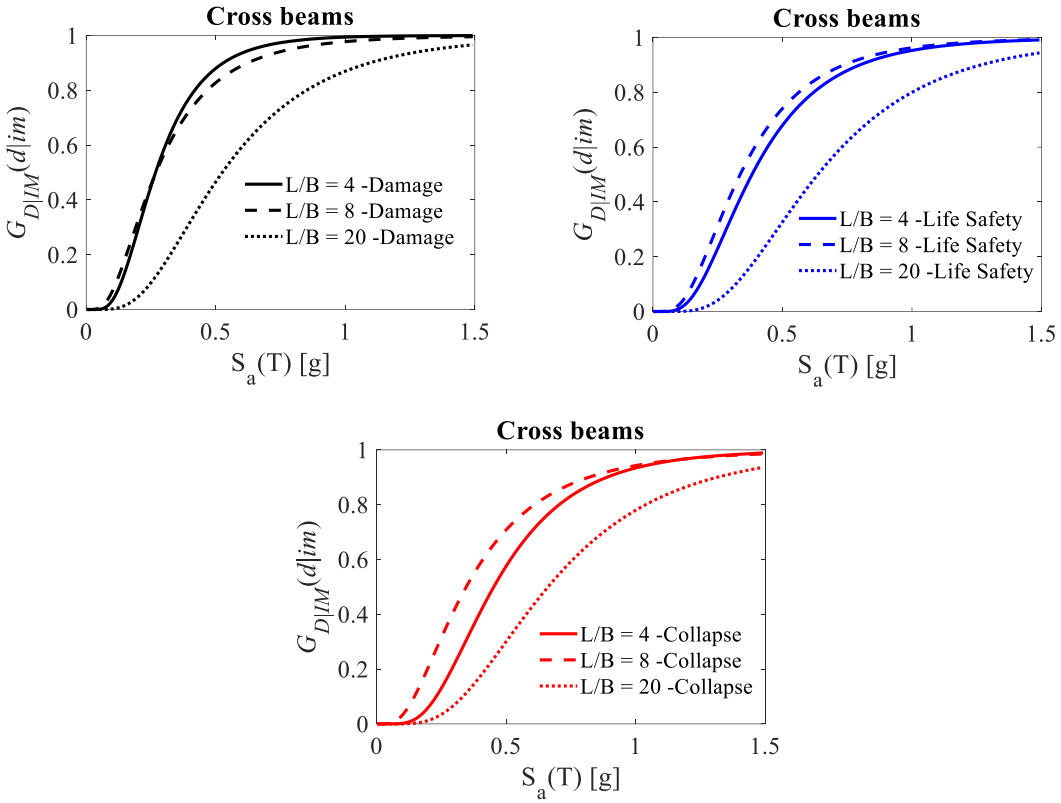

Figure 5.64. Comparison of fragility curves for cross beams of SCC bridges at different limit states.

The fragility of abutments is commented referring to the Damage limit state only (Figure 5.65), since no appreciable failures are observed for more severe performance thresholds. It is possible to see that the behaviour of abutments is similar among the case studies up to Sa(T)=0.3g; then, a higher vulnerability is associated to the configuration L/B=4. This can be related to the absence of piers, so that shear forces are resisted only by bearings and abutments, and transferred from the superstructure through the cross beams, which have a higher vulnerability too.

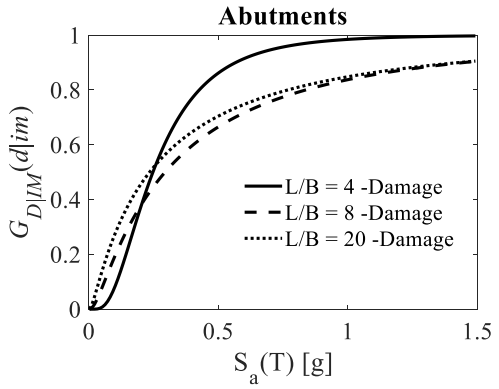

Figure 5.65. Comparison of fragility curves for abutments of SCC bridges at Damage limit state.

Concerning bearings (Figure 5.66), the longest the bridge the higher the fragility of the component. This can be explained by the higher amount of shear forces in the longitudinal direction resisted by the fixed devices (on the left abutment). In case of single span bridges, the spectral accelerations on which the curves are built are from two to three times the corresponding ones in case of multi-span configurations. Finally, the analysis of piers is carried out comparing the case study L/B=8 and L/B=20 (Figure 5.67). For all the considered limit states, piers belonging to the longer bridge present a higher fragility. This information adds to the characterization of the differences between the performance of short and long bridges.

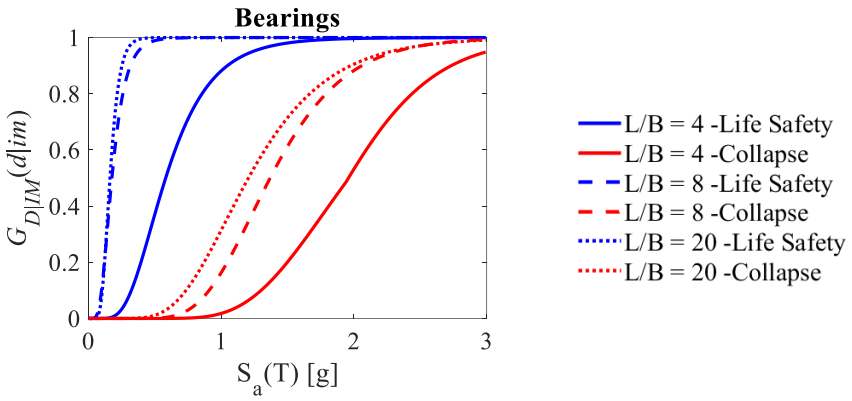

Figure 5.66. Comparison of fragility curves for bearings of SCC bridges at Life Safety and Collapse limit state.

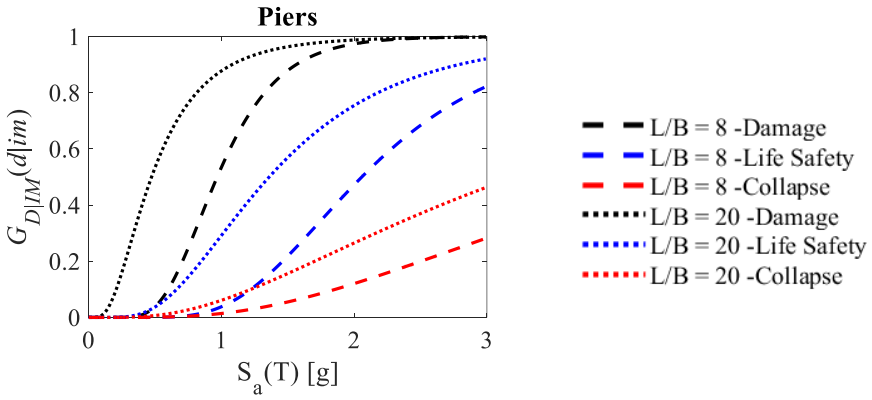

Figure 5.67. Comparison of fragility curves for piers of SCC bridges at different limit states.

5.2.2 Effects of compliant base and degradation

Analyses with different ageing conditions and the presence of compliance at foundation level under the piers are performed to highlight the degree of reliability of the models with design characteristics and fixed base in the face of an existing bridge structure. The following Figure 5.68 and Figure 5.69 provide a comparison between fragility curves for L/B=8 and L/B=20 at different ageing and structural conditions. Results of the analysis on the case study L/B=4 revealed that effects of ageing are of negligible importance for the considered structural configuration, in which ageing could be applied only to the

resisting shear force of bearings in the fixed directions. It is worth noting that, as already observed, as the total length of the bridge increases, the vulnerability of bearing devices increases as well, so it can be assumed that major influence of ageing on the steel component that determine the resistance of the bearings could have a higher impact on longer spans and multi-span configurations.

Looking at the case studies L/B=8 and L/B=20, it is evident that effects of both ageing and SSI are mostly evident on piers, where they are explicitly modelled. The response of other structural components is slightly affected by the behaviour of piers. Higher influence is observed on the cross beams, even if it is possible to consider that fixed base results are representative of the component behaviour. For what concerns piers, ageing (dot and dashed lines) changes the vulnerability of the structural component largely, especially at Life Safety and Collapse limit states. In particular, starting from the fixed base condition (blue and red solid lines), the 50% of overcoming damage or failure corresponds to lowering values of spectral acceleration up to almost half of the initial value.

More in detail, for L/B=8 (Figure 5.68), in case of Life Safety limit state, fragility curves change so that 50% probability of damage goes from Sa(T)=2.0g at design condition to Sa(T)=1.75g for 25 years ageing and Sa(T)=1.5g for 50 years ageing, that corresponds to a decrease of the frequency of occurrence of the corresponding earthquake event from 25'000 to 10'000 years return period. In case of Collapse, the influence of ageing is even higher, since 50% probability is now overcome in the IM domain, at Sa(T)=2.0g. For L/B=20 (Figure 5.69), major differences are noticeable at Collapse limit state, for which the probability of failure in the *IM* range 1.0g < Sa(T) < 2.0g is doubled and for Sa(T)>2.0g more than doubled.

The presence of compliant base furtherly increases the vulnerability of piers, since higher displacements are expected in case of flexible foundation. This influence is increasingly evident as the performance threshold is more severe in both the structural configurations. For L/B=8, in case of Life Safety and Collapse (light blue and orange curves), results for the design condition with fixed base almost overlap the 50-years-ageing condition with compliant base. Ageing on the compliant base configurations implies a reduction of the spectral accelerations where severe damage or collapse occurs up to 20%. A similar approach can be used to analyse results for L/B=20, where the probability of overcoming severe damage or total failure is increased by 10%. Although severe damage on piers is expected at very high values of *IM*, when all the other structural components have already experienced damage or collapse and the overall capacity of the bridge is compromised, the changed fragility of piers may largely affect the post-earthquake scenario for what concerns potential indirect consequences, as it will be shown in next Chapter 6.

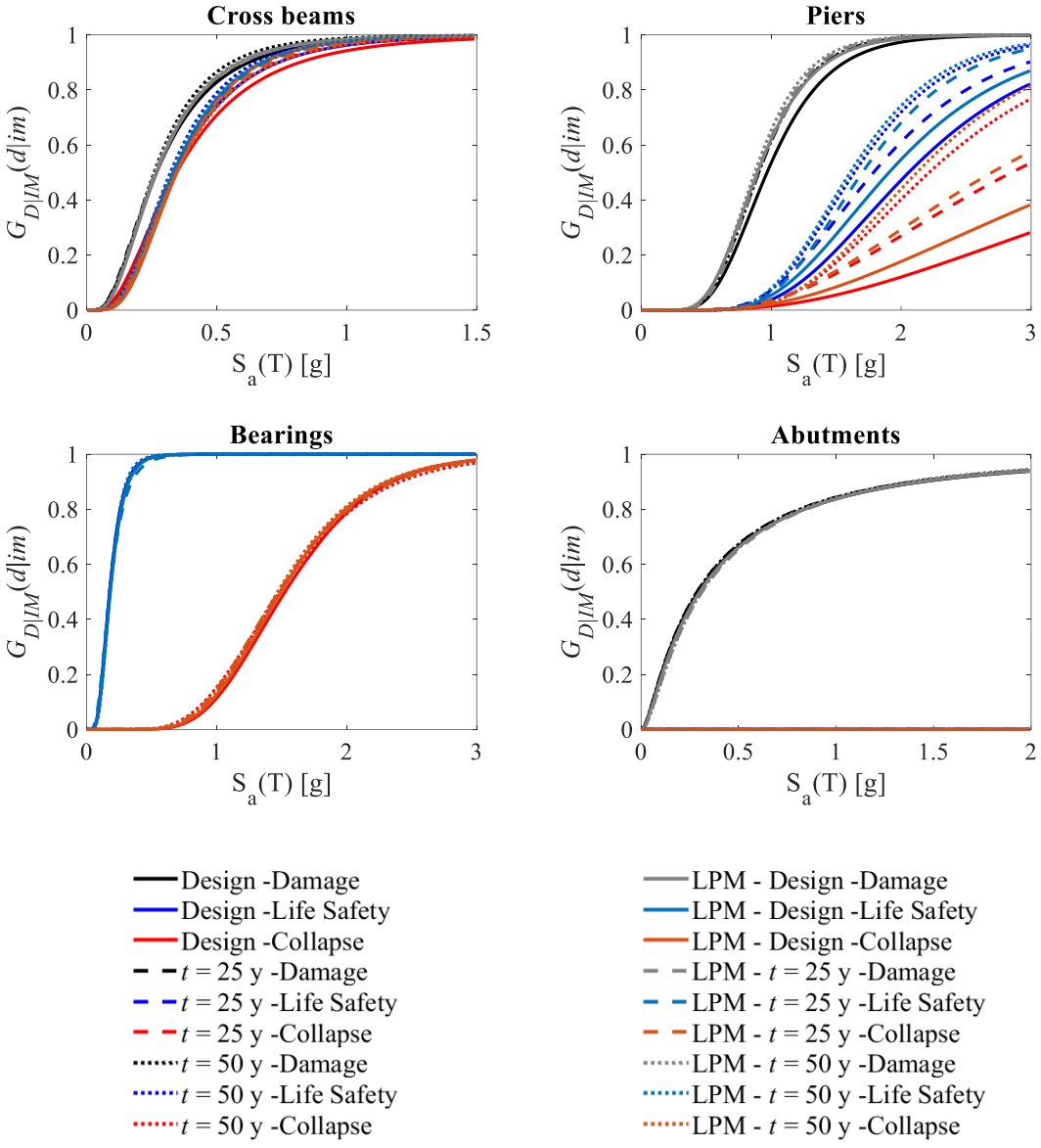

Figure 5.68. Comparison of fragility curves for different ageing conditions and compliance of the foundation system – case study L/B = 8.

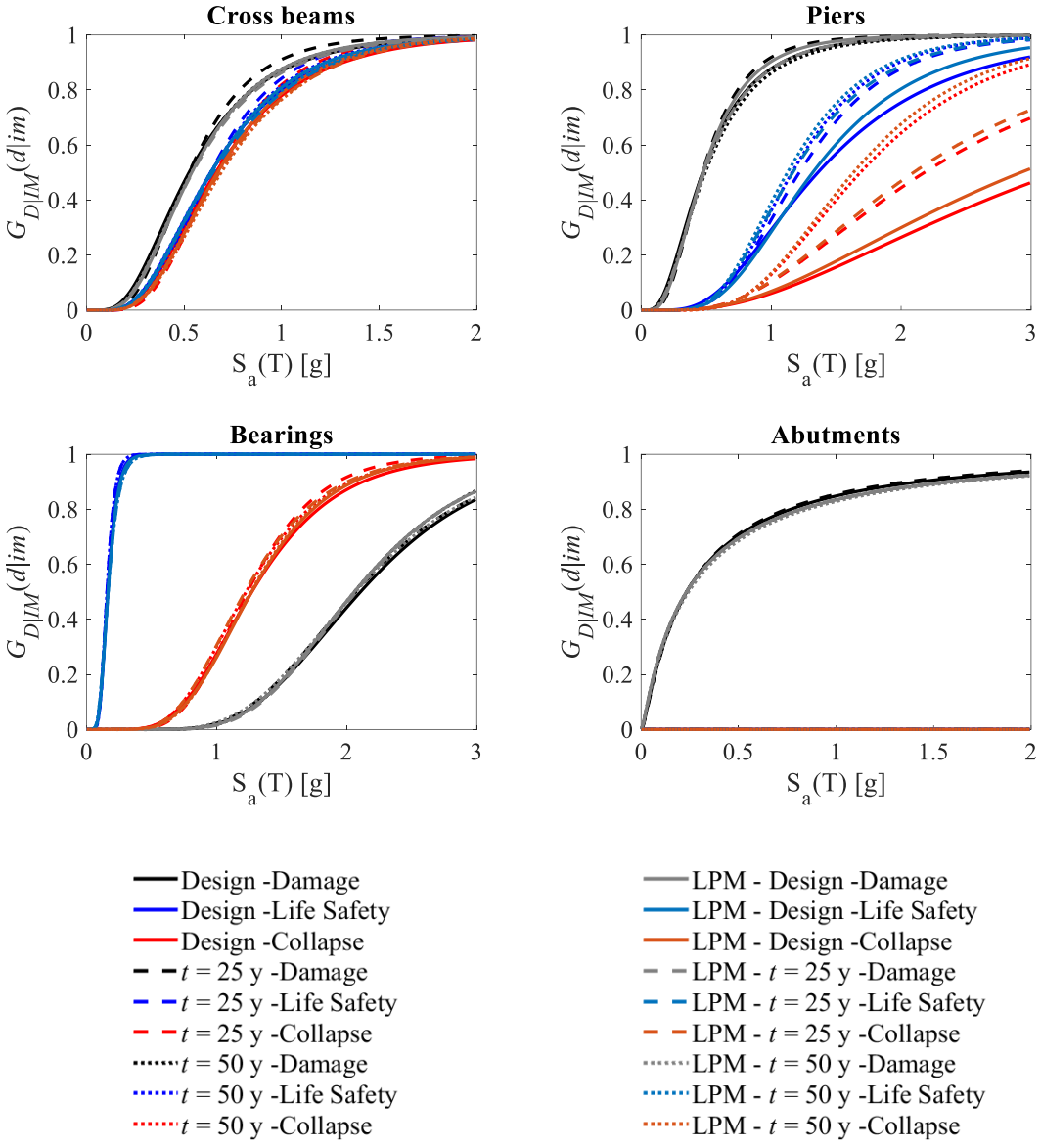

Figure 5.69. Comparison of fragility curves for different ageing conditions and compliance of the foundation system – case study L/B = 20.

5.3 Chapter's references

Boore, D. M., & Joyner, W. B. (1997). Site amplifications for generic rock sites. *Bulletin of the seismological society of America*, *87*(2), 327-341.

Carbonari, S., Minnucci, L., Gara, F., Dezi, L., Dall'Asta, A. (2017). The Role of End Cross-beams on the Distribution of Seismic Induced Shear Actions on the Shear Connection in Steel-Concrete Composite Bridge Decks. *Atti delle XXVI Giornate Italiane della Costruzione in Acciaio*, Venezia 28-29/09/2017.

Dezi, L., Carbonari, S., Dall'Asta, A., Gara, F., & Minnucci, L. (2018). Seismic behaviour of steel-concrete composite bridge decks. In *Steel and Steel-concrete composite structures in seismic areas: advances in research and design*. Research Project RP3, ReLUIS-DPC 2014-2018. Napoli: Doppia Voce. ISBN 978-88-89972-74-8, 451-478.

Mangalathu, S., Heo, G., & Jeon, J. S. (2018). Artificial neural network based multi-dimensional fragility development of skewed concrete bridge classes. *Engineering Structures*, *162*, 166-176.

Minnucci, L., Carbonari, S., Dall'Asta, A., Dezi, L., Gara, F. (2019). Local failure mechanisms of existing steel-concrete composite decks. *Atti delle XXVII Giornate Italiane della Costruzione in Acciaio*, Bologna 3-5/10/2019.

Ramanathan, K. N. (2012). *Next generation seismic fragility curves for California bridges incorporating the evolution in seismic design philosophy* (Doctoral dissertation, Georgia Institute of Technology).

Scozzese, F., Tubaldi, E., & Dall'Asta, A. (2020). Assessment of the effectiveness of multiple-stripe analysis by using a stochastic earthquake input model. *Bulletin of Earthquake Engineering*, *18*(7), 3167-3203.

Xie, Y., & DesRoches, R. (2019). Sensitivity of seismic demands and fragility estimates of a typical California highway bridge to uncertainties in its soil-structure interaction modeling. *Engineering Structures*, *189*, 605-617.

6. A step forward: a holistic framework for assessing direct and indirect consequences of bridge fragility

In previous Chapter 2 and Chapter 3, an overview on the vulnerability of existing bridges and the analysis of the available information on the Marche region bridge stock have shown the importance and the need for a comprehensive framework in which the analysis of the regional infrastructures must include the assessment against both vertical and seismic loads and must be extended to the evaluation of direct and indirect consequences.

In this Chapter, a holistic probabilistic framework for the assessment of direct and indirect consequences of bridge fragility is proposed. Following the PEER's scheme, the framework is composed by different steps that can be evaluated in sequence. The framework includes the analysis of vulnerability, risk and loss connected to both vertical loads and seismic actions, as well as the concepts of degradation, Structural Health Monitoring (SHM) and maintenance/retrofit interventions, with the aim of furnishing detailed and constantly updated results about the existing bridge structural condition. A synthetic representation of the proposed framework is depicted in Figure 6.1.

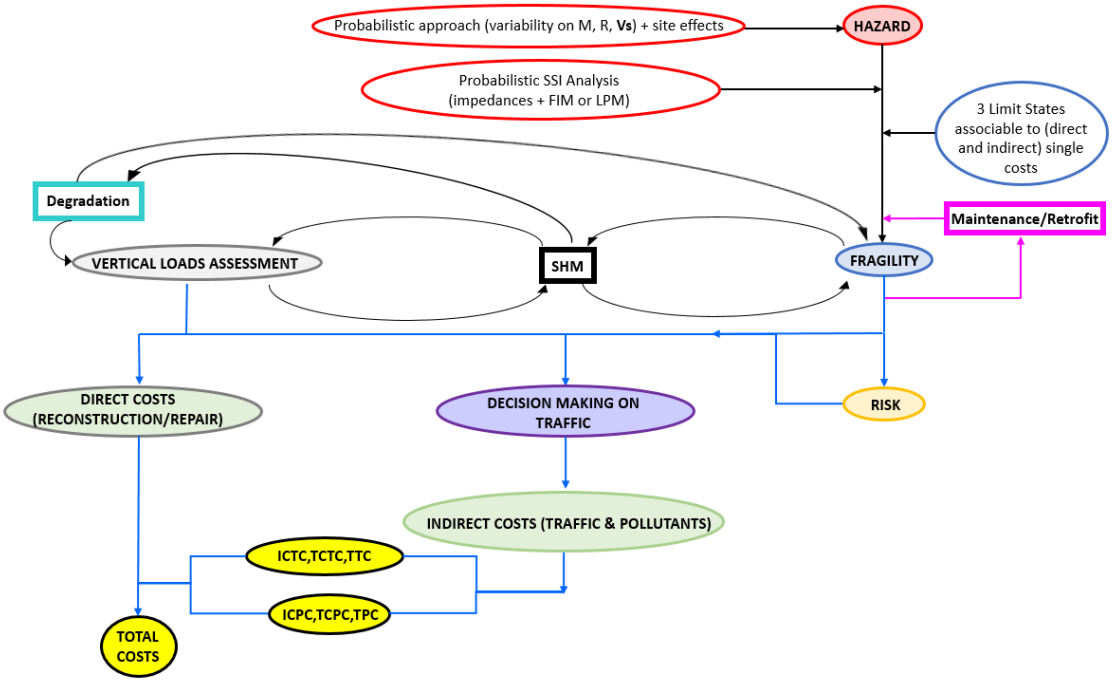

Figure 6.1. A holistic framework for the evaluation of direct and indirect consequences of bridge fragility.

In the following Sections 6.1, 6.2, 6.3 and 6.4 a deepening on the different steps required by the framework is provided, including the analysis of the available tools and proposals for the development of the framework in a probabilistic perspective. Then, in Section 6.5 an application of the framework is carried out, exploiting the already available methodologies and the results from the previous Chapters. The regional scenario of the

Marche region is considered for the quantification of direct and indirect consequences of the seismic fragility on the existing bridges along one of the two analysed regional routes.

6.1 Hazard

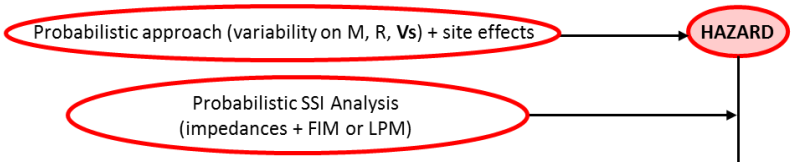

Figure 6.2. Hazard analysis and associated steps.

The probabilistic approach described in §2.4 holds, in which the variability of the seismic input is considered by sampling (via direct Monte-Carlo like simulation method) magnitude and epicentral distance from the relative probability density functions. An additional variability that shall be taken into account concerns the subsoil, whose mechanical characteristics affect the maximum amplitude and the frequency content of the generated seismic signals. It is known that both intrinsic and spatial variability affect the definition of soil mechanical properties (Phoon & Kulhawy, 1999; Uzielli et al., 2006; Mayne et al., 2009); it is also known that, among all the parameters defining the soil properties, the shear wave velocity V_S has a large influence on the amplitude and frequency content of surface ground motions, as obtained by (Bazzurro & Cornell, 2004; Rathje et al., 2010; Barani et al., 2013); a thorough discussion and an original contribution on these aspects will be provided in Chapter 7.

For the purpose of the following elaborations, the characteristics of the soil are condensed in V_{S30} parameter, i.e., the average shear wave velocity within the first 30 m under the ground level of the site of interest. This choice will be justified by the results showed in Chapter 7. Up to now, V_{S30} has been considered without any variability, since the adopted value for V_{S30} has been deterministically chosen. A substantial improvement of the adopted approach would be given by the introduction of a proper probabilistic distribution for V_{S30}, in order to obtain seismic signals from the sampling in a more realistic 3-D stochastic domain (M, R, V_{S30}). This probabilistic distribution could be derived from either detailed experimental campaigns or, in absence of test data, from the literature review (Jones et al., 2002; Rathje et al., 2010; Griffiths et al., 2016). As a result, the number of possible combinations of the triplet (M, R, V_{S30}) for the generation of seismic signals will increase proportionally to the number of sampled V_{S30}.

It is also recognized the importance of spatial variability of ground motion in case of long structures like bridges; the non-synchronism, that can manifest as the wave passage effect, the loss of coherency and, most of all, possible amplitude effects caused by local site conditions, has a key role in the definition of the seismic input under the supporting elements (Sextos, 2003a; Lupoi, 2005; Capatti et al., 2017). Since local site effects strongly affect not only the ground motion peak acceleration and spectral amplitude, but also the Soil-Structure Interaction (SSI) phenomena (Sextos, 2003b), which are of non-

negligible importance in case of bridges (Carbonari et al., 2010), they could be included in the generation of a more realistic seismic database to be applied under seismic bridge structures, through a 1-D or 2-D local response analysis, even considering soil nonlinearities, as shown in the methodology by (Capatti et al., 2017). The variability of the shear wave velocity and of seismic signal due to local site effects are still studied in the recent literature (Passeri et al., 2019) and may be the object of study for a harmonized framework on the topic.

Independently from the adopted approach, it has been already mentioned that SSI can have detrimental effects on the bridges' structural response, but its effects are usually neglected in the practical design for seismic vulnerability assessment, and possible unfavourable interactions between the site and the structure response may be responsible of unexpected structural damage. The introduction of SSI effects in the framework ensures a more reliable description of the bridge seismic response, as already shown in Chapter 5, and locates at an intermediary point between the Hazard and the Fragility. The improvement of this step would be provided by the introduction of variability on soil and foundation parameters reflecting their intrinsic aleatoric nature. Few works deal with the adoption of a probabilistic approach for the SSI problem, and very little attention is paid on the probabilistic assessment of the soil-foundation system only. In the following Chapter 7 a new study on the probabilistic response of deep foundations is presented; in the study, the focus is on the variability of the Impedance and the Foundation Input Motion (FIM) functions depending on the variability of three main parameters describing the characteristics of the subsoil system, i.e., the soil density, the concrete elastic modulus of the piles and the shear wave velocity. As main result, it appears that even for the combined system soil-foundation the variability of the shear wave velocity plays a key role in the definition of the variability of the overall response.

6.2 Fragility

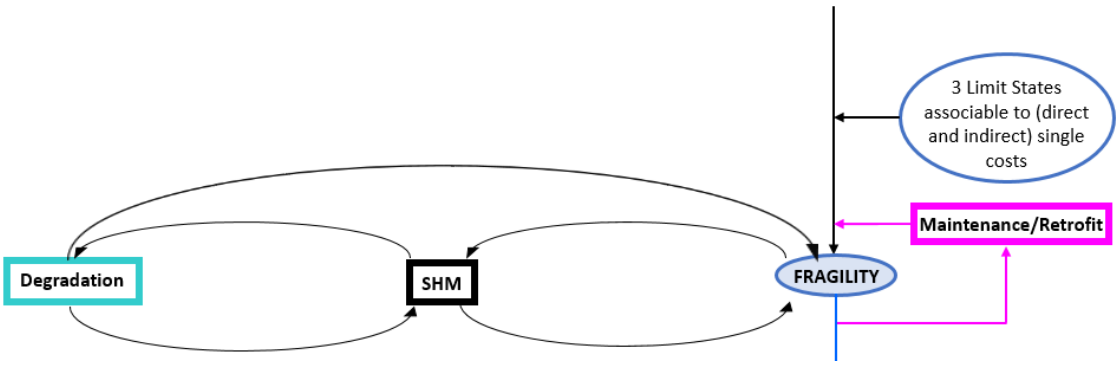

Figure 6.3. Fragility analysis and associated steps.

As a preliminary step to the evaluation of the fragility, the definition of performance levels useful to assess the bridge performance is required. The choice can be made basing

on the overall structural behaviour, so choosing a unique EDP, or evaluating the single components performance, to which different EDPs are associated. A strategic choice for the performance levels should consider the possibility to associate them not only a physical mechanism of damage, but also the quantification of consequences after the damage itself, that translates into repair or reconstruction costs, if direct consequences are evaluated, or traffic and environmental emissions, if indirect consequences are considered. The adoption of such a strategy is already well known in the literature and widely adopted in case of bridge structures (Mackie & Stojadinović, 2006; Padgett & DesRoches, 2007; HAZUS, 2013). For example, in HAZUS four limit states are identified concerning the level of damage (slight, moderate, extensive, complete), to be investigated both at component level (for railway bridges) and at system level, and the associated economic impact is expressed with a damage ratio, that is a fraction of the whole bridge replacement cost (Figure 6.4, Figure 6.5 and Figure 6.6).

Table 15.16: Default Replacement Values of Transportation System Components

System	Replacement Value (thous. $)	Label	Component Classification
Highway	10,000	HRD1	Major Roads (value based on one km length, 4 lanes)
	5,000	HRD2	Urban Streets (value based on one km length, 2 lanes)
	20,000	HWB1/HWB2	Major Bridges
	5,000	HWB8, 9, 10, 11, 15, 16, 20, 21, 22, 23, 26, 27	Continuous Bridges
	1,000	HWB3, 4, 5, 6, 7, 12, 13, 14, 17, 18, 19, 24, 25, 28	Other Bridges
	20,000	HTU1	Highway Bored/Drilled Tunnel (value based on liner)
	20,000	HTU2	Highway Cut and Cover Tunnel (value based on liner)

Figure 6.4. HAZUS Table 15.16: Default Replacement Values of Transportation System Components.

Table 15.18: Damage Ratios for Highway System Components

Classification	Damage State	Best Estimate Damage Ratio	Range of Damage Ratios
Roadways	slight	0.05	0.01 to 0.15
	moderate	0.20	0.15 to 0.4
	extensive/ complete	0.70	0.4 to 1.0
Tunnel's Lining	slight	0.01	0.01 to 0.15
	moderate	0.30	0.15 to 0.4
	extensive	0.70	0.4 to 0.8
	complete	1.00	0.8 to 1.0
Bridges	slight	0.03	0.01 to 0.03
	moderate	0.08	0.02 to 0.15
	extensive	0.25	0.10 to 0.40
	complete	1.00*	0.30 to 1.00

Figure 6.5. HAZUS Table 15.18: Damage ratios for highway system components.

Column		slight extensive complete	0.05 0.25 0.8
Abutment		slight moderate extensive	0.02 0.075 0.15
Connection		moderate extensive	0.01 0.02
Deck		slight	0.05

Figure 6.6. HAZUS Table 15B.1: Subcomponents for the Railway System.

In this Thesis, a proposal for the evaluation of three useful limit states (Damage, Life Safety, Collapse) has been illustrated in previous Chapter 4. In particular, the considered performance thresholds are associable to current design codes (see NTC2018) as well as to economically quantifiable damage mechanisms at component level, basing on the available literature. This choice allows a better estimate of the damage consequences on each bridge structure and leads to a more detailed estimation of costs on the network. It holds that other and different performance levels can be analysed depending on the requests of the stakeholders.

Fragility curves can be built according to the procedure adopted in Chapter 2, with the multiple purpose of the global and local assessment within the bridge structure, also taking into account multiple failure modes and the damage extension. These latter aspects are fundamental for the quantification not only of seismic risk, but also for the costs of interventions and the optimization of the retrofitting and maintenance works. The improvement furnished by the proposed novel approach lays in the possibility of an easier, more direct and more accurate quantification of costs related to the structural interventions and the consequent decision-making by the stakeholders.

6.2.1 Degradation, Maintenance, Retrofit and Structural Health Monitoring

The accuracy in the evaluation of fragility both before and after the adoption of intervention measures strictly depends on the accuracy of numerical models on which the fragility analyses are performed. The need for numerical models that realistically represent the response of the real structure both in the design and in the validation of the executed works leads to a constant updating process that reflects, as a result, on the updating of the fragility curves. It appears that two are the main aspects taking place on the real structure that influence a good and reliable modelling and its consequent response in terms of fragility: the first is the presence of damaged elements and the evolution of degradation phenomena, such as the corrosion on steel elements or the cracking of concrete components; the second concerns the presence of structural details due to maintenance or retrofit works, that both locally and globally may affect the structural performance.

In the first case, the aging and deterioration may develop in various forms within a bridge structure, such as spalling of RC members, corrosion of steel reinforcement in RC columns, build-up of debris leading to corrosion of steel bearings and so on. These components compromise the primary force resisting system of bridges under both vertical and seismic loading and consequently have a potentially significant impact on the bridge performance. In addition, given the time-dependent nature of bridge deterioration phenomena, the analysis of the bridge response becomes part of a constant updating process that must follow and represent the evolving vulnerability of the structure in time. Many studies dealt with the evaluation of degradation effects on the fragility of existing bridges, in which the deterioration phenomena occurring on concrete or steel elements are often modelled as a physical time-dependent modification of the structural members' geometry or in the strength of the construction materials. Regarding RC members, the corrosion on steel rebars, which is often related to the presence of the sea or to the massive use of chloride-laden deicing salts, has been widely investigated in the literature about the bridge fragility (Enright & Frangopol, 1999; Vu & Stewart, 2000; Choe et al., 2008; Choe et al., 2009; Ghosh & Padgett, 2010; Biondini et al., 2014; Rao et al., 2017a; Rao et al., 2017b). Corrosion is recognized as the most influencing degradation phenomenon affecting the vulnerability of bridge structures, and among its possible consequences (i.e. reduction of the resisting section, reduction of the reinforcement ratio, reduction of the concrete strength due to the cracking, reduction of the steel strength), the reduction of the rebars' area has the highest impact on the fragility of columns (Rao et al., 2017a; Mangalathu et al., 2018). It is also worth noting that spalling of the RC members, especially of bridge columns, has significant influence on the seismic fragility of the whole structure (Simon et al., 2010). In case of steel members, the severity of deterioration will depend on how long the metal is exposed to water, oxygen, and salt. Kayser & Nowak (1989) proposed a corrosion damage model to investigate effects of different forms of corrosion on the carrying capacity of steel girder bridges. They concluded that the web is typically the critical element under shear and vertical loads, particularly for shorter span bridges with no bearing stiffeners. Czarnecki & Nowak (2008) developed a time-variant reliability-based model for evaluation of steel highway bridges with regard to corrosion, with the aim of improving the analysis of carrying capacity of existing bridges. Finally, corrosion on bearing anchor bolds leads to reduced ultimate lateral strength of the bearing device, as observed by (Hoeke et al., 2009; Ghosh & Padgett, 2010). Degradation phenomena may have not only structural but also economic and social consequences, that may be considered in the time-dependent analysis of bridge fragility (Dong et al., 2013).

The aggressive environmental conditions previously illustrated, that may be responsible of degradation and together with the ever-increasing traffic loading contribute to the progressive deterioration of existing bridges, lead to risky structural deficiencies that should be prevented to ensure the bridge proper functioning. Since the importance of bridges considered as single structures or as parts of a road network is crucial from the safety and the socio-economic point of view, an adequate maintenance plan to keep their

satisfactory performance in their lifetime is necessary. Many research studies dealt with the elaboration of optimization strategies for bridge maintenance, in which the variability of the bridge conditions in time and the uncertainty about the evolution of degradation are taken into account. The integration of such aspects in the analysis of the bridge performance is fundamental to minimize the intervention costs, bringing them on budget and avoiding too common wastes of money into repair or reconstruction interventions not in due time. Moreover, a good maintenance organization allows to maintain the efficiency of the road network viability even if partially closed to traffic and other alternative paths are made available. Examples of these studies can be found in (Liu & Frangopol, 2005; Liu & Frangopol, 2006; Frangopol, 2011; Bocchini & Frangopol, 2011; Zhang & Wang, 2017). With the aim of assessing a single bridge structural health conditions and at the same time provide efficient instructions about how, when and where it is necessary to allocate funds for interventions in a bridge network, Bridge Management Systems (BMSs) are thus developed and help decision-makers to keep bridges in an acceptable level for public services in the network. A BMS is a rational and interactive database in which information about the organization of maintenance and all the correlated activities can be critically compared and filtered basing on interesting parameters (i.e., a maximum budget) to select optimum solutions both in a short-time perspective and most of all, if smartly queried, for the life-cycle management in the future. Efforts in the improvement of existing bridges databases for the building of efficient BMSs have been involving the research for the last 20 years (Estes & Frangopol, 2003; Pellegrino et al., 2011; Amini et al., 2016; Hurt & Schrock, 2016), but much more effort must be done to assess the role of maintenance within a comprehensive framework for the analysis of bridge fragility, especially in Italy, where no National BMSs exist yet.

The adoption of repair or retrofit measures may affect the bridge response significantly, so that the analysis of the bridge structure in the upgraded condition may be necessarily combined with the adoption of reliable numerical models useful to predict the bridge behaviour and to forecast its performance under seismic events. Usually, repair or retrofit works involve only few bridge component separately, so that the improvement on specific elements is certainly reached; however, the effects on other non-retrofitted components, as well as on the entire structure, may be not beneficial, and the need for a detailed analysis on the single element categories is required (Padgett & DesRoches, 2008a). Fragility curves for retrofitted bridges have been developed considering either retrofit interventions on single components (Kim & Shinozuka, 2004; Karim & Yamazaki, 2007) or on multiple components, in this case assessing the impact of the interventions on the various bridge elements (Padgett & DesRoches, 2008b). As a result, the analysis of fragility curves for retrofitted bridges allows to predict the most effective retrofit measures in reducing probable damage at both component and system level, thus evaluating and comparing the cost effectiveness of different vulnerability mitigation strategies. The optimization of repair and retrofit interventions is usually treated as a part of wider frameworks on life-cycle costs and cost-benefit analysis (Padgett et al., 2010; Dong et al., 2015).

In the light of all the above, the importance of a reliable modelling for capturing the behaviour of an existing bridge subjected to deterioration phenomena or modified by structural interventions is fundamental in the fragility assessment. Generally, numerical models only occasionally are calibrated with respect to the measured response of the investigated structural system, although it is well known in the literature that the calibration of structural models on the base of the measured response has a strong impact on the evaluation of structural properties, damage detection and damage forecast (Doebling et al., 1996; Sohn & Law, 2000; Sohn et al., 2003). In particular, different damage detection techniques have been developed in the Structural Health Monitoring (SHM) context for the quality assessment and capacity rating, as well as for retrofitting evaluation of performed repairs (Arici & Mosalam, 2003; Basu, 2005; Malekjafarian et al., 2015; Loh et al., 2015; Moughty & Casa, 2017). The importance of SHM lies not only in the monitoring of present structural conditions, but also in the ability of forecasting the evolution of damage through the continuous monitoring and so of predicting the change of the structural properties, the latter being fundamental in the definition of a numerical model for fragility analysis, through a continuous updating of information (Behmanesh et al., 2015; Behmanesh & Moaveni, 2016). Moreover, fragility is built referring to a selected IM, which is often estimated through analytical Ground Motion Prediction Equations (GMPEs), depending on seismic source and site features. The choice of the independent variables in GMPEs may influence the definition of the fragility function improperly. In order to properly include the above aspects, which are generally neglected in conventional seismic vulnerability assessment, a more reliable risk assessment framework should involve strong-motion measurements (Chiou et al., 2008), system identification, model updating and structural performance evaluation through monitoring systems (Teughels & De Roeck, 2004), as well as the most recent GIS technologies (Molina et al., 2010). The employment of system identification techniques, based on experimental data and numerical model calibrations, may have a strong impact in the reduction of the uncertainties in the description of both bridge response and earthquake signals. In addition, identification tools can improve the prediction of the soil response under seismic action, which is a fundamental aspect in the definition of a robust numerical soil-structure model to consider effects of SSI adequately, especially in case of large-scale problems as bridge networks, where local site effects can be significant. Machine learning algorithms may manage the multiple aspect of the SHM within the framework, such as acquisition, processing and analysis of data from the continuous monitoring as well as the numerical modelling updating/upgrading.

6.3 Vertical loads assessment

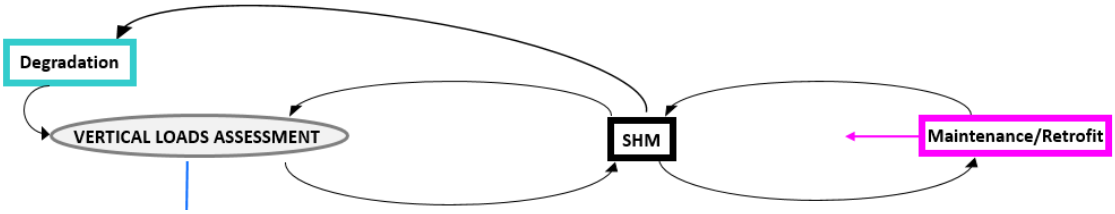

Figure 6.7. Vertical load assessment and associated steps.

The functionality of bridges can be compromised not only by their inadequacy towards seismic (or more generally, natural) hazard, but even before by the failure to satisfy the assessment of the carrying capacity with regard to vertical and traffic loads. Extensive or localized damage due to the natural process of ageing, to the occurrence of exceptional events other than natural hazards (for instance, vehicle impacts) and also to the aforementioned effect of degradation due to environmental exposure may lead to the loss of design requirements and, as a consequence, to the recalculation of the allowable traffic flow.

The transit conditions are the central point of the new Italian Guidelines (Ministero delle Infrastrutture e dei Trasporti, 2020), that assign different levels of vulnerability to the considered structure based on different parameters of investigation to be verified. The methodology proposed in the Guidelines resides in a multi-layered approach for the quick or thorough estimation of the vulnerability; the level of deepening depends on the global and local bridge health conditions, the exposure to different types of hazard and the outcomes of the vertical load assessment. As a consequence, the assignment of the considered bridge to a specific level of vulnerability, called *class of attention*, is followed by different decisions about the viability (involving not only the specific bridge, but also the road network of pertinence). In the Guidelines, the problem about vertical loads is explicitly taken into account through the *structural and foundation class of attention*. The parameters mainly affecting the assignment to a specific level of vulnerability with regard to the vertical loads are: the amount of traffic load on the structure (the actual to be compared to the design one); the level of defectiveness, linked to the ageing condition of the structure; the rapidity of deterioration processes due to the exposure to environmental factors; the codes of the original design project (in the most of cases, prior to the current codes); the geometry and the adopted materials in the actual conditions. Whereas necessary, that is in case of at least a medium *class of attention*, the level of detail for the analysis and the estimation of the bridge vulnerability is deepened through further visual inspections, in situ tests and numerical analyses, and more refined investigation criteria must be adopted for a safer choice about the level of usability of the structure.

It is evident that even in case of vertical loads, the concepts of degradation, maintenance, retrofit and structural health monitoring can be well contextualized and result fundamental for an adequate prediction of the bridge network functionality and the

relative economic, social and environmental consequences. The measures of prevention against ageing, deterioration, natural hazards and damage/collapse due to increased or accidental loads can be found in the same tools useful for a more reliable forecast of the structural fragility, that is a good plan of maintenance, the organization and prioritization of retrofitting interventions, the continuous monitoring of the structural health conditions, all of these within a process of constant updating. Moreover, in order to quantify more accurately the bridge performance under traffic loads, the monitoring could be employed to collect data about the traffic volume and probabilistic load models can be developed in case of specific bridges of strategic importance (Stewart, 2001). In this case, the proposed novel methodology for the analysis of failure modes and damage extension could be reformulated choosing a suitable parameter to be used as *IM* for the vertical loads.

6.4 Direct and Indirect costs

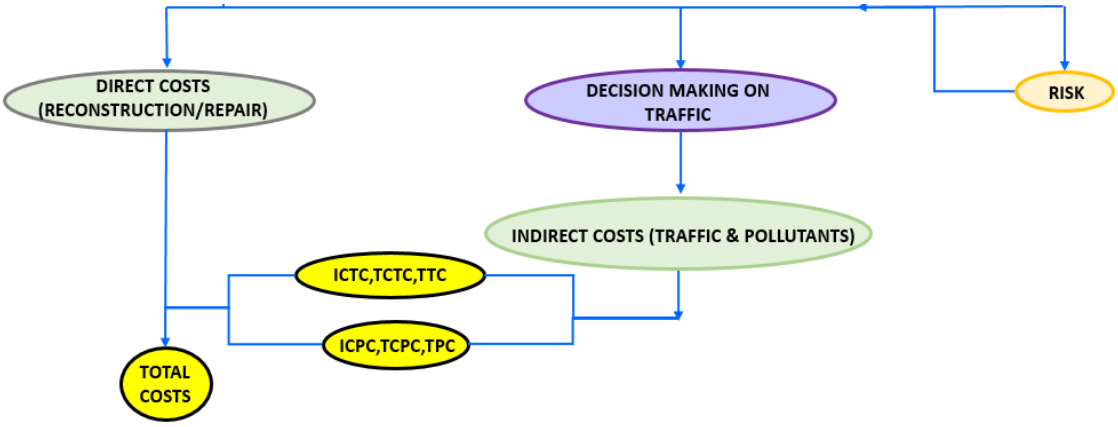

Figure 6.8. Risk and costs analysis and associated steps.

The next step after the fragility is the computation of risk. As already explained in Chapter 2, following the PEER's framework, the risk results as the convolution of hazard and fragility or of hazard and vulnerability. In the first case, the analysis aims to quantify the MAF of exceedance of a seismic demand level as a function of *IM*; in the second, the analysis aims to quantify the MAF of exceedance of a certain level of (economic, social,…) loss in the *IM* domain. The evaluation of risk has a central role in the decision-making and in the long-term scheduling of activities by the stakeholders.

It is worth observing that, if a vulnerability model is adopted, the analysis of risk coincides with the analysis of costs. However, the quantification of costs through a vulnerability model implies that an easily computable correlation between structural damageability and losses can be defined, that actually may result extremely complicated for what concerns indirect costs (i.e. those related to the consequences of the bridge failure), given the large number of influencing parameters on the socio-economic or environmental loss estimate, or inaccurate for what concerns direct costs (i.e., those related to the construction, maintenance and reparation of the structure only), since the remaining service life and the

possible inflation rates highly influence the evolution of costs in time and cannot be neglected.

Different proposal for the quantification of costs linked to the risk analysis have been made in the literature, mainly focusing on the best estimate of direct costs (Stewart, 2001; Padgett et al., 2010; Ghosh & Padgett, 2011) or including indirect costs under necessary several approximations and assumptions regarding the traffic-related costs (Kendall et al., 2008; Mackie et al., 2010; Alipour et al., 2011). In the latter case, an accurate evaluation of the transport relevance and related socio-economic impacts would include differentiated zoning for demand passengers and freight, as well as the creation or acquisition of studies, if any, for the assignment of passenger and freight traffic and the estimation of accessibility indices of territorial areas characterized by significant concentration of settlement, production density and logistic sites. It appears that the required data should come from multiple sources and many different institutions, which is often difficult to coordinate and onerous from the point of view of timing. At the same time, it is known that the economic losses are imputable as much or more to indirect costs than direct costs (Kendall et al., 2008; Mackie et al., 2010). A compromise between a too heavy research work on traffic information and the use of conventional non-accurate assumptions is provided in a recent paper by (Kilanitis & Sextos, 2019), where multiple traffic scenarios are considered and simulated with the aid of a dynamic traffic assignment engine (Zhou & Taylor, 2014), and time-variant roadway indicators are introduced to quantify the sustainability of the road network in terms of traffic user costs and environmental impact using information directly from the fragility analysis.

In the present framework, for what concerns the direct costs estimation, in absence of detailed studies, the three proposed limit states of Damage, Life Safety and Collapse considered in this Thesis can be associated to the HAZUS Slight, Extensive and Complete damage conditions as a first approximation. The damage ratios illustrated in Figure 6.5 and Figure 6.6 can be adopted, a total reconstruction cost for bridges equal to 1400 €/m^2, and a cost of 0.5% the total reconstruction cost can be assumed for ordinary maintenance (de Miranda, 2019).

The framework presented in this Thesis considers different parameters to properly evaluate the indirect costs. Hereinafter, the explanation of the adopted approach concerning indirect costs is provided. Since the effects of the alteration of traffic are the primary responsible of indirect costs, the adoption of measures and criteria for the traffic regulation after a seismic event or in the following of a vertical load assessment must be necessarily introduced, calling them decision-making on traffic. Being part of a more general decision-making process, these measures and criteria should be established by the stakeholders such as the operators of the infrastructural system, the construction companies, the local and regional authorities, depending on the expected time and resources allowable for the intervention works, and some necessary hypothesis have been made at this regard. The novel aspect in the proposed logical flow that leads to the quantification of indirect costs resides in associating consequences to the damage of

specific bridge components instead to the entire bridge behaviour. At this scope, results from the application of the proposed methodology for the seismic fragility analysis (or, in case of vertical loads, from the assessment towards a probabilistic distribution of traffic) could be directly employed. Evaluating the single component behaviour, the failure modes or the damage extension, a more reliable description of post-disaster scenarios is offered and, at the same time, an attempt for the optimization of the decision-making is made.

6.4.1 Decision making on traffic

Starting from the considered limit states, 3 possible consequence on the traffic flow are outlined:

- Damage → partial or null closure of the bridge in the longitudinal direction (even if all the structural components experienced a light damage, the bridge can remain open);
- Life Safety → the closure of the bridge depends on the structural component: if piers, bearings or abutments are extensively damaged, the bridge must be closed; in case of damage on the superstructure, it can remain open);
- Collapse → total closure of the bridge.

The decision making on the closure of road lanes implies the partial or total reduction of traffic flow. Four possible traffic flow reduction conditions are outlined:

- Traffic Condition 1 (TC 1): closure of emergency line – no reduction of traffic flow
- Traffic Condition 2 (TC 2): -50% heavy traffic flow (trucks) and -25% light traffic flow (vehicles)
- Traffic Condition 3 (TC 3): -75% heavy traffic flow and -50% light traffic flow
- Traffic Condition 4 (TC 4): total closure of the bridge

Closure times and percentages of traffic flow can be furnished by the stakeholder or taken from the available data/literature. In this Thesis times and percentages are suggested as an estimate, relating limit states with the conditions of traffic closure. The latter are inspired by the Guide Lines by Braga et al. (2019) for highway roads (Table 4.2).

Table 6.1. Conditions of transversal distribution of moving loads.

Condition\Lane	Emergency	Low velocity	High velocity	Fast lane
1	Closed	Trucks	Trucks	Vehicles
2	Closed	Trucks	Vehicles	Vehicles
3	Closed	Closed	Trucks	Vehicles

To associate a certain limit state to one of the traffic flow conditions, two preliminary steps must be addressed:

1) the evaluation of the expected value of *IM* for the seismic event of interested at the specific site of the bridge of interest within the road network;
2) the analysis of the probability of exceedance of different limit states for each of the bridge components at the estimated *IM* from their respective fragility curves.

For what concerns step n°1 and for the next application purposes, the following assumptions are taken about the seismic scenario: a single seismic point source is considered (a more realistic and refined multiple faults scenario could be used); the GMPE recently proposed by Lanzano et al. (2019) is adopted to estimate the expected *IM* values along the infrastructural network.

It is briefly recalled that the GMPE by Lanzano revises and updates the ground motion model for shallow crustal earthquakes in Italy (ITA10) proposed by Bindi et al. (2011) with the strong motion recorded after the recent seismic sequences of 2012 in Emilia (Northern Italy) and 2016-2017 in Central Italy. The new model allows to investigate a wide magnitude range (even higher than previous 6.9) of seismic events and considers site effects, accounted for by a linear dependence on the time-averaged shear-wave velocity V_{S30}. From the proposed model (ITA18) new GMPEs allow to estimate the mean value of the natural logarithm of the selected *IM* and its dispersion, the latter being representative of between-event and site-to-site variability. In case the spectral acceleration at the fundamental period of the structure (Sa(T)) is selected as *IM*, the new GMPEs are suitable for the analysis of structure with vibration periods up to 10 s. The general expression adopted for the new set of GMPEs (ITA18) is:

$$log_{10}Y = a + F_M(M_w, SoF) + F_D(M_w, R) + F_S(V_{S30}) + \varepsilon \qquad (38)$$

in which Y is the observed *IM*, a is the offset, SoF is the style of faulting (strike, reverse or normal), $F_M(M_w, SoF)$ is the source function, $F_D(M_w, R)$ is the distance function, $F_S(V_{S30})$ is the site term, and ε is the error associated with the median prediction.

Using the Eq. (38), it is possible to evaluate the expected value for *IM* in the site of interest (characterized by a certain V_{S30}), for a certain seismic magnitude M_w and at a certain distance R from the seismic source. For each bridge of the network, a specific value of *IM* can be obtained to predict the probability of exceedance at different limit states.

Once done step n° 1, step n° 2 requires that a comparison between the different probabilities of exceedance from the fragility curves related to the analysed limit states is carried out. The comparison aims to quantify the most probable damage condition on the structure at the occurrence of an input from the considered seismic scenario. There can be several criteria to establish which limit state is the most likely to verify, depending on economic parameters, expert judgements and so on, to be endorsed among the involved stakeholders. In this work, a hypothesis on the criterion of choice of the limit state to analyse is made. For the evaluation of indirect costs, it is assumed that the structure lays

in the limit state L if L has the highest probability of occurrence, being the latter the difference between the probability of exceedance of L and the probability of exceedance relative to the next worse limit state L+1 (Figure 6.9). More precisely, if l is the number of considered limit states and d_l are the associated performance thresholds on the damage parameter D, the probability $P_l|IM$ that the structure is in the l-th limit state can be calculated as follows:

$$P_l|IM = P(D \geq d_l|IM) - P(D \geq d_{l+1}|IM) \tag{39}$$

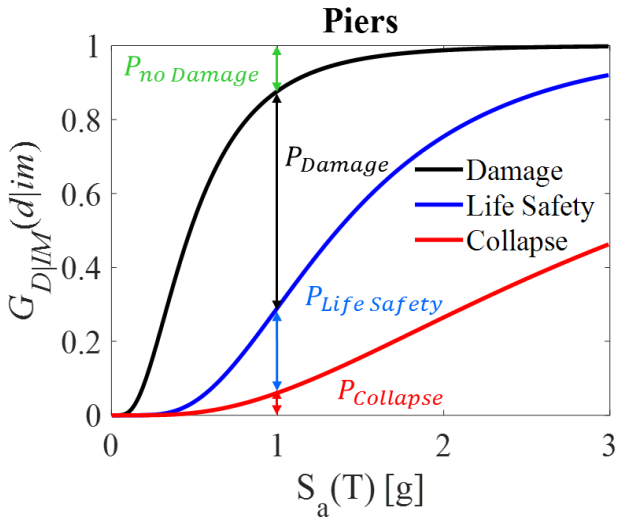

Figure 6.9. Example of graphical evaluation of occurrence probabilities for different limit states (piers).

This is the passage from a probabilistic world to a deterministic one, but it can be justified since the choice of an action regarding the traffic flow (reduction or not) is always deterministic. On the other hand, a probabilistic analysis of the decision-making process is always possible, in order to evaluate the *most probable* scenario of consequences associated to a bridge fragility condition, establishing a variability on the fragility curves that may derive from uncertainties related to various parameters affecting the structural response, such as the geometry, the mechanical parameters or the subsoil conditions (already commented in previous §6.1). For the purposes of the application of the framework, in this Thesis the first approach is followed.

The analysis of the most probable limit state is diversified for the bridge components. The need for a component level analysis is due to the different impact that damage on certain structural elements can have not only in terms of structural response, but also for what concerns potential direct and indirect consequences. It is recognized that failure on the supporting elements (piers, bearings, abutments) may have serious consequences for the bridge stability, while it is generally true that damage on the superstructure may not lead to analogous results. In this Thesis, a differentiation between consequences is made concerning damage on elements belonging to the superstructure and those under them. The analysis can be extended and further detailed where necessary.

Once the limit state to observe is defined, a relationship between it and the correspondent traffic flow reduction can be outlined. Even in this case, several choices can be made based on multiple economic, environmental or other criteria that the stakeholders should provide. For the following applications, in this framework the relationships between limit states and traffic flow conditions are illustrated in the following:

- Damage (D) on superstructure → Traffic Condition 1
- Damage on abutments, piers, bearings → Traffic Condition 2
- Life Safety (LS) on deck, links → Traffic Condition 3
- Life Safety (LS) on abutments, piers, bearings → Traffic Condition 4
- Collapse (C) → Traffic Condition 4

As a consequence, different periods for the restoration of the normal traffic flow are assumed. For each couple limit state-traffic condition, the time is the maximum considering that different components can experience damage at the same time and are repaired simultaneously. Different assumptions can be considered basing on expert judgements (Table 6.2). Moreover, the traffic restoration time could be probabilistically simulated to add some uncertainties in the process. In this Thesis, the following assumption are made:

- D + TC 1 → 1 day
- D + TC 2 → 7 days
- LS + TC 3 → 30 days
- LS + TC 4 → 150 days
- C on superstructure → TC4 → 90 days
- C on piers, bearings, abutments → TC4 → 450 days

Table 6.2. Conditions of transversal distribution of moving loads.

Limit State\Traffic Condition	TC1	TC2	TC3	TC4
D	1	7	-	-
LS	-	-	30	150
C	-	-	-	≥90

Looking at the entire road network, the presence of bridges implies that different damage conditions, traffic conditions and subsequent recovery times can verify. An example of the evolution of the road network functionality basing on the recovery times assumed in this Thesis is depicted in the following Figure 6.10.

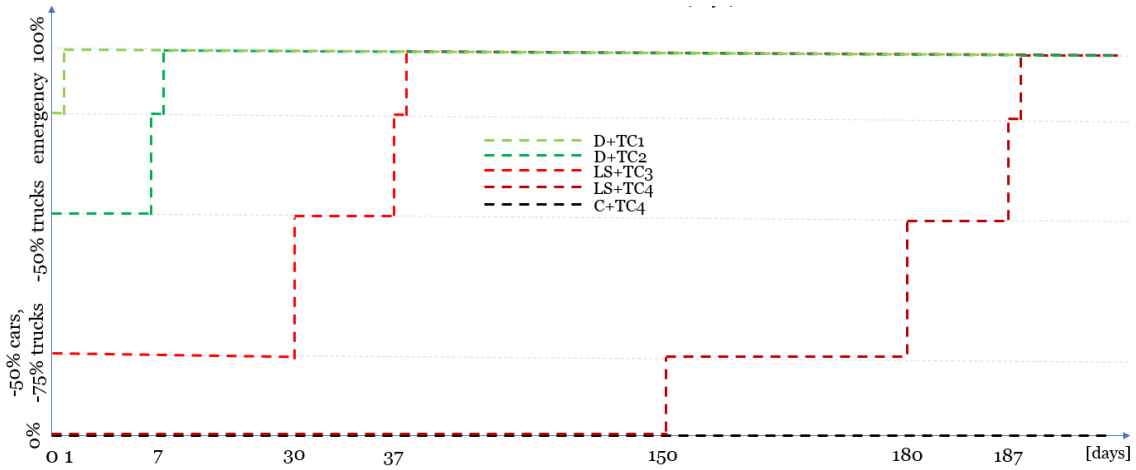

Figure 6.10. Example of evolution of the road network functionality relating to different traffic and damage scenarios.

6.4.2 Quantification of traffic and environmental costs

The quantification of indirect costs according to the previously explained criteria presupposes that a certain travel path is examined within the road network. In particular, an origin (O) and a destination (D) must be individuated, as well as alternative roads and paths, which must be included for a correct forecast of the traffic volume on the entire network during partial or total closures of the damaged bridges. The insertion of an interruption in the normal traffic flow due to the decision-making outcomes implies that new roads are automatically considered by traffic users to complete the O-D itinerary. Likely these new paths include easily accessible ways and users give priority to fast roads in order not to furtherly extend the journey times. Other conditions could arise during travelling, such as the interruption of the journey, the change of destination and so on. The analysis of traffic could result as very expensive, especially in absence of statistical data on the most frequent O-D itineraries or the preferential alternative ways.

In this Thesis, it is assumed that the O-D route remains fixed and the roads that constitute the alternative paths are selected as the fastest after the principal one that is where there are the considered bridge structures. The focus is on costs due to the increase of the travelling length to complete the O-D route and the resultant emissions of pollutants. The first ones will be called Traffic Costs (TC), while the second ones Pollutant Costs (PC). Some data are required to calculate TC and PC, to link the increased length of the alternative O-D path to a monetary loss in currency, and some definitions are introduced as listed below:

- **IMR** (Identified Mobility Index - Indice di Mobilità Rilevata (in Italian)) **[vehicles/day]**: it expresses the amount of traffic flow on the examined link as an average on the time period (monthly or yearly) and on the number of available tracking stations;

- **$SVTC_j$** (Single Vehicle Traffic Cost) [**€/km/vehicle**]: represents the equivalent cost of journey per unit length per single vehicle for the j-th examined vehicle category;
- **$SVPC_j$** (Single Vehicle Pollutant Cost) [**€/km/vehicle**]: represents the cost associated to the journey in terms of pollutant emission per unit length per single vehicle for the j-th examined vehicle category;
- **$T_{1,j}$** [**h**]: is the average travel time on the original O-D road path in absence of working zones for the j-th vehicle category;
- **$T_{2,j}$** [**h**]: is the average travel time on the network in presence of working zones for the j-th vehicle category;
- **V_j** [**km/h**]: is the average speed on the original O-D road path in absence of working zones for the j-th vehicle category;
- **$L_{1,j}$** [**km**]: is the length of the original O-D road path for the j-th vehicle category;
- **$L_{2,j}$** [**km**]: is the length of the alternative O-D road path for the j-th vehicle category.

The IMR, SVTC and SVPC indexes can be easily found on national or regional databases about traffic volumes and environmental emissions. In this Thesis, a detailed analysis on the available data about regional traffic flows and emissions associated to the vehicles that run on the SS76 and SS77 roads is carried out. T_1 and T_2 for the j-th vehicle category can be calculated with the aid of dedicated software for traffic simulation; in this Thesis, the open-source dynamic traffic assignment engine by Zhou & Taylor (2014) is exploited. Further details about the outcomes of the analysis on traffic/emission data and the adopted tools will be commented in next §6.6.2 and §6.6.3, respectively. Considering the average speed in normal traffic flow conditions V_j, it can be assumed that cars and trucks have to travel on the fictitious longer path $L_{2,j}$, which can be calculated proportionally to the length of the link under recovery:

$$\mathbf{L_{2,j} = V_j \times T_{2,j}} \tag{40}$$

This choice is due to the fact that in Italy the available data on traffic costs as well as pollutant emissions costs are expressed in €/km (per car/truck).

Once the parameters listed above are known, indirect costs associated to the consequences of the reduced functionality of the road network can be calculated. Some indicators are proposed to quantify the effects of the traffic alteration on the considered O-D path; it is worth noting that each of them is associated to one of the various recovery phases of the bridge (see Figure 6.10), so they result time-dependent.

For what concerns TC:

- **ICTC** (Incremental Category Traffic Cost) [**€/vehicle**]: for the j-th vehicle category, the cost related to the lengthening of the journey can be calculated as an increment on the standard traffic cost on the original path L_1.

$$ICTC_j = SVTC_j \times \left(L_{j,2} - L_{j,1}\right) \quad (41)$$

- **TCTC** (Total Category Traffic Cost) [**€/day**]: for the j-th vehicle category, two different TCTC can be calculated, corresponding to the free-flow condition (1) and the ongoing works condition (2). For $k = 1,2$,

$$TCTC_{j,k} = SVTC_j \times L_k \times IMR_k \quad (42)$$

- **TTC** (Total Traffic Cost) **[€]**: each recovery phase t_i is characterized by a total cost. For each j-th vehicle category, with $j = 1, \dots, N_j$, and N_j equal to the total number of vehicle categories,

$$TTC_{i,k} = (\sum_{j=1}^{N_j} TCTC_{j,k}) \times t_i \quad (43)$$

- **TFTC** (Total Final Traffic Cost) **[€]**: costs associated to single recovery phases are summed. For each recovery time t_i, with $i = 1, \dots, N_t$, and N_t equal to the total number of recovery phases,

$$TFTC_k = \sum_{i=1}^{N_t} TTC_{i,k} \quad (44)$$

For the comparison of the ante- and post-operam situations, the percentage increment of TCTC and TTC can be calculated:

- **TCTC$_{PI}$** (Total Category Traffic Cost – Percentage Increment) **[%]**:

$$TCTC_{j,PI} = \left(\frac{TCTC_{j,2}}{TCTC_{j,1}} - 1\right) \times 100 \quad (45)$$

- **TTC$_{PI}$** (Total Traffic Cost – Percentage Increment) **[%]**:

$$TTC_{i,PI} = \left(\frac{TTC_{i,2}}{TTC_{i,1}} - 1\right) \times 100 \quad (46)$$

- **TFTC$_{PI}$** (Total Final Traffic Cost – Percentage Increment) **[%]**:

$$TFTC_{PI} = \left(\frac{TFTC_2}{TFTC_1} - 1\right) \times 100 \quad (47)$$

For what concerns PC:

- **ICPC** (Incremental Category Pollutant Cost) [**€/vehicle**]: for the j-th vehicle category, the cost related to the increment of pollutant emissions due to the lengthening of the journey can be calculated as follows

$$ICPC_j = SVPC_j \times \left(L_{j,2} - L_{j,1}\right) \quad (48)$$

- **TCPC** (Total Category Pollutant Cost) [**€/day**]: for the j-th vehicle category, two different TCPC can be calculated, corresponding to the free-flow condition (1) and the ongoing works condition (2). For $k = 1,2$,

$$TCPC_{j,k} = SVPC_j \times L_k \times IMR_k \quad (49)$$

- **TPC** (Total Pollutant Cost) **[€]**: each recovery phase t_i is characterized by a total cost. For each j-th vehicle category, with $j = 1, \dots, N_j$, and N_j equal to the total number of vehicle categories,

$$TPC_{i,k} = (\sum_{j=1}^{N_j} TCPC_{j,k}) \times t_i \quad (50)$$

- **TFPC** (Total Final Pollutant Cost) **[€]**: costs associated to single recovery phases are summed. For each recovery time t_i, with $i = 1, \dots, N_t$, and N_t equal to the total number of recovery phases,

$$TFPC_k = \sum_{i=1}^{N_t} TPC_{i,k} \quad (51)$$

For the comparison of the ante- and post-operam situations, the percentage increment of TCPC and TPC can be calculated:

- **TCPC$_{PI}$** (Total Category Pollutant Cost – Percentage Increment) **[%]**:

$$TCPC_{j,PI} = \left(\frac{TCPC_{j,2}}{TCPC_{j,1}} - 1\right) \times 100 \quad (52)$$

- **TPC$_{PI}$** (Total Pollutant Cost – Percentage Increment) **[%]**:

$$TPC_{i,PI} = \left(\frac{TPC_{i,2}}{TPC_{i,1}} - 1\right) \times 100 \quad (53)$$

- **TFPC$_{PI}$** (Total Final Pollutant Cost – Percentage Increment) **[%]**:

$$TFPC_{PI} = \left(\frac{TFPC_2}{TFPC_1} - 1\right) \times 100 \quad (54)$$

In the next Section 6.6, an application of the framework is carried out analysing the SS76 road in the Marche region. As previously mentioned, the analysis of the available databases about viability, traffic flow and related emissions is performed. Results deriving from Chapter 5 about the fragility of RCLS and SCC bridges are employed to calculate the indirect costs indicators associated to the damage of the bridge typologies present on the SS76. Three structural configurations are considered, in order to highlight

the impact of ageing and compliance of the foundation system on the indirect costs. Finally, the comparison of results from direct and indirect costs for the SS76 bridges is carried out. As a result, it is found that indirect costs may have a high impact on the economic management of the bridges, especially if compared to the ordinary maintenance costs.

6.5 Application: the case study of the SS76 road

An application of the proposed framework is carried out assuming as case study the bridge network pertaining to the SS76 road. Starting from the results obtained in previous Chapter 5, the framework is crossed following the PEER-based methodology up to the evaluation of indirect costs from traffic and pollutant emissions, as shown in the synthetic flow chart in Figure 6.11. In particular, effects of degradation and compliant base have been considered in the construction of fragility curves and results from the fragility of the bridge components are adopted for the successive decision-making phase. Combining traffic conditions and the degree of damage on each component, different time lengths are defined for the intervention works along the network. Basing on these, indirect costs associable to the traffic and the pollutant emissions are computable.

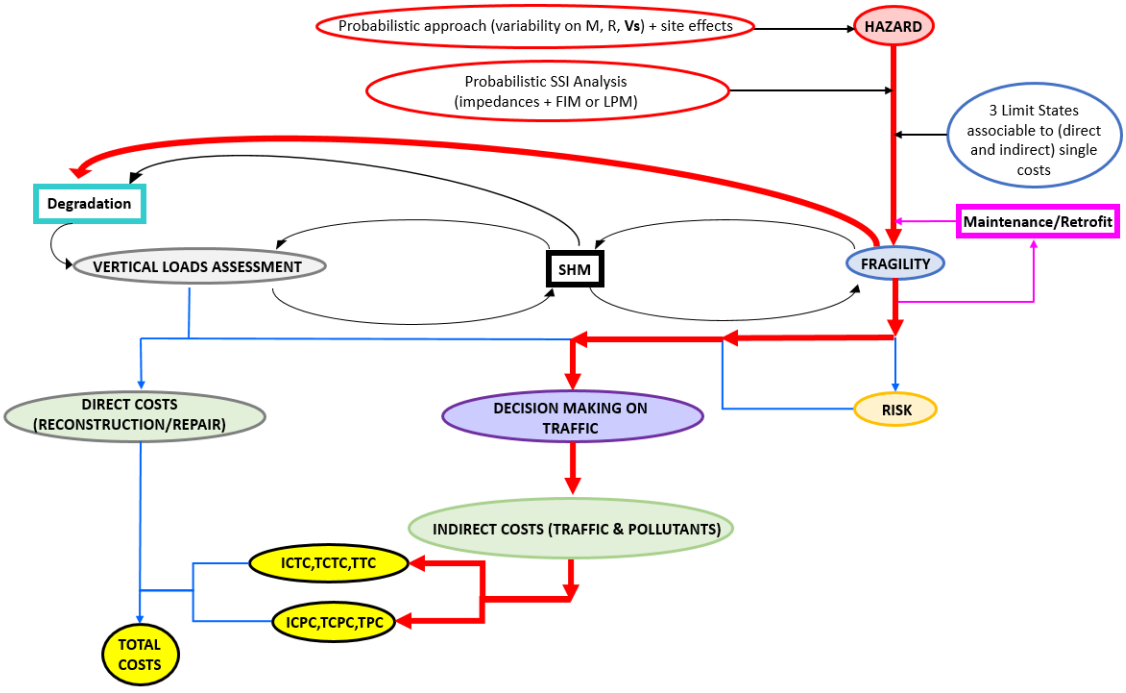

Figure 6.11. Followed path (in bold red) within the proposed framework for the application on the SS76 case study.

The SS76 counts 15 RCLS and 12 SCC viaducts of main importance, dislocated from West to East as depicted in the following Figure 6.12. As already illustrated in previous Chapter 4, different geometries have been associated to the SS76 bridges. To summarize the considered bridges and the associated geometries for the numerical analyses, Table

6.3 and Table 6.4 are here below reported, where RCLS bridges are highlighted in orange and SCC bridges in black. The viaducts names are listed following the bridges spatial order from the hinterland to the coast.

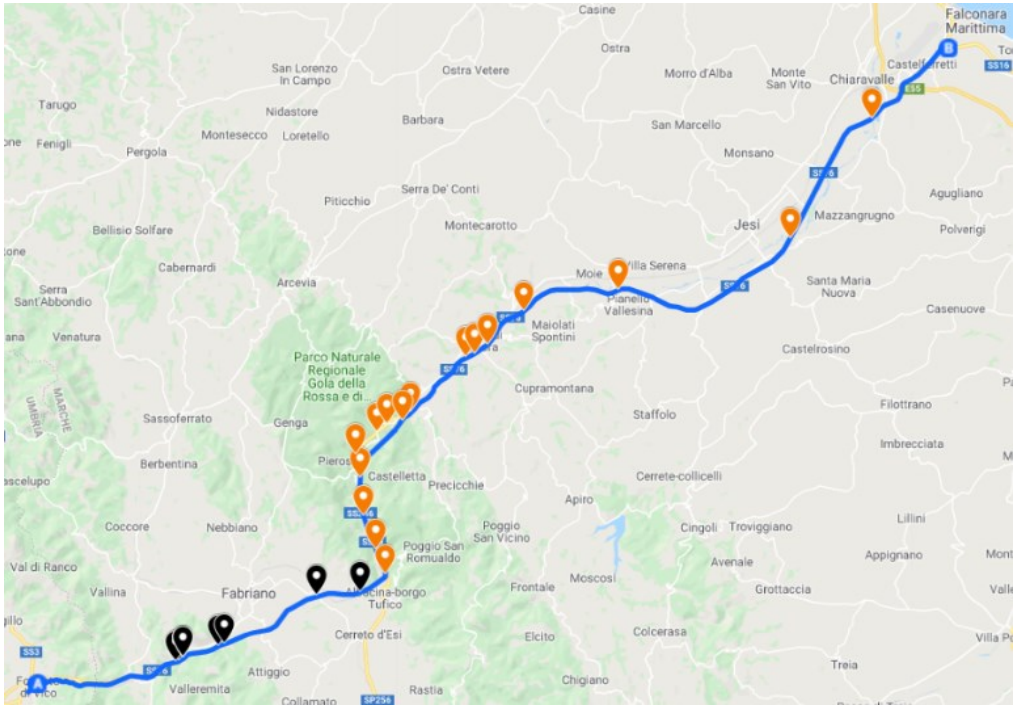

Figure 6.12. Surveyed bridges along SS76. Orange marker: viaducts with RC deck; black marker: viaducts with SCC deck.

Table 6.3. SS76 bridges and associated geometries for the numerical analyses: RCLS bridges.

Name	Latitude	Longitude	L/B*	N_{spans}*
Esino	43.35283	12.99907	10	5
Mariani	43.38307	12.98459	10	5
Gattuccio	43.40177	12.98202	10	5
Esino II	43.41353	12.97982	10	5
Esino III	43.42413	12.9945	10	5
Esino IV	43.42808	13.00125	10	5
Gola della Rossa	43.43616	13.02023	20	10
Serra San Quirico	43.45587	13.04715	20	10
Angeli	43.46201	13.05673	10	5
Esinante	43.46414	13.06303	20	10
Collefreddo	43.46808	13.07012	10	5
Spontini	43.4847	13.09555	20	10
Castelbellino	43.49459	13.15893	10	5
Esino I	43.52131	13.27668	20	10
Esino II	43.5811	13.33345	20	10

Table 6.4. SS76 bridges and associated geometries for the numerical analyses: SCC bridges.

Name	Latitude	Longitude	L/B*	N_{spans}*
Giano Ovest (Sx)	43.31086	12.85769	4	1
Giano Ovest (Dx)	43.31086	12.85769	8	2
Camporegio	43.3115	12.85983	8	2
Valleremita (Sx)	43.31471	12.86608	20	5
Valleremita (Dx)	43.31471	12.86608	20	5
Malvaioli (Sx)	43.31868	12.88675	4	1
Malvaioli (Dx)	43.31868	12.88675	4	1
Vetralla (Sx)	43.32007	12.89125	8	2
Vetralla (Dx)	43.32007	12.89125	8	2
Giano Est	43.34425	12.95745	20	5
Albacina (Sx)	43.34534	12.98265	20	5
Albacina (Dx)	43.34534	12.98265	20	5

For this application, the SS76 road network is also composed by other minor roads, where the maximum allowed transit speed is equal or lower than that on SS76. These alternative roads have been selected among all the possible to minimize the elongation of the journey in case of bridge partial or total closure, that means that at least one alternative road for each direction is considered in correspondence of each bridge, and, if more than one alternative ways are available, the one with the highest transit speed is evaluated. This assumption can be integrated through more detailed studies on the regional traffic flows and modified according to further information from the stakeholders.

The involved roads are statal, provincial, municipal or local. Acceleration or deceleration ramps are included to simulate the income or outcome of vehicles from the principal path on the SS76. According to the Italian road code, the maximum allowed speed on the typologies present on the network is illustrated in Table 6.5 and adopted for the successive traffic analyses.

Table 6.5. Maximum transit speed for the road typologies on the SS76 network.

Road Typology	Maximum speed [km/h]
SS – Statal roads	110
SP – Provincial roads	90
SC – Connection roads (municipal or local, out of the city centre)	70
RM – acceleration/deceleration Ramps	40

6.5.1 GIS analysis

As a preliminary phase to the analysis of the traffic flow in the SS76 network, the roads pertaining to the SS76 are filtered from the regional road GIS-database, available on the Marche region website: https://www.regione.marche.it/Regione-Utile/Paesaggio-Territorio-Urbanistica-Genio-Civile/Cartografia-e-informazioni-Territoriali/Repertorio#item2582. The database contains the regional traffic graph that fully returns the entire road network present on the Marche territory; in addition to the state and provincial roads, it includes the connecting roads of the ISTAT 2011 centres and nuclei, the railways and all the secondary roads connecting the scattered settlements. The database is organized through different tabs and can be queried selecting various indicators (i.e. the road name, category, maximum allowed speed, number of lanes, etc.). The GIS interface consists of two vector files: Linear Elements (Polyline) and Point Elements (Point).

In the following, Figure 6.13 shows the entire SS76 road network, while Figure 6.14 reports the selected roads highlighted with different colours according to the relevant road category. In both cases, the analysed RCLS and SCC viaducts are shown in blue on the SS76 road. The SS76 road network consists of 1097 linear elements, of which 527 form the SS76 road, 283 are provincial roads, 250 are municipal or local roads and 37 are acceleration or deceleration ramps.

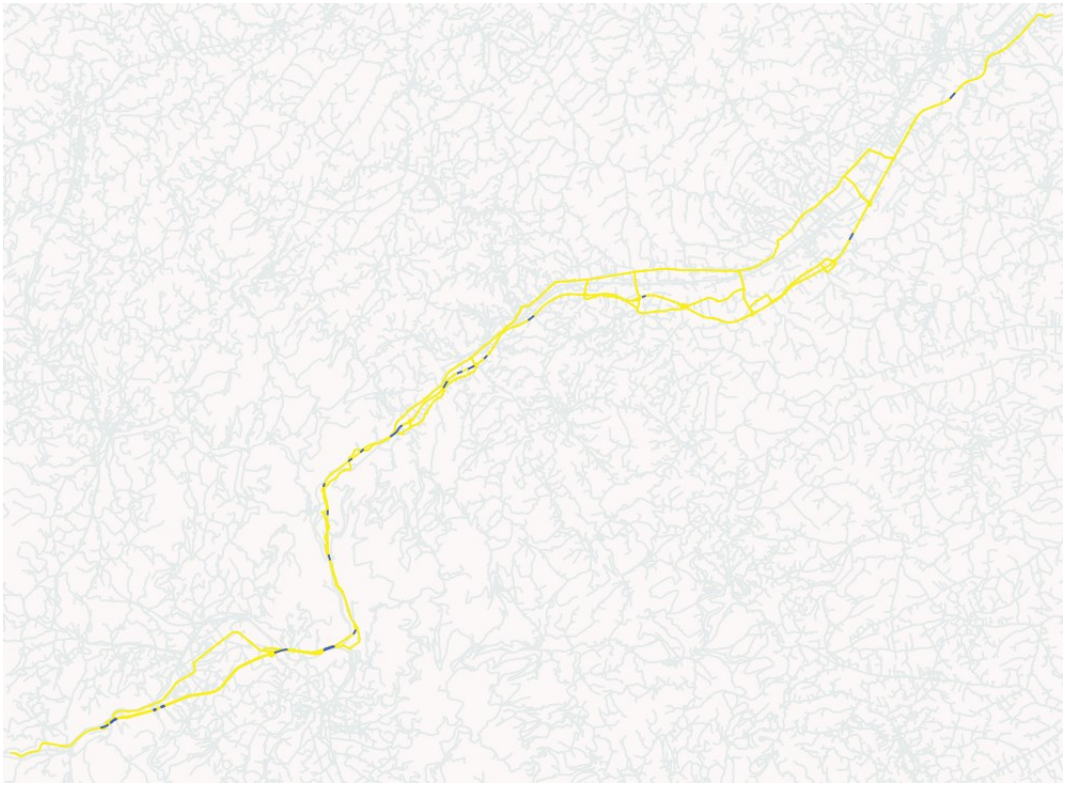

Figure 6.13. Complete SS76 road network (in yellow) with considered viaducts (in blue).

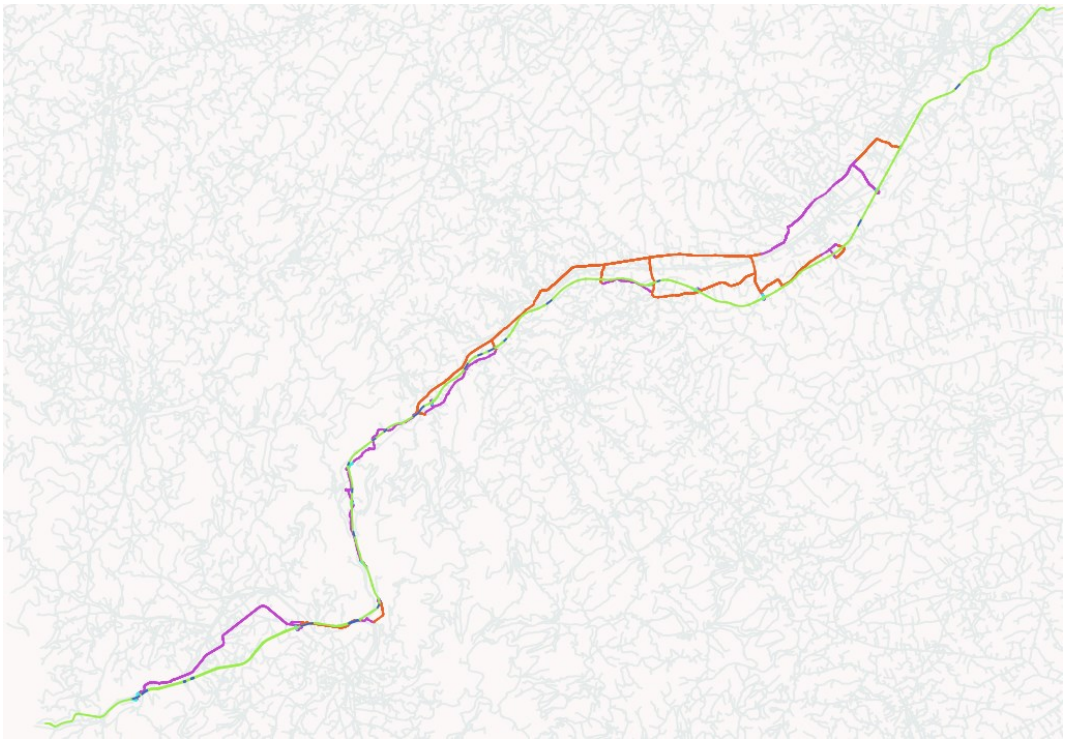

Figure 6.14. SS76 road network with the differentiation of the road typologies: green = SS76; red = provincial roads; purple = local and municipal roads; cyan = acceleration/deceleration ramps; blue = viaducts on the SS76.

6.5.2 Analysis of traffic data, traffic and emission costs

6.5.2.1 Traffic data

Information about the distribution of traffic on the existing road network are provided by the stakeholders. In case of SS76, the observatory of ANAS collects traffic data and furnishes the daily traffic flow on different tracking stations, based on the number of detected heavy and light vehicles. The traffic flow data are bidirectional values, calculated with reference to counting sections. If the counting section consists of two distinct stations, one for each of the two directions of travel, the section refers to the station located at the shortest kilometre. The number of vehicles is calculated as the arithmetic average of the traffic measured in the valid days that constitute the reference sample; a day of data is considered valid if the control unit does not report malfunctions and if the data for at least 98% of the 288 intervals of 5 minutes scheduled in a day are loaded into the system. In relation to the calculation method, for each station it is verified that the number of days with valid data is greater than half the number of days of the year.

For what concerns traffic on the SS76 road, data for 2017 are considered. 4 tracking stations along the SS76 road resulted active, as shown in the following Table 6.6, Table 6.7 and Table 6.8. Due to the absence of more detailed data, in order to simulate a uniform traffic flow from the hinterland to the coast, a calculation of the average number of vehicles in transit is made, considering three categories of vehicles: SOV (Single

Occupancy Vehicles – very light cars), HOV (High Occupancy vehicles – vehicles with more than 1 occupant, such as normal weight cars and medium-small buses), heavy vehicles (trucks or big buses). In particular, Table 6.6 shows the observed traffic flow in 2017, distinguishing between SOV, HOV and truck flows. Table 6.7 reports the analysis of the distribution of data for each direction. Table 6.8 shows the evaluation of the traffic flow for each vehicle category as a weighted average on the 4 tracking stations. Finally, Table 6.9 shows the calculation and the assignment of traffic flow reductions for each traffic category and traffic condition on the SS76 road. The number of vehicles in transit on SS76 road changes basing on the different scenario of damage on the SS76 bridges. As a fundamental step of the decision-making process, the traffic flow reduction is calculated according to the Traffic Conditions evaluated in previous §6.4.1.

Table 6.6. Tracked daily traffic flow on the SS76 road (source: ANAS - 2017).

Name of the tracking station	IMR	IMR - trucks	IMR - SOV and HOV
Km 32.000, Genga(AN) one-way values	11544 5772	1439 719.5	10105 5052.5
Km 4.200, Fabriano(AN) one-way values	6094 3047	1022 511	5072 2536
Km 53.085, Monte Roberto(AN) one-way values	20172 10086	1914 957	18258 9129
Km 69.640, Camerata Picena(AN) one-way values	21684 10842	2240 1120	19444 9722

Table 6.7. Distribution of tracked daily traffic flow on the SS76 road.

Name of the tracking station	Vehicle category	%	IMR [vehicles/day]
Km 32.000, Genga(AN) (one-way values)	SOV HOV trucks	30 70 100	1515.75 3536.75 719.5
Km 4.200, Fabriano(AN) (one-way values)	SOV HOV trucks	30 70 100	760.8 1775.2 511
Km 53.085, Monte Roberto(AN) (one-way values)	SOV HOV trucks	30 70 100	2738.7 6390.3 511
Km 69.640, Camerata Picena(AN) (one-way values)	SOV HOV trucks	30 70 100	2916.6 6805.4 1120

Table 6.8. Calculation and assignment of vehicles for each traffic category on the SS76 road.

Vehicle category	IMR [vehicles/day]	IMR/TOTAL [%]
SOV	1983	26.66
HOV	4627	62.22
trucks	827	11.12
TOTAL	7437	100

Table 6.9. Calculation and assignment of traffic flow reductions for each traffic category and traffic condition TC on the SS76 road.

			Traffic Flow Reduction Factor (TFRF) [%]				IMR			
Vehicle category	IMR [vehicles /day]	IMR [%]	TFRF [%] TC1	TFRF [%] TC2	TFRF [%] TC3	TFRF [%] TC4	IMR TC1	IMR TC2	IMR TC3	IMR TC4
SOV	1983	26.66	0	25	50	100	1983	1487	992	0
HOV	4627	62.22	0	25	50	100	4627	3470	2314	0
trucks	827	11.12	0	50	75	100	827	414	207	0
TOTAL	7437	100					7437	5371	3512	0

6.5.2.2 Traffic costs

For each vehicle category, the traffic costs can be estimated basing on the information available on the ACI website: www.aci.it. In particular, ACI offers a service that allows to calculate the mileage costs necessary to quantify the amount of refunds for employees or professionals who use their vehicle while carrying out activities in favour of their employer. These costs are expressed in €/km and represent an attempt to evaluate the amount of costs incurred by the road users. With the ACI service, one can find:

- the value of the cost per kilometre for the individual models of car, motorcycle, moped, off-road vehicle, van (from 2018);
- the value of the cost per kilometre for the individual truck models (from 2012);
- the price of fuel (since 2000);
- tax deductibility limits from business income for travel expenses (since 2000).

With the calculation of mileage costs it is possible to view the values for each individual vehicle, selecting the following parameters: category of vehicles (passenger car, motorcycle, moped, off-road), list of brands (Alfa Romeo, BMW, etc..), power supply (petrol, diesel, etc..), calculation date (starting from 1/1/2018).

For the current application, 7 vehicle types are considered belonging to the 3 vehicle categories illustrated above, taking into account some common and widespread typologies on the regional transport fleet. Table 6.10 reports the vehicle typologies, the associated user costs and the assumed percentage distribution on the regional traffic flow.

Table 6.10. Single Vehicle Traffic Costs (SVTC) for vehicle categories and typologies on the SS76 road.

Vehicle category and type	SVTC [€/km/vehicle]	[%]	IMR/TOTAL [%]	averaged [%]
(1) SOV - SMART FORTWO COUPÉ 0.9 90CV - MY2014	0.2209	100	26.66	26.66
(2) HOV - GRANDE PUNTO 1.4 - 77CV	0.2576	50	62.22	31.11
(3) HOV - OPEL ZAFIRA Elegance	0.3581	35		21.777
(4) HOV - IVECO-FIAT ECODAILY 35S17V - MIDIVAN	0.4164	15		9.333
(5) Truck - IVECO-FIAT Daily 50c15v 3.0 hpi	0.5714	30	11.12	3.336
(6) Truck - IVECO-FIAT Ml120e18/p	0.5323	30		3.336
(7) Truck - SCANIA R500 lb 4x2 Cr 19 highline	0.5677	40		4.448

6.5.2.1 Emission costs

The emission costs are here evaluated. In this case, the recent "EMEP/EEA air pollutant emission inventory guidebook" (herein after called the Guidebook) from the European Environment Agency (EEA, 2019), together with the "Guidelines for Reporting Emissions and Projections Data" by the United Nations Economic Commission for Europe (UNECE) convention on Long-range Transboundary Air Pollution (LRTAP convention), provides concise guidance on how to compile an air pollutant emissions inventory, focusing on a twofold purpose: to provide procedures to enable users to compile emission inventories that meet quality criteria for transparency, consistency, completeness, comparability and accuracy, and to provide estimation methods and emission factors for inventory compilers at various levels of sophistication. The use of the Guidebook relates to the latest version of the EMEP/CORINAIR Atmospheric Emissions Inventory Guidebook published in July 2018. In particular, chapter 1.A.3.b.i-iv "Road transport" (https://www.emisia.com/utilities/copert/documentation/) provides the methodology, emission factors and relevant activity data enabling exhaust emissions for the following categories of road vehicles:

- passenger cars (SOV or HOV), differentiated by small, medium or large size;
- light commercial vehicles (< 3,5 t),
- heavy-duty vehicles (>3,5 t) and buses.

The most important pollutants emitted by road vehicles include:

- ozone precursors (CO, NOx, NMVOC);
- greenhouse gases (CO_2, CH_4, N_2O);
- acidifying substances (NH_3, SO_2);
- particulate matter mass (PM) including black carbon (BC) and organic carbon (OC);
- carcinogenic species (PAHs and POPs);
- toxic substances (dioxins and furans);

- heavy metals.

The Emission Factors (EF) illustrated in the following Table 6.11 are relevant to the considered vehicle categories and vehicle typologies. Three pollutant emissions are examined: the carbon monoxide CO and the volatile organic compounds VOC, assuming petrol as employed fuel. The emission factors are expressed in g/km/vehicle. In the following, the SVPC are specialized consistently with the corresponding pollutant.

Table 6.11. Emission factors for vehicle categories and typologies on the SS76 road.

Vehicle category and type	EF_CO [g/km/vehicle]	EF_VOC [g/km/vehicle]
(1) SOV - SMART FORTWO COUPÉ 0.9 90CV - MY2014	0.3648	0.0196
(2) HOV - GRANDE PUNTO 1.4 - 77CV	0.3648	0.0196
(3) HOV - OPEL ZAFIRA Elegance	0.3648	0.0196
(4) HOV - IVECO-FIAT ECODAILY 35S17V - MIDIVAN	0.5731	0.0214
(5) Truck - IVECO-FIAT Daily 50c15v 3.0 hpi	0.5731	0.0214
(6) Truck - IVECO-FIAT Ml120e18/p	3.558	2.647
(7) Truck - SCANIA R500 lb 4x2 Cr 19 highline	3.558	2.647

The monetary quantification of pollutant emissions can be made taking into account the consequences that the release of pollutants in the air may have on environment and human being. Values for emission costs derive from a recent research by Čokorilo et al. (2019) and Preiss et al. (2008). According to these documents, for each of the European countries the basic unit costs of emissions for NOx, SOx, NMVOC and PM in 2000 were determined, considering socio-economic characteristics of the investigated countries and their geographical position. These costs refer to the pollutants impact on human health, loss of biodiversity, crops & materials and global warming. Given the estimated average gross domestic product growth at the European level of 2% in the period up to 2030 and 1% in the period from 2030 to 2050, it is possible to determine the unit cost of pollutants for any year in the range from 2000 to 2050. For what concerns CO, the Unit Cost of Emission (UCE) is directly derived from the work by Čokorilo et al. (2019). Table 6.12 offers a synthetic view of the adopted UCEs for CO and VOC emissions, expressed in € per tonne, with reference to the results for Italy in current 2020.

Table 6.12. Single Vehicle Pollutant Costs (SVPC) for considered pollutant emissions.

UCE_CO [€/t]	UCE_VOC [€/t]
106.5	861.0

As a consequence, the SVPCs (Single Vehicle Pollutant Costs) can be calculated as the product of the emission factors and the unit costs of emission, and the correspondent values are shown in Table 6.13.

Table 6.13. Single Vehicle Pollutant Costs (SVPC) for considered pollutant emissions and vehicle typologies.

Vehicle category and type	SVPC_CO [€/km/vehicle]	SVPC_VOC [€/km/vehicle]
(1) SOV - SMART FORTWO COUPÉ 0.9 90CV - MY2014	0.0389	0.0169
(2) HOV - GRANDE PUNTO 1.4 - 77CV	0.0389	0.0169
(3) HOV - OPEL ZAFIRA Elegance	0.0389	0.0169
(4) HOV - IVECO-FIAT ECODAILY 35S17V - MIDIVAN	0.0610	0.0184
(5) Truck - IVECO-FIAT Daily 50c15v 3.0 hpi	0.0610	0.0184
(6) Truck - IVECO-FIAT Ml120e18/p	0.3789	2.2791
(7) Truck - SCANIA R500 lb 4x2 Cr 19 highline	0.3789	2.2791

6.5.3 NEXTA-DTALite application

The analyses of traffic flows are developed through the specific and dedicated software NeXTA (Zhou & Taylor, 2014). NEXTA (Network EXplorer for Traffic Analysis) is an open-source graphical user interface (GUI) that aims to facilitate the preparation, post-processing and analysis of transportation assignment, simulation and scheduling datasets. The traffic simulation analyses are performed through the DTALite (Light-weight Dynamic Traffic Assignment Engine), that uses a computationally simple but theoretically rigorous traffic queuing model in its light weight mesoscopic simulation engine With both open-source traffic simulation engine and graphic user interface (GUI), the software suite of DTALite + NEXTA aims to:

- provide an open-source code base to enable transportation researchers and software developers to expand its range of capabilities to various traffic management analysis applications;
- present results to other users by visualizing time-varying traffic flow dynamics and traveller route choice behaviour in an integrated 2D/3D environment.

The software architecture of DTALite aims to integrate many rich modelling and visualization capabilities into an open-source dynamic traffic assignment model suitable for practical everyday use within the context of an entire large-scale metropolitan area network. The features of the adopted version of NeXTA (version 3) include:

- convenient import of network and demand data from other planning models based on GIS shape files
- multi-layer management for transportation layer

- integrated sensor and simulated data management and visualization
- click-and-drag network/control creation and editing interface based on background image
- improved loading and display time-dependent link-based speed, density, queue and bottleneck for large-scale network datasets
- capability of loading large networks with more than 60k links, and simulation results with more than10M trips.
- click-and-define a path and show path-based speed, density and emission contour
- vehicle trajectories-based analysis for generating traffic mobility, emission and reliability Measures of Efficiency (MOEs) for many categories.
- built-in interfaces with Google Earth and GIS shape files
- generation of default movements and signal control data for fast deployment

The GIS-based data on the SS76 road network illustrated in §6.5.1 have been implemented within NeXTA, where the network is modelled from the union of 1025 nodes and 2002 links and sub-links. For each link element, information about the road type, the number of lanes, the maximum allowed speed and the traffic reduction are editable, so that different and multiple traffic scenarios can be evaluated. In particular, in presence of working areas, it is possible to set the daily time interval during which the normal traffic flow conditions (herein, the free flow conditions) are altered.

For what concerns the current application, the working zones correspond to the viaducts under damage or collapse conditions at the occurrence of the investigated seismic intensity. Figure 6.15 shows the graphical restitution of the SS76 road network with implemented working areas on its bridges.

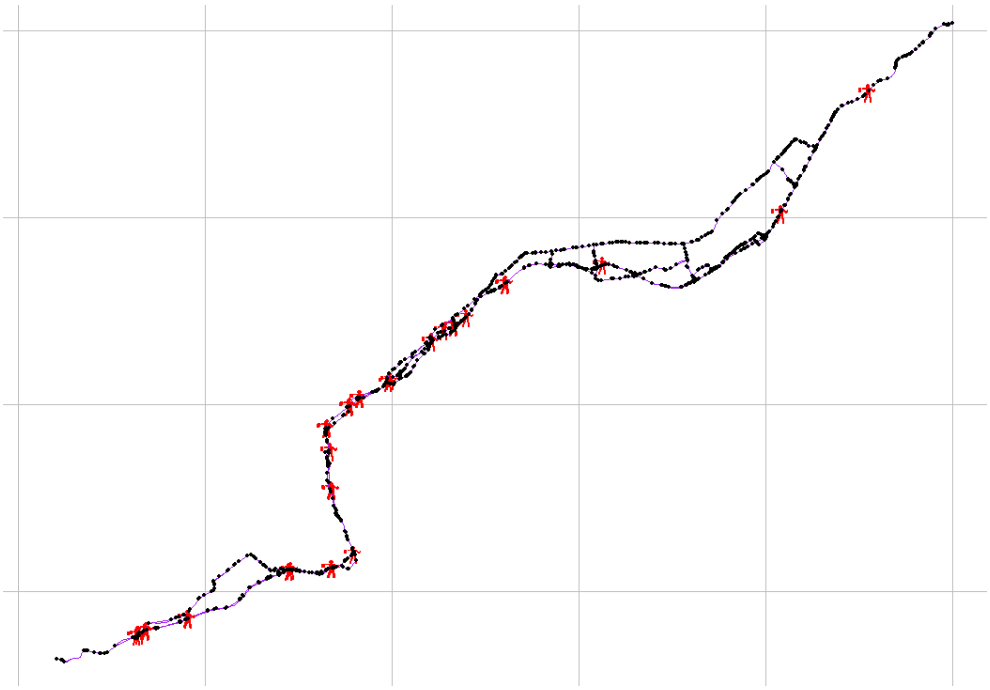

Figure 6.15. SS76 road network with working areas on the viaducts.

To associate a degree of damage to the SS76 viaducts, and the consequent alteration of traffic flow, a seismic event characterized by a magnitude $M = 6.5$ with epicentre located in the city of Fabriano is considered. The epicentral distances R can be calculated for the viaducts on SS76 and the procedure illustrated in §6.4.1 is followed to estimate different values for IM and the corresponding damage condition on the viaduct components. In absence of more detailed data concerning the subsoil category in correspondence of the viaduct foundations, the shear wave velocity V_{S30} in each bridge site is evaluated basing on the corresponding subsoil class according to the NTC2018 classification (NTC2018). The attribution of a soil class to each bridge site is made through the stand-alone software SCC-Italy following the work by Forte et al. (2019). Table 6.14 summarizes the soil characteristics and the expected IM values (Sa(T=1 s)) in correspondence of the SS76 viaducts for the assumed seismic magnitude at the relevant epicentral distances.

Table 6.14. SS76 bridges and associated epicentral distances, subsoil shear wave velocities and expected spectral acceleration values; in orange, RCLS bridges; in black, SCC bridges.

Name	R [km] (from Fabriano)	Subsoil Class	V_{S30} [m/s]	IM = Sa(T=1 s) [g]
Esino	7.60	B	450	0.2216
Mariani	7.67	C	255	0.3151
Gattuccio	8.84	E	255	0.2842
Esino II	9.71	E	255	0.2644
Esino III	11.37	C	255	0.2324
Esino IV	12.06	B	450	0.1545
Gola della Rossa	13.74	C	255	0.1970
Serra San Quirico	16.83	C	255	0.1635
Angeli	17.86	C	255	0.1546
Esinante	18.38	C	255	0.1504
Collefreddo	19.09	C	255	0.1450
Spontini	21.85	C	255	0.1271
Castelbellino	26.38	C	255	0.1054
Esino I	35.81	C	255	0.0772
Esino II	43.39	C	255	0.0632
Giano Ovest (Sx)	5.41	C	255	0.3887
Giano Ovest (Dx)	5.41	C	255	0.3887
Camporegio	5.24	C	255	0.3951
Valleremita (Sx)	4.63	B	450	0.2926
Valleremita (Dx)	4.63	B	450	0.2926
Malvaioli (Sx)	3.28	C	255	0.4727
Malvaioli (Dx)	3.28	C	255	0.4727
Vetralla (Sx)	2.98	B	450	0.3386
Vetralla (Dx)	2.98	B	450	0.3386
Giano Est	4.18	C	255	0.4366
Albacina (Sx)	6.22	C	255	0.3602
Albacina (Dx)	6.22	C	255	0.3602

The just found *IM* values are used to find the highest probability of occurrence among the considered performance levels and then to associate to each viaduct a traffic condition. To evaluate the consequence of damage more reliably, fragility curves from the analysis with compliant base and ageing condition t = 50 years are employed. In the following, a comparison in terms of traffic and emission costs between the free flow scenario and the presence of working zones is provided.

Finally, to perform traffic simulation analyses, among the different available traffic flow models, the Newell's simplified Kinematic Wave Model is adopted (Newell, 1993). The O-D path is built assuming as starting station the first West node of the SS76 road and ending station the easternmost node, corresponding to the municipality of Falconara Marittima (Figure 6.16). Even in this case, specific studies on the analysis of the local traffic flows provided by the stakeholders may improve the level of accuracy of next results.

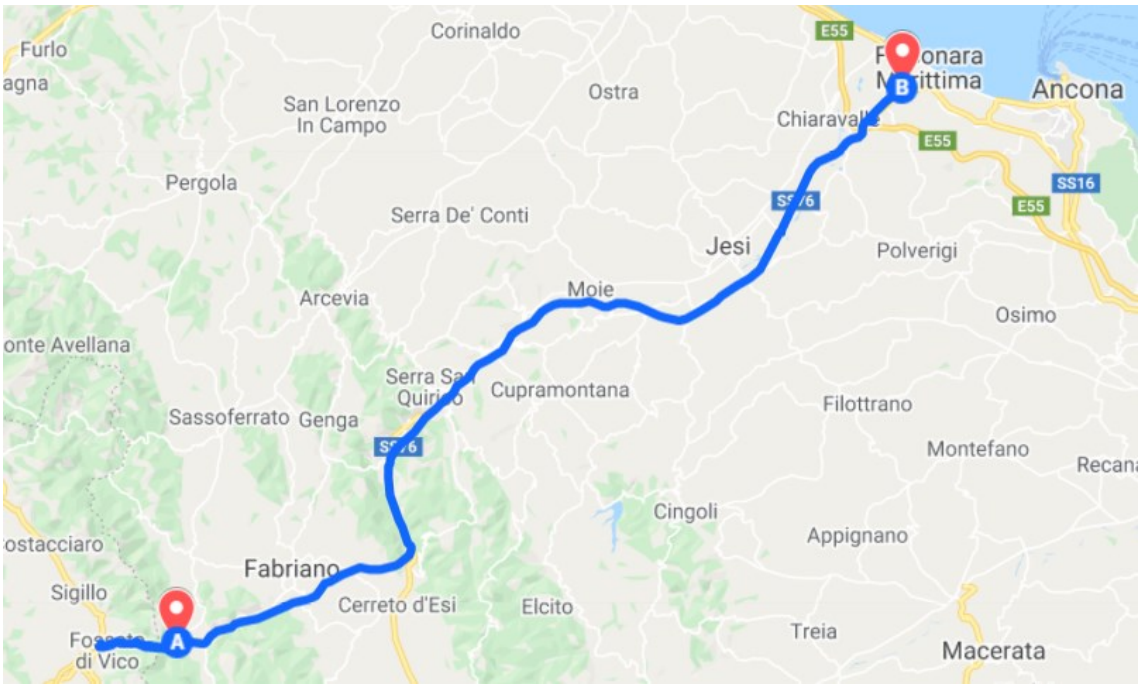

Figure 6.16. O-D points (red markers on A=Origin, B=Destination) and path (in blue) for traffic simulation on SS76.

6.5.4 Results

In this section, results of the application of the framework for the analysis of direct and indirect costs are commented. Three configurations are examined to perform the analysis of consequences on SS76 viaducts: the design condition, with fixed columns at the base (*Design, Fixed Base*); the ageing condition to the present days, with fixed columns at the base (*t = 50 y, Fixed Base*); the ageing condition to the present days, with compliant base under the piers (*t = 50 y, LPM*). The outcomes of the decision-making process on the fragility results are summarized in Table 6.15, where both the limit state/traffic condition

couple and the associated recovery time are reported. It is immediate to see that the three conditions not only represent a significant change in the structural response, as already commented in previous Chapter 5, but also strongly affect the management of the road network for the duration of the intervention works. The viaducts whose recovery time length changed from one configuration to another are highlighted in light grey.

Table 6.15. Examined structural configurations for the analysis of direct and indirect costs.

	Design, Fixed Base		t = 50 y, Fixed Base		t = 50 y, LPM	
Name	Limit State/Traffic Condition	Recovery Time [days]	Limit State/Traffic Condition	Recovery Time [days]	Limit State/Traffic Condition	Recovery Time [days]
Esino	D + TC2	7	D + TC2	7	D + TC2	7
Mariani	LS + TC4	90	LS + TC4	90	LS + TC4	90
Gattuccio	LS + TC4	90	LS + TC4	90	LS + TC4	90
Esino II	LS + TC4	90	LS + TC4	90	LS + TC4	90
Esino III	LS + TC4	90	LS + TC4	90	LS + TC4	90
Esino IV	LS + TC4	90	LS + TC4	90	LS + TC4	90
Gola della Rossa	D + TC2	7	D + TC2	7	D + TC2	7
Serra San Quirico	D + TC2	7	D + TC2	7	D + TC2	7
Angeli	D + TC2	7	D + TC2	7	D + TC2	7
Esinante	D + TC2	7	D + TC2	7	D + TC2	7
Collefreddo	D + TC2	7	D + TC2	7	D + TC2	7
Spontini	D + TC2	7	D + TC2	7	D + TC2	7
Castelbellino	D + TC2	7	D + TC2	7	D + TC2	7
Esino I	D + TC2	7	D + TC2	7	D + TC2	7
Esino II	D + TC2	7	D + TC2	7	D + TC2	7
Giano Ovest (Sx)	D + TC1	1	LS + TC4	90	LS + TC4	90
Giano Ovest (Dx)	D + TC1	1	LS + TC4	90	LS + TC4	90
Camporegio	D + TC1	1	LS + TC4	90	LS + TC4	90
Valleremita (Sx)	D + TC2	7	D + TC2	7	D + TC2	7
Valleremita (Dx)	D + TC2	7	D + TC2	7	D + TC2	7
Malvaioli (Sx)	D + TC1	1	LS + TC4	90	LS + TC4	90
Malvaioli (Dx)	D + TC1	1	LS + TC4	90	LS + TC4	90
Vetralla (Sx)	D + TC1	1	LS + TC4	90	LS + TC4	90
Vetralla (Dx)	D + TC1	1	LS + TC4	90	LS + TC4	90
Giano Est	D + TC2	7	D + TC2	7	C + TC4	150
Albacina (Sx)	D + TC2	7	D + TC2	7	C + TC4	150
Albacina (Dx)	D + TC2	7	D + TC2	7	C + TC4	150

For the sake of brevity, the calculation of the traffic and emission costs according to the indexes in Eq. (41)-(54) is illustrated for the third configuration (*t = 50 y, LPM*), since it can be assumed as the most representative of the actual bridges' characteristics. The recovery scenario associated to the third configuration consists in the evolution in time of

the number of bridges that need intervention works, marked by three phases: the first one predicts the partial or total closure for all the SS76 viaducts for the first 7 days; in the second one, viaducts with 90 or 150 days recovery time are still closed, for the remaining (90-7) = 83 days; in the third one, (150-7-(90-7)) = 60 days are left for the recovery of the last remained damaged viaducts (Giano Est, Albacina Sx and Albacina Dx). The evolution of the recovery scenario is summarized in Figure 6.17.

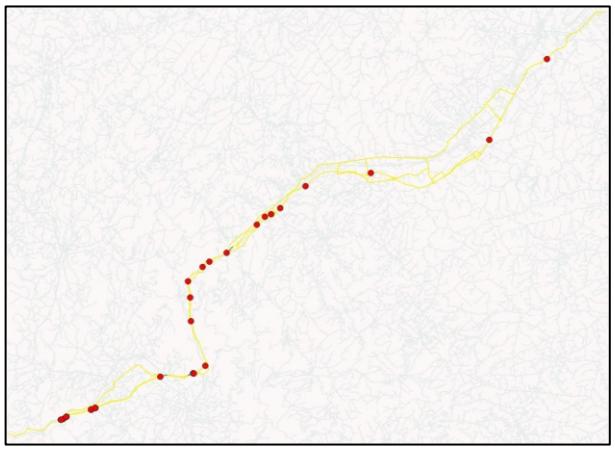

(a)

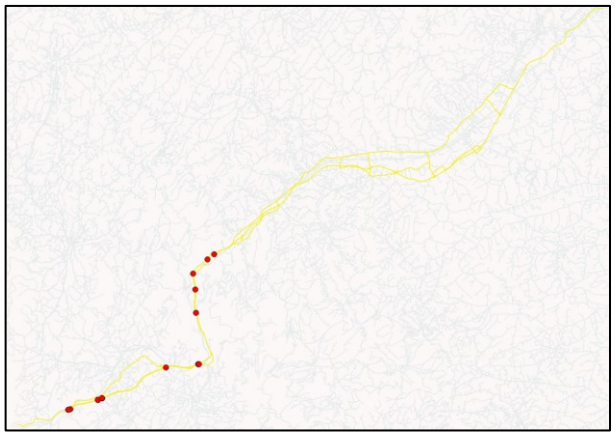

(b)

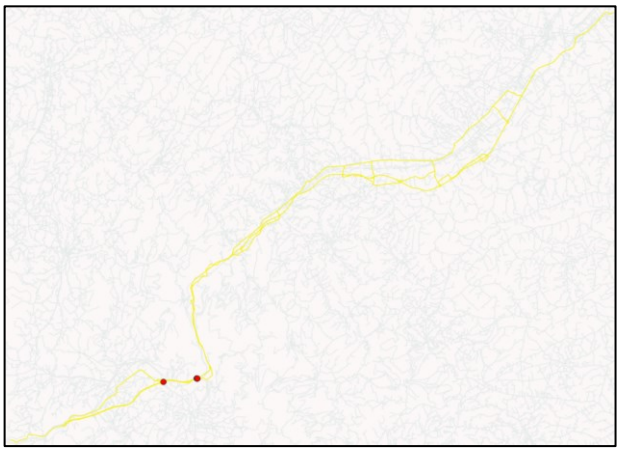

(c)

Figure 6.17. Evolution of the recovery scenario: (a) 1st phase (1-7 days); (b) 2nd phase (8-90 days); (c) 3rd phase (91-150 days).

In the following, the calculation of the traffic and pollutant emission indexes is provided. First, the Incremental Category Traffic Cost (ICTC) (Eq. (41)) is evaluated for each vehicle type (Figure 6.18). This information is useful for the traffic user. The ICTC progressively reduces from the 1st to the 3rd phase of the recovery period, and the improvement of the SS76 road conditions between the 1st and the 2nd phase slightly affects the improvement of the relative traffic conditions, confirming the strong impact of extremely damaged bridges on the overall viability.

Analogously, the Incremental Category Pollutant Costs (ICPCs) are evaluated (Figure 6.19), according to Eq. (48). It is interesting to notice that, in case of trucks, the emission costs are up to 4 times higher than the user costs. This information may be used to furtherly investigate the local environmental impact of emissions in case of queues for the SS76 adjacent areas.

Figure 6.20 and Figure 6.21 show the comparison between the free flow condition and the ongoing work condition for each phase of the recovery scenario, in terms of Total Category Traffic Cost (TCTC – Eq. (42)) and Percentage Increment of Total Category Traffic Cost ($TCTC_{PI}$ – Eq. (45)), for SOV-HOV and trucks, respectively. In this case, very heavy trucks involve the maximum increment of TCTC. This information may be useful to additionally improve the decision-making process, choosing to allow the transit only for the vehicle categories that have the lowest increment of costs for the users.

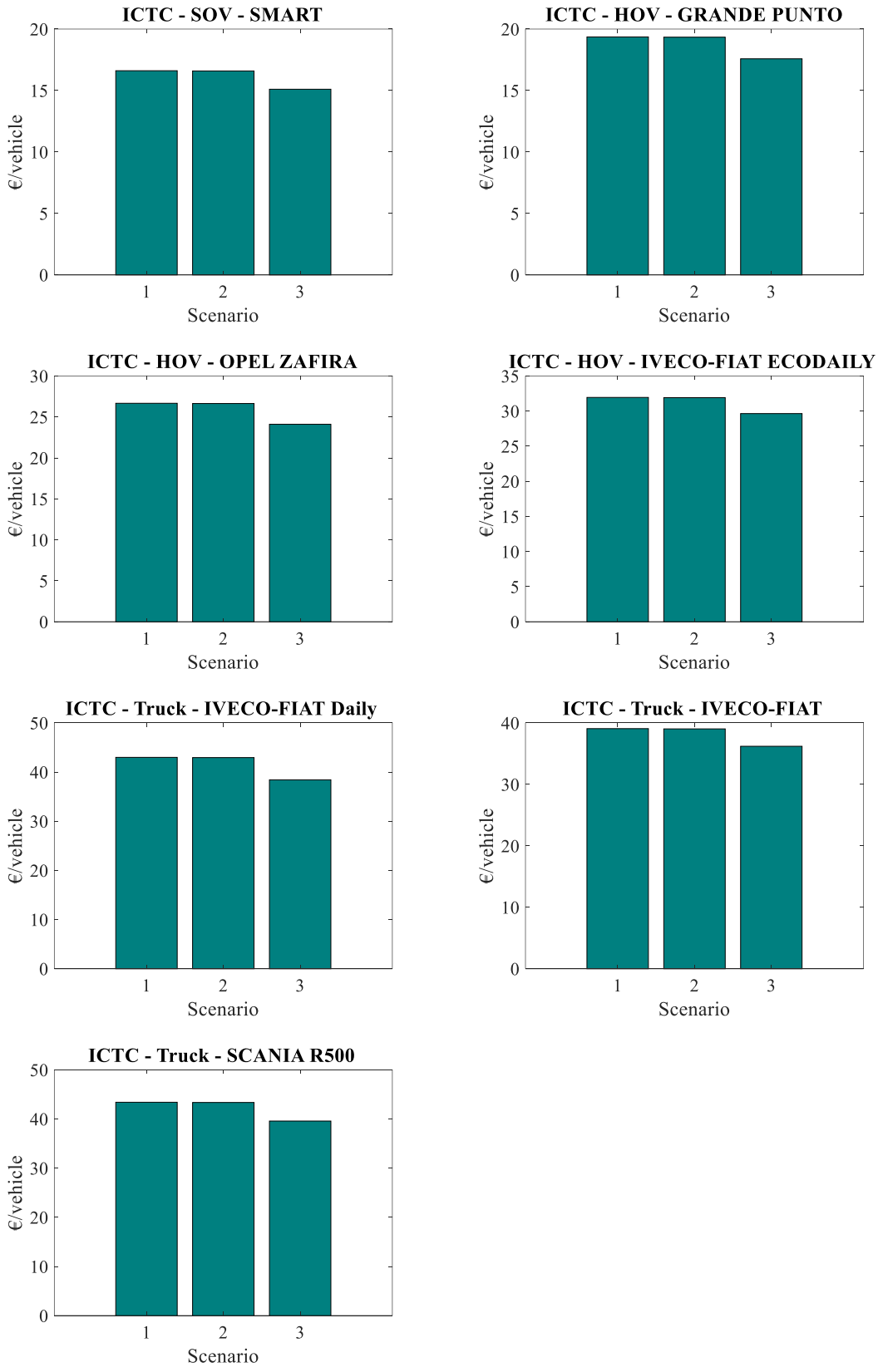

Figure 6.18. Incremental Category Traffic Costs (ICTCs) for the considered recovery scenarios.

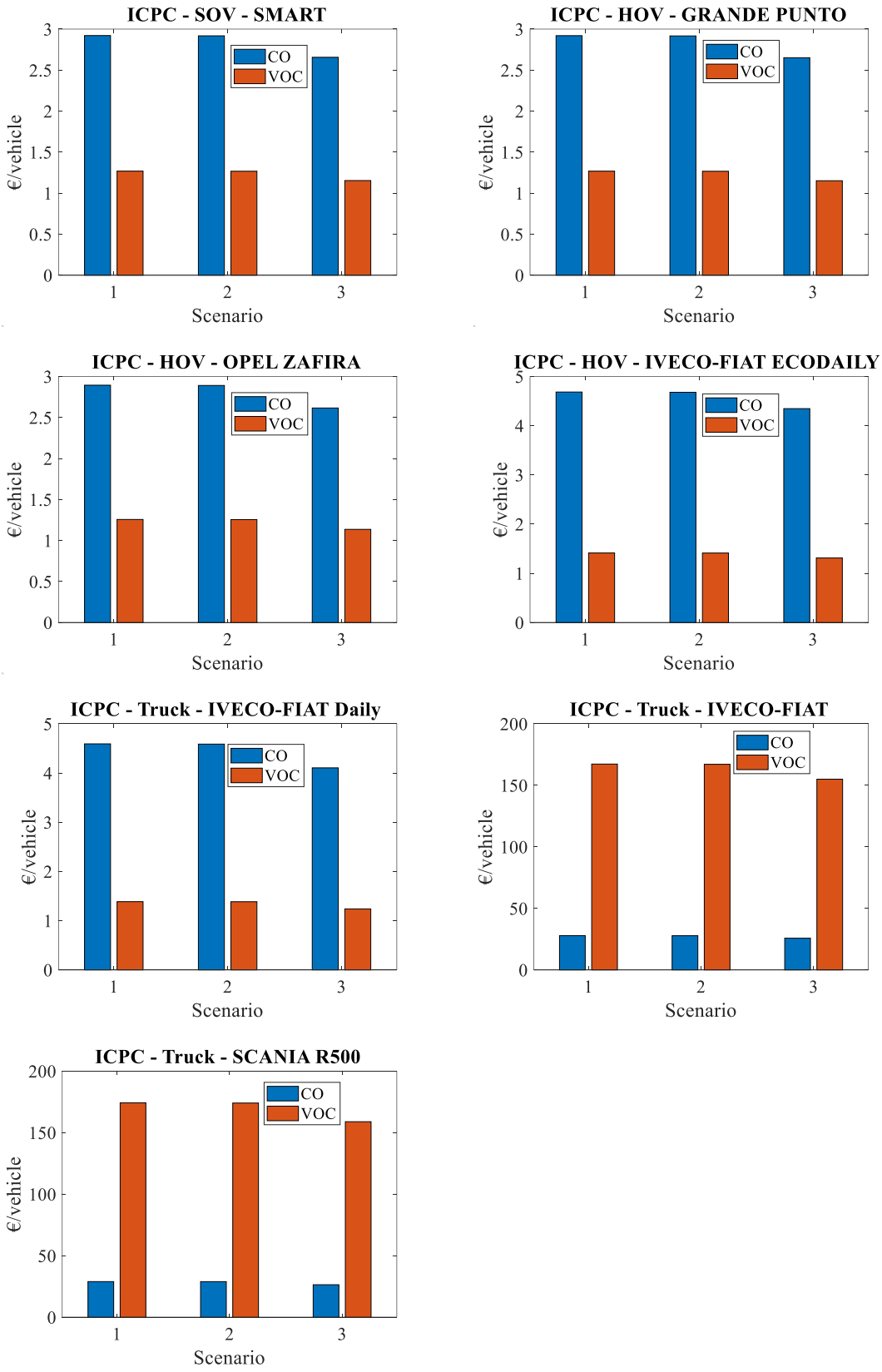

Figure 6.19. Incremental Category Pollutant Costs (ICTCs) for the considered recovery scenarios.

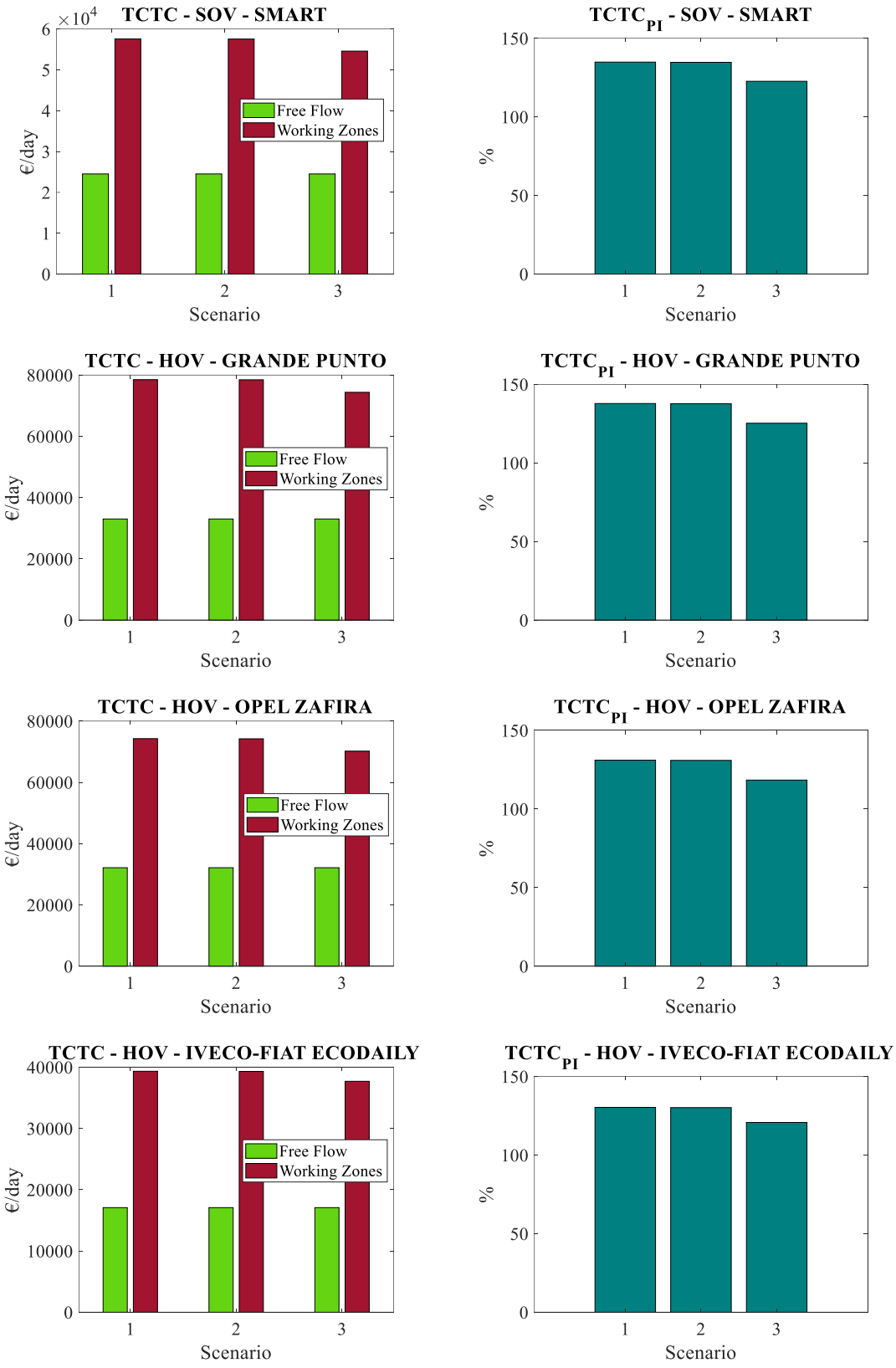

Figure 6.20. Total Category Traffic Costs (TCTCs) and Total Category Traffic Costs Percentage Increment ($TCTC_{PI}$) for the considered recovery scenarios – SOV and HOV.

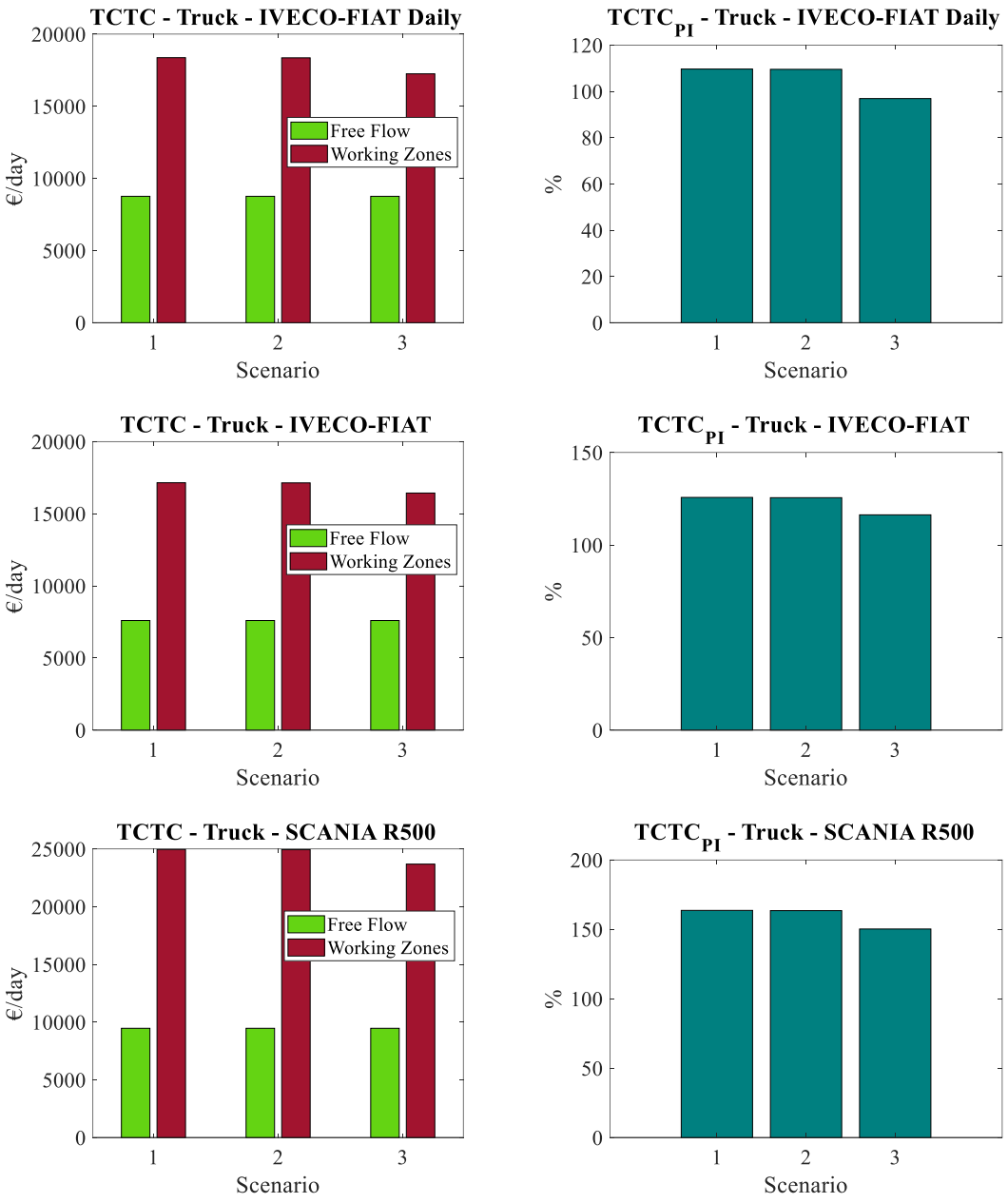

Figure 6.21. Total Category Traffic Costs (TCTCs) and Total Category Traffic Costs Percentage Increment ($TCTC_{PI}$) for the considered recovery scenarios – trucks.

Analogously, the Total Category Pollutant Costs (TCPCs) and the associated Percentage Increments ($TCPC_{PI}$) are evaluated according to Eq. (49) and Eq. (52), respectively. Figure 6.22 shows that SOVs and HOVs vehicles produce a consistent increment of emission costs for CO, while trucks are responsible of larger VOC emission costs. It is interesting to notice that in case of SOVs and HOVs, user costs (TCTCs) are 4-5 times higher than environmental costs (TCPCs), while an opposite trend can be recognized in case of medium-high weight trucks. This information may represent another aspect for the improvement of the decision-making.

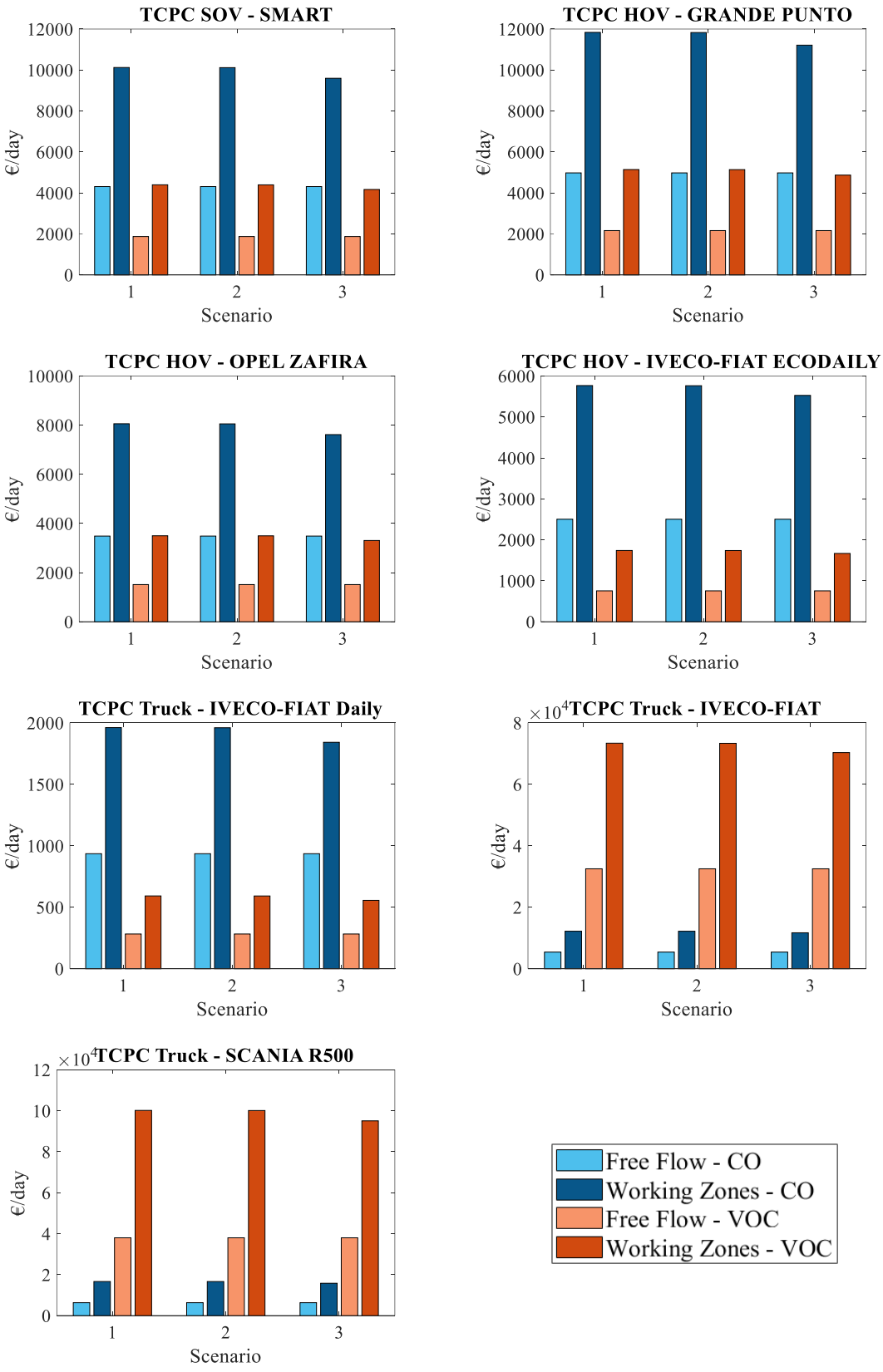

Figure 6.22. Total Category Pollutant Costs (TCPCs) for the considered recovery scenarios.

Finally, the Total Traffic Costs (TTCs – Eq. (43)) and the Total Pollutant Costs (TPCs – Eq. (50)) are calculated in each recovery phase. Figure 6.23 and Figure 6.24 compare total costs associated to the absence and the presence of intervention works for the entire duration of the recovery phase.

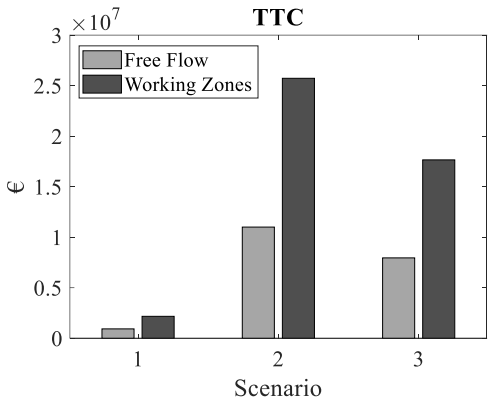

Figure 6.23. Total Traffic Costs (TTCs) for the considered recovery scenarios.

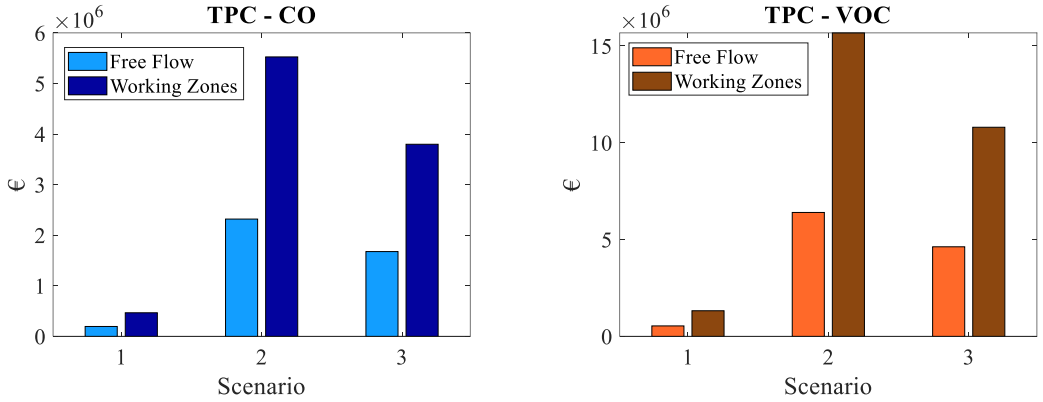

Figure 6.24. Total Pollutant Costs (TPCs) for the considered recovery scenarios.

In order to quantify the increment of indirect costs, Table 6.16 offers a comparison between the free flow condition and the presence of working areas along the SS76 road. It suggests that the presence of damages on the viaducts implies more than a doubling of the normal costs of emissions and traffic for users.

Table 6.16. Total Final Costs for Traffic (TFTC) and Pollutants (TFPC) and Percentage Increments ($TFTC_{PI}$, $TFPC_{PI}$) for free flow and altered traffic flow conditions.

Condition	TFTC [€]	TFPC_CO [€]	TFPC_VOC [€]	TFPC [€]
Free Flow	19,884,640	4,191,097	11,566,525	15,757,622
Working Zones	45,547,269	9,789,562	27,798,144	37,587,706
	$TFTC_{PI}$ [%]	$TFPC\_CO_{PI}$ [%]	$TFPC\_VOC_{PI}$ [%]	$TFPC_{PI}$ [%]
	129.5 %	133.6 %	140.3 %	138.5 %

To highlight the impact of indirect costs and at the same time stress the attention on the importance of the maintenance operations, Table 6.17 offers a synthetic view of the Total Reconstruction Costs (TRCs), the annual Maintenance Costs (MCs) and, basing on the analysed damage scenario, the Partial Reconstruction Costs (PRCs) associated to the interventions on the SS76 viaducts. PRCs are derived from FEMA's HAZUS (2013) Table 15.18 and Table 15B.1, previously reported in Figure 6.5 and Figure 6.6, respectively. The results are also related to the above mentioned estimates on the reconstruction costs and ordinary maintenance costs suggested by Professor de Miranda for Italian bridges (de Miranda, 2019).

Table 6.17. Evaluation of reconstruction costs and maintenance costs for the viaducts on SS76.

	t = 50 y, LPM				
Name	Total Reconstruction Cost (TRC) [€]	Maintenance Cost (MC) [€/year]	Limit State/Traffic Condition	Recovery Time [days]	Partial Reconstruction Cost (PRC) [€]
Esino	2,625,000	13,125	D + TC2	7	131,250
Mariani	3,062,500	15,312.5	LS + TC4	90	765,625
Gattuccio	2,625,000	13,125	LS + TC4	90	656,250
Esino II	1,312,500	6,562.5	LS + TC4	90	328,125
Esino III	2,187,500	10,937.5	LS + TC4	90	546,875
Esino IV	2,187,500	10,937.5	LS + TC4	90	546,875
Gola della Rossa	11,812,500	59,062.5	D + TC2	7	590,625
Serra San Quirico	4,812,500	24,062.5	D + TC2	7	240,625
Angeli	3,062,500	15,312.5	D + TC2	7	153,125
Esinante	4,375,000	21,875	D + TC2	7	218,750
Collefreddo	2,187,500	10,937.5	D + TC2	7	109,375
Spontini	4,375,000	21,875	D + TC2	7	218,750
Castelbellino	1,750,000	8,750	D + TC2	7	87,500
Esino I	4,812,500	24,062.5	D + TC2	7	240,625
Esino II	4,812,500	24,062.5	D + TC2	7	240,625
Giano Ovest (Sx)	875,000	4,375	LS + TC4	90	218,750
Giano Ovest (Dx)	1,750,000	8,750	LS + TC4	90	437,500
Camporegio	2,625,000	13,125	LS + TC4	90	656,250
Valleremita (Sx)	4,375,000	21,875	D + TC2	7	218,750
Valleremita (Dx)	4,375,000	21,875	D + TC2	7	218,750
Malvaioli (Sx)	875,000	4,375	LS + TC4	90	218,750
Malvaioli (Dx)	875,000	4,375	LS + TC4	90	218,750
Vetralla (Sx)	1,750,000	8,750	LS + TC4	90	437,500
Vetralla (Dx)	1,750,000	8,750	LS + TC4	90	437,500
Giano Est	96,25,000	48,125	C + TC4	150	1,443,750
Albacina (Sx)	6,125,000	30,625	C + TC4	150	918,750
Albacina (Dx)	7,875,000	39,375	C + TC4	150	1,181,250
TOTAL COST [€]	98,875,000	494,375/year			11,681,350

It is immediate to recognize that required direct costs (in this application, only the PRCs would be necessary for the restoration of the road network) are sensibly lower than indirect ones (Table 6.18). Moreover, the adoption of maintenance measures to keep the viaducts structural characteristics at a proper level would imply a huge money saving.

Table 6.18. Comparison of direct and indirect costs for viaducts on SS76.

	TFTC [€]	TFPC [€]	TRC [€]	MC [€] (50 years)	PRC [€]
t = 50 y, LPM	45,547,269	37,587,706	98,875,000	24,718,750	11,681,350

Finally, a brief comment on the different impact of initial assumptions on the structural characteristics of investigated bridges can be traced from the results in Table 6.19. The comparison between indirect costs in the three different examined configurations shows that effects of the compliance at the foundation level are predominant with respect to ageing for a reliable estimate of the economic impact. Moreover, the analysis of the viaducts' performance including ageing and SSI leads to a not negligible difference in terms of costs than the adoption of simpler modelling assumptions.

Table 6.19. Comparison of Total Final Costs for Traffic (TFTC) and Pollutants (TFPC) for the examined structural configurations.

	TFTC [€]	TFPC_CO [€]	TFPC_VOC [€]	TFPC [€]	
t < 10 y, Fixed Base	26,523,773	5,696,664	16,160,307	21,856,971	
t = 50 y, Fixed Base	27,661,814	5,941,211	16,854,969	22,796,180	+ 4.30 %
t = 50 y, LPM	45,547,269	9,789,562	27,798,144	37,587,706	+ 71.98 %

Although the calculations offered in this example represent an attempt to estimate the economic impact of bridge damage due to an earthquake, it is possible to say that the results underline the necessity for a good plan of maintenance, that it is not yet drawn up at regional level. The awareness on the maintenance problem and the investment of resources in this field represent a challenge for the future of Italian bridges. For what concerns effects of ageing and SSI, results confirm the importance of a realistic modelling strategy, especially regarding the compliance of the foundation system, that is usually neglected in ordinary design and assessments. A failure to take into account fundamental structural aspects such as age-dependency and SSI could lead to dangerous underestimations of earthquake consequences.

6.6 Chapter's references

Alipour, A., Shafei, B., & Shinozuka, M. (2011). Performance evaluation of deteriorating highway bridges located in high seismic areas. *Journal of Bridge Engineering*, *16*(5), 597-611.

Amini, A., Nikraz, N., & Fathizadeh, A. (2016). Identifying and evaluating the effective parameters in prioritization of urban roadway bridges for maintenance operations. *Australian Journal of Civil Engineering*, *14*(1), 23-34.

Arici, Y., & Mosalam, K. M. (2003). System identification of instrumented bridge systems. *Earthquake engineering & structural dynamics*, *32*(7), 999-1020.

Barani, S., De Ferrari, R., & Ferretti, G. (2013). Influence of soil modeling uncertainties on site response. *Earthquake Spectra*, *29*(3), 705-732.

Basu, B. (2005). Identification of stiffness degradation in structures using wavelet analysis. *Construction and building materials*, *19*(9), 713-721.

Bazzurro, P., & Cornell, C. A. (2004). Ground-motion amplification in nonlinear soil sites with uncertain properties. *Bulletin of the Seismological Society of America*, *94*(6), 2090-2109.

Behmanesh, I., & Moaveni, B. (2016). Accounting for environmental variability, modeling errors, and parameter estimation uncertainties in structural identification. *Journal of Sound and Vibration*, *374*, 92-110.

Behmanesh, I., Moaveni, B., Lombaert, G., & Papadimitriou, C. (2015). Hierarchical Bayesian model updating for structural identification. *Mechanical Systems and Signal Processing*, *64*, 360-376.

Bindi, D., Pacor, F., Luzi, L., Puglia, R., Massa, M., Ameri, G., & Paolucci, R. (2011). Ground motion prediction equations derived from the Italian strong motion database. *Bulletin of Earthquake Engineering*, *9*(6), 1899-1920.

Biondini, F., Camnasio, E., & Palermo, A. (2014). Lifetime seismic performance of concrete bridges exposed to corrosion. *Structure and Infrastructure Engineering*, *10*(7), 880-900.

Bocchini, P., & Frangopol, D. M. (2011). A probabilistic computational framework for bridge network optimal maintenance scheduling. *Reliability Engineering & System Safety*, *96*(2), 332-349.

Braga, F., Del Grosso, A., Franchin, P., Mancini, G., Pinto, P. (2019). Linee Guida AT - Metodologia per l'analisi di transitabilità di ponti e viadotti esistenti (in Italian).

Capatti, M. C., Tropeano, G., Morici, M., Carbonari, S., Dezi, F., Leoni, G., & Silvestri, F. (2017). Implications of non-synchronous excitation induced by nonlinear site

amplification and of soil-structure interaction on the seismic response of multi-span bridges founded on piles. *Bulletin of Earthquake Engineering*, *15*(11), 4963-4995.

Carbonari, S., Dezi, F., & Leoni, G. (2011). Seismic soil–structure interaction in multi-span bridges: application to a railway bridge. *Earthquake engineering & structural dynamics*, *40*(11), 1219-1239.

Chiou, B., Darragh, R., Gregor, N., & Silva, W. (2008). NGA project strong-motion database. *Earthquake Spectra*, *24*(1), 23-44.

Choe, D. E., Gardoni, P., Rosowsky, D., & Haukaas, T. (2008). Probabilistic capacity models and seismic fragility estimates for RC columns subject to corrosion. *Reliability Engineering & System Safety*, *93*(3), 383-393.

Choe, D. E., Gardoni, P., Rosowsky, D., & Haukaas, T. (2009). Seismic fragility estimates for reinforced concrete bridges subject to corrosion. *Structural Safety*, *31*(4), 275-283.

Čokorilo, O., Ivković, I., & Kaplanović, S. (2019). Prediction of Exhaust Emission Costs in Air and Road Transportation. *Sustainability*, *11*(17), 4688.

Czarnecki, A. A., & Nowak, A. S. (2008). Time-variant reliability profiles for steel girder bridges. *Structural Safety*, *30*(1), 49-64.

de Miranda, M. (2019). Durabilità di ponti e viadotti: come garantire la sicurezza dei ponti esistenti (in Italian).

Doebling, S. W., Farrar, C. R., Prime, M. B., & Shevitz, D. W. (1996). *Damage identification and health monitoring of structural and mechanical systems from changes in their vibration characteristics: a literature review* (No. LA-13070-MS). Los Alamos National Lab., NM (United States).

Dong, Y., Frangopol, D. M., & Sabatino, S. (2015). Optimizing bridge network retrofit planning based on cost-benefit evaluation and multi-attribute utility associated with sustainability. *Earthquake Spectra*, *31*(4), 2255-2280.

Dong, Y., Frangopol, D. M., & Saydam, D. (2013). Time-variant sustainability assessment of seismically vulnerable bridges subjected to multiple hazards. *Earthquake Engineering & Structural Dynamics*, *42*(10), 1451-1467.

EEA, 2019. EMEP/EEA air pollutant emission inventory guidebook 2019. EEA Report No 13/2019. Available at: https://www.eea.europa.eu/publications/emep-eea-guidebook-2019 (08- 09-2020).

Enright, M. P., & Frangopol, D. M. (1998). Probabilistic analysis of resistance degradation of reinforced concrete bridge beams under corrosion. *Engineering structures*, *20*(11), 960-971.

Estes, A. C., & Frangopol, D. M. (2003). Updating bridge reliability based on bridge management systems visual inspection results. *Journal of Bridge Engineering*, *8*(6), 374-382.

FEMA. (2013). Hazus—MH 2.1: Technical manual. *Multi-hazard loss estimation methodology, earthquake model*.

Forte, G., Chioccarelli, E., De Falco, M., Cito, P., Santo, A., & Iervolino, I. (2019). Seismic soil classification of Italy based on surface geology and shear-wave velocity measurements. *Soil Dynamics and Earthquake Engineering*, *122*, 79-93.

Frangopol, D. M. (2011). Life-cycle performance, management, and optimisation of structural systems under uncertainty: accomplishments and challenges 1. *Structure and infrastructure Engineering*, *7*(6), 389-413.

Ghosh, J., & Padgett, J. E. (2010). Aging considerations in the development of time-dependent seismic fragility curves. *Journal of Structural Engineering*, *136*(12), 1497-1511.

Ghosh, J., & Padgett, J. E. (2011). Probabilistic seismic loss assessment of aging bridges using a component-level cost estimation approach. *Earthquake Engineering & Structural Dynamics*, *40*(15), 1743-1761.

Griffiths, S. C., Cox, B. R., Rathje, E. M., & Teague, D. P. (2016). Surface-wave dispersion approach for evaluating statistical models that account for shear-wave velocity uncertainty. *Journal of Geotechnical and Geoenvironmental Engineering*, *142*(11), 04016061.

Hoeke, L. J., Moser, R. D., Singh, P. M., Kahn, L. F., & Kurtis, K. E. (2009). Degradation of steel girder bridge bearing systems by corrosion. *National Association of Corrosion Engineers, P. O. Box 218340 Houston TX 77084 USA.[np]. 22-26 Mar*.

Hurt, M. A., & Schrock, S. D. (2016). *Highway bridge maintenance planning and scheduling*. Butterworth-Heinemann.

Jones, A. L., Kramer, S. L., & Arduino, P. (2002). *Estimation of uncertainty in geotechnical properties for performance-based earthquake engineering*. Pacific Earthquake Engineering Research Center, College of Engineering, University of California.

Karim, K. R., & Yamazaki, F. (2007). Effect of isolation on fragility curves of highway bridges based on simplified approach. *Soil Dynamics and Earthquake Engineering*, *27*(5), 414-426.

Kayser, J. R., & Nowak, A. S. (1989). Capacity loss due to corrosion in steel-girder bridges. *Journal of Structural Engineering*, *115*(6), 1525-1537.

Kendall, A., Keoleian, G. A., & Helfand, G. E. (2008). Integrated life-cycle assessment and life-cycle cost analysis model for concrete bridge deck applications. *Journal of Infrastructure Systems*, *14*(3), 214-222.

Kilanitis, I., & Sextos, A. (2019). Integrated seismic risk and resilience assessment of roadway networks in earthquake prone areas. *Bulletin of earthquake engineering*, *17*(1), 181-210.

Kim, S. H., & Shinozuka, M. (2004). Development of fragility curves of bridges retrofitted by column jacketing. *Probabilistic Engineering Mechanics*, *19*(1-2), 105-112.

Lanzano, G., Luzi, L., Pacor, F., Felicetta, C., Puglia, R., Sgobba, S., & D'Amico, M. (2019). A Revised Ground-Motion Prediction Model for Shallow Crustal Earthquakes in ItalyA Revised Ground-Motion Prediction Model for Shallow Crustal Earthquakes in Italy. *Bulletin of the Seismological Society of America*, *109*(2), 525-540.

Liu, M., & Frangopol, D. M. (2005). Balancing connectivity of deteriorating bridge networks and long-term maintenance cost through optimization. *Journal of Bridge Engineering*, *10*(4), 468-481.

Liu, M., & Frangopol, D. M. (2006). Optimizing bridge network maintenance management under uncertainty with conflicting criteria: Life-cycle maintenance, failure, and user costs. *Journal of structural Engineering*, *132*(11), 1835-1845.

Loh, C. H., Hung, T. Y., Chen, S. F., & Hsu, W. T. (2015, July). Damage detection in bridge structure using vibration data under random travelling vehicle loads. In *J. Phys. Conf. Ser* (Vol. 628, p. 012044).

Lupoi, A., Franchin, P., Pinto, P. E., & Monti, G. (2005). Seismic design of bridges accounting for spatial variability of ground motion. *Earthquake engineering & structural dynamics*, *34*(4-5), 327-348.

Mackie, K. R., & Stojadinović, B. (2006). Post-earthquake functionality of highway overpass bridges. *Earthquake engineering & structural dynamics*, *35*(1), 77-93.

Mackie, K. R., Wong, J. M., & Stojadinović, B. (2010). Post-earthquake bridge repair cost and repair time estimation methodology. *Earthquake Engineering & Structural Dynamics*, *39*(3), 281-301.

Malekjafarian, A., McGetrick, P. J., & OBrien, E. J. (2015). A review of indirect bridge monitoring using passing vehicles. *Shock and vibration*, *2015*.

Mangalathu, S., Jeon, J. S., & DesRoches, R. (2018). Critical uncertainty parameters influencing seismic performance of bridges using Lasso regression. *Earthquake Engineering & Structural Dynamics*, *47*(3), 784-801.

Mayne, P. W., Coop, M. R., Springman, S., Huang, A. B., & Zornberg, J. (2009). SOA-1: Geomaterial behavior and testing. In *Proceedings of the 17th International Conference*

on Soil Mechanics and Geotechnical Engineering: 5–9 October 2009, Alexandria, Egypt (pp. 2777-2872). Millpress, Rotterdam, the Netherlands.

Ministero delle Infrastrutture e dei Trasporti, D.M.17.01.2018, *Aggiornamento delle "Norme Tecniche per le Costruzioni"*, G.U. n.42, 20.02.2018 (in Italian).

Ministero delle Infrastrutture e dei Trasporti, *Linee Guida per la Classificazione e Gestione del Rischio, la Valutazione della Sicurezza ed il Monitoraggio dei Ponti Esistenti*, 17.04.2020 (in Italian).

Molina, S., Lang, D. H., & Lindholm, C. D. (2010). SELENA–An open-source tool for seismic risk and loss assessment using a logic tree computation procedure. *Computers & Geosciences*, *36*(3), 257-269.

Moughty, J. J., & Casas, J. R. (2017, June). Evaluation of the Hilbert Huang transformation of transient signals for bridge condition assessment. In *Proceedings of the Annual European Safety and Reliability Conference (ESREL 2017), Portoroz, Slovenia* (pp. 18-22).

Newell, G.F. (1993). A simplified theory of kinematic waves in highway traffic I: General theory. II: Queuing at freeway bottlenecks. III: Multi-destination flows. *Transportation Research, Part B, 27*(4), 281–313.

Padgett, J. E., & DesRoches, R. (2007). Bridge functionality relationships for improved seismic risk assessment of transportation networks. *Earthquake Spectra*, *23*(1), 115-130.

Padgett, J. E., & DesRoches, R. (2008a). Three-dimensional nonlinear seismic performance evaluation of retrofit measures for typical steel girder bridges. *Engineering Structures*, *30*(7), 1869-1878.

Padgett, J. E., & DesRoches, R. (2008b). Methodology for the development of analytical fragility curves for retrofitted bridges. *Earthquake Engineering & Structural Dynamics*, *37*(8), 1157-1174.

Padgett, J. E., Dennemann, K., & Ghosh, J. (2010). Risk-based seismic life-cycle cost–benefit (LCC-B) analysis for bridge retrofit assessment. *Structural Safety*, *32*(3), 165-173.

Passeri, F., Foti, S., Cox, B. R., & Rodriguez-Marek, A. (2019). Influence of epistemic uncertainty in shear wave velocity on seismic ground response analyses. *Earthquake Spectra*, *35*(2), 929-954.

Pellegrino, C., Pipinato, A., & Modena, C. (2011). A simplified management procedure for bridge network maintenance. *Structure and Infrastructure Engineering*, *7*(5), 341-351.

Phoon, KK & Kulhawy, FH (1999) Evaluation of geotechnical property variability. *Canadian Geotechnical Journal* , *36* (4), 625-639.

Preiss, P.; Friedrich, R.; Klotz, V. (2008). NEEDS New Energy Externalities Developments for Sustainability—Deliverable No. 1.1-RS 3a—Report on the procedure and data to generate averaged/aggregated data. Available online: http://www.needs-project.org/.

Rao, A. S., Lepech, M. D., & Kiremidjian, A. (2017b). Development of time-dependent fragility functions for deteriorating reinforced concrete bridge piers. *Structure and Infrastructure Engineering*, *13*(1), 67-83.

Rao, A. S., Lepech, M. D., Kiremidjian, A. S., & Sun, X. Y. (2017a). Simplified structural deterioration model for reinforced concrete bridge piers under cyclic loading. *Structure and Infrastructure Engineering*, *13*(1), 55-66.

Rathje, E. M., Kottke, A. R., & Trent, W. L. (2010). Influence of input motion and site property variabilities on seismic site response analysis. *Journal of geotechnical and geoenvironmental engineering*, *136*(4), 607-619.

Sextos, A. G., Kappos, A. J., & Pitilakis, K. D. (2003). Inelastic dynamic analysis of RC bridges accounting for spatial variability of ground motion, site effects and soil–structure interaction phenomena. Part 2: Parametric study. *Earthquake Engineering & Structural Dynamics*, *32*(4), 629-652.

Sextos, A. G., Pitilakis, K. D., & Kappos, A. J. (2003). Inelastic dynamic analysis of RC bridges accounting for spatial variability of ground motion, site effects and soil–structure interaction phenomena. Part 1: Methodology and analytical tools. *Earthquake engineering & structural dynamics*, *32*(4), 607-627.

Simon, J., Bracci, J. M., & Gardoni, P. (2010). Seismic response and fragility of deteriorated reinforced concrete bridges. *Journal of Structural Engineering*, *136*(10), 1273-1281.

Sohn, H., & Law, K. H. (2000). Bayesian probabilistic damage detection of a reinforced-concrete bridge column. *Earthquake engineering & structural dynamics*, *29*(8), 1131-1152.

Sohn, H., Farrar, C. R., Hemez, F. M., Shunk, D. D., Stinemates, D. W., Nadler, B. R., & Czarnecki, J. J. (2003). A review of structural health monitoring literature: 1996–2001. *Los Alamos National Laboratory, USA*, *1*.

Stewart, M. G. (2001). Reliability-based assessment of ageing bridges using risk ranking and life cycle cost decision analyses. *Reliability Engineering & System Safety*, *74*(3), 263-273.

Teughels, A., & De Roeck, G. (2004). Structural damage identification of the highway bridge Z24 by FE model updating. *Journal of Sound and Vibration*, *278*(3), 589-610.

Uzielli, M., Lacasse, S., Nadim, F., & Phoon, K. K. (2006). Soil variability analysis for geotechnical practice. *Characterization and engineering properties of natural soils*, *3*, 1653-1752.

Vu, K. A. T., & Stewart, M. G. (2000). Structural reliability of concrete bridges including improved chloride-induced corrosion models. *Structural safety*, *22*(4), 313-333.

Zhang, W., & Wang, N. (2017). Bridge network maintenance prioritization under budget constraint. *Structural safety*, *67*, 96-104.

Zhou, X., & Taylor, J. (2014). DTALite: A queue-based mesoscopic traffic simulator for fast model evaluation and calibration. *Cogent Engineering*, *1*(1), 961345.

7. Probabilistic modelling of uncertainties in the soil-foundation system

Classically, SSI analyses are performed with a deterministic approach that disregards the importance of accounting for uncertainties in soil properties derived from geotechnical site investigations. These uncertainties are related to the spatial variability of the geological condition, to the limited number of measurements, and to testing and measurement procedure errors.

Probabilistic analyses can be used to model uncertainties of parameters affecting the system behaviour and to evaluate its scattered response. With new computational capacities, the probabilistic approach is becoming a common practice in the research, when studying response of prototypal structural systems, or in the practice when analysing strategic structures. However, it is not yet common to adopt a full probabilistic perspective to approach the study of SSI phenomena.

Lutes et al. (2000) studied effects of soil and superstructure uncertainties on SSI of a shallow foundation introducing a deterministic variability range on the nominal values of shear stiffness and Poisson's ratio of the soil and the shear stiffness and damping of the superstructure. Cottereau et al. (2007) evaluated uncertainties on the impedance matrix directly, without applying a probabilistic distribution on the fundamental variables that rule the problem and lead to the definition of the impedance matrix itself. Moghaddasi et al. (2011) performed Monte Carlo simulations to evaluate the probabilistic seismic response of a single degree of freedom system, considering geometrical and mechanical uncertainties of both the soil-foundation system, represented through a shallow foundation frequency independent lumped parameter model, and the structure, assuming deterministic variability ranges for the random variables. However, no detailed studies have been yet developed regarding the probabilistic dynamic behaviour of pile foundations although the variability and uncertainties of the geotechnical properties play an important role in their dynamic response. Hence, the definition of probabilistic models describing the dynamic properties of the soil-foundation system needs further investigations in order to better address the effects of uncertainty relative to the soil and foundations on the superstructure response.

This Chapter presents the analysis of the dynamic behaviour of pile foundation in a probabilistic framework, in which uncertainties are accounted for through probabilistic distributions of the main parameters governing the soil-foundation dynamic response. Frequency dependent impedance functions of both single piles and square pile groups as well as kinematic response factors are investigated. Starting from the probabilistic distributions of the selected random variables, assumed to be uncorrelated, samples are derived using the Quasi-Random Sampling (QRS) technique (Sobol' et al., 1992) that allows a reliable probabilistic distribution of the output quantities to be obtained with a limited computational effort. Probabilistic analyses are performed by using a numerical

model developed by the Authors for the kinematic interaction analysis of single piles and pile groups (Dezi et al., 2016). The model accounts for the pile-soil-pile interaction, the soil hysteretic and radiation damping, which all affect the dynamic behaviour of deep foundations. The variability of the output quantities is presented and discussed. In addition, sensitivity studies are developed to show the influence of variability of each considered random variable on the system response.

7.1 Modelling of the soil-pile foundation interaction

Many different models are available in the literature to evaluate the dynamic stiffness and the kinematic response of pile group foundations (Dobry et Gazetas, 1988; Padrón et al., 2007; Dezi et al., 2009; Álamo et al., 2016). Among them, the numerical model proposed by Dezi et al. (2016) permits to perform 3D kinematic interaction analyses of vertical and inclined piles, considered as elastic Euler-Bernoulli beam elements embedded in an infinite horizontally layered viscoelastic soil. Soil layers are assumed to be independent and the pile-soil-pile interactions at each layer is described by Green's functions derived in the frequency domain from the dynamics of oscillating rigid disks, accounting for both hysteretic and radiation damping (Dobry et al., 1982; Gazetas & Dobry, 1984; Makris & Gazetas, 1993). An example of a pile group foundation and the relevant finite element model is depicted in Figure 2.1.

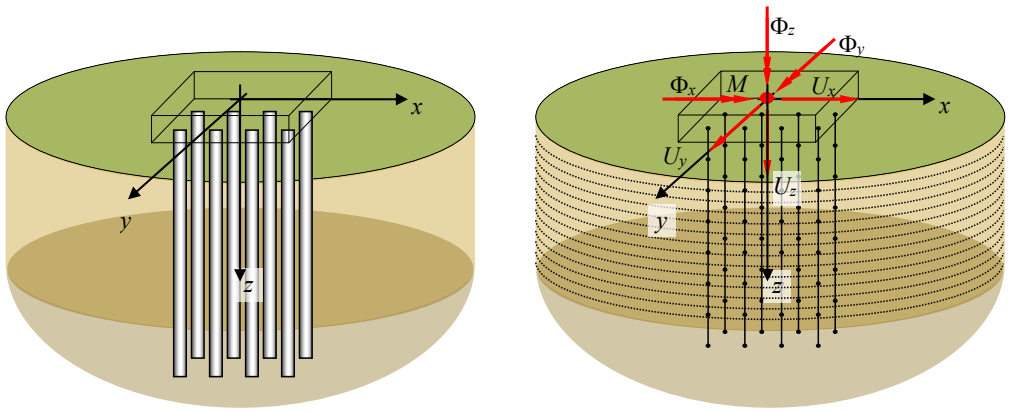

Figure 7.1. (a) Soil-foundation system; (b) BEM-FEM model.

Because of the problem linearity, the dynamic equilibrium of a vertical pile foundation is expressed by the following complex valued system of linear algebraic equations in the frequency domain

$$\left(\mathbf{K}_p - \omega^2\mathbf{M}_p + \mathbf{K}_s(\omega)\right)\mathbf{d}(\omega) = \mathbf{f}(\omega) \qquad (1)$$

where $\mathbf{K}_p$ and $\mathbf{M}_p$ are the global stiffness and mass matrices of piles, respectively, $\mathbf{K}_s(\omega)$ is the impedance matrix of the soil, $\mathbf{d}(\omega)$ is the piles nodal displacement vector and $\mathbf{f}(\omega)$ is the vector of external loads due to the free-field motion and the pile-soil-pile interaction

forces. The impedance matrix of the soil and the vector of external loads are obtained by assembling contribution of all the E elements as

$$\mathbf{K}_s(\omega) = \sum_{e=1}^{E} \int_0^{L_e} \mathbf{N}^T \mathbf{D}_s^{-1}(\omega, z) \mathbf{N} dz \tag{2a}$$

$$\mathbf{f}(\omega) = \sum_{e=1}^{E} \int_0^{L_e} \mathbf{N}^T \mathbf{D}_s^{-1}(\omega, z) \mathbf{u}_{ff} dz \tag{2b}$$

where L_e is the finite element length, $\mathbf{N}$ is the matrix of the interpolating polynomials, $\mathbf{u}_{ff}$ is the vector collecting the free-field motion components in the x, y and z directions (Figure 2.1b) while $\mathbf{D}_s(\omega, z)$ is the local soil-pile compliance matrix assembled considering Green's functions available in the literature (Dezi et al., 2016).

The pile cap is modelled with a rigid body constraint between the pile heads and by a Master node (M) having 6 degrees of freedom. By denoting the geometric matrix of the kinematic constraint by $\mathbf{A}$, Equation (1) assumes the form

$$\tilde{\mathbf{K}}(\omega)\tilde{\mathbf{d}}(\omega) = \tilde{\mathbf{f}}(\omega) \tag{3}$$

where

$$\tilde{\mathbf{K}}(\omega) = \mathbf{A}^T \left(\mathbf{K}_p - \omega^2 \mathbf{M}_p + \mathbf{K}_s(\omega) \right) \mathbf{A} \tag{4a}$$

$$\tilde{\mathbf{f}}(\omega) = \mathbf{A}^T \mathbf{f}(\omega) \tag{4b}$$

In Equation (3), $\tilde{\mathbf{d}}(\omega)$ is the vector collecting the six displacement components of M and the displacement components of the remaining non-constrained pile nodes.

Equation (3) can be partitioned as follows to separate displacements of the master node ($\mathbf{U}_M$) from those of the embedded pile nodes:

$$\begin{pmatrix} \tilde{\mathbf{K}}_{MM} & \tilde{\mathbf{K}}_{MS} \\ \tilde{\mathbf{K}}_{SM} & \tilde{\mathbf{K}}_{SS} \end{pmatrix} \begin{pmatrix} \mathbf{U}_M \\ \mathbf{d}_S \end{pmatrix} = \begin{pmatrix} \tilde{\mathbf{f}}_M \\ \tilde{\mathbf{f}}_S \end{pmatrix} \tag{5}$$

By condensing system (5) on the master node *dofs*, the following expressions for the complex impedance matrix ($\mathfrak{I}$) and the complex FIM ($\mathbf{U}_M$) can be derived:

$$\mathfrak{I}(\omega) = (\tilde{\mathbf{K}}_{MM} - \tilde{\mathbf{K}}_{MS}\tilde{\mathbf{K}}_{SS}^{-1}\tilde{\mathbf{K}}_{SM}) \tag{6a}$$

$$\mathbf{U}_M(\omega) = \mathfrak{I}^{-1}(\tilde{\mathbf{f}}_M - \tilde{\mathbf{K}}_{MS}\tilde{\mathbf{K}}_{SS}^{-1}\tilde{\mathbf{f}}_S) \tag{6b}$$

In case of double-symmetric pile configurations, by suitably positioning M at the intersection between the two symmetry planes, the impedance matrix has the form

$$\mathfrak{I}(\omega) = \begin{bmatrix} \mathfrak{I}_x & 0 & 0 & 0 & \mathfrak{I}_{x-ry} & 0 \\ & \mathfrak{I}_y & 0 & \mathfrak{I}_{y-rx} & 0 & 0 \\ & & \mathfrak{I}_z & 0 & 0 & 0 \\ & & & \mathfrak{I}_{rx} & 0 & 0 \\ & sym & & & \mathfrak{I}_{ry} & 0 \\ & & & & & \mathfrak{I}_{rz} \end{bmatrix} \tag{7}$$

With reference to Figure 2.1b, $\mathfrak{I}_x, \mathfrak{I}_y, \mathfrak{I}_z$ are the translational frequency dependent impedances along x, y and z, respectively, whereas $\mathfrak{I}_{rx}, \mathfrak{I}_{ry}, \mathfrak{I}_{rz}$ are the rotational impedance components and $\mathfrak{I}_{x-ry}, \mathfrak{I}_{y-rx}$ are the coupled roto-translational terms.

Material properties, of both piles and soil, and geometric parameters are involved in the definition of the impedance matrix. The pile stiffness and mass matrices overall depend on the elastic modulus of the pile material, the pile diameter and the pile length. The pile-soil-pile interaction, affecting the global dynamic stiffness matrix of the soil-foundation system and the external loads (Equation (2)), is captured by the soil compliance matrix $\mathbf{D}_s(\omega, z)$ that assumes the form

$$\boldsymbol{D}_s(\omega, z) = \begin{bmatrix} \boldsymbol{D}_{11} & \cdots & \boldsymbol{D}_{1q} & \cdots & \boldsymbol{D}_{1n} \\ \vdots & & \vdots & & \vdots \\ \boldsymbol{D}_{p1} & \cdots & \boldsymbol{D}_{pq} & \cdots & \boldsymbol{D}_{pn} \\ \vdots & & \vdots & & \vdots \\ \boldsymbol{D}_{n1} & \cdots & \boldsymbol{D}_{nq} & \cdots & \boldsymbol{D}_{nn} \end{bmatrix} \tag{8}$$

Sub-matrices $\boldsymbol{D}_{pq}(\omega, z)$ appearing in Equation (8) contain the elastodynamic Green's functions expressing the soil displacements at the location of the p-th pile at depth z, due to a time-harmonic unit point load acting at the location of the q-th pile at the same depth. They are expressed as

$$\boldsymbol{D}_{pq}(\omega, z) = \boldsymbol{G}_{pq}^T(z)\boldsymbol{\Psi}_{pq}(\omega, z)\boldsymbol{G}_{pq}(z)\boldsymbol{\mathfrak{D}}(\omega, z) \tag{9}$$

where

$$\boldsymbol{\mathfrak{D}}(\omega, z) = \begin{bmatrix} \dfrac{k_h(\omega) - i\omega c_h(\omega)}{k_h^2(\omega) + \omega^2 c_h^2(\omega)} & 0 & 0 \\ 0 & \dfrac{k_h(\omega) - i\omega c_h(\omega)}{k_h^2(\omega) + \omega^2 c_h^2(\omega)} & 0 \\ 0 & 0 & \dfrac{k_v(\omega) - i\omega c_v(\omega)}{k_v^2(\omega) + \omega^2 c_v^2(\omega)} \end{bmatrix} \tag{10}$$

collects soil displacements at the position of the applied force and matrix $\boldsymbol{G}_{pq}^T\boldsymbol{\Psi}_{pq}\boldsymbol{G}_{pq}$ describes the displacement attenuation from point q to point p within each layer (Makris & Gazetas, 1992; Mylonakis & Gazetas, 1998). Terms appearing in Equation (10) are

formulated as follows (Dobry et al., 1982; Gazetas & Dobry, 1984; Makris & Gazetas, 1993):

$$k_h = 1.67E_s\left(\frac{E_p}{E_s}\right)^{-0.053} \tag{11a}$$

$$c_h(\omega) = \frac{1}{2}\pi d\rho_s V_s\left[\mathrm{Re}\left(-i\frac{H_1^{(2)}\frac{\pi\omega d}{8V_s}}{H_0^{(2)}\frac{\pi\omega d}{8V_s}}\right)+\frac{V_c}{V_s}\mathrm{Re}\left(-i\frac{H_1^{(2)}\frac{\pi\omega d}{8V_c}}{H_0^{(2)}\frac{\pi\omega d}{8V_c}}\right)\right] + 2\xi_s\frac{k_h}{\omega} \tag{11b}$$

$$k_v(\omega) = 0.6\,E_s\left(1+\frac{1}{2}\sqrt{\frac{\omega d}{V_s}}\right) \tag{11c}$$

$$c_v(\omega) = \pi d\rho_s V_s\left[\mathrm{Re}\left(-i\frac{H_1^{(2)}\frac{\pi\omega d}{8V_s}}{H_0^{(2)}\frac{\pi\omega d}{8V_s}}\right)\right]+2\xi_s\frac{k_v}{\omega} \tag{11d}$$

where E_p and E_s are the pile material and soil Young's modulus, respectively, while ξ_s is the hysteretic damping ratio of the soil. Furthermore, V_c is the velocity of the compression–extension waves, which can be expressed as a function of the shear wave velocity (Lysmer's analogue velocity), d is the pile diameter and $H_0^{(2)}$ and $H_1^{(2)}$ are the zero-order and first-order Hankel functions of second kind.

7.2 Probabilistic model

Uncertainties related to modelling, which can be reduced by improving and refining the models, are included among epistemic uncertainties, while the inherent variability of data gives rise to aleatoric uncertainties, which can be characterized by statistical models and probabilistic laws. Concerning the former, it is worth mentioning that the adopted numerical model has been validated through comparisons with results obtained from more refined modelling approaches (Dezi et al., 2016) and through comparisons based on available data from experimental tests (Capatti et al., 2017; Dezi et al., 2019). As for the aleatoric uncertainties, these represent an essential aspect of the geotechnical engineering, and several works from the geotechnical literature deal with the characterization of soil properties based on field tests, resulting in the definition of probabilistic trends for the density, the degree of saturation, the cohesion, the friction angle and many other features (Phoon & Kulhawy, 1999; Uzielli et al., 2006; Mayne et al., 2009). Concerning piles, variability of the parameters can be closely associated with the uncertainties on construction material properties. In particular, the use of concrete involves the adoption of probabilistic models regarding the compressive strength, density and the elastic

modulus, which are widely adopted in the literature when reliability or fragility analyses are performed (Bartlett & MacGregor, 1996; Nielson, 2005; Stefanidou & Kappos, 2017). Less important uncertainties usually characterise steel reinforcements whose behaviour is thus considered to be deterministic in this study.

Since pile-soil-pile interaction phenomena are strongly affected by geotechnical parameters, which are sources of uncertainty, a probabilistic approach for the assessment of the soil-foundation system dynamic behaviour is necessary. Considering Equations (11), the soil density ρ_s, the shear wave velocity V_s and the concrete elastic modulus E_p are assumed as independent random variables in this study. Probabilistic models assumed for above variables are deduced from the available technical literature. In particular:

- a normal distribution is considered for the soil density (Jones et al., 2002);
- a lognormal distribution is considered for the shear wave velocity (Jones et al., 2002; Moon & Ku, 2016; Griffiths et al., 2016);
- the concrete elastic modulus E_p is derived from the cylindrical compressive strength f_c that is assumed to be a lognormally distributed random variable (CNR, 2014).

The remaining mechanical parameters, namely soil and concrete Poisson's moduli (ν_s, ν_p), soil and concrete damping ratios (ξ_s, ξ_p) and concrete density ρ_p, are assumed to be deterministic since their variability on the overall dynamic response of the foundation is limited under the assumption of linear soil behaviour (Jin et al., 2000; Cottereau et al., 2007). It is worth observing that most of the damping capacity of the soil-foundation system are attributable to radiation phenomena that are provided by the first addenda of Equations (11b) and (11d) as a function of the above defined random variables.

For the purpose of this paper, by limiting furtherly the analysis to square pile groups, the problem previously stated can be turned in a non-dimensional form so that the impedance matrix (7) can be rewritten as

$$\boldsymbol{\Pi}\left(\rho_s, V_s, E_p; a_0\right) = \begin{bmatrix} \Pi_1 & 0 & 0 & 0 & \Pi_3 & 0 \\ & \Pi_1 & 0 & -\Pi_3 & 0 & 0 \\ & & \Pi_4 & 0 & 0 & 0 \\ & & & \Pi_2 & 0 & 0 \\ & sym & & & \Pi_2 & 0 \\ & & & & & \Pi_5 \end{bmatrix} \tag{12}$$

where ρ_s, V_s and E_p are parameters that are considered subjected to uncertainties,

$$a_0 = \frac{\omega d}{\mu_{V_s}} \tag{13}$$

is the non-dimensional frequency and

$$\Pi_1(\rho_s, V_s, E_p; a_0) = \frac{\Im_i}{\rho_s \mu_{V_s}^2 d} \quad \text{for } i = x, y \tag{14a}$$

$$\Pi_2(\rho_s, V_s, E_p; a_0) = \frac{\Im_{ri}}{\rho_s \mu_{V_s}^2 d^3} \quad \text{for } i = x, y \tag{14b}$$

$$\Pi_3(\rho_s, V_s, E_p; a_0) = \frac{\Im_{i-rj}}{\rho_s \mu_{V_s}^2 d^2} \quad \text{for } i = x, y \text{ and } j = y, x \tag{14c}$$

$$\Pi_4(\rho_s, V_s, E_p; a_0) = \frac{\Im_z}{\rho_s \mu_{V_s}^2 d} \tag{14d}$$

$$\Pi_5(\rho_s, V_s, E_p; a_0) = \frac{\Im_{rz}}{\rho_s \mu_{V_s}^2 d^3} \tag{14e}$$

In addition to the previous relationships relevant to the foundation dynamic compliance, transfer functions between the free field motion and the FIM can be considered to be representative for the foundation kinematic response. These are represented by ratios between FIM components and free field motion at the soil outcrop. By considering the earthquake shaking to be constituted by vertically travelling shear waves, because of the square layout of pile groups considered, the following transfer functions can be defined:

$$I_U(\rho_s, V_s, E_p; a_0) = \frac{U_i}{U_{ff,i}} \qquad I_\Phi(\rho_s, V_s, E_p; a_0) = \frac{\Phi_i d}{U_{ff,i}} \qquad \text{for } i = x, y \tag{15a, b}$$

where $U_{ff,x}$ and $U_{ff,y}$ are the free field displacements at the soil outcrop, and U_x, U_y, Φ_y and Φ_x are the translational and rotational non-null displacement components of the foundation Master node (M), respectively (Figure1b).

Once suitable statistical distributions are adopted for the random variables ρ_s, V_s and E_p, Equations (14) and (15) will return impedances and transfer functions with their own distributions that will be investigated in this paper.

7.2.1 Sensitivity index

Sensitivity analysis can be defined as "*the study of how uncertainty in the output of a model (numerical or otherwise) can be apportioned to different sources of uncertainty in the model input*" (Saltelli et al., 2004). In the sequel, a brief recall of the methodology adopted to compute the sensitivity indexes is provided considering the frequency-dependent nature of quantities at hand. Impedances Π_j $(j = 1, \dots, 5)$ and kinematic transfer functions I_α, $(\alpha = U, \phi)$, derived in the previous section, depend on the three independent aleatoric variables ρ_s, V_s and E_p, each characterised by a specific probability distribution. By denoting by Y the generic function and by X_k $(k = 1, \dots, 3,)$ the aleatoric variables

$$Y = g(X_1, X_2, X_3; a_0) \tag{16}$$

generically represents one of equations (14) and (15). The sensitivity analysis aims at discovering the dependence of the fluctuation in the output from the uncertainties characterizing the input variables X_k (Saltelli et al., 2004). To this purpose, variance-based methods for sensitivity analysis allow to monitor the influence of each random variable on the final variability amount and interaction effects among variables, assuming variance as a measure of uncertainty into the entire range of variability of each input variable. The influence of the single parameter X_k on the output can be evaluated moving on the so-called first path of variance-based sensitivity method. In order to measure how uncertainties of the generic variable affect uncertainties of the model, the following sensitivity indexes can be considered

$$S_k(a_0) = \frac{V_{X_k}\left(E_{X_{\sim k}}(Y|X_k)\right)}{V(Y)} \tag{17}$$

where $V_{X_k}\left(E_{X_{\sim k}}(Y|X_k)\right)$ is the variance, taken over the k-th variable, of the expected value of Y conditioned on k-th variable and taken over all variables but the k-th one, and $V(Y)$ is the total variance. S_k is the first order sensitivity index of X_k (Saltelli et al., 2004) varying between 0 and 1; the higher the index, the higher the importance of the variable. As the considered variables are independent, the following relationship holds:

$$\sum_k S_k(a_0) = 1 \tag{18}$$

It is worth noticing that the adopted sensitivity indexes vary with the nondimensional frequency a_0. In an attempt to measure the overall importance of the variable parameter over the frequency range considered, the following mean value can be defined:

$$\bar{S}_k = \frac{1}{A_0}\sum_{a_0=0}^{A_0} S_k(a_0) \tag{19}$$

which is also varying between 0 and 1 and satisfy condition analogous to (18).

7.3 Investigated foundation systems

Floating vertical piles embedded in a homogeneous soil deposit are considered; geometric parameters of foundations are assumed to be deterministic. Single piles, 2x2 and 3x3 square pile groups (Figure 7.2) are investigated. Two pile slenderness ratios L/d (representative of realistic short and long piles), and three pile spacing-diameter ratios s/d (consistently with realistic engineering applications) are considered for a total of 14 geometric models.

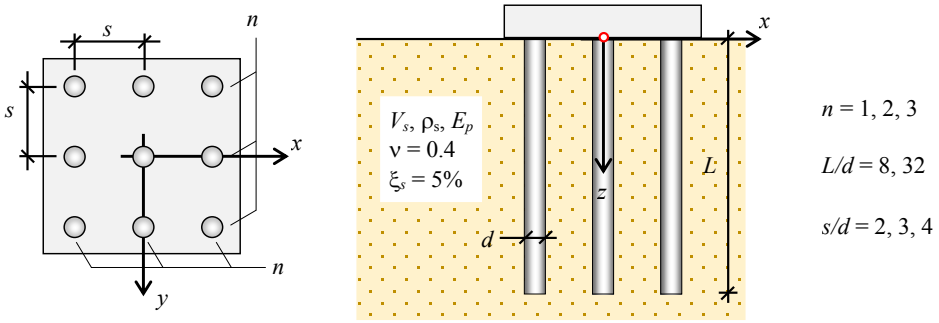

Figure 7.2. Scheme of investigated soil-foundation systems.

As already discussed, soil density, shear wave velocity and concrete modulus of elasticity are considered to be aleatoric while the other mechanical parameters, necessary to define the model, are considered to be deterministic. Table 6.2 reports parameters (mean values and standard deviation) of the probability distributions adopted for the aleatoric parameters. Instead, Table 7.2 lists the deterministic values adopted for the other parameters.

Table 7.1. Statistical distributions for ρ_s, V_s, E_c.

Uncertainties	Probabilistic Distribution	μ	σ
Soil density ρs [t/m3]	Normal	1.75	σ=0.175
Shear wave velocity V_s [m/s]	Lognormal	100, 200, 300	σ_{ln} = 0.39
Concrete cylindric strength [MPa] (for concrete elastic modulus E_p: $E_p = 22000\left(\frac{fc+8}{10}\right)^{0.3}$)	Lognormal	20.12	σ_{ln} (f_c) = 0.20

Table 7.2. Deterministic parameters.

Mechanical parameters	value
Soil Poisson's ratio ν_s [-]	0.40
Soil damping ξ_s [-]	0.05
Pile material Poisson's ratio (concrete) ν_p [-]	0.20
Pile material density (concrete) ρ_p [t/m^3]	2.50

7.4 Generation of samples

The propagation of the uncertainties through the numerical model starts with a sampling procedure on the independent random variables according to their probability distributions. Monte Carlo random Sampling (MCS) (Rubinstein & Kroese, 2016) represents the most widespread tool for probabilistic analysis thanks to its simplicity of

implementation. With random sampling from uncorrelated variables, each sample element is generated independently of all other sample elements, and all the subsets in the variable space have the same probability of realization. The reliability of the Monte Carlo method is proportional to the number of performed simulations and a high accuracy in the results, which can be measured with a goodness fit test (Massey, 1951; Cochran, 1952), generally requires a huge number of simulations. This implies a not-negligible computational effort, especially in a numerical model with more than one independent input parameters. Engineering problems are often affected by the issue of calculation cost, hence several different probabilistic approaches capable of reducing the required number of analyses without a significant loss in the accuracy of the final output have been developed in the last years, with numerous applications in seismic and risk analyses (Engelund & Rackwitz, 1993; Helton & Davis, 2003; Au & Beck, 2003).

Among the latter, the Quasi-Random Sampling (QRS) technique, based on low discrepancy Sobol' sequence (Sobol' et al., 1992), is adopted in this paper. The QRS technique implements Low Discrepancy Sequences (LDSs) to generate samples that are not random, in the sense of completely unpredictable, because the algorithm following the LDS ensures the selection of new points keeping them away from previous selected ones. Anyway, samples are still random, in the sense that they are distributed in the sample domain. This approach allows reducing the generation of clusters (i.e. overlapping of samples) or gaps (i.e. empty spaces among samples) in the sample domain, assuring the minimum discrepancy, that is to place sample points as uniformly as possible in the variability domain. As an example, by considering a three-dimensional parameter space of p_1, p_2 and p_3 variables, for which sampling is performed through a uniform distribution in the interval [0,1], (i.e. $P_{ij} \sim U(0,1)$, with $i = 1,2,3$ and $j = 1,2,\dots,N$, where N is the number of realizations and U denotes the uniform distribution), the random MCS provides sampling of the 3D domain in Figure 7.4a that, in case of small sample sizes, may generate important clusters or gaps (as can be observed from the 2D section). On the contrary, the Sobol' LDS, even for rather small numbers of simulations, allows to obtain a good sample distribution in terms of discrepancy with a very fast computational algorithm (Figure 7.4b).

7.4.1 Efficiency of Quasi Random Sampling

The efficiency of the QRS on the sampling of the independent variables previously defined was proven in the research paper by Minnucci et al. (2019), where the QRS is adopted to simulate the parameter variability in a single-pile foundation model and, with reference to results of sensitivity analyses, the adequate number of samples to get the required reliability of results is evaluated. More in detail, a preliminary study on the optimal number of required analyses is developed to validate the adopted sampling procedure, assuming results from the standard MCS as benchmark. The comparison is made on the basis of results of the sensitivity analyses. Referring to equation (18), where k may represent ρ_s, V_s and E_p, values of $\sum_k S_k(a_0)$ greater than 1 suggests that a not sufficiently high number of samples have been considered. A comparison between MCS

and Sobol' QRS is shown in Table 7.3 in terms of the mean value $\bar{S}$ of the sum of sensitivity indexes within the investigated frequency range

$$\bar{S} = \frac{1}{A_0} \sum_{a_0=0}^{A_0} \sum_k S_k(a_0) \tag{21}$$

computed for different total numbers of processed analyses. It is worth noting that QRS performs much better than MCS. A reduction of the number of samples is gradually applied to reach an optimum on the minimum number of analyses to be performed with a maximum loss in precision minor or equal to 1%. As a result, 10.000 is chosen as the number of analyses to perform.

Table 7.3. Evaluation of the sum of first-order sensitivity indexes.

	Number of simulations			
	125000 (MCS)	25000 (QRS)	10000 (QRS)	5000 (QRS)
$\bar{S}$	1.164	1.002	1.006	1.012

For the current applications, $s = 2000$ samples are generated according to the QRS for the i-th random variable (with $i = 1, \ldots, k$ and $k = 3$) so that a total of $N = s(k + 2) = 10.000$ analyses for each soil-foundation geometric model are performed. The parameter distributions obtained through Sobol' QRS are illustrated in Figure 7.3 for the investigated random variables.

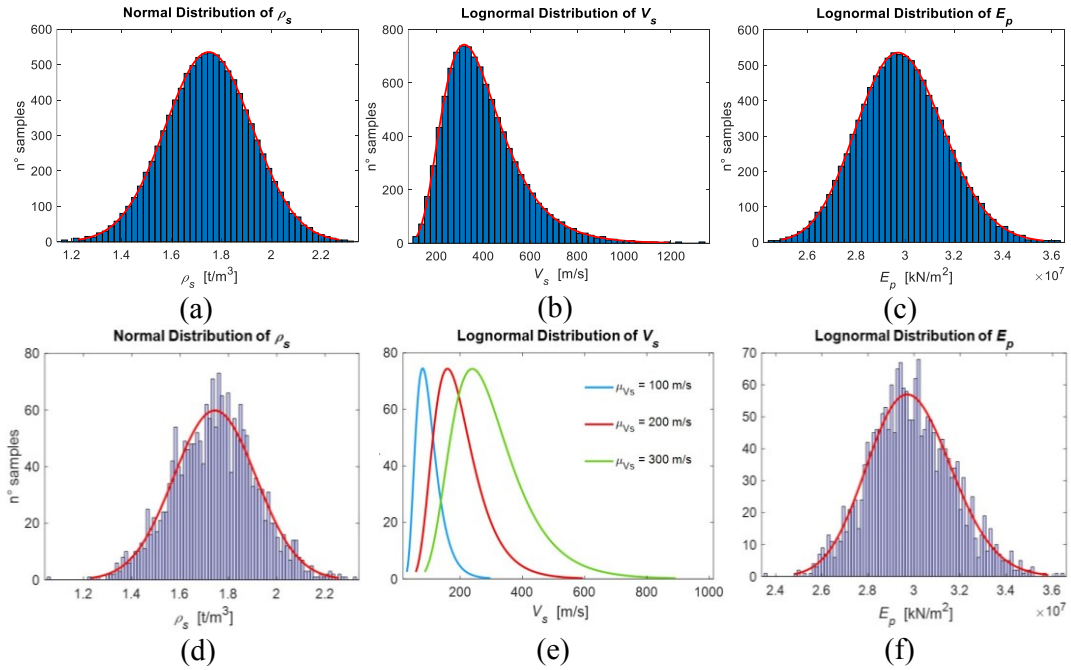

Figure 7.3. Sample distributions for the random variables: (a) ρ_s, (b) V_s and (c) E_p with Quasi Random technique; (d) ρ_s, (e) V_s and (f) E_p with Monte Carlo simulation.

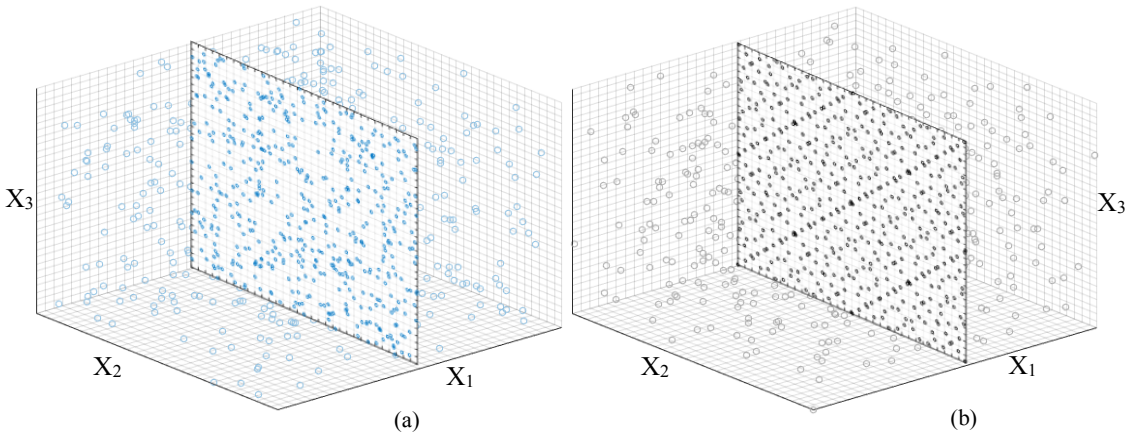

Figure 7.4. Comparison of (a) MCS and (b) QRS adopting Sobol' Sequence for a uniformly distributed 3-dimensional variable X_i, i=1,2,3 (512 samples).

7.4.2 Calculation of sensitivity indexes from Sobol's sequence

The computation of the sensitivity index previously introduced requires a large number of simulations since the presence of uncertainties must not be addressed to the lack of samples. In this sense, MCS presents some drawbacks, as already discussed in the previous section, resulting in a too much great calculation effort. In order to limit the computational effort of the first order sensitivity index, the following procedure, based on the Sobol' sequence, is adopted (Saltelli et al., 2008; Saltelli et al., 2010):

1. the QRS is used to get a n x $2k$ matrix of samples (where $k = 3$ is the number of random variables) from which, by halving, two n x k matrices (A, B) are obtained;
2. matrix C_c, $c = 1, \dots, k$ is assembled, in which all columns are derived from B, excepting the c-th one, taken from A;
3. the probabilistic analysis is performed using A, B and C_c, in order to obtain the n x 1 output vectors at each frequency $y_A(a_0), y_B(a_0), y_{C_c}(a_0)$;
4. the first order sensitivity index depending on the non-dimensional frequency is calculated from

$$S_{i,f} = \frac{y_A(a_0) \cdot y_{C_c}(a_0) - f_0^2}{y_A(a_0) \cdot y_A(a_0) - f_0^2} \tag{21}$$

in which

$$f_0^2 = \left(\frac{1}{n} \sum_{i=1}^{n} y_A(a_0)^i \right)^2 \tag{22}$$

7.5 Probabilistic soil-foundation dynamic analyses

In this section, results of the probabilistic soil-foundation dynamic analyses performed through the numerical model by Dezi et al. (2016) are presented, focusing on the foundation impedance functions and the kinematic response factors. The latter provide a measure of the filtering effect induced by the deep foundation on the free-field motion and can be used to compute the FIM (Equation (6b)). Impedance functions and kinematic response factors are evaluated in the non-dimensional frequency range 0-1, which always assures that the frequency range of practical interest in the field of seismic engineering is included. The latter is assumed to be 0-10 Hz since in this range earthquakes have their highest energy content and structures have their fundamental vibrational periods. As already mentioned, 10000 samples are generated for each foundation geometric layout and dynamic analyses are performed within the non-dimensional frequency range 0-1, for an overall amount of 420000 applications. As a result, a probabilistic distribution of the output quantities can be outlined, highlighting the inner variability of the impedance functions and the kinematic response factors for each foundation layout.

7.5.1 Variability of impedances

For the sake of brevity, the probability density function of impedances given the non-dimensional frequency are shown only for some case studies discussing peculiar trends of results. The latter are obtained through a data fitting process assuming a Generalized Extreme Value distribution (GEV), which represents a family of continuous probability density functions developed to deal with extreme deviations from the median values and suits well for all the investigated frequencies. Different probability density functions were also taken into account but revealed not able to approximate distributions of data in the whole analysed frequency range: analogously with the probabilistic models adopted for the random variables, the lognormal distribution for example can be suitably used for real parts of impedances at low frequencies, where the shear wave velocity mainly governs the foundation response, while the normal distribution revealed capable to interpret variability of impedances at high frequency, due to the higher contribution of the soil density to the response. However, both fails in handing negative values of dynamic stiffnesses and cannot be used if the variability of results includes both positive and negative realizations. A complete overview of results will be presented later with focus on the first two statistical moments. However, unless otherwise specified, comments below can be considered of general validity and apply to all the investigated foundations. Figure 7.5 shows the variability of the real and imaginary parts of the non-dimensional translation impedance Π_1 of the 2x2 foundation for s/d = 4, L/d = 32 and Vs = 300 m/s. In detail, Figure 7.5a shows the contour lines of the 3D GEV distribution of the non-dimensional impedance function realizations (real and imaginary parts), depending on non-dimensional frequency. The contour line, that represents the places of equal probability density, is highlighted through a colour scale from blue to white progressively changing by increasing the data frequency of occurrence. In the same graph three significant quantities are highlighted to characterize the output distribution in a

probabilistic perspective: the red solid line fits the mean value trend of impedances, the red dashed one covers the median value and the dotted black one the mode on frequencies. Figure 7.5b shows curves representing the density distribution of impedance values given selected a_0 values (0, 0.25, 0.50, 0.75 and 1.00); vertical dashed blue lines are used in Figure 7.5a to show sections of the 3D domain. As for real parts, it is worth observing that the scattering of data, which is overall important, varies sensibly with frequency and presents a reduction in the a_0 range 0.3-0.6 as highlighted by the yellow area in the graph (Figure 7.5a) and in the corresponding density function (middle graph of Figure 7.5b). Overall, the mean value does not coincide with the mode, i.e. with the most frequent value, in all the frequency range; the same happens with respect to the median value. Differences among mean, median and mode are higher in the low-medium non-dimensional frequency range (0-0.5) where the mean value is higher that the median which in turn is higher than the mode: this aspect, which is also typical of the lognormal distribution, is due to the fact that the dynamic stiffness in the low-medium frequency range is mainly governed by the shear wave velocity that is characterised by a lognormal distribution, while at higher frequencies the contribution of masses on the dynamic impedance increases, so that the probability distribution of the soil density (which is normal) becomes evident (right graph of Figure 7.5b). Concerning imaginary parts, a trend can be recognised for the data dispersions: by increasing frequency an overall increase of the scattering of the non-dimensional imaginary translational impedances is observed. It is worth mentioning that data at 0 frequency provides information on the static stiffness of the soil-foundation system; in this sense, transverse distribution of imaginary parts is not shown for $a_0 = 0$ since damping (mainly due to radiation phenomena) tends to zero for the static condition.

By adopting a similar approach, Figure 7.6 shows analysis outcomes in terms of real and imaginary parts of vertical non-dimensional impedance Π_4 of the 3x3 foundation for s/d = 3, L/d = 8 and V_s = 200 m/s. For this component of the impedance matrix both real and imaginary parts are characterised by an increasing scattering of values with frequency; this is clearly evident from both Figure 7.6a and Figure 7.6b. It is worth noting that the data scattering is extremely high, for both the real and imaginary parts, for non-dimensional frequencies higher than about 0.6. Finally, similar considerations with respect to the three statistical parameters hold and the mean value practically coincides with both the median and the mode ones up to $a_0 = 0.5$ for both the real and imaginary parts of the impedance component. Similarly, Figure 7.7 refers to real and imaginary parts of rotational non-dimensional impedance Π_2 for the 2x2 foundation with s/d = 2, L/d = 8 and V_s = 100 m/s. Concerning trends of data scattering, some similarities with data of Figure 7.5, relevant to the translational impedance of the same foundation embedded in a stiffer soil, can be noted. Indeed, the variability of real part shows a reduction of the scattering in the non-dimensional frequency range 0.3-0.75 while scattering of imaginary parts progressively increase with frequency.

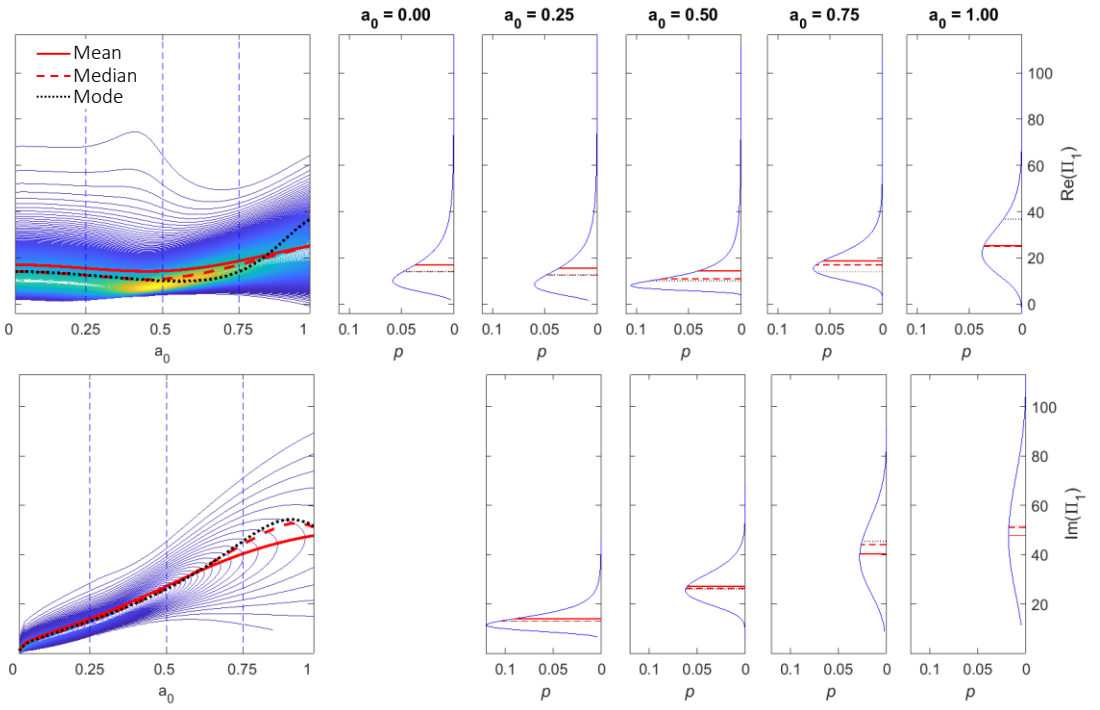

(a) (b)

Figure 7.5. (a) Variability of Π_1 (real and imaginary parts) and (b) distributions of values at selected frequencies - Case 2x2, s/d = 4, L/d = 32, V_s = 300 m/s.

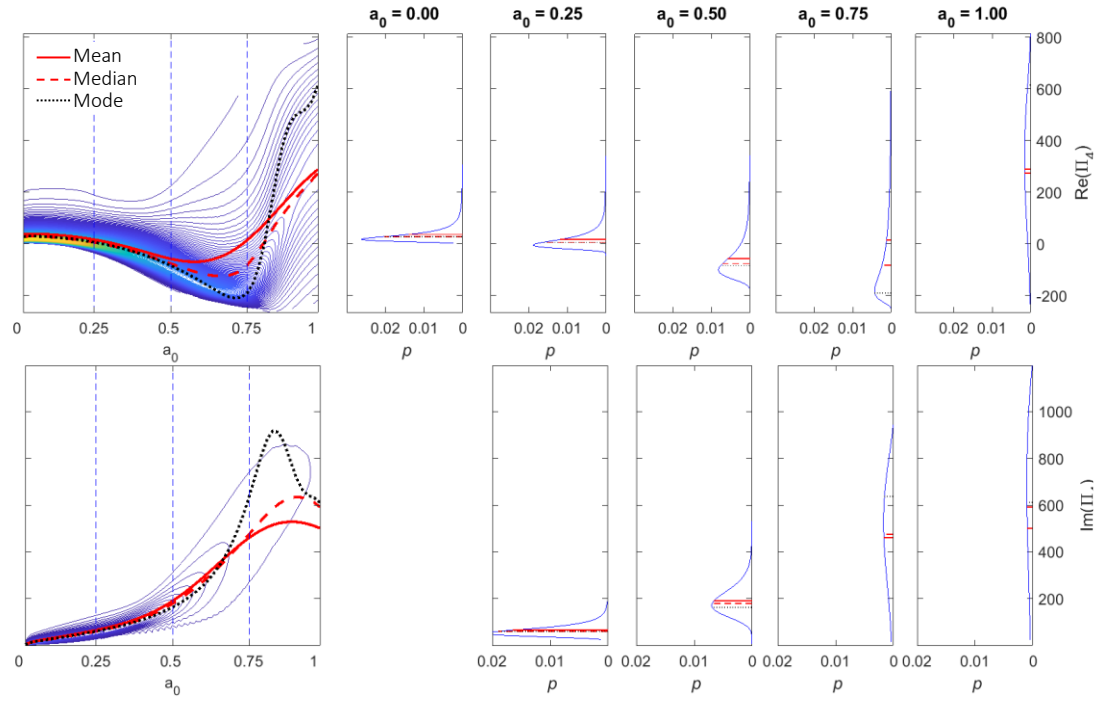

(a) (b)

Figure 7.6. (a) Variability of Π_3 (real and imaginary parts) and (b) distributions of values at selected frequency values - Case 3x3, s/d = 3, L/d = 8, V_s = 200 m/s.

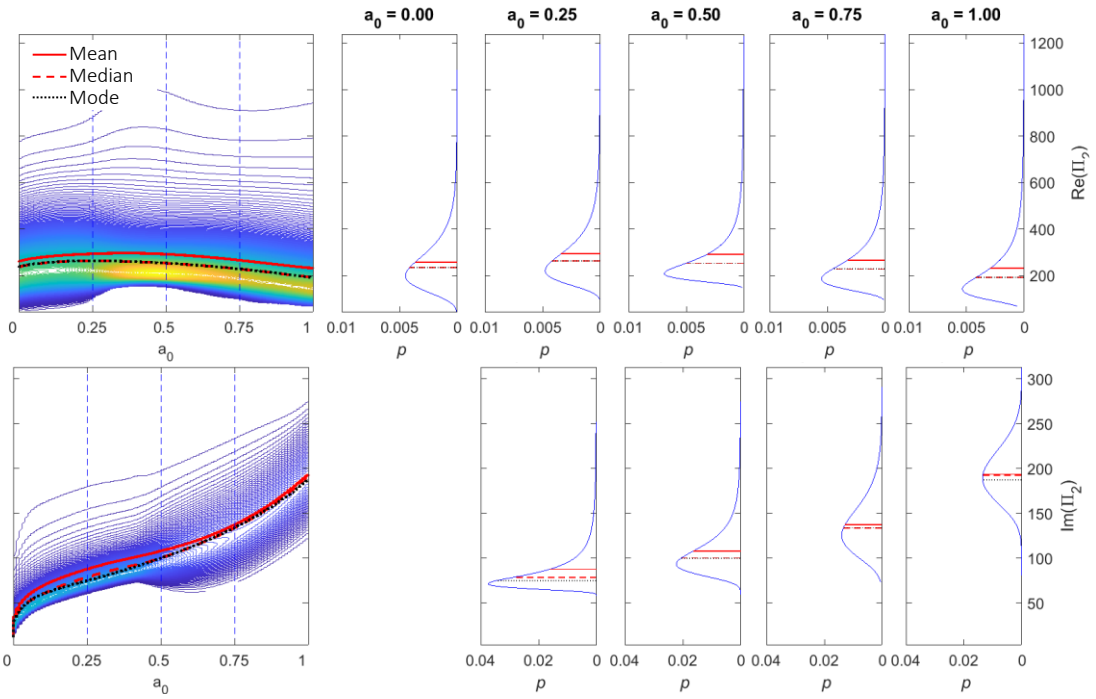

Figure 7.7. (a) Variability of Π_2 (real and imaginary parts) and (b) distributions of values at selected frequencies - Case 2x2, s/d = 2, L/d = 8, Vs = 100 m/s.

From a qualitative point of view, previous considerations concerning the mean, mode and median values hold even if in this case, less important differences between values are obtained in the whole investigated frequency range.

Finally, Figure 7.8 shows real and imaginary parts of the coupled non-dimensional roto-translational impedance Π_3 of the 3x3 foundation with $s/d = 4$, $L/d = 32$ and $V_s = 200$ m/s. As well known, the coupled behaviour, typical of deep foundations, stems from equilibrium of kinematic bending moments at the pile heads due to translations through axial forces in piles; thus, variability of the coupled roto-translational impedance reflects those of translational and vertical ones. In this sense, similarities in the data scattering with respect to translational (Figure 7.5) and vertical (Figure 7.6) impedances are evident although the latter refer to different case studies. In fact, presented cases are enough to highlight peculiar trends of results from the overall case analysed foundations.

A complete overview of results from case studies relevant to the single piles, the 2x2 and 3x3 foundations is shown in in the sequel in terms of the first two statistical moments and the relevant Coefficient Of Variation (COV). Figure 7.9 shows the frequency dependent mean values, standard deviations and the COVs of real and imaginary parts of the non-dimensional impedance functions of the investigated single piles. Some comments about

trends of standard deviations and COVs are provided. Standard deviations of all the impedance components present trends that reflect those of the mean values for both the real and imaginary parts. Thus, COVs are almost independent on the case study and constant with frequency for both the real and imaginary parts of translational, vertical and coupled roto-translational impedances. Overall, real parts have higher COVs than imaginary parts with values of about 70%, 50% and 25% for the translational, coupled roto-translational and vertical impedances, respectively. COVs of the rotational impedance present different trends: higher values are obtained for short piles than for long ones and COVs generally increase by reducing the soil dynamic properties. Π_5, namely the non-dimensional torsional impedance, is not reported consistently with the adopted model for the soil-foundation analysis, which neglects the torsional behaviour of the single pile (Dezi et al., 2016; Carbonari et al., 2016).

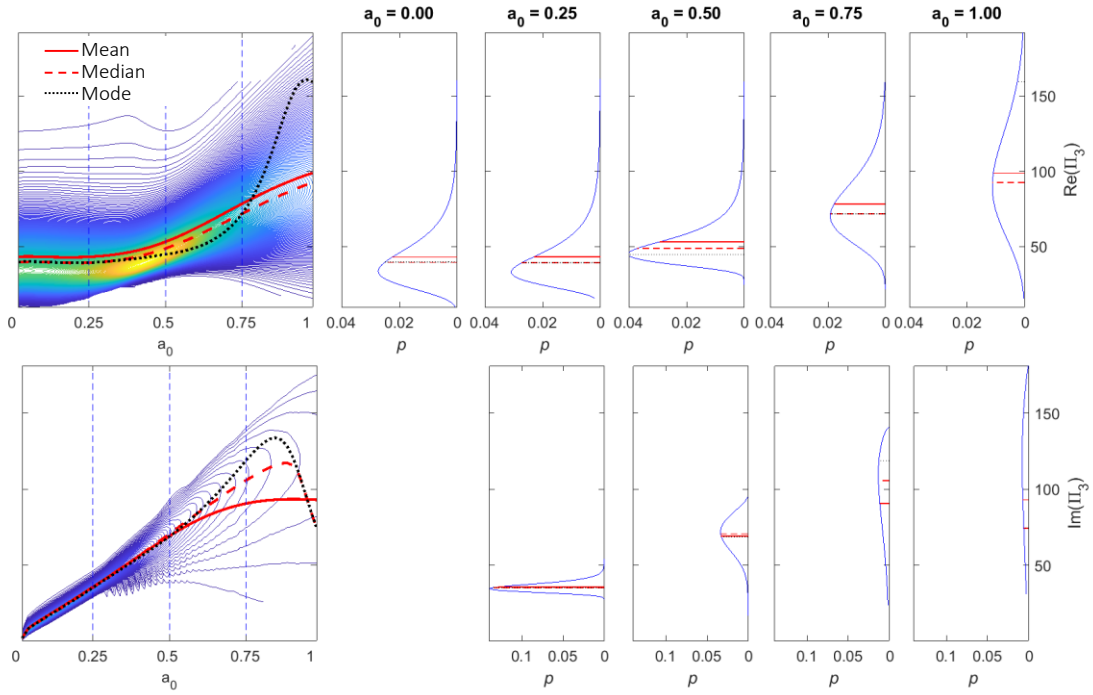

Figure 7.8. (a) Variability of Π_3 (real and imaginary parts) and (b) transverse distributions of values at selected frequency Case 3x3, s/d = 4, L/d = 32, Vs = 200 m/s.

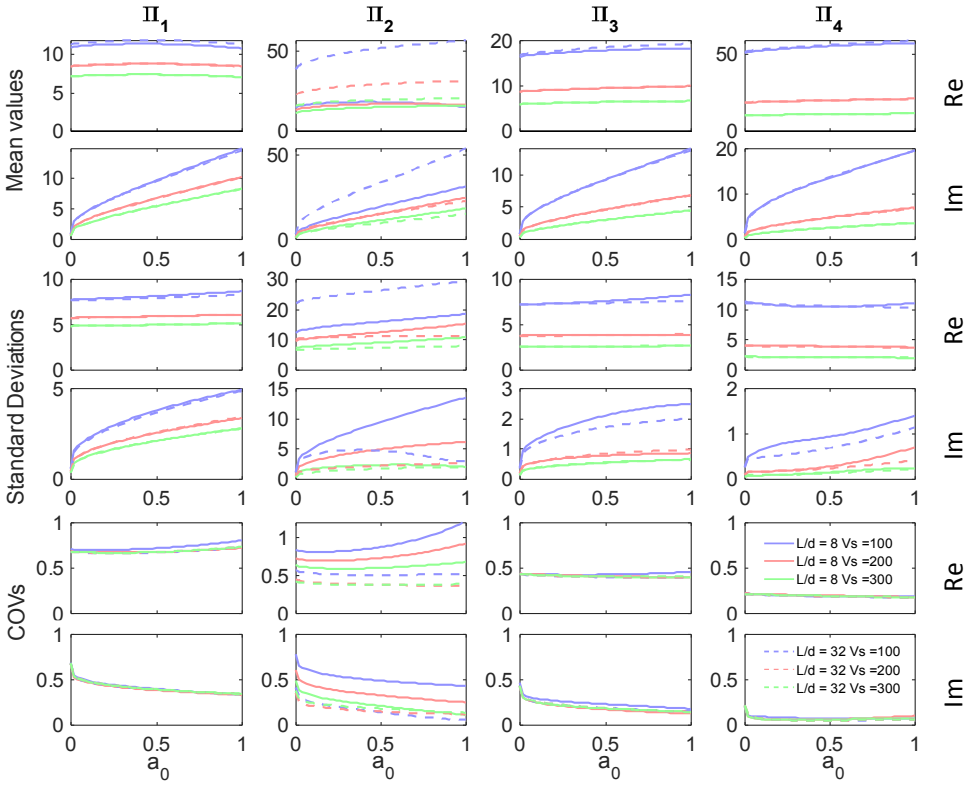

Figure 7.9. Frequency dependent mean values, standard deviations and COVs of real and imaginary parts of non-dimensional impedances of single piles.

Figure 7.10 shows the frequency dependent mean values, standard deviations and the COVs of real part of the non-dimensional impedance functions of the 2x2 foundations. Herein the variability and the scattering of results will be discussed: it can be observed that standard deviations are overall very high, particularly for the non-dimensional translational (Π_1) and vertical (Π_4) impedances for which COVs are within 80-100% up to a non-dimensional frequency of 0.5 and 0.3 for the translational and vertical components, respectively. For higher frequencies COVs of both impedances are characterised by very high peaks due to the mean values approaching null or nearly null values; high values simply express a variation of almost null quantities. This phenomenon affects mainly foundations in soft soils for which the sign inversion of the dynamic stiffnesses occurs at lower frequencies with respect to foundations in medium or stiff soils. The non-dimensional rotational impedance Π_2 and the coupled roto-translational impedance Π_3 are characterised by lower values of COVs (around 30-70%) in the whole frequency range. For Π_2 COVs of long piles are higher than those of short piles and increase with the *s*/*d* ratio. Finally, COVs of the torsional impedance Π_5 are the only one presenting a clear increasing trend with frequency passing from 60-70%, typical of low frequencies, to 70-110% at high frequencies.

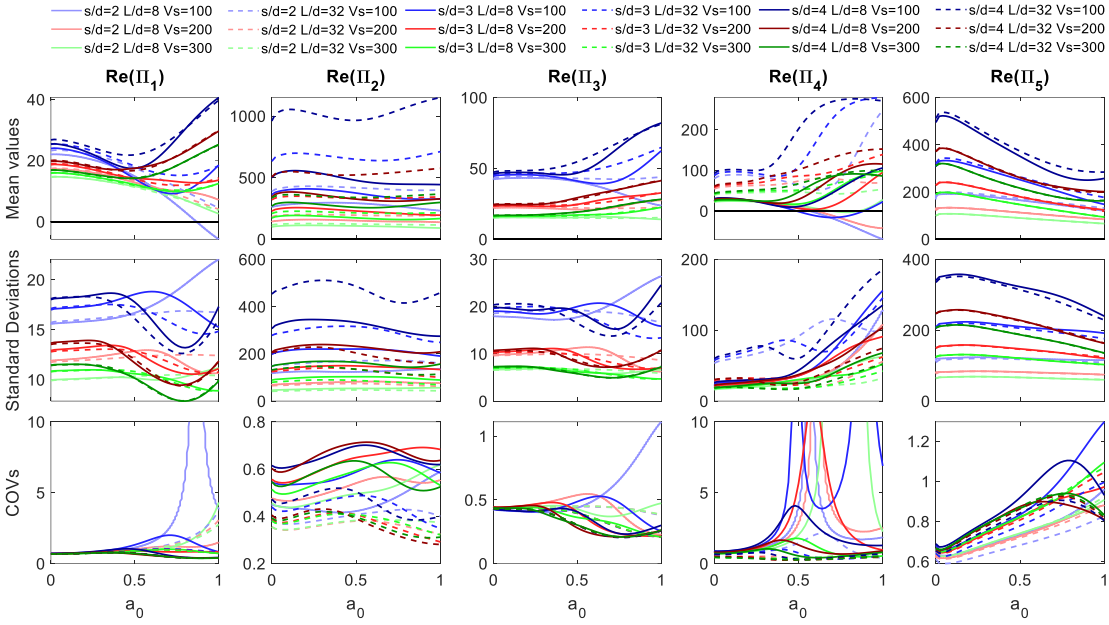

Figure 7.10. Frequency dependent mean values, standard deviations and COVs of real parts of non-dimensional impedances of 2x2 foundations.

In a similar way, Figure 7.11 shows quantities relevant to the imaginary components of impedances. Mean values show the typical increasing trend with frequency, characterised in some cases by peaks of resonance that for the highest pile *s*/*d* ratio fall within the investigated non-dimensional frequency range. Differently from mean values, standard deviations are almost constant in the frequency range 0-0.5 for all the impedance components (excepting for the static values, presenting very low standard deviations); for frequencies higher than 0.5, standard deviations increase rapidly and almost linearly with frequency. This issue gives rise to the peculiar convex trends of the COVs, which decrease in the frequency range 0-0.5 and increase for higher frequencies. It is worth observing that COVs are included in the range 10-60%, excepting static of quasi-static values, which not deserve attention since the mean values of imaginary parts of impedances tend to zero.

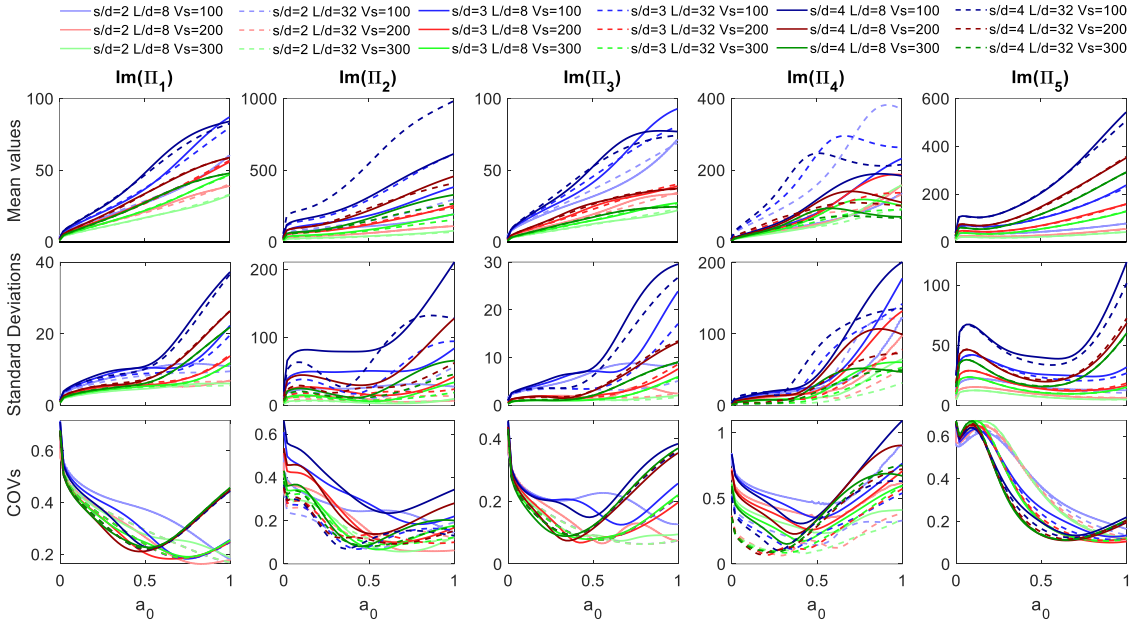

Figure 7.11. Frequency dependent mean values, standard deviations and COVs of imaginary parts of non-dimensional impedances of 2x2 foundations.

Figure 7.12 shows the frequency dependent mean values, standard deviations and COVs of the real parts of the non-dimensional impedance functions of the 3x3 foundations. At a glance, similarities with results of the 2x2 foundations can be recognised. For example, standard deviations are overall very high, particularly for the non-dimensional translational (Π_1) and vertical (Π_4) impedances for which COVs are within 80-100% up to a non-dimensional frequency of 0.3 and 0.2 for the translational and vertical components, respectively. Like previously, for higher frequencies COVs are characterised by peaks due to mean values approaching null or nearly null values; however, it is worth noting that these phenomena occur at lower frequencies with respect to 2x2 foundations and affect a higher number of investigated foundations. Trends of COVs of the non-dimensional rotational impedance Π_2 and the coupled roto-translational impedance Π_3 are similar to that observed for the 2x2 foundations but with a higher variability; anyway, COVs do not overcome 100% (if cases producing peaks are neglected; indeed, for 3x3 foundations the latter occur more frequently in the investigated frequency range than for the 2x2 foundations). Finally, COVs of the torsional impedance Π_5 (included in the range 90-150% excluding peaks) are slightly higher than those of 2x2 foundations.

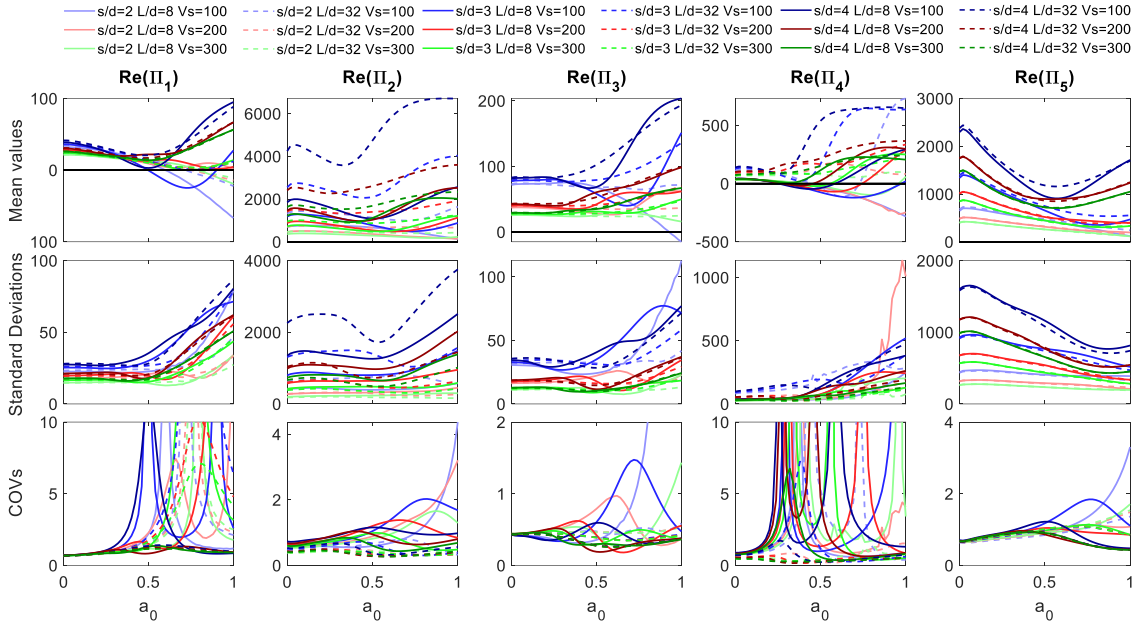

Figure 7.12. Frequency dependent mean values, standard deviations and COVs of real parts of non-dimensional impedances of 3x3 foundations.

Figure 7.13 shows quantities relevant to the imaginary components of the non-dimensional impedances of 3x3 foundations. In this case, similarities with results from 2x2 foundations are more evident and previous comments relevant to COVs completely hold. It is worth observing some jagged curves arising from convergence issues relevant to applications characterised by very low shear wave velocities.

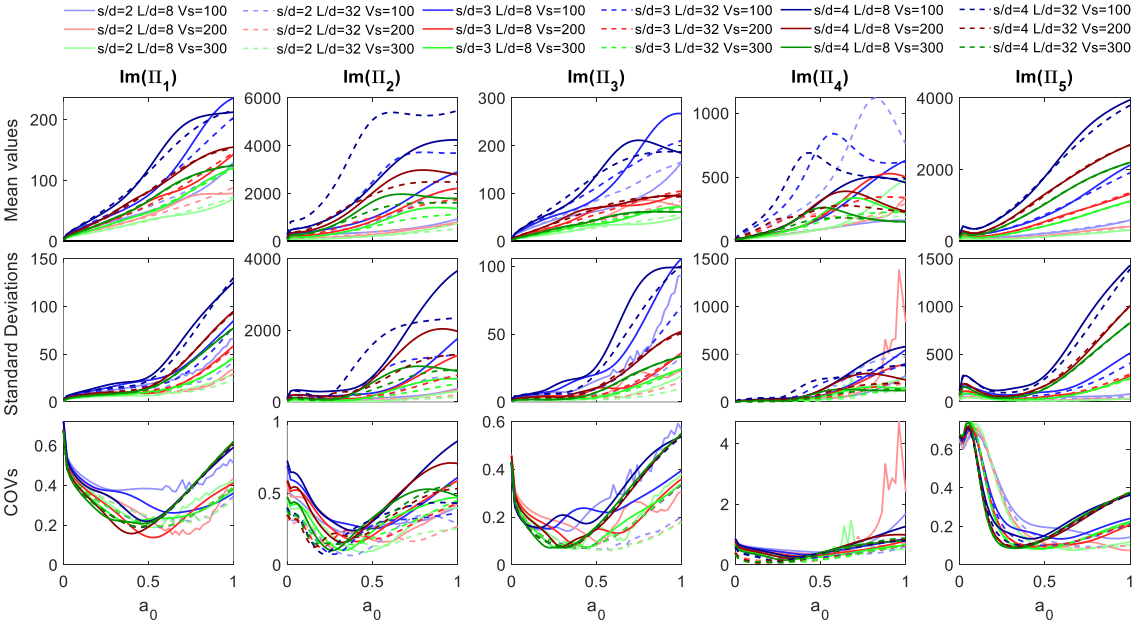

Figure 7.13. Frequency dependent mean values, standard deviations and COVs of imaginary parts of non-dimensional impedances of 3x3 foundations.

7.5.1.1 Correlation coefficients

In this section the Pearson correlation coefficient ρ_{xy} is adopted to provide a measure of the linear correlation between the non-dimensional impedances and the random variables of the problem (V_s, ρ_s, E_p). As well known, Pearson's correlation coefficient is the covariance of the two variables divided by the product of their standard deviations and assumes values in the range [-1,1]:

$$\rho_{xy} = \frac{\sigma_{xy}}{\sigma_x \sigma_y} \tag{23}$$

For the sake of brevity only few cases of the investigated ones will be shown being possible a generalization of the comments. Figure 7.14 collects in a matrix of graphs the frequency-dependent correlation coefficients between the non-dimensional impedances and the random variables of the 2x2 foundation with $s/d = 3$, $L/d = 8$, $V_s = 100$ m/s. Results of this analysis case are representative of foundations with short piles embedded in soft soils. It can be observed an almost complete absence of a linear correlation between real and imaginary parts of impedances and the pile Young's modulus. A similar conclusion can be drawn with respect to the soil density for the non-dimensional frequency lower than 0.5. On the contrary, correlation coefficients tends to increase (up to 0.5) for higher non-dimensional frequencies (i.e. greater than 0.5); this is in line with comments about the statistical position parameters and the contribution of the soil density on the foundation dynamic stiffnesses. On the contrary, a linear clear correlation between impedances and the soil shear wave velocity is evident for a wide range of the non-dimensional frequency in the interval 0-1. In detail, a linear positive correlation holds between both real and imaginary parts of all the impedance components in the non-dimensional frequency range 0-0.5; for higher frequencies, the linear correlation is partially lost (e.g. for impedance Π_4, correlation turns negative for frequencies higher than about 0.6), in contrast with the increasing values of the correlation coefficients relevant the soil density.

Figure 7.15 collects the correlation coefficients relevant to the 2x2 foundation with $s/d = 3$, $L/d = 32$, $V_s = 100$ m/s; results are representative of foundations with long piles embedded in soft soils. Even in this case, an almost null correlation between real and imaginary parts of impedances and the pile Young's modulus is evident, although positive non null correlation coefficients (up to about 0.5) are obtained for imaginary parts of Π_2 and Π_3 in the non-dimensional frequency range 0.25-0.75. Similar considerations, extended to all the imaginary parts of impedances, hold for correlations with the soil density.

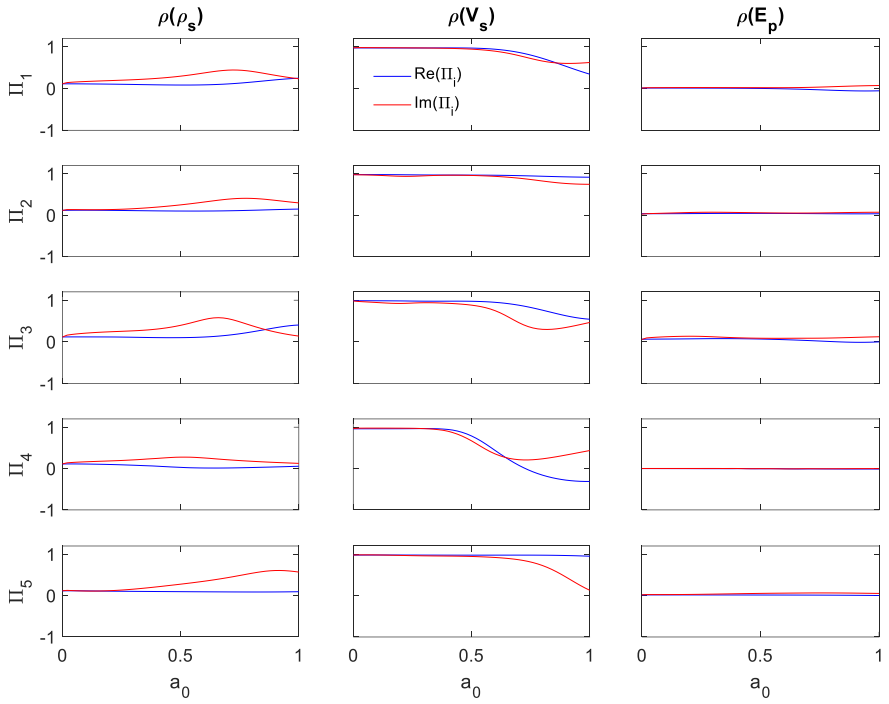

Figure 7.14. Correlation coefficients between non-dimensional impedances (real and imaginary parts) and the independent random variables for 2x2 foundation, s/d = 3, L/d = 8, Vs = 100 m/s.

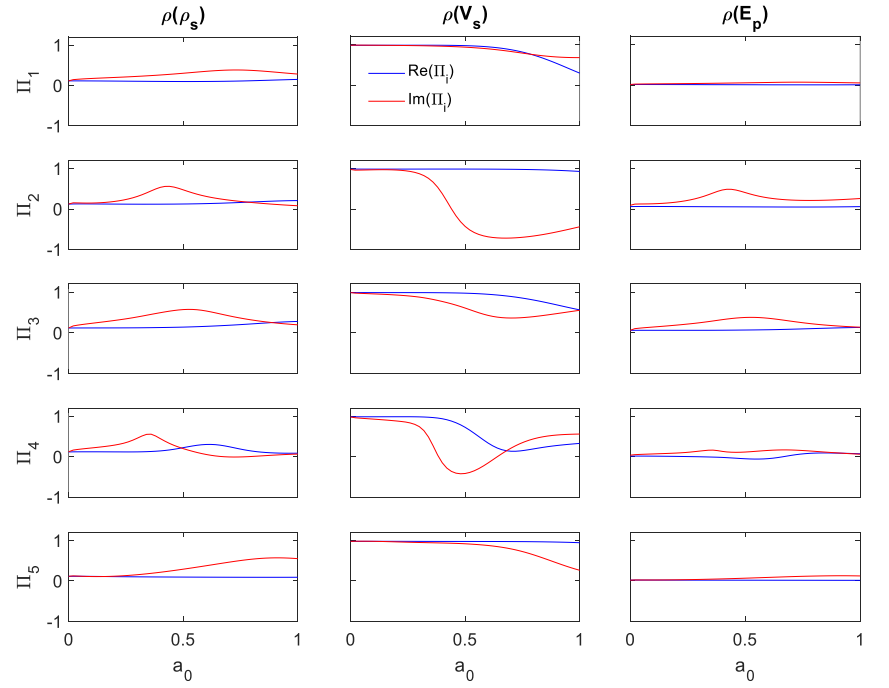

Figure 7.15. Correlation coefficients between non-dimensional impedances (real and imaginary parts) and the independent random variables for 2x2 foundation, s/d = 3, L/d = 32, Vs = 100 m/s.

Again, the highest correlations are observed with respect to the soil shear wave velocity. In detail, a positive linear correlation characterises all the real parts of impedance

components up to a frequency of 0.75, for Π_1 and Π_3, up to a frequency of about 0.5 for Π_4, and in the whole frequency range for Π_2 and Π_5. As for imaginary parts, the linear correlation is partially lost at a frequency of about 0.2-0.5, depending on the impedance component. It is worth observing that a decrease of the correlation coefficient relevant to the shear wave velocity is always almost in contrast with an increase of coefficients relevant to the soil density and the pile Young's modulus.

7.5.1.2 Sensitivity indexes

In this section the first order sensitivity indexes $\bar{S}_i$ for ρ_s, V_s and E_p are presented and discussed. Table 7.4, Table 7.5 and Table 7.6 and collect the sensitivity indexes of all the case studies relevant to the single pile foundations, the 2x2 foundations and the 3x3 foundations. Bar charts are constructed within the table to provide at a glance the importance of the index (green and red colours are used for the real and imaginary parts, respectively). From an overall point of view, V_s is primarily responsible for the global variability of the results. In general, for real parts sensitivity indexes of V_s are higher than 0.90 in all the considered pile configurations, with values over 0.95 in most cases. About imaginary parts, a different behaviour can be delineated. It is interesting to observe that, with reference to single piles, the pile Young's modulus contributes even larger than the soil shear wave velocity to the variability of imaginary parts of the non-dimensional rotational impedance Π_2, and a higher influence of the soil density on Π_2, Π_4 and Π_5 is evident with respect to pile groups. On the other hand, considering pile group foundations, the variability of E_p scarcely contributes to the variability of impedances, while sensitivity indexes of V_s generally exceed 0.80, especially for translational impedance functions Π_1, where the minimum value is 0.90. Furthermore, it is worth observing the influence of the soil density variability for Π_3 and Π_5, where $\bar{S}_i$ generally assumes values between 0.15 and 0.20. It can be concluded that V_s can be adopted as the most important random variable of the problem.

Table 7.4. Sensitivity indexes for 2x2 foundations.

$\frac{s}{d}$	$\frac{L}{d}$	V_s	Π_1			Π_2			Π_3			Π_4			Π_5		
			ρ_s	V_s	E_p	ρ_s	V_s	E_p	ρ_s	V_s	E_p	ρ_s	V_s	E_p	ρ_s	V_s	E_p
			Re	Re	Re	Re	Re	Re	Re	Re	Re	Re	Re	Re	Re	Re	Re
			Im	*Im*	*Im*	*Im*	*Im*	*Im*	*Im*	*Im*	*Im*	*Im*	*Im*	*Im*	*Im*	*Im*	*Im*
2	8	100	0.01	0.99	0	0.01	0.98	0.01	0.01	0.98	0.01	0.01	0.99	0	0.01	0.99	0
			0.07	*0.93*	*0*	*0.07*	*0.92*	*0.01*	*0.13*	*0.86*	*0.01*	*0.03*	*0.97*	*0*	*0.06*	*0.94*	*0*
		200	0.02	0.98	0	0.01	0.99	0	0.04	0.96	0	0.01	0.99	0	0.01	0.99	0
			0.1	*0.9*	*0*	*0.08*	*0.92*	*0*	*0.14*	*0.86*	*0*	*0.04*	*0.95*	*0.01*	*0.14*	*0.86*	*0*
		300	0.03	0.97	0	0.01	0.99	0	0.05	0.95	0	0.01	0.99	0	0.01	0.99	0
			0.06	*0.94*	*0*	*0.06*	*0.94*	*0*	*0.08*	*0.91*	*0.01*	*0.04*	*0.96*	*0*	*0.15*	*0.85*	*0*
	32	100	0.01	0.99	0	0.02	0.98	0	0.03	0.97	0	0.01	0.99	0	0.01	0.99	0
			0.07	*0.92*	*0.01*	*0.17*	*0.7*	*0.13*	*0.12*	*0.72*	*0.16*	*0.05*	*0.95*	*0*	*0.08*	*0.92*	*0*
		200	0.01	0.99	0	0.02	0.98	0	0.03	0.96	0.01	0.01	0.99	0	0.01	0.99	0
			0.09	*0.91*	*0*	*0.16*	*0.83*	*0.01*	*0.15*	*0.76*	*0.09*	*0.05*	*0.95*	*0*	*0.16*	*0.83*	*0.01*
		300	0.03	0.97	0	0.02	0.98	0	0.04	0.95	0.01	0.02	0.98	0	0.01	0.99	0
			0.07	*0.93*	*0*	*0.1*	*0.89*	*0.01*	*0.11*	*0.84*	*0.05*	*0.05*	*0.95*	*0*	*0.17*	*0.83*	*0*
3	8	100	0.01	0.99	0	0.02	0.98	0	0.02	0.98	0	0.01	0.99	0	0.01	0.99	0
			0.07	*0.93*	*0*	*0.18*	*0.69*	*0.13*	*0.18*	*0.71*	*0.11*	*0.06*	*0.94*	*0*	*0.08*	*0.91*	*0.01*
		200	0.01	0.99	0	0.02	0.98	0	0.03	0.96	0.01	0.03	0.97	0	0.01	0.99	0
			0.09	*0.91*	*0*	*0.19*	*0.76*	*0.05*	*0.17*	*0.76*	*0.07*	*0.03*	*0.96*	*0.01*	*0.18*	*0.82*	*0*
		300	0.03	0.97	0	0.02	0.98	0	0.04	0.95	0.01	0.03	0.97	0	0.01	0.99	0
			0.06	*0.94*	*0*	*0.14*	*0.83*	*0.03*	*0.11*	*0.86*	*0.03*	*0.05*	*0.94*	*0.01*	*0.18*	*0.82*	*0*
	32	100	0.01	0.99	0	0.02	0.98	0	0.02	0.98	0	0.05	0.95	0	0.01	0.99	0
			0.07	*0.93*	*0*	*0.08*	*0.82*	*0.1*	*0.23*	*0.67*	*0.1*	*0.07*	*0.89*	*0.04*	*0.07*	*0.93*	*0*
		200	0.01	0.99	0	0.02	0.98	0	0.03	0.96	0.01	0.03	0.97	0	0.01	0.99	0
			0.09	*0.91*	*0*	*0.08*	*0.82*	*0.1*	*0.17*	*0.76*	*0.07*	*0.07*	*0.91*	*0.02*	*0.14*	*0.86*	*0*
		300	0.03	0.97	0	0.02	0.98	0	0.04	0.95	0.01	0.03	0.97	0	0.01	0.99	0
			0.06	*0.94*	*0*	*0.11*	*0.82*	*0.07*	*0.11*	*0.86*	*0.03*	*0.06*	*0.92*	*0.02*	*0.15*	*0.85*	*0*
4	8	100	0.01	0.99	0	0.02	0.98	0	0.02	0.98	0	0.02	0.97	0.01	0.01	0.99	0
			0.07	*0.93*	*0*	*0.03*	*0.9*	*0.06*	*0.24*	*0.67*	*0.09*	*0.07*	*0.82*	*0.11*	*0.08*	*0.92*	*0*
		200	0.01	0.99	0	0.02	0.98	0	0.03	0.96	0.01	0.02	0.97	0.01	0.01	0.99	0
			0.09	*0.91*	*0*	*0.06*	*0.86*	*0.08*	*0.17*	*0.76*	*0.07*	*0.06*	*0.86*	*0.08*	*0.16*	*0.84*	*0*
		300	0.03	0.97	0	0.02	0.97	0.01	0.04	0.95	0.01	0.02	0.97	0.01	0.01	0.99	0
			0.06	*0.94*	*0*	*0.07*	*0.84*	*0.09*	*0.11*	*0.87*	*0.02*	*0.06*	*0.89*	*0.05*	*0.17*	*0.83*	*0*
	32	100	0.01	0.99	0	0.02	0.98	0	0.02	0.98	0	0.02	0.98	0	0.01	0.99	0
			0.07	*0.93*	*0*	*0.06*	*0.87*	*0.07*	*0.24*	*0.67*	*0.09*	*0.09*	*0.83*	*0.08*	*0.09*	*0.91*	*0*
		200	0.01	0.99	0	0.02	0.98	0	0.03	0.96	0.01	0.02	0.97	0.01	0.01	0.99	0
			0.09	*0.91*	*0*	*0.11*	*0.83*	*0.06*	*0.17*	*0.76*	*0.07*	*0.08*	*0.87*	*0.05*	*0.18*	*0.82*	*0*
		300	0.03	0.97	0	0.02	0.98	0	0.04	0.95	0.01	0.03	0.97	0	0.01	0.99	0
			0.06	*0.94*	*0*	*0.11*	*0.82*	*0.07*	*0.11*	*0.87*	*0.02*	*0.07*	*0.9*	*0.03*	*0.18*	*0.82*	*0*

Table 7.5. Sensitivity indexes for single piles.

Foundation	$\frac{L}{d}$	V_s	Π_1			Π_2			Π_3			Π_4		
			ρ_s	V_s	E_p	ρ_s	V_s	E_p	ρ_s	V_s	E_p	ρ_s	V_s	E_p
			Re	Re	Re	Re	Re	Re	Re	Re	Re	Re	Re	Re
			Im	*Im*	*Im*	*Im*	*Im*	*Im*	*Im*	*Im*	*Im*	*Im*	*Im*	*Im*
Single pile	8	100	0.01	0.99	0	0.02	0.93	0.05	0.02	0.98	0	0.02	0.98	0
			0.03	*0.97*	*0*	*0.12*	*0.56*	*0.32*	*0.05*	*0.94*	*0.01*	*0.03*	*0.97*	*0*
		200	0.01	0.99	0	0.02	0.93	0.05	0.02	0.98	0	0.02	0.98	0
			0.03	*0.97*	*0*	*0.08*	*0.4*	*0.51*	*0.06*	*0.9*	*0.04*	*0.06*	*0.94*	*0*
		300	0.01	0.99	0	0.02	0.93	0.05	0.02	0.98	0	0.02	0.98	0
			0.03	*0.97*	*0*	*0.09*	*0.36*	*0.55*	*0.06*	*0.92*	*0.02*	*0.07*	*0.92*	*0.01*
	32	100	0.01	0.99	0	0.02	0.93	0.05	0.02	0.98	0	0.02	0.98	0
			0.03	*0.97*	*0*	*0.12*	*0.21*	*0.67*	*0.02*	*0.93*	*0.05*	*0.1*	*0.8*	*0.1*
		200	0.01	0.99	0	0.02	0.93	0.05	0.02	0.98	0	0.02	0.98	0
			0.03	*0.97*	*0*	*0.12*	*0.24*	*0.64*	*0.06*	*0.92*	*0.02*	*0.06*	*0.88*	*0.06*
		300	0.01	0.99	0	0.02	0.93	0.05	0.02	0.98	0	0.02	0.98	0
			0.03	*0.97*	*0*	*0.12*	*0.21*	*0.64*	*0.06*	*0.92*	*0.02*	*0.06*	*0.91*	*0.03*

Table 7.6. Sensitivity indexes for 3x3 foundations.

$\frac{s}{d}$	$\frac{L}{d}$	V_s	Π_1			Π_2			Π_3			Π_4			Π_5		
			ρ_s	V_s	E_p	ρ_s	V_s	E_p	ρ_s	V_s	E_p	ρ_s	V_s	E_p	ρ_s	V_s	E_p
			Re	Re	Re	Re	Re	Re	Re	Re	Re	Re	Re	Re	Re	Re	Re
			Im	*Im*	*Im*	*Im*	*Im*	*Im*	*Im*	*Im*	*Im*	*Im*	*Im*	*Im*	*Im*	*Im*	*Im*
2	8	100	0.03	0.97	0	0.01	0.99	0	0.01	0.95	0.04	0.01	0.99	0	0.01	0.99	0
			0.05	*0.92*	*0.03*	*0.05*	*0.93*	*0.02*	*0.05*	*0.86*	*0.09*	*0.03*	*0.97*	*0*	*0.18*	*0.82*	*0*
		200	0.02	0.98	0	0.01	0.99	0	0.02	0.96	0.02	0.01	0.99	0	0.01	0.99	0
			0.08	*0.92*	*0*	*0.06*	*0.94*	*0*	*0.09*	*0.88*	*0.03*	*0.04*	*0.95*	*0.01*	*0.2*	*0.8*	*0*
		300	0.02	0.98	0	0.01	0.99	0	0.03	0.96	0.01	0.01	0.99	0	0.02	0.98	0
			0.07	*0.93*	*0*	*0.05*	*0.94*	*0.01*	*0.08*	*0.9*	*0.02*	*0.05*	*0.95*	*0*	*0.15*	*0.85*	*0*
	32	100	0.03	0.97	0	0.01	0.99	0	0.03	0.92	0.05	0.11	0.89	0	0.01	0.99	0
			0.05	*0.9*	*0.05*	*0.08*	*0.91*	*0.01*	*0.1*	*0.8*	*0.1*	*0.04*	*0.87*	*0.11*	*0.23*	*0.73*	*0.04*
		200	0.01	0.99	0	0.01	0.99	0	0.03	0.94	0.03	0.02	0.98	0	0.01	0.99	0
			0.08	*0.9*	*0.02*	*0.08*	*0.92*	*0*	*0.11*	*0.82*	*0.07*	*0.07*	*0.93*	*0*	*0.26*	*0.73*	*0.01*
		300	0.01	0.99	0	0.02	0.98	0	0.03	0.95	0.02	0.02	0.97	0.01	0.02	0.98	0
			0.07	*0.92*	*0.01*	*0.07*	*0.93*	*0*	*0.1*	*0.85*	*0.05*	*0.06*	*0.94*	*0*	*0.2*	*0.8*	*0*
3	8	100	0.02	0.98	0	0.02	0.98	0	0.01	0.94	0.04	0.1	0.83	0.07	0.01	0.99	0
			0.06	*0.93*	*0.01*	*0.12*	*0.86*	*0.02*	*0.1*	*0.85*	*0.05*	*0.05*	*0.83*	*0.12*	*0.34*	*0.65*	*0.01*
		200	0.01	0.99	0	0.03	0.97	0	0.02	0.97	0.01	0.03	0.95	0.02	0.01	0.99	0
			0.08	*0.92*	*0*	*0.09*	*0.9*	*0.01*	*0.13*	*0.77*	*0.1*	*0.07*	*0.91*	*0.02*	*0.31*	*0.69*	*0*
		300	0.01	0.99	0	0.03	0.97	0	0.03	0.96	0.01	0.03	0.96	0.01	0.02	0.98	0
			0.07	*0.93*	*0*	*0.08*	*0.91*	*0.01*	*0.12*	*0.82*	*0.07*	*0.07*	*0.93*	*0*	*0.23*	*0.77*	*0*
	32	100	0.01	0.99	0	0.03	0.97	0	0.02	0.96	0.02	0.03	0.96	0.01	0.01	0.99	0
			0.07	*0.93*	*0*	*0.11*	*0.83*	*0.06*	*0.18*	*0.69*	*0.13*	*0.08*	*0.85*	*0.07*	*0.27*	*0.73*	*0*
		200	0.01	0.99	0	0.03	0.97	0	0.02	0.97	0.01	0.04	0.93	0.03	0.01	0.99	0
			0.08	*0.92*	*0*	*0.08*	*0.88*	*0.04*	*0.17*	*0.78*	*0.05*	*0.08*	*0.89*	*0.03*	*0.25*	*0.75*	*0*
		300	0.01	0.99	0	0.03	0.97	0	0.03	0.96	0.01	0.04	0.95	0.01	0.02	0.98	0
			0.07	*0.93*	*0*	*0.07*	*0.9*	*0.03*	*0.13*	*0.84*	*0.03*	*0.07*	*0.92*	*0.01*	*0.18*	*0.82*	*0*
4	8	100	0.01	0.99	0	0.02	0.98	0	0.02	0.98	0	0.02	0.91	0.07	0.01	0.99	0
			0.07	*0.93*	*0*	*0.03*	*0.92*	*0.05*	*0.22*	*0.68*	*0.1*	*0.08*	*0.82*	*0*	*0.31*	*0.69*	*0*
		200	0.01	0.99	0	0.02	0.97	0.01	0.02	0.97	0.01	0.02	0.95	0.03	0.01	0.99	0
			0.08	*0.92*	*0*	*0.03*	*0.94*	*0.03*	*0.17*	*0.78*	*0.05*	*0.07*	*0.85*	*0.08*	*0.27*	*0.73*	*0*
		300	0.01	0.99	0	0.03	0.97	0	0.03	0.96	0.01	0.03	0.95	0.02	0.02	0.98	0
			0.07	*0.93*	*0*	*0.03*	*0.95*	*0.02*	*0.13*	*0.84*	*0.03*	*0.06*	*0.89*	*0.05*	*0.2*	*0.8*	*0*
	32	100	0.01	0.99	0	0.02	0.98	0	0.02	0.98	0	0.1	0.82	0.08	0.01	0.99	0
			0.07	*0.93*	*0*	*0.04*	*0.92*	*0.04*	*0.21*	*0.69*	*0.1*	*0.06*	*0.85*	*0.09*	*0.35*	*0.65*	*0*
		200	0.01	0.99	0	0.02	0.97	0.01	0.02	0.97	0.01	0.02	0.97	0.01	0.01	0.99	0
			0.08	*0.92*	*0*	*0.04*	*0.93*	*0.03*	*0.17*	*0.78*	*0.05*	*0.09*	*0.83*	*0.08*	*0.3*	*0.7*	*0*
		300	0.01	0.99	0	0.03	0.97	0	0.03	0.96	0.01	0.03	0.96	0.01	0.02	0.98	0
			0.07	*0.93*	*0*	*0.04*	*0.94*	*0.02*	*0.13*	*0.84*	*0.03*	*0.08*	*0.86*	*0.06*	*0.22*	*0.78*	*0*

7.5.2 Variability of Kinematic response factors

In this section the variability of the Foundation Input Motion (FIM) given that of the random variables is addressed and discussed. Typical trends of the kinematic translational and rotational response factors are shown in Figure 7.16 for a set or samples from a 2x2 foundation layout; apart the very high variability of results, which is clearly evident and will be addressed in the sequel with details relevant to the foundation layout, it can be observed that typical trends of the translational factor are characterised by a plateau of unit value that extends from 0 up to a frequency depending on the shear wave velocity of the soil deposit (the higher the soil shear wave velocity, the higher the plateau extension is) followed by a rapid reduction of the parameter and by a subsequent oscillation around a mean almost constant value. Furthermore, values greater than one 1 (up to 1.2) be obtained for very stiff soils. On the contrary, the rotational kinematic response factor assumes nearly zero values at very low frequencies and increases rapidly with frequency presenting, similarly to the kinematic parameter, oscillations for higher frequencies.

Above trends, well known from the literature [52], determine intrinsic difficulties in the identification of probabilistic models for the kinematic parameters since oscillations of curves affect sensibly the probability of getting certain values of the parameter; this will be shown in the sequel discussing the variability of the parameters from a probabilistic point of view.

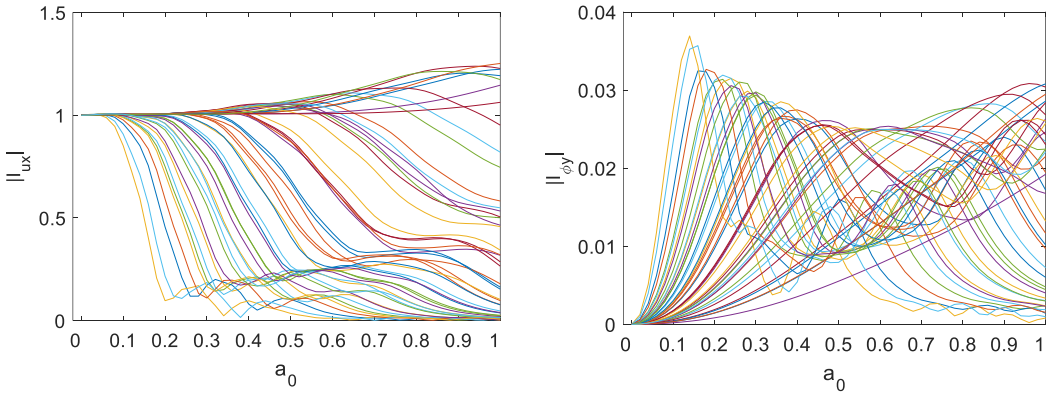

Figure 7.16. Typical trends of kinematic response factors (samples from case 2x2, s/d = 4, L/d = 32, V_s = 300 m/s).

In order to highlight the considerable variation of the kinematic response factors in the non-dimensional frequency domain, results are presented in the form of boxplots. Figure 7.17 and Figure 7.18 show the variability of the translational (I_U) and rotational (I_ϕ) kinematic response factors for only two case studies belonging to 2x2 and 3x3 foundations, being possible a generalization of comments concerning the main statistical parameters. In graphs of both figures, median values are traced with white circles with a blue dot in the centre while mean values are identified with red solid lines. Blue bars at each frequency value embraces values between the 25th and the 75th percentile while grey whiskers refers to the 10th and 90th percentile. Concerning translational factors, differently from impedances, a small range (0-0.2 for short piles and 0-0.15 for long piles) at low frequency can be identified in which the dispersion of results is negligible; in these ranges, the parameter can be described by its mean value. Overall, for $a_0 >$ 0.15-0.2, the variability of I_U generally increases with frequency, and in case of long piles it stabilizes at a frequency of about 0.4, 0.6 and 0.8 for V_s = 100, 200 and 300 m/s respectively. It is worth observing that highest values, occurring for high values of the shear wave velocity, never overcome 1.2. Concerning rotational kinematic response factors, the dispersion of the outcomes is almost symmetric with respect to the mean values and increases rapidly for $a_0 > 0$. However, it is worth noticing that for $a_0 >$ 0.5-0.6 results maintain the same dispersion or slightly decrease it till the end of the investigated frequency domain. Both means and medians have a convex development and are attested at quite close values. For both translational and rotational kinematic response factors, Figure 7.17 and Figure 7.18 also shows curves representing the density distribution of parameters given a selected a_0 value (0, 0.25, 0.50, 0.75 and 1.00); distribution demonstrate the absence of a clear trend

and the practical difficulty to define a probabilistic model for the parameter, at least for certain frequency ranges.

As already done for impedances, the first two statistical moments and the relevant COVs of the two kinematic response factors are shown in the following to provide a complete survey on the analysis results. Figure 7.19a refers to the investigated single piles; overall mean values present trends, with respect to V_s and L/d, that are well known from the technical literature and commenting about these goes beyond the aim of this work. On the contrary, it is worth discussing about standard deviations that, for the translational factor, increase significantly and almost linearly with frequency from 0 to about 0.4 with a gradient that depends on the shear wave velocity (up to $a_0 > 0.6$, the gradient reduces by increasing the soil shear wave velocity). COVs of the translational factors follow a similar trend. Concerning the rotational parameters, it is worth observing that mean values increase up to stabilise at about $a_0 = 0.6$ while standard deviations increase in the whole frequency range from 0 to about 0.2. Consequently, COVs present a pseudo-parabolic trend like that previously observed for impedances with the highest values ranging between 100-120%.

Figure 7.19b and Figure 7.19c, referring to 2x2 and 3x3 pile group respectively, are discussed together in view of their similarities in terms of results variability. As a general observation for mean values, the scattering of curves relevant to the same shear wave velocity can be attributed mainly to the different pile spacing, although the latter does not reflect in a significant dispersion of COVs for the same results. This confirms that V_s plays the most relevant role in the definition of the kinematic problem. Furthermore, it is possible to see that, for a given s/d, L/d and V_s, standard deviations and COVs have almost the same behaviour for the 2x2 and 3x3 pile foundations. Indeed, standard deviations of the translational factor generally increases almost linearly with frequency up to a non-dimensional frequency of 0.5-0.75, depending on the shear wave velocity, and then stabilises or slightly decreases. On the contrary, COVs are always ascending, from 0 to about 80% in the majority of cases and to 120% for low V_s and long piles. With respect to the rotational factor, trends of standard deviations are quite similar to that of the mean values while COVs present the pseudo-parabolic trend already discussed in this section, with values moving from 200% at very low frequencies to about 50% at medium-high frequency.

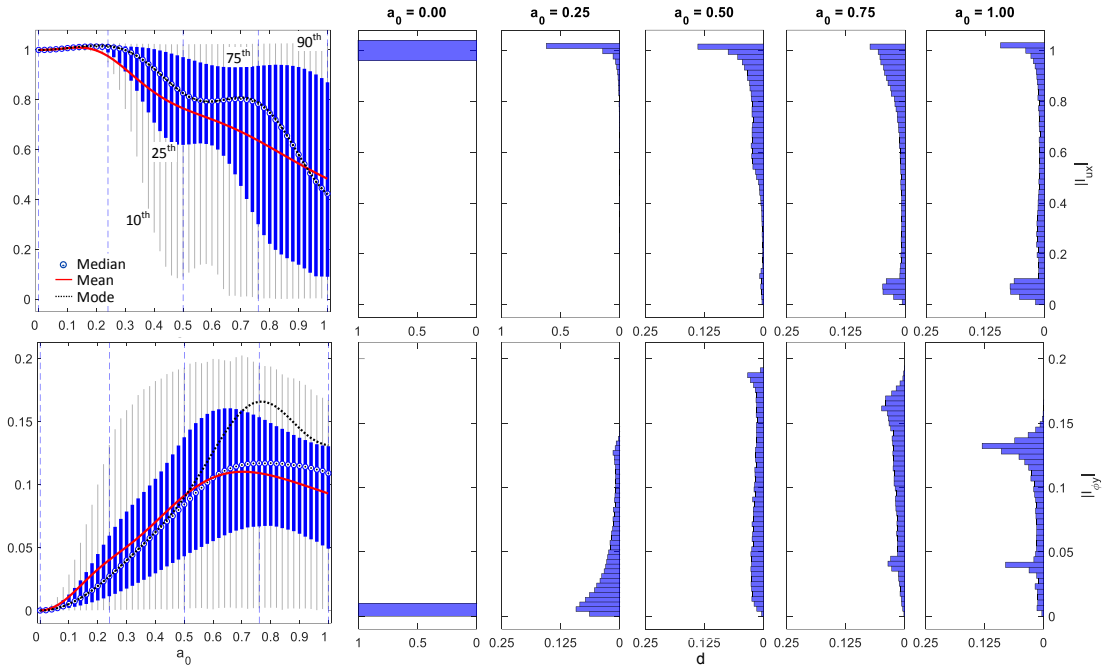

Figure 7.17. Variability of (a) I_U and (b) I_Φ for 2x2 foundation, s/d = 3, L/d = 8, V_s = 200 m/s.

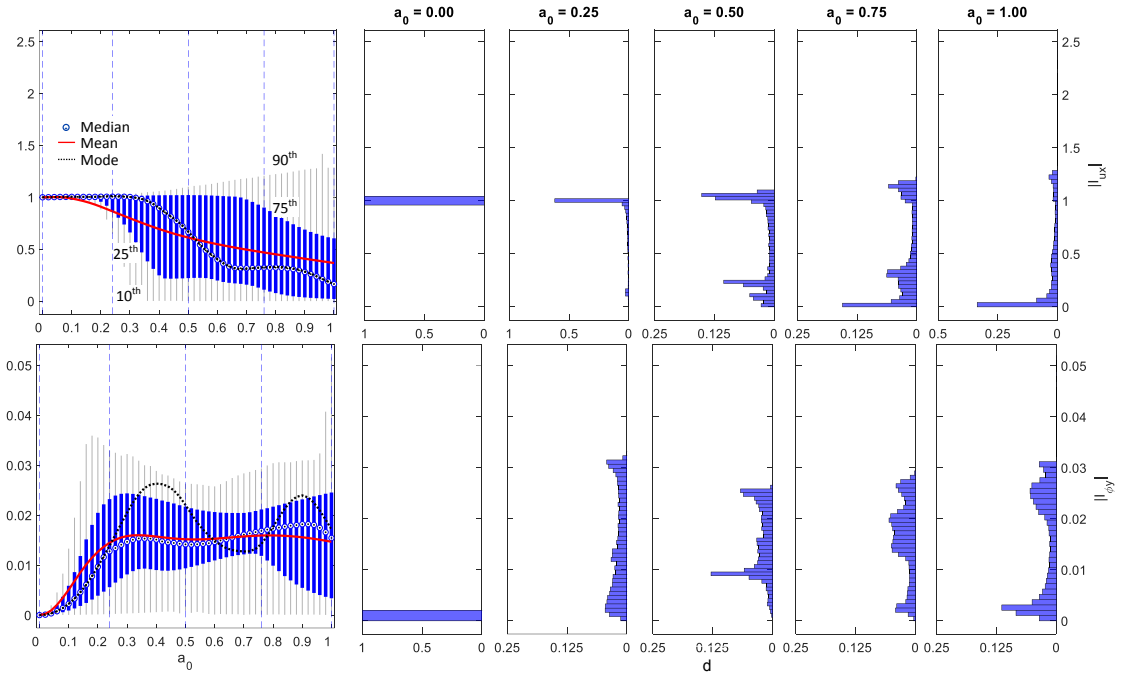

Figure 7.18. Variability of (a) I_U and (b) I_Φ for 3x3 foundation, s/d = 4, L/d = 32, V_s = 100 m/s.

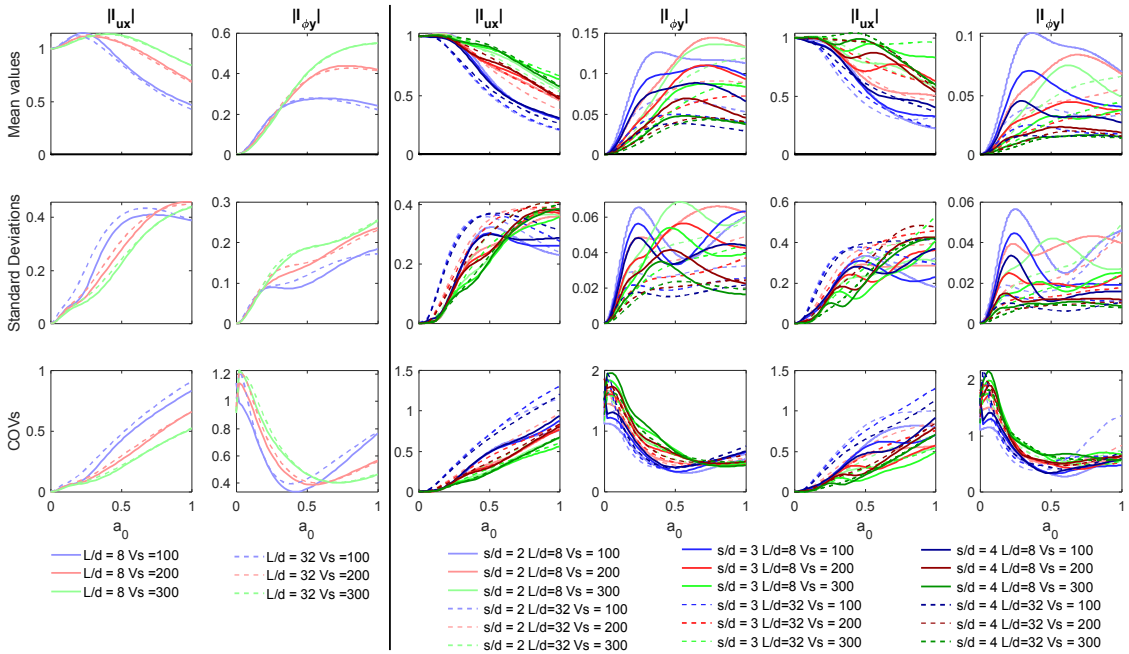

Figure 7.19. Frequency dependent mean values, standard deviations and COVs of FIM components of single pile foundations.

7.5.2.1 Correlation coefficients

It is possible to provide a measure of the linear correlation between kinematic response factors and the three main random variables through the Pearson correlation coefficient. For the sake of brevity, only few cases will be shown to illustrate and discuss general trends found for all the applications. Figure 7.20 shows the frequency-dependent correlation coefficients between the random variables and the kinematic response factors of the 2x2 foundation with s/d = 4, L/d = 8, V_s = 300 m/s, representative of short piles. For both translational and rotational factors there is no appreciable correlation between the variation of results and that of soil density or concrete elastic modulus, since no significant variations of the Pearson's coefficient around 0 in the considered frequency domain are observed. Regarding the shear wave velocity, it is clear that the variability of kinematic response factors depends on V_s in a nonlinear manner, and a different behaviour can be highlighted for I_U and I_Φ. For the former, the correlation is positive, and tends to become perfectly linear as the frequency value increases (up to 0.9 for high values of a_0). Oscillations on the correlation coefficients have a correspondence with the shape of boxplots, where the dispersion of results is not constant along the frequency axis, and it is possible to put in evidence a monotonic positive trend for correlation coefficients at a_0 > 0.5. An inverse correlation can be recognized for I_Φ; the correlation coefficient lies between -0.5 and -0.9, so that as the rotational factors increase the shear wave velocity decreases, and tends to become 0 at high frequencies, contrary to the translational factors. Nevertheless, the influence of soil density or concrete Young's modulus is negligible,

since the correlation coefficients are equal to 0 for all the considered frequencies in this case too.

Figure 7.21 collects the correlation coefficients relevant to the 2x2 foundation with s/d = 4, L/d = 32, V_s = 300 m/s, representative of long piles. Previous considerations concerning the soil density and the pile concrete Young's modulus hold for both I_U and I_Φ. Indeed, it is possible to find strong similarities in the V_s correlation coefficients for short and long piles in case of the translational factor.

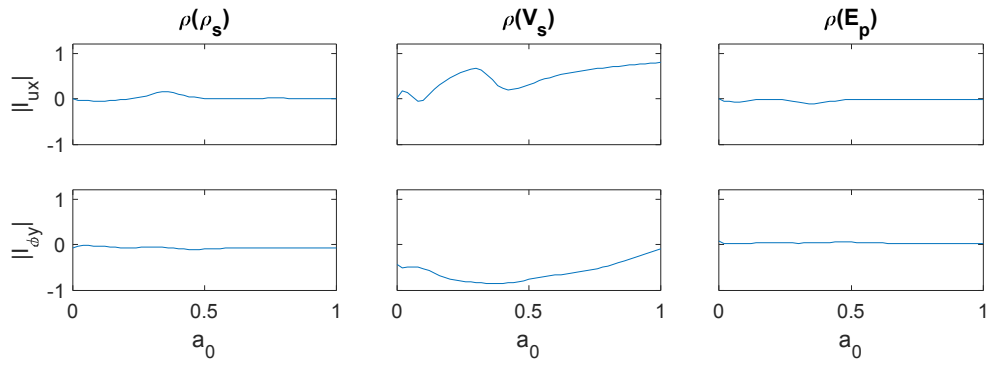

Figure 7.20. Correlation coefficients between kinematic response factors and the independent random variables for 2x2 foundation, s/d = 4, L/d = 8, Vs = 300 m/s.

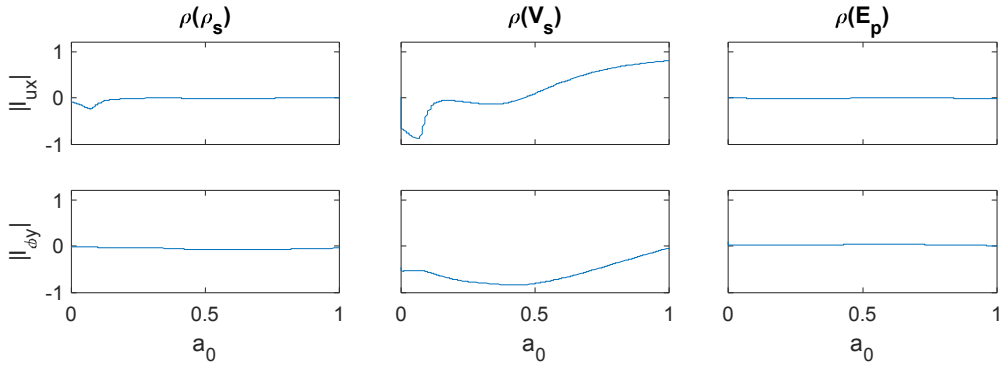

Figure 7.21. Correlation coefficients between kinematic response factors and the independent random variables for 2x2 foundation, s/d = 2, L/d = 32, Vs = 300 m/s.

7.5.2.2 Sensitivity indexes

The first order sensitivity indexes $\bar{S}_i$ for ρ_s, V_s and E_p are presented and discussed in this section. Table 7.7 and Table 7.8 collect the sensitivity indexes of all the case studies relevant to the considered pile group foundations (2x2 and 3x3) and the single pile, respectively. As previously, bar charts are plotted within the table to provide at glance interpretation of the data collected. Similarly to impedances, the shear wave velocity sensitivity indexes are almost unitary (always higher than 97%), confirming that Vs is primarily responsible for the overall variability of the results, especially in the case of

single piles. Very low sensitivity indexes are obtained for the soil density (less than 11%) and the pile concrete Young's modulus (less than 3%).

Table 7.7. Sensitivity indexes for pile group foundations.

$\frac{s}{d}$	$\frac{L}{d}$	V_s	I_U			I_Φ		
			ρ_s	V_s	E_p	ρ_s	V_s	E_p
			2x2 *3 x 3*	2x2 *3 x 3*	2x2 *3 x 3*	2x2 *3 x 3*	2x2 *3 x 3*	2x2 *3 x 3*
2	8	100	0.03 *0.05*	0.97 *0.92*	0 *0.03*	0.01 *0.05*	0.99 *0.93*	0 *0.02*
		200	0.02 *0.08*	0.98 *0.92*	0 *0*	0.01 *0.06*	0.99 *0.94*	0 *0*
		300	0.02 *0.07*	0.98 *0.93*	0 *0*	0.01 *0.05*	0.99 *0.94*	0 *0.01*
	32	100	0.03 *0.05*	0.97 *0.9*	0 *0.05*	0.01 *0.08*	0.99 *0.91*	0 *0.01*
		200	0.01 *0.08*	0.99 *0.9*	0 *0.02*	0.01 *0.08*	0.99 *0.92*	0 *0*
		300	0.01 *0.07*	0.99 *0.92*	0 *0.01*	0.02 *0.07*	0.98 *0.93*	0 *0*
3	8	100	0.02 *0.06*	0.98 *0.93*	0 *0.01*	0.02 *0.12*	0.98 *0.86*	0 *0.02*
		200	0.01 *0.08*	0.99 *0.92*	0 *0*	0.03 *0.09*	0.97 *0.9*	0 *0.01*
		300	0.01 *0.07*	0.99 *0.93*	0 *0*	0.03 *0.08*	0.97 *0.91*	0 *0.01*
	32	100	0.01 *0.07*	0.99 *0.93*	0 *0*	0.03 *0.11*	0.97 *0.83*	0 *0.06*
		200	0.01 *0.08*	0.99 *0.92*	0 *0*	0.03 *0.08*	0.97 *0.88*	0 *0.04*
		300	0.01 *0.07*	0.99 *0.93*	0 *0*	0.03 *0.07*	0.97 *0.9*	0 *0.03*
4	8	100	0.01 *0.07*	0.99 *0.93*	0 *0*	0.02 *0.03*	0.98 *0.92*	0 *0.05*
		200	0.01 *0.08*	0.99 *0.92*	0 *0*	0.02 *0.03*	0.97 *0.94*	0.01 *0.03*
		300	0.01 *0.07*	0.99 *0.93*	0 *0*	0.03 *0.03*	0.97 *0.95*	0 *0.02*
	32	100	0.01 *0.07*	0.99 *0.93*	0 *0*	0.02 *0.04*	0.98 *0.92*	0 *0.04*
		200	0.01 *0.08*	0.99 *0.92*	0 *0*	0.02 *0.04*	0.97 *0.93*	0.01 *0.03*
		300	0.01 *0.07*	0.99 *0.93*	0 *0*	0.03 *0.04*	0.97 *0.94*	0 *0.02*

Table 7.8. Sensitivity indexes for single piles.

Foundation	$\frac{L}{d}$	V_s	I_U			I_Φ		
			ρ_s	V_s	E_p	ρ_s	V_s	E_p
Single pile	8	100	0	1	0	0.01	0.99	0
		200	0	1	0	0	1	0
		300	0.01	0.99	0	0	1	0
	32	100	0.01	0.99	0	0.01	0.99	0
		200	0.01	0.99	0	0.01	0.99	0
		300	0	1	0	0	1	0

7.6 Conclusive remarks

A probabilistic investigation on the dynamic behaviour of deep foundations has been presented with the purpose of addressing effects of intrinsic uncertainties in the main parameters governing the soil-piles interaction problem on the soil-foundation dynamic impedance and kinematic response factors. In detail, the soil density, the shear wave velocity and the concrete elastic modulus of the piles are assumed as uncorrelated random variables and probabilistic distributions from the available literature are assigned to reproduce their uncertainties and a Quasi-Random simulation technique is exploited to generate samples. Floating piles in homogeneous deposits are analysed considering different pile layouts and statistic parameters of the output quantities, derived from a total of 420000 analyses, are presented and discussed.

From an overall point of view the following main aspects can be highlighted concerning the variability of the soil-foundation impedances:

- the GEV distribution can be adopted to approximate the variability of impedance functions in the whole investigated frequency range, which is of practical interest for seismic engineering applications. More in detail, for low frequencies a lognormal distribution can also be suitable employed, in line with the positive values of impedances and with the distribution of the shear wave velocity which mainly affect impedances at low frequencies. At higher frequencies, where the contribution of the soil density becomes higher and the dynamic stiffness may achieve negative values, the lognormal distribution fails and a GEV distribution must be adopted.

- Standard deviations of all real parts of impedance components of single piles reflects mean values within the whole investigated frequency range and COVs, ranging between 20-50%, are almost independent on the case study and constant with frequency. Only COVs of the rotational impedance depends on the investigated case and assumes highest values for short piles and soft soils.

- Standard deviations of real part of impedances of pile foundations are overall very high, particularly for the non-dimensional translational and vertical impedances for which COVs are within 80-100% up to a non-dimensional frequency ranging from 0.2 to 0.5 depending on the component and the foundation layout. The non-dimensional rotational impedance and the coupled roto-translational impedance are characterised by lower values of COVs (around 30-70%) in the whole frequency range. Finally, COVs of the torsional impedance are characterised by a clear increasing trend with frequency.

- Standard deviations of imaginary parts of impedances of pile foundations are almost constant in the frequency range 0-0.5 for all the impedance components; for higher frequencies, standard deviations increase rapidly and almost linearly with frequency. This issue gives rise to peculiar convex trends of the COVs, which decrease in the frequency range 0-0.5 and increase for higher frequencies.

- The Pearson correlation coefficient reveals an almost complete absence of a linear correlation between real and imaginary parts of impedances and the pile Young's modulus. A similar conclusion holds for the soil density for non-dimensional frequencies lower than 0.5. On the contrary, correlation coefficients relevant to the soil density tends to increase (up to 0.5) for higher frequencies, in line with the contribution of the soil density on the foundation dynamic stiffnesses.

- The Pearson correlation coefficient demonstrates a linear clear correlation between impedances and the soil shear wave velocity for a wide range of the non-dimensional frequency in the interval 0-1. A linear positive correlation holds between both real and imaginary parts of all the impedance components in the non-dimensional frequency range 0-0.5, which is partially lost for higher frequencies.

- Sensitivity indexes of the shear wave velocity evaluated from real and imaginary parts of impedances outcomes are higher than 0.90 for all the considered pile configurations; thus, the shear wave velocity configures as the main and most important variable that determines the variability of impedances. An exception to this overall trend is only represented by the imaginary part of the rotational non-dimensional impedance of the single piles, for which the pile Young's modulus contributes even larger than the soil shear wave velocity to define the impedance variability.

From an overall point of view the following main aspects can be highlighted concerning the variability of the soil-foundation kinematic response factors:

- differently from impedances, peculiar variability of kinematic response factors makes it difficult to select a suitable distribution from those available in the literature, independently on the frequency.

- For single piles, standard deviations of the translational factor increase significantly and almost linearly with frequency with a gradient that depends on the shear wave velocity. COVs of the translational factors follow a similar trend. Concerning the rotational parameters, standard deviations increase in the whole frequency range and COVs present a pseudo-parabolic trend ranging between 100-120%.

- For pile groups, standard deviations of the translational factor generally increase almost linearly with frequency up to a non-dimensional frequency of 0.5-0.75, depending on the shear wave velocity, and then stabilises or slightly decreases. On the contrary, COVs are always ascending with frequency up to 120% for low shear wave velocities and long piles. With respect to the rotational factor, COVs present a pseudo-parabolic trend with values moving from 200% at very low frequencies to about 50% at medium-high frequency.

- The Pearson correlation coefficient reveals that there is no linear correlation between results and soil density or concrete elastic modulus. The kinematic response factors depend nonlinearly on the shear wave velocity; for the translational parameter the correlation is positive and tends to become perfectly linear as the frequency approaches 0.9. For the rotational parameter, an inverse correlation can be recognized.

- Similarly to impedances, the shear wave velocity sensitivity indexes are almost unitary (always higher than 97%), confirming that V_s is primarily responsible for the overall variability of the results, especially in the case of single piles.

Overall the probabilistic investigation clearly outlines that the variability of the dynamic response of single piles and pile groups is mainly governed by uncertainties in the soil shear wave velocity; while frequency-dependent probabilistic models can be theoretically defined for impedances, models for kinematic response parameters are difficult to be defined starting from distributions available in the literature.

7.7 Chapter's references

Álamo, G. M., Martínez-Castro, A. E., Padrón, L. A., Aznárez, J. J., Gallego, R., & Maeso, O. (2016). Efficient numerical model for the computation of impedance functions of inclined pile groups in layered soils. *Engineering Structures*, *126*, 379-390.

Au, S. K., & Beck, J. L. (2003). Subset simulation and its application to seismic risk based on dynamic analysis. *Journal of Engineering Mechanics*, *129*(8), 901-917.

Bartlett, F. M., & MacGregor, J. G. (1996). Statistical analysis of the compressive strength of concrete in structures. *Materials Journal*, *93*(2), 158-168.

Capatti, M. C., Carbonari, S., Dezi, F., Gara, F., & Leoni, G. (2017). Validation of a 3D model for dynamic soil-structure-interaction of pile foundations by means of in situ tests. *Validation of a 3D model for dynamic soil-structure-interaction of pile foundations by means of in situ tests*, 68-77.

Carbonari, S., Morici, M., Dezi, F., & Leoni, G. (2016). Analytical evaluation of impedances and kinematic response of inclined piles. *Engineering Structures*, *117*, 384-396.

CNR. Guide for the probabilistic assessment of the seismic safety of existing buildings. Report CNR-DT 212/2013*,* CNR – Advisory Committee on Technical Recommendations for Construction, Rome; 2014.

Cochran, W. G. (1952). The $\chi 2$ test of goodness of fit. *The Annals of mathematical statistics*, 315-345.

Cottereau, R., Clouteau, D., & Soize, C. (2007). Construction of a probabilistic model for impedance matrices. *Computer Methods in Applied Mechanics and Engineering*, *196*(17-20), 2252-2268.

Dezi F, Roia D, Capatti MC, Carbonari S, Gara F, Leoni G, Morici M. (2019). Evaluation of dynamic soil-pile interaction based on both full scale in situ tests and numerical simulations. In *7th International Conference on Earthquake Geotechnical Engineering (ICEGE)*, CRC Press.

Dezi, F., Carbonari, S., & Leoni, G. (2009). A model for the 3D kinematic interaction analysis of pile groups in layered soils. *Earthquake Engineering & Structural Dynamics*, *38*(11), 1281-1305.

Dezi, F., Carbonari, S., & Morici, M. (2016). A numerical model for the dynamic analysis of inclined pile groups. *Earthquake Engineering & Structural Dynamics*, *45*(1), 45-68.

Dobry, R., & Gazetas, G. (1988). Simple method for dynamic stiffness and damping of floating pile groups. *Geotechnique*, *38*(4), 557-574.

Dobry, R., Vicente, E., O'Rourke, M., & Roesset, M. (1982). Horizontal stiffness and damping of single piles. *Journal of Geotechnical and Geoenvironmental Engineering*, *108*(GT3).

Engelund, S., & Rackwitz, R. (1993). A benchmark study on importance sampling techniques in structural reliability. *Structural safety*, *12*(4), 255-276.

Gazetas, G., & Dobry, R. (1984). Simple radiation damping model for piles and footings. *Journal of Engineering Mechanics*, *110*(6), 937-956.

Griffiths, S. C., Cox, B. R., Rathje, E. M., & Teague, D. P. (2016). Surface-wave dispersion approach for evaluating statistical models that account for shear-wave velocity uncertainty. *Journal of Geotechnical and Geoenvironmental Engineering*, *142*(11), 04016061.

Helton, J. C., & Davis, F. J. (2003). Latin hypercube sampling and the propagation of uncertainty in analyses of complex systems. *Reliability Engineering & System Safety*, *81*(1), 23-69.

Jin, S., Lutes, L. D., & Sarkani, S. (2000). Response variability for a structure with soil–structure interactions and uncertain soil properties. *Probabilistic Engineering Mechanics*, *15*(2), 175-183.

Jones, A. L., Kramer, S. L., & Arduino, P. (2002). *Estimation of uncertainty in geotechnical properties for performance-based earthquake engineering*. Pacific Earthquake Engineering Research Center, College of Engineering, University of California.

Lutes, L. D., Sarkani, S., & Jin, S. (2000). Response variability of an SSI system with uncertain structural and soil properties. *Engineering Structures*, *22*(6), 605-620.

Makris, N., & Gazetas, G. (1993). Displacement phase differences in a harmonically oscillating pile. *Geotechnique*, *43*(1), 135-150.

Makris, N., & Gazetas, G. (1992). Dynamic pile-soil-pile interaction. Part II: Lateral and seismic response. *Earthquake engineering & structural dynamics*, *21*(2), 145-162.

Massey Jr, F. J. (1951). The Kolmogorov-Smirnov test for goodness of fit. *Journal of the American statistical Association*, *46*(253), 68-78.

Mayne, P. W., Coop, M. R., Springman, S., Huang, A. B., & Zornberg, J. (2009). SOA-1: Geomaterial behavior and testing. In *Proceedings of the 17th International Conference on Soil Mechanics and Geotechnical Engineering: 5–9 October 2009, Alexandria, Egypt* (pp. 2777-2872). Millpress, Rotterdam, the Netherlands.

Mylonakis, G., & Gazetas, G. (1998). Vertical vibration and additional distress of grouped piles in layered soil. *Soils and foundations*, *38*(1), 1-14.

Minnucci, L., Dezi, F., Carbonari, S., Morici, M., Gara, F., & Leoni, G. (2019). Effects of uncertainties of soil and pile mechanical properties on the dynamic stiffness of single piles in homogenous deposits. In *COMPDYN 2019: 7th International Conference on Computational Methods in Structural Dynamics and Earthquake Engineering, Crete, Greece, 24-26 June 2019*.

Moghaddasi, M., Cubrinovski, M., Chase, J. G., Pampanin, S., & Carr, A. (2011). Probabilistic evaluation of soil–foundation–structure interaction effects on seismic structural response. *Earthquake engineering & structural dynamics*, *40*(2), 135-154.

Moon, S. W., & Ku, T. (2016). Empirical estimation of soil unit weight and undrained shear strength from shear wave velocity measurements. In *5th International Conference on Geotechnical and Geophysical Site Characterisation, ISC 2016* (pp. 1247-1252). Australian Geomechanics Society.

Nielson, B. G. (2005). *Analytical fragility curves for highway bridges in moderate seismic zones* (Doctoral dissertation, Georgia Institute of Technology).

Padrón, L. A., Aznárez, J. J., & Maeso, O. (2007). BEM–FEM coupling model for the dynamic analysis of piles and pile groups. *Engineering Analysis with Boundary Elements*, *31*(6), 473-484.

Phoon, KK & Kulhawy, FH (1999) Evaluation of geotechnical property variability. *Canadian Geotechnical Journal* , *36* (4), 625-639.

Rubinstein, R. Y., & Kroese, D. P. (2016). *Simulation and the Monte Carlo method* (Vol. 10). John Wiley & Sons.

Saltelli, A., Annoni, P., Azzini, I., Campolongo, F., Ratto, M., & Tarantola, S. (2010). Variance based sensitivity analysis of model output. Design and estimator for the total sensitivity index. *Computer physics communications*, *181*(2), 259-270.

Saltelli, A., Ratto, M., Andres, T., Campolongo, F., Cariboni, J., Gatelli, D., ... & Tarantola, S. (2008). *Global sensitivity analysis: the primer*. John Wiley & Sons.

Saltelli, A., Tarantola, S., Campolongo, F., & Ratto, M. (2004). *Sensitivity analysis in practice: a guide to assessing scientific models* (Vol. 1). New York: Wiley.

Sobol' IM, Turchaninov VI, Levitan YL, Shukhman BV. Quasirandom sequence generators. Institute of Applied Mathematics, Russian Academy of Sciences, Moscow; 1992.

Stefanidou, S. P., & Kappos, A. J. (2017). Methodology for the development of bridge-specific fragility curves. *Earthquake Engineering & Structural Dynamics*, *46*(1), 73-93.

Uzielli, M., Lacasse, S., Nadim, F., & Phoon, K. K. (2006). Soil variability analysis for geotechnical practice. *Characterization and engineering properties of natural soils*, *3*, 1653-1752.

Conclusions

This Thesis aims to revise and improve some aspects of the probabilistic framework used to assess the fragility and the risk (post-scenario costs, consequences, etc.) of existing bridges and viaducts, assumed as key components of a wider infrastructural system. The study is conducted by considering earthquakes as main natural source of hazard, although the proposed methodologies as well as the whole framework could be easily extended and used to analyse hazards other than the seismic one (e.g., flood-induced actions such as scour or hydrodynamic pressure, landslides, etc.).

More in detail, the main original contributions provided by the present work concern the following aspects:

1) development of a novel methodology for the fragility analysis of existing bridges at a level of detail deeper than the commonly adopted;
2) development of simple formulas for estimating a Lumped Parameter Model (LPM) reproducing Soil-Structure Interaction (SSI) effects on deep foundations;
3) characterization and analysis of the seismic response of some common bridge typologies, which also result widespread on the Italian territory, taking into account SSI and degradation effects;
4) development of a holistic framework for the probabilistic assessment of bridge vulnerability and risk under seismic and vertical loads, including the proposed methodologies and the analysis of consequences in terms of direct and indirect costs;
5) probabilistic analysis of deep foundations in homogeneous soils for the quantification of the effects of uncertainties affecting the behaviour of both soil and pile properties on the embedded system, whose response is analysed in terms of impedance functions and kinematic response factors.

More in detail, the proposed methodology for the fragility assessment aims at offering an insight on the failure mechanisms most likely to occur and the evolution of damage within the bridge structure. The information deriving from the application of the proposed methodology results of strategic importance for the optimization and the prioritization of interventions in case of occurrence of an earthquake, both in the maintenance phase and in case of repair or reconstruction works. A mathematical description of two new approaches for the evaluation of fragility as an alternative to the classical fragility representation is provided, concerning the analysis of failure modes and the damage extension. In the first case, the failure mode analysis investigates the concomitance of more than one single fragility mechanism that may occur on the structure. In the second case, the damage extension analysis provides for an insight on the fragility related to a significative subset of components involved in a certain failure mechanism.

Since the role of SSI is recognized as crucial for the response of bridges, a novel approach for the quantification of SSI effects is developed, consisting in the approximation of an

already existing Lumped Parameter Model with easy-to-compute formulas reproducing the behaviour of end-bearing pile foundations in homogeneous soils. The efficiency of the proposed formulas is proved in comparison with the original LPM and a more refined SSI model. The formulas are easy to implement in FE codes and allow considering SSI effects in time-domain analyses.

In this Thesis, bridges taken from the Italian bridges stock are used as case study to show the potentialities of the proposed methods. This choice is mainly dictated by the high vulnerability of the existing Italian infrastructural system, the most of which has been built before the emanation of the current codes concerning the performance-based design and the fulfilment of the structural requirements in presence of seismic action. Two bridge typologies are recognized as the most common in the Italian infrastructural scenario: the Reinforced Concrete with Link Slab (RCLS) bridges and the Steel Concrete Composite (SCC) bridges. As the investigation concerns existing structures, effects of ageing are explicitly modelled and the presence of possible interaction phenomena between soil and foundations is taken into account through the proposed LPM formulas for a more accurate description of the expected response. The adopted case studies result representative not only of the most common typologies on the national territory, but also of the regional scenario of the Marche region, where two longest and most economically influencing main routes are investigated, the SS76 and the SS77 roads, and a statistical analysis of the principal characteristics of existing bridges is carried out. The analysis of the investigated bridge classes through the proposed methodology offers information at a suitable level of detail not only for the assessment of the structural performance but also for the successive analysis of direct and indirect costs associable to post-earthquake scenarios.

For what concerns the fragility of RCLS bridges, the following remarkable results can be put in evidence:

- The simulated design project for piers determines a low fragility at Life Safety and Collapse limit states in both the examined structural configurations; for what concerns Damage limit state, the fragility of piers result always lower than the fragility of other structural components. Longer bridges (L/B=20) present a higher vulnerability on piers than medium-length ones (L/B=10);
- Link slab bars are the most fragile component of RCLS bridges at all the considered limit states. In particular, in both the examined structural configurations, a higher probability of failure is observed in correspondence of the last structural joint, where the superstructure is connected to the right abutment.
- For what concerns the analysis of damage extension, high percentages (>50%) of involved link bars and bearings are observed at all the considered limit states within values for the *IM* inferior than 1.0g;
- For what concerns the analysis of failure modes, the fragility of only links mostly concurs to the determination of the global fragility of the structure for low values

of *IM*. Damage or collapse of the other structural elements verifies at higher *IM* values and results always concomitant among the components.

- Effects of ageing and compliant base are mostly evident on piers, whose fragility results increased. Major consequences of ageing and compliant base are observed at Damage and Life Safety limit states; in the latter case, the probability of exceeding severe damage remains low at very high *IM* values. An exception is offered by the combination of strong ageing and compliant base in case of long bridges (L/B=20), where results at Life Safety limit state from the analysis with fixed base result too conservative.

For what concerns the fragility of SCC bridges:

- The behaviour of cross beams is similar on short bridges (single and double span – L/B = 4 and L/B = 8) and presents a higher fragility than in case of medium-length bridges /L/B = 20) at all the considered limit states;
- In all the examined bridge configurations, cross beams are the most fragile component at collapse limit state; a higher fragility can be observed on end cross beams (corresponding to abutments);
- Comparing the different geometric configurations, a significative change in the fragility of bearings can be observed at Life Safety limit state. In particular, the fragility of the component increases with the length of the bridge. Bearings result more vulnerable than other structural components in case of double-span (L/B = 8) and multi-span (L/B = 20) bridges. Moreover, bearings corresponding to the fixed constraint in the longitudinal direction result as the most vulnerable;
- A significative contribution to the global fragility at Damage limit state is offered by the active response of abutments, especially in case of single-span bridges; no severe damage nor collapse is expected for other mechanisms in the considered *IM* range;
- The fragility of piers in SCC bridges is higher than in RCLS bridges. Nevertheless, piers remain the less vulnerable component within the structure. The fragility of piers increases with the increase of the bridge length;
- In case of single-span bridges (L/B = 4), the global fragility can be attributed to the concomitance of damage on cross beams and abutments, cross beams and bearings and cross beams only for medium-high seismic intensities at Damage, Life Safety and Collapse limit states, respectively;
- In case of double-span bridges (L/B = 8), the failure mechanisms concurring to the global fragility are related to cross beams, bearings and abutments, similarly to the single-span case. At Damage limit state, the fragility of piers adds at *IM* = 1.0g.
- In case of multi-span bridges (L/B = 20), a higher vulnerability of central piers is observed; the fragility of abutments, bearings and cross beams mainly governs the global fragility for *IM* < 1.0 g at Damage, Life Safety and Collapse limit state, respectively; for higher seismic intensities, the concomitance of damage on piers at both Damage and Life Safety limit state is appreciable. In case of multi-span

bridges, damage on half of the cross beams and the bearing set fixed in longitudinal direction is very likely to occur since low seismic intensities, corresponding to low return periods. Damage on piers rapidly evolves from half of the total to the total number, at both Damage and Life Safety limit state;

- Effects of ageing and compliant base are mostly evident on piers, whose fragility results increased. Major consequences of ageing and compliant base are observed at Life Safety and Collapse limit states. Between the two factors, ageing mostly influences the behaviour of piers, particularly at Collapse limit state. In this case, the probability of exceeding collapse is doubled.

The proposed fragility methodology can be integrated in a wider framework for the probabilistic assessment of existing bridge structures. This comprehensive framework for the analysis of bridges' vulnerability and risk has the purpose of furnishing a detailed and reliable insight on the performance of existing bridges with regards not only to the seismic action but also to the vertical loads assessment, a major problem in the Italian context. The framework extends the concepts of hazard and fragility introducing innovative cues for the characterization of the bridges' behaviour in presence of Soil-Structure Interaction phenomena. The framework is flexible for the analysis of fragility and risk also in case of different natural hazards potentially affecting bridge structures. Aspects linked to the maintenance problem, the degradation phenomena, the relevance of structural health monitoring techniques are discussed and incorporated in the description of the framework. Information deriving from the development of the framework's steps are suitable for the final quantification of costs associated to direct and indirect consequences on the road network the examined bridges belong to.

An application of the framework is carried out exploiting the methodologies and the results obtained in this Thesis on the examined regional scenario for the quantification of direct and indirect consequences of the bridge fragility on a main route of interest. The application offers a starting point to discuss the potential impact of an earthquake occurrence on the damageability and the consequent level of functionality of the SS76 road in the Marche region. Regarding the analysis of the road network functionality, results of the fragility analysis on the selected case studies are employed to determine possible post-earthquake scenarios along the SS76 road. Different recovery times are associated to the SS76 bridges after the occurrence of a selected earthquake event. Information about the daily traffic on the selected path are derived from regional databases and 7 vehicle categories are analysed to evaluate costs for different kind of users. The viability of the traffic flow on the selected O-D path is simulated through a dedicated open-source engine in which the SS76 and the associated alternative routes are modelled. Results are elaborated according to different indexes useful to quantify the functionality of the road network. The performance indicators are defined and calculated at the evolution of the recovery scenario. For each phase of the recovery plan, the analysis of costs associated to the altered traffic viability and the associated vehicle emissions is provided. Finally, the total cost of indirect consequences is compared to the expected reconstruction and maintenance costs. The quantification of traffic and environmental

costs shows that indirect consequences are of not-negligible importance in case of infrastructural systems.

In order to summarize the main results, the following aspects can be highlighted:

- At network level, heavy vehicles (trucks) are responsible of high pollutant emission daily costs; on the contrary, given the higher number of SOV and HOV on the analysed context, light vehicles are associated to higher daily traffic costs;
- Traffic and pollutant costs in presence of working zones due to the post-earthquake damage scenario are more than doubled compared to the free flow condition;
- Final traffic costs, obtained from the sum of traffic costs in each recovery phase, are of the same order of magnitude of final pollutant costs;
- Direct cost associated to the reconstruction of bridges' damaged components are sensibly lower than indirect costs;
- The adoption of an ordinary plan of maintenance in the service life of the structures would allow for a huge save of money;
- The analysis with the assumption of fixed base under the piers leads to a significative underestimation of the costs associated to the restoration of the road network functionality. The role of ageing and Soil-Structure Interaction is of primary importance for a reliable estimation of indirect consequences.

Future challenges in the development and the improvement of the proposed framework concern the introduction of a probabilistic approach for the analysis of Soil-Structure Interaction effects in the quantification of fragility and risk of existing bridges. A not negligible impact of the soil and foundation characteristics on the response of bridge structures can be recognized at both hazard and fragility level. Nevertheless, few works in the literature provide a dedicated insight on the SSI probabilistic characterization and the adoption of probabilistic tools for the quantification of SSI effects still needs further investigations. At this scope, a probabilistic study of the behaviour of deep foundations in homogeneous soils has been carried out to furnish a clearer view on the parameters that mostly influence the response of the soil-pile combined system. Moreover, an attempt to describe the response in terms of impedance functions and foundation input motion (FIM) through probabilistic distribution is made. Three parameters that mainly affect the soil and pile response are considered as aleatoric, and probabilistic distributions derived from the geotechnical available literature are employed. An efficient sampling technique is implemented to derive the parameters' samples and to perform interaction analyses on different foundation geometrical configurations and soil typologies. A non-dimensional approach is adopted to investigate impedance and FIM functions on a suitable frequency domain for structural engineering applications. Sensitivity analyses are carried out to establish the influence of the independent variables on the behaviour of the embedded system.

From the ongoing research results on the topic, the following main aspects can be remarked:

- The Generalized Extreme Values (GEV) distribution can be adopted to approximate the variability of impedance functions in the whole investigated frequency range, which is of practical interest for seismic engineering applications. More in detail, for low frequencies a lognormal distribution can also be suitable employed, in line with the positive values of impedances and with the distribution of the shear wave velocity which mainly affect impedances at low frequencies. At higher frequencies, where the contribution of the soil density becomes higher and the dynamic stiffness may achieve negative values, the lognormal distribution fails and a GEV distributions must be adopted;
- FIM functions are unlikely to be approximated by a single probability distribution on the entire frequency range. A dedicated study on the possibility of approximation of FIM with more than one probability distribution can be considered a future goal for this research;
- In case of impedances, the Pearson correlation coefficient reveals an almost complete absence of a linear correlation between real and imaginary parts of impedances and the pile Young's modulus or the soil density, in the latter case for non-dimensional frequencies lower than 0.5. For higher frequencies, the higher contribution of the soil density to the foundation dynamic stiffness reflects into an increase of the Pearson coefficient up to 0.5. In case of the shear wave velocity, a linear correlation with the analysis results is evident in the whole frequency domain.
- For what concerns the FIM, the Pearson correlation coefficient reveals that there is no linear correlation between results and soil density or concrete elastic modulus. The kinematic response factors depend nonlinearly on the shear wave velocity; for the translational parameter the correlation is positive and tends to become perfectly linear as the frequency approaches 0.9. For the rotational parameter, an inverse correlation can be recognized.
- The shear wave velocity configures as the main and most important variable that determines the variability of both impedances and FIM functions. In case of impedances, sensitivity indexed associated to the shear wave velocity are always higher than 0.9; an exception to this overall trend is only represented by the imaginary part of the rotational non-dimensional impedance of the single piles, for which the pile Young's modulus contributes even larger than the soil shear wave velocity to define the impedance variability. In case of FIM, the predominant contribution of the variability of the shear wave velocity to the variability of the response is even more evident, since sensitivity indexes are almost unitary (always higher than 97%), confirming that V_S is primarily responsible for the overall variability of the results, especially in the case of single piles.

Additional future developments of this work shall extend the application of the proposed methodology for the fragility assessment to other bridge typologies. Given the flexibility of the approach, the evaluation of failure mechanisms other than the already analysed and the employment of the proposed approach for the analysis of failure consequences at network level could be carried out with a higher level of detail. The methodologies proposed in this Thesis about the fragility, the quantification of costs related to the performance of road networks and the probabilistic analysis of SSI effects can be suitable for other applications in the civil engineering field, concerning other sources of hazard. Efforts in the harmonization of the adopted instruments within a unique analysis framework are the challenge of the future research.

Appendix

Table A. Parameters of the LPM closed-form formulas (§2.5.2).

Ω_i	n	α	β	χ	δ	ε	ϕ	φ	γ	κ
Ω_1	1	2.2068	0	0.00145	0.21021	-	-	-	-	-
	2	3.9501	0.2037	-0.00023	0.21056	-	-	-	-	-
	3	5.57664	0.2693	-0.00149	0.21084	-	-	-	-	-
	4	7.13818	0.3002	0.00065	0.21080	-	-	-	-	-
	5	8.65519	0.3177	0.00557	0.21054	-	-	-	-	-
Ω_2	1	1	-0.4485	0	0	0	-	-	-	-
	2	0.72831	2.74226	-2.37E-07	0.00023	3.78511	-	-	-	-
	3	0.83961	1.08683	5.603E-07	-0.0028	27.03892	-	-	-	-
	4	0.95976	0.19168	4.784E-07	0.00222	67.01696	-	-	-	-
	5	1.02683	-0.0973	-1.82E-06	0.01657	115.9066	-	-	-	-
Ω_3	1	1	-0.1808	1.669E-07	0.00048	21.36234	-	-	-	-
	2	0.54884	0.17127	-5.35E-07	0.00593	30.29008	-	-	-	-
	3	0.80035	0.47078	-1.83E-06	0.01228	39.31741	-	-	-	-
	4	0.96114	0.74962	-2.04E-06	0.0154	48.6382	-	-	-	-
	5	1.08628	0.76012	-3.07E-06	0.02388	60.16417	-	-	-	-
Ω_4	1	-0.4928	0	0.00158	0.47346	-	-	-	-	-
	2	-1.1531	0.1359	-0.00232	0.47388	-	-	-	-	-
	3	-1.899	0.18094	0.00154	0.47356	-	-	-	-	-
	4	-2.7132	0.20184	0.01592	0.47244	-	-	-	-	-
	5	-3.5833	0.21328	0.03704	0.47094	-	-	-	-	-
Ω_5	1	0	0	0	0	-	-	-	-	-
	2	0	0	0	0	-	-	-	-	-
	3	-0.6084	-0.2399	4.53695	0.24911	-	-	-	-	-
	4	-2.2774	0.78598	3.8906	0.15478	-	-	-	-	-
	5	-2.7947	1.06496	3.2542	0.24101	-	-	-	-	-
Ω_6	1	3.22514	0	0.30245	0.23005	-	-	-	-	-
	2	3.97101	0.48106	0.38126	0.3291	-	-	-	-	-
	3	5.31738	0.66483	0.30408	0.38741	-	-	-	-	-
	4	7.53143	0.77205	0.47104	0.39779	-	-	-	-	-
	5	9.72955	0.84712	0.39294	0.42266	-	-	-	-	-
Ω_7	1	5.663E-05	5.77E-05	-0.03354	232.7635	30019.93	0.88453	-0.00040	-	-
	2	0.000779	-0.0008	-0.06386	433.5887	171694.2	1.75513	-0.3441	-	-
	3	0.00282	-0.0036	-0.12227	1037.128	344937.2	1.40658	-0.4403	-	-
	4	0.00694	-0.0095	-0.16538	1691.237	471922.6	1.13963	-0.4831	-	-
	5	0.01353	-0.0190	-0.19653	2367.728	571263.4	0.94006	-0.5009	-	-
Ω_8	1	-2.13E-07	-2.13E-07	-2.13E-07	0.18159	-485.846	-2091490	2.07403	0.0189	-
	2	0.000333	-0.0011	0.00103	-0.0226	79.50082	-2438.3769	-3.4868	2.3118	-
	3	0.00534	-0.0151	0.0127	-0.28697	1334.937	-14314.01	-7.9606	1.3516	-
	4	0.00533	-0.0147	0.01223	0.01035	-43.42026	140587.364	1.29069	1.0771	-
	5	0.01998	-0.0557	0.0477	0.01182	-38.2927	191842.092	0.33118	0.9119	-
Ω_9	1	2.977E-06	2.98E-06	2.976E-06	-0.12533	521.4217	435223.645	2.60335	0.0079	-
	2	0.000180	-0.0001	0.00065	-0.00267	19.15515	59971.3804	0.73802	0.5798	-
	3	0.000962	-0.0028	0.00351	-0.00575	27.28366	53174.8551	1.65464	1.0916	-
	4	0.00312	-0.0115	0.01319	-0.00363	17.37703	39454.3998	2.68146	1.4816	-
	5	0.00864	-0.0344	0.03942	-0.00291	15.06353	32917.2645	3.01846	1.6982	-
Ω_{10}	1	106,6317	-1,03E-05	0,0848421	28,68086	1,46576	-0,45835	-	-	-

Ω_i	n	α	β	χ	δ	ε	ϕ	φ	γ	κ
	2	0,08192	-2,38E-05	0,4290812	85,40291	0,57299	-0,51224	-	-	-
	3	0,12816	-3,09E-05	0,7208385	116,5395	0,45263	-0,47394	-	-	-
	4	0,16591	-3,03E-05	9,08E-01	133,7845	0,37313	-0,41934	-	-	-
	5	0,19934	-2,47E-05	1,01E+00	143,3302	0,31734	-0,36691	-	-	-
Ω_{11}	1	0	0	0	0	0	0	-	-	2000
	2	9,69E-01	-19,6	3,07E+00	-1,67E-07	9,87E-06	-7,652E-05	-	-	442
	3	1,06354	-3,38	0,88332	-0,00126	8,74E-02	-0,4559935	-	-	300
	4	1,04904	-0,511	5,99E-01	-,002421	2,33E-01	0,06260198	-	-	0
	5	1,03754	0,60216	0,41476	-0,0017	4,65E-01	7,8268823	-	-	0
Ω_{12}	1	6,02211	0,59049	0,05557	-0,00079	0,30204318	16,4602273	-	-	0
	2	0,61742	0,47699	0,18137	0,010835	-0,2495260	22,687036	-	-	0
	3	0,87509	0,21319	0,28866	0,013036	-0,4340227	26,3905513	-	-	0
	4	0,97493	0,20027	0,33256	0,013930	-0,5180498	35,3765775	-	-	0
	5	1,02386	0,15193	0,35794	0,011682	-4,36E-01	4,68E+01	-	-	0
Ω_{13}	1	1.5	0.25392	-5.28E-10	-2.371E-05	1.42514	-	-	-	-
	2	1.75344	1.34909	-1.41E-06	0.00499	16.00872	-	-	-	-
	3	1.93871	1.36806	-5.30E-06	0.01874	59.18202	-	-	-	-
	4	2.04008	1.37436	-0.000013	0.04497	141.34578	-	-	-	-
	5	2.10388	1.37774	-2.47E-05	0.08709	273.41737	-	-	-	-
Ω_{14}	1	1.5	-0.6641	4.358E-08	-0.00019	0.59767	-	-	-	-
	2	3.43807	-8.4452	-9.22E-05	0.39579	-4.61503	-	-	-	-
	3	2.87355	-1.0518	3.562E-05	-0.13316	322.13418	-	-	-	-
	4	2.74287	-2.3445	0.000284	-0.94663	2353.98912	-	-	-	-
	5	2.69686	-2.7295	0.00152	-3.97363	7635.85437	-	-	-	-
Ω_{15}	1	1.5	-3.0349	2.983E-07	-0.00077	2.70754	-	-	-	-
	2	1.94311	-1.9263	2.074E-06	0.01241	39.82764	-	-	-	-
	3	2.83271	0.5482	-3.39E-06	0.02146	23.50052	-	-	-	-
	4	3.1257	2.2111	-7.73E-06	0.02901	32.50647	-	-	-	-
	5	3.17766	2.70347	-1.80E-05	0.05597	72.5556	-	-	-	-